ΕΘΝΙΚΟ ΜΕΤΣΟΒΙΟ ΠΟΛΥΤΕΧΝΕΙΟ
Σχολή Πολιτικών Μηχανικών
Εργαστήριο Εδαφομηχανικής

NATIONAL TECHNICAL UNIVERSITY
School of Civil Engineering
Soil Mechanics Laboratory

Δ Ι Δ Α Κ Τ Ο Ρ Ι Κ Η Δ Ι Α Τ Ρ Ι Β Η

Μεταπλαστική Απόκριση και Κατάρρευση Συστημάτων Πλαισίου–Θεμελιώσεως, και Σεισμική Μόνωση μέσω Λικνισμού

Φανή Μ. Γελαγώτη

Διπλωματούχος Πολιτικός Μηχανικός
Ε.Μ.Π. – 2004

Master of Science
Mechanics Material and Computing
Carnegie Mellon University, U.S.A. – 2006

Επιβλέπων: ***Καθηγητής Γ. Γκαζέτας***

Αθήνα, Οκτώβριος 2010

ΕΘΝΙΚΟ ΜΕΤΣΟΒΙΟ ΠΟΛΥΤΕΧΝΕΙΟ
Σχολή Πολιτικών Μηχανικών
Εργαστήριο Εδαφομηχανικής

NATIONAL TECHNICAL UNIVERSITY
School of Civil Engineering
Soil Mechanics Laboratory

D O C T O R A L T H E S I S

Metaplastic Response and Collapse of Frame–Foundation Systems, and the Concept of Rocking Isolation

Fani M. Gelagoti

Diploma in Civil Engineering
NTUA – 2004

Master of Science
Mechanics Material and Computing
Carnegie Mellon University, U.S.A. – 2006

Supervised by: ***Professor George Gazetas***

Athens, October 2010

7-μελής Επιτροπή εξέτασης της Διδακτορικής Διατριβής

Γεώργιος Γκαζέτας (Καθηγητής ΕΜΠ, Σχολή Πολ. Μηχ.)

Νικόλαος Μακρής (Καθηγητής Πανεπιστημίου Πατρών, Σχολή Πολ. Μηχ.))

Μιχαήλ Καββαδάς (Αναπλ. Καθηγητής ΕΜΠ, Σχολή Πολ. Μηχ.)

Κ. Πιτιλάκης (Καθηγητής ΑΠΘ, Σχολή Πολ. Μηχ.)

Ε. Βιντζηλαίου (Καθηγήτρια ΕΜΠ, Σχολή Πολ. Μηχ.)

Ε. Σαπουντζάκης (Αν. Καθηγητής ΕΜΠ, Σχολή Πολ. Μηχ.)

Ν. Γερόλυμο (Λέκτορας, Σχολή Πολ. Μηχ.)

Acknowledgments

I feel most thankful for having had the opportunity to be supervised by my advisor, Professor George Gazetas, *since my very early steps in engineering research. Ever since its commencement, my research has been guided by his invaluably inspirational advice and I do hope the completion of this thesis is offering me just one of a series of opportunities to thank him.*

A very special mention is reserved for Dr Ioannis Anastasopoulos, *who has had a very vigorous role in co-supervising my thesis. His active participation in all stages of this research has offered me precious support, for which I am honestly grateful.*

This work forms part of the EU research project "DARE" ("Soil-Foundation-Structure Systems Beyond Conventional Seismic Failure Thresholds : Application to New or Existing Structures and Monuments"), which is funded through the 7th Framework Programme "Ideas", Support for Frontier Research — Advanced Grant, under contract number ERC-2008-AdG 228254-DARE.

ΔΙΔΑΚΤΟΡΙΚΗ ΔΙΑΤΡΙΒΗ

Φανής Μ. Γελαγώτη

Μεταπλαστική Απόκριση και Κατάρρευση Συστημάτων Πλαισίου–Θεμελιώσεως, και Σεισμική Μόνωση μέσω Λικνισμού

Εκτενής Περίληψη

Οποιαδήποτε, έστω και αδρομερής, επισκόπηση της σύγχρονης βιβλιογραφίας του αντισεισμικού σχεδιασμού, θα ήταν πλημμελής εάν παρέλειπε την αναφορά στην αυξανόμενη σύγχρονη τάση “δημιουργικής αμφισβήτησης” των συμβατικών (και καθιερωμένων μέσα από τους διεθνείς Κανονισμούς) μεθόδων οι οποίες βασίζονται στον υπολογισμό δυνάμεων. Αντί αυτής, προτείνεται η προσέγγιση του σχεδιασμού με γνώμονα τις μετακινήσεις, τόσο των δομικών στοιχείων της κατασκευής (*Δομοστατικός Σχεδιασμός Ανωδομής*) όσο και της θεμελίωσης (*Γεωτεχνικός Σχεδιασμός Θεμελιώσεως*). Η νέα λογική σχεδιασμού προτείνει την (υπό-προϋποθέσεις) εγκατάλειψη της σχετικής κανονιστικής απαγόρευσης, προκρίνοντας την δημιουργία “πλαστικής άρθρωσης” *υπό* την διεπιφάνεια θεμελιώσεως εδάφους (υλοποιούμενης είτε μέσω αποκόλλησης του πρώτου ή αστοχίας φέρουσας ικανότητας του τελευταίου). Κατ’ αυτόν τον τρόπο περιορίζεται η αδρανειακή φόρτιση που δύναται να μεταδοθεί στην ανωδομή **(Σχήμα i)**. Μία τέτοια λογική έχει αποτελέσει αντικείμενο μελέτης διεθνώς, η δε διερεύνηση τής εφαρμοσιμότητάς της σε απλές επιφανειακές θεμελιώσεις έχει επιχειρηθεί τόσο αναλυτικά όσο και πειραματικά. Στην παρούσα διδακτορική διατριβή επιδιώκεται η ολοκληρωμένη διερεύνηση της αποτελεσματικότητας της ιδέας αυτής σε επίπεδο όχι ενός απλού

θεμελίου αλλά μίας πλαισιωτής κατασκευής. Ως εκ τούτου, κύριο αντικείμενο της έρευνας αποτελεί η μελέτη της μή-γραμμικής και ανελαστικής αλληλεπίδρασης συστημάτων θεμελιώσεως–εδάφους–πλαισίου υποβαλλομένων σε ισχυρή εδαφική διέγερση που ενίοτε υπερβαίνει κατά πολύ την συμβατική διέγερση σχεδιασμού. Η εργασία διαρθρώνεται σε ***5 βασικές ενότητες***:

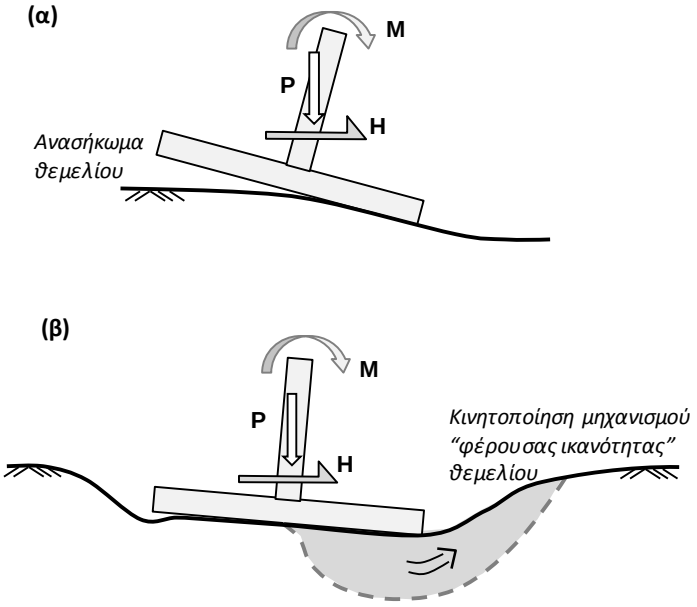

Σχήμα i. Μη-γραμμική ανελαστική απόκριση θεμελιώσεως (α) μέσω ανασηκώματος του θεμελίου (όταν $FS_v \geq 2$) και (β) μέσω κινητοποιήσεως του μηχανισμού "φέρουσας ικανότητας" του εδάφους (όταν $FS_v < 2$).

Αντικείμενο της *πρώτης ενότητας* είναι η βαθμονόμηση και επαλήθευση ενός αξιόπιστου καταστατικού προσομοιώματος ικανού να αναπαράγει με πιστότητα την μή-γραμμική λικνιστική απόκριση συστημάτων θεμελιώσεως επί αργιλικού και αμμώδους εδάφους. Το προσομοίωμα ενσωματώνεται στον κώδικα πεπερασμένων στοιχείων ABAQUS και χρησιμοποιείται στις επακόλουθες αναλύσεις.

Η *δεύτερη ενότητα* αποτελεί τον κυρίως κορμό της διεξαχθείσης έρευνας: μελετά ενδελεχώς την δυναμική απόκριση σε επιβαλλόμενη σεισμική διέγερση ρεαλιστικώς απλών πλαισιωτών κατασκευών επί εδαφικής στρώσης. Συγκρίνεται ποιοτικά και

ποσοτικοποιείται η αποτελεσματικότητα της νέας φιλοσοφίας έναντι του συμβατικού σχεδιασμού.

Στην *τρίτη ενότητα* της διατριβής αναπτύσσεται μια απλοποιημένη μεθοδολογία προκαταρκτικού σχεδιασμού της θεμελίωσης με εφαρμογή της προτεινόμενης προσέγγισης. Βάσει αυτής υπολογίζεται η μέγιστη και η ελάχιστη ανεκτή διάσταση του θεμελίου ώστε να εξασφαλίζεται η αποτελεσματικότητα της προτεινόμενης λογικής σχεδιασμού.

Οι αναλύσεις των ενοτήτων 2 και 3 πραγματοποιήθηκαν θεωρώντας συνθήκες μονοδιάστατης εδαφικής ενίσχυσης. Προκειμένου να ληφθούν υπόψιν διδιάστατα κυματικά φαινόμενα τα οποία ενδέχεται να αλλοιώνουν τον τελικώς επιβαλλόμενο κραδασμό, στην *τέταρτη ενότητα* διενεργείται ενδελεχής μελέτη της επίδρασης της διδιάστατης γεωμετρίας εδαφικής κοιλάδας στην παραγόμενη στην επιφάνεια σεισμική διέγερση.

Η επίδραση της παραγόμενης στην επιφάνεια παρασιτικής *κατακόρυφης* συνιστώσας της σεισμικής κίνησης σε επιφανειακώς θεμελιωμένη στην θέση αυτή πλαισιωτή κατασκευή, μελετάται στην τελευταία *πέμπτη ενότητα* της διατριβής. Η περιγραφή των αναλύσεων και τα κύρια αποτελέσματα συνοψίζονται ανά ενότητα στις επόμενες παραγράφους της εκτενούς περίληψης.

Ενότητα 1

Απλοποιημένο Καταστατικό Προσομοίωμα για την Ανακυκλική Απόκριση Επιφανειακών Θεμελίων

1.1. Εισαγωγή

Παρότι στη βιβλιογραφία απαντάται ένα σημαντικό πλήθος ιδιαιτέρως αξιόλογων καταστατικών προσομοιωμάτων της εδαφικής συμπεριφοράς [e.g., *Prevost, 1980; Houlsby, 1986; Jefferies, 1993; Whittle & Kavvadas, 1994; Pestana, 1994; Pestana & Whittle, 1995; 1999; Gajo & Wood, 1999; Jeremic et al., 1999; Kavvadas & Amorosi, 2000; Puzrin & Houlsby, 2001a; 2001b; 2001c; Einav et al., 2003; Houlsby & Puzrin, 2006*], τα πλέον λεπτομερή εξ αυτών προορίζονται συνήθως για χρήση από εξειδικευμένους χρήστες σε ειδικούς αριθμητικούς κώδικες, ή απαιτούν την βαθμονόμηση ενός μεγάλου αριθμού παραμέτρων, καθιστώντας δύσκολη την εφαρμογή τους στην πράξη. Σε μία προσπάθεια υπέρβασης μέρους των ανωτέρω δυσχερειών, στο πρώτο κεφάλαιο της διατριβής προτείνεται και επαληθεύεται ένα απλοποιημένο προσομοίωμα (τροποποίηση του ενσωματωμένου στον αριθμητικό κώδικα ABAQUS προσομοιώματος “κινηματικής κράτυνσης”), προκειμένου με επιτυχία να αναπαραχθεί η συμπεριφορά θεμελίων υποκειμένων σε λικνιστική ταλάντωση επί αργιλικού ή αμμώδους εδάφους. Το εν λόγω προσομοίωμα απαιτεί την βαθμονόμηση δύο μόνον παραμέτρων, καθιστώντας το έτσι ελκυστικό για εφαρμογή σε πρακτικά προβλήματα παρότι εν γένει δεν μπορεί να θεωρηθεί ως γενικής χρήσεως και καθολικής ισχύος όπως συζητείται παρακάτω.

1.2. Καταστατικές Σχέσεις

Το προσομοίωμα συνδυάζει μή-γραμμική κινηματική κράτυνση με συσχετισμένο νόμο πλαστικής ροής, με το κριτήριο διαρροής *Von Mises* (καταλλήλως τροποποιημένο ώστε να λαμβάνει υπόψιν την επίδραση της μέσης ορθής τάσης σε άμμους).

Επομένως, η μέγιστη τάση διαρροής για αργίλους ορίζεται ως

$$\sigma_{\mathrm{y}} = \sqrt{3} S_u \tag{1.1}$$

όπου S_u η αστράγγιστη διατμητική αντοχή, ενώ για άμμους

$$\sigma_{\mathrm{y}} = \sqrt{3}\left(\frac{\sigma_1 + \sigma_2 + \sigma_3}{3}\right)\sin\varphi \tag{1.2}$$

όπου η τάση διαρροής εκφράζεται συναρτήσει της μέσης οκταεδρικής τάσης και της γωνίας διατμητικής αντοχής φ. Η εξέλιξη των δύο συνιστωσών του νόμου κράτυνσης (κινηματικής και ισοτροπικής) δίδεται σε μονοδιάστατη απεικόνιση στο **Σχήμα 1.1**.

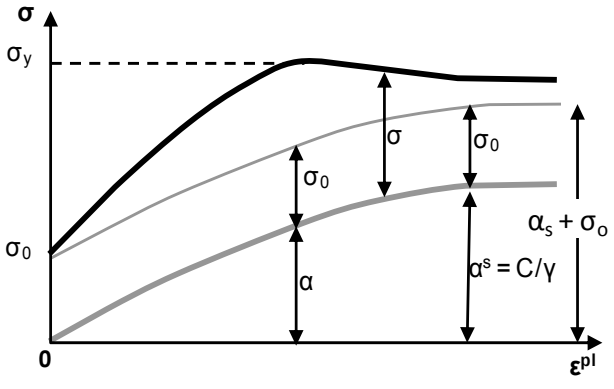

Σχήμα 1.1. Εξέλιξη του νόμου κράτυνσης του καταστατικού Προσομοιώματος.

Ως εγγενείς περιορισμοί του προσομοιώματος αναφέρονται η αδυναμία του να αναπαραγάγει αφενός την ανάπτυξη υπερπιέσεων πόρων στις αργίλους και

αφετέρου την διαστολική συμπεριφορά της άμμου. Εντούτοις ο μέν πρώτος περιορσισμός θεωρείται ως μικρής σημασίας για το εξεταζόμενο πρόβλημα δυναμικής αλληλεπίδρασης αργιλικού εδάφους-θεμελίου δεδομένης της ταχείας φύσεως της σεισμικής φόρτισης, ενώ ο έτερος θα δειχθεί στα επόμενα ότι δεν επηρεάζει την συμπεριφορά του συνολικού συστήματος εδάφους–θεμελίου.

Το τροποποίημένο καταστατικό προσομοίωμα έχει εισαχθεί στον κώδικα ABAQUS μέσω υπορουτίνας. Η βαθμονόμηση του προσομοιώματος βασίζεται στις παραμέτρους: (i) αντοχή: S_u ή, φ; c (ii) αρχική δυσκαμψία: G_o , V_s ; και (iii) στις *καμπύλες G-γ* των *Ishibashi & Zhang [1993]* **(Σχήμα 1.2)**.

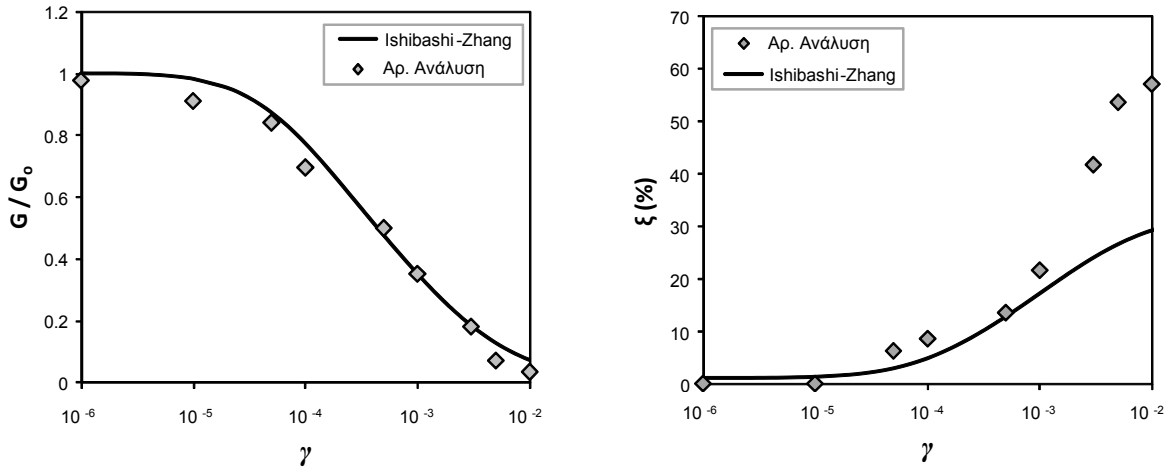

Σχήμα 1.2. Βαθμονόμηση τροποποιημένου καταστατικού προσομοιώματος για άμμο. Σύγκριση των υπολογισθεισών καμπυλών G–γ και ξ–γ με τις δημοσιευμένες των *Ishibashi and Zhang [1993]* για τάση εγκιβωτισμού σ_{vo} = 50 kPa.

1.3. Επαλήθευση του Προσομοιώματος για Άργιλο

Οι αριθμητικές προβλέψεις συγκρίνονται με τα πειραματικά αποτελέσματα των *Gajan et al. [2005]*. Τα πειράματα αυτά είχαν εκτελεστεί στον φυγοκεντριστή του Πανεπιστημίου Davis (ΗΠΑ), συνίσταντο δε σε κατακόρυφη φόρτιση θεμελίου ακολουθούμενη από σειρά κύκλων αργής ανακυκλικής φόρτισης σε τρία στάδια αυξανομένου πλάτους επιβαλλόμενης μετακίνησης.

Αριθμητικό Προσομοίωμα

Το 3-διάστατο προσομοίωμα πεπερασμένων στοιχείων (Π.Σ.) απεικονίζεται στο **Σχήμα 1.3** (κατά το ήμισυ λόγω συμμετρίας). Τόσο τα στοιχεία του εδάφους όσο και του θεμελίου έχουν προσομοιωθεί με χρήση οκτακομβικών στοιχείων ενώ η διεπιφάνειά τους με τα λεγόμενα στοιχεία “κενού” (gap elements), τα οποία επιτρέπουν την ολίσθηση και την αποκόλληση του θεμελίου από το έδαφος ανάλογα με την φόρτιση. Η συμπεριφορά του εδάφους καθορίζεται από το καταστατικό προσομοίωμα που περιγράφηκε παραπάνω, η βαθμονόμηση του οποίου πραγματοποιήθηκε με βάση την αρχικό πείραμα κατακόρυφης φόρτισης του θεμελίου.

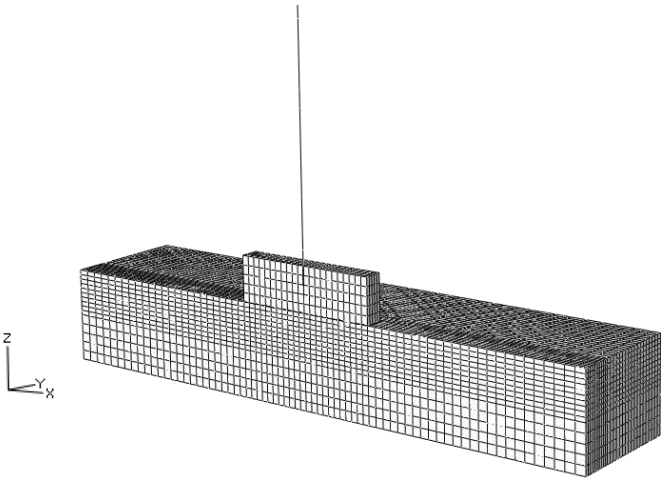

Σχήμα 1.3. Χρησιμοποιηθέν 3-Δ προσομοίωμα πεπερασμένων στοιχείων

Αξιολόγηση Αποτελεσμάτων

Η σύγκριση της αριθμητικής πρόβλεψης με τις πειραματικές μετρήσεις απεικονίζεται στο **Σχήμα 1.4** για όλους τους κύκλους φόρτισης. Στον πρώτο κύκλο η ανάλυση υπερεκτιμά την μέγιστη θετική ροπή, ενώ η απόκλιση είναι μειωμένη στην αντίθετη κατεύθυνση (**Σχ. 1.4α**). Η σύγκριση είναι πολύ ικανοποιητική σε όρους στροφής–καθίζησης (**Σχήμα 1.4β**) τόσο ως προς τον υπολογισμό της καθίζησης ανά κύκλο φόρτισης όσο καί της συνολικής. Αξίζει πάντως να παρατηρηθεί ότι αντίθετα με τα πειραματικά αποτελέσματα οι παραχθέντες αριθμητικά βρόχοι είναι ενδεικτικοί συμπεριφοράς στην οποία δεσπόζει το ανασήκωμα. Αυτή η διαφορά ενδεχομένως οφείλεται σε τοπικού χαρακτήρα προϋπάρχουσες πλαστικοποιήσεις κάτω από το θεμέλιο στο πείραμα (πιθανόν αποτέλεσμα προηγουμένων δοκιμών). Κατά την διάρκεια του δευτέρου σταδίου, οι παραγόμενοι βρόχοι υστέρησης (**Σχήματα 1.4 γ-δ**), τόσο πειραματικά όσο και αναλυτικά φανερώνουν σημαντική απώλεια ενέργειας στην διεπιφάνεια θεμελίου-εδάφους. Στο τελικό στάδιο, τόσο το πείραμα όσο και η ανάλυση αναδεικνύουν την εντόνως μή γραμμική συμπεριφορά του συστήματος εδάφους-θεμελιώσεως (**Σχήμα 1.4ε**). Η πλήρης ανάπτυξη της οριακής ροπής του θεμελίου (M_{ult} ≈ 300 kNm) είναι σαφώς αναγνωρίσιμη στην καμπύλη $M-\theta$ (αύξηση στροφής υπό σταθερή ροπή). Η μή-συμμετρική ωστόσο μορφή της πειραματικής καμπύλης δεν είναι δυνατόν να αναπαραχθεί. Τέλος, όπως φαίνεται και στο (**Σχήμα 1.4στ**), το προσομοίωμα εξακολουθεί να προβλέπει με επιτυχία την συμπεριφορά σε όρους στροφής–καθίζησης (ακόμη και στο τρίτο στάδιο όπου οι επιβαλλόμενες μετακινήσεις είναι αρκετά σημαντικές).

1.4. Επαλήθευση του Προσομοιώματος για Άμμο

Χρησιμοποιούνται πειραματικά δεδομένα από το Ερευνητικό πρόγραμμα TRISEE, στα πλαίσια του οποίου διεξήχθησαν στο εργαστήριο ELSA (JRC, Ισπρα, Ιταλία), δοκιμές αργής ανακυκλικής φόρτισης θεμελίου (**Σχήμα 1.5)** επί υγρής (μη-κορεσμένης) άμμου, υψηλής (HD) και χαμηλής (LD) πυκνότητας *[Faccioli et al, 2001*]. Ενώ στην πρώτη περίπτωση ο στατικός κατακόρυφος συντελεστής ασφαλείας του θεμελίου (ήτοι οι παράμετροι αντοχής του εδαφικού υλικού) είναι σαφώς υπολογισμένος (FS = 5, $\phi_p = 43^o$), για την χαλαρή άμμο οι δημοσιευμένοι υπολογισμοί κυμαίνονται από FS = 2 έως FS = 7. Λόγω της έντονης αυτής διασποράς στην τιμή του FS, κατά την αριθμητική προσομοίωση υιοθετήθηκαν δύο εναλλακτικά σενάρια (FS =3, $\phi_p = 30^o$ και FS=5, $\phi_p = 35^o$).

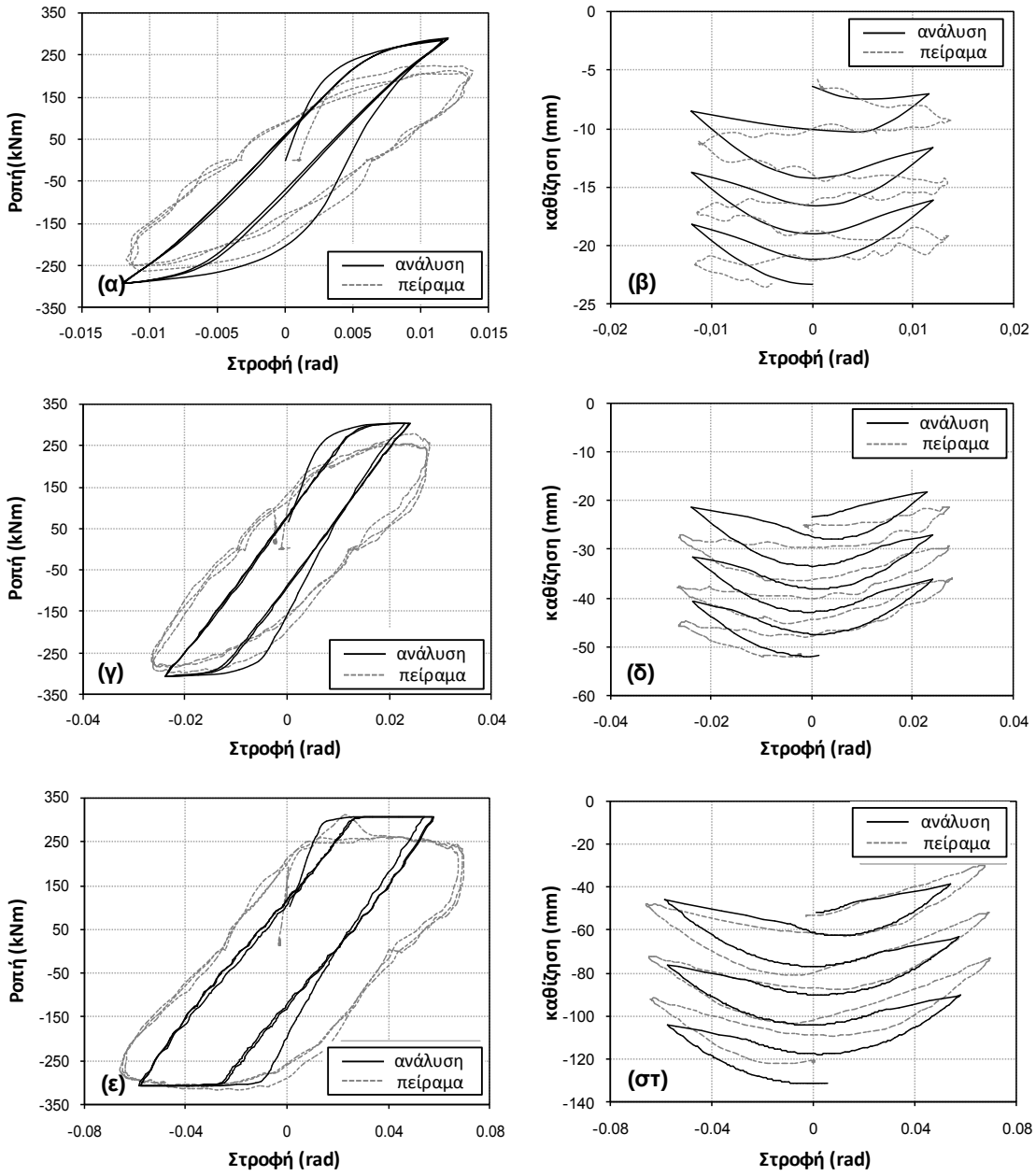

Σχήμα 1.4. Σύγκριση αριθμητικής πρόβλεψης με πειραματικές μετρήσεις ανά στάδιο ανακυκλικής φόρτισης σε όρους ροπής-στροφής και καθίζησης-στροφής του θεμελίου.

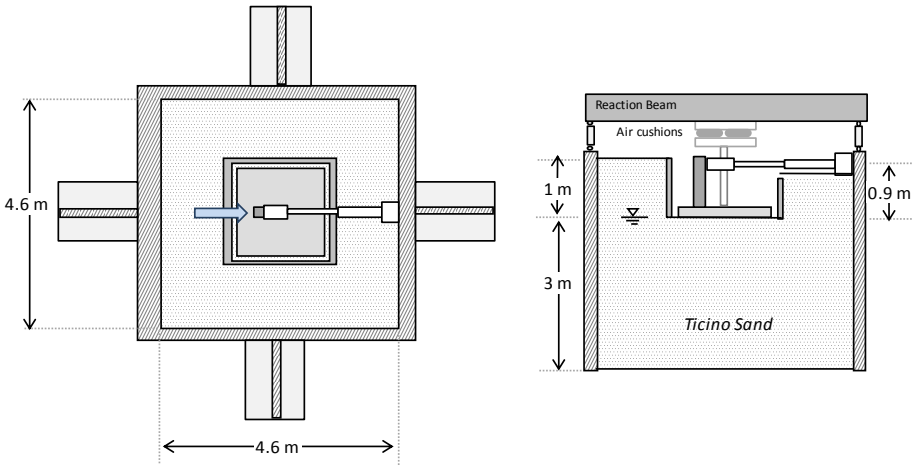

Σχήμα 1.5. Σκαριφηματική απεικόνιση της πειραματικής διάταξης μελέτης της μη-γραμμικής συμπεριφοράς θεμελίων υποβαλλόμενων σε οριζόντια ανακυκλική φόρτιση (πηγή: Faccioli et al, 2001).

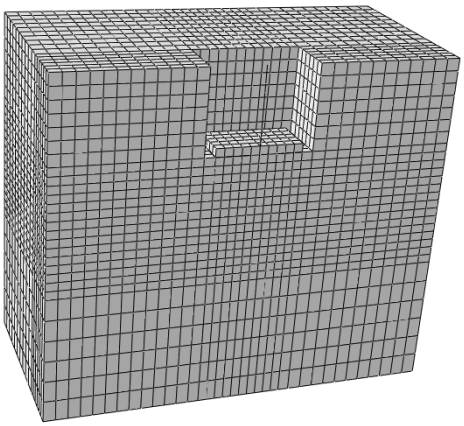

Σχήμα 1.6. Χρησιμοποιηθέν 3-Δ προσομοίωμα πεπερασμένων στοιχείων για την αναπαραγωγή των πειραμάτων μεγάλης κλίμακας 1-g που διεξήχθησαν στο εργαστήριο ELSA στα πλαίσια του ερευνητικού προγράμματος TRISEE

Αριθμητική Προσομοίωση και Αποτελέσματα

Προσομοιώνεται η Τρίτη Φάση του πειράματος κατά την οποία στην κορυφή της κατασκευής επιβάλλονται ημιτονοειδείς κύκλοι μετακίνησης αυξανόμενου πλάτους, μέχρις πλήρους ενεργοποίησης της φέρουσας αστοχίας του εδάφους.

Η μεθοδολογία προσομοίωσης είναι όμοια με αυτήν που ακολουθήθηκε στην περίπτωση της αργίλου. Το τρισδιάστατο αριθμητικό προσομοίωμα όπως καταστρώθηκε στον κώδικα ABAQUS δίνεται στο **Σχήμα 1.6**.

Για την βαθμονόμηση του καταστατικού προσομοιώματος χρησιμοποιούνται δημοσιευμένα αναλυτικά αποτελέσματα των *Allottey & El Naggar [2008].* Βάσει αυτών, για την πυκνή άμμο υιοθετήθηκε $C = 8500\sigma_y$ ενώ για την χαλαρή $C = 6000\sigma_y$.

Όπως δείχνει το **Σχήμα 1.7α** γιά την πυκνή άμμο η σύγκριση της αριθμητικής πρόβλεψης με την πειραματική μέτρηση είναι άκρως ικανοποιητική σε όρους υστερητικών βρόχων ροπής-στροφής, αρκετά δε ικανοποιητική σε όρους οριζόντιας επιβαλλόμενης δύναμης-μετακίνησης (**Σχήμα 1.7β**): προβλέπεται με ακρίβεια τόσο η οριακή τιμή της ροπής αντοχής όσο και η σιγμοειδής μορφή του βρόχου M-θ (χαρακτηριστική μή-γραμμικής συμπεριφοράς του θεμελίου λόγω ανασηκώματος).

Αντίθετα με την συμπεριφορά του θεμελίου επί πυκνής άμμου όπου το ανασήκωμα δεσπόζει, στην χαλαρή άμμο ο κύριος μηχανισμός αστοχίας του θεμελίου είναι η βύθισή του εντός του εδάφους, όπως υποδεικνύει το πειραματικό αποτέλεσμα και επιβεβαιώνει η αριθμητική ανάλυση (**Σχήμα 1.8** για $FS_v \approx 3$).

Σε συμφωνία με την μετρηθείσα πειραματικώς τιμή, η αριθμητικώς υπολογισθείσα τιμή της ροπής αντοχής του συστήματος είναι $M_{ult} \approx 40$ kNm. Σε όρους οριζόντιας δύναμης–μετακίνησης, το σενάριο FS = 3 οδηγεί σε υπολογισμό μεγαλυτέρων μετακινήσεων από ότι το FS = 5. Πάντως, κανένα σενάριο δεν αναπαράγει την αποτυπωθείσα πειραματικώς έντονη μη-συμμετρικότητα της ολίσθησης του θεμελίου (προς τις αρνητικές τιμές του άξονα x).

Ανακυκλική Καθίζηση (Πυκνή και Χαλαρή Άμμος)

Η μέγιστη μετρηθείσα καθίζηση είναι της τάξης των 2 cm για την πυκνή άμμο και 7 cm για την χαλαρή αντιστοίχως. Το αριθμητικό προσομοίωμα για την πυκνή άμμο προβλέπει ικανοποιητικά το πριονωτό σχήμα της καμπύλης χρονικής εξέλιξης της

καθιζήσεως (ενδεικτικό του ανασηκώματος του θεμελίου), υπερεκτιμά όμως ελαφρώς την τελική τιμή της **(Σχήμα 1.9α**) . Στην περίπτωση της χαλαρής άμμου, το σενάριο FS = 5 δίνει την πλέον ικανοποιητική πρόβλεψη (**Σχήμα 1.9β**).

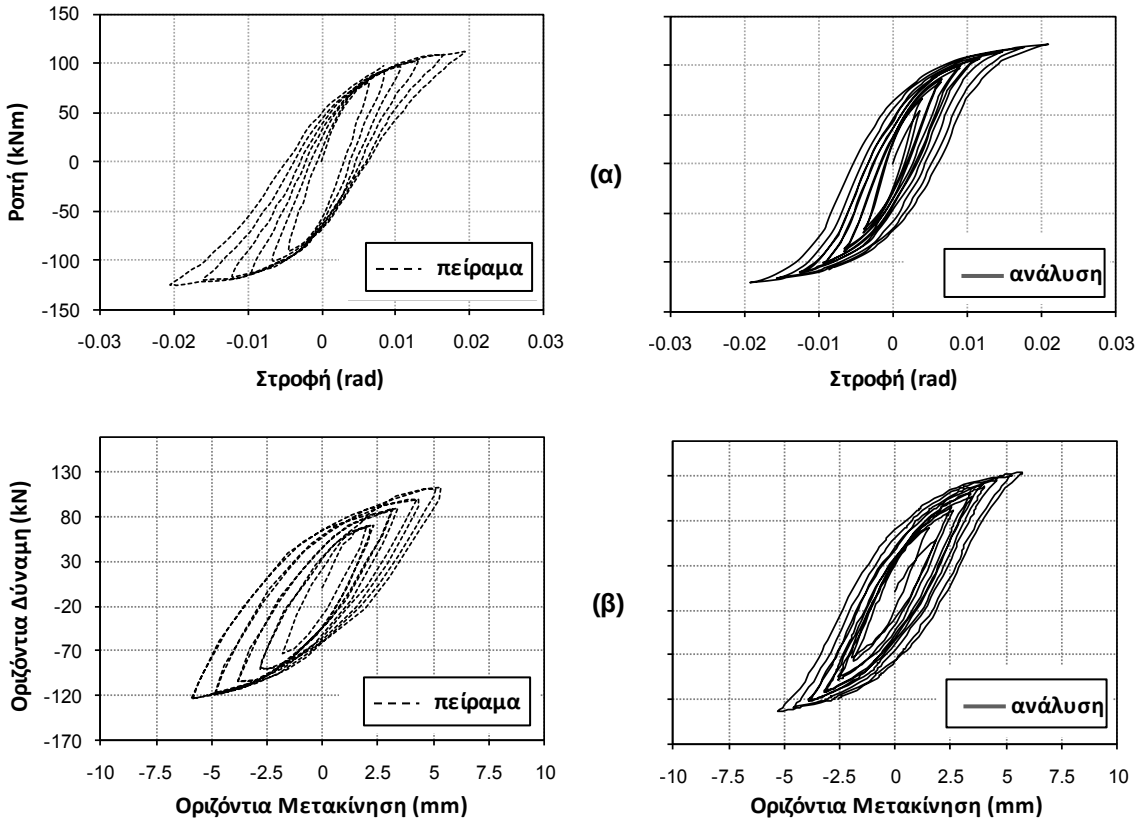

Σχήμα 1.7. Σύγκριση αριθμητικής πρόβλεψης με τις πειραματικές μετρήσεις σε όρους (**α**) υστερητικών βρόχων ροπής-στροφής και (**β**) οριζόντιας επιβαλλόμενης δύναμης-μετακίνησης για το πείραμα της πυκνής άμμου.

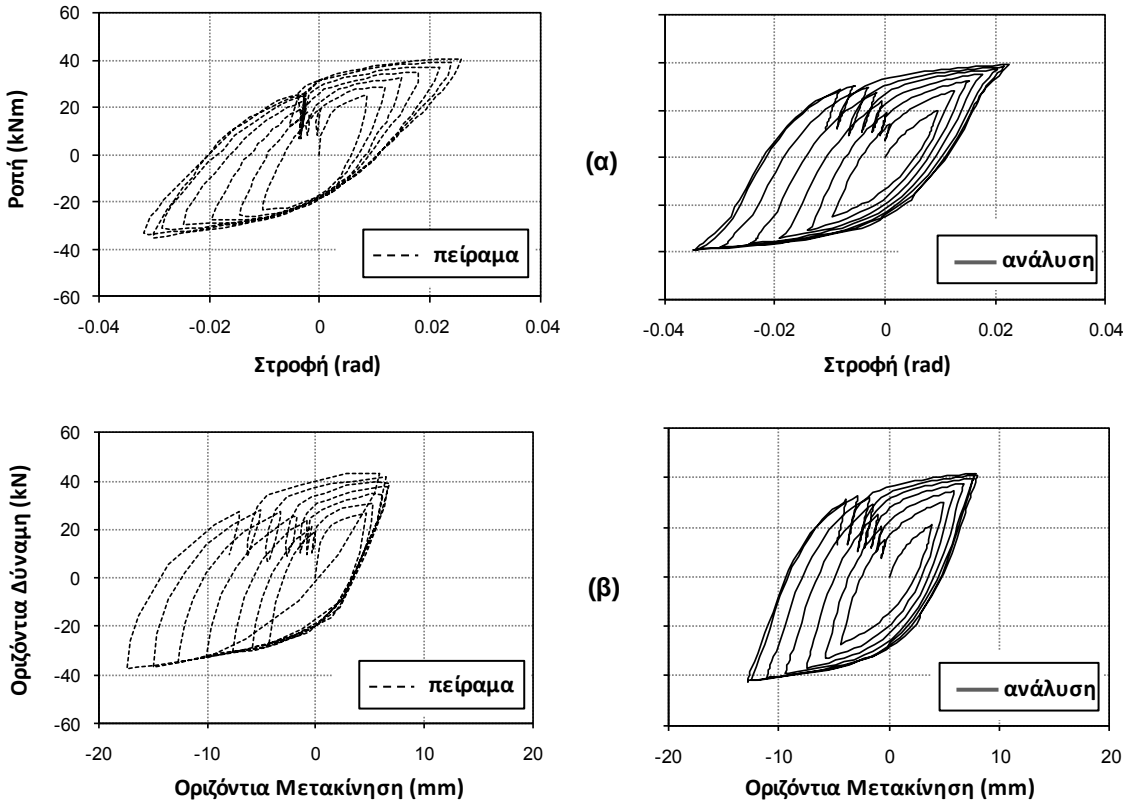

Σχήμα 1.8. Σύγκριση αριθμητικής πρόβλεψης (με θεώρηση $FS_v \approx 3$) με τις πειραματικές μετρήσεις σε όρους (α) υστερητικών βρόχων ροπής-στροφής και (β) οριζόντιας επιβαλλόμενης δύναμης-μετακίνησης για το πείραμα σε χαλαρή άμμο.

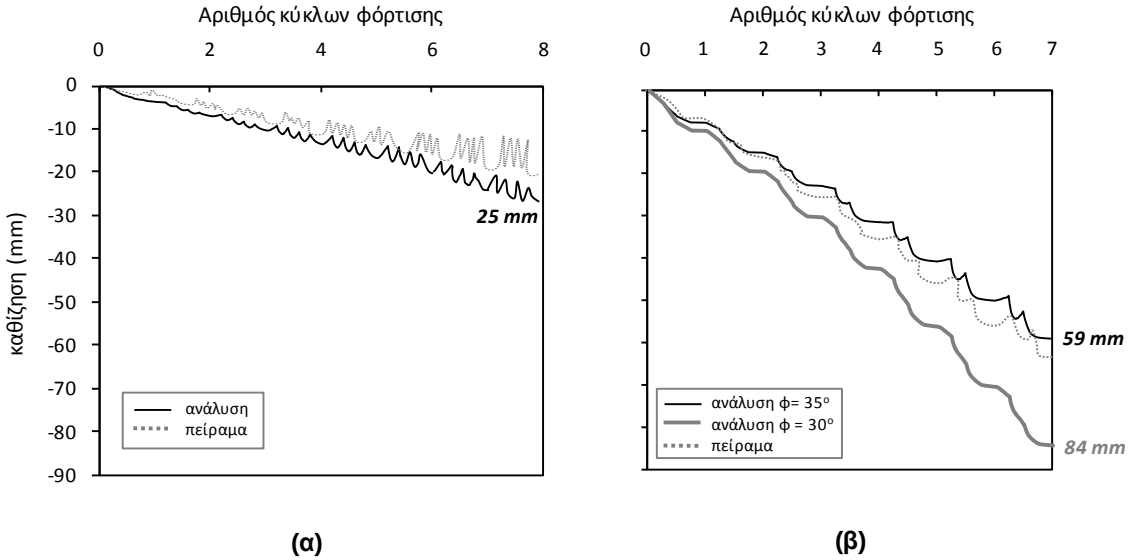

Σχήμα 1.9. Εξέλιξη καθιζήσεων ανά κύκλο φόρτισης: Σύγκριση πειράματος με τις προβλεψεις της αριθμητικής ανάλυσης για πείραμα σε: (α) πυκνή και (β) χαλαρή άμμο.

Ενότητα 2:

Μη-Γραμμική και Ανελαστική Συμπεριφορά Θεμελιώσεων: Εφαρμογή στην Σεισμική Προστασία Πλαισιωτών Φορέων

2.1 Εισαγωγή

Ως γνωστόν, η φιλοσοφία των σύγχρονων αντισεισμικών Κανονισμών απαγορεύει τόσο την εξάντληση της φέρουσας ικανότητας του εδάφους όσο και την δυνατότητα σημαντικής αποκόλλησης (> 50 %) του θεμελίου από το έδαφος. Προς τούτο εισάγονται σημαντικοί πρόσθετοι συντελεστές ασφαλείας έναντι των εν λόγω μηχανισμών αστοχίας. Εντούτοις, εξαιτίας του ανακυκλικού και κινηματικού χαρακτήρα της σεισμικής φόρτισης, η ενεργοποίηση της μή-γραμμικής ανελαστικής απόκρισης της θεμελίωσης δεν συνιστά υποχρεωτικώς αστοχία υπό ισχυρή σεισμική ένταση. Αντιθέτως μάλιστα, πρόσφατες μελέτες καταδεικνύουν την ενδεχομένως ευνοϊκή δράση της και προτείνουν μέχρι και την ενσωμάτωση σχετικών οδηγιών στους Κανονισμούς [*Paolucci, 1997; Pecker, 2000; FEMA-356, 2000; Makris & Roussos, 2000; Pecker & Pender, 2000; Faccioli et al., 2001; Kutter et al., 2003; Gazetas et al., 2003; 2007; Harden and Hutchinson, 2006; Paolucci et al., 2008; Kawashima et al., 2007; Gajan & Kutter, 2008; Chatzigogos et al., 2009; Anastasopoulos et al., 2010a*]. Βάσει των ανωτέρω, θα ήταν ενδεχομένως εφικτή η αναθεώρηση της υφισταμένης φιλοσοφίας προς μία κατεύθυνση σχεδιασμού που θα επέτρεπε την εκδήλωση των προαναφερθέντων μηχανισμών αστοχίας, εφόσον βέβαια τα παραγόμενα μετακινησιακά μεγέθη παραμένουν εντός αποδεκτών ορίων.

Στην παρούσα ενότητα διερευνάται η αποτελεσματικότητα της εν λόγω προσέγγισης για την περίπτωση πλαισιωτών φορέων. Στα παραδείγματα που εξετάζονται επιχειρείται η λικνιστική σεισμική μόνωση των κατασκευών ευνοώντας κατά τον σχεδιασμό την μή-γραμμική απόκριση της θεμελίωσης μέσω του μηχανισμού του ανασηκώματος. Στο **Σχήμα 2.1** περιγράφεται σκαριφηματικά η βασική ιδέα του προτεινομένου σχεδιασμού: συγκρίνεται η απόκριση σε οριζόντια φόρτιση 2 πανομοιότυπων πλαισίων επί μεμονωμένων πεδίλων, σχεδιασμένων: (α) συμβατικά, σύμφωνα με τον ισχύοντα αντισεισμικό κανονισμό και (β) νεωτεριστικά, ακολουθώντας την προτεινόμενη μεθοδολογία. Στην πρώτη περίπτωση, οι διαστάσεις των θεμελίων είναι τέτοιες ώστε να εξασφαλίζουν πρακτικώς συνθήκες πάκτωσης των υποστυλωμάτων στην βάση τους, και επομένως, η επιβαλλόμενη φόρτιση να μεταφράζεται σε δομητική επιπόνηση της ανωδομής, μέχρις εξαντλήσεως της διατιθέμενης πλαστιμότητας του υποστυλώματος η οποία συνεπάγεται *κατάρρευση* του πλαισίου. Αντιθέτως στην λικνιστικώς μονωμένη κατασκευή τα θεμέλια εσκεμμένα υποδιαστασιολογούνται ώστε όταν η επιβαλλόμενη φόρτιση υπερβεί μια “κρίσιμη” τιμή να ανασηκώνονται. Επιτυγχάνεται έτσι ουσιαστικά ο περιορισμός της μεταδιδόμενης έντασης στην ανωδομή.

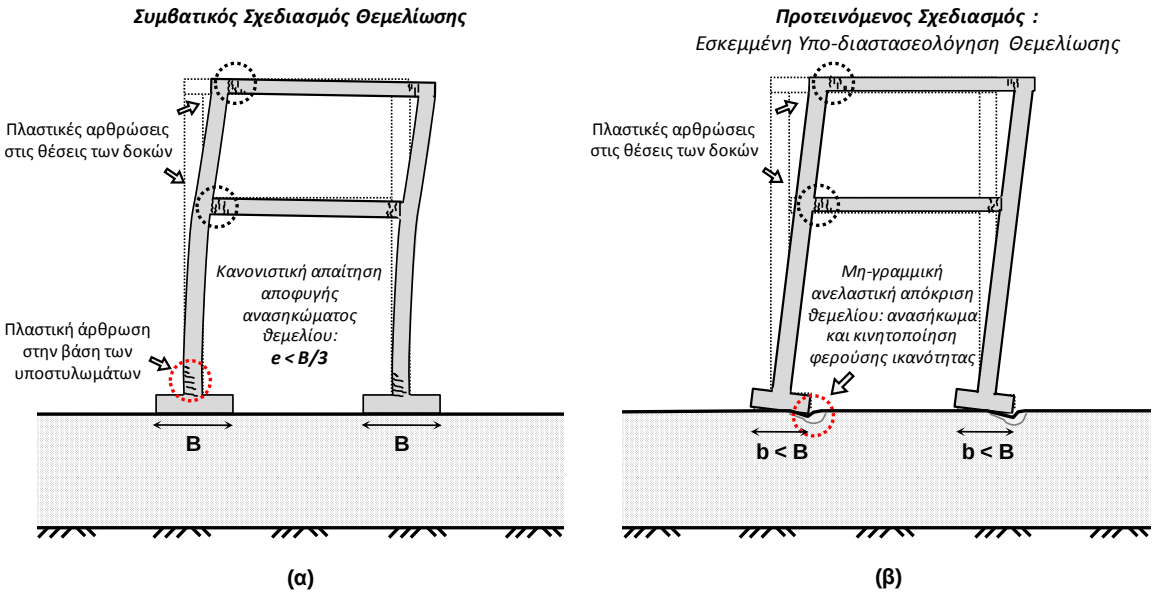

Σχήμα 2.1: Συγκριτική απόκριση 2 πανομοιότυπων (σε όρους ανωδομής) πλαισιωτών κατασκευών επί μεμονωμένων πεδίλων σχεδιασμένων: (**α**) συμβατικά σύμφωνα με τον ισχύοντα αντισεισμικό κανονισμό και (**β**) ακολουθώντας την προτεινόμενη μεθοδολογία.

2.2 Ιδιότητες της Κατασκευής

Σχεδιασμός Ανωδομής

Τα χαρακτηριστικά του (υπό-μελέτην) πλαισίου παρουσιάζονται στο **Σχήμα 2α.** Η κατασκευή έχει μελετηθεί συμβατικά σύμφωνα με τον ΕΑΚ 2000 θεωρώντας επιτάχυνση σχεδιασμού A_d = 0.36 g, και συντελεστή συμπεριφοράς q = 3.5.

Συμβατικός Σχεδιασμός Θεμελιώσεως

Προκειμένου να ικανοποιηθούν οι απαιτήσεις περιορισμού της εκκεντρότητας του κανονισμού e < B/3, η ελάχιστη διάσταση του τετραγωνικού θεμελίου προκύπτει B = 1.7 m. Ο επιτυγχανόμενος έτσι συντελεστής ασφαλείας έναντι κατακορύφων φορτιών είναι: $FS_V \approx 8$ υπό στατικές συνθήκες και $FS_E \approx 1.93$, υπό σεισμικές (ψευδοστατικώς εφαρμοζόμενες).

Μη Συμβατικός Σχεδιασμός Θεμελιώσεως (Νέα Προσέγγιση)

Υιοθετείται διάσταση θεμελίου B = 1.40 m, η οποία εξασφαλίζει μεν επαρκή συντελεστή ασφαλείας υπό στατικές συνθήκες (FS_V = 5.9) αλλά δεν ικανοποιεί το (συμβατικό) κριτήριο της εκκεντρότητας. Η ροπή αντοχής του εν λόγω θεμελίου [*Gourvenec, 2007*], υπό κατακόρυφο φορτίο N_v (προερχόμενο από το σύνολο των μή σεισμικών δράσεων) προκύπτει M_{ult} ≈ 100 kNm, ενώ η ροπή αντοχής του συμβατικώς σχεδιασμένου υποστυλώματος είναι M_{RD} ≈ 165 kNm. Σύμφωνα με τα παραπάνω, ορίζεται ο συντελεστής απομείωσης της αντοχής ως προς αυτήν του υποστυλώματος ως CRF = M_{RD} / M_{ult}, ο οποίος για το υπό εξέταση παράδειγμα είναι ίσος με CRF = 1.63.

2.3 Αριθμητική Προσομοίωση

Θεωρώντας συνθήκες επίπεδης παραμόρφωσης, καταστρώθηκε και βαθμονομήθηκε καταλλήλως προσομοίωμα πεπερασμένων στοιχείων (**Σχ. 2.2 β**) στον κώδικα ABAQUS, το οποίο ενσωματώνει το περιγραφέν στην πρώτη ενότητα της διατριβής καταστατικό προσομοίωμα. Η χρονοϊστορία της επιτάχυνσης επιβάλλεται στους κόμβους της βάσης του προσομοιώματος, ενώ στα πλευρικά του όρια θεωρούνται συνθήκες ελευθέρου πεδίου. Το έδαφος θεωρείται στιφρή άργιλος με αντοχή S_u = 150 kPa.Για την προσομοίωση της ανωδομής χρησιμοποιείται το ίδιο καταστατικό προσομοίωμα καταλλήλως τροποποιημένο, ώστε να αναπαράγει την μή γραμμική σχέση ροπής–καμπυλότητας των μελών ωπλισμένου σκυροδέματος. Οι παράμετροι του προσομοιώματος βαθμονομήθηκαν με βάση την καμπύλη μονοτονικής φόρτισης της κάθε διατομής, η οποία υπολογίστηκε με χρήση του κώδικα X-tract 2000 σύμφωνα με στοιχεία των [Vintzilaiou et al., 2007]. Το αποτέλεσμα της

βαθμονόμησης σε μονοτονική και ανακυκλική φόρτιση για το υποστύλωμα του ισογείου παρουσιάζεται στο **Σχήμα 2.2 γ.**

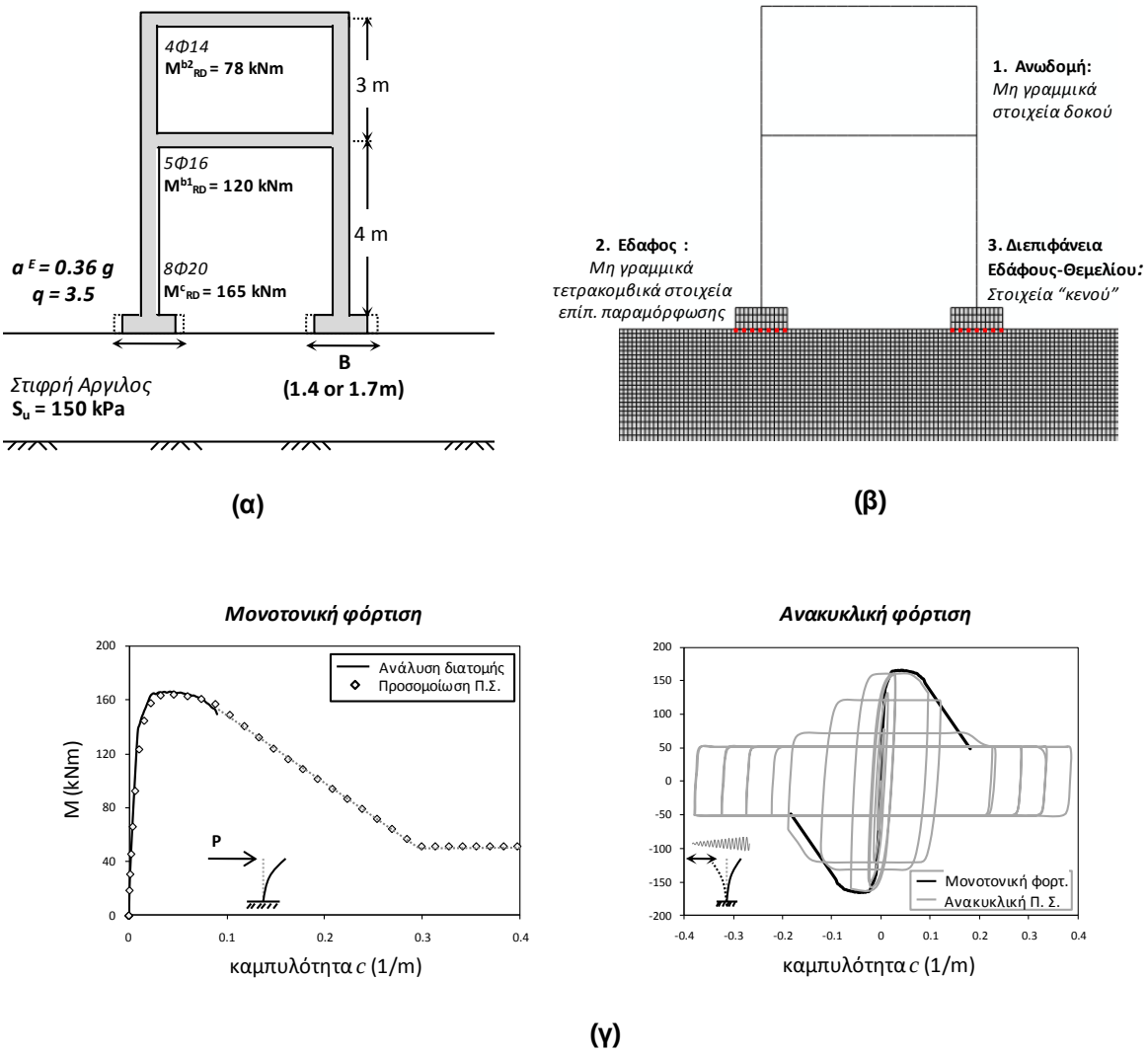

Σχήμα 2.2. (**α**) Γεωμετρικά χαρακτηριστικά και καμπτικές ροπές αντοχής των στοιχείων της ανωδομής (κατά Ε.Α.Κ 2000), (**β**) προσομοίωμα πεπερασμένων στοιχείων: θεώρηση συνθηκών επίπεδης παραμόρφωσης, ρεαλιστική προσομοίωση γεωμετρικών μη-γραμμικοτήτων (δυνατότητα ανασηκώματος και P-δέλτα φαινόμενα), καθώς και της ανελαστικής συμπεριφοράς της ανωδομής και του υποκείμενου εδάφους.

2.4 Πλαίσιο υποβαλλόμενο σε Στατική Φόρτιση Push-Over:

Απόκριση του Συστήματος

Στο **Σχήμα 2.3** συγκρίνεται το αποτέλεσμα (καμπύλη P-δ) της ανάλυσης για το συμβατικώς σχεδιασμένο πλαίσιο (θεμέλιο B = 1.7 m) και το σχεδιασμένο σύμφωνα με την προτεινόμενη μεθοδολογία (B = 1.4 m). Η απόκριση χωρίζεται σε τρεις διακριτές φάσεις:

(α) Στην αρχική φάση, κατά την οποία *καί* τα δύο πλαίσια αποκρίνονται καμπτικώς μέχρις διαρροής των δοκών (**Σχήμα 2.3**, Σημείο Α).

(β) Στην ενδιάμεση φάση κατά την οποία τα δομικά στοιχεία του συμβατικού συστήματος πλαστικοποιούνται εντόνως έως ότου εξαντληθεί πλήρως η διατιθέμενη πλαστιμότητά τους (σημείο Β) οπότε το σύστημα βαίνει προς κατάρρευση. Απεναντίας, το υποδιαστασεολογημένο σύστημα αποκρίνεται λικνιστικά μεν διά του ανασηκώματος του θεμελίου, καμπτικά δε έως ότου οι κόμβοι του πλαισίου αναπτύξουν πλαστικές αρθρώσεις στις θέσεις των δοκών (Σημείο C).

(γ) Στην τελική φάση, η οποία υφίσταται *μόνον* για το μή-συμβατικό σύστημα, όταν πιά κυριαρχεί το ανασήκωμα των θεμελίων μέχρι την πλήρη ανατροπή του πλασίου (σημείο D). Κατά την διάρκεια του τρίτου σταδίου το “λικνιστικώς μονωμένο”, σύστημα εκφυλίζεται εξιδανικευμένα σε δύο μονοβάθμιους ταλαντωτές κινηματικώς μόνον αλληλο-εξαρτημένους μέσω των οριζοντίων δοκών.

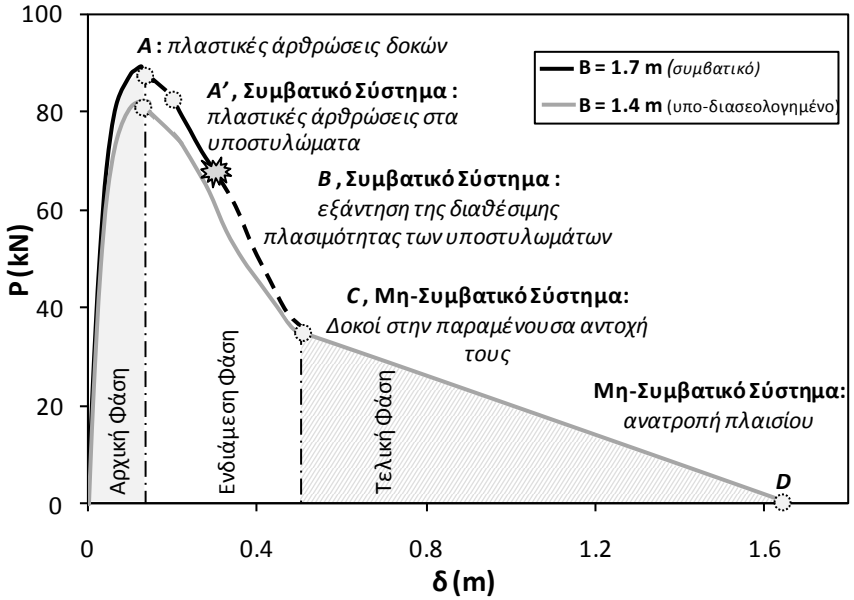

Σχήμα 2.3. Στατική ανάλυση επιβαλλόμενης μετακίνησης για τις 2 εναλλακτικές λύσεις

Απόκριση της Θεμελίωσης

Επίδραση της Αυξομείωσης του Αξονικού Φορτίου

Στο **Σχήμα 2.4α** απεικονίζεται η εξέλιξη του αξονικού φορτίου καθενός υποστυλώματος λόγω ανασηκώματος με την επιβαλλόμενη μετακίνηση δ. Κατά την ***αρχική φάση***, η μείωση του αξονικού φορτίου του αριστερού υποστυλώματος συνοδεύεται από ίση αύξηση του φορτίου στο δεξιό με το άθροισμά τους να διατηρείται προφανώς σταθερό. Η συμπεριφορά είναι ενδεικτική της πλαισιωτής λειτουργίας της κατασκευής: η εξωτερικώς επιβαλλόμενη ροπή παραλαμβάνεται μέσω ζεύγους αξονικών δυνάμεων, πέραν αυτών που αναπτύσσονται λόγω στατικών φορτίων. Στις επόμενες φάσεις, η πλαισιωτή λειτουργία περιορίζεται (λόγω πλαστικοποίησης των δοκών) και η αξονική δύναμη αμφοτέρων των υποστυλωμάτων τείνει προς την αρχική (στατική) τιμή της.

Η επίδραση της αξονικής δύναμης N στην καμπύλη ροπής–στροφής του θεμελίου δίδεται στο **Σχ. 2.4β**. Όπως αναμενόταν [*Houlsby & Puzrin, 1999; Bransby, 2001;*

Taiebat & Carter, 2002; Gourvenec, 2007], για συντελεστή ασφαλείας FS_V μεγαλύτερο του 2, αύξηση του N συνεπάγεται αύξηση της οριακής ροπής του θεμελίου. Επομένως, στον σχεδιασμό σύμφωνα με την προτεινόμενη λογική, η πιθανή διακύμανση του φορτίου πρέπει να λαμβάνεται υπόψιν διότι αυξάνοντας την πραγματική αντοχή του θεμελίου διακυβεύεται η αποτελεσματικότητα του αντισυμβατικού σχεδιασμού (καθώς αυξάνεται τελικώς η ένταση που είναι δυνατόν να μεταδοθεί στην ανωδομή).

Επιρροή της διακύμανσης του μοχλοβραχίονα M/Q

Η εξέλιξη του λόγου M/Q με την επιβαλλόμενη μετακίνηση δ φαίνεται στο **Σχήμα 2.4γ.** Στην *αρχική φάση*, καθώς το πλαίσιο δεν έχει υποστεί βλάβες, η τιμή του λόγου M/Q κυμαίνεται περί την αρχική της τιμή μεταξύ 1.9 και 2.5. Κατά την διάρκεια της *ενδιάμεσης φάσης*, ο λόγος M/Q τείνει προς την τιμή 4.8, ήτοι το ύψος απ' την βάση του κέντρου μάζας του προαναφερθέντος εξιδανικευμένου μονοβαθμίου ταλαντωτή. Στην *τελική φάση*, ο λόγος M/Q μειώνεται καθώς, παρότι η αντοχή του θεμελίου έχει λάβει την οριακή της τιμή (M=σταθερό) το σύστημα εξακολουθεί να διαθέτει αποθέματα διατμητικής αντοχής, με αποτέλεσμα η τιμή της διατμητικής δύναμης Q να αυξάνει. Όπως προκύπτει και από το **Σχήμα 2.4δ**, η διακύμανση της τιμής του λόγου M/Q δεν επηρεάζει ουσιωδώς την οριακή ροπή του θεμελίου, αλλά επιδρά στην στροφή ανατροπής, και επομένως θα πρέπει να λαμβάνεται υπόψιν στον σχεδιασμό με την νέα μεθοδολογία καθώς χαμηλή τιμή της οριακής στροφής συνεπάγεται κίνδυνο ανατροπής του θεμελίου.

Η επιρροή των ανωτέρω μηχανισμών αποτυπώνεται στην υπολογιζόμενη καμπύλη ροπής-στροφής των θεμελίων κατά την φόρτιση Push-Over του πλαισίου (**Σχ. 2.4ε**). Πράγματι, η αντοχή του δεξιού θεμελίου (το κατακόρυφο φορτίο του οποίου

αυξάνει κατά την φόρτιση) υπερβαίνει σαφώς αυτήν του αριστερού στο οποίο όμως η χαμηλότερη τιμή του λόγου M/Q του εξασφαλίζει μεγαλύτερη στροφή ανατροπής.

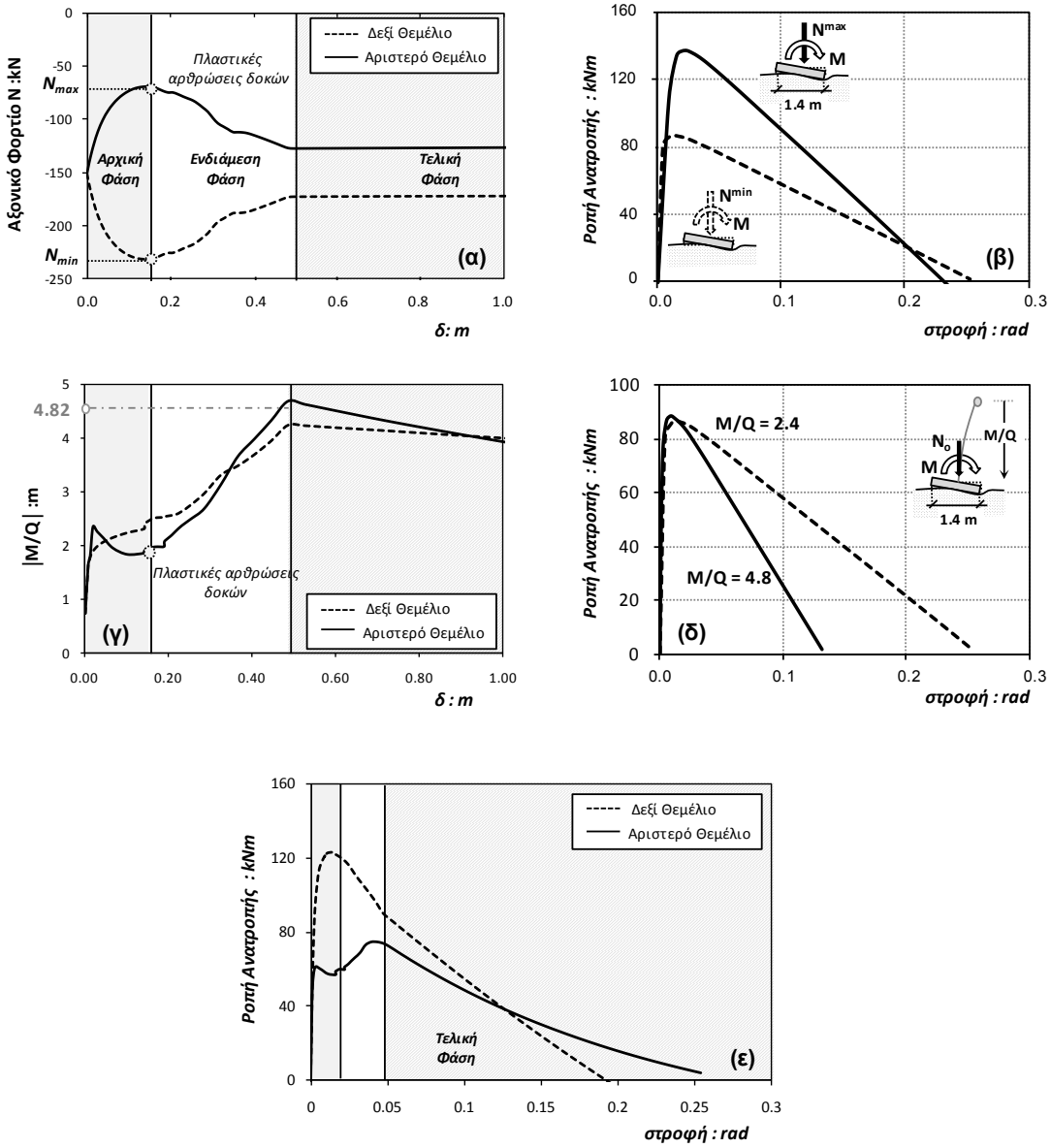

Σχήμα 2.4. Επίδραση της μεταβολής του αξονικού φορτίου (**α, β**) και του λόγου M/Q (**γ, δ**) στην μέγιστη ανελαστική απόκριση επιφανειακού θεμελίου (μέγιστη ροπή M_{ult} και οριακή στροφή θ_{ult}), (**ε**) "πραγματική" καμπύλη ροπής αντοχής-στροφής των θεμελίων του πεδίλου

2.5 Απόκριση σε Δυναμική Φόρτιση

Αποσκοπώντας στη συγκριτική αξιολόγηση των εναλλακτικών μεθόδων θεμελιώσεως, τα δύο συστήματα έχουν υποβληθεί σε 24 χρονοϊστορίες καταγεγραμμένων επιταχύνσεων ποικίλων χαρακτηριστικών (**Σχήμα 2.5**), πολλές από τις οποίες ξεπερνούν κατά πολύ την αντοχή σχεδιασμού του πλαισίου. Σε σεισμό ήπιας έντασης (π.χ. El Centro, 1940, μπλέ γραμμή), η συμπεριφορά των δύο εναλλακτικών είναι συγκρίσιμη, και εντός των ορίων λειτουργικότητας. Αναλυτικά παρουσιάζονται τα αποτελέσματα για το πλέον καταστροφικό σενάριο (Takatori , M_s 7.2 Kobe 1995 earthquake-κόκκινη γραμμή).

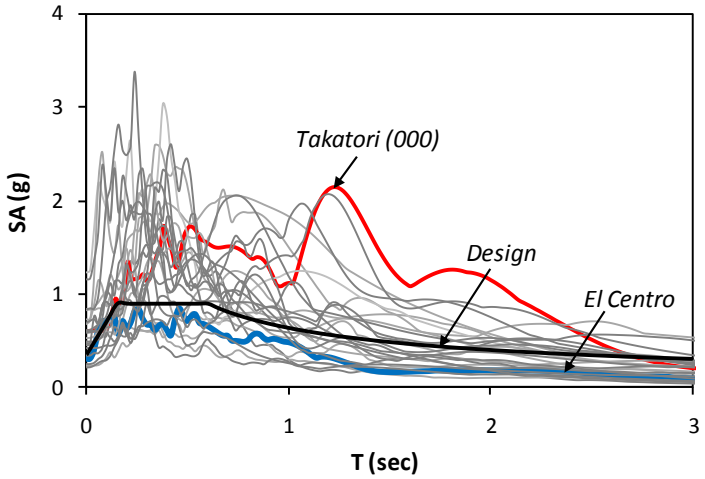

Σχήμα 2.5. Φάσματα απόκρισης των επιταχυνσιογραφημάτων που χρησιμοποιήθηκαν κατά τις δυναμικές αναλύσεις

Αναλυτικό Παράδειγμα

Όπως απεικονίζεται στο **Σχήμα 2.6**, το συμβατικώς θεμελιωμένο σύστημα δεν είναι ικανό να παραλάβει την τεράστια σεισμική δράση και οδηγείται σταδιακά σε κατάρρευση (**Σχ. 2.6 α και β**). Αντιθέτως, στο θεμελιωμένο σύμφωνα με την νέα προσέγγιση σύστημα, τα υποστυλώματα συμπεριφέρονται ελαστικά (**Σχ. 2.6β**). Τα υποδιαστασιολογημένα θεμέλια αναπτύσσουν σημαντική στροφή και ανασηκώνονται προστατεύοντας την ανωδομή (**Σχήμα 2.6γ**). Η σεισμική καθίζηση

είναι ασήμαντη (0.5 cm). Εντούτοις, παρότι η δομητική αστοχία αποφεύγεται, η ανάπτυξη των στροφών οδηγεί σε σημαντική κινηματικού χαρακτήρα καταπόνηση. Η διαφορική οριζόντια μετακίνηση ισογείου-1^{ου} ορόφου φτάνει τα 50cm (**Σχήμα 2.6δ**) αν και η παραμένουσα τιμή της δεν ξεπερνά τα 5cm, αντιστοιχούσα σε λόγο σχετικής διαφορικής μετάθεσης της τάξης του 2%. Επομένως, παρότι οι βλάβες σε μη δομικά μέλη και στις δοκούς πρέπει να θεωρούνται βέβαιες, η δομητική αστοχία των υποστυλωμάτων αποφεύγεται παρά την σφοδρότητα του σεισμού.

2.6 Συγκεντρωτικά Αποτελέσματα και Συμπεράσματα

Στο **Σχήμα 2.7** παρατίθενται τα αποτελέσματα για όλα τα εξετασθέντα σεισμικά σενάρια σε όρους: (α) λόγου κατανάλωσης πλαστιμότητας στο ισόγειο $\mu_{αναπτυχθείσα}/\mu_{διαθέσιμη}$, (β) συνολικού λόγου διαφορικής οριζόντιας μετακίνησης ορόφου προς ύψος ορόφου δ / h , *(γ)* διαφορικής οριζόντιας μετακίνησης ορόφου λόγω κάμψης (και όχι λόγω στροφής θεμελίου) δ_C / h και (δ) καθίζησης.

Όταν το συμβατικώς θεμελιωμένο σύστημα υπόκειται σε σεισμικές διεγέρσεις που υπερβαίνουν τον σεισμικό κραδασμό σχεδιασμού, οι βλάβες των υποστυλωμάτων είναι σαφώς μή επισκευάσιμες (**Σχήμα 2.7α**). Παρότι σε όρους συνολικής διαφορικής μετακίνησης (**Σχήμα 2.7β**) τα δύο συστήματα φαίνεται ότι συμπεριφέρονται ισοδύναμα, σε όρους διαφορικής μετακίνησης λόγω καμπτικής καταπόνησης (**Σχήμα 2.7γ**) η απόκριση του υπο-διαστασιολογημένου συστήματος είναι σαφώς ευνοϊκότερη. Όπως προκύπτει από τους υπολογισθέντες λόγους δ_C / h, οι βλάβες των υποστυλωμάτων του «λικνιστικώς μονωμένου» πλαισίου είναι

ασήμαντες για τουλάχιστον το 50% των περιπτώσεων, ενώ για τις υπόλοιπες διατηρούνται εντός των ορίων επισκευασιμότητας [Priestley et al., 2007].

Εν κατακλείδι συμπεραίνεται ότι η καμπτική καταπόνηση της ανωδομής είναι δυνατόν να περιορισθεί με υπο-διαστασιολόγηση των θεμελίων ώστε να αποκριθούν μη-γραμμικά εξαντλώντας τήν φέρουσα ικανότητά τους. Ετσι περιορίζουν την μεταδιδόμενη στα υποστυλώματα ένταση στα επίπεδα της δικής τους (μικρότερης) ροπής αντοχής. Αν και η στροφή του θεμελίου συνεπάγεται σημαντική κινηματική επιπόνηση και βλάβες στα μη δομικά μέλη επί του πλαισίου, η δομητική αστοχία των υποστυλωμάτων αποφεύγεται ακόμη και όταν η σεισμική ένταση υπερβαίνει κατά πολύ την αντοχή σχεδιασμού της κατασκευής.

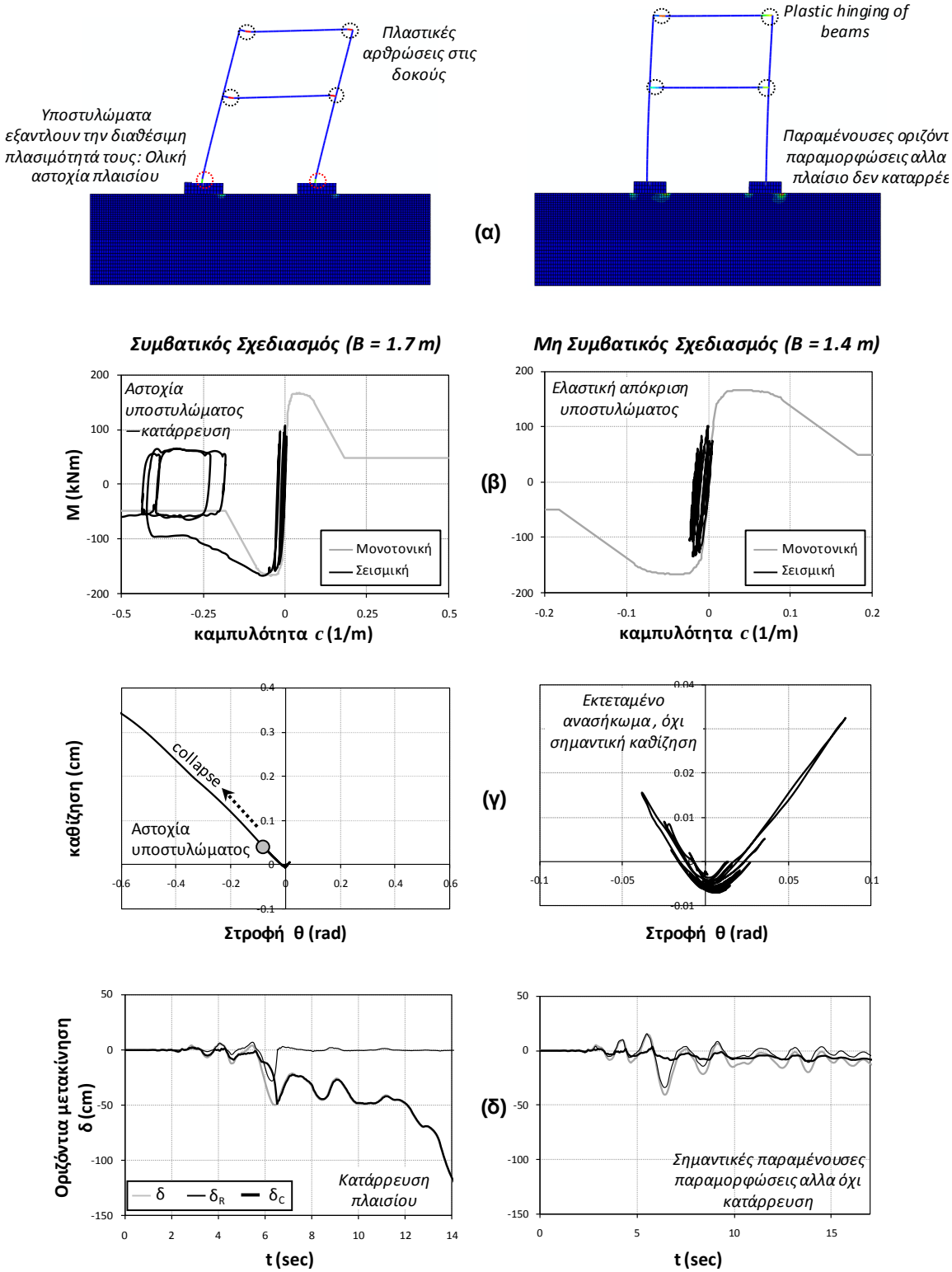

Σχήμα 2.6: Συγκριτική Συμπεριφορά των 2 εναλλακτικών σχεδιασμών θεμελίωσης (συμβατικός σχεδιασμός *B* = 1.7 m ; μη συμβατικός, *B* = 1.4 m) όταν το πλαισίο διεγείρεται από εξαιρετικά ισχυρό σεισμικό κραδασμό που κατά πολύ υπερβαινει τον σεισμό σχεδιασμό του πλαισίου (καταγραφή Takatori,Kobe 1995): (**α**) παραμορφωμένος κάνναβος πεπερασμένων στοιχείων και ισοϋψεις πλαστικών παραμορφώσεων, (**β**) βρόχοι καμπτικής ροπής - καμπυλότητας στην βάση του υποστυλώματος, (**γ**) βρόχοι καθίζησης-στροφής θεμελίου (*w–ϑ*) και (**δ**) χρονοϊστορία οριζόντιας μετακίνησης στο επίπεδο του ισογείου.

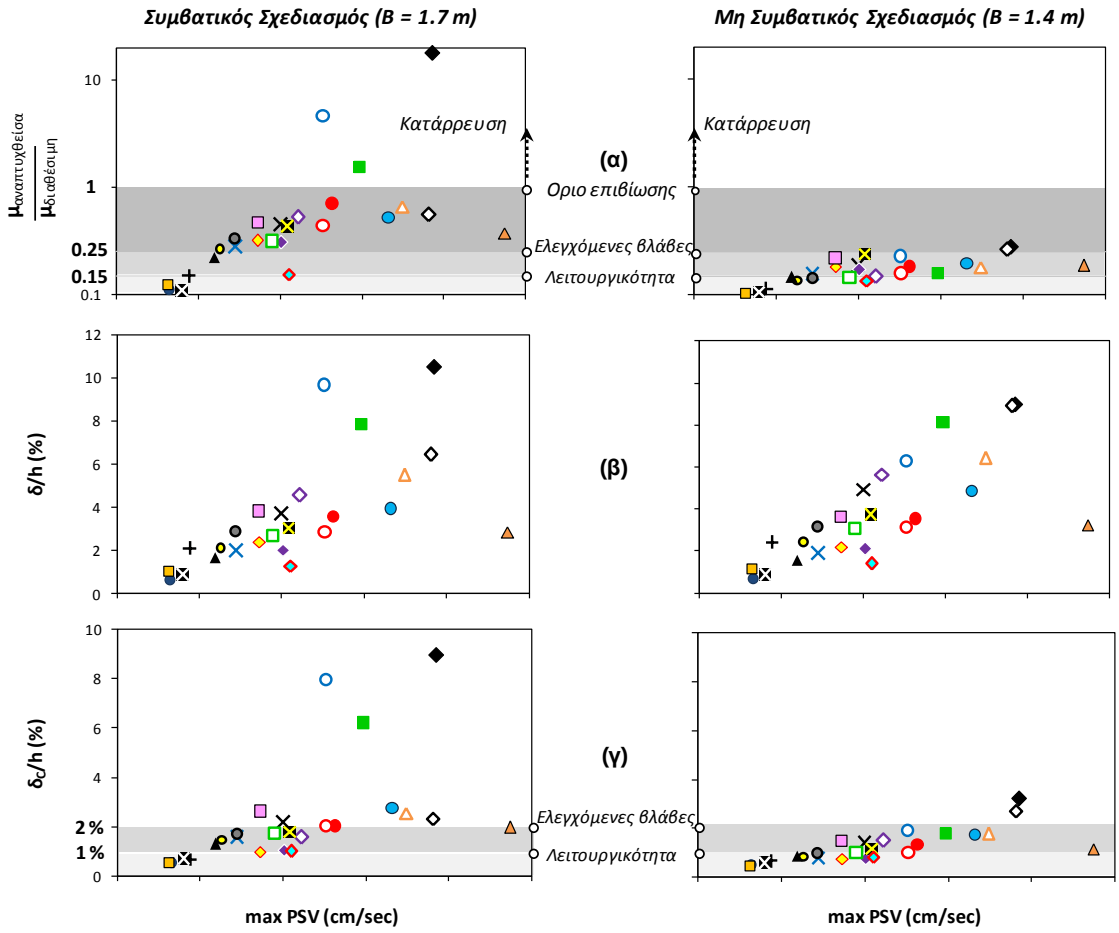

Σχήμα 2.7: Συνοπτική παρουσίαση της σεισμικής απόκρισης των 2 εναλλακτικών συστημάτων θεμελίωσης σαν συνάρτηση της μέγιστης φασματικής ταχύτητας *SV* σε όρους λόγου (**α**) απαιτούμενης προς διατιθέμενης καμπυλότητας στην βάση του υποστυλώματος (**β**) παραμένουσας οριζόντιας μετακίνησης στο επίπεδο του ισογείου και (**γ**) λόγου διαφορικής οριζόντιας μετακίνησης προς ύψος ισογείου οφειλόμενου αποκλειστικώς σε καμπτική καταπόνηση των υποστυλωμάτων. Οι στάθμες επιτελεστικότητας ακολουθούν τον ορισμό των *Priestley et al. (1996)*

2.7 Επεκτείνοντας την Εφαρμοσιμότητα της Νέας Προσέγγισης

Τα αποτελέσματα των παρουσιασθεισών αναλύσεων ανέδειξαν την αποτελεσματικότητα της προτεινόμενης προσέγγισης όταν ο Συντελεστής Ασφαλείας των υπό-διαστασιολογημένων θεμελίων είναι $FS_V \approx 5.3$ υπονοώντας κατ' ουσίαν ότι η περαιτέρω μείωσή του θα απαιτήσει την ανάπτυξη μεγαλύτερης στροφής του θεμελίου κατά την επιβαλλόμενη ισχυρή φόρτιση. Το εύλογον του επιχειρήματος ελέγχεται συγκρίνοντας τη συμπεριφορά του πλαισίου επί θεμελίων με στατικόν συντελεστή ασφαλείας $FS_V = 4$, υλοποιούμενου με δύο μεθόδους:

(α) Θεμέλια πλάτους B = 1.2 m επί εδάφους με αστράγγιστη διατμητική αντοχή S_u = 150 kPa, (αντιστοιχούν σε Ροπή Αντοχής M_{ult} = 100 kNm)

(β) Θεμέλια πλάτους B=1.6 m επί εδάφους με αστράγγιστη διατμητική αντοχή S_u = 85 kPa (Ροπή Αντοχής M_{ult} = 145 kNm)

Τα αποτελέσματα της ανάλυσης των δύο συστημάτων υποβαλλομένων στην ισχυρότατη διέγερση Takatori (Kobe 1995) επιβεβαιώνουν την αύξηση των αναπτυσσομένων μετακινησιακών μεγεθών του πλαισίου από τις τιμές που είχαν προκύψει με τον υψηλότερο συντελεστή ασφαλείας. Ως προς την μεταξύ τους σύγκριση, οι δύο εναλλακτικές, διαθέτουσες τον ίδιον συντελεστή ασφαλείας (FS_V = 4), αναπτύσσουν αντίστοιχη μέγιστη στροφή ($\theta \approx 0{,}08$ rad) στην θεμελίωση (**Σχ.2.8β**) και επομένως αντίστοιχους λόγους συνολικής διαφορικής οριζόντιας μετάθεσης ισογείου δ (**Σχ.2.8γ**). Ωστόσο, σε όρους διαφορικής οριζόντιας μετάθεσης λόγω καμπτικής παραμόρφωσης, η εναλλακτική λύση B = 1.2 m, είναι εμφανώς

ευνοϊκότερη για την κατασκευή — αποτέλεσμα της μειωμένης ροπής αντοχής και του συνακόλουθου περιορισμού της μεταδιδόμενης έντασης στην ανωδομή.

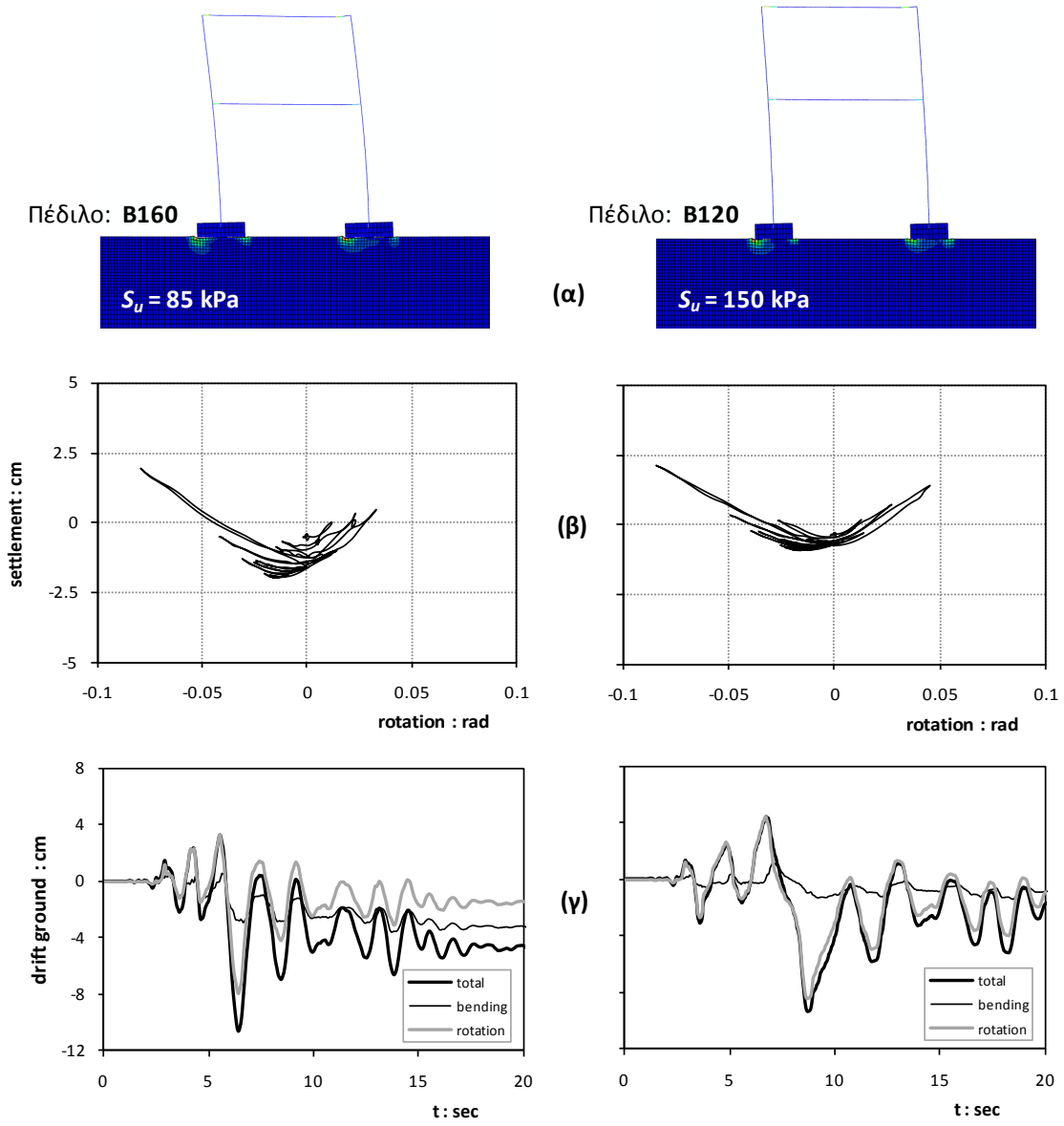

Σχήμα 2.8: Απόκριση πλαισίων επί θεμελίων με $FS_V = 4$ στην διέγερση Takatori (Kobe, 1995): (α) ισοϋψείς παραμενουσών πλαστικών παραμορφώσεων, (β) ροπή-καθίζηση θεμελίων και (γ) χρονοϊστορίες λόγου διαφορικής μετακίνησης ισογείου.

Ενότητα 3:

Απλοποιημένη Μέθοδος Σχεδιασμού Θεμελιώσεων με βάση την Νέα Προσέγγιση

3.1 Προτεινόμενη Μεθοδολογία

Αντικείμενο της Ενότητας αυτής αποτελεί η ανάπτυξη μιας απλοποιημένης μεθοδολογίας για την εφαρμογή της νέας λογικής σχεδιασμού, σε απλούς πλαισιωτούς φορείς επί επιφανειακών θεμελίων. Προκειμένου η μέθοδος να είναι εφαρμόσιμη με επιτυχία δύο αντικρουόμενα κριτήρια ως προς τις διαστάσεις του θεμελίου θα πρέπει να ικανοποιούνται ταυτόχρονα: (i) να είναι αρκετά μικρές ώστε η οριακή του ροπή να μην υπερβεί αυτήν του υποστυλώματος και (ii) αρκετά μεγάλες ώστε να εξασφαλίζεται ένα ικανοποιητικό περιθώριο ασφαλείας έναντι ανατροπής, χωρίς ωστόσο να διακυβεύεται η γενική ευστάθεια της κατασκευής (FS_V > 3). Προκύπτει δηλαδή η ανάγκη υπολογισμού ενός άνω και ενός κάτω ορίου της διάστασης B.

3.2 Εκτίμηση του Ανω Ορίου

Για τον προσδιορισμό ενός ασφαλούς άνω ορίου η ελάχιστη τιμή του *συντελεστή απομείωσης* CRF, πρέπει να λαμβάνει την τιμή 2, ώστε αφενός μεν να αποκλειστεί το ενδεχόμενο υπέρβασης της ροπής αντοχής του υποστυλώματος λόγω διακύμανσης του κατακορύφου φορτίου N, αφετέρου δε να συνυπολογιστούν πιθανές

αβεβαιότητες ως προς την πραγματική αντοχή του εδάφους και της ανωδομής, ή φαινόμενα δυναμικής υπεραντοχής.

3.3 Εκτίμηση του Κάτω Ορίου

Ο υπολογισμός του ελάχιστου πλάτους του θεμελίου απαιτεί γνώση τόσο της οριακής στροφής ανατροπής του πλαισίου ϑ_{top} (αντοχή) όσο και της μέγιστης επιβαλλόμενης στροφής λόγω σεισμού ϑ_{dem} (απαίτηση), όπως εξηγείται παρακάτω.

Απλοποιημένη Μέθοδος για την Εκτίμηση της θ_{top}

Η οριακή τιμή της στροφής του πλαισίου θα αναπτυχθεί κατά την διάρκεια της τρίτης και τελευταίας φάσης του **Σχήματος 2.4ε.** Στην φάση αυτή, το πλαίσιο έχει ουσιαστικώς εκφυλιστεί σε δύο μονοβάθμιους ταλαντωτές, και αποκρίνεται στο επιβαλλόμενο φορτίο μέσω λικνισμού με ασήμαντη κάμψη. Όπως φαίνεται στο **Σχήμα 3.1** οι υπολογισθείσες καμπύλες ροπής-στροφής των δύο θεμελίων διαστάσεων B x B περιβάλλονται αρκετά ικανοποιητικά από τις καμπύλες ροπής–στροφής δύο μονοβαθμίων ταλαντωτών επί θεμελίων επίσης διαστάσεων B x B, οι οποίοι αντιστοιχούν απλοποιητικά σε δύο ακραίους συνδυασμούς αξονικού φορτίου N και μοχλοβραχίονα M/Q:

Ταλαντωτής Α: N = N_{FD} = 247 kN, M/Q = 2.4 (ήτοι οι ψευδοστατικώς υπολογιζόμενες τιμές των μεγεθών N και M/Q σύμφωνα με τον ΕΑΚ2000, Παρ. 5.2)

Ταλαντωτής Β: N = 135 kN, M/Q = 4.8 (ήτοι οι οριακές τιμές των μεγεθών N και M/Q κατά την τρίτη φάση της απόκρισης).

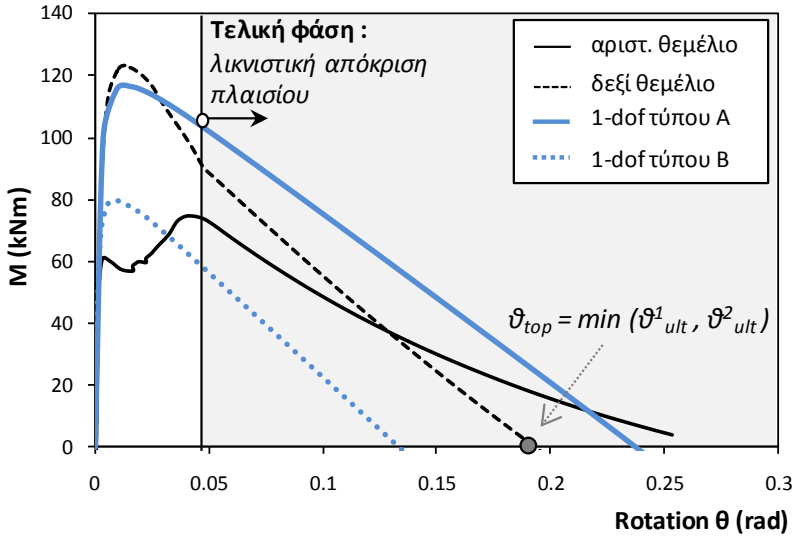

Σχήμα 3.1. Πλαίσιο υποβαλλόμενο σε στατική φόρτιση ελεγχόμενης μετακίνησης: Σύγκριση της καμπύλης M-θ των πεδίλων του πλαισίου με τις αντίστοιχες καμπύλες 2 "ισοδύναμων" μονοβαθμίων συστημάτων τύπου A και B, διάστασης θεμελίου B=1.40 m.

Δεδομένου ότι η πλήρης μή-γραμμική ανάλυση Push-Over του όλου πλαισίου (επί εδαφικής στρώσης) δεν είναι πρακτικώς εφαρμόσιμη κατά τον σχεδιασμό, η παρούσα έρευνα κατέληξε ότι ο απλούστερος τρόπος υπολογισμού της στροφής ανατροπής του πλαισίου είναι η εφαρμογή συντελεστή ασφαλείας 1.5 στην οριακή στροφή που υπολογίζεται από την φόρτιση Push-Over του ταλαντωτή Α. Δεδομένου μάλιστα ότι ο στατικός συντελεστής ασφαλείας του θεμελίου είναι αρκετά υψηλός, η βύθισή του λόγω πλαστικοποίησης του εδάφους δείχθηκε ήδη ότι είναι ασήμαντη. Αρα, χωρίς ουσιώδη βλάβη της γενικότητας, ο εξιδανικευμένος ταλαντωτής στην φάση έναρξης της ανατροπής είναι δυνατόν να απλοποιηθεί έτι περαιτέρω ως ένα άκαμπτο σώμα επί άκαμπτης βάσης. Η βασική ορθότητα της απλοποητικής αυτής παραδοχής επιβεβαιώνεται στο **Σχήμα 3.2**, όπου η πρόβλεψη της θ_{ult} με χρήση του άκαμπτου σώματος ($\theta_{ult} = \tan^{-1}(b/h) \approx b/h$) συγκρίνεται με τον ακριβή υπολογισμό της με χρήση τριδιάστατου αριθμητικού προσομοιώματος. Όπως αναμενόταν, όσο

μικρότερος είναι ο συντελεστής ασφαλείας τόσο μικρότερη είναι η ακρίβεια της απλοποίησης. Λαμβάνοντας πάντως υπόψιν ότι σε πραγματικές κατασκευές ο Συντελεστής Ασφαλείας σπανίως κείται κάτω του 3, η απλοποίηση θεωρείται εξαιρετικά εύλογη.

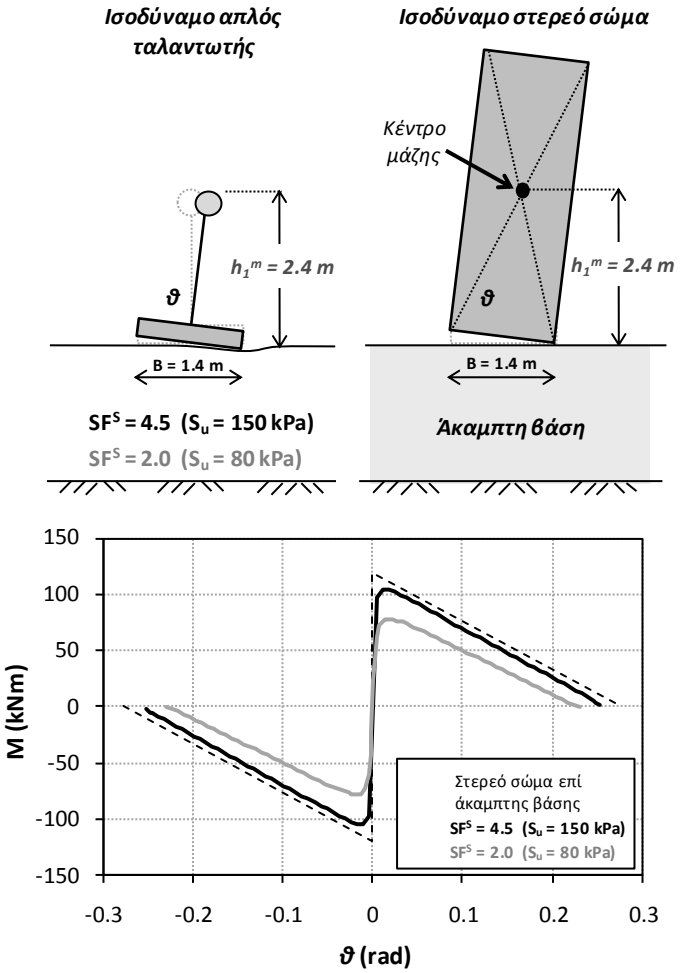

Σχήμα 3.2. Σύγκριση μετα-πλαστικής απόκρισης *M–ϑ του* μονοβαθμίου ταλαντωτή τύπου Α εδραζομένου επί μη-γραμμικού εδάφους με S_u*= 150 kPa* (μαύρη γραμμή) και S_u*= 80 kPa* (γκρι γραμμή) με την απόκριση του ισοδύναμου στερεού σώματος επί άκαμπτης βάσης.

Συντηρητικός Υπολογισμός της Σεισμικής Απαίτησης θ_{dem}

Η οριακή στροφή ϑ_{top} *αντιστοιχεί σε οριακή μετακίνηση* δ_κ στο κέντρο μάζας της κατασκευής. Επομένως, η ζητούμενη ασφαλής διάσταση του θεμελίου θα πρέπει να ικανοποιεί την απαίτηση $\boldsymbol{\delta_\kappa > \delta_\varepsilon}$ όπου δ_ε η σεισμικώς επιβαλλόμενη μετακίνηση ("απαίτηση"). Διευκρινίζεται ότι στην παρούσα έρευνα δεν αναζητείται μια μέθοδος υπολογισμού της πραγματικής σεισμικής απαίτησης, αλλά ένας απλοποιητικός τρόπος συντηρητικής εκτίμησης της μέγιστης πιθανής μετακίνησης $\boldsymbol{\delta_\varepsilon}$. Στα πλαίσια αυτά, ως μέτρο της απαίτησης προτείνεται η μέγιστη τιμή της φασματικής μετακίνησης του επιταχυνσιογραφήματος σχεδιασμού (SD_{max}). Δεδομένου ότι η ιδιοπερίοδος της λικνιστικά αποκρινόμενης κατασκευής μεταβάλλεται ραγδαία από την αρχική της τιμή T_{el} (τείνοντας ασυμπτωτικά προς το άπειρο λίγο πριν απ'την ανατροπή) η θεώρηση μίας συγκεκριμένης τιμής φασματικής μετακίνησης θα ήταν ανεπαρκής. Θεωρείται επίσης αυτονόητο ότι η μέγιστη μετακίνηση SD_{max} μόνον από σύμπτωση θα ήταν πιθανόν να αναπτυχθεί όντως στο πλαίσιο. Ωστόσο στόχος της έρευνας είναι να καταδειχθεί ότι η τιμή αυτή αποτελεί συντηρητική μόνον εκτίμηση της πραγματικής μετακίνησης και άρα εύλογη εκτίμηση του ζητούμενου δείκτη $\boldsymbol{\delta_\varepsilon}$. Η ισχύς της υπόθεσης αυτής εξετάζεται στις επόμενες παραγράφους.

Στερεό Σώμα υποβαλλόμενο σε απλούς παλμούς: Σύγκριση με Αναλυτικές Λύσεις

Στο **Σχήμα 3.3α** απεικονίζεται ενδεικτική σύγκριση της ακριβούς λύσης των Zhang & Makris [2001] (γραμμοσκιασμένη περιοχή) με την εκτίμηση της απλοποιητικής μεθοδολογίας (διακριτά σημεία), για στερεό σώμα επί άκαμπτης βάσης υποβαλλομένου σε παλμούς ημιτόνου και συνημιτόνου, ενώ στο **Σχήμα 3.3β** η

εκτίμηση της απλοποιητικής μεθοδολογίας συγκρίνεται με την ακριβή λύση των Gerolymos et al. [2005] για σώματα υποβαλλόμενα σε παλμούς Ricker. Όπως προκύπτει από την επισκόπηση των Σχημάτων 3.3, η υπολογιζόμενη επιτάχυνση ανατροπής με βάση το $\boldsymbol{SD_{max}}$ δεν είναι συντηρητική σε όλο το φάσμα των εξετασθεισών συχνοτήτων. Κατόπιν αυτού, η διεξαχθείσα έρευνα κατέληξε ότι είναι αναγκαία η εφαρμογή ενός συντελεστή ασφαλείας της τάξης του 1.4 στην εκτίμηση με βάση το $\boldsymbol{SD_{max}}$, ώστε να εξασφαλίζεται συντηρητικός υπολογισμός σε όλες τις περιπτώσεις.

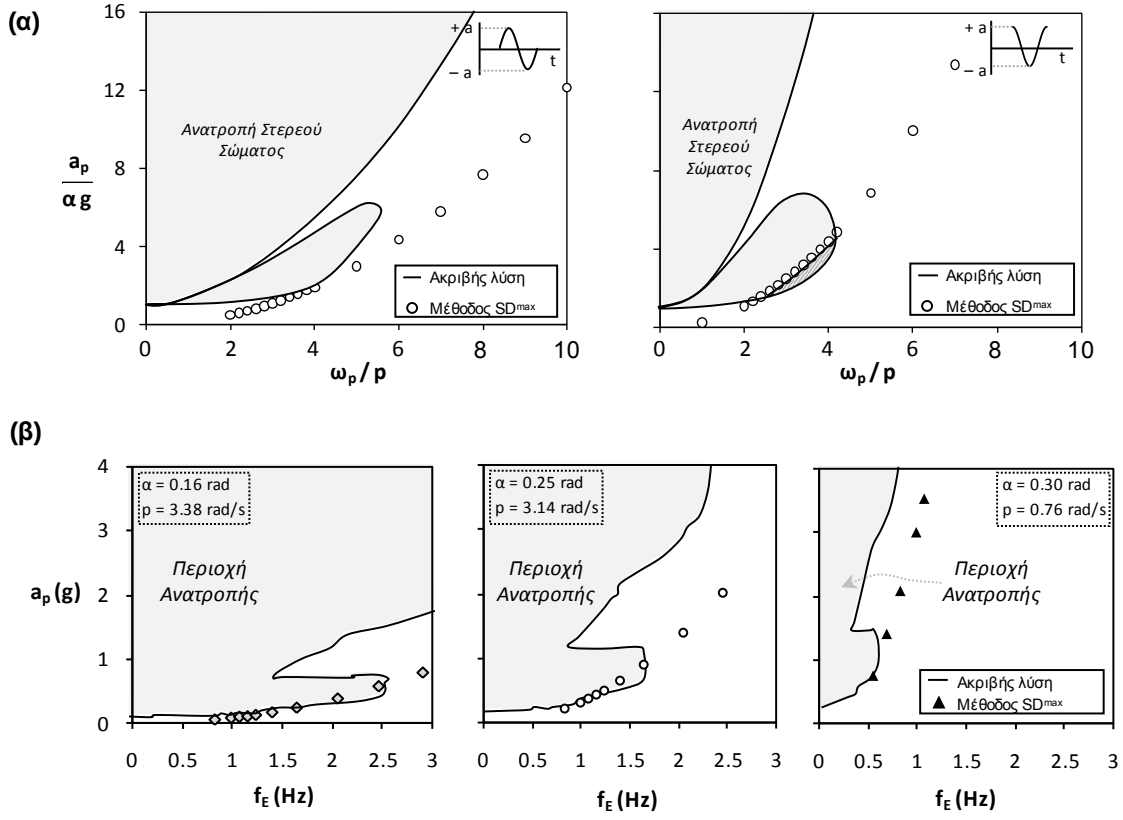

Σχήμα 3.3. Σύγκριση της προτεινόμενης προσεγγιστικής μεθοδολογίας με τις ακριβείς λύσεις (**α**) των Zhang & Makris (2001) και (**β**) των Gerolymos et al. (2005) για τον λικνισμό στερεών σωμάτων επί άκαμπτης βάσης διεγειρόμενων από απλούς παλμούς σε όρους φασμάτων λικνισμού (rocking spectra).

Εφαρμογή της Μεθοδολογίας σε Διώροφο Πλαίσιο επί Μη Γραμμικού Εδάφους

Ακολουθώντας την παραπάνω διαδικασία, η οριακή στροφή του μελετηθέντος στην προηγούμενη ενότητα διωρόφου πλαισίου επί θεμελίων διαστάσεων 1.1 x 1.1 m υπολογίζεται ως ϑ_{ult} = 0.14 rad, η οποία αντιστοιχεί σε δ_K = 71 cm (στο κέντρο μάζας του πλαισίου). Η ισχύς επομένως της μεθοδολογίας θα επαληθευτεί εφόσον η κατασκευή παραμένει ασφαλής έναντι ανατροπής για σεισμούς των οποίων η μέγιστη φασματική μετακίνηση δεν ξεπερνά τα 71 cm. Προκειμένου να εκτιμηθούν τα πιθανά περιθώρια ασφαλείας της απλοποιητικής μεθόδου, διερευνάται η δυναμική απόκριση του πλαισίου σε διεγέρσεις ανηγμένες σε μέγιστη φασματική μετακίνηση $SD_{max} = 1.1\ \delta_K$ (≈ 78 cm) και $SD_{max} = .0.9\ \delta_K$ (≈ 64 cm).

Σε όλες τις περιπτώσεις, για $SD_{max} = 0.9\ \delta_K$ η απλοποιητική εκτίμηση είναι συντηρητική. Αρα προκύπτει, ότι η εφαρμογή ενός συντελεστή ασφαλείας της τάξης μόλις του 1.1 θα ήταν απολύτως ικανοποιητική. Αρκετά ενθαρρυντικό είναι το γεγονός ότι ακόμη και όταν $SD_{max} = 1.1\ \delta_K$, η ανατροπή επέρχεται σε δύο μόνον σεισμικά σενάρια από τα 24 συνολικά Το γεγονός αυτό πάντως δεν θεωρείται ανησυχητικό λόγω του μή-ρεαλιστικού δυσμενούς χαρακτήρα των ανηγμένων χρονοϊστοριών (PGA ≈ 2g).

Ενότητα 4:

Κυματική Διάδοση εντός μαλακής Αλλουβιακής Κοιλάδας:

Δημιουργία παρασιτικής Κατακόρυφης Συνιστώσας

4.1 Εισαγωγή

Παρότι τα φαινόμενα τοπογραφικής ενίσχυσης λόγω διδιάστατης κυματικής διάδοσης έχουν μελετηθεί ενδελεχώς στην βιβλιογραφία, συνήθως οι αναλύσεις γίνονται με χρήση ελαστικών αναλύσεων και εξιδανικευμένων παλμών (*Trifunac, 1971; Wong &; Harmsen & Harding, 1981, Sánchez-Sesma & Luzón, 1995, Bao et al., 1996, Bielak et al., 1999, 2000*). Περιορισμένη μόνον προσοχή έχει αφιερωθεί στη διερεύνηση της επίδρασης κυρίων παραμέτρων του προβλήματος όπως το συχνοτικό περιεχόμενο της κίνησης και οι “λεπτομέρειές” της (π.χ. διάρκεια, αριθμός κύκλων, διαδοχή παλμών) λαμβάνοντας υπόψιν την μη γραμμική εδαφική απόκριση. Η εμβάθυνση στον ρόλο των παραπάνω παραγόντων, οι οποίοι ενδέχεται να μεταβάλλουν σημαντικά την αναπτυσσόμενη κίνηση στην επιφάνεια εδαφικών κοιλάδων (θέσεις θεμελιώσεως κατασκευών), επιχειρείται στην τέταρτη ενότητα της διατριβής. Επιπλέον, ιδιαίτερη βαρύτητα δίδεται στη μελέτη της γένεσης μίας παρασιτικής *κατακόρυφης* συνιστώσας της κίνησης, απόρροια της διδιάστατης γεωμετρίας και μόνον. Λόγω του ότι η συνιστώσα αυτή αναμένεται να είναι σύγχρονη και ομοιοσυχνοτική με την οριζόντια συνιστώσα θεωρείται και πολύ πιο επιζήμια για τις κατασκευές.

4.2 Γεωμετρία του Προβλήματος και Μέθοδος Ανάλυσης

Μελετάται η πολύ μαλακή αλλουβιακή κοιλάδα Ohba στην Ιαπωνία (*Tazoh et al. [1984]*). Η ταχύτητα διάδοσης του διατμητικού κύματος V_S κυμαίνεται μεταξύ 40 και 65 m/s στο έδαφος και περί τα 400 m/s στο υπόβαθρο. Το αριθμητικό προσομοίωμα για τις δυναμικές εν χρόνω αναλύσεις απεικονίζεται στο **Σχήμα 4.1**. Σε όλες επόμενες περιπτώσεις τα αποτελέσματα αναφέρονται σε επιβολή στην βάση του προσομοιώματος χρονοϊστορίας αποκλειστικώς οριζόντιας επιτάχυνσης.

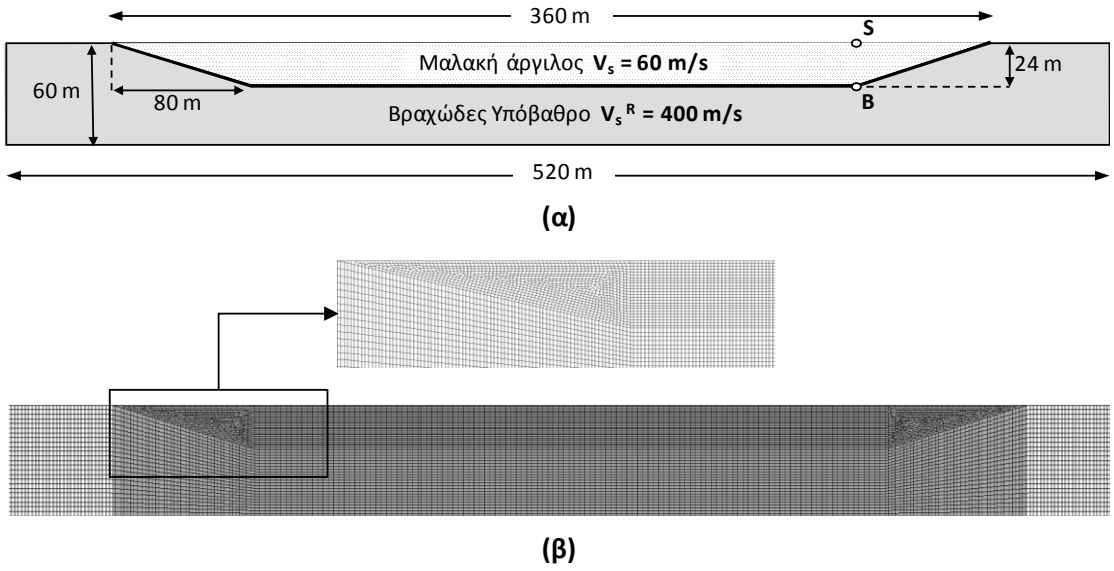

Σχήμα 4.1: (**α**) Απλοποιημένη γεωμετρία της κοιλάδας Ohba. (**β**) το αριθμητικό προσομοίωμα πεπερασμένων στοιχείων που χρησιμοποιήθηκε στις δυναμικές αναλύσεις. Σε μεγέθυνση η πυκνή διακριτοποίηση πλησίον του άκρου της κοιλάδας.

Προκειμένου να αποφευχθούν μή ρεαλιστικές ανακλάσεις κυμάτων, τοποθετούνται στη βάση του προσομοιώματος απορροφητικά σύνορα ενώ στα πλευρικά του όρια αναπαράγονται συνθήκες ελευθέρου πεδίου. Τα στοιχεία του δικτύου είναι αρκετά μικρών διαστάσεων για την αναπαραγωγή πιθανών υψίσυχνων κυματομορφών. Η ισχύς της αριθμητικής μεθοδολογίας έχει επιβεβαιωθεί από τους *Tazoh et al. [1988], Fan et al. [1992] and Psarropoulos et al. [2007]*.

4.3 Ο ρόλος του Συχνοτικού περιεχομένου

Στο **Σχήμα 4.2** απεικονίζεται η χωρική κατανομή του συντελεστή τοπογραφικής επιδείνωσης $AG = A_{2D}/A_{1D}$ (λόγος των PGA διδιάστατης προς μονοδιάστατης ανάλυσης) όταν η κοιλάδα υποβάλλεται σε παλμούς Ricker (ελαστικές αναλύσεις με ξ=2%). Με τον υψίσυχνο παλμό Ricker3 (**Σχήμα 4.2(α)**), η απόκριση της κοιλάδας είναι εμφανώς μονοδιάστατη στο κέντρο. Διδιάστατα φαινόμενα εντοπίζονται στις άκρες όπου τα κύματα υπόκεινται σε πολλαπλές ανακλάσεις (εντός των οριοθετουμένων από το υπόβαθρο εδαφικών πρισμάτων) προκαλώντας επιδείνωση (*AG* ≈ 1.3). Σε αντίστοιχα συμπεράσματα έχουν καταλήξει μεταξύ άλλων οι *Sánchez-Sesma et al. [1988]*, ενώ η συγκεκριμένη κατανομή του συντελεστή επιδείνωσης εξηγεί ενδεχομένως την κατανομή των παρατηρηθεισών βλαβών επί εδαφικών κοιλάδων σε διάφορους καταγεγραμμένους σεισμούς (π.χ. Palos Grandes, 1997)

Μειουμένης της συχνότητας του κραδασμού (Ricker 1 : f_o = 1 Hz) η χωρική κατανομή του συντελεστή AG τροποποιείται δραστικά (**Σχήμα 4.2(β)**). Το παραγόμενο κύμα είναι λιγότερο ευαίσθητο στην τοπογραφική ανωμαλία ως αποτέλεσμα της μικρότερης συχνότητας του παλμού. Ακολούθως, η επιδείνωση λόγω πολλαπλών ανακλάσεων (πλησίον των άκρων) που παρατηρήθηκε στην προηγούμενη περίπτωση επισκιάζεται πλέον από την υπερθετική συμβολή των αντιρρόπως διαδιδόμενων προς το κέντρο επιφανειακών κυμάτων Rayleigh. Τα τελευταία συντελούν στην μετάθεση της περιοχής μέγιστης επιδείνωσης (*AG* = 1.7) πλησίον του κέντρου. Περαιτέρω μείωση της συχνότητας του παλμού (Ricker 0.5, **Σχήμα 4.2(γ)**), οδηγεί σε εξομάλυνση της κατανομής των συντελεστών επιδείνωσης AG. Η παρατηρούμενη χωρική κατανομή τους είναι ενδεικτική φαινομένων

διδιάστατου συντονισμού, επιβεβαιώνοντας πληθώρα σχετικών δημοσιευμένων μελετών (*Bard and Bouchon, 1985; Moczo et al, 1996; Hill et al, 1990*).

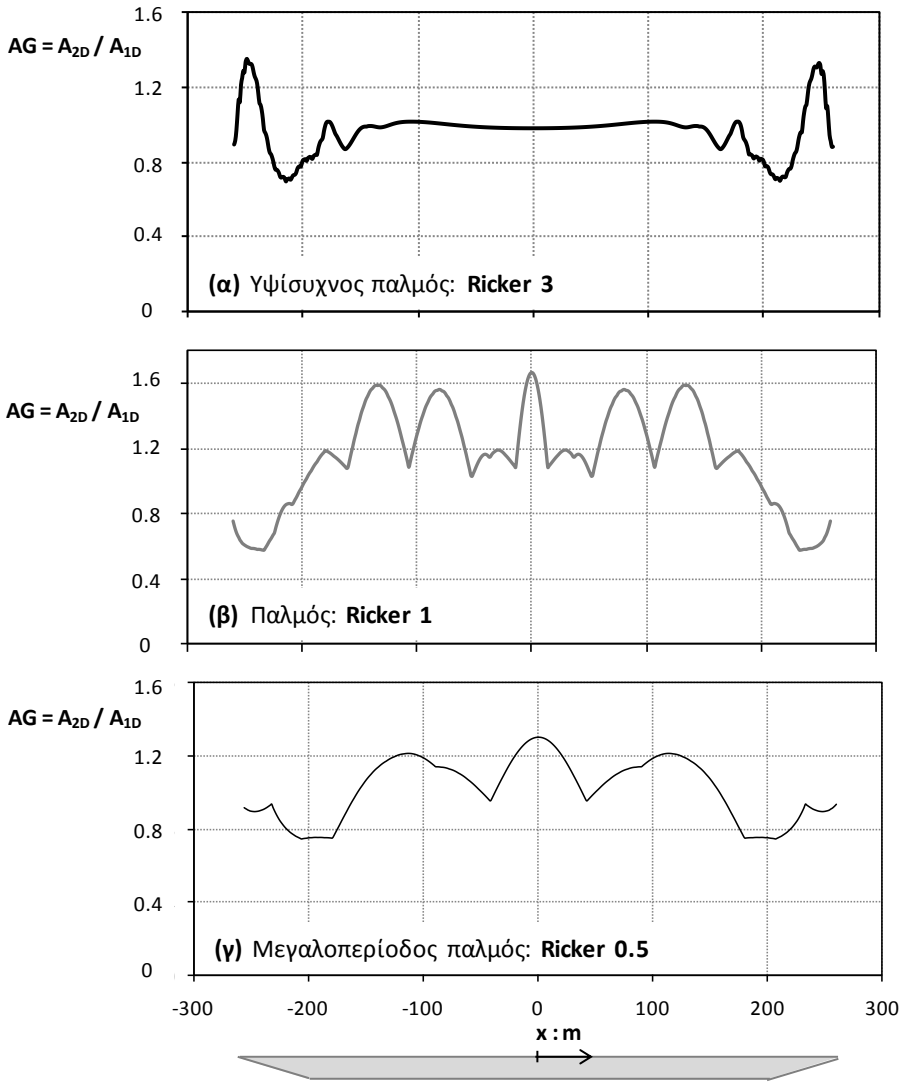

Σχήμα 4.2. Κατανομή του συντελεστή εδαφικής επιδείνωσης AG όταν η κοιλάδα διεγείρεται (**α**) από τον υψίσυχνο παλμό Ricker 3, (**β**) από τον παλμό Ricker1 και από τον εξαιρετικά μεγαλοπερίοδο παλμό Ricker 0.5. Θεώρηση ελαστικής εδαφικής απόκρισης με συντελεστή βισκοελαστικής απόσβεσης ξ = 2 %.

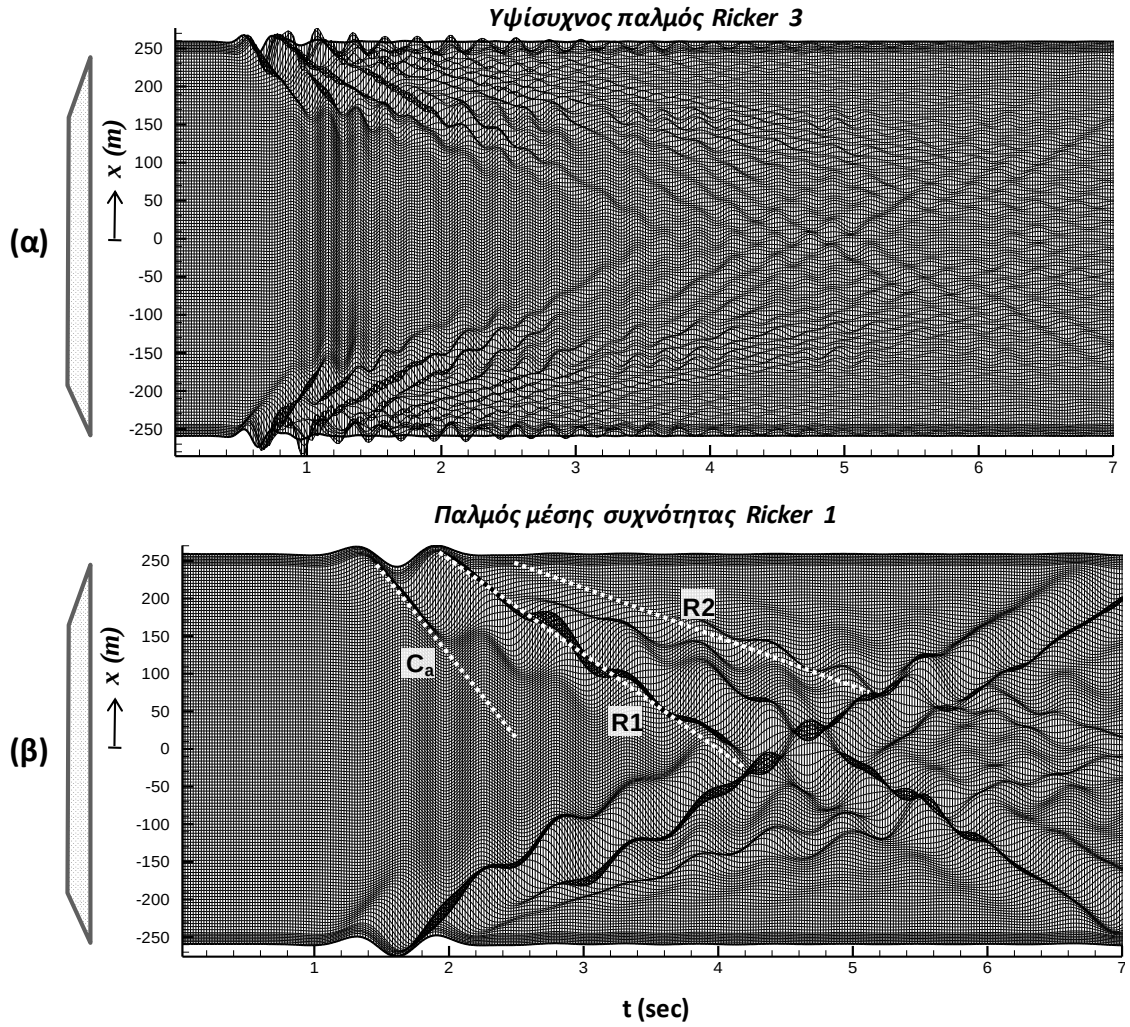

Σχήμα 4.3: Επιρροή του συχνοτικού περιεχομένου της διέγερσης στο παραγόμενο κυματικό πεδίο όταν η κοιλάδα διεγείρεται από (**α**) τον υψίσυχνο παλμό Ricker 3, (**β**) τον παλμό Ricker 1 και (**γ**) τον παλμό υψηλής περιόδου Ricker 0.5.

Τα ανωτέρω επαληθεύονται καί από την μορφή των παραγομένων συνθετικών σεισμογραφημάτων (**Σχήμα 4.3**). Στον ενδιάμεσης-συχνότητας παλμό Ricker1, απεικονίζονται καθαρά οι 2 πρώτες ιδιομορφές των διαδιδομένων προς το κέντρο επιφανειακών κυμάτων (R1, R2). Η συμβολή των τελευταίων προκαλεί ενισχύσεις, παρατηρούμενες σχεδόν σε όλο το μήκος της κοιλάδας. Αντιθέτως με τον υψίσυχνο παλμό Ricker3 (**Σχήμα 4.3β**), παρότι δημιουργείται ένα εξαιρετικά πολύπλοκο κυματικό πεδίο, τα διαδιδόμενα προς το κέντρο της κοιλάδας κύματα εξασθενούν

ταχέως (λόγω της απόσβεσης), με αποτέλεσμα την απουσία οποιασδήποτε ενίσχυσης σε περιοχές εκτός των άκρων.

4.4 Επιρροή των Χαρακτηριστικών της Διέγερσης

Στην περίπτωση της ελαστικής απόκρισης χαρακτηριστικά της διέγερσης όπως ο αριθμός των κύκλων, η διάρκεια, το συχνοτικό περιεχόμενο δεν φαίνεται να επηρεάζουν την ενίσχυση στις άκρες της κοιλάδας, αλλά επιδρούν ουσιωδώς στη γένεση επιφανειακών κυμάτων, υπευθύνων για την επιδείνωση του κραδασμού στο κέντρο της (*Bard & Bouchon, 1980, Fishman & Ahmad, 1995*): η αύξηση του αριθμού των σημαντικών κύκλων φόρτισης αυξάνει προφανώς την πιθανότητα ενισχυτικής συμβολής επιφανειακών κυμάτων αντιρρόπως διαδιδόμενων προς το κέντρο της κοιλάδας και κατακορύφως διαδιδόμενων από την βάση, με τελικό αποτέλεσμα την επιδείνωση του κραδασμού.

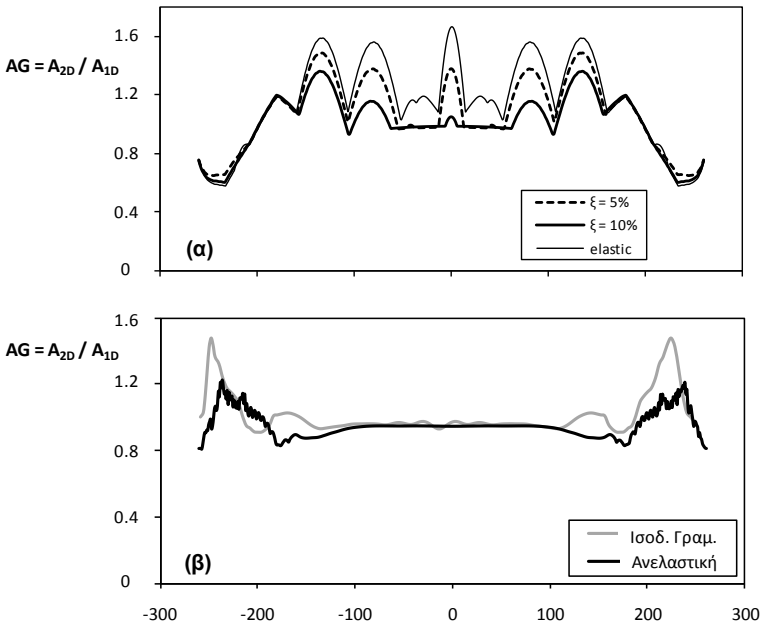

Σχήμα 4.4. Χώρική κατανομή του συντελεστή εδαφικής επιδείνωσης AG για κοιλάδα διεγειρόμενη από παλμό Ricker 1: (**α**) με θεώρηση σταδιακώς αυξανομένου ποσοστού απόσβεσης ξ και (**β**) με θεώρηση ισοδύναμης γραμμικής απόκρισης (γκρί γραμμή) και πλήρους μη γραμμικής συμπεριφοράς (μαύρη γραμμή)

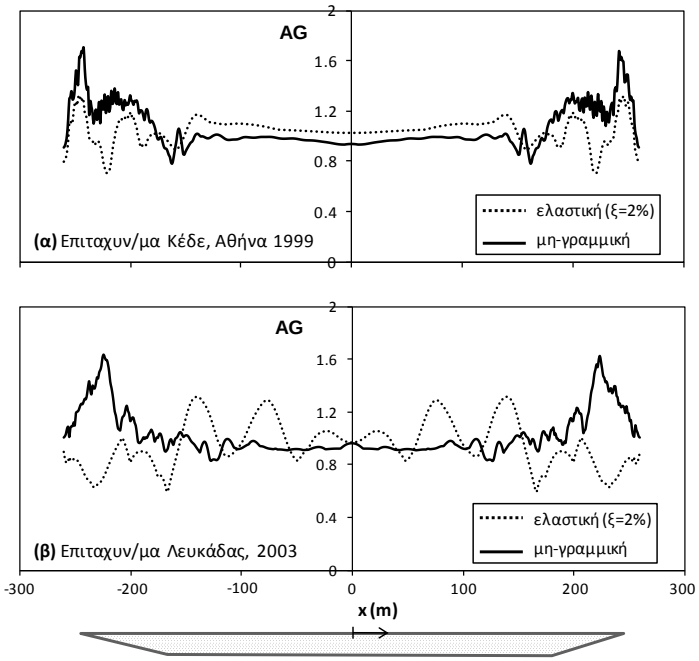

Σχήμα 4.5. Επιρροή της εδαφικής μη-γραμμικότητας στην σεισμική απόκριση της κοιλάδας όταν η διέγερση είναι (**α**) η καταγραφή Κέδε του σεισμού της Αθήνας (1999) και (**β**) το επιταχυνσιογράφημα της Λευκάδας (2003). Με μαύρη γραμμή απεικονίζεται το αποτέλεσμα της πλήρους μή-γραμμικής ανάλυσης, ενώ με την εστιγμένη η απόκριση της κοιλάδας με θεώρηση ελαστικής εδαφικής συμπεριφοράς.

4.5 Μή-Γραμμική Απόκριση του εδάφους

Οι μη γραμμικές αναλύσεις της κοιλάδας υποβαλλομένης τόσο σε εξιδανικευμένους παλμούς όσο και σε πραγματικά επιταχυνσιογραφήματα, επιβεβαιώνουν την σημασία της μή γραμμικότητας, η οποία τροποποιεί σημαντικά την διδιάστατη απόκριση του σχηματισμού. Πέραν της πλήρως μή-γραμμικής ανάλυσης, ισοδύναμες γραμμικές αναλύσεις καθώς και ελαστικές με αυξημένη ιξωδοελαστική απόσβεση ξ, αξιοποιούνται εν προκειμένω στην αξιολόγηση εναλλακτικών (απλούστερων) μεθόδων ανάλυσης οι οποίες λαμβάνουν έμμεσα υπόψιν την μή γραμμική εδαφική συμπεριφορά. Αποδεικνύεται ότι η αύξηση του ποσοστού αποσβέσεως ξ ορθώς εκτιμά την μείωση της επιδείνωσης στο κέντρο της κοιλάδας, είναι όμως ανεπαρκής στην αναπαραγωγή των φαινομένων που λαμβάνουν χώρα στα άκρα του σχηματισμού. Αντιστοίχως, η πρόβλεψη της ισοδύναμης γραμμικής ανάλυσης

(Αριθμητικός κώδικας QUAD4M, Hudson et al, 1994), αν και σαφώς πλησιέστερη στην πραγματική μή γραμμική εδαφική απόκριση, αναπαράγει μέρος μόνον του συνόλου των φαινομένων **(Σχήμα 4.4)**. Ως εκ τούτου, η διεξαγωγή πλήρους μη γραμμικής ανάλυσης προκρίνεται ως η αναγκαία λύση.

Ένα από τα πιο ενδιαφέροντα ευρήματα της έρευνας αφορά στο παράδοξο της αύξησης (και όχι μείωσης όπως συνήθως έχει παρατηρηθεί) της τοπογραφικής επιδείνωσης στα άκρα της κοιλάδας λόγω της μη γραμμικότητας του εδάφους (**Σχήμα 4.5).** Γενεσιουργό αίτιο του φαινομένου εικάζεται ο εξής μηχανισμός: Τα αρχικώς προσπίπτοντα κύματα, προκαλούν διαρροή του εδάφους πλησίον της διεπιφάνειάς του με τον βράχο δημιουργώντας στην περιοχή μία πλαστικοποιημένη ζώνη, στην οποία «παγιδεύονται» τα μετέπειτα προσπίπτοντα κύματα (λόγω των επόμενων κύκλων σεισμικής φόρτισης). Πράγματι, επιβεβαιώνοντας την ισχύ του μηχανισμού, το φαινόμενο είναι ισχυρότερο για την διέγερση της Λευκάδας από ότι για την διέγερση ΚΕΔΕ.

4.6 Δημιουργία Παρασιτικής Κατακόρυφης Συνιστώσας

Όπως ήδη αναφέρθηκε, η διέγερσή της κοιλάδας με αμιγώς οριζόντια σεισμική κίνηση αναπόφευκτα δημιουργεί λόγω της διδιάστατης γεωμετρίας και μία παρασιτική κατακόρυφη συνιστώσα. Στα πλαίσια της διατριβής επιχειρείται μία πρώτη απόπειρα επαλήθευσης του μηχανισμού, υποβάλλοντας το προσομοίωμα σε πραγματικά επιταχυνσιογραφήματα. Πράγματι, (**Σχήμα 4.6α**) η εξαίτηση με την οριζόντια μόνον (A_h) συνιστώσα του επιταχυνσιογραφήματος Λευκάδας (2003), παράγει μία σημαντική κατακόρυφη συνιστώσα A_v στην επιφάνεια της κοιλάδας η οποία σε όρους μέγιστης τιμής είναι συγκρίσιμη με την οριζόντια (max $A_v \approx 0.6$ max

A_h*)*. Επιπλέον (**Σχ. 4.6β**), ως συνέπεια της γεωμετρίας, η κατακόρυφη παρασιτική συνιστώσα A_v είναι εν φάσει με την οριζόντια. Αξίζει μάλιστα να σημειωθεί ότι αντίθετα με την καταγραφείσα κατακόρυφη συνιστώσα της σεισμικής κίνησης "Λευκάδας" η οποία, ως αποτέλεσμα κυμάτων P είναι ιδιαιτέρως υψίσυχνη και επομένως ασήμαντη για τις κατασκευές [*Fardis et al., 2003*], η παρασιτική συνιστώσα **(Σχ.4.6γ)** χαρακτηρίζεται από συχνοτικό περιεχόμενο πρακτικώς όμοιο με αυτό της οριζοντίας. Ετσι πολλαπλασιάζεται η πιθανότητα επιζήμιας δράσης στις κατασκευές.

Ολοκληρώνοντας, θεωρήθηκε ιδιαιτέρου πρακτικού ενδιαφέροντος η διερεύνηση της ευαισθησίας της παρασιτικής κατακόρυφης συνιστώσας στην μή-γραμμική απόκριση του εδάφους **(Σχήμα 4.7)**. Για την περίπτωση της υψίσυχνης διέγερσης ΚΕΔΕ **(Σχήμα 4.7α**), η κατανομή του λόγου A_v / A_h παραμένει πρακτικώς ανεπηρέαστη, ενώ για τις περιπτώσεις ενδιάμεσης και χαμηλής συχνότητας διεγέρσεις Λευκάδας και Yarimca **(Σχήμα 4.7β)** αντιστοίχως, η μή-γραμμικότητα όχι μόνον δεν τροποποιεί την γενική τάση, αλλά στις περιοχές των άκρων επιφέρει ακόμη και αύξηση της τιμής του λόγου A_v / A_h στα άκρα της κοιλάδας. Η αύξηση αυτή είναι αποτέλεσμα κυρίως της απομείωσης της οριζόντιας επιτάχυνσης (μείωση του παρονομαστή στον λόγο A_v / A_h) αποκαλύπτοντας την εν γένει περιορισμένη ευαισθησία της παρασιτικής συνιστώσας στη μή γραμμική απόκριση του εδάφους.

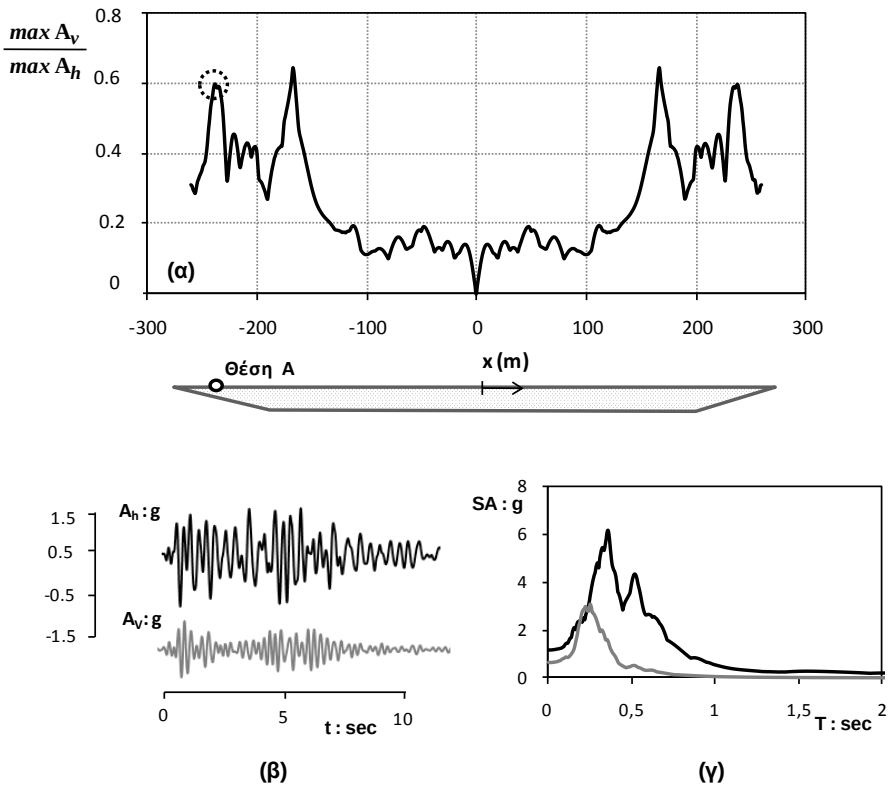

Σχήμα 4.6. (**α**) Χωρική κατανομή του λόγου max A_v/max A_h κατά μήκος της επιφάνειας της κοιλάδας όταν η τελευταία διεγείρεται από το επιταχυνσιογράφημα του σεισμού της Λευκάδας (2003), (**β**) παραγόμενες χρονοϊστορίες επιτάχυνσης (οριζόντιας και κατακόρυφης) και (**γ**) ελαστικά φάσματα απόκρισης στη θέση Α όπου ο λόγος max A_v/max A_h λαμβάνει τοπικά μέγιστη τιμή.

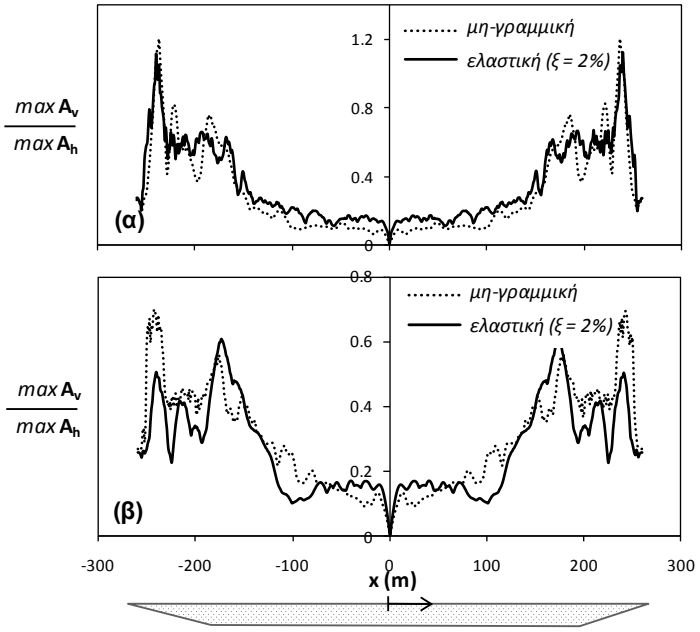

Σχήμα 4.7. Επιρροή της μη-γραμμικής συμπεριφοράς του εδάφους στην παρασιτικώς αναπτυσσόμενη κατακόρυφη συνιστώσα: κοιλάδα διεγειρόμενη (**α**) από την υψίσυχνη καταγραφή του ΚΕΔΕ (Αθήνα, 1999) και (**β**) από την μακροπερίοδη καταγραφή της Yarimca (Kocaeli, 1999).

Ενότητα 5:

Σεισμική Αλληλεπίδραση Εδάφους-Θεμελιώσεως-Πλαισίου σε Περιοχές Εντόνου Γεωμορφικού Αναγλύφου

5.1 Εισαγωγή

Αντικείμενο ετούτης της ενότητας είναι η διερεύνηση των επιζήμιων συνεπειών της παρασιτικής κατακόρυφης συνιστώσας σε κατασκευές θεμελιωμένες πλησίον των άκρων εδαφικής κοιλάδας. Όπως διαπιστώθηκε στην προηγούμενη ενότητα, η εν λόγω συνιστώσα είναι αφενός “εν συγχροτισμώ” με την οριζόντια συνιστώσα της κίνησης και αφετέρου είναι πολύ λιγότερο ευαίσθητη στην μή γραμμική εδαφική απόκριση. Δεδομένου ωστόσο ότι τα ως άνω συμπεράσματα έχουν εξαχθεί από ανάλυση μιάς συγκεκριμένης μαλακής εδαφικής κοιλάδας, εξετάζεται αρχικώς η δυνατότητα γενίκευσής τους μέσω αναλύσεων μιας σκληρότερης εδαφικής κοιλάδας και εν συνεχεία επιχειρείται η αδιαστατοποίηση του προβλήματος ώστε τα παραγόμενα αποτελέσματα να δύνανται να θεωρηθούν ως γενικής ισχύος, ανεξάρτητα από την συγκεκριμένη γεωμετρία του προβλήματος και τις ιδιότητες των εδαφικών υλικών. Στον κυρίως κορμό της τρέχουσας ενότητας μελετάται με χρήση προσομοιώματος πεπερασμένων στοιχείων η σεισμική απόκριση μίας ρεαλιστικώς απλής πλαισιωτής κατασκευής θεμελιωμένης επιφανειακώς πλησίον του άκρου της κοιλάδας.

5.2 Γενίκευση των Αποτελεσμάτων : μέτριας σκληρότητας κοιλαδα

Το εξετασθέν πρόβλημα απεικονίζεται στο **Σχήμα 5.1.** Ως εξαίτηση στην βάση του προσομοιώματος έχουν χρησιμοποιηθεί καταγραφές από ιστορικούς σεισμούς μετρίας έως σημαντικής εντάσεως (**Σχ. 5.1β**) οι οποίοι παρουσιάζουν ποικιλία ως προς τα χαρακτηριστικά τους (ένταση, συχνοτικό περιεχόμενο και αριθμός κύκλων φόρτισης)

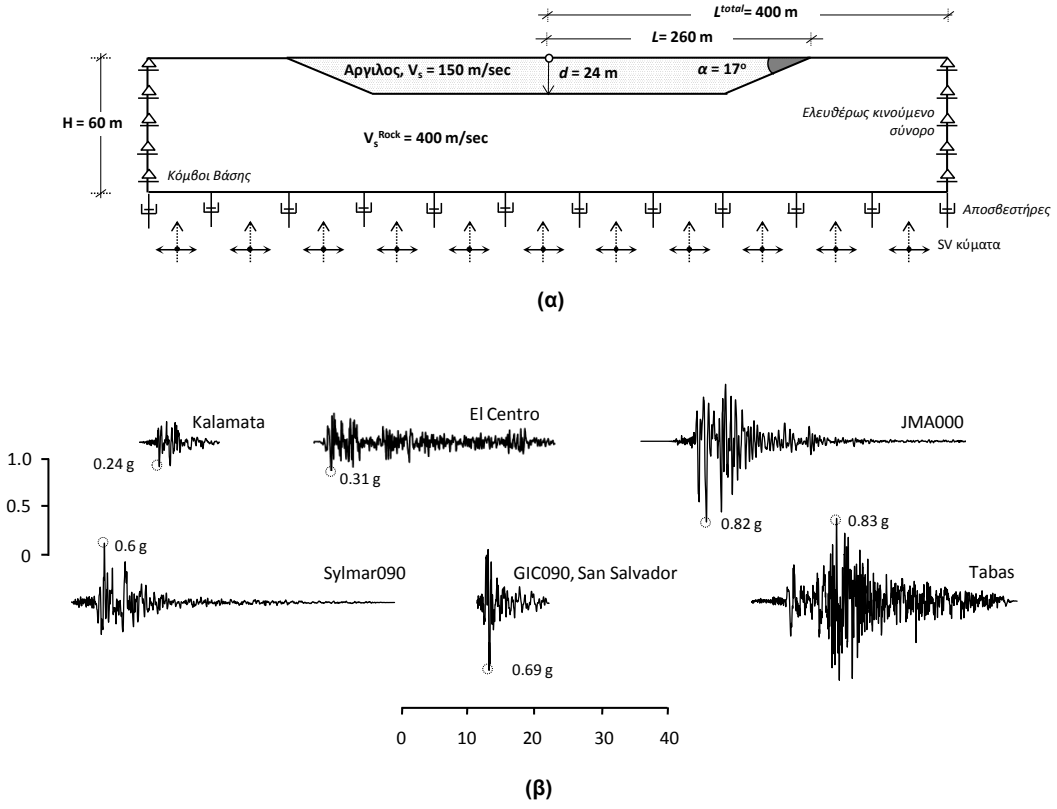

Σχήμα 5.1: (**α**) Σχηματική απεικόνιση του αριθμητικού προσομοιώματος της κοιλάδας, (**β**) χρονοϊστορίες επιταχυνσιογραφημάτων που χρησιμοποιήθηκαν ως διεγέρσεις βάσης του προσομοιώματος Π.Σ.

Τα αποτελέσματα παρουσιάζονται συγκεντρωτικά στο **Σχήμα 5.2** και επιγραμματικά συνοψίζονται ως εξής:

- Όταν το έδαφος είναι ελαστικό, η "κοιλαδική" ενίσχυση (AG = α_{2D} / α_{1D}) είναι σαφώς *μή* προβλέψιμη. Περιοχές συσσωρευμένης ενίσχυσης διαδέχονται περιοχές με ασήμαντη ενίσχυση κατά σχεδόν-χαοτικόν τρόπο, ενώ η κατανομή των ενισχύσεων επηρεάζεται εντόνως από τα χαρακτηριστικά της διέγερσης.
- Η μή γραμμική εδαφική συμπεριφορά απλοποιεί δραστικά την παρατηρούμενη απόκριση της κοιλάδας. Σε όλες τις περιπτώσεις, η όποια κοιλαδική ενίσχυση περιορίζεται εντός των εδαφικών πρισμάτων (γραμμοσκιασμένες περιοχές). Μάλιστα δε, η επιδείνωση στα ακραία σύνορα της κοιλάδας είναι πιθανόν ακόμη και να ξεπεράσει την αντίστοιχη υπό ελαστικές συνθήκες
- Η παρασιτική συνιστώσα όχι μόνον δεν εκφυλίζεται λόγω μή-γραμμικής εδαφικής απόκρισης αλλά ενδέχεται ακόμη και να ξεπεράσει την τιμή της αντίστοιχης οριζόντιας επιτάχυνσης (λόγω μειώσεως της τελευταίας). Πάντως, στο μή γραμμικό πρόβλημα η εν λόγω συνιστώσα αναπτύσσεται πάντοτε πλησίον των άκρων της κοιλάδας.

5.3 Διαστατική Ανάλυση

Ελαστική Συμπεριφορά

Στις έως τώρα παρουσιασθείσες αναλύσεις η γεωμετρία της κοιλάδας έχει θεωρηθεί σταθερή. Αποσκοπώντας στην απεξάρτηση των αποτελεσμάτων από την γεωμετρία της κοιλάδας, επιχειρήθηκε η αδιαστατοποίηση του προβλήματος όπως περιγράφεται παρακάτω (**Σχ. 5.3α**) . Αγνοώντας σε πρώτη φάση την μή γραμμικότητα, τα αποτελέσματα αδιαστατοποιούνται εφόσον ο λόγος $\chi = \lambda/D$ (μήκος κύματος προς πάχος της κοιλάδας) παραμένει σταθερός, με αποτέλεσμα

βέβαια να διατηρείται σταθερός και ο λόγος της δεσπόζουσας συχνότητας του εδαφικού προφίλ προς αυτήν της σεισμικής διέγερσης:

$$\chi \equiv \frac{\lambda}{D} = \frac{V_S}{f \times D} = \frac{4\,V_S}{4 \times f \times D} = \frac{4\,T_{διέγερσης.}}{T_{κοιλάδας}} \qquad (5.1)$$

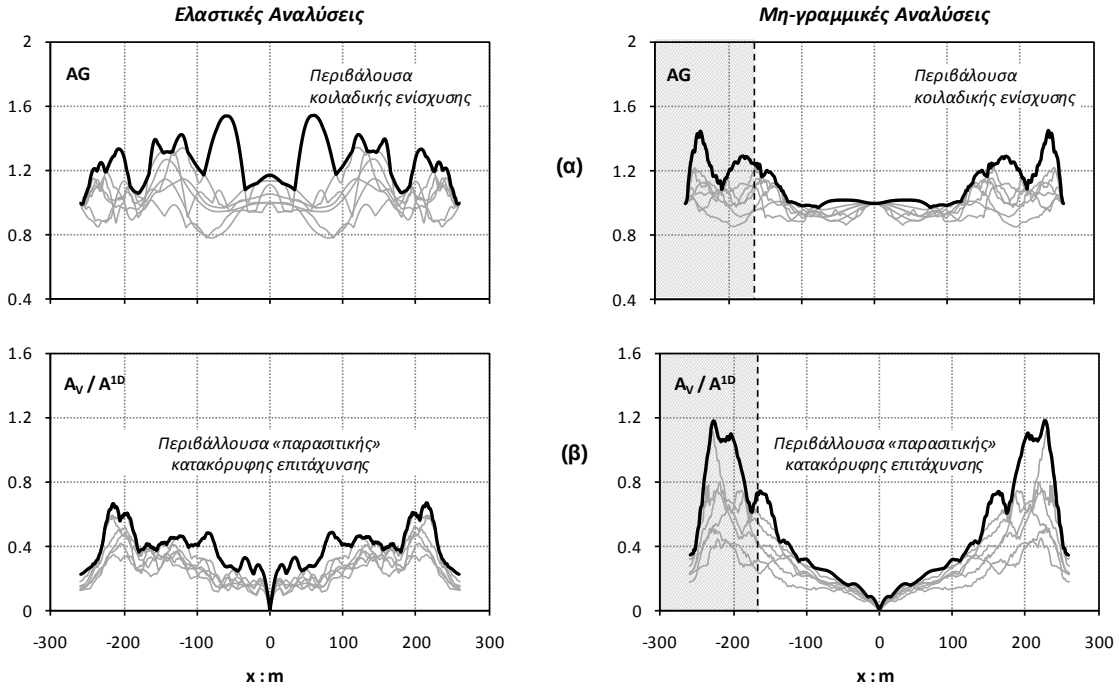

Σχήμα 5.2: (**α**) Χωρική κατανομή του συντελεστή κοιλαδικής ενίσχυσης (AG) και (**β**) του λόγου της «παρασιτικώς» αναπτυσσόμενης κατακόρυφης επιτάχυνσης στην επιφάνεια της κοιλάδας προς την αντίστοιχη τιμή της οριζοντίας (υπό 1-διάστατες συνθήκες) για γραμμική (αριστερά) και μη-γραμμική εδαφική απόκριση (δεξιά) Με έντονη μαύρη γραμμή απεικονίζεται η περιβάλλουσα.

Με τον τρόπο αυτόν επιτυγχάνεται η ορθή αναπαραγωγή της επίδρασης τόσο της κυματικής διάδοσης (αφού τα παραγόμενα μήκη των κυμάτων εξαρτώνται από τις διαστάσεις της κοιλάδας) καθώς και της 1-διάστατης εδαφικής ενίσχυσης αφού ο λόγος των συχνοτήτων διέγερσης/εδαφικού προφίλ παραμένει σταθερός . Η αδιάστατη αυτή παράμετρος χ είναι δυνατόν να θεωρηθεί ως μέτρο της «ικανότητας» των παραγόμενων σεισμικών κυμάτων να "αντιληφθούν" την διδιάστατη γεωμετρία της κοιλάδας. Στη λογική αυτήν, χαμηλές τιμές του λόγου χ

είναι ενδεικτικές μικρού μήκους κύματος σχετικά με τις διαστάσεις της κοιλάδας, που οδηγεί σε αυξημένη ικανότητα αντίληψης της γεωμετρίας και επομένως αναπαραγωγής των κυματικών ανακλάσεων που είναι δυνατόν να δημιουργηθούν λόγω αυτής. Η σύγκριση των αναλύσεων για μία συγκεκριμένη τιμή του λόγου χ σε αδιάστατους όρους απεικονίζεται στο **Σχήμα 5.4β**.

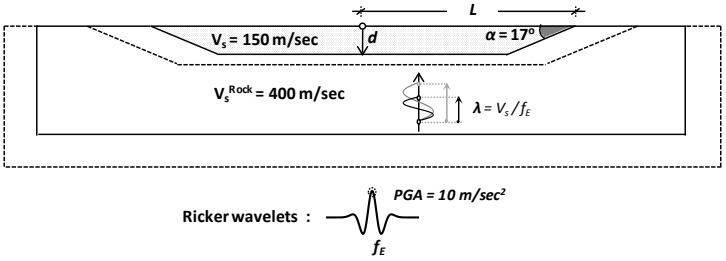

χ	Γεωμετρίες Κοιλάδας		
	τύπου 1 [L, d] = [260, 24]	*τύπου 2* [L, d] = [390, 36]	*τύπου 3* [L, d] = [520, 48]
6.25	f_E = 1 Hz	f_E = 0.67 Hz	f_E = 0.5 Hz
3.125	f_E = 2 Hz	f_E = 1.33 Hz	f_E = 1 Hz
2	f_E = 3 Hz	f_E = 2 Hz	f_E = 1.5 Hz

(α)

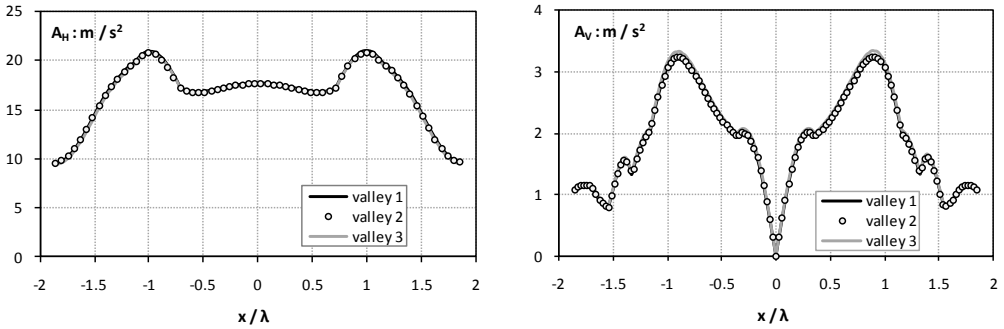

(β)

Σχήμα 5.3: Διαστατική ανάλυση με θεώρηση *ελαστικής* απόκρισης του εδαφικού υλικού της κοιλάδας: (**α**) εξετασθείσες γεωμετρίες και ομοδοποίηση αυτών βάσει του συντελεστή $\chi = \lambda / d$, και (**β**) τυπικό αποτέλεσμα της διαστατικής ανάλυσης (χ = 6.25).

Μή Γραμμική Συμπεριφορά

Θεωρώντας μή γραμμική την συμπεριφορά του εδάφους, η αδιαστατοποίηση θα πρέπει πλέον να λαμβάνει υπόψιν πέραν των ανωτέρω (διατήρηση σταθερού λόγου

$\chi = \lambda/D$) καί την αντοχή του εδαφικού υλικού. Ως εκ τούτου, προκειμένου να αδιαστατοποιηθεί επιτυχώς το μή γραμμικό πρόβλημα, απαιτείται ο λόγος των αντοχών των δύο προφίλ (S_{u1}/S_{u2}) να ισούται με τον λόγο των διαστάσεων των δύο κοιλάδων (D_1/D_2). **Το Σχήμα 5.4** επιβεβαιώνει την επιτυχή αδιαστατοποίηση του προβλήματος τόσο σε όρους χωρικής κατανομής των συντελεστών επιδείνωσης, όσο και χρονοϊστοριών των δύο συνιστωσών της επιτάχυνσης στο σημείο Α.

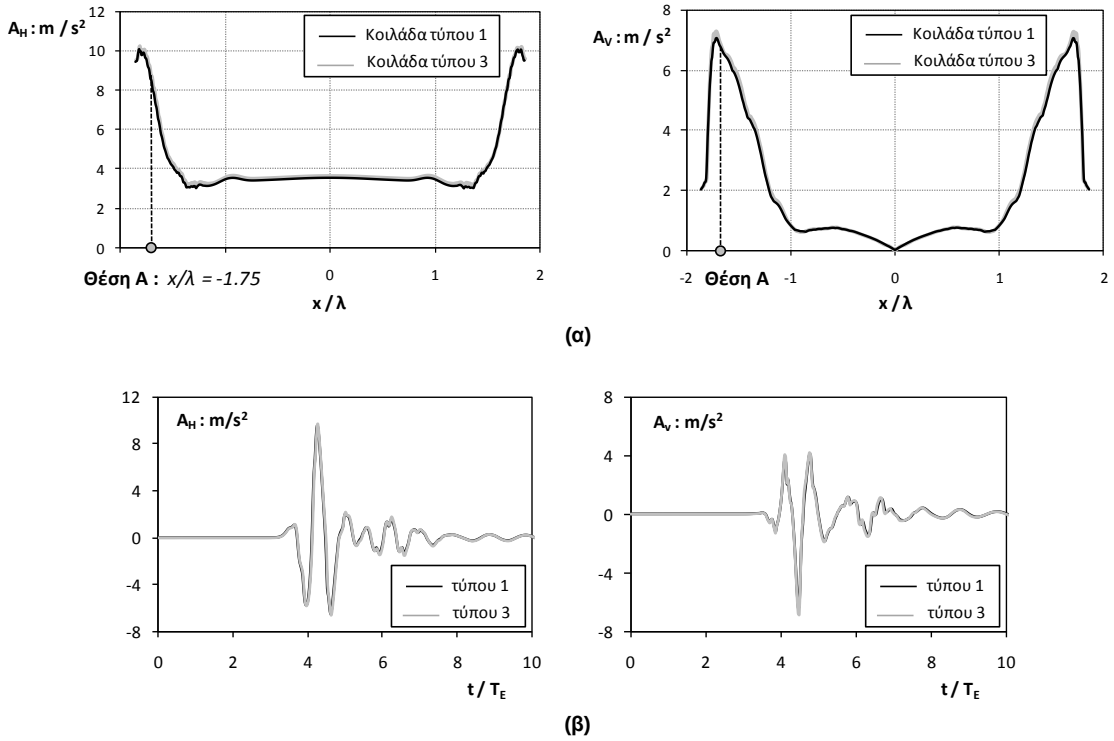

Σχήμα 5.4: Διαστατική ανάλυση με θεώρηση *ανελαστικής* εδαφικής απόκρισης. Τα αποτελέσματα παρουσιάζονται σε όρους (**α**) χωρικής κατανομής των μεγίστων επιταχύνσεων (οριζοντίων και κατακορύφων) και (**β**) χρονοϊστοριών επιταχύνσεων στην θέση Α.

5.4 Απόκριση Πλαισιωτής Κατασκευής σε Διέγερση Επηρεασμένη από Φαινόμενα Κοιλάδας

Μελετάται με χρήση πεπερασμενών στοιχείων η σεισμική συμπεριφορά ενός ρεαλιστικώς απλού πλαισίου εξ ωπλισμένου σκυροδέματος θεμελιωμένου πλησίον

του άκρου κοιλάδας όπου η παρασιτική κατακόρυφη συνιστώσα είναι μεγάλη. Η επίλυση/ανάλυση διενεργείται σε 2 στάδια :

(i) αρχικώς υπολογίζεται η επιφανειακή απόκριση της κοιλάδας χωρίς την παρουσία του πλαισίου σε αποκλειστικώς οριζόντια διέγερση στο βραχώδες υπόβαθρο

(ii) Οι παρογόμενες χρονοϊστορίες οριζόντιας και παρασιτικής κατακόρυφης επιτάχυνσης του πρώτου σταδίου (στην θέση θεμελιώσεως του πλαισίου) χρησιμοποιούνται ως διέγερση ενός αποζευγμένου προσομοιώματος το οποίο περιλαμβάνει μόνον το έδαφος εγγύς του πλαισίου.

Για να ποσοτικοποιηθεί η επίδραση της παρασιτικής κατακόρυφης συνιστώσας, συγκρίνεται η απόκριση του πλαισίου υποβαλλομένου στην οριζόντια μόνον συνιστώσα της επιτάχυνσης με την απόκριση του πλαισίου υποβαλλομένου στην συνδυασμένη οριζόντια και παρασιτική-κατακόρυφη συνιστώσα. Για λόγους πληρότητας παρατίθενται και τα αποτελέσματα από την δυναμική ανάλυση του πλαισίου επί του αυτού εδαφικού προφίλ, θεωρώντας συνθήκες ελευθέρου πεδίου (δηλ. ανεπηρέαστου από φαινόμενα κοιλάδας).

Επιζήμια επίδραση της Παρασιτικής Κατακόρυφης Συνιστώσας : Μηχανισμοί

Αποτέλεσμα της σύγχρονης με την οριζόντια παρασιτικής κατακόρυφης συνιστώσας είναι, ανάλογα με τη φορά της φόρτισης άλλοτε η μείωση κι άλλοτε η αύξηση του αξονικού φορτίου των υποστυλωμάτων. Αμφότερα τα φαινόμενα είναι πιθανόν να είναι ιδιαιτέρως επιβλαβή για την κατασκευή όπως εξηγείται παρακάτω.

Αύξηση του Αξονικού Φορτίου

Στο **Σχήμα 5.4** απεικονίζονται συγκριτικά οι παραμορφωμένοι κάνναβοι-αποτελέσματα των δυναμικών αναλύσεων του πλαισίου (ισοϋψείς πλαστικών παραμορφώσεων). Απουσία της παρασιτικής συνιστώσας το πλαίσιο αποκρίνεται στην επιβαλλόμενη ισχυρή σεισμική διέγερση μέσω κυρίως ανασηκώματος από το έδαφος θεμελιώσεως, με αποτέλεσμα τον περιορισμό του αδρανειακού φορτίου που μεταφέρεται από την θεμελίωση στην ανωδομή. Ο παλμός της οριζόντιας επιτάχυνσης προκαλεί στροφή των δύο θεμελίων και, φυσικά, κινηματικού χαρακτήρα καταπόνηση της ανωδομής. Όταν ωστόσο ο παλμός αυτός συνοδεύεται από έναν "συγχροτισμένο" κατακόρυφο παλμό, αυξάνει το (μεταφερόμενο μέσω της αξονικής δύναμης του υποστυλώματος) κατακόρυφο φορτίο του θεμελίου **(Σχήμα 5.4α)** την χρονική στιγμή t = 3.8 s. Ετσι, το ανασήκωμα του τελευταίου περιορίζεται ή και ακυρώνεται. Όντως, την χρονική στιγμή αυτήν η στροφή του δεξιού θεμελίου μειώνεται κατά 80% (**Σχ. 5.4β** γκρί γραμμή) σε σχέση με την τιμή της απουσία κατακόρυφης συνιστώσας— επιβεβαίωση της αδυναμίας του θεμελίου να ανασηκωθεί. Ως εκ τούτου, το υποστύλωμα αποκρίνεται στην επιβαλλόμενη σεισμική ένταση καμπτικά, όπως ξεκάθαρα φαίνεται και στα παραχθέντα διαγράμματα ροπής καμπυλότητας του υποστυλώματος (**Σχήμα 5.4γ).** Όπως μάλιστα προκύπτει από την σύγκριση των τριών περιπτώσεων που απεικονίζονται, έαν είχαμε αγνοήσει την παρασιτική κατακόρυφη συνιστώσα, θα συμπεραίναμε εσφαλμένα ότι η "κοιλαδική" ενίσχυση δεν προκαλεί ουσιώδη επιδείνωση της καταπόνησης του πλαισίου: αύξηση μόλις κατά 10% της αναπτυσσόμενης καμπυλότητας στο υποστύλωμα σε σχέση με την καμπυλότητα υπό συνθήκες ελευθέρου πεδίου.

Μείωση του Αξονικού Φορτίου

Οι πιθανές επιπτώσεις της μείωσης του αξονικού φορτίου εξαιτίας της παρασιτικής κατακόρυφης συνιστώσας επεξηγούνται στο **Σχήμα 5.5**. Η βασική συνέπεια ενός "συγχροτισμένου" παλμού κατακόρυφης επιτάχυνσης με φορά προς τα κάτω, είναι η δυνητική απώλεια της επαφής θεμελίου-εδάφους. Πιθανό αποτέλεσμα: μία κινηματικώς αναπτυσσόμενη μόνιμη παραμόρφωση του υποστυλώματος όπως επεξηγείται παρακάτω. Ιδού γιατί: Συνεπεία της δράσης του κύριου οριζόντιου παλμού το αξονικό φορτίο του αριστερού θεμελίου είναι μειωμένο λόγω της λικνιστικής παραμόρφωσης του πλαισίου την στιγμή εκείνη δέχεται ταυτόχρονα την αδρανειακή δύναμη ενός κατακόρυφου παλμού φοράς προς τα άνω. Ο τελευταίος οδηγεί σε στιγμιαία πλήρη αποκόλληση του θεμελίου από το έδαφος, όπως μαρτυρούν και οι θετικές τιμές της αξονικής δύναμης (**Σχήμα 5.6α**). Μετά την επανεπαφή του με το έδαφος το θεμέλιο έχει πλέον μετατεθεί ελαφρώς προς τα αριστερά σε σχέση με την αρχική του θέση ενώ το δεξιό θεμέλιο έχει παραμείνει αμετακίνητο στην οριζόντια διεύθυνση (**Σχήμα 5.6β**): συνέπεια, η μή-αναστρέψιμη παραμόρφωση του υποστυλώματος. Η τελευταία αντανακλάται στην παραμένουσα καμπυλότητα του υποστυλώματος η οποία απεικονίζεται στο **Σχήμα 5.6γ,** φυσικά δε διατηρείται καί κατά τους επόμενους κύκλους φόρτισης.

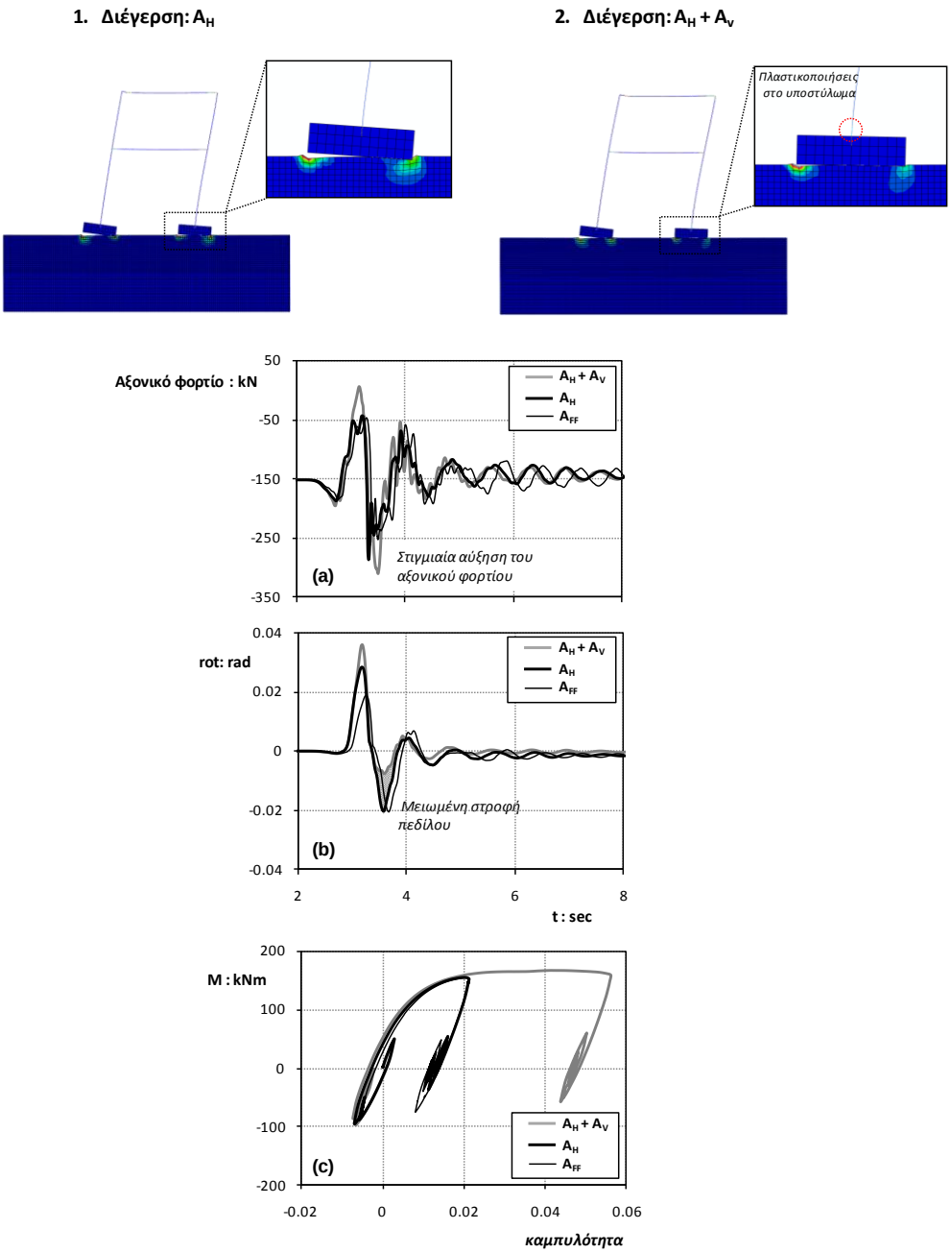

Σχήμα 5.5: Πλαίσιο επί μεμονομένων πεδίλων διεγειρόμενο από (1) μόνον οριζόντια επιτάχυνση και (2) ταυτόχρονη δράση οριζόντιας και κατακόρυφης (παρασιτικώς αναπτυσόμενης στα όρια κοιλαδικού σχηματισμού) επιτάχυνσης. Η ταυτόχρονη παρουσία της κατακόρυφης επιτάχυνσης (**α**) αυξάνει έστω και στιγμιαία το αξονικό φορτίο στο δεξιό υποστύλωμα (**β**) εμποδίζοντας το ανασήκωμά του και (**γ**) προκαλώντας σημαντικές πλαστικοποιήσεις (αυξημένες απαιτήσεις καμπυλότητας)

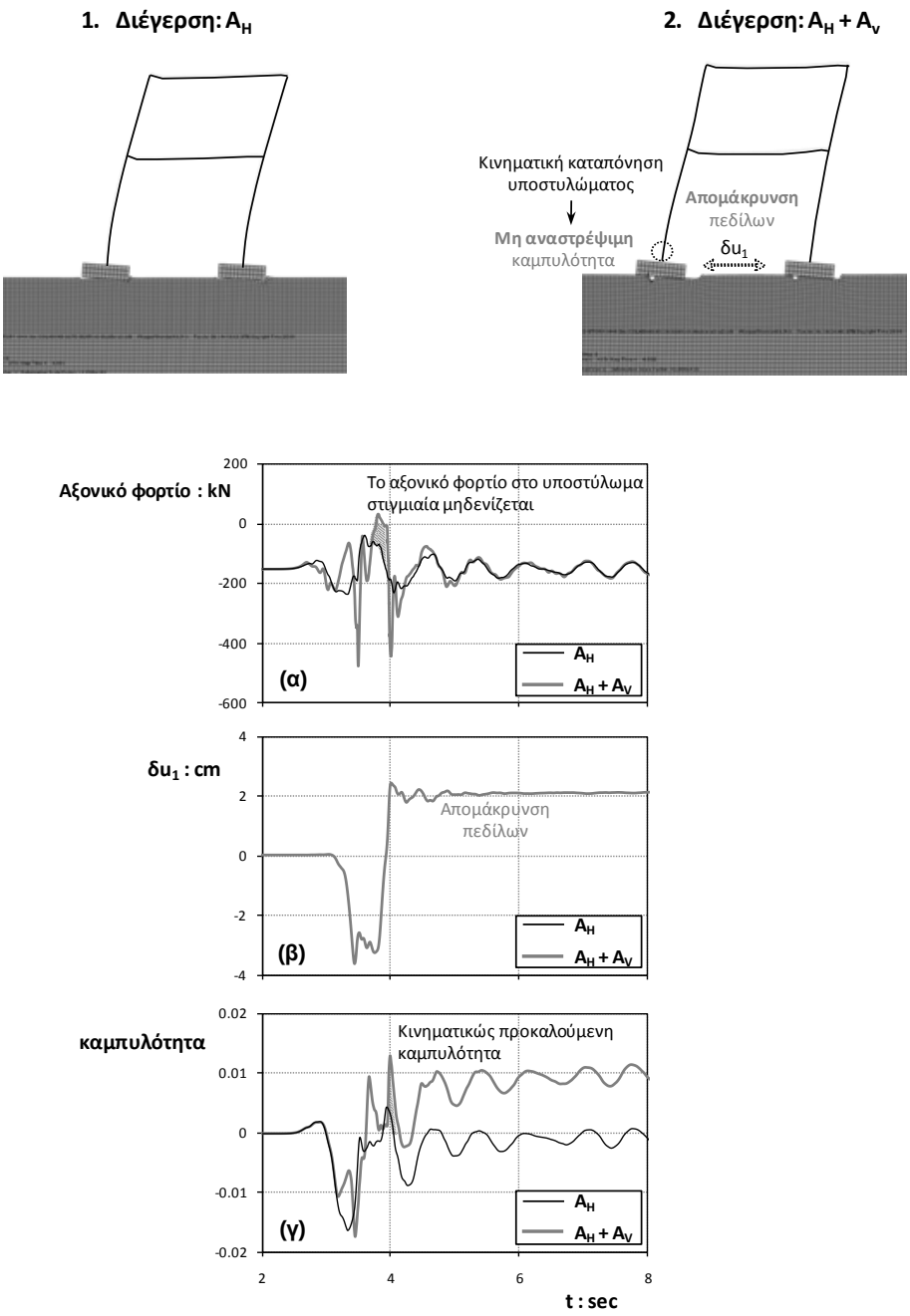

Σχήμα 5.6: Πλαίσιο επί μεμονομένων πεδίλων διεγειρόμενο από (1) μόνον οριζόντια επιτάχυνση και (2) ταυτόχρονη δράση οριζόντιας και κατακόρυφης (παρασιτικώς αναπτυσόμενης στα όρια κοιλαδικού σχηματισμού) επιτάχυνσης. Η ταυτόχρονη παρουσία της κατακόρυφης επιτάχυνσης (με κατεύθυνση προς τα πάνω) (**α**) μηδενίζει έστω και στιγμιαία το αξονικό φορτίο στο αριστερό υποστύλωμα. (**β**) Όταν το πέδιλο ανακτά εκ νέου επαφή με το έδαφος έχει ελαφρώς μετατοπιστεί σε σχέση με την αρχική του θέση. **(γ)** αυξάνοντας σημαντικά τις απαιτήσεις πλασιμότητας του αριστερού υποστυλώματος

Πλαίσιο Υποβαλλόμενο σε Καταγραφείσες Διεγέρσεις

Για επιβεβαίωση των ανωτέρω σχετικά με την επιζήμια επιρροή της παρασιτικής κατακόρυφης συνιστώσας στην σεισμική απόκριση του πλαισίου, παρουσιάζονται στην ενότητα αυτήν τα αποτελέσματα από την δυναμική ανάλυση του πλαισίου υποβαλλομένου πλέον σε δύο πραγματικούς σεισμικούς κραδασμούς: το ήπιας έντασης επιταχυνσιογράφημα της Καλαμάτας (σεισμός 1986) και το ισχυρό επιταχυνσιογράφημα Tabas (σεισμός Iran, 1978). Όπως γίνεται αντιληπτό, για την ήπιας έντασης διέγερση **(Σχήμα 5.7),** η συμπεριφορά του πλαισίου είναι ουσιαστικά ελαστική και η ύπαρξη της κατακόρυφης συνιστώσας δεν επηρεάζει την απόκρισή του. Αντιθέτως, τα φαινόμενα είναι εντονότερα όταν η κοιλάδα διεγείρεται από το ισχυρό επιταχυνσιογράφημα του Tabas **(Σχήμα 5.8α**), το οποίο παράγει στα άκρα της κοιλάδας (όπου και η θεμελίωση του πλαισίου) τις χρονοϊστορίες οριζόντιας και κατακόρυφης επιτάχυνσης του **Σχήματος 5.8β**. Η επιδείνωση της συμπεριφοράς λόγω της παρασιτικής κατακόρυφης συνιστώσας είναι εμφανής: δραματική αύξηση της καμπτικής επιπόνησης, εξαιρετικά αυξημένη καμπυλότητα στο υποστύλωμα, και διαφορική σχετική μετάθεση ορόφου ενδεικτική πλήρους αστοχίας του πλαισίου.

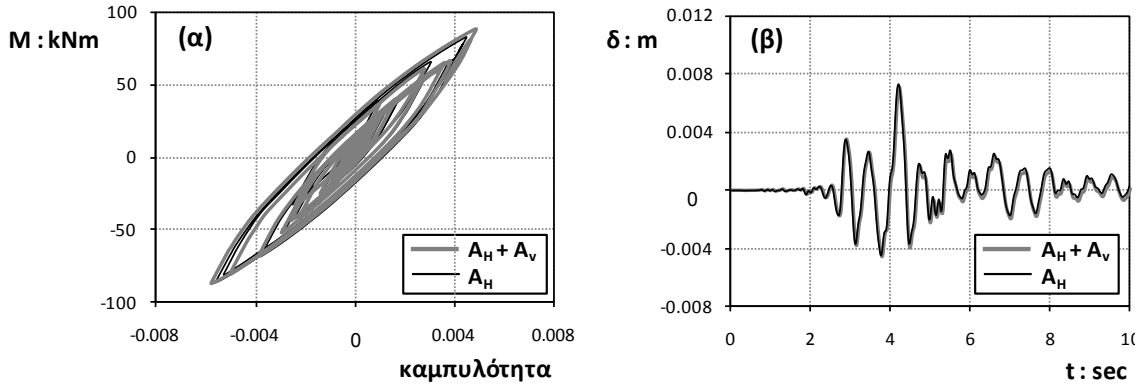

Σχήμα 5.7: Συγκριτική απόκριση πλαισίου διεγειρομένου από αποκλειστικώς οριζόντια επιτάχυνση (μαύρη γραμμή) και από ταυτόχρονη δράση οριζόντιας και κατακόρυφης επιτάχυνσης (γκρι γραμμή): (**α**) ροπή καμπυλότητα στην βάση του υποστυλώματος και (**β**) διαφορική οριζόντια μετακίνηση ισογείου. Διέγερση: Καλαμάτας, 1986.

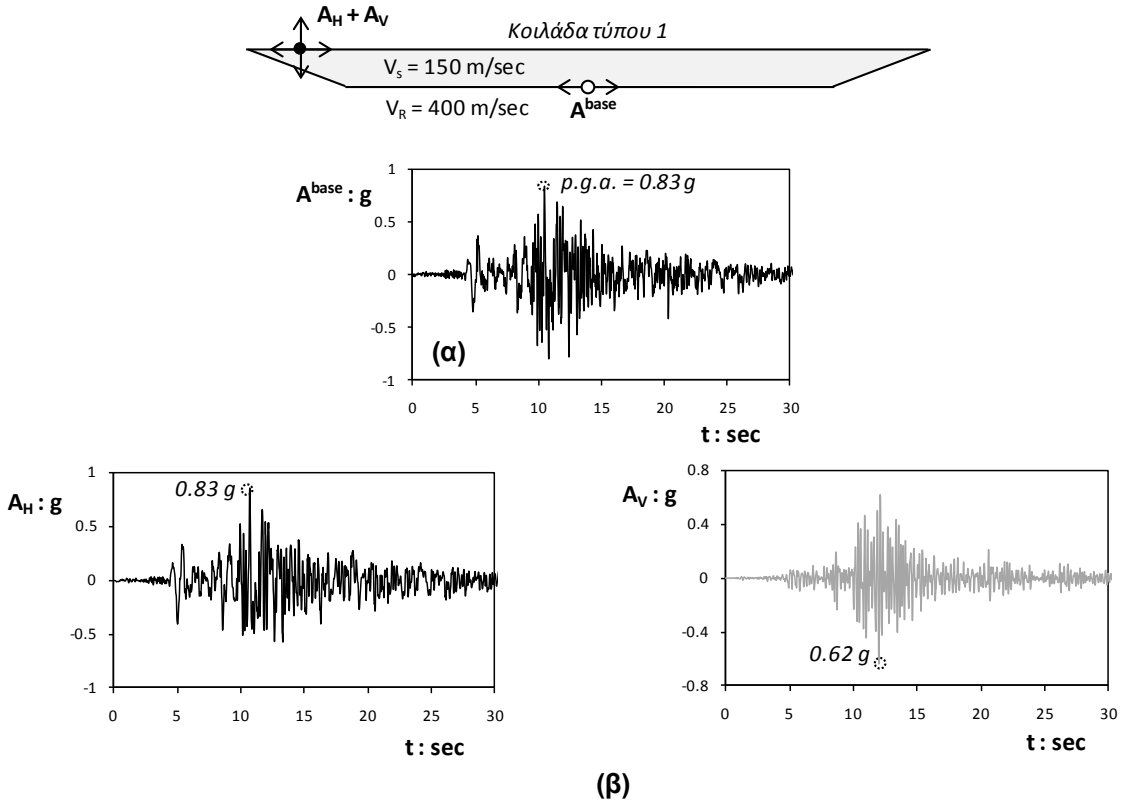

Σχήμα 5.8: (α) Κοιλάδα τύπου 1 διεγειρόμενη από την οριζόντια επιτάχυνση της καταγραφής Dayhook στον σεισμό του Tabas (1978) και (β) χρονοϊστορίες οριζόντιας (μαύρη) και κατακόρυφης (γκρι γραμμή) επιτάχυνσης στην θέση της μέγιστης κατακόρυφης συνιστώσας.

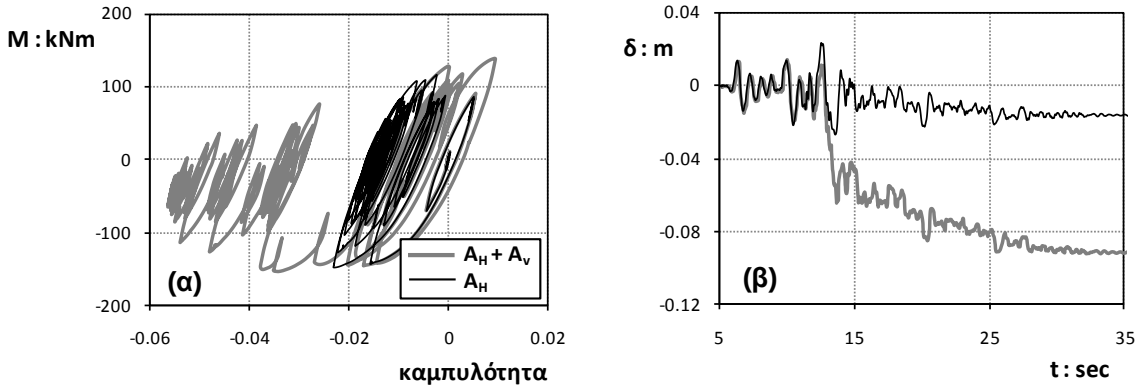

Σχήμα 5.9: Συγκριτική απόκριση πλαισίου διεγειρόμενου από αποκλειστικώς οριζόντια επιτάχυνση (μαύρη γραμμή) και από ταυτόχρονη δράση οριζόντιας και κατακόρυφης επιτάχυνσης (γκρι γραμμή): (**α**) Διάγραμμα ροπής-καμπυλότητας στην βάση του υποστυλώματος, και (**β**) χρονοϊστορία διαφορικής οριζόντιας μετακίνησης ισογείου. Διέγερση: Καταγραφή Tabas (Ιράν, 1978).

Βιβλιογραφία

Ελληνικός Αντισεισμικός Κανονισμός ΕΑΚ (2000) ΥΠΕΧΩΔΕ, Αθήνα, Ελλάδα

Ελληνικός Κανονισμός Ωπλισμένου Σκυροδέματος (2000) ΥΠΕΧΩΔΕ, Αθήνα, Ελλάδα

Allotey N.K., El Naggar M.H. (2008), "An investigation into the Winkler modeling of the cyclic response of rigid footings", *Soil Dynamics and Earthquake Engineering*, 28(1), pp. 44–57.

Anastasopoulos I., Gazetas G., Loli M., Apostolou M, Gerolymos N. (2010a), "Soil Failure can be used for Earthquake Protection of Structures", *Bulletin of Earthquake Engineering*, Vol. 8, p.p. 309-326.

Bao H., Bielak J., Ghattas O., Kallivokas L.F., O' Hallaron D.R., Shewchuk J., & Xu J. (1996), "Earthquake ground motion modeling on parallel computers", *Proceedings of ACM/IEEE Supercomputing Conference*, Pittsburgh, USA.

Bard P.Y. & Bouchon M.A. (1980), "The seismic response of sediment filled valleys. Parts 2. The Case of incident P and SV waves", *Bulletin of the Seismological Society of America*, Vol.70, No. 5, pp. 1921-1941.

Bard, P. Y. and Bouchon, M. (1985). "The two-dimensional resonance of sediment-filled valleys", *Bull. Seism. Soc. Am.*, 75, 519-541.

Bielak J., Hisada Y., Bao H., Xu J & Ghattas O. (2000), "One - vs two - or three-dimensional effects in sedimentary valleys", *Proceedings of the 12th World Conference on Earthquake Engineering*, New Zealand.

Bielak J., Xu J. & Ghattas O. (1999), "Earthquake Ground motion and Structural Response in alluvial Valleys", *Journal of Geotechnical and Geoenviromental Engineering*, Vol. 125, No. 5, pp. 413-423.

Bransby M.F. (2001), "Failure envelopes and plastic potentials for eccentrically loaded surface footings on undrained soil", *International Journal for Numerical and Analytical Methods in Geomechanics*, 25, pp. 329-346.

Chatzigogos C.T., Pecker A., Salencon J. (2009), "Macroelement modeling of shallow foundations", *Soil Dynamics and Earthquake Engineering*, Vol. 29, No. 6, pp. 765–781.

Einav I., Puzrin A.M, Houlsby G.T. (2003), "Continuous Hyperplastic Models for Overconsolidated Clays", *Mathematical and Computer Modelling, special issue on Mathematical Models in Geomechanics*, Proceedings of symposium at Scilla di Reggio Calabria, 19-22 September, Vol. 37, No. 5/6, pp 515-523

Faccioli E., Paolucci R., Vivero G. (2001), "Investigation of seismic soil–footing interaction by large scale cyclic tests and analytical models", Proceedings, *4th International Conference on Recent Advances in Geotechnical Earthquake Engineering and Soil Dynamics*, S. Prakash (Ed.), Paper no. SPL-5, San Diego, CA.

Fan K., "*Seismic Behavior of Pile Groups*", (1992), PhD Thesis, SUNY at Buffalo.

Fardis, N., Georgarakos, P., Gazetas, G., & Anastasopoulos, I. (2003), "Sliding Isolation of Structures: Effect of Horizontal and Vertical Acceleration", *Proceedings of the FIB International Symposium on "Concrete Structures in Seismic Regions"*, Athens, Greece (in CD-Rom).

Fishman K. L. & Ahmad S., (1995), "Seismic response for alluvial valleys subjected to SH, P and SV waves", *Soil Dynamics and Earthquake Engineering*, Vol. 14, pp. 249-258.

Gajan S., Kutter B.L., Phalen J.D., Hutchinson T.C., Martin G.R. (2005), "Centrifuge modeling of load-deformation behavior of rocking shallow foundations", *Soil Dynamics and Earthquake Engineering*, 25, pp. 773–783

Gajan, S. & Kutter, B. L. (2008), "Capacity, settlement, and energy dissipation of shallow footings subjected to rocking", *Journal of Geotechnical and Geoenvironmental Engineering*, ASCE, 134 (8), pp 1129-1141.

Gajo, A., & Muir Wood, D. A.,(1999), "Kinematic hardening constitutive model for sands: a multiaxial formulation", *International Journal of Numerical and Analytical Methods in Geomechanics*, Vol 23, pp. 925–65.

Gazetas G., Apostolou M., and Anastasopoulos I. (2003), "Seismic Uplifting of Foundations on Soft Soil, with Examples from Adapazari (Izmit 1999, Earthquake)", *BGA International Conference on Foundation Innovations, Observations, Design & Practice*, Univ. of Dundee, Scotland, September 25, pp. 37–50.

Gazetas, G., Anastasopoulos, I., Apostolou, M., (2007), "Shallow and deep foundations under fault rupture or strong seismic shaking", *4th International Conference on Earthquake Geotechnical Engineering*, Thessaloniki, Greece.

Gerolymos N., Gazetas G., Tazoh T. (2005), "Seismic Response of Yielding Pile in Non-Linear Soil", *Proc. 1st Greece –Japan Workshop, Seismic Design, Observation, and Retrofit of Foundations*, pp. 25-36, Athens 11-12 October.

Gourvenec S. (2007), "Shape effects on the capacity of rectangular footings under general loading", *Géotechnique*, 57(8), pp. 637–646.

Harden, C., Hutchinson, T. (2006), "Investigation into the Effects of Foundation Uplift on Simplified Seismic Design Procedures", *Earthquake Spectra*, 22 (3), pp. 663–692.

Harmsen S., & S. Harding, (1981), "Surface Motion over a sedimentary valley for incident plane P and SV waves", *Bulletin of the Seismological Society of America*, Vol. 71, No. 3, pp. 655-67

Hill J., BENZ H., Murphy M., & G. Schuster,(1990), "Propagation and Resonance of the SH waves in the Salt Lake Valley, Utah", *Bulletin of the Seismological Society of America*, Vol. 80, No. 1, pp. 23-42.

Houlsby G.T. (1986), "A General Failure Criterion for Frictional and Cohesive Materials", *Soils and Foundations*, Vol. 26, No. 2, pp 97-101.

Houlsby G.T. & Puzrin A.M. (2006), "*Principles of Hyperplasticity*", Springer : Berlin.

Hudson M., Idriss I.M., and Beikae M. (1994), *QUAD4M*—A computer program to evaluate the seismic response of soil structures using finite element procedures and incorporating a compliant base, Center for Geotechnical Modeling, Dept. of Civil and Environmental Engineering, Univ. of Calif., Davis.

Ishibashi,I. and Zhang, X. (1993), "Unified dynamic shear moduli and damping ratios of sand and clay", *Soils and Foundations*, Vol. 33(1), pp. 12-191.

Jefferies M.G. (1993), "Nor-sand: A simple critical state model for sand", *Géotechnique*, Vol. 43, pp. 91–103.

Jeremic B., Runesson K., and Sture S. (1999), "A model for elastic-plastic pressure sensitive materials subjected to large deformations", *International Journal of Solids and Structures,* 36, 31/32, pp 4901-4918.

Kavvadas M. and A. Amorosi, (2004), "A constitutive model for structured soils", *Geotechnique*, Vol 50, No 1, pp 263-273.

Kawashima K., Nagai T., Sakellaraki D. (2007), "Rocking Seismic Isolation of Bridges Supported by Spread Foundations", *Proc. of 2nd Japan-Greece Workshop on Seismic Design, Observation, and Retrofit of Foundations*, April 3-4, Tokyo, Japan, pp. 254–265.

Kutter B.L, Martin G., Hutchinson T.C., Harden C., Gajan S., Phalen J.D. (2003), "Status report on study of modeling of nonlinear cyclic load–deformation behavior of shallow foundations", *University of California, Davis, PEER Workshop*.

Makris, N., & Roussos, Y., (1998), ‘‘Rocking response and overturning of equipment under horizontal pulse-type motions.’’ *Rep. No. PEER- 98/05, Pacific Earthquake Engrg. Res. Ctr.*, University of California, Berkeley, California.

Moczo, P., Labfik, P., Kristek, J, and . Hron (1996), “Amplification and Differential Motion due to an Antiplane 2D Resonance in the Sediment Valleys Embedded in a Layer over the Half-Space”, *Bulletin of the Seismological Society of America*, Vol. 86, No. 5, pp. 1434-1446

NEHRP Commentary on the Guidelines for the Seismic Rehabilitation of Buildings, FEMA publication 274; October 1997.

Paolucci R, Pecker A., (1997) “Seismic bearing capacity of shallow strip foundation on dry soils”, *Soils and Foundations*; Vol. 37(3), pp. 95-105.

Paolucci R., Shirato M., Yilmaz M.T. (2008), “Seismic behaviour of shallow foundations: Shaking table experiments vs numerical modeling”, *Earthquake Engineering and Structural Dynamics*, Vol. 37, pp. 577–595.

Pecker A. & Pender M.J., (2000), “Earthquake Resistant Design of Foundations: New Construction”, Invited paper, *GeoEng2000*, Vol 1, pp. 313-332.

Pestana J.M. (1994), “*A unified constitutive model for clays and sands”*, Sc.D. Thesis, Department of Civil & Environmental Engineering, Massachusetts Institute of Technology, Cambridge, MA.

Pestana J.M., and Whittle A.J. (1995), “Compression model for cohessionless soils”, *Géotechnique*, Vol. 45, No. 4, pp. 611-631.

Pestana J.M., and Whittle A.J. (1999), "Formulation of a unified constitutive model for clays and sands", *Int. Journal for Numerical and Analytical Methods in Geomechanics*, 23, pp. 1215-1243.

Prévost, J.H., (1980) "Mechanics of Continuous Porous Media", *International Journal of Engineering Science*, 18 (5), pp. 787-800

Priestley, M.J.N., Calvi G.M., Kowalsky M.J. (2007) "*Displacement-Based Seismic Design of Structures*" IUSS Press, ISBN 88-6198-000-6

Priestley, M.J.N., Seible, F. and Calvi, G.M. (1996), "*Seismic Design and Retrofit of Bridges"*, John Wiley and Sons, New York.

Psarropoulos P.N., Tazoh T., Gazetas G., & Apostolou M. (2007), "Linear and Nonlinear Valley Amplification Effects on Seismic Ground Motion", *Soils and Foundations*, Vol. 47, No. 5, pp. 857-871.

Puzrin, A.M. and Houlsby, G.T. (2001a), "Strain-based plasticity models for soils and the BRICK model as an example of the hyperplasticity approach", *Géotechnique*, Vol. 51, No. 2, pp 169-172

Puzrin, A.M. and Houlsby, G.T. (2001b), "Fundamentals of Kinematic Hardening Hyperplasticity", *International Journal of Solids and Structures*, Vol. 38, No. 21, pp 3771-3794

Puzrin, A.M. and Houlsby, G.T. (2001c) "On the Non-Intersection Dilemma in Multi-Surface Plasticity", *Géotechnique*, Vol. 51, No. 4, pp 369-372

Sánchez-Sesma F.J. & Luzón F. (1995), "Seismic response of three-dimensional alluvial valleys for incident P, S, and Rayleigh waves", *Bulletin of the Seismological Society of America*, Vol. 85, No. 1, pp. 269-284.

Sánchez-Sesma, F. J., Chavez-Garcia F., & Bravo M.A. (1988), "Seismic response of a class of alluvial valley for incident SH waves", *Bulletin of the Seismological Society of America*, Vol.78, No.1, pp. 83-95.

Taiebat H.A., and Carter J.P. (2002), "Bearing capacity of strip and circular foundations on undrained clay subjected to eccentric loads", *Géotechnique*, 52(1), pp. 61–64.

Tazoh T., Dewa K., Shimizu K., & Shimada M. (1984), "Observations of earthquake response behavior of foundation piles for road bridge", *Proceedings of the 8th World Conference on Earthquake Engineering*, Vol. 3, pp. 577-584.

Tazoh T., Shimizu K. & Wakahara (1988), "Seismic observations and analysis of grouped piles", *Shimizu Technical Research Bulletin*, Vol. 7, pp. 17-32.

Trifunac M.D., (1971), "Surface motion of a semi-cylindrical alluvial valley for incident plane SH waves", *Bulletin of the Seismological Society of America*, Vol. 61, pp. 1755-1770.

Vintzilaiou E., Tassios T.P., Chronopoulos M. (2007) "Experimental validation of seismic code provisions for RC columns", *Engineering Structures,* 29, p.p., 1153-1164

Whittle A.J. and M. Kavvadas, (1994),"Formulation of the MIT-E3 constitutive model for overconsolidated clays", *Journal of the Geotechnical Engineering Division*, ASCE, Vol 120, No 1, pp 173-198.

Wong H.L. & Trifunac M.D. (1974), "Surface motion of a semi-elliptical alluvial valley for incident plane SH waves", *Bulletin of the Seismological Society of America*, Vol. 64, No. 5, pp. 1389-1408.

Zhang J., Makris N. (2001), "Rocking response of free-standing blocks under cycloidal pulses", *Journal of Engineering Mechanics*, ASCE, 127 (5), pp. 473–483.

TABLE OF CONTENTS

CHAPTER 4: Simplified Method for Foundation Design of Rocking–isolated Frames

CHAPTER 5: Seismic Wave Propagation in a Very Soft Alluvial Valley :

Sensitivity to Soil Nonlinearity, Generation of Parasitic Vertical Component

Introduction—Motivation of the Study

A growing population of pioneering researchers is currently pointing out the need of a skeptical look against the philosophy of current codes of practice. Performance based design (i.e. design based on acceptable displacements) is steadily gaining ground among structural engineers opposing the holistic applicability of the nowadays prevailing capacity design.

The latter accepts that structural damage is unavoidable and understands that the increase of structural strength is not always associated with increased safety levels. Therefore modern seismic design principles, aim to control seismic damage rather than to avoid it. Through proper reinforcement detailing it is intended to ensure that critical structural members can sustain loads that exceed their capacity without collapsing,

while failure *"is guided"* to less important structural members (beams instead of columns) and to non-brittle mechanisms (bending instead of shearing) [Park & Paulay, 1976].

On the other hand, a crucial goal of current seismic *foundation* design, particularly as entrenched in the respective codes [e.g. EC8], is to *avoid full mobilisation of strength* in the foundation by *"guiding"* failure to the superstructure. To this end, *over-strength* factors (capacity design) and (explicit and implicit) factors of safety larger than 1 are introduced against each of those “failure” modes.

Were the code provisions neglected, shallow foundations subjected to severe seismic shaking could experience detachment from the supporting soil due to the large overturning moments (arising from inertial and gravitational forces). The ensuing rotational uplift would possibly lead to a large increase of the imposed stresses on the soil under the edge of the footing. Yet, the occurrence of such an event does not necessarily imply failure — owing to the *cyclic* and *kinematic* nature of the seismic excitation: a bearing capacity “failure” mechanism may produce only a small rotation before the direction of motion is reversed.

Performance-based design in earthquake geotechnics (i.e., design on the basis of limiting the maximum and permanent displacements and rotations of facilities during the design earthquake) has its justification on the above consequences of the cyclic and kinematic character of motion. Thus, the concept of allowing significant *foundation uplifting* (implying a geometric nonlinearity) and mobilization of ultimate bearing capacity (implying material inelasticity) during strong shaking has been suggested in

recent years as a substantial deviation from the conventional design philosophy [e.g., FEMA-356, 2000]. In fact a significant body of pragmatic evidence provide a robust justification of the idea that allowing nonlinear-inelastic foundation response is not only unavoidable, but may even be beneficial [Paolucci, 1997; Pecker, 1998, 2003; Martin & Lam, 2000; Makris & Roussos, 2000; Comartin et al., 2000; Pecker & Pender, 2000; Faccioli et al., 2001; Kutter et al., 2003; Gazetas et al., 2003; 2007; Paolucci et al., 2008; Kawashima et al., 2007; Gajan & Kutter, 2008].

Motivated by, but certainly notwithstanding the controversial nature of the aforementioned concepts, this research will attempt to provide exploitable insight into the ***Metaplastic Response and Collapse of Frame–Foundation Systems, and the Concept of Rocking Isolation***, in honest hope that results may be functional both in the design of new and the upgrading of existing structures.

1

Literature Review

1.1 From Conventional SSI analysis to Non-Linear Design of Foundations

The need to assess Soil, Foundation and Structure Non-Linearity

The dynamic response of structures under strong ground shaking and the associated complex soil-structure interaction phenomena have been thoroughly investigated over the last 40 years. One of the important contributions was that of *Jennings and Bielak in 1973,* who studied how soil compliance may influence the seismic response of super-structures. A comprehensive description of the state-of-art information on the dynamic Soil-Structure interaction problem can be found in *Mylonakis, et al 2006*:

"During earthquake shaking, soil deforms under the influence of the incident seismic waves and ''carries'' dynamically with it the foundation and the supported structure. In turn, the induced motion of the superstructure generates inertial forces which result in dynamic stresses at the foundation that are transmitted into the supporting soil. Thus, superstructure-induced deformations develop in the soil while additional waves emanate

from the soil– foundation interface. In response, foundation and superstructure undergo further dynamic displacements, which generate further inertial forces and so on.

The above phenomena occur simultaneously. However, it is convenient (both conceptually and computationally) to separate them into two successive phenomena referred to as *''kinematic interaction''* and *''inertial interaction'' (Kausel et al 1976; Kramer, 1996; Stewart et al, 1999; Kim and Stewart, 2003)*, and obtain the response of the Soil–Foundation– Structure system as a superposition of these two interaction effects:

(a) ***"Kinematic interaction'' (KI)*** refers to the effects of the incident seismic waves to the system shown in **Fig. 1.1b**, which consists essentially of the foundation and the supporting soil, with the mass of the superstructure set equal to zero (in contrast to the complete system of **Fig. 1.1a**). The main consequence of KI is that it leads to a ''foundation input motion'' (FIM) which is different (usually smaller) than the motion of the free-field soil and, in addition, contains a rotational component. *Luco (1971), Elsabee et al. (1977), Harada et al. (1981), Tassoulas (1984), Wolf (1994)* have proposed some of the most widely used simple expressions for estimating the translational and rocking components of this foundation motion for both surface and embedded foundations and for different type of incident seismic waves. These expressions are of the form $U_G = U_A \times I(\omega)$ and correlate in the frequency domain the free-field motion U_A (that can be determined through 1-dimesional wave propagation analysis) with the experienced motion (translational or rocking) at the foundation level.

(b) ***''Inertial interaction'' (II)*** refers to the response of the complete Soil–Foundation–Structure system to the excitation by D'Alembert forces associated

with the acceleration of the superstructure due to the *KI* **(Fig. 1.1b).** For a surface or embedded foundation, II analysis is also conveniently performed in two steps, as shown in **Fig. 1.1c**: first compute the foundation dynamic impedance (''springs'' and ''dashpots'') associated with each mode of vibration, and then determine the seismic response of the structure and foundation supported on these springs and dashpots, and subjected to the kinematic accelerations $a_k(t)$ of the base. A number of analytical studies have been conducted to estimate the foundation impedance for each vibration mode. Among others *Richart et al (1970),* V*eletsos and Nair (1975), Kausel and Roesset (1975), Gazetas (1983)* studied the seismic interaction of structures on hysteretic foundations, *Luco (1974), Gazetas and Roesset (1976), Gazetas (1980), Wong and Luco (1985), Guzina and Pak (1998), Vrettos (1999),* extended the solutions to account for non-homogeneous soil profiles, while *Stokoe and Richart (1974), Novak (1985), Gazetas and Stokoe (1991), Gazetas (1991), and Gazetas and Mylonakis (1998)* provided both analytical solutions and experimental evidence on the dynamic response of an embedded foundation on a soil medium.

Despite the indisputable value of all the aforementioned studies in understanding the mechanisms of the complex Soil-Foundation-Structure interaction problem there is one significant assumption/limitation: the system is considered to behave elastically(i.e. the soil behaviour was idealized as a linear visco-elastic material, and the elastic structure is always considered to have full contact with the underlying soil). However, over the last years there is a growing awareness of the need to consider also non-linear soil structure interaction in the seismic analysis and design *(Paolucci 1997; Pecker, 1998, 2006;*

Apostolou and Gazetas; 2004, Gazetas et al, 2007; Pender; 2007). Three types of non-linearity at the soil-foundation level are recognized **(Figure 1.2)**. These are:

i. *Sliding at the soil-foundation interface* when the transmitted horizontal force exceeds the available frictional resistance. As pointed out by *Newmark (1965)*, under seismic conditions, due to the oscillatory nature of the loading, such an exceedance and the associated sliding it is not necessarily related with failure.

ii. *Seperation and Uplift of the Foundation,* when the seismic overturning moment exceeds the footing moment capacity. Since *1963 Housner* realized that this rocking oscillations may be particularly beneficial to the seismic response of the super-structure.

iii. *Plastification of the supporting soil,* which may considerably modify the experienced ground motion at the foundation level.

This urgent need to explicitly account for the aforementioned non-linear phenomena in the cotemporary earthquake design has emerged from:

(a) *The fact that the intensity of the recorded ground accelerations over the last 20 years had significantly exceeded the design accelerations*. [A few examples: the 1994 Northridge earthquake with an Ms of 6.8 and a maximum recorded P.G.A. of a = 0.98 g (Rinaldi 228 record); the 1995 Kobe earthquake (Ms = 7.2) with a maximum recorded acceleration of a= 0.85 g (JMA record); the 1986 San Salvador earthquake (Ms=5.6) and a =0.75g; the 2007 Niigata earthquake in northern Japan where an acceleration of a=1.20 g was recorded]. Under such a severe shaking, preventing the “plastic hinging” in the foundation system is a formidable task. And in fact, it may not even be desirable since enormous ductility demands would be imposed to superstructure. Alternatively, allowing inelastic soil-

foundation response might be beneficial for the superstructure by isolating the transmitted accelerations to the latter.

(b) *The need to seismically upgrading/retrofitting an older/traditional building*. A common procedure is by inserting a shear wall that will undertake most of the inertia-driven shear force. Yet, since the existing structural system is already carrying the vertical load, this newly added element will transmit a disproportionately large horizontal force and overturning moment onto the foundation. Accounting for soil-foundation inelasticities in the design of such a shear wall might be the only rational procedure: the conventional design that aims to increase the structural capacity by increasing the stiffness of some elements, unavoidably entails that the forces transmitted onto the foundation will also be increased, to the point that it might not be technically or economically feasible to undertake them "elastically".

(c) *A philosophical change being under way in structural earthquake engineering* **:** from strength-based design (involving force considerations) to performance-based design (involving displacement considerations). *Geotechnical* earthquake engineering has also been slowly moving in this direction **:** gravity retaining walls are indeed allowed to slide. It is therefore considered as appropriate for soil–foundation–structure interaction (SFSI) to also move from imposing "safe" limits on forces and moments acting on the foundation (aiming at avoiding pseudo-static "failure") to performance–based design in which all possible conventional "failure" mechanisms are allowed to develop, while ensuring that maximum and permanent displacements and rotations would be acceptable.

An increased amount of research has also been conducted further extending the principle of performance based design (which allows the non-linear behavior of structural members provided that specific displacement acceptance criteria are met) to even allowing for rocking of structural members during earthquake loading. A review of recent advances to non-linear structural design is attempted in the following paragraphs.

1.2 Performance Based Design

Structural seismic design has been undergoing a critical reappraisal in recent years, with the emphasis changing from “strength” to “performance”. While in conventional seismic design methods, the objective is to provide *life safety* (strength and ductility) and *damage control* (serviceability drift limits), the performance-based design is a more general philosophy in which the design criteria are expressed in terms of achieving stated performance objectives when the structure is subjected to stated levels of seismic hazard. In this direction the Structural Engineers Association of California [*SEAOC, 2000*] has defined the marriage of the structural performance and earthquake intensity as a ‘*Performance Level*’, and a suite of performance levels as a ‘*Performance Objective’*. Four performance levels are defined:

Fully Operational: Facility continues in operation with negligible damage.

Operational: Facility continues in operation with minor damage and minor disruption in nonessential services.

Life Safe: Life safety is substantially protected, damage is moderate to extensive.

Near Collapse: Life safety is at risk, damage is severe, structural collapse is prevented.

The relationship between these performance levels and earthquake design level is summarised in **Figure 1.3** (*OES, 1995*).

1.2.1 Force-Based Assesment

As the understanding on the importance of inelastic structural response under strong earthquake events increased, so did the necessity to accurately quantify the inelastic deformation capacity of structural components. Despite the wide-spread agreement that

inelastic time-history analysis is the most accurate approach of seismic design, the method is not yet mature enough for use by design professionals. To this end, a number of simple assessment approaches (generally based on push over analysis) have been developed over the years aiming to correlate the displacement demand of a specific earthquake to the displacement capacity of the structure and thus to estimate the expected structural damage without conducting full non-linear time-history analysis. Some of the most commonly used Force-Based Assessment approaches are described in the ensuing.

N2 Method

Fajfar et al (1997) provided an update on the N2 method. In this approach, the seismic displacement demand is estimated by response spectrum analysis of an equivalent single-degree-of-freedom (SDOF) bilinear model, representing the first elastic mode of the structure. This displacement demand is compared with the results of a push-over analysis of a multi-degree-of-freedom (MDOF) representation of the structure and with the use of a Park-Ang damage model local inelastic deformations are extracted.

Capacity Spectrum Method

The *Capacity Spectrum Method* (CSM) proposed by *Freeman (1998)* compares the capacity of a structure to resist lateral forces to the demands of earthquake response spectra in a graphical representation that allows a visual evaluation of how the structure will perform when subjected to earthquake ground motion. The structural capacity is represented by a lateral load force (V at the base of the building)-displacement (lateral roof displacement Δ_R) diagram that accounts for sequential yielding of structural elements as the structure is laterally displaced beyond its elastic limits. To be directly

comparable to demand response spectra, Δ_R and V are converted to a spectral set of coordinates (S_d and S_a respectively) by assuming the structure is of a single-degree-of freedom. Likewise the earthquake demand is also represented by a set of response spectra. To graphically estimate the earthquake demand on a structure, the capacity spectrum and the family of damped response spectra are plotted together on an ADRS format (i.e. S_a vs S_d coordinates with period T lines radiating from the origin) as illustrated in **Figure 1.4**. The intersection of the capacity spectrum with the appropriately damped response spectrum represents the estimated earthquake demand.

Fajfar (1998) has recently combined the two approaches, but using inelastic spectra, related to displacement-ductility demand, rather than equivalent viscous damping (see **Figure 1.5**). This presumes that the shape of the hysteretic response of the structure is irrelevant, or requires some modification to the demand for structures with non-structural hysteretic response.

1.2.2 Performance-based design Approches

A great amount of work has been conducted on the development of design procedures that aim to complement the conventional seismic design by addressing some performance based criteria.

Bertero and Zagajeski (1979) and *Fintel and Ghosh (1982)* proposed force-based code design for preliminary strength determination, with inelastic time-history analyses to check inelastic deformation. A similar approach was suggested by *Hatamoto et al (1990)* and *Stone and Taylor (1994)* for buildings and bridges respectively, but using local damage indices rather than inelastic deformation as the acceptance criteria. *Kappos (1997)* proposed a modified version of the aforementioned procedures specialized for

frame structures: beam strength is based on forces reduced from modal elastic analysis using code force-reduction factors, while column strength is based on the results of inelastic time-history analyses using code spectrum-compatible accelerograms. Capacity design principles are then employed to determine the required shear strength of members and joints. The time-history analyses are also used to check that storey drifts and local inelastic deformations are within acceptable limits. According to *Priestley (2000)* the procedure of Kappos might reduce some of the potential conservatism associated with capacity design of columns, but consequent savings are likely to be minimal, while it is also not clear that a MDOF modal analysis is a better starting point than a simple SDOF model for ductile structures, since it is clear that inelastic action primarily reduces the force levels associated with the first mode, while having comparatively minor effect on the higher modes. Thus a force-based design approach which applies a constant force-reduction factor to all modes is likely to greatly underestimate the importance of higher modes, which is implicitly accounted for in simplified capacity design procedures (*Paulay and Priestley, 1992*). *Fardis and Panagiotakos (1997*) suggested another simplified design procedure according to which seismic design forces for ductile elements are calculated for the serviceability level earthquake

1.3 Direct Displacement-Based Design Methodology

All the aforementioned methods despite their undisputable value in suggesting design procedures that aim to reduce local damage, are basically force-based procedures that involve an addition of a displacement check to ensure that acceptable performance

levels are achieved in the design earthquake *Priestley (2000).* Therefore, an alternative design procedure known as "direct displacement-based design" has been developed (*Priestley (1992), Priestley and Calvi (1997), Priestley and Kowalsky (2000)*), where the overall performance of the building is controlled as a function of the design process.

In the displacement-based design the engineer specifies a target displacement rather than a displacement limit. Hence the structural system is designed so as to sustain a predefined level of damage under a predefined level of earthquake intensity. Strength and stiffness are not variables in this procedure, bud are the end results. A brief yet comprehensive description of the basic steps involved in Displacement Based Design is attempted in the following:

Step 1: Application of the Substitute Structure Approach to obtain an equivalent elastic system

The application of displacement-based design procedure requires the use of the ***Substitute Structure Approach*** *(introduced by Gulkan and Sozen in 1974)* according to which an inelastic system may be replaced by an equivalent elastic system. The latter is known as the substitute structure and is characterized by: (a) an effective stiffness, K_{eff}; (b) an effective damping, ζ_{eff}; and (b) effective period , T_{eff}.

To better illustrate this consider the inelastic force–displacement hysteretic response of a typical well confined concrete bridge pier (**Figure 1.6**). According to the Substitute Structure Approach this response can be modeled with an equivalent elastic secant stiffness $K_{eff}$to the maximum response point (denoted by the dotted line) coupled with an equivalent viscous damping value, ζ_{eff} (which is related to the hysteretic energy absorbed by the system). [The equivalent viscous damping consists of two components:

one due to the hysteretic energy dissipation, ζ_{hyst}, and the other due to viscous damping, ζ_{vis}] . Since the effective properties of the substitute structure are elastic, a set of elastic response spectra can be used for design. Therefore, the substitute structure approach allows an inelastic system to be designed and analyzed using elastic response spectra.

Step 2: Definition of the design Displacement

To define the design displacement of a structure, specific criteria that relate quantitatively the experienced damage with the observed strain limits, the permanent displacements or drifts need to be established. For example for a reinforced concrete bridge column it is common to assume that the yield displacement will be achieved when the serviceability limit state is reached (i.e. onset of cover concrete crushing, or the development of crack widths of a size that might require injection grouting after an earthquake). Up to this point the structure is assumed to behave elastically. Similarly, the maximum (ultimate) design displacement will be achieved when the 'damage control' limit state is reached (i.e. beyond this point the structural repair is not economically feasible). Having established a relation between the design displacement and the limit state of the structure, it is then straightforward to relate these limit states to acceptable plastic curvatures, and thus to plastic drift ratios.

The effective damping is estimated by *applying Jacobsen's approach* to the *Takeda* degrading-stiffness-hysteretic response which yields the following relation:

$$\zeta_{eff} = 0.05 + \frac{1-\left(\frac{1-r}{\mu_\Delta}\right)- r\sqrt{\mu_\Delta}}{\pi} \qquad (1.1)$$

where 0.05 corresponds to a 5% viscous damping, r is the ratio of the post-elastic structural response curve to that of the initial elastic structural response curve (see **Figure 1.7**) and μ_Δ is the structural element ductility defined as $\mu_\Delta = \frac{\Delta_m}{\Delta_y}$

Step 3: Define a set of suitable displacement Elastic Response Spectra

In order to design for a displacement, a set of suitable displacement response spectra (DRS) must be employed. **Figure 1.8** presents a typical DRS that can be used in performance-based design analyses. This particular DRS corresponds to an artificial accelerogram designed to satisfy a EuroCode7 design acceleration response spectrum

Step 4: Calculate the maximum Force of the system

For given values of design displacement and effective damping, the elastic displacement response spectra can be used to estimate the effective period of the substitute structure, T_{eff}. By following a procedure similar to that described in **Figure 1.9** the period T_{eff} is obtained at the point that the appropriate DRS curve (corresponding to the level of effective damping previously calculated) intersects with the maximum design displacement. For the simplest case of a single-degree-of-freedom (SDOF) oscillator, the effective period is related to the effective stiffness at maximum response, K_{eff} by the relation:

$$K_{eff} = \frac{4\pi^2 M}{T_{eff}^2} \qquad (1.2)$$

Therefore, the maximum lateral force, *F*, is easily obtained by multiplying the effective stiffness by the target maximum displacement. Once the lateral force is established, the system can be designed.

Since 1995, when the idea of displacement based design was first introduced a great number of studies followed that extended its application to more complex structural

systems. Among them of particular interest is the work of *Kowalsky et al (1995)* who applied the above procedure in the design of RC bridge columns, while *Calvi and Kingsley (1995)* tested its applicability to multi-degree of freedom bridge structures. They concluded that the displacement based method may possess significant difficulties when applied to structures that experience modes of response that significantly deviate from their single dominant mode. Some years later *Priesley and Kowalsky (2000)* proposed a slightly modified procedure that could be applicable to concrete buildings as well. In 2002 *Kowalsky* implemented a displacement-based procedure for the design of multi-span bridge systems. The procedure was applied to a series of four span bridge structures, and dynamic inelastic time-history analyses were performed to provide verification.

1.4 The Concept of Rocking Isolation: Application to Structural Members

The work of Housner, who first recognized the possible positive role of rocking on the seismic response of structures, motivated further studies on the subject. *Priestley et al. (1978)* complemented Housner's results by providing additional experimental data (rocking of a model slender structure on a 1-g shaking table), while he proposed a simplified design method to estimate the maximum rocking displacement for a single-degree-of-freedom rocking structure using an equivalent response spectra approach. This metholodoly, that is based on the assumption that a rocking block may be represented by a (SDOF) oscillator of constant damping, whose period depends on the amplitude of rocking, was later embedded in the FEMA 356 document to compute rotations of slender structures.

Later, *Makris and Konstantinidis (2003), questioned the reliability of this* simple spectrum analysis method and concluded that the information involved in the exact rocking spectrum cannot be obtained by other simplified approaches. *Huckelbridge and Clough (1978)* examined experimentally the effect of partial lift-off on a multistorey model structure and confirmed the benefit of uplift action in reducing the strength and ductility demands of the frame. *Meek (1978)* investigated parametrically the dynamic response of tipping core-braced buildings using a simplified first-mode model (**Figure 1.10**). It was concluded that for structures with natural frequency between 0.5 and 4 Hz, tipping could notably reduce the pseudo-acceleration to values considerably less than the fixed-base response, and the reduction is even greater for more slender structures.

Two of the most widely studied methods of rocking isolation of structural members are discussed in the ensuing.

1.4.1 Application of Post-tensioned Energy dissipating Mechanisms

Motivated by the Northridge (1997) earthquake, where numerous structures experienced major damage, a significant amount of research (mainly expressed by the structural engineers) was conducted on the development and promotion of novel isolating concepts. "*Jointed ductile systems*", for both frame and wall systems, were suggested as an alternative to the traditional "cast-in-place" solutions within the framework of the U.S. PRESSS (PREcast Seismic Structural System Structural). In these new typologies pure precast elements are connected though unbonded post-tensioning techniques; the inelastic demand is accommodated within the connection itself (beam-column, column-foundation, wall-foundation critical interface) where a "controlled rocking" motion occurs with opening and closing of existing gap; as a consequence, a

very limited level of damage is expected in the structural elements which are maintained in the elastic range (*Priestley, 1996; Priestley et al, 1999)*. *Stanton et al, 1997* experimentally *manifested* the promising efficiency and high flexibility of such hybrid pre-cast concrete beam-to-column systems compared to the performance of the corresponding monolithic systems.

Christopoulos et al (2002) extended the "controlled rocking" connections, to steel frames. **Figure 1.11** illustrates the implementation of this idea. In his work the simulation of the PTED (post-tensioned energy dissipating) connection was achieved by incorporating a flag-shaped hysteretic model, with self-centering capability **(Figure 1.12)**. This flag-shaped hysteretic behaviour can be fully defined by simply incorporating a post-yielding stiffness parameter and an energy-dissipation parameter as shown in **Figure 1.13**. An ensemble of 20 historical earthquake records corresponding to ordinary ground motions having a probability of exceedance of 10% in 50 years, in California was used as an input in their parametric study. It was demonstrated that a flag-shaped hysteretic SDOF system of equal or lesser strength can always be found to match or better the response of an elastoplastic hysteretic SDOF system in terms of displacement ductility and without incurring any residual drift from the seismic event. A typical numerical example from this study is presented in **Figure 1.14.** It is clear that the "controlled rocking" system demonstrates less energy dissipation, but significantly reduced the produced residual drifts.

1.4.2 Controlled Rocking

"Controlled Rocking" is innovative beam-to-column connection that combines self-centring characteristics as well as energy dissipation. The most significant feature of

these connections was their capacity to ensure small residual drifts, through self-centering capabilities, even when significant inelastic transient deformations were mobilized during the seismic response. The first applications of this hybrid concept were performed to bridge piers by *Mander and Chen (1997).* Similar work was conducted at University of California, San Diego (*Hewes and Priestley;* 2001) where the seismic performance of precast segmented piers with unbonded post-tension cables have been tested both experimentally and analytically. **Figure 1.15** illustrates the application of this rocking isolation concept on bridges as accomplished by the use of a "hybrid" system (that allows restricted detachment of the pier from the foundation). A number of alternative solutions, which rely on the use of post-tensioned bars or tendons (bonded or partially unbonded during the casting) have been proposed by *Zatar and Mutsuyoshi, 2000; Kawashima, 2002; Ikeda et al, 2002*. It was verified that employing pre-stressing tendons in RC bridge piers could result in subsequent reductions of residual displacements, restrain-associated cracking, and enhanced concrete shear strength.

Kurama et al, (2002) applied the "controlled rocking" concept to pre-cast concrete walls and concluded that the amount of post-tensioning force and the initial stress and eccentricity of the post-tensioning steel are the key parameters affecting the behavior of such wall systems. The efficiency of rocking isolation on partially pre-stressed concrete cantilever walls had been experimentally investigated by *Holden et al (2003).* **Figure16** schematically compares the hysteretic behaviour of three alternative wall systems: (a) a conventional reinforced concrete system; (b) a fully prestressed precast concrete system; and (c) a partially prestressed "hybrid" concrete system. For the last two prestressed wall systems the tendons, if left un-bonded over a certain length, remain elastic during rocking. In this way the elastic restoring force essentially prevents residual lateral

displacements from. Since the concrete is not bonded to the tendons, considerably less cracking is induced than in monolithic walls. One the other hand monolithic systems can dissipate larger amounts of energy, but this is provided through structural damage and stiffness degradation, as well as residual drift. In contrast, prestressed-only systems dissipate little energy, which is expected to lead to larger displacement demands than for those systems where energy dissipation can take place. One the other hand partially pre-cast pre-stressed systems are “hybrid” systems that intended to combine the benefits of both systems, thus providing a good level of energy dissipation and showing self-centering characteristics as well as no damage. Experimental data form *Holden et al study* provide enough evidence on this theoretically expected response: The conventional precast reinforced wall (experimentally implemented as in **Figure 1.17a**)performed very well in terms of the ductility capacity and energy absorption capability, reaching 2.5% drift before significant strength degradation occurred, while the precast partially prestressed wall unit (**Figure 1.17b**) achieved slightly higher drift levels (in excess of 3%) but no visible damage to the wall panel prior to failure.

Palermo et al (2004) further examined the comparative advantages of a hybrid solution both at local (bridge piers) and global level (bridge systems) against the conventional monolithic connection. Both systems had been represented with lumped plasticity models: elastic beam elements representing the bridge piers and inelastic rotational springs at the critical interface sections modeling the rocking motion in hybrid system or the formation of plastic hinge for the monolithic connection **(Figure 1.18).** Non-linear time-history analyses on different bridge configurations had shown no substantial differences in terms of maximum displacements for the two connection examined, with slightly higher values (10-15 %) for the less-dissipative hybrid systems.

More important outcome is that the use of “controlled rocking” solutions results in negligible residual displacement, while values in order of 20% of the maximum pier drift/displacement are expected when monolithic connections are adopted.

1.5 Non-Linear and Inelastic Response of Soil Foundation Systems

In all the above studies the nonlinear capacity of the system is exploited at the superstructure level alone, typically permitting the energy dissipation at suitably selected points through formation of plastic hinges or insertion of isolation/dissipation devices, while in the same framework any damage at the foundation level is prohibitted. In other words, the geotechnical designer must ensure that the below-ground the support system will not even reach a number of "thresholds" that would statically imply failure. Thus, mobilisation of the *bearing-capacity failure* mechanism, severe foundation uplifting sliding, or any relevant combination are not allowed.

However, thanks to the *cyclic* and *kinematic* nature of the seismic excitation, mobilization of the bearing capacity failure mechanism under severe seismic shaking does not necessarily imply failure. In fact, a growing body of evidence , both analytical and experimental, suggests that allowing such nonlinear-inelastic foundation response is not only unavoidable, but may even be beneficial [*Paolucci, 1997; Pecker, 1998, 2003; Martin & Lam, 2000; Makris & Roussos, 2000; Pecker & Pender, 2000; Faccioli et al., 2001; Kutter et al., 2003; Gazetas et al., 2003; 2007; Gajan et al., 2005; Paolucci et al., 2008; Kawashima et al., 2007; Gajan & Kutter, 2008; Chatzigogos et al., 2009 ; Anastasopoulos et al., 2009*]. The first realization of the aforementioned studies into practice can be found in *Federal Emergency Management Agency NEHRP Guidelines* for the seismic retrofit of buildings (1997) and the associated *Applied Technology Council* document (*ATC 40*) , where alternative design methods associated with the response of shear walls subjected to lateral earthquake induced rocking are discussed.

1.5.1 Theoretical Studies

The current state–of–the art in nonlinear analysis of foundations involve the development of macro-element models [*Paolucci, 1997; Cremer et al., 2001; 2002; Le Pape & Sieffert, 2001; Pecker, 2002; Paolucci et al., 2008*] or advanced winkler models [*Taylor et. al, 1981; Psycharis, 1983; Psycharis and Jennings, 1983; Yim and Chopra, 1984, 1985; Nakaki and Hart, 1987; Filiatrault et al, 1992; Fenves 1998; Anderson, 2003; Chen and Lai; 2003*; *Houlsby et al., 2005; Harden et al., 2005*; *Allotey and Naggar, 2003, 2007; Raychowdhury and Hutchinson, 2009*]and less often coupled simulations with FE models. A quite detailed inventory on the most representative theoretical studies on the subject can be found in the next paragraphs where some recent advances in the numerical modelling of Soil-Foundations systems are described.

1.5.2 Experimental Evidence

Aside from the theoretical studies, a significant number of experimental work has been conduct in parallel to enhance the understanding on the mechanics of foundation uplifting and mobilization of ultimate bearing capacity during strong shaking

Foundation rocking

One of the first attempts to provide experimental evidence on the non-linear response of Soil-Foundation systems under lateral loading were the large-scale experiments conducted in the framework of TRISEE project. Two tests were performed, with relative densities 45% (LD test) and 85% (HD test). The set-up consisted of a shallow foundation (1m x 1m in plan) resting on saturated uniform sand layer (*Negro et al, 2000*). The specimens were subjected both to a realistic time-history of horizontal force and overturning moment (representative of the seismic actions transmitted by the super-

structure to the foundation during an earthquake) and to a series of displacement cycles of increasing amplitude up to the ultimate capacity of the soil-foundation system. The experimental data manifested the completely different response of the two test : The HD test experienced substantial foundation uplift under eccentric loading as demonstrated by the characteristic “s-shape” of the overturning moment-rotation curve (**Figure 1.19a**). This effect does not appear for LD conditions, where “punching” is the prevailing failure mode and foundation sinks into the sand preventing any uplift effects **(Figure 1.19b).**

Gajan et al (2005) and *Gajan and Kutter (2009)* had recognized that soil nonlinearity may act as an energy dissipation mechanism and thus potentially reducing shaking demands exerted on the building. To provide experimental evidence of the above statement, they conducted a great number of centrifuge experiments where the response of shear wall footings under cyclic and earthquake loading was investigated. Their parametric studies involve different footing dimensions, depth of embedment, initial static vertical factor of safety, soil density, and soil type. **Figure 1.20** portrays the set up of the centrifuge experiment. Some of their most important findings are:

i. the moment capacity was not observed to degrade with cycling, but due to the deformed shape of the footing–soil interface and uplift associated with large rotations and stiffness degradation was observed (**Figure 1.21**).

ii. Permanent deformations beneath the footing accumulate with increasing number of cycles of loading but the rate of settlement accumulation decreases as the footing embeds itself.

iii. For a particular FS_V footings with a large moment to shear ratio dissipate considerably more energy through rocking and suffer less permanent settlement than footings with a low moment to shear ratio.

iv. Shallow foundations with a sufficiently large *A*/*Ac ratio (where A is the actual footing Area and Ac is the area required to support the vertical and shear loads)* suffer small permanent settlements and have a well defined moment capacity.

Based on the above the authors suggested that shallow foundations with a sufficiently large *A*/*Ac* may be effectively used as energy dissipation devices to restrain loads transmitted to the superstructure.

Shirato et al (2007) and *Paolucci et al* (2008) explored the soil-foundation-structure interaction phenomena by performing a series of large-scale shaking table tests at the Public Works Research Institute in Tsukuba, Japan. The test model, that consisted of a steel rack at the top, a 0.5m sided square foundation block at the bottom and a short steel beam with I cross-section connecting the two massive blocks, was lying on nearly homogeneous sand layer of Dr = 80% (see **Figure 1.22**). The achieved static safety factor was rather high and was estimated to be equal to F_s=29. The model had been excited by a different excitation motions that range from sinusoidal-type waveforms to actual recorded accelerograms (e.g. JMA record). It was concluded that the soil–foundation system initiates significant yielding when the ultimate load levels are attained, and the foundation keeps in contact with the underlying soil only in the proximity of the foundation edges revealing significant foundation uplift. However, during the unloading phases and the subsequent reloading phases, the area of the contact zone does not increase remarkably, thus implying a permanent reduction of the foundation–soil contact area **(Figure 1.23).** This results in an overall degradation of the dynamic foundation impedances, and in turn, elongation of the natural period of the soil–foundation system.

A similar evidence of a curved soil surface formation beneath the foundation was also found by *Gajan et al (2005)*.

Soil Yielding

Zeng and Steedman (1998) studied the behaviour of buildings on shallow foundations under earthquake loading by conducting centrifuge tests on dry or saturated sand speciments. Their work provided new insights into the mechanism of seismic bearing capacity failure. They concluded that the striking phenomenon of sudden foundation failure near the end of an earthquake is triggered by a combination of a critical permanent rotation and significant but well below the maximum ground acceleration. A direct implication is that an earthquake with moderate cycles is more likely to cause bearing capacity failure of foundations than an earthquake with just one or two strong cycles.

Maugeri et al (2000) tested experimentally the seismic bearing capacity failure mechanism of shallow foundations by performing 1-g shaking table experiments on dry sand. The foundation was subjected to a vertical eccentric load and to a sine dwell-type acceleration. The measured response **(Figure 1.24)** correlates well with the kinematic failure mechanism proposed by *Paolucci and Pecker, (1997) and Richard et al., (1993)*.

On the seismic bearing capacity of foundations was also the work of *Knappet et al (2006).* A series of 1g shaking table experiments had been carried at Cambridge University in order to determine seismic induced displacements. To accurately measure the development of the failure mechanism within the soil, the technique of Particle Image Velocimetry (PIV), combined with high-speed videography and photogrammetry had been utilized. The experimental data **(Figure 1.25)** confirm the analytical results of *Paolucci and Pecker, (1997)* illustrating that for structures where the centre of mass is

significantly above the foundation level (moment-dominant response), seismic bearing capacity is expected to be drastically reduced due to uplift.

1.6 *Non-linear dynamic Response of Shallow Foundations*

Scope of this chapter is to present a brief (yet comprehensive) overview of the different approaches used to model the *Non-Linear* Soil-Foundation-Structure Interaction (SFSI) problem for the case of shallow footings. Phenomena associated with geometric non-linearities (i.e. sliding and rocking of the foundation), gap formation between the footing and soil, dynamic settlement-densification, and energy dissipation stemming from the non-linear soil behavior need to be realistically captured to completely describe the problem. The modeling approaches may be broadly divided into the following categories:

(a) *Analytical Methods* (which involve analytical solutions, Winkler models and the Macroelement method)

(b) *Hybrid Methods;* The term hybrid reflects the fact that the SSI problem is tackled by combining different numerical techniques.

(c) *Direct approaches* primarily expressed by the Finite Element method.

In the methods presented in the ensuing the structural system is simulated with an increasing level of sophistication either as a combination of [M, Q, N] loading representing the (static or inertia) loading transferred from the superstructure to the foundation level, as a rigid block (neglecting the structural stiffness), or as an 1-dof or even a multi-degree of freedom system.

1.6.1 Analytical Methods

Rocking Response of a Rigid Block

Housner, in his pioneering work of 1963, was the first to observe that foundation uplift may be responsible for the good performance of seemingly unstable structures during erthquakes. Motivated by the Chilean earthquakes of 1960's he studied the dynamics of

a rigid block rocking on a rigid horizontal base, and demonstrated that there is a scale effect which makes the larger of two geometrically similar blocks more stable than the smaller block (**Figure 1.26**).

Following Housner's seminal paper a large number of studies have been presented to address the complex dynamics of the free-standing block. *Yim et al. (1980)* adopted a probabilistic approach and conducted a numerical study using artificially generated ground motions to show that the rocking of a block is extremely sensitive to system parameters. Similar conclusions (which were further justified by experimental data) had been drawn from the work of *Aslam et al*. (1980). The authors studied the rocking and overturning response of rectangular blocks of various sizes and aspect ratios under several strong motion earthquakes. The sensitivity of overturning to small changes in base geometry and coefficient of restitution as well as to the type of the ground motion had been highlighted. Thus it was concluded that it may be difficult to use data from observations on standing and overturned rigid bodies after an earthquake to provide useful information on the intensity of ground motion. *Spanos and Koh (1984)* on the same problem identified ''safe'' and ''unsafe'' regions and developed analytical methods for determining the fundamental and subharmonic modes of the system. Their study was extended by *Hogan (1989, 1990)*, who further elucidated the mathematical structure of the problem. The block of **Figure 1.27(a)** was excited by a cosine pulse of the form:

$$a_H = \beta\, \alpha\, g \cos(\Omega\tau + \varphi) \tag{1.3}$$

and the complicated dynamics of its response were investigated. Following similar procedure with that proposed by *Spanos and Koh,* he concluded that that the domain of maximum transients of his solutions appears relatively ordered and possesses a high degree of predictability despite the chaotic nature that is present in the asymptotic part

of the solutions. A typical result of his work is presented in **Figure 1.27(b).** The horizontal axis corresponds to initial values x_o of the angular displacement and the vertical axis to initial values y_o of the angular velocities. Note that although at the figure corners it is evident the great unpredictability of the problem (i.e. a small change in the initial conditions may produce completely different asymptotic response), yet the central part of the figure elucidates a quite ordered response (i.e. n=1 or n=3 are the dominant orbits).

The steady state rocking response of rigid blocks was also studied analytically and experimentally by *Tso and Wong (1989 a,b)*. Although their theoretical study was not as in-depth as the one presented by *Hogan (1989),* their experimental work provided valuable support to the theoretical findings.

Of exceptional interest is the work presented some years later by *Makris and Roussos (1998, 2000)* who studied the rocking response of a rigid block subjected to trigonometric pulses and near-source ground motions. Inspired by the latest recorded earthquakes. Firstly, they deducted that under a half-sine pulse, a rigid block overturns during its free vibration regime and not at the instant that the pulse expires. Subsequently, the rigid block dynamics under various cycloidal pulses (to account for some near-source ground motions characteristics) were examined. It was found that the toppling of a smaller block is more sensitive to the peak ground acceleration, whereas the toppling of larger block depends mostly on the incremental ground velocity. Moreover, it was concluded that the high-frequency fluctuations that occasionally override the long-duration (near-source pulse) in an actual earthquake record may be crucial for the toppling of a smaller block, whereas a larger block will only overturn due to the long-duration pulse. One year later *Zhang and Makris (2001*) investigated further

the response of a free-standing block under a cosine and a sinus pulse. They reveal that the block may overturn with two different modes: (a) by exhibiting one or more impacts; and (b) without exhibiting any impact. Yet the existence of the second mode results in a safe region that is located over the minimum overturning acceleration spectrum. The shape of this region depends not only on the geometric properties of the block under study and the shape of the excitation motion, but also is sensitive to the coefficient of restitution and to the nonlinear nature of the problem. Typical results of their study are depicted on **Figures 1.28 – 1.29.** In the first one the overturning acceleration spectra (computed utilizing the linear and the non-linear formulation) of a specific rigid block excited by a one-sine pulse is illustrated, while **Figure 6** provides the same information for the same block excited by a one-cosine pulse. In *2005 Gerolymos et al* investigated the same highly unpredictable problem by means of artificial neural network modeling. After successfully comparing their results with the analytical solution of *Zhang and Makris, 2001*, they used this powerful tool to predict the response of the rigid block subjected to a variety of idealized pulses that resemble near-fault ground motion characteristics (i.e. Ricker pulses, T-Ricker etc) and even to real earthquake records. They concluded that the overturning of a block becomes more chaotic to predict (revealed by the presence of even more "safe islands" on the overturning acceleration spectrum) as the complexity of the excitation pulse increases. **Figure 1.30** schematically illustrates the above statement by comparing the overturning acceleration spectrum obtain for a specific block subjected to (a) a real earthquake record (i.e Duzce, 1999 record) and (b) to a suitably fitted mathematical Ricker pulse.

Biot (2006) investigated analytically the role of ground elasticity on the rocking motion of a building and derived useful expressions on the influence of the soil and foundation

uplift on the natural period of a structure. In his work the soil medium was assumed to be a semi-infinite elastic body, while the building rocking was represented by a pair of opposite distributed loads at distance 2ξ (ξ varies accordingly to assumed structure dimensions) as depicted in **Figure 1.31**. It was established that for the case of a rigid structure of mass M whose center of gravity is at a height h above the ground and rests on a foundation of width 2l, and assuming that the axis of rotation is located at the surface of the soil, the frequency of the rocking motion is given by the equation:

$$f = \frac{1}{2\pi}\sqrt{\frac{c}{mK^2} - \frac{gh}{K^2}} \qquad (1.4)$$

where c is the elastic stiffness coefficient of the soil and K is the radius of gyration of the structure with respect to the rocking axis. The second term under the radical represents the destabilizing influence of gravity. The limit case where $\frac{c}{mK^2} = \frac{gh}{K^2}$ (i.e when the tipping moment due to gravity equals the restoring moment of the soil) corresponds to statical instability and results in $f = 0$ (or to infinite fundamental period of the structure). Recently, *Palmeri and Makris (2008)* revisited the rocking response of rigid structures to account for phenomena associated with the presence of a flexible viscoelastic foundation layer. The effect of the stiffness and damping of the foundation was presented in terms of rocking spectra and the response was compared with those of the rigid block rocking on a monolithic base. Some interesting features were highlighted: for instance, less slender and smaller blocks tend to separate easier, whereas the smaller the angle of slenderness, the less sensitive the response to the flexibility of the foundation.

Winkler based models

One of the most popular methods to engineering practitioners for modeling soil-foundation-structure interaction problems (basically due to its simplicity, minimal computational effort and ease of implementation) is the beam-on-Winkler Foundation (BWF) approach. The idea dates back to 1867 and indicates that the physical soil medium may be replaced by a system of continuously distributed springs along the foundation width. Besides its inherent assumption that the discretely placed springs react independently from each other, thus ignoring the coupling effects between neighboring springs, the BWF method has been widely used to assess the study the rocking and uplift response of linear structures (*Chopra and Yim, 1984; Psycharis and Jennings, 1983*)and more recently to investigate the effect of both uplift and yield on structural response (*Taylor et. al, 1981; Filiatrault et al, 1992; Anderson, 2003; Chen and Lai; 2003*). A collection of the most representative publications on the subject is presented in the following paragraphs.

Psycharis (1983) and Psycharis and Jennings, 1983 studied the dynamics of rigid blocks and flexible systems that experience partial foundation uplift. The structure was supported through (a) a simple two-spring viscously damped foundation (**Figure 1.32**) and (b) a Winkler type foundation (springs-dashpots). The non linearity at the foundation interface has been taken into account by 3 distinct mechanism: (1) the use of viscous dampers, (2) the use of nonlinear springs (elastic-perfectly plastic) and (3) an impact mechanism that allows energy dissipation during impact. He concluded that the two-spring foundation system though simple may be a good approximation of the system response.

Similar to the work of Psycharis, *Yim and Chopra (1984)* and *Chopra and Yim (1985)* evaluated the response of single-degree-of-freedom (sdof) and multi-degree-of-freedom (mdof) systems. The numerical approximation of the system consists of a linear structure of mass *m,* lateral stiffness *k* and lateral damping *c,* which is supported by two idealized foundation systems (**Figure 1.33**): (a) a two-element type system which involves only two spring-dashpot elements at the footing edges and (b) a Winkler type foundation system (pairs of spring-damper elements equally distributed along the foundation width). In both systems the horizontal slippage between the foundation and the supporting elements is prohibited and the stiffness and damping coefficients of the foundation model are assumed constant, independent of displacement amplitude or the excitation frequency. A primary conclusion of this work was that foundation flexibility and uplift have little effect on higher modes of vibration.

A few years later, *Nakaki and Hart (1987)* used elastic, no-tension Winkler springs with viscous dampers to study the rocking response of a shearwall supported on a mat foundation **(Figure 1.34a)**. The inelastic shearwall structure was modeled utilizing a non-linear stiffness degrading hysteretic model. Nakaki's and Hart's findings illustrate the beneficial role of foundation uplift, which may significantly reduce the structural ductility demand of the superstructure **(Figure 1.34b).**

In an application to bridge modeling, *Fenves 1998* developed a composite spring model properly calibrated to capture the cumulative permanent settlement observed due to rocking of shallow footings under large amplitude cyclic motions. More Recently *Houlsby et al., 2005* proposed a generalized (yet simplified) Winkler model to study the response of shallow foundations under cyclic loading. The model utilizes the concepts of hyperplasticity to simulate the experienced non-linear stress-displacement response. The

produced results closely resemble the system behavior obtained experimentaly and by conducting more sophisticated numerical analyses.

Harden et al., 2005 studied the behavior of shallow strip footings supporting rocking-dominated shearwall buildings. To this end, they developed a Winkler-based model that shares common features with a material originally formulated by *Boulanger et al, 1999* for describing the behaviour of pile tip under cyclic loading. Each material is capable to simulate both the "far-field" (i.e elastic response of the footing) and "near-field" (i.e the permanent displacements) and to do so it consist of an ensemble of linear and nonlinear springs, gap elements and a dashpot, to account for radiation damping. Schematically the conceptual configuration of the "material" is depicted in **(Figure 1.35).** The main attributes of the model that make it particularly applicable to shallow foundation problems are summarized as follows: (a) it has a non-symmetric backbone (i.e reduced ultimate strength in tension), (b) under cyclic loading, the material does not attain full stiffness until the strain reaches the unloading strain of the previous cycle. In that sense, the material is able to capture phenomena such the cumulative settlement of the foundation. The accuracy of the model has been extensively tested against centrifuge and 1-g experiments in both sandy and clayey materials.

Of exceptional interest is also the recently published work of *Allotey and Naggar (2003, 2007, 2008)*. They developed a Winkler-based approach to investigate the response of rigid footings under monotonic and cyclic conditions. The proposed cyclic response curve (**Figure 1.36)** comprises of a no-tension multi-linear degrading model. Two different paths of loading are distinguished. The standard reload curve which simulates loading of the original soil, and the direct reload curve (DRC) that simulates loading through a developed slack zone. The shape of the hysteresis loops may be

controlled by proper model parameters. The authors have extensively validated their model against centrifuge tests by *Gajan et al,* and large scale 1-g tests (TRISEE experiment). As indicated by **Figure 1.37** the *Allotey and Naggar* model compares quite satisfactorily with the experimental data in terms of Moment-Rotation and settlement-rotation loops. Howerer, it seems to systematically underpredict the permanent horizontal displacements. This is mainly attributed to the limited coupling between horizontal and vertical-rotational responses.

A critical review on the effectiveness of spring models for the simulation of shallow foundations on soil can be found in the work of *Pender 2007.* The author highlights some of the inherent deficiencies arising from the use of discrete spring elements. He compares the response of a rectangular rigid footing supported on a bed of uniformly distributed springs to that of a footing resting on a continuous soil assuming both linear and non-linear soil behaviour. He concluded that for given footing dimensions the rotational stiffness computed with the winkler approach is considerably less than that arising from the continuous medium assumption **(Figure 1.38)**. The underlying reason is that the spring model doesn't take into account the interaction between the neighboring springs and thus the calculated reaction pressure at each point depends only on the displacement at that point. This incompatibility between the two simulations may be remedied in the elastic case by adding an additional rotational spring beneath the footing. Yet if soil nonlinearity is taken into account the assumption of uniform spring elements it is possible to better represent the accomplished rotational stiffness (because the induced non-linearity tends to decrease more rapidly the rotational stiffness compared to the vertical one). A possible solution to bridge this gap between the linear

and the nonlinear response is the use of a bed of non-linear spring elements coupled with a non-linear rotational spring at the center of the footing.

Lastly *Raychowdhury and Hutchinson, 2009* developed a new Winkler model that is built upon the work of *Harden et al* and complements the *Allotey and Naggar* model. In this newer version of the BNWF model, the vertical springs are of variable stiffness in order to simulate correctly not only the rocking, uplift and settlement but also the rotational stiffness of the system. This idea follows the FEMA 273 document that recommends the use of stiffer springs at the edge of the foundation compared to the central part. Moreover, horizontal springs are attached to the sides of the footing to capture the sliding and passive resistance. A schematic representation of the idealized BNWF model is depicted in **Figure 1.39**. Model evaluation was conducted by simulating the response of a number of centrifuge experiments that cover a wide range of shallow foundation problems. It was concluded that the proposed winkler model may quite reasonably predict not only the measured footing behaviour in terms of moment, shear, settlement and rotational demands but also the general hysteresis response (**Figure 1.40**).

Macro-elements models

A further alternative strategy to study the complex soil-foundation interaction is by employing the macro-element concept. In this approach the entire soil-foundation system is replaced by one single element that describes the generalized force-displacement behavior of a point (normally at the center of the footing) in the vertical, horizontal and rotational dimensions. A comparative advantage of this approach that makes it especially popular to structural engineers is that the produced element can be

makes it especially popular to structural engineers is that the produced element can be embedded in F.E. codes as a typical link/spring element in order to study the dynamic response of complicated structural systems accounting for the non-linear SFSI phenomena.

The concept of the ‘‘macroelement’’ was initially introduced by *Nova and Montrasio in 1991.* The authors abandoned the conceptual framework of elasticity for the prediction of settlements of foundations under static eccentric loading and instead proposed the use of a global linearized elastoplastic model with isotropic hardening and non-associated flow rule. We proceed with some detail on the formulation of the Nova and *Montrasio* macroelement, since it is consider being the starting point for all the sub-sequent work on the subject. The principal elements of their formulation are presented hereafter:

Firstly, the generalized stress variable vector *Q* is defined as:

$$Q \equiv \begin{Bmatrix} \xi \\ h \\ m \end{Bmatrix} \equiv \frac{1}{V_M} \begin{Bmatrix} V \\ H/\mu \\ M/(\psi B) \end{Bmatrix} \tag{1.5}$$

while the generalized strain variable vector q as follows:

$$q \equiv \begin{Bmatrix} \eta \\ \varepsilon \\ \zeta \end{Bmatrix} \equiv V_M \begin{Bmatrix} \upsilon \\ \mu u \\ \psi B \theta \end{Bmatrix} \tag{1.6}$$

V, H, M correspond to the concentrated axial, shear and moment loading of the foundation and, u and θ are the produced vertical and horizontal displacements and rotations at the center of mass of the foundation **(Figure 1.41).** The V_M is the ultimate vertical load of the footing, B stands for the foundation width and ψ, μ are constitutive parameters that can be experimentally evaluated. (The authors propose that μ equals

$$h^2 + m^2 - \xi^2 (1 - \xi)^{2\beta} \quad (1.7)$$

To account for soil isotropic hardening the loading function is given by :

$$f(Q, \rho_c) = h^2 + m^2 - \xi^2 (1 - \frac{\xi}{\rho_c})^{2\beta} .. \quad (1.8)$$

where ρ_c is a function of the "memory" of the system used to describe a common feature of soil material that as the plastic strain increases the strength may also increase simultaneously (hardening) . From a geometrical standpoint (*Eq. 1.6)* represents a closed form surface in the Q space that shares common shape with the surface described by *Eq (1.5)* , while it coincides with the latter when ρ_c = 1. The proposed plastic flow used is non-associated and thus the plastic potential is given by the expression:

$$g(Q) = \lambda^2 h^2 + x^2 m^2 - \xi^2 (1 - \frac{\xi}{\rho_g})^{2\beta} \quad (1.9)$$

where ρ_g is just a scaling factor parameter with no physical meaning, and parameters λ and x are defined as $\lambda = \mu/\mu_g$ and $x = \psi/\psi_g$ with μ_g and ψ_g being parameters to be experimentally specified. In case λ=x=1 the plastic potential and the loading function coincide and the flow rule degenerates to associated**.** To summarize the macroelement presented consist of nine parameters that first need to be determined via simple experimental tests. After that, it may quite satisfactorily predict the induced settlements. **Figure 1.42** summarizes the model performance in various tests where both inclined loading and overturning moment are present.

Based on the Nova and Montrasio formulation *Paolucci in 1997* was the first to apply the macroelement approach to study the response of structures subjected to real earthquake loading. A year later *Pedretti 1998* further improved the performance of the Nova and Montrasio model and extended its applicabilty to footings subjected to cyclic loading. In this work, the simplified elastoplastic model with isotropic hardening was

replaced by the more sophisticated bounding surface plasticity model (*Dafalias and Hermann, 1982)*. The basic concept of this plasticity theory (illustrated in **Figure 1.43**) lies on the assumption that the loading surface may be replaced by a so called "bounding surface". Each Point P (describing a particular loading state) within this surface can be mapped through a specified "mapping" rule to a conjugate point I_p lying on the bounding surface. The plastic modulus, that describes the soil behavior after its yield point, is defined as a continuous function of the distance between the I_p and the P points. A fundamental advantage of this formulation (especially in cyclic problems) is that the model establishes a smooth transition between elastic and plastic behavior particularly in unloading-reloading phases.

Le Pape and Sieffert (2001) derived another macro-element model based on a thermodynamically coherent framework. According to their theoretical approach the global non-associated behaviour of the foundation is not only a consequence of a local non-associated flow, but is the result of the total energy balance of the soil domain under study. *Crémer 2001 and Crémer et al 2001* exploited further the macro-element concept and presented an element in which two separate mechanisms of non-linearity were introduced: *(a) material nonlinearity generated by soil plastification and (b) geometric nonlinearities due to footing uplift*. The model is based on the assumption that the total footing displacement may be obtained by adding the effect of each one of the above mechanisms. In terms of generalized kinematic parameters the system response is described by the following relation:

$$q = q^{el} + q^{pl} + q^{up} \tag{1.10}$$

where q^{el} denotes the elastic displacements, q^{pl} the plastic displacements and q^{up} the footing displacements associated with the uplift. To describe the nonlinear soil response

a multi-yield elasto-plastic constitutive law with kinematic hardening for cohesive soil (*Prevost's model, 1978*) was adopted. Another important modification of this model is the definition of the non-associative flow rule. Instead of using the standard formula described by *Eq. 1.7* (according to which the plastic potential and the loading surface are basically described by the same expression) Cremer proposed a slightly modified rule:

$$g(Q) = \left(\frac{Q_V}{\kappa}\right)^2 + \left(\frac{Q_M}{\xi}\right)^2 + Q_N^2 - 1 \qquad (1.11)$$

Q_N, Q_V, Q_M stand for the axial, shear and moment loading applied on the foundation center and κ, ξ are constitutive parameters that need to be calibrated. **Figure 1.44** schematically illustrates the definition of the plastic potential in the Q_V, Q_N space. Note that in this plasticity model the loading surface $g(Q)$ is growing inside the failure surface $f(Q)$ and is related to the latter to a certain yielding level. To describe the foundation uplift a simple geometric model was utilized. Equations (1.12-1.14) summarize the basic mechanical- geometrical characteristics:

Initiation of Uplift:

$$Q_M = \frac{Q_N}{4} \qquad (1.12)$$

It is worth noting that the use of Equation (1.12) is based on the assumption of a parabolic stress distribution beneath the footing and implies that the onset of footing uplift takes place when the eccentricity ratio e_o equals ¼ . (Compared to 1/6 which is the value obtained if a constant stress distribution beneath the footing was assumed)

During Uplift :

$$\frac{Q_M}{Q_{M_o}} = 2 - \frac{q_{M_o}}{q_M} = 1 + \delta \qquad (1.13)$$

$$\frac{\dot{q_N}}{\dot{q_M}} = -\frac{\delta}{2}. \qquad (1.14)$$

In Equation 1.12 Q_{M_o}corresponds to the required moment for uplift onset, q_{M_o} is the footing rotation at that instance, and δ is a parameter that expresses the percentage of the footing area being detached from the underlying soil. The Moment-rotation relationship (described by Eq. 1.11) is illustrated in **Figure 1.45.** Lastly, by Eq. 1.12 a relationship between the derivative of vertical displacement and increment of footing rotation is established. It is worth mentioning that the above formulations are valid only if the underlying soil is elastic. Yet uplift behaviour is strongly coupled and influenced by soil yielding as the latter may induce an irreversible uplift behaviour. To tackle this coupled problem Crémer et al have built an uplift surface which moves inside an uplift domain. Each surface corresponds to an uplift percentage. **Figure 1.46** schematically illustrates these "iso-separation" surfaces superimposed on the failure criterion of the plasticity model. A direct outcome is that the only values of separation that may be reached during uplift are those located inside the failure criterion. Another important consequence is that the moment of uplift onset is no longer a linear function of the vertical load Q_N.

Recently, *Grange et al (2008*) modified the plasticity model of *Cremer et al (2001), (2002)* to account for circular footings under 3-dimensional loading. *Chatzigogos et al (2009, 2010)* further extended the original formulation of Crémer and proposed that the irreversible elastoplastic soil behavior may be described by a bounding surface hypoplastic model the definition of which is independent of the ultimate loads of the system.

At the same time *Paolucci et al (2008)* upgraded the original *Paolucci (1997)* formulation by introducing a stiffness degradation model that aims to describe in an indirect way the coupled uplift-soil plasticity phenomena, while *Shirato et al (2008(a,b))*

presented a macro-element in which an uplift model had been added in the *Nova and Montrasio* approach.

1.6.2 Hybrid Methods

The basic idea of hybrid modeling approach is that the total soil-structure system is partitioned in two distinct sub-domains (**Figure 1.47**). One substructure is the *near-field* and consists of the structure to be analysed under the prescribed loading conditions and a finite portion of soil immediately surrounding its base. This near-field may encompasses extremely complex phenomena such as arbitrary foundation geometries, soil heterogeneities/non-linearities and complicated foundation-superstructure systems.

The second substructure (the *far-field*) is a semi-infinite half-space which shares a common interface with the near-field and is considered to be sufficiently distant from the foundation-structure system so that it can be realistically assumed that the energy transmitted from the structural system to the far-field does not provoke non-linear effects. Since the far field radiates energy in the form of waves travelling away from the foundation, a realistic model must reflect this behaviour.

The two distinct domains may be modeled by different computational methods such as finite element or finite difference models, spectral elements, boundary integral methods etc. The combination of these alternative numerical approaches may offer significant advantages (mostly in decreasing the computational time) in the non-linear SSI problem that cannot provided by a single method on its own. A variety of hybrid methodologies are available that date back to 1980. *Mita and Luco (1987)* utilized the boundary integral together with the finite-element method to investigate the dynamic response of embedded foundations, while *Bielak et al (1991)* used a similar method to

study site effects. *Fäh et al (1993, 1994)* developed a hybrid procedure that combines the modal summation with finite differences method, to examine 2D wave scattering phenomena in two sedimentary valleys: the Friuli basin in Italy (1993) and the Mexico City Valley (1994). *Zahradník and Moczo (1996*) used the discrete-wavenumber and finite-differences methods to analyse the seismic wave fields at localized 2D near-surface structures that are excited by a point source.

It is beyond the scope of this study to refer separately to the formulation of all of the above methods. In the ensuing, attention will be focused on 3 hybrid methodologies for different reasons. The first one (developed by Gupta and his co-workers) is one of the earliest attempts in hybrid modeling, while the second is the DRM method which is indeed an effective algorithm that can be used to solve extremely diversive applications (i.e., modeling the propagation of seismic waves through a complex and heterogeneous domain from the fault-source to the ground surface, or study the non-linear dynamic soil –foundation-structure interaction). Lastly, this review will be complemented by describing the spectral element method, which has been extensively used for the simulation of SSI problems.

Gupta et al, 1980 tackled the problem of soil-structure interaction under dynamic conditions analytically by transforming the equation of motions in the frequency domain as follows:

The equation of motion for the near-filed sub-domain gives

$$m\ddot{u} + c\dot{u} + ku = p(t) + f(t) \qquad (1.15)$$

where u is the relative displacement of the near field against the motion of the surrounding far-field domain, and $\dot{u}$ and $\ddot{u}$ are the corresponding velocity and acceleration. The term $p(t)$ describes the inertia loading of the structure due to the

earthquake loading, while the $f(t)$ term stands for the interaction forces between the two domains acting on the interface. Equation (1.13) when transformed into the frequency domain yields:

$$(-\omega^2 m + i\omega c + k)U(\omega) = P(\omega) + F(\omega). \quad (1.16)$$

and by substituting $(-\omega^2 m + i\omega c + k)$ by $S(\omega)$ we get the simpler expression

$$S(\omega)U(\omega) = P(\omega) + F(\omega) \quad (1.17)$$

where S is the complex value impedance matrix of the near-field. Equation (1.15) can be written in partitioned form as follows:

$$\begin{bmatrix} S_{ss} & S_{sb} \\ S_{sb}^T & S_{bb} \end{bmatrix} \begin{Bmatrix} u_s \\ u_b \end{Bmatrix} = \begin{Bmatrix} P_s \\ P_b \end{Bmatrix} + \begin{Bmatrix} 0 \\ F_b \end{Bmatrix} \quad (1.18)$$

Accordingly the equation of motion for the far-field when transformed into the frequency domain results to:

$$S_f(\omega)U_f(\omega) = F_f(\omega) \quad (1.19)$$

Taking account the compatibility and equilibrium conditions on the interface, Equations (1.16) and (1.17) may be combined to describe the response of the whole system:

$$\begin{bmatrix} S_{ss} & S_{sb} \\ S_{sb}^T & S_{bb} + S_f \end{bmatrix} \begin{Bmatrix} u_s \\ u_b \end{Bmatrix} = \begin{Bmatrix} P_s \\ P_b \end{Bmatrix}. \quad (1.20)$$

The originality of the developed methodology lies in the numerical trick used to obtain the far-field impedance matrix. First of all, the interface has been judiciously chosen to be hemispherical in form so that it provides a smooth surface along which mathematical boundary conditions can easily be satisfied. Then the domain has been divided into infinitesimally thin soil elements (extending to infinity in the direction normal to the hemispherical surface cavity), proposing a technique that may be thought of as the dynamic equivalent of the Winkler model (**Figure 1.48**). The dynamic load-deflection relationship of each of these infinitesimal soil elements is described through impedance

elements, the real parts of which represent stiffness and the imaginary parts radiation damping. The impedance functions of the system as formulated by the superposition of the all the above elements is discretized at the interface nodal points to obtain the far-field impedance matrix that will be assembled into the matrix of Equation (1.18) in order to determine the $U(\omega)$ of the system. The displacement time histories may be obtained by applying inverse Fourier Transform:

$$u(t) = \frac{1}{2\pi}\int_{-\infty}^{\infty} U(\omega)e^{i\omega t}d\omega \qquad (1.21)$$

Domain Reduction Method (DRM)

An alternative sub-structuring approach for dynamic analyses has been developed by Bielak and his co-workers (Bielak &*Cristiano, 1984; Cremonini et al, 1988; Loukakis, 1988; Bielak et al, 2003*). The proposed methodology aims to reduce the domain that has to be numerically modeled, by subdividing the problem into two sequential parts. First, a background structure is considered (Ω^+) from which the localized geological features have been deleted, and the corresponding ground motion is calculated. During this step the computation requires a grid mesh that is only as fine as dictated by the softest material in the background model. In the second step, only a reduced region of interest (Ω) which contains the localized feature (such as a sedimentary valley, a topographic relief or even a foundation-structure system) is modeled to the desired accuracy taking into account all possible induced non-linearities (**Figure 1.49**). The ground motion obtained in the first step is subsequently used to determine a set of localized equivalent forces, which are then applied as input over a local domain (Ω). An outside benefit of the proposed procedure is that all the waves of the exterior region Ω^+ are outgoing. This

suggests that the size of the Ω^+ region may be drastically reduced provided that suitable absorbing boundaries are utilized to limit the propagation of spurious waves.

Spectral Element Method (SEM)

The spectral element method has been used for more than 25 years in computational fluid dynamics (*Patera, 1984*). However it has recently gained interest for studying 2-D (*Seriani et al., 1992; Cohen et al. ,1993; Priolo et al. 1994*) and 3-D (*Komatitsch, 1997; Faccioli et al., 1997; Seriani, 1998; Komatitsch et al., 2000; Paolucci et al., 1999*) seismic wave propagation and SSI problems. The SEM method instead of using the strong formulation to solve the equation of motion (as dictated by the Finite Element Method), is based on the weak formulation. One of the nice attributes of that formulation is that the stress-free surface boundary condition is naturally satisfied and doesn't have to be imposed explicitly. Moreover the mass matrix M is diagonal by construction thus allowing for significant reduction in the complexity and the computational cost of the algorithm.

1.6.3 Direct Methods (Coupled Approach)

Direct methods treat the non-linear SSI problem globally, without decomposing the domain into sub-structures. Among direct methods the most broadly used is the finite element method. Both the structure and the foundation soil are modeled together in one single system through an assemblage of finite elements. The method is extremely popular basically due to its flexibility to model irregular problems that may involve arbitrary geometries or abnormal soil stratification. Moreover, F.E. may also comprehend both soil elasto-plastic constitutive behavior and geometric non-linearities at the soil-foundation interface (i.e. detachment of the foundation from the underlying soil, foundation rocking response, sliding and P-δ effects of the superstructure). Yet, the

constantly increasing computational capacity is continuously enhancing the applicability of F.E modeling confronting even complex non-linear 3-D problems which were considered impossible in the past. The most important drawback of this approach is that the soil which is essentially semi-infinite in nature is normally modeled by a finite-size model having rigid boundaries which obstruct energy from radiating away from the foundation. One way to mitigate this problem is to place the boundaries of the model sufficiently far from the structure in order to eliminate the effects of the undesirable boundary-reflections. However, such an action leads to extremely large systems which may introduce a severe penalty on the required computer time. Therefore, the use of viscous and transmitting boundary elements is an appealing alternative to minimize errors associated with a finite-size model. They basically consist of a series of dashpots placed normally and tangentially at boundary nodes. The optimal absorption is achieved for perpendicularly impinging waves and by no means the angle of wave-incidence should exceed the 30^{o} to achieve accurate solutions *(Zdravkovic and Kontoe, 2008).*

Since the original work of *Wolf and Darbre (1984) Wolf and Obernhuber (1985) and Wolf (1985)* on the non-linear Soil Foundation Structure Interaction, where phenomena such as foundation uplift and soil stiffness had initially been introduced **(Figure 1.50),** direct methods and particularly F.E. have experienced a significant growth. A great portion of the work conducted has been oriented to the estimation of the bearing capacity of footings under combined loading. Following the experimental and analytical findings of *Ticof, 1977; Butterfield, 1981; Georgiadis and Butterfield, 1988;* Tan, 1990; Dean *et al*., 1992; *Gottardi and Butterfield, 1993; Butterfield and Gottardi, 1995;* Murff, 1994; a significant number of numerical studies was performed to estimate the 3D yield loci in V-H-M space of various foundation systems (shallow foundation, skirted footings

e.t.c) accounting for different soil and loading conditions. In the following paragraphs some of the most relevant works are briefly described.

Houlsby and Martin (1992) simulated the non-linear response of a spudcan foundation (offshore foundation) on clay (**Figure 1.51**). The soil model is described by an incremental plasticity model which employs a yield surface and a plastic flow rule which is properly calibrated through small-scale laboratory tests. It was found that the model may quite reasonably reproduce important features of the observed behaviour, but fails in simulating cyclic loading events. *Tani and Craig in 1995* utilized a FE code to investigate the influence of linearly increasing undrained shear strength with depth on the bearing capacity of shallow foundations, under both plane strain and axisymmetric conditions. Their numerical results have been validated against centrifuge experiments. The effect of pre-loading on the bearing capacity of a surface foundation lying on a normally consolidated stratum has been thoroughly examined by *Bransby (2002)*. In his FE analyses a Cam Clay model was chosen to describe the non-linear soil response. It was concluded that the application of a vertically dead weight loading may significantly increase the foundation capacity especially in terms of horizontal loading (**Figure 1.52).** *In 1999, Bransby and Randolph* studied the response of a skirted footing under combined vertical (V), moment (M) and horizontal (H) loading. In this foundation system (extensively used in offshore engineering) the presence of the skirt has a binary role: on one hand it allows suction to develop when uplift loadings are applied resulting in an increased uplift capacity, while on the other, during compressive loading the achieved confinement within the skirts results in increased bearing capacity. A two dimensional F.E. model had been utilized to deduce the ultimate footing loading. The soil was modelled as an elastic-plastic Tresca material with a linearly increasing with depth

undrained shear strength. It was found that the shape of the yield locus was similar to that predicted by relevant research works in V-M and V-H space, but differed significantly in M-H representation. The bearing capacity of skirted footings under combined loading had been also investigated by *Gourvenec and Randolph (2003)*. In this study emphasis was given on the effect of shear strength heterogeneity. The degree of heterogeneity was defined in terms of a non-dimensional non-homogeneity factor. It was concluded that under combined loading conditions, the load capacity for heterogeneous soil conditions cannot be estimated by simply scaling the failure locus obtained for homogeneous conditions by a factor related to the degree of heterogeneity.

Another significant work on the field was that of *Taiebat and Carter (2000).* They conducted 3-dimensional finite-element analyses of circular foundations lying on a homogeneous and purely cohesive soil. The foundations were assumed to adhere fully to the soil (i.e. compressive, tensile and shear stresses may develop at the interface between the footing and the soil). The three-dimensional failure locus in V-H-M space was presented, and an equation that approximates the shape of the failure locus was also suggested. A similar work has been published by *Gourvenec 2007* where the ultimate limit states of rectangular footings with varying (B/L) ratios (under combined vertical (V), moment (M) and horizontal (H) loading) were presented. In this study 2 distinct footing/soil interface conditions are considered: interface unable to sustain tension and interface with unlimited tensile resistance. Results are presented as failure envelopes in V-H, V-M and V-M-H space accompanied by extremely useful analytical expressions. The main outcome of this work is that for footings unable to sustain tension the footing aspect ratio does not affect the shape of the failure envelope: therefore the ultimate limit state of a footing may be derived from a unique envelope scaled

appropriately and a closed-form expression is proposed to describe the shape of this normalized failure envelope. This is certainly not the case when the footings are able to sustain tension and hence the shape of failure envelope is controlled by footing geometry and dimensions. Typical results from this work are displayed in **Figure 1.53.**

In all the above studies, despite the great amount of sophistication involved in describing the limit state of complicated foundation systems, relatively little attention had been drawn to realistically simulate the superstructure (the most common approach is to replace the structural system by combined M, Q, N loading) and the geometric non-linearities associated with the latter (i.e. P-delta effects). Only recently, *Anastasopoulos et al, (2009)* conducted fully coupled FE numerical analyses to investigate the rocking response of a 1-dof bridge pier lying on a stiff clay profile. The nonlinear response of both the pier and the underlying soil were simulated utilizing a properly calibrated plastic model with kinematic hardening. The footing-soil interface has been modeled accordingly to simulate geometric nonlinearities at the foundation level, while P-delta phenomena where also taken into account **(Figure 1.54**). Subjecting the pier to an ensemble of recorded accelerograms well beyond the structure's design, the authors manifested the beneficial role of rocking and soil yielding in dissipating the seismic energy, hence protecting the superstructure from collapse. **Figure 1.55** illustrates this "fail-safe" response of the under-designed system that not only survives collapse but also experiences minimal residual drift. The only price to pay is the relatively high settlements that for the case displayed here (pier subjected to the devastating Takatori accelerogram recorded during the Kobe, 1995 earthquake) exceeded 20 cm.

1.7 2D Wave Propagation Phenomena

1.7.1 Theoretical Studies

Analytical Solutions

The scattering of earthquake waves from surface and subsurface inhomogeneities has been extensively studied during the past fifty years. Pioneering work in this area was done in the 60's and early 70's. Early attempts involve the study of the elastic wave propagation problems in horizontally stratified media with irregular and regular interfaces (*Herrera, 1964; Tsai 1969; Aki and Larner, 1970; Boore, 1970*). Closed form exact analytical solutions on the 2d diffraction problem (using separation of variables and expansion of the solution in a basis of orthogonal functions) were obtained by *Trifunac (1971, 1973)* for semicircular and by Wong and *Trifunac (1974a, b)* for semi-elliptical valleys and canyons subjected to plane *SH* waves. Their work revealed the prominent role of surface topography on the resulting surface motion: the amplification of surface displacement changes rapidly from one point to another, but the amplification is always less than 2. The angle of incidence of plane SH waves γ (see **Figure** 1.**56**), and. the ratio of λ/r (with r being the dimension of the subsurface irregularity and λ the wavelength of the incident wave) control the trends and the complication of the amplification pattern.

The diffraction problem of dilatational (P) and vertically polarized shear (SV) incident waves has received less attention due to its complexity (the orthogonal wave functions developed in classical physics are not separable for the half-space surface due to coupling of the boundary conditions). *Lee (1984)* and *Lee and Cao (1989)* overcame this difficulty for a semi-spherical valley and canyon by expanding the spherical wave functions further into power series that could match all the boundary conditions. Following a similar procedure *Cao and Lee (1990)* analytically tackled the scattering of

plane P waves by circular and cylindrical canyons by approximating the surface of the half-space close to the canyon by a cylindrical surface with very large radius and represented the scattered waves in Fourier-Bessel series. *Todorovska and Lee (1991)* extended further the applicability of the *Cao and Lee (1999)* method by studying the scattering of plane elastic *SH* waves from shallow circular alluvial valleys with variable depth.

Despite the value of the aforementioned analytical methods in highlighting the main mechanisms involved in the 2-d diffraction problems, their applicability is limited to special geometries assuming elastic wave propagation. To this end, a number of numerical methods (boundary integral equations, finite difference and finite elements methods) have been developed over the years to study the dynamics of more complex irregularities of arbitrary shape. In the ensuing the main advances in the 2D and 3D valley amplification effects are briefly presented and the most significant outcomes are summarized.

Boundary element Algorithms and other approximate numerical techniques

The boundary integral equation method was firstly introduced by *Wong and Jennings (1975)* for a canyon of arbitrary shape. Their work was followed by series of methods using different types of integral equations. (i.e., *Sánchez-Sesma and Esquivel (1979), Wong (1982), Dravinski (1982), Sánchez-Sesma et al. (1985), Kawase (1988), Niwa and Hirose (1985), Bouchon et al (1989), Gaffet and Bouchon (1991)). Jongmans and Campilo (1993)* used the boundary integral equation method of *Gaffet and Bouchon (1991)* to predict amplification effects in Ubaye Valley. The 2-d model utilized in their study consists of a series of branches of cosine and straight lines and is depicted in **Figure 1.57**.

Although the numerical simulations were able to explain some general features of the recorced spectral ratios, some important discrepancies existed between synthetic and experimental amplifications: modeling results systematically underestimated the recorded amplification effects.

Sanchez-Sesma et al (1993) proposed the use of an indirect boundary integral formulation (BEM) to study the physics of diffraction problems. The method was validated against the theoretical solutions of *Trifunac (1971)* for the response of a semicircular valley subjected to oblique incident *(φ* = 30^{o}) harmonic SH waves, and *Dravinski and Mossessian (1987)* for the case of again a semicircular valley excited by oblique incident SV and Rayleigh waves *(φ* = 30^{o}). Afterwards the BEM was utilized to study the response of semielliptical soft deposits under incident Rayleigh waves. It was concluded that even a relatively mild heterogeneity can generate important variations in both amplitude and polarization of the ground motion. A very soft shallow deposit was also analysed against incident SH and SV waves. Very large amplifications were computed and the contour maps of transfer functions in the frequency-space domain *(f-x)* reveal a fine structure in which locally generated surface waves play a significant role for frequencies higher than the one that controls the 1D response at the centre **(Figure 1.58)**. *Sanchez-Sesma and Luzon in 1995* extended further this work to account for diffraction phenomena associated with the 3-dimesional basin geometry. It was revealed that even in a simple axisymmetric case, 3-dimensional diffractions result in extremely complicated amplification patterns.

Fishman and Ahmad (1995) studied the seismic response of two-dimensional alluvial valleys of semi-elliptical cross-section subjected to SH, P and SV waves. Using a rigorous boundary element algorithm they studied the influence of key parameters, such as,

valley depth, impedance ratio, frequency, and angle of incidence on surface ground motion. Furthermore, the case of a valley within a layered half-space has been analyzed and results were compared with those obtained for a valley within a homogeneous half-space.

Recent studies with BEM involve the work of *Semblat and Duval (2000)* and *Kham et al (2002)* .Of extremely interest is also the work of Bard and Bouchon (1980(a,b)). The latter using the Aki-Larner technique extended in the time domain, investigated thoroughly the dynamic response of bi-dimensional valleys of various geometrical and elastic parameters to vertically incident SH, P and SV waves both in frequency and time-domain. They concluded that irrespectively of the type of the incident wave, the valley behaviour is quantitatively similar: non-planar interface causes surface waves (Love waves when the valley is excited by SH waves and Rayleigh waves when subjected to P and SV waves) to be generated at the valley edges and propagate laterally inside the basin **(Figure 1.59)**. The amplitude of these waves is greatly controlled by the velocity contrast, the valley shape and the frequency content of the excitation and may under circumstances be even higher than the disturbance associated with the direct incident signal.

Paolucci et al (1992) presented a simplified methodology to study the SH wave propagation in a class of wedge-shaped alluvial valleys. The proposed method that is based on the assumption that these wedge-shaped valleys may be divided into simple elements for which the scalar Green's functions can be easily determined, allows for fast parametric analyses both for the prediction of the seismic valley response and for interpretation of existing instrumental data. The scalar Green's function at a point $P(r, \varphi)$ due to a harmonic antiplane load at a source $S(r_o, \varphi_o)$ is expressed as a superposition of the contributions of 4N source points in unbounded homogeneous medium, located on

the circle of ray r_o. **Figure 1.60** schematically summarizes the above procedure for the case of a rigid base valley assuming N=3.

Finite difference Methods

Harmsen and Harding (1981) were among the first to apply finite difference techniques to study the response of a sedimentary basin in an isotropic elastic half-space to vertically incident compressional and shear sources. In this study of primary interest was also the formation of Rayleigh waves over the flank of the basin and the effect of soil anisotropy on the latter **(Figure 1.61).** In 1983 *Otsuki and Harumi* investigated the effect of subsurface inhomogeneity on the surface motion. The examined geometry **(Figure 1.62)** that consists of a cliff with a soft layer and filled land, was subjected to vertically incident SV waves. It was found that the surface displacement is very much influenced by surface irregularities when the incident wavelengths are comparable to the size of the topographic features. Moreover the combining incident SV and Rayleigh waves were assumed to be responsible for a zone of large amplification near the slope crest. Another interesting work is that of *Mozco et al (1996)*, who parametrically investigated possible 2D resonance phenomena in different parabolic valley geometries using finite difference algorithm. **Figure 1.63** summarizes their main findings: a 2D resonance is observed in all the four valleys examined despite the fact that the valley-layer velocity contrasts are well below the existence curve of *Bard and Bouchon (1985*).

Hill et al (1990) conducted a comprehensive study in order to delineate some of the important factors controlling low frequency *SH* wave amplification observed in the Salt Lake Basin in Utah. Towards this end, a finite-difference method was used to simulate SH-wave propagation and resonance phenomena in a group of two-dimensional models

of the Salt Lake Basin corresponding to different levels of basin complexity as illustrated in **Figure 1.64** (from a 1-dimensional profile to a relative complicated asymmetric basin structure). Results indicate that the low-frequency *SH* amplification (0.2 to 2.0 Hz) is greater over the deepest part of the basin and is primarily attributed to multiple reflections inside the two near surface low-velocity layers **(Figure 1.65)**. Their predictions of site amplification are somewhat verified by comparing synthetic spectral ratios with measured spectral ratios determined from nuclear explosions. The numerical findings of *Hill et al* had been further affirmed by the work of *Olsen et al (1995).* In this later work a more sophisticated 3D finite-difference model was utilized to study the 0.2 to 1.2 Hz elastodynamic site amplification in the Salt Lake Valley. Simulations were carried out for a P wave propagating vertically from below and for P waves propagating horizontally to the north, south, east, and west. Their results revealed that for steeply incident P waves, the impedance decrease and resonance effects associated with the deeper basin structure control the amplification of the initial P-wave arrival, whereas reverberations in the near-surface unconsolidated sediments were responsible for the large-amplitude coda waves. These reverberations were mainly caused by *P-to-S* converted waves, and their strength was found to be highly sensitive to the incidence angle of the source.

Fäh et al. (1993, 1995) used a hybrid technique based on mode summation and finite differences to simulate 2-Hz ground motion in Rome for the 13 January 1915 Fucino earthquake. They found peak accelerations of up to 60 cm/sec^2 and maximum amplification factors of 5–6 within the 2D basin model of Rome with respect to a 1D model, caused by resonance effects and excitation of local surface waves. According to their study the largest amplification was observed at the edge of the sedimentary basin of the Tiber River valley. Some years later *Natale and Nunziata (2004)* employed the

same hybrid method to study the 2D wave effects at Sellano Valley during the 1997–1998 Umbria seismic sequence.

During the months that followed the 1994 M6.7 Northridge earthquake, several acceleration stations were deployed in the San Fernando basin to record aftershock data so as to indirectly estimate site-amplification effects. In parallel, a significant amount of numerical models have been constructed to reproduce analytically the observed valley response. *Haase et al. (1996), Pitarka and Irikura (1996)*and *Hauksson and Haase (1997)* proposed different 2D cross sections models of the San Fernado valley, while more sophisticated 3D models have been utilized by *Olsen et al (1995)* and *Olsen and Archuleta (1996)*. In 1999 *Scrivner and Helmberger* using a two-dimensional finite difference numerical technique (*Vidale et al., 1985; Helmberger and Vidale, 1988*) modeled the seismic response of San Fernado valley under two distinct aftershocks with similar epicenters, but with different hypocentral depths: a shallow (4 km) and deep (16 km) event. The main objective of that work was to decide upon a valley structure and soil properties that may replicate the main features of the observed response: the deep event was mostly insensitive to the basin, while recorded waveforms from the shallow event manifest the existence of large basin-generated surface waves. The recorded waveforms also indicated interactions of the wavefield with structure below the basin. The numerical model that fitted best the measured response included a slow upper basin down to 1.5 km, a deeper basin down to 3.5 km, and a gradient in the background model at 5.5 km depth. The velocity contrast between the upper and lower basins needed to be large to generate multiple cycles in the surface waves. The velocity contrast and depth of the upper basin were sensitive parameters of the upper basin, whereas the waveforms

were less sensitive to the steepness of the basin edge. The location of the bottom of the deep basin, relative to the source, was found to be another important parameter.

Olsen et al (2000), using a powerful finite difference algorithm simulated viscoelastic wave propagation in a three-dimensional model of the upper Borrego Valley, southern California, for a M 4.9 earthquake with epicenter 5 km north of the valley. The simulation reproduces quite well the overall pattern of ground motions at the basin surface **(Figure 1.66)** and borehole sites (as recorded by the implemented surface and deep downhole array) and shows a good correlation of the observed to the synthetic waveforms **(Figure 1.67)**: the first wave arrival was nicely reproduced while the model cannot capture the late arrivals. In another study *Olsen et al (2006)* utilized the already developed powerful numerical algorithm to estimate long-period (>1 Hz) ground motions for possible earthquake scenarios for a 3D velocity model of Rome. They discriminate two possible mechanisms of seismic hazard in Rome: (1) seismic waves from Alban Hills at an average distance of 25 km from Rome which may generate large peak motions and (2) seismic waves form Apennines regions (80-100 km away) that may result in ground motions of extended durations causing significant damage on the built environment.

Another extremely ambitious project was that conducted by *Hartzell et al (2006)* who utilizing the 3D finite difference code of *Liu and Archuleta (2002)*, constructed a 3D velocity and attenuation model of the Santa Clara Valley. Waveforms were calculated to an upper frequency of 1 Hz using a parallelized code. **Figure 1.68** depicts the 3-dimensional geologic structure of the model while **Figure 1.69** shows a typical outcome of their study for a specific earthquake scenario.

Of particular interest is the work of *Kamiyama and Matsukawa (2002)* who formulated an iterative numerical method for analyzing nonlinear earthquake response

of irregular grounds. The method (PSM) combines the principles of the equivalent linear method with that of pseudo-spectral techniques. *Kamiyama and Fukuchi (2007)* utilized PSM to investigate the effects of induced non-linearity to wave scattering phenomena by studying the response of two ground models to vertically incident Ricker wavelets: a soft surface layer (assumed to behave nonlinearly) which forms (a) symmetric trapezoidal basin and (b) an asymmetric basin over a bed halfspace. They concluded that when the soil response is considered linear the irregularity of the surface layer plays an important role in generating some secondary waves that travel horizontally along the surface. These horizontally traveling waves overlap with those direct vertically propagating amplifying the ground motion at the valley surface. Contrarily to the linear response, when the soft soil is allowed to respond non-linearly, the horizontally traveling waves are less pronounced due to the increased damping effects (increasing strain results in increased damping values). Another important outcome of this study was that the effects of material nonlinearity were observed to be more remarkable for the secondary waves, which appear in the later phases of the motions, rather than for the direct waves of vertical propagation.

Finite Elements Methods

An extremely thorough study on the 2D site effects of the Salt Lake valley in Utah had been conducted by *Benz and Smith (1988)*. The authors using a non-Galerkin finite-element formulation and an explicit finite-difference technique (*Kelly et al., 1976) investigated the valley response under both* near- and far field earthquakes. **Figure 1.70** illustrates the cross-sections of the simplified numerical model along with the four kinematic source simulations. Synthetic seismograms from vertically incident plane-wave

sources and buried double-couple sources predict large amplitude Rayleigh-wave propagation from the edges of the basin and, in general, an almost uniform site amplification pattern. On the other hand, in the case of the near-field simulations, the produced amplification seems to be overshadowed by the source directivity effects: the maximum amplification is observed near the surface projection of the fault while the amplification rapidly decays as the distance from the fault increases.

Papageorgiou and Kim (1991) studied the seismic response (due to antiplane line (point) sources and incident plane *SH* waves) of Caracas valley at Venezuela through a 2-D model of its NS cross-section through the Palos Grandes district .It was concluded that the steeply sloped northern edge of the valley was a more efficient generator and reflector of surface waves than the mildly sloped southern edge. Also the spectral amplification and time response characteristics of this asymmetric wedge-shaped valley were highly controlled by the direction of incidence of the excitation waves **(Figure 1.71)**. The same 2-D model of the valley was then used to simulate also the antiplane response of the valley to synthetic strong motions equivalent--in amplitude,frequency content, and duration--to those that most likely were generated by the 29 July 1967 Caracas earthquake. The analysis revealed that for the specific event the peak acceleration was fairly uniform across the valley, varying from 0.15 to 0.21 g, while on the contrary, peak velocities and peak rotational (torsional) strains varied considerably (factor of 2 to 3) across the valley.

In all the preceding studies emphasis was given in the proper simulation of the complicated wave-field pattern by ignoring phenomena associated with inelastic soil response. Towards this direction was the work of *Zhang and Papageorgiou (1996)* who using *a hybrid* numerical technique that combines the boundary integral equation

method with the finite-element method (Zhang *et al.,* 1995) estimated the severity of ground motion that the Marina District experienced during the 1989 Loma Prieta mainshock. To validate their numerical algorithm, initially the elastic response of a two-dimensional model of a cross section of the Marina District was simulated and compared with the recorded aftershock data. Subsequently, the same 2-dimensional model was excited by the ground-motion time histories recorded at an adjacent rock outcrop site during the mainshock **(Figure 1.72)**. To account for the effect of soil nonlinearities, an iterative procedure, referred to as the "equivalent linear approach", was adopted according to which the values of soil damping and stiffness are selected to be consistent with the level of strain at. Their conclusions suggest that, in general, the damping characteristics of soil deposits (reflecting the amount of induced non-linearity) are a key factor in controlling the nature of the overall response of a sedimentary basin.

Bielak and Ghattas in 1999 studied the earthquake response of a small valley in Kirovakan in order to explain the spatial distribution of the structural damage during the 1988 Armenia earthquake. The results of the 2D finite elements simulations show striking differences with respect to the corresponding 1D soil amplification analyses. In particular, it was concluded that the peak ground response and structural response were almost twice as large for the 2D as for the 1D model. Moreover, the 2D model exhibits, a new set of resonant frequencies and concomitant ‘‘mode shapes’’ across the valley, which are directly related to the rapid oscillation (both spatial and with frequency) of the ground amplification ratio along the valley **(Figures 1.73 and 1.74)**. These results provided a meaningful explanation of the observed irregular damage distribution: two identical structures located in the same vicinity or two slightly different structures

located essentially on the same site experienced significantly different earthquake motion and therefore different level of damage.

Puglia et al (2007) utilized the finite element code QUAD4M (*Hudson et al., 1994*) to conduct two-dimensional time domain analyses in order to explain complex site amplification phenomena in the town of San Giuliano di Puglia, during the Molise 2002 earthquake sequence. Two different geometries of the geological structure have been hypothetized : (a) a syncline ("basin" model) and (b) an overthrust ("wedge"model). The numerical modeling for the aforementioned structures is depicted in **Figure 1.75**. The analyses provided a PGA distribution along the ground surface increasing from the edges to the center of the clay deposit, and characterized by significant longitudinal fluctuations. This result is consistent with the irregular seismic damage distribution.

The effects of basin edge slope on the dynamic response of horizontal soil deposits have been also investigated by *Ciliz et al (2007)*. To this end, 24 basin models of trapezoidal cross section were generated to represent different valley geometries (i.e. depth of basin, slope of basin edge), while the non linear stress strain behavior of soils had been also incorporated using an equivalent linear method. To quantify the effects of basin edge slope the dimensionless ratio PGA^{2D}/PGA^{1D} was introduced. It was concluded that a significant shadow area (where the predictions of the 1D analyses were conservative compared to that of the 2D analyses by a factor of as low as 0.30) could be observed in almost all cases examined. Besides, the PGA^{2D}/PGA^{1D} values were decreasing with increasing slope inclination. However, beyond this region one-dimensional analysis results were unconservatively biased by a factor as high as 1.2, with maximum being the 2D amplification at a region between 0.8 to 1.4 (in dimensionless terms).

1.7.2 Observational Evidence

Lately, the critical issue of capturing the real aggravation mechanisms and the necessity to confirm the theoretical results has led to the development of fully instrumented test-sites, which serve as large scale natural laboratories. The Euroseistest in the Volvi basin in Greece [*Pitilakis, 2004; Chavez-Garcia et al., 2000; Raptakis et al., 2000; Makra et al., 2001; 2005*], the Japanese seismograph arrays in Ashighara Valley [Ohtsuki & Harumi, 1983; Ohtsuki et al., 1984] and Ohba Valley [Tazoh et al., 1988; Gazetas et al., 1993], the alluvial Valley of Parkway in New Zealand [Chavez-Garcia et al., 1998], the Coachella Valley in California [Field, 1996], and the Valley of Nice in France [Sanchez-Sesma et al., 1988], are some of the best known test sites. Their merits include : (i) the high density of the installed accelerograph arrays, (ii) the detailed knowledge of subsoil geometry and soil mechanical properties, and (iii) the accumulation of records. Site response analysis confirmed the importance of 2D geometry effects, clearly suggesting that 1D soil amplification phenomena may be significantly contaminated (*aggravated*) by laterally propagating surface waves. Although such studies have offered valuable insights, in most cases only weak ground motions have been recorded so far.

One of the first attempts to provide observational evidence of the importance of 2D and 3D site effects was that of *King and Tucker (1984)*. In this early work in order to measure the dependence of valley site's response on key parameters (such as, input signal's azimuth and incidence angle, the position of the site within the valley, frequency, valley dimension, and the impedance contrast of the valley sediments to the basement rock) a number of field experiments had been designed. The valley under study was 400 m wide and 700 m long, with a maximum sediment thickness of 60 m. The average seismic impedance contrast between the sediments and underlying basement rock was

about 6:1. Their findings correspond to elastic valley response as the input motions were weak, varying between 10^{-5} and 10^{-3} g. Results from this study show apparent site amplifications: Ratios of Fourier spectra from soil sites to spectra from nearby rock sites were as much as a factor of ten, depending strongly on the frequency and the distance of the site from the valley edge. In fact ground motion at valley-edge and mid-valley sites, separated by less than 100 m, differed by as much as a factor of five. On the other hand the response to earthquake motion of a valley was found slightly to depend on the input signal's azimuth and the angle of incidence.

The work of *Frankel (1994)* had considerably contributed in the better understanding of the basin induced surface waves. Utilizing measured data from three dense arrays deployed in the San Bernardino Valley, he showed that the long duration of shaking with periods of 1 to 3 sec that followed the aftershocks of the Big Bear and Landers earthquakes may be only attributed to short-period surface waves propagating in the valley. Indeed comparison of the observed records with synthetics determined from a flat layered velocity models indicates that these surface waves could not be generated near the source, but must have been produced by trapping of the incident S wave near the edge of the Valley **(Figure 1.76).**

Field (1996) based on measurements of a linear array deployed in the Coachella Valley, California, during the 1992 Landers/Big Bear aftershock sequence provided experimental evidence that the seismic response of the site was clearly dominated by basin-edge-induced waves: Sediment to bedrock spectral ratios computed using short windows that exclude the basin-edge-induced waves imply that the multi-dimensional effects are significant only below 4 Hz, where they increase amplifications by an approximate factor of 2. In the same pace was also the work of *Malagnini et al (1996)*

who based on explosion, earthquake (only low intensity events), and ambient noise recordings collected at the eastern edge of a Pliocene sediment-filled valley, nearby the town of San Casciano dei Bagni deducted extremely high amplification amplitudes. **Figure 1.77** clearly demonstrates the above observation with the left figure incorporating the observed amplifications that may be attributed only to the direct S waves, while the right figure illustrates the experienced amplifications where all wave trains were taken into account. It is clear that these later arrivals significantly amplify the valley response for frequencies below 2.5 Hz.

In *1999 Chávez-García* et al employing data from a dense seismograph array that operated for more than 2 months in the alluvial basin of Parkway in New Zealand studied the amplification phenomena associated both with 1D and 2D valley response. The primary conclusion of this work was that it may be extremely difficult to differentiate between 2D and 1D site effects, if try to do so in the frequency domain (as they both appear at the same frequency range). A side outcome was that a stable direction of propagation for edge-generated Rayleigh waves was distinguished irrespectively of the excitation events confirming that valley geometry strongly controls the produced wave-forms. Stephenson (2007) by exploiting data recorded by a temporary dense seismometer array again at the Parkway valley, distinguished strongly 2-d phenomena site effects associated with both transverse and longitudinal waves, while quite interestingly he provided evidence of a ‘‘cellular mode of resonant response’’ of the valley similar to that suggested by *Bard and Bouchon* in their numerical studies.

Additional evidence on the importance of basin generated surface waves was presented by *Cornou et al (2003b)* by studying the site effects in Grenoble Basin in French Alps. In an attempt to explain the large amplification and the significant duration

increase of ground even for moderate-size events, a dense array of 29 seismometers had been established. Utilizing a methodology developed by *Cornou et al, 2003a* (which is based on time–frequency coherence and multiple signal classification algorithm) the complex recorded wave field was decomposed and the distinguished wave arrivals have been identified. It was concluded that the ground motion inside the valley was dominated by basin-edge-induced waves (60% Rayleigh waves and 40% Love waves) that carry 4 times more energy than the direct wave field, regardless of the type of event considered. Similar were the findings of *Hartzell et al (2003)*, who analyzing the ground motion records from a 52-element dense seismic array near San Jose in California, concluded that the observed amplification pattern (who is almost the same for both local and regional events) may be attributed to the generation/trapping of surface waves above the shallowing basement of the basin.

From an engineering perspective, valuable are the findings of *Safak (2007)* who investigated the effects of surface waves on structural response and presented both observational and analytical confirmations of their significance. He suggested that surface waves may be particular critical for long-period structures, such as tall buildings and base-isolated structures since their energy is mainly concentrated at long periods. Moreover because of their long duration, surface waves can push a damaged structure into complete collapse because of the additional hysteretic deformation cycles that the structure goes through. **Figure 1.78** clearly illustrates the above statement by comparing the response of 2-second elasto-plastic oscillator when subjected to an excitation of 20 seconds (where the late arrivals that are associated with surface waves have artificially been removed) and when excited by the entire record.

Figures of Chapter 1

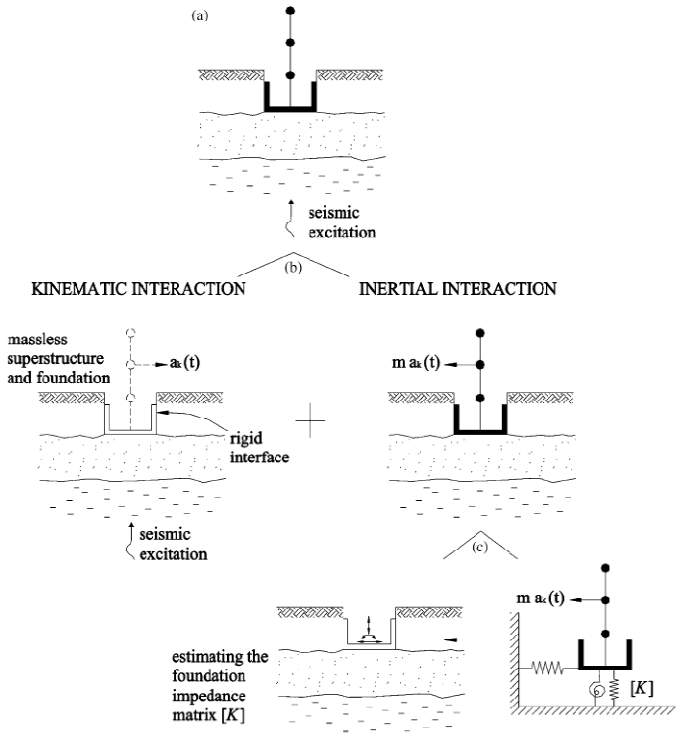

Figure 1.1: (a) The geometry of soil–structure interaction problem; (b) decomposition into kinematic and inertial response; (c) two-step analysis of inertial interaction (after *Mylonakis et al, 2006*).

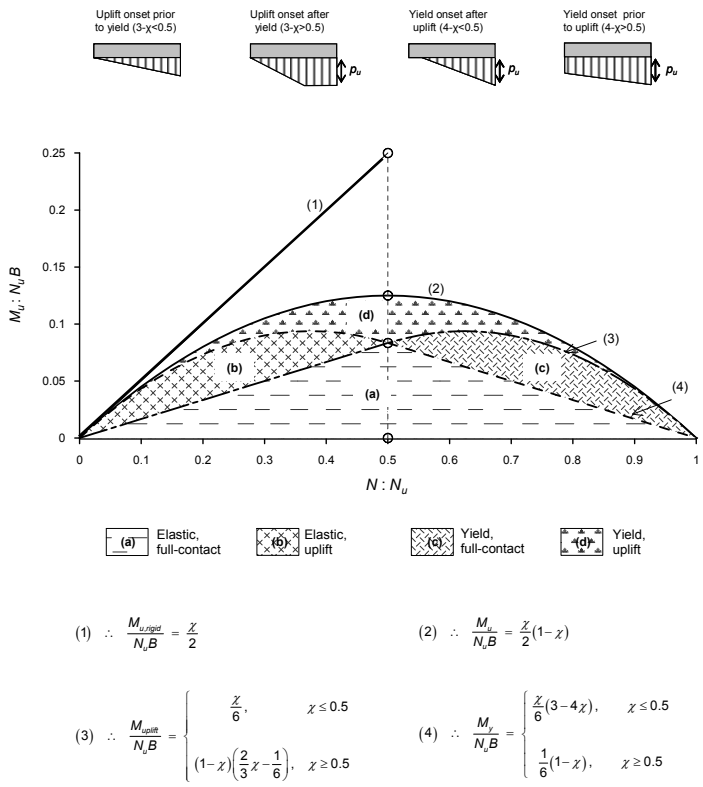

Figure 1.2: Interaction curves in the normalised N–M plane for bearing capacity failure on rigid (1) or deformable (2) soil. Decomposition of uplifting and soil-yielding mechanisms (*after Gazetas et al, 2007*)

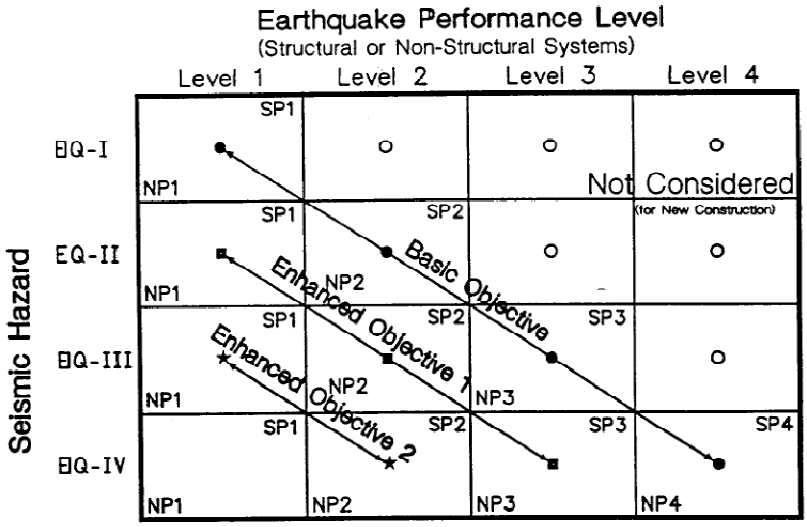

Figure 1.3: Relationship between earthquake design level and performance level (*after OES, 1995*)

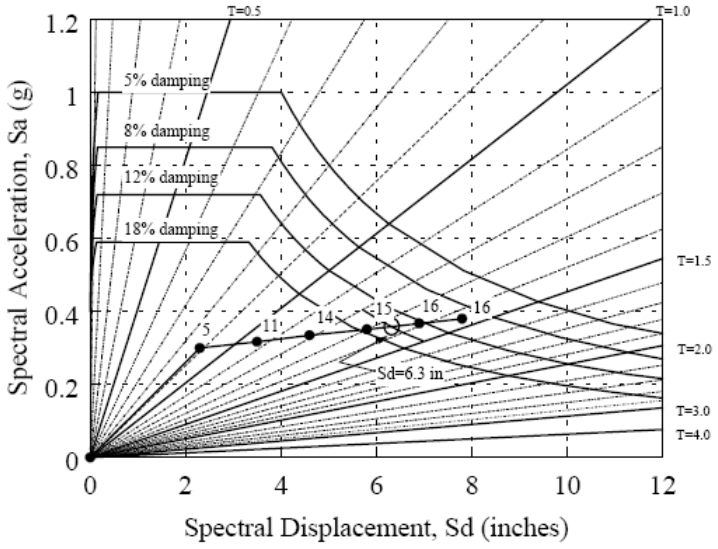

Figure 1.4: Graphical solution using the Capacity Design Spectrum approach (*after Freeman, 1998*)

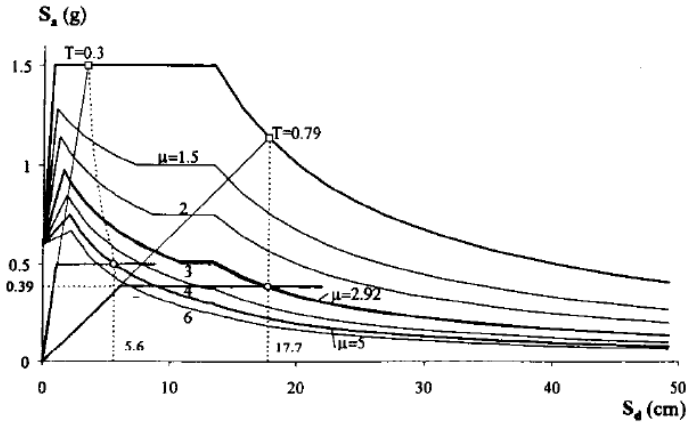

Figure 1.5: Modification of Capacity Spectrum Method utilizing inelastic response spectrum proposed by *Fajfar (1998)*

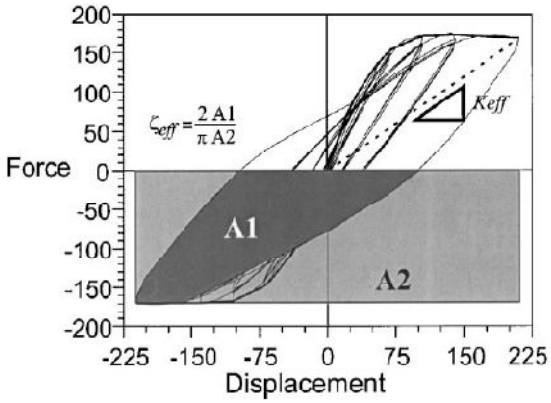

Figure 1.6: *Step 1* of the Displacement-based Design Approach: Determine the effective Stiffness and Damping Properties of the equivalent 1-dof system

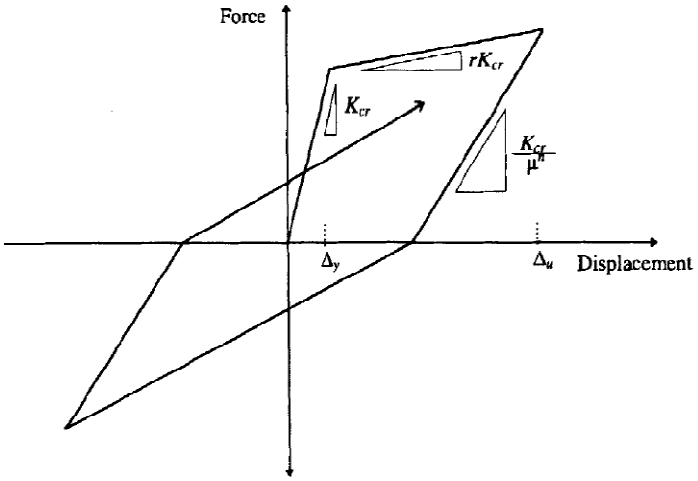

Figure 1.7: *Step 2* of the Displacement-based Design Approach: Estimation of effective damping according to Tadeka degrading stiffness hysteresis

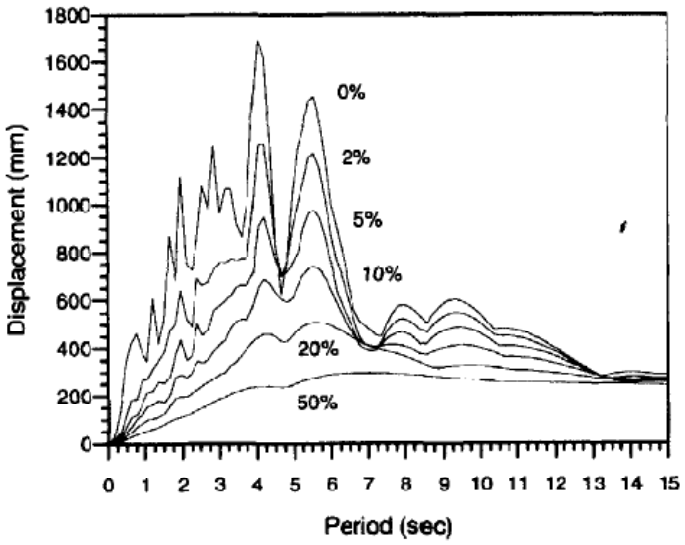

Figure 1.8: *Step 3* of the Displacement-based Design Approach: Decide upon a Displacement response spectra

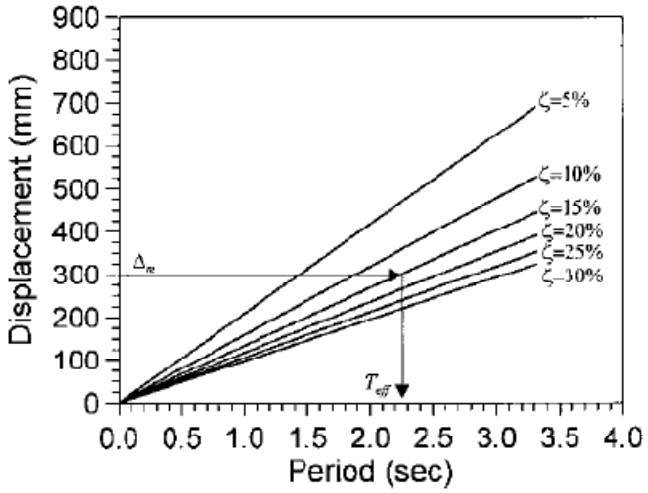

Figure 1.9: *Step 4* of the Displacement-based Design Approach: Obtaining the effective period (at the point of the maximum Displacement) from a Elastic Displacement Response Spectrum for a given allowable displacement

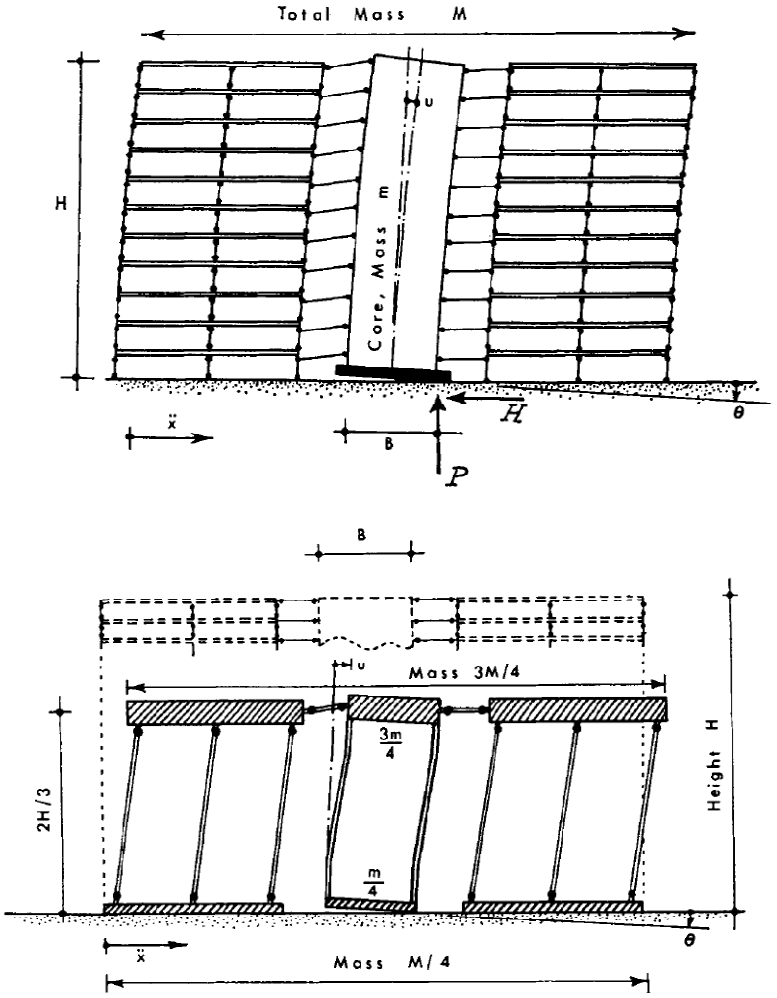

Figure 1.10: Model of core-stiffened building and equivalent simplified first-modal system analyzed (after *Meek, 1978*)

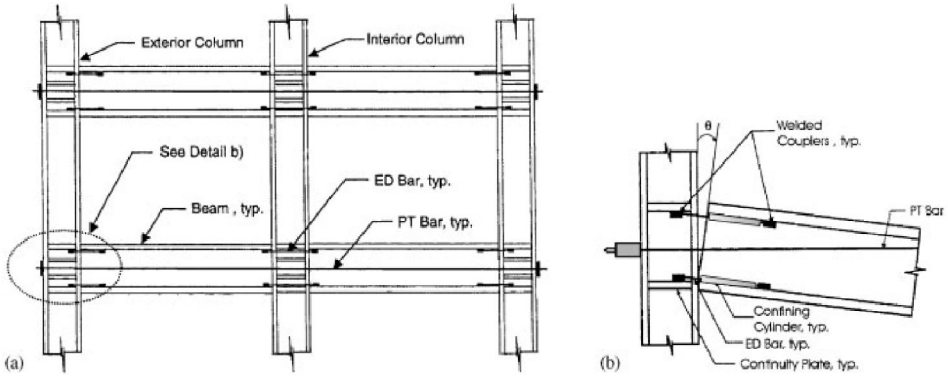

Figure 1.11: Concept of PTED steel connection: (a) steel frame with PTED connections; (b) deformed configuration of exterior PTED connection (after *Christopoulos, et al 2002*)

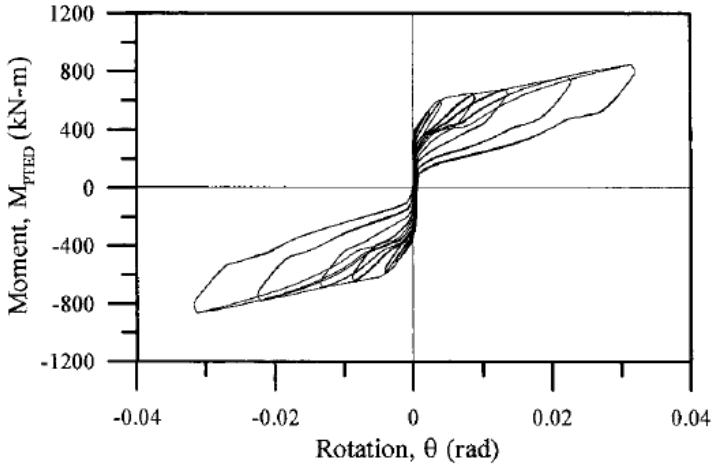

Figure 1.12: Experimental moment–rotation curve of a PTED connection (after *Christopoulos, et al 2002)*

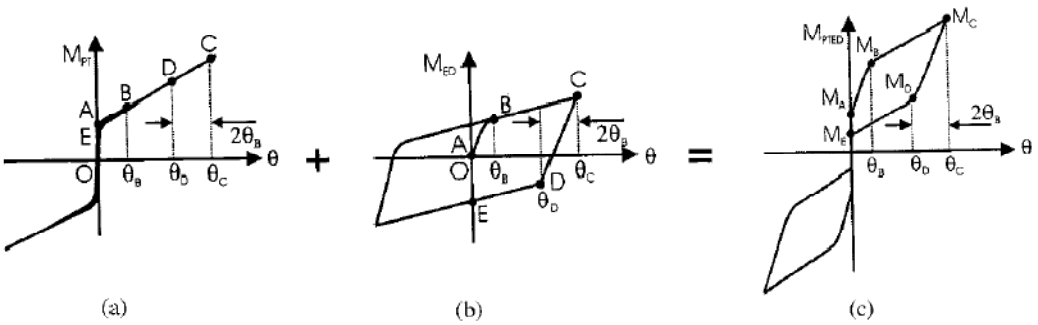

Figure 1.13: Idealized hysteretic behaviour of the PTED beam-to-column connection: (a) contribution of PT Bars; (b) contribution of ED bars; and (c) moment–rotation relationship of PTED connection *(Christopoulos, et al 2002)*

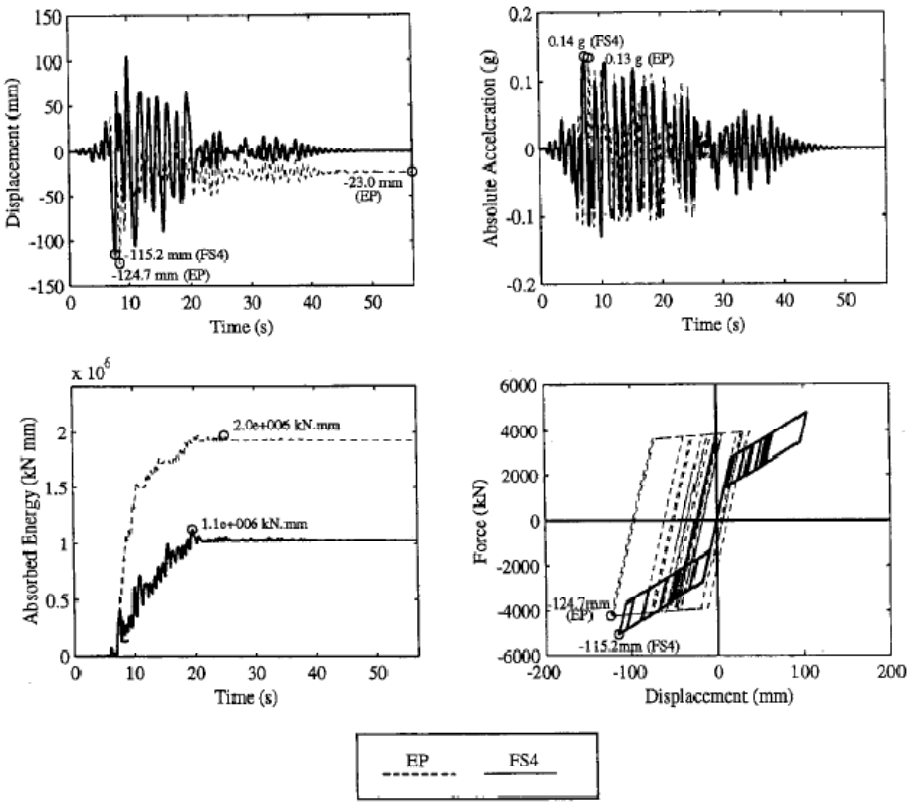

Figure 1.14: Comparative results on the response of EP and FS4 systems under 130% of Loma Prieta record (a) displacement time-history; (b) acceleration time-history; (c) absorbed energy time-history; and (d) force–displacement response *(Christopoulos, et al 2002)*.

Figure 1.15: Application of the "controlled rocking" concept to enhance the seismic performance of bridge piers

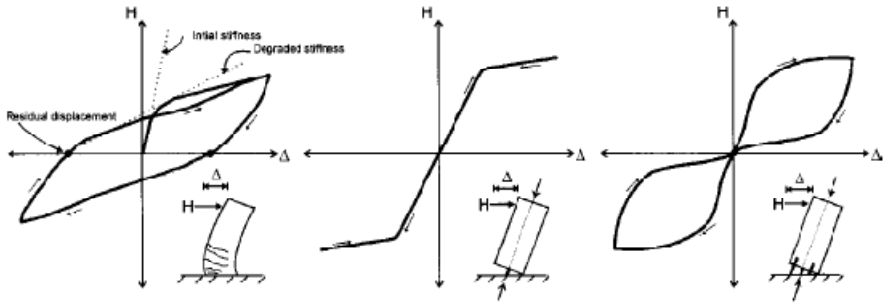

Figure 1.16: Hysteretic response of various structural wall systems : (a) conventional system; (b) fully pre-stressed system; (c) partially prestressed "hybrid" concrete system

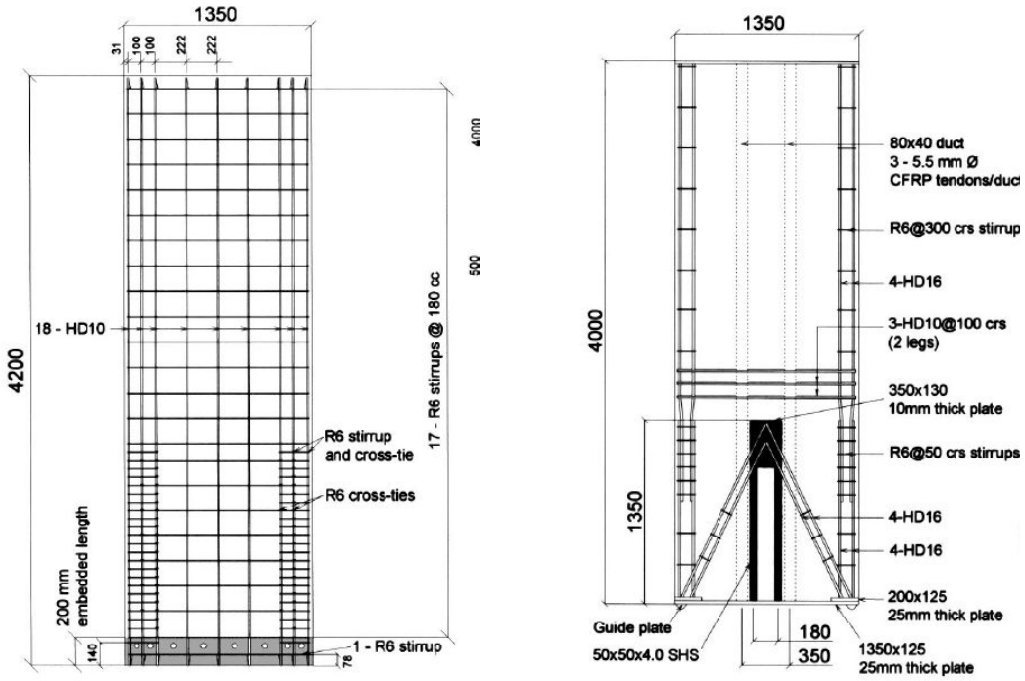

Figure 1.17: Details of experimental Configuration of (a) the conventional precast reinforced wall and (b) of the "hybrid" system proposed by *Holden el al, 2003.*

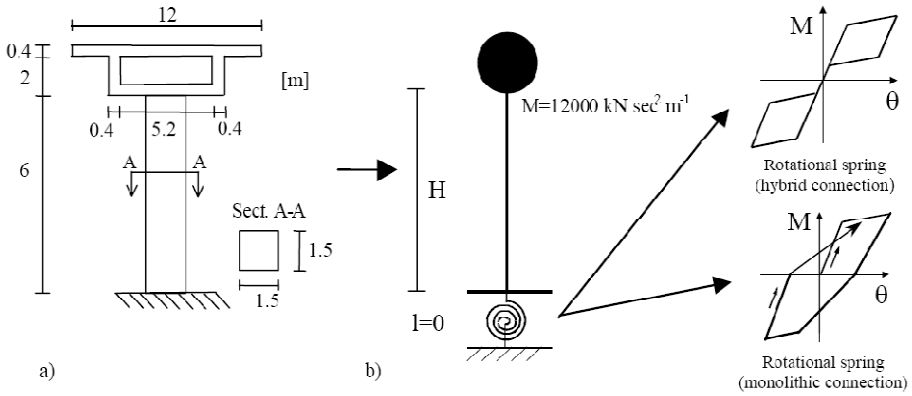

Figure 1.18: a) Pier and deck geometrical data; b) SDOF Modeling (after Palermo et al, 2004)

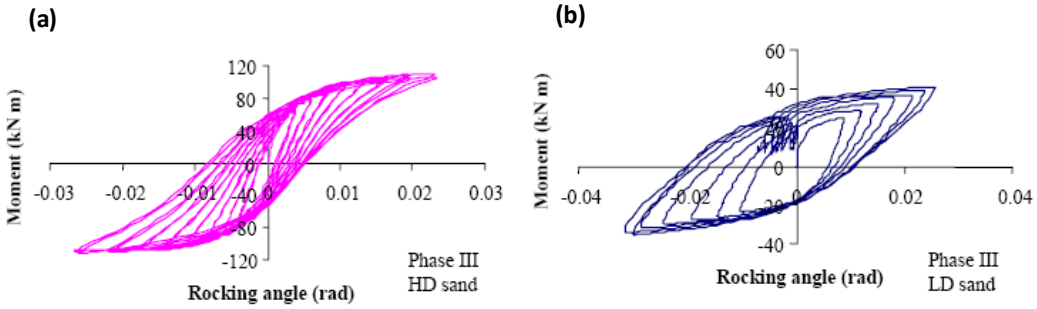

Figure 1.19: Experimentally deduced overturning moment vs. rocking angle of the foundation subjected to slow-cyclic lateral load: (a) assuming HD and (b) LD conditions (after: *Negro et al, 2000*)

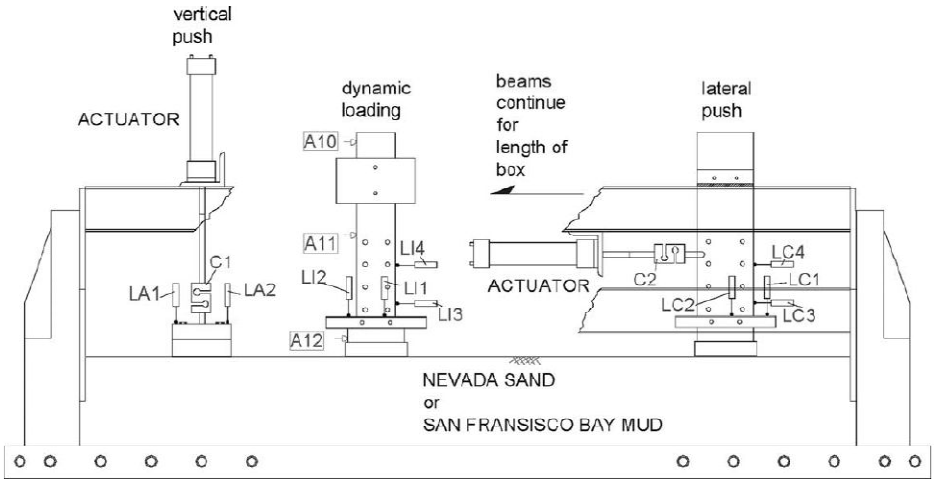

Figure 1.20: Experimental set up for vertical push, slow cyclic lateral push and dynamic loading tests (after *Gajan et al, 2005*)

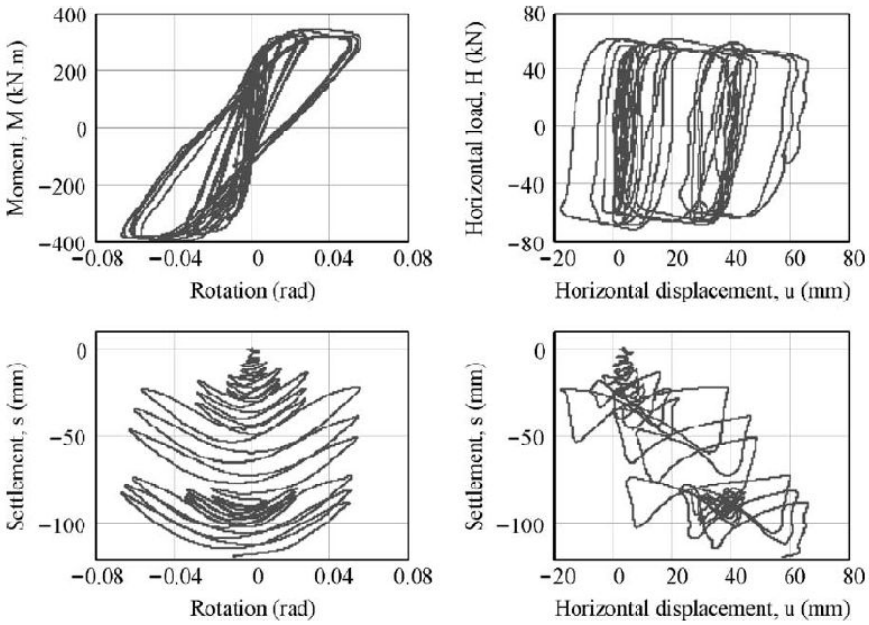

Figure 1.21: Results for the slow cyclic lateral push test (case study: dry sand (Dr 80%), footing length 2.84 m, width 0.65 m, embedment 0.0 m, FS 6.7, lateral load applied at height 4.9 m (after *Gajan et al, 2005*)

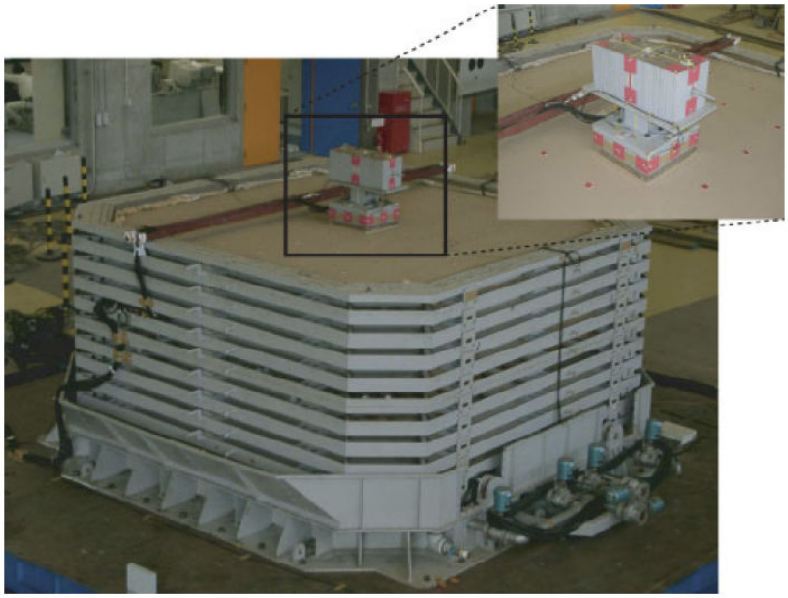

Figure 1.22: Picture of the experimental set-up, including the test model (source: *Paolucci et al, 2008*)

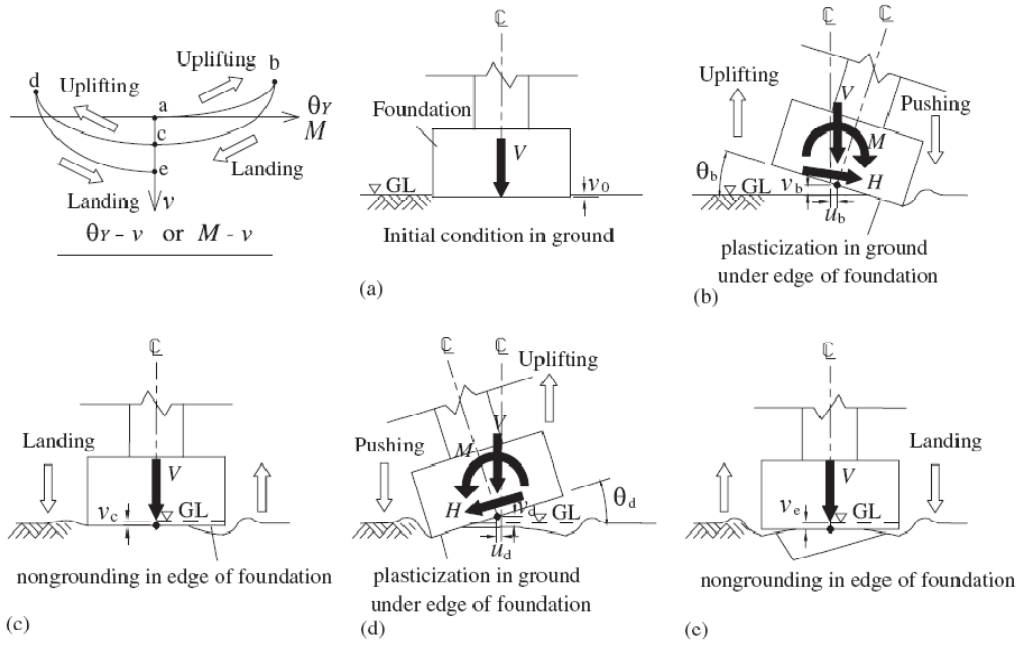

Figure 1.23: Sketch of subsequent yielding phases of foundation–soil interaction as observed from shaking table experiments (after *Paolucci, 2008*)

Figure 1.24: Snapshot of the experiment (*source: Maugeri et al, 2000*)

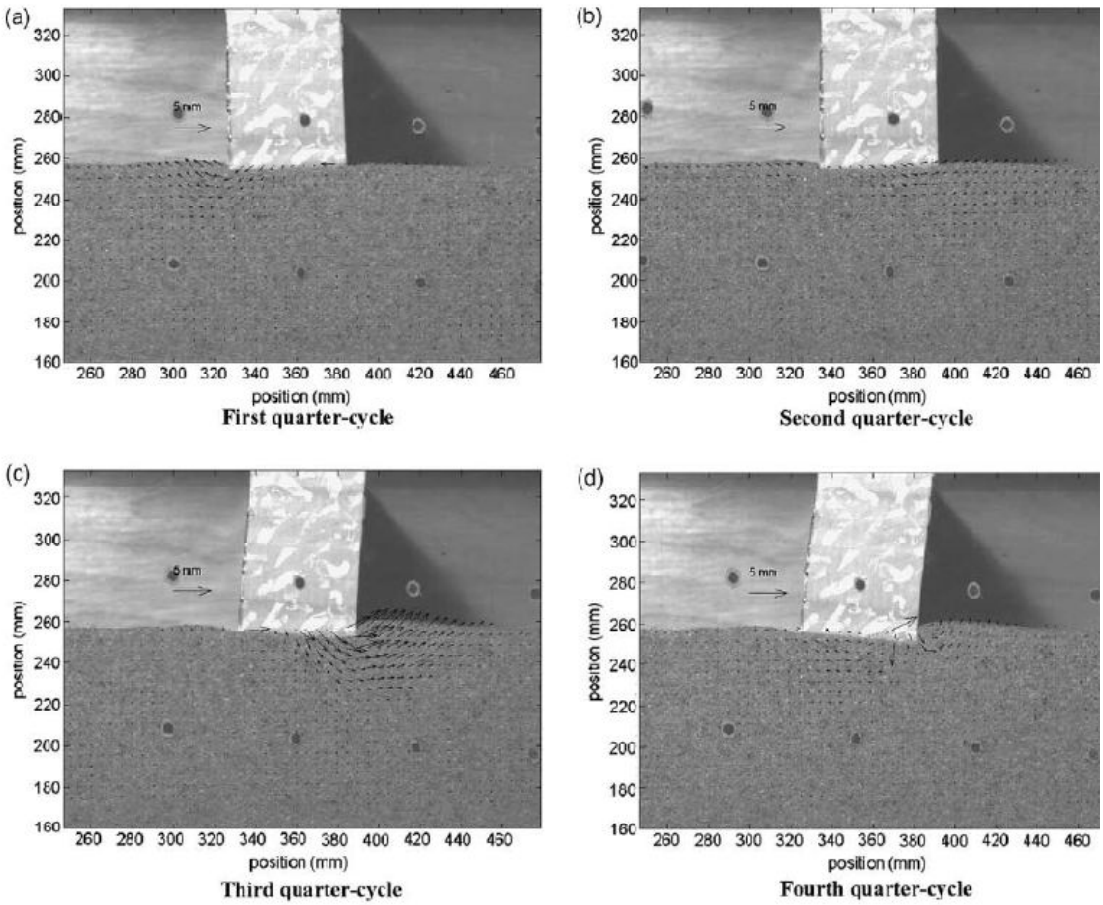

Figure 1.25: Displacement field beneath the foundation deduced from PIV analysis (*source: Knappet et al, 2006*)

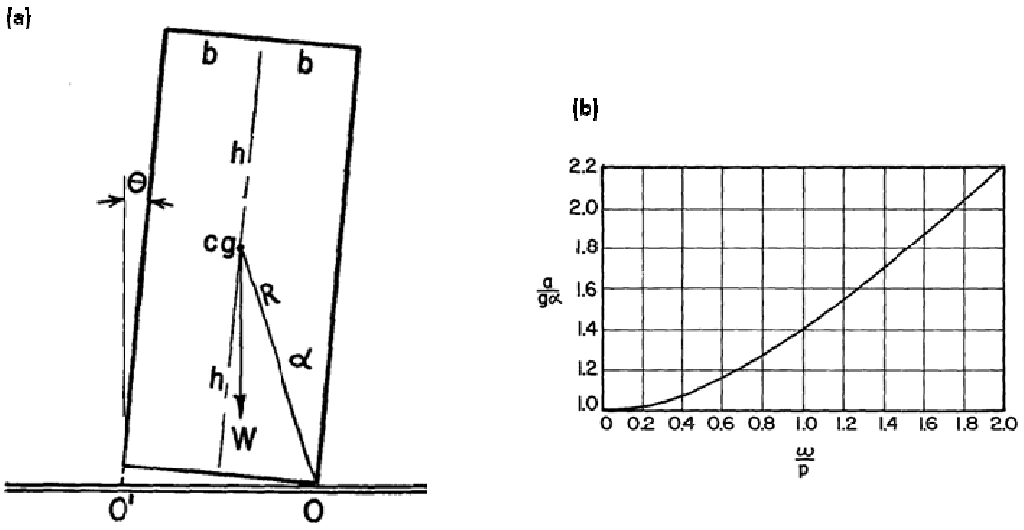

Figure 1.26: (a) Problem definition: Rocking of a rigid block on a rigid base and (b) example result from *Housner's* work; constant acceleration α of duration t1 required for overturning (case study of a rigid block excited by a sinusoidal acceleration)

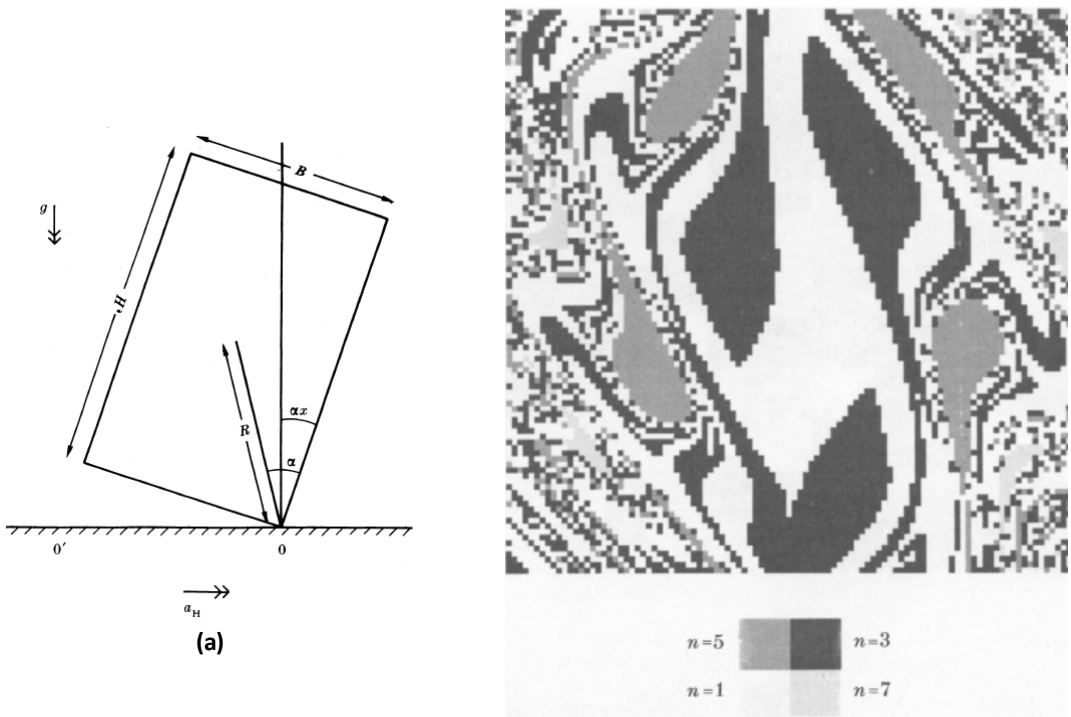

(a) **(b)**

Figure 1.27: (a) Definition sketch of the Rocking Block and (b) typical result; domain of attraction of the four subharmonic orbits [case study: α=0.001, ν=0.925, β=2.5, ω=9.0], (after: *Hogan, 1989*)

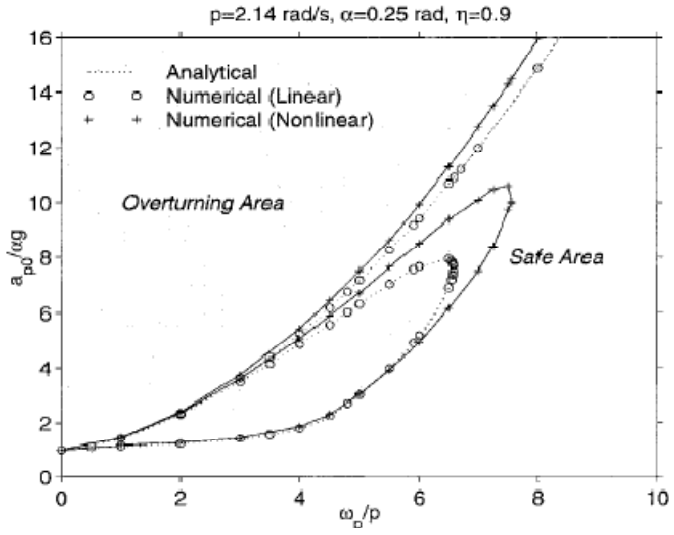

Figure 1.28: Overturning Acceleration Spectra of Slender Block under One-Sine Pulse computed both with a Linear and Nonlinear formulation. [case study: p=2.14 rad/sec, α =0.25 rad and n=0.9], (after *Zhang & Makris, 2001*)

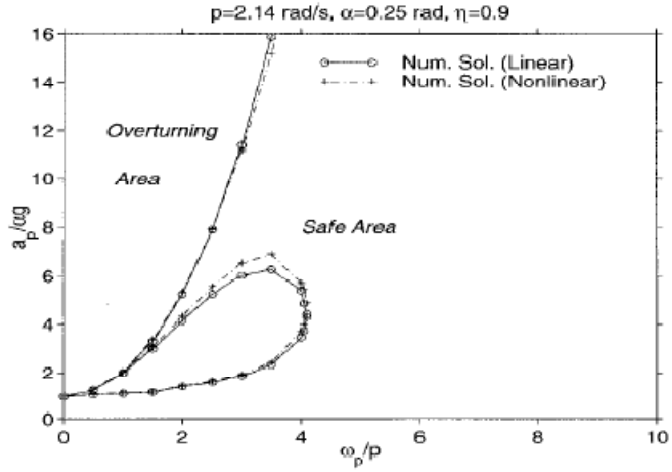

Figure 1.29: Overturning Acceleration Spectra of Slender Block under One-Cosine Pulse computed both with a Linear and Nonlinear formulation. [case study: p=2.14 rad/sec, α =0.25 rad and n=0.9], (after *Zhang & Makris, 2001*)

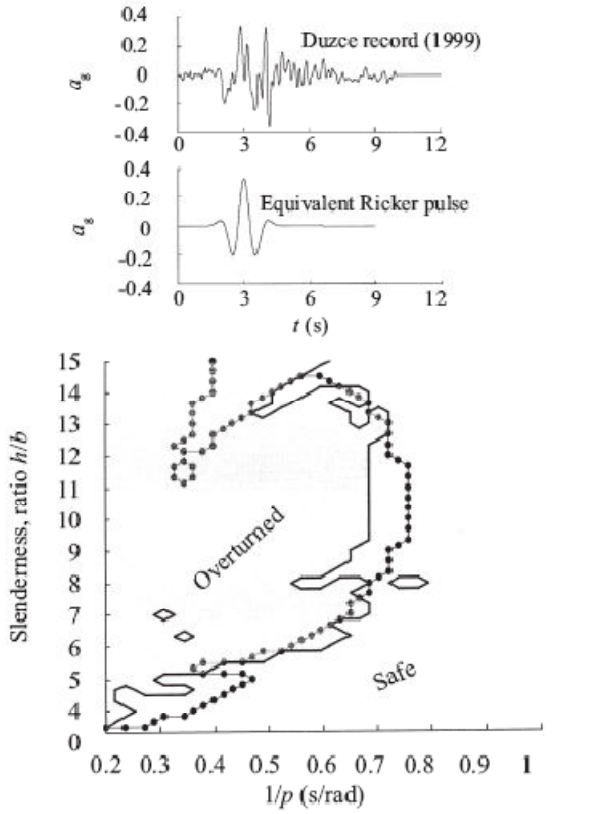

(a) Under two excitations: (i) the Duzce record (Kocaeli 1999 earthquake), and (ii) a suitably fitted ("equivalent") Ricker wavelet

Figure 1.30: Relationship between slenderness ratio and size parameter (1/p) required for the overturning of a rigid block. The continuous line corresponds to the result obtained when the excitation was the Duzce record, and the dotted line to the suitably "fitted" Ricker wavelet (after*: Gerolymos et al, 2007*)

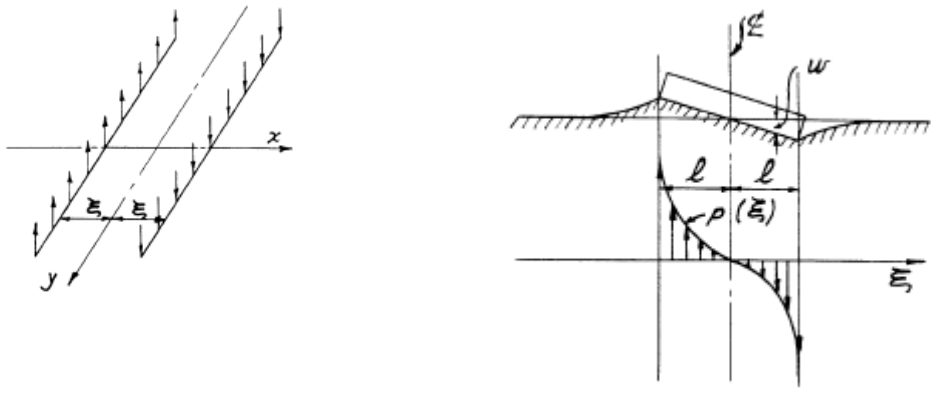

Figure 1.31: Problem Definition and pressure distribution under a rocking rigid slab (after: *Biot, 2006)*

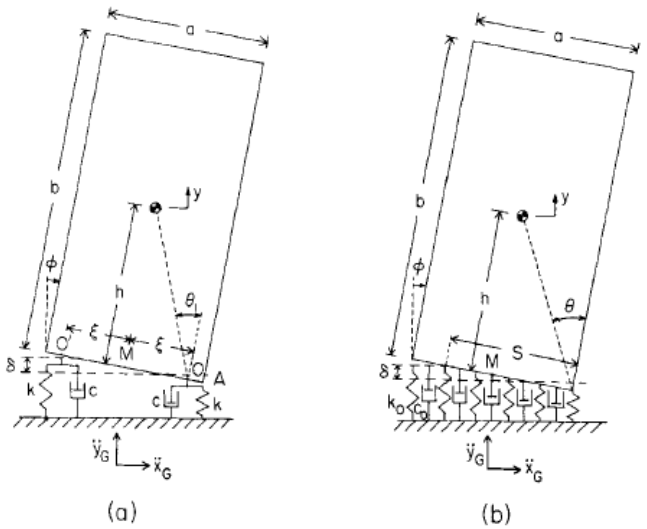

Figure 1.32: Rocking block on (a) two-spring foundation and (b) Winkler foundation

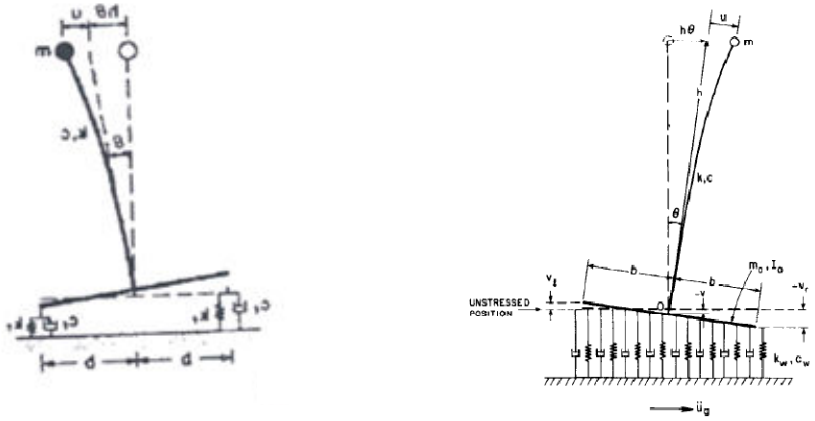

Figure 1.33: Flexible Structure supported on **(a)** a simple two-spring viscously damped foundation and **(b)** on a winkler type foundation (*after Yim and Chopra (1984) and Chopra and Yim, 1985*)

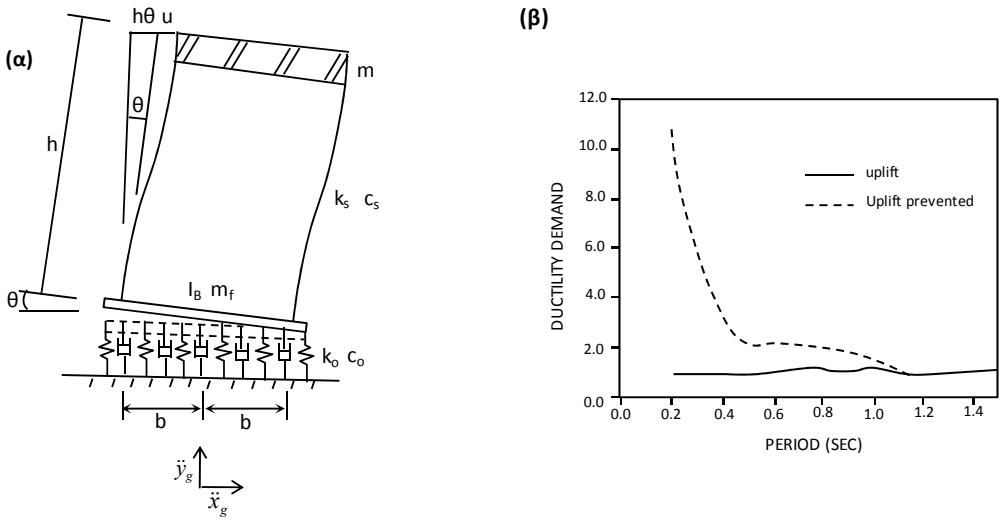

Figure 1.34: (a) Winkler-foundation system below an inelastic shear wall and (b) ductility demand vs period allowing or preventing uplift (after: *Nakaki and Hart, 1987)*

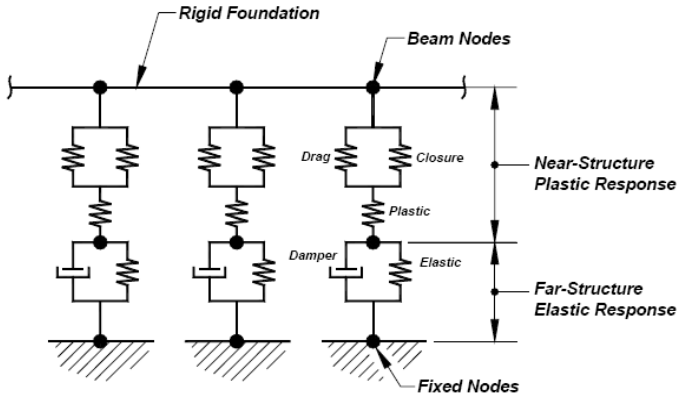

Figure 1.35. Typical configuration of the "material" utilized by *Harden et al, 2005*

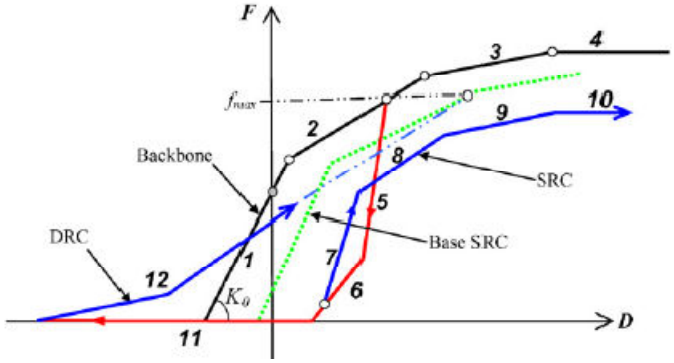

Figure 1.36. Cyclic response curve for the nonlinear Allotey and El Naggar Winkler model.

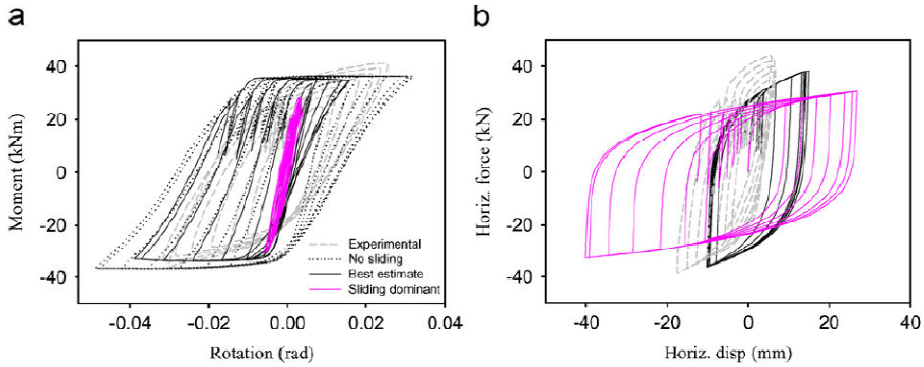

Figure 1.37. Comparison of computed results utilizing the Allotey and El Naggar Nonlinear Winkler model with experimental data in terms of moment–rotation and horizontal force–displacement response, Case study: LD test, in the TRISEE 1-g experiment.

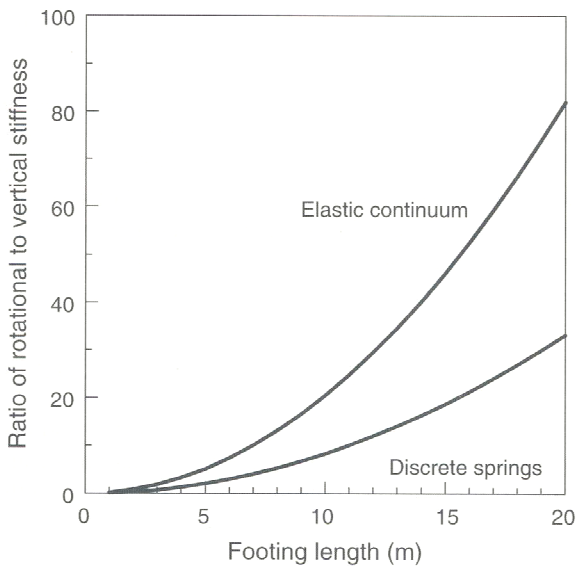

Figure 1.38. Ratio of the rotational to vertical stiffness of square rigid shallow footings, for a uniform elastic foundation material and the foundation represented as a bed of discrete springs (after: *Pender, 2007*)

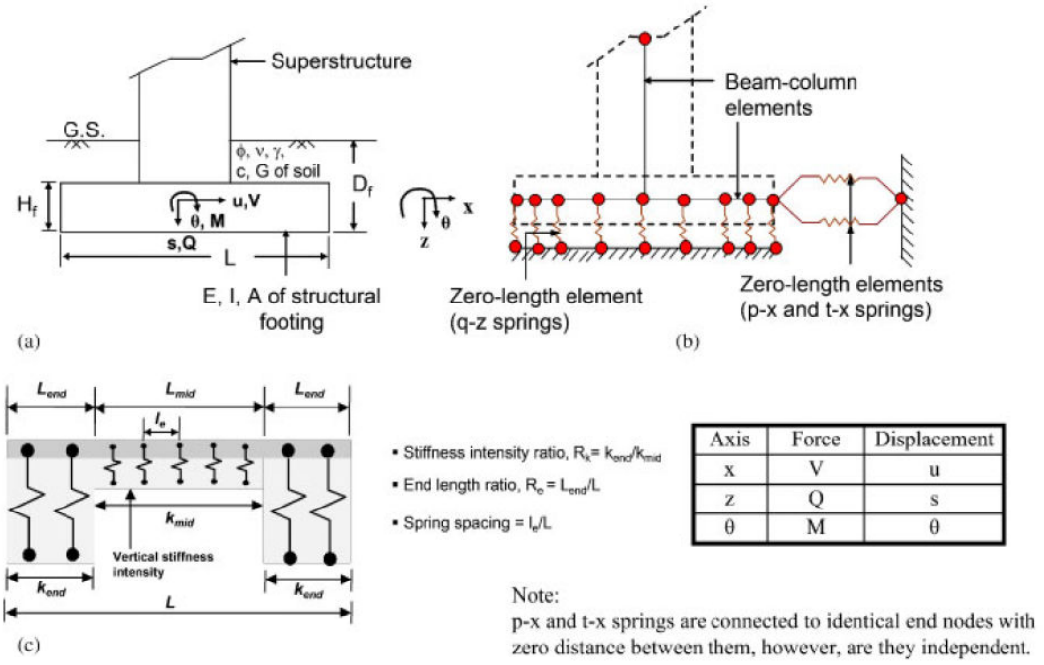

Figure 1.39: Proposed BNWF model: (a) hypothesized footing–structural system; (b) idealized model; and (c) variable vertical stiffness distribution (*Raychowdhury & Hutchinson, 2008*)

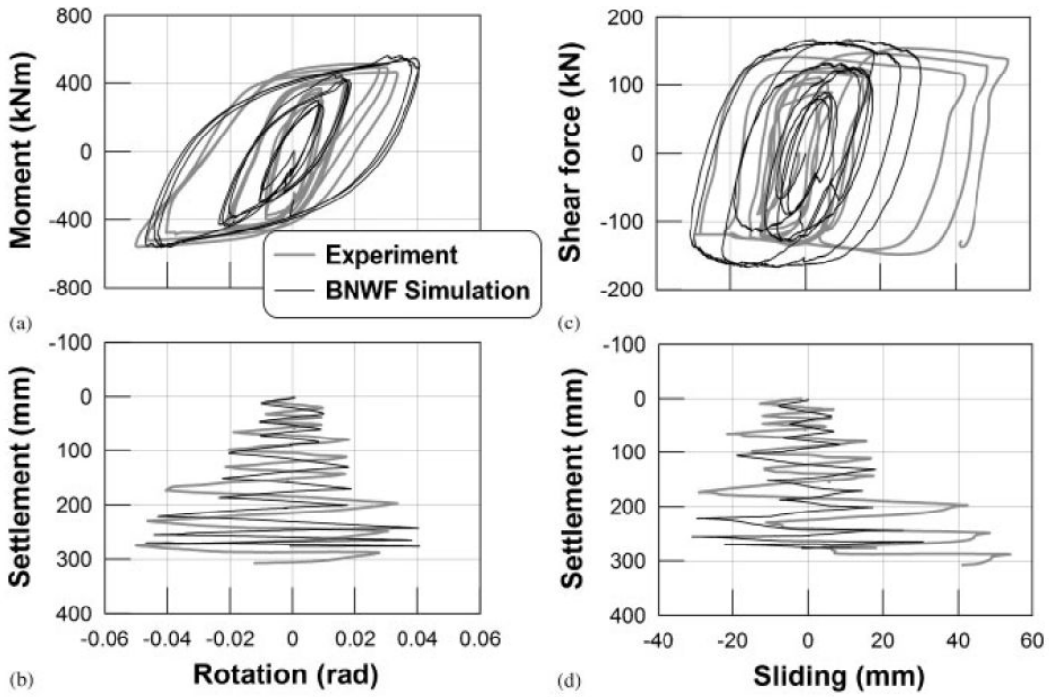

Figure 1.40: Comparison of the experimental results with the proposed winkler model (case study: static cyclic test on dense sand with *D*r=80%, FSv=2.3 and *M/HL*=1.20): (a) moment–rotation; (b) settlement–rotation; (c) shear–sliding; and (d) settlement–sliding. (*after Raychowdhury & Hutchinson, 2008)*

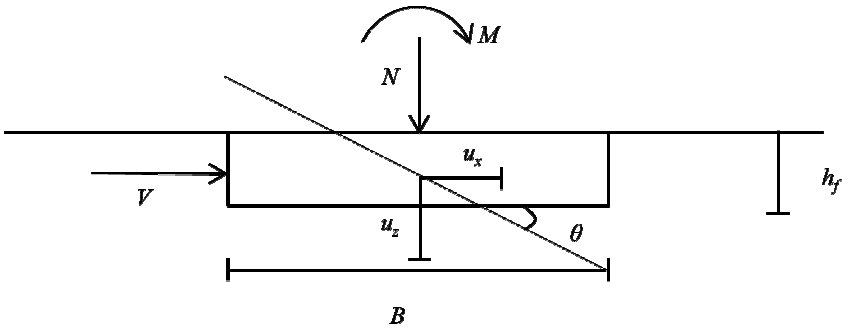

Figure 1.41: Problem Definition according to *Nova and Montrasio (1991)*

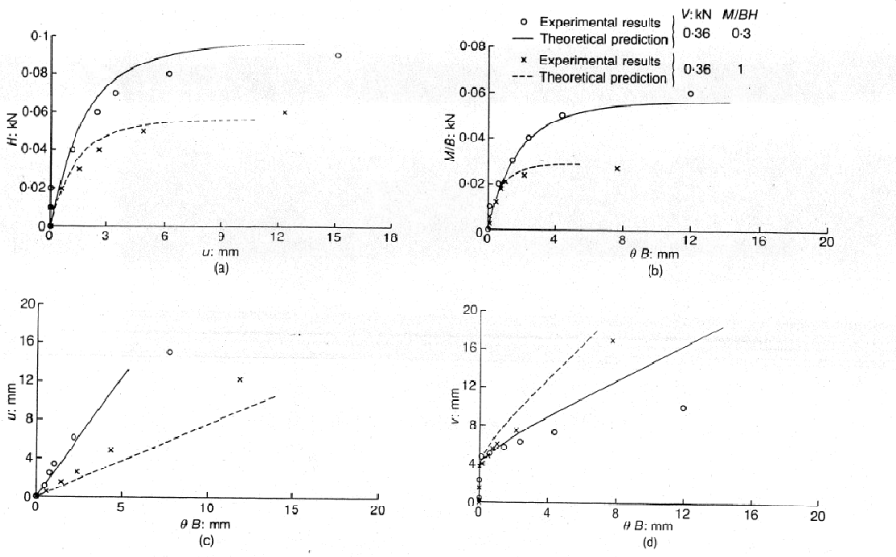

Figure 1.42: Comparison between experimental and calculated results by applying the Nova-Montrasio macroelement

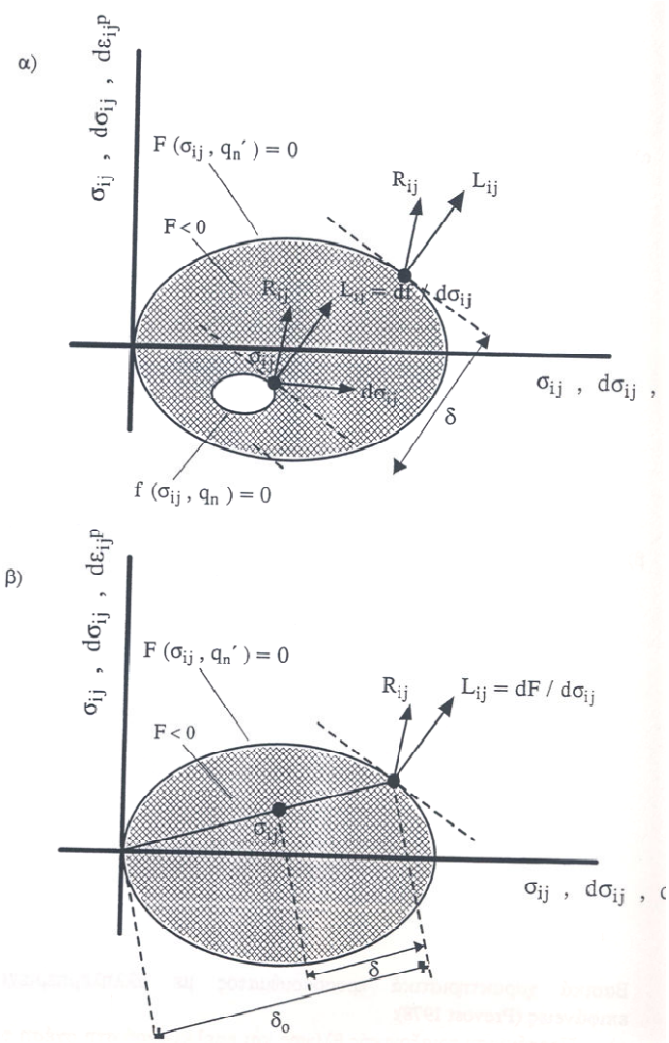

Figure 1.43: Bounding surface model: Each Point P (describing a particular loading state) within this surface can be mapped through a specified "mapping" rule to a conjugate point I_p lying on the bounding surface.

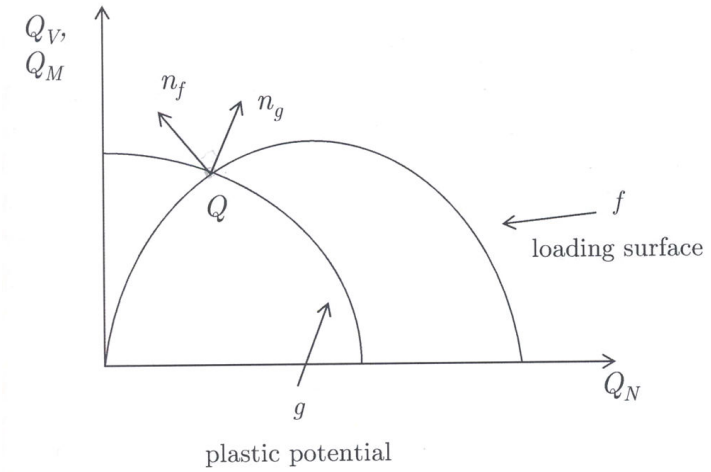

Figure 1.44: Crémer definition of the plastic potential (after *Crémer at al, 2001*)

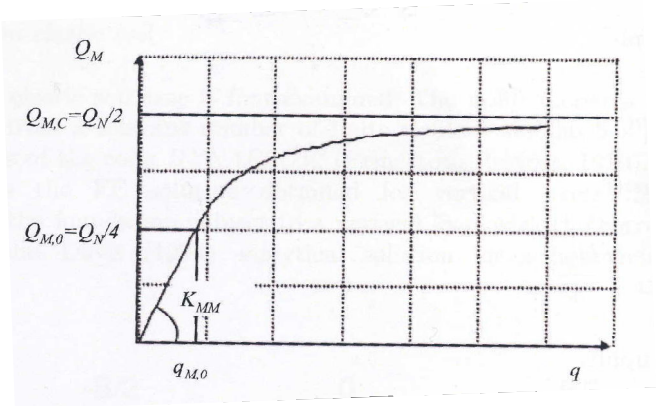

Figure 1.45: Moment Rotation relationship for a foundation on an elastic soil (after *Crémer at al, 2001*)

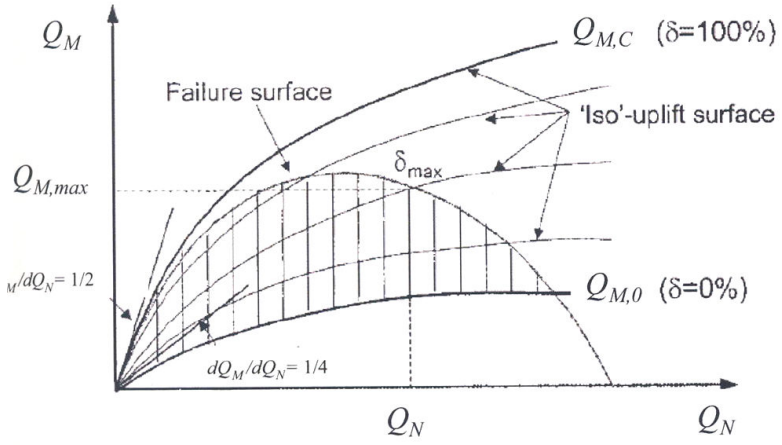

Figure 1.46: Iso-uplift surface and failure criterion in the Q_M + Q_N plane (after *Crémer at al, 2001*)

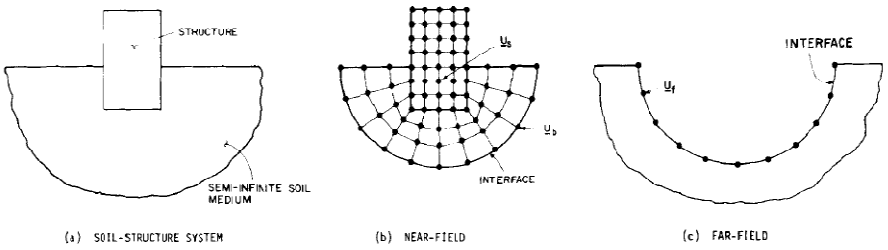

Figure 1.47: Hybrid modeling of soil-structure interaction problems (after *Gupta and Lin, 1982)*

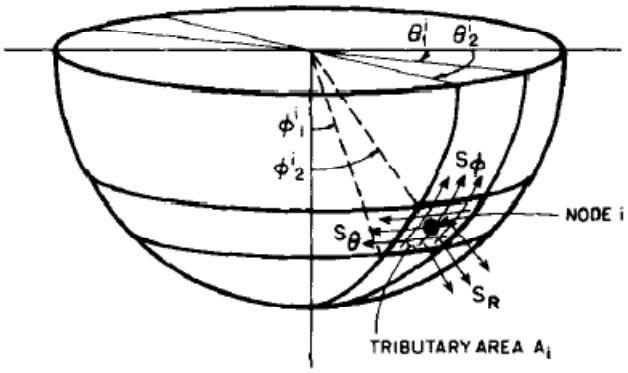

Figure 1.48: Disretization of the far-field domain to infinitesimally small soil elements (*after Gupta et al, 1980*)

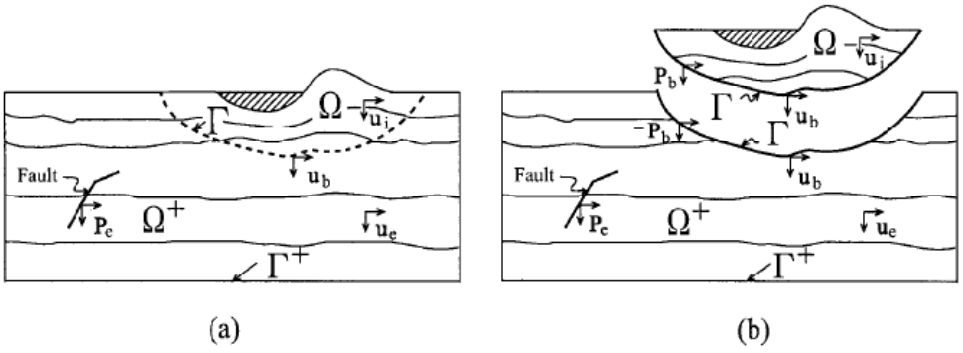

Figure 1.49: Schematic Representation of the DRM Method as applied in a seismic propagation problem. The region under study is divided into two subdomains; (a) Ω^+, which includes the seismic source, represented by nodal forces P_e, and (b) Ω, which contains the localized geological features. The two regions are partitioned explicitly across the interface Γ. *(after Bielak et al, 2003)*

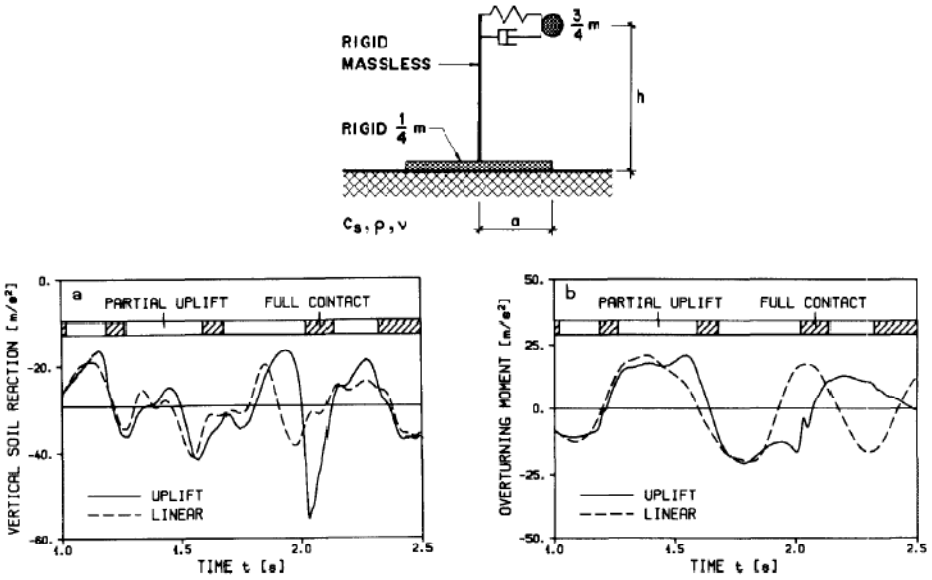

Figure 1.50: The model of the investigated structure in the work of Wolf & Oberhuber, 1985 (top figure) and a typical result of their study: comparison of vertical soil reaction and overturning moment time histories by assuming both full contact conditions and by allowing foundation uplift (bottom).

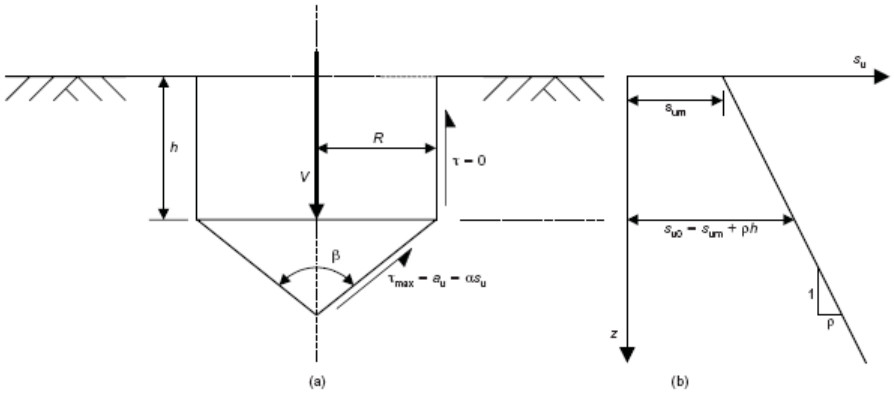

Figure 1.51: (a) Outline of the spudcan footing analysed by *Houlsby & Martin* (2003), and (b) variation of the undrained shear strength with depth.

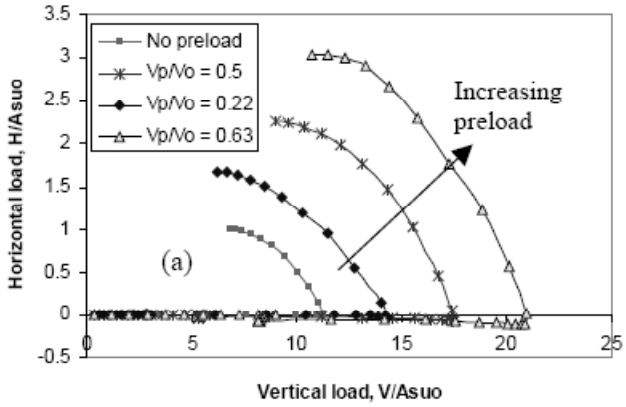

Figure 1.52: Typical Result from Bransby (2002): effect of preload consolidation on the V-H yield locus

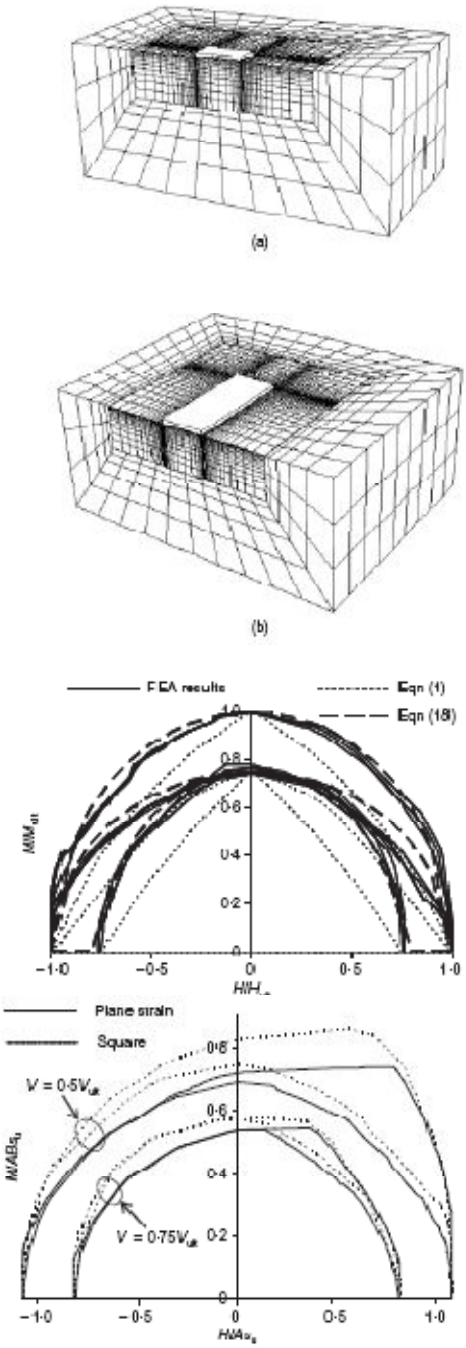

Figure 1.53: Finite Element Models utilized by *Gourvenec, 2007* (top figure); produce failure envelopes (in normalized load space) for VHM loading considering zero-tension interface (middle); comparison of the failure envelopes when zero-tension and unlimited tension interfaces are assumed.

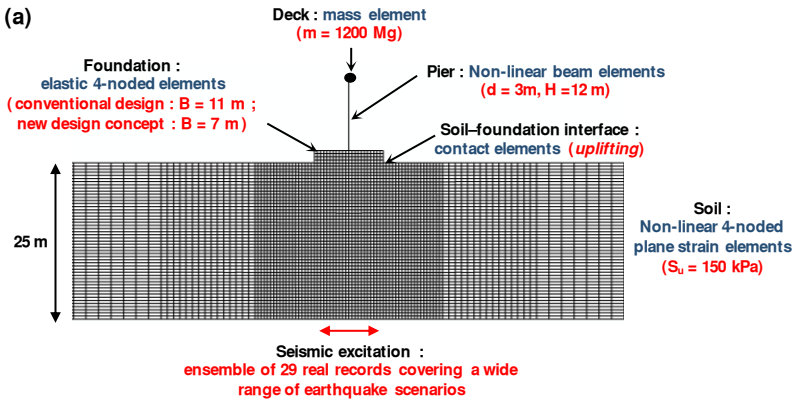

Figure 1.54: Overview of the finite element modeling : plane-strain conditions are assumed, taking account of material (soil and superstructure) inelasticity and geometric (uplifting and P-Δ effects) nonlinearities. (after *Anastasopoulos et al 2009*)

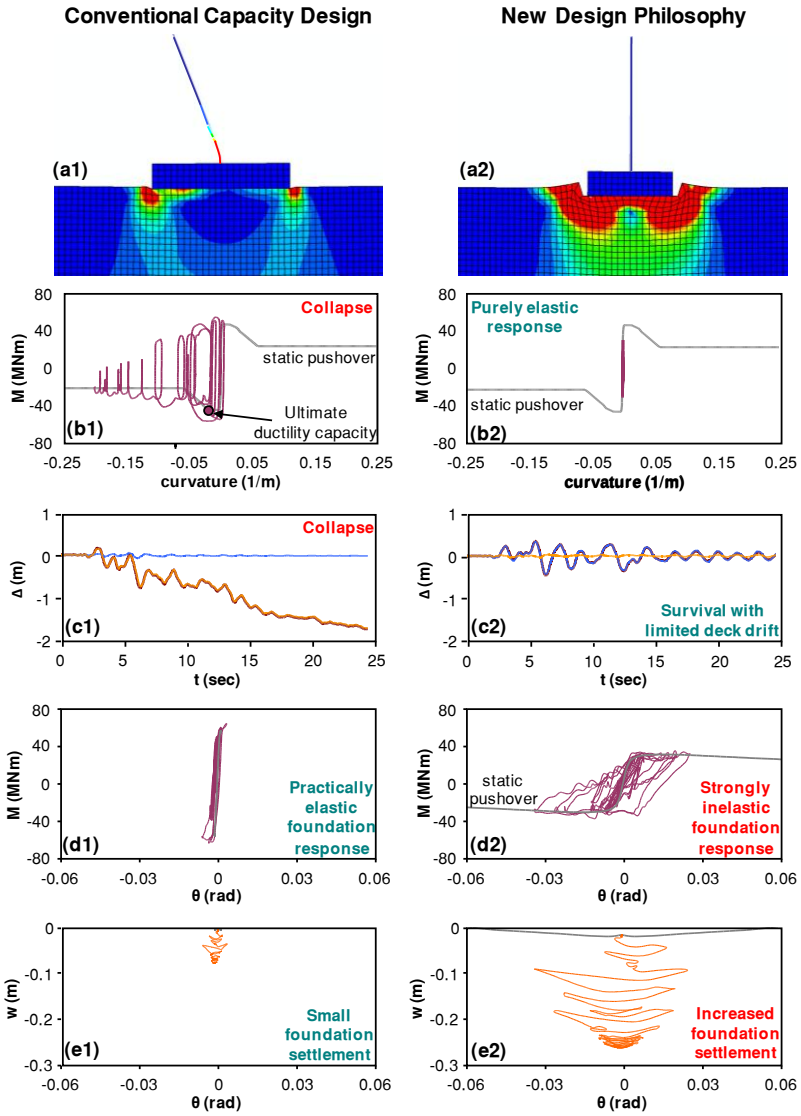

Figure 1.55: Comparison of the response of the two alternatives subjected to a large intensity earthquake (Takatori, 1995), exceeding the design limits. (after *Anastasopoulos et al 2009*)

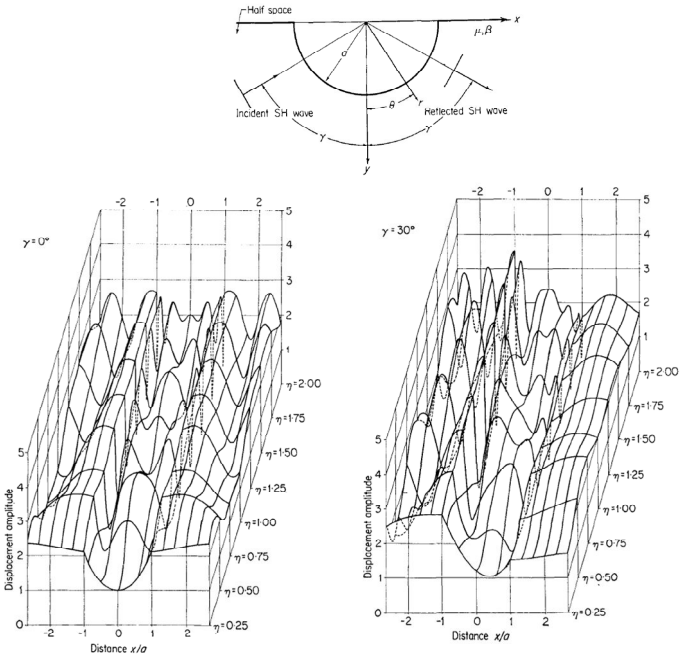

Figure 1.56: (top) Geometry of the semi-cylindrical canyon and the surrounding half-space studied by *Trifunac, 1971*. Surface displacement amplitudes for incident SH waves with γ=0^o and γ=30^o(bottom).

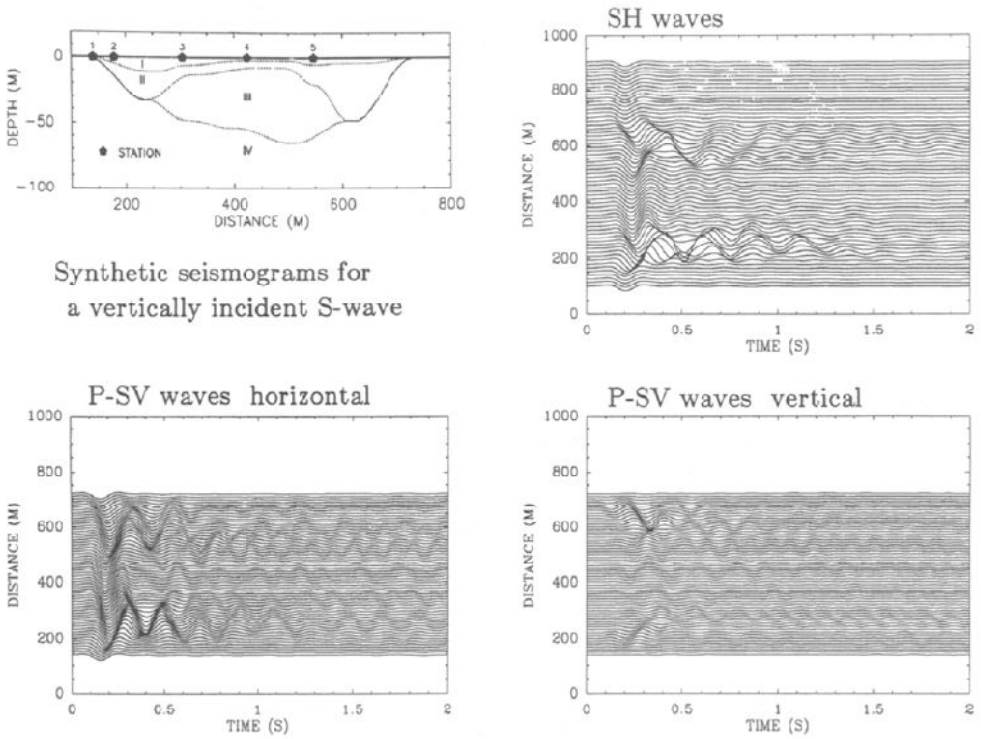

Figure 1.57: 2D model used in the numerical simulations and synthetic seismograms computed for vertical incident waves (after *Jongmans and Campilo, 1993)*

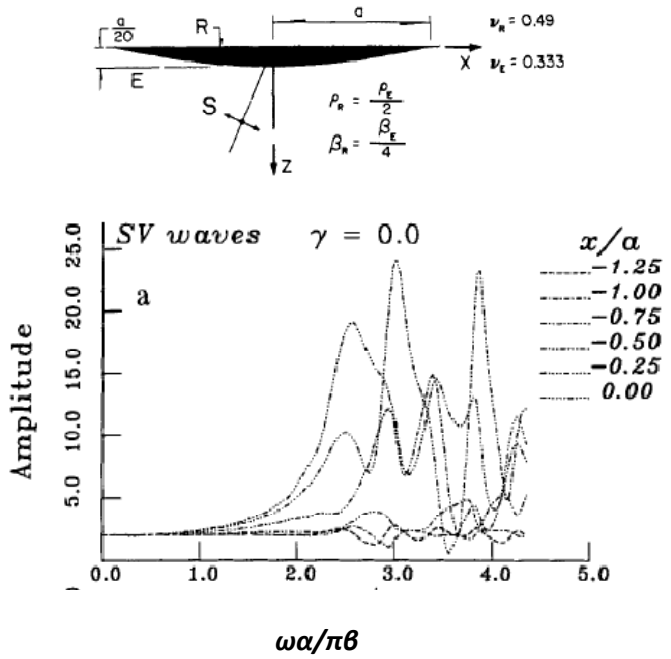

Figure 1.58: Incidence of a plane SV wave with incidence angle of 0". Frequency response for surface receivers equally spaced between x = - 1.25a and x = 0.0 at the surface of a shallow parabolic valley *(Sanchez- Sésma et al, 1993).*

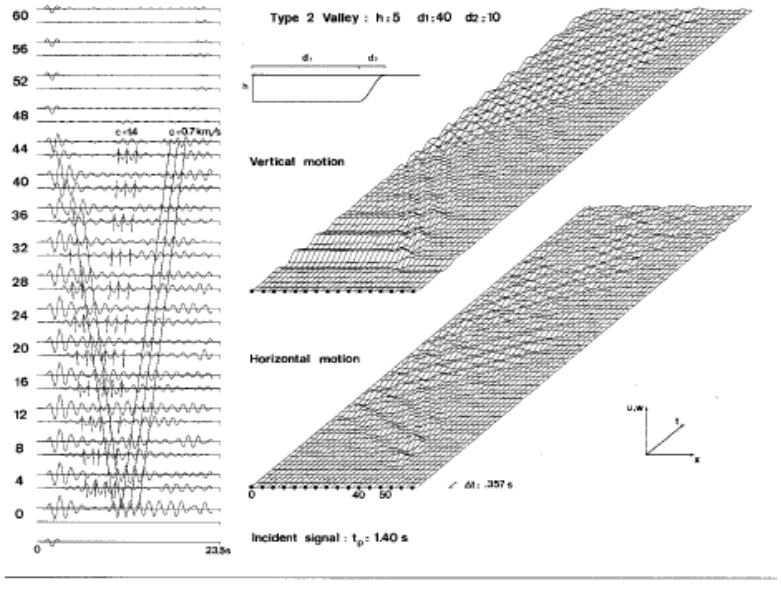

Figure 1.59: Response of a high contrast type 2 valley with maximum depth 500 m and half width 5 km to a vertically incident P Ricker wavelet of characteristic period T_p = 1.40 sec. Left: the traces represent the horizontal and vertical displacements at the valley surface. Right: Diagrams showing the temporal and the spatial evolution of the surface displacement components. (*after: Bard and Bouchon, 1980(b)*)

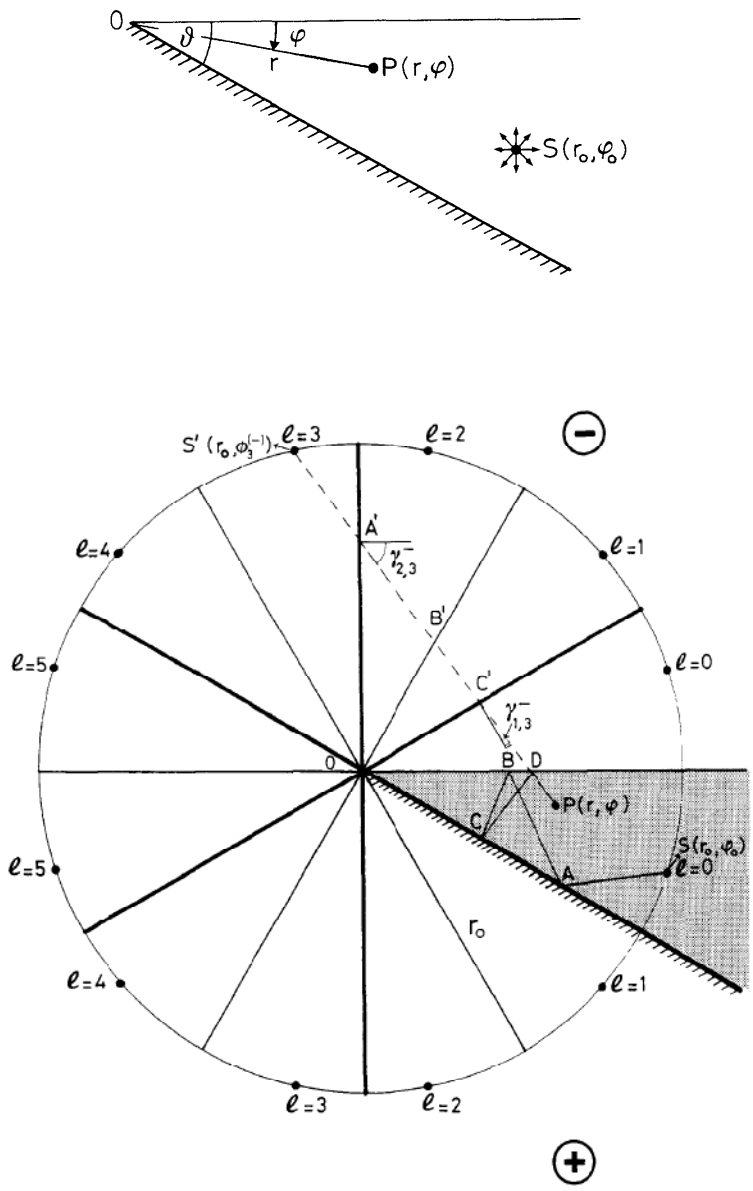

Figure 1.60: Construction of the 4N image point sources contributing to motion at *P(r,* ϕ), for the case N = 3. One of the 4N ray paths is shown (SABCDP), together with its equivalent obtained by method of images (the straight line *S'A'B'C'DP).(after: Paolucci et al, 1992)*

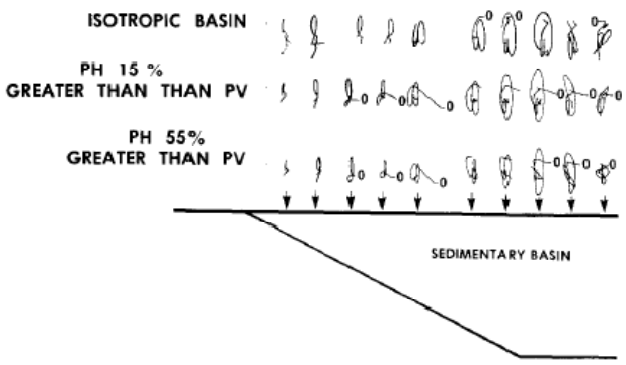

Figure 1.61: Rayleigh waves at various sites for three basin materials; top: isotropic, middle:-bottom transversely isotropic with different levels of anisotropy; Two Rayleigh orbits are distinguished. It was concluded that anisotropy only slightly affects the formation of the scattered waveforms.

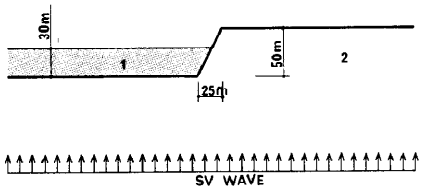

(a)

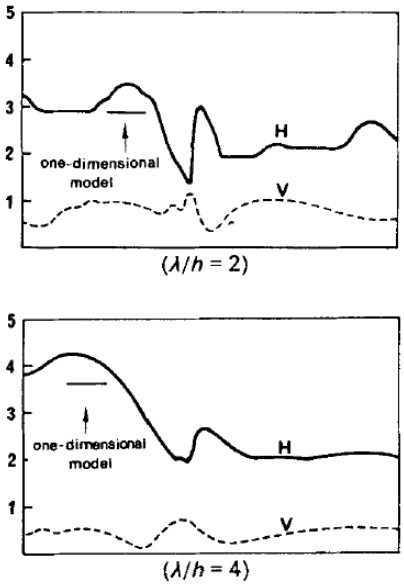

(b)

Figure 1.62: (a)Analytical model of a cliff with a soft layer and filled land and (b) Distributions of maximum horizontal and vertical surface displacements compared with results calculated by one-dimensional model (after *Otsuki and Harumi, 1983*)

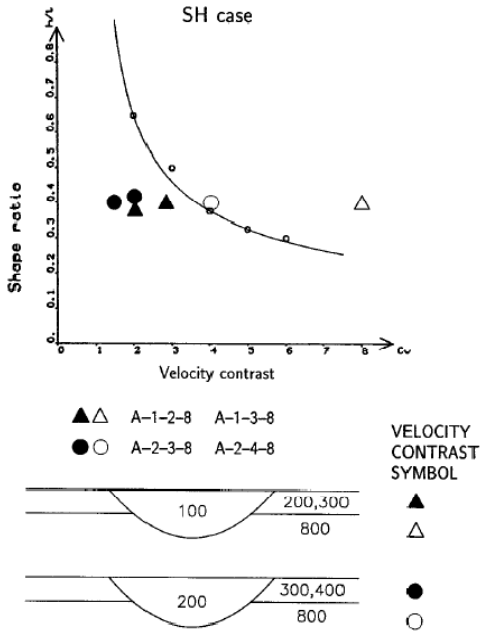

Figure 1.63: Comparison of the studied valley models with Bard and Bouchon's (1985) existence condition represented by the shape ratio-velocity contrast curve

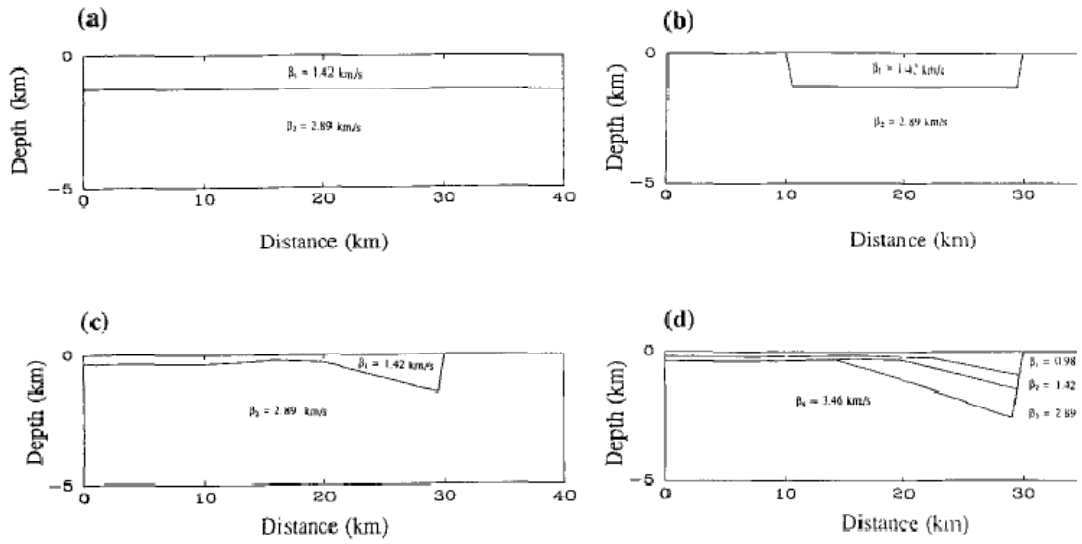

Figure 1.64: 2-dimensional basin models used to investigate the effects of basin complexity on the seismic response to a vertically incident SH waves. *(Hill et al, 1990)*

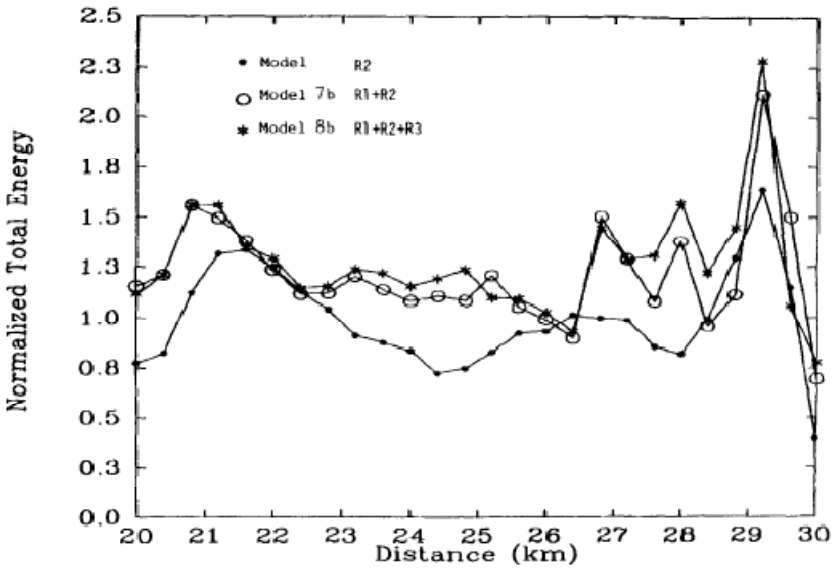

Figure 1.65: Total normalized kinetic energy of the seismic traces for the different basin models of the Salt Lake valley*(Hill et al, 1990)*

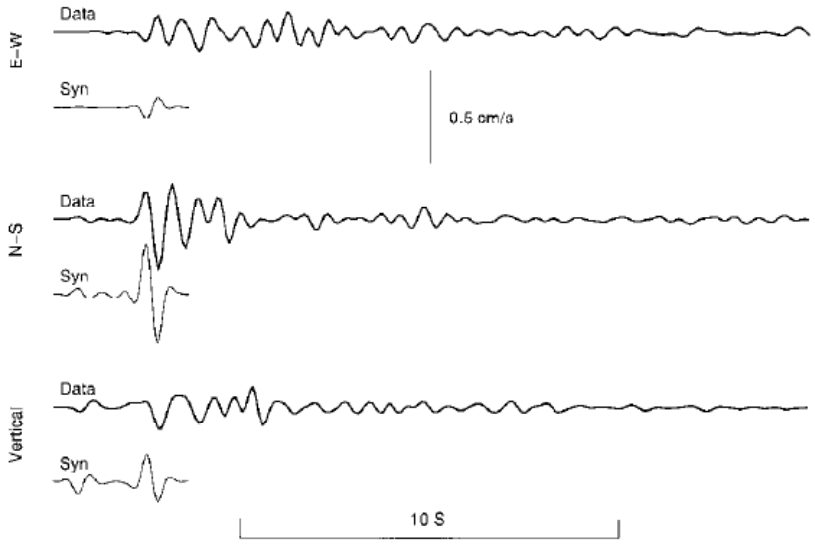

Figure 1.66: Comparison of simulated particle velocities at a depth of 300 m to recordings at the deepest borehole station *(after Olsen et al, 2000)*

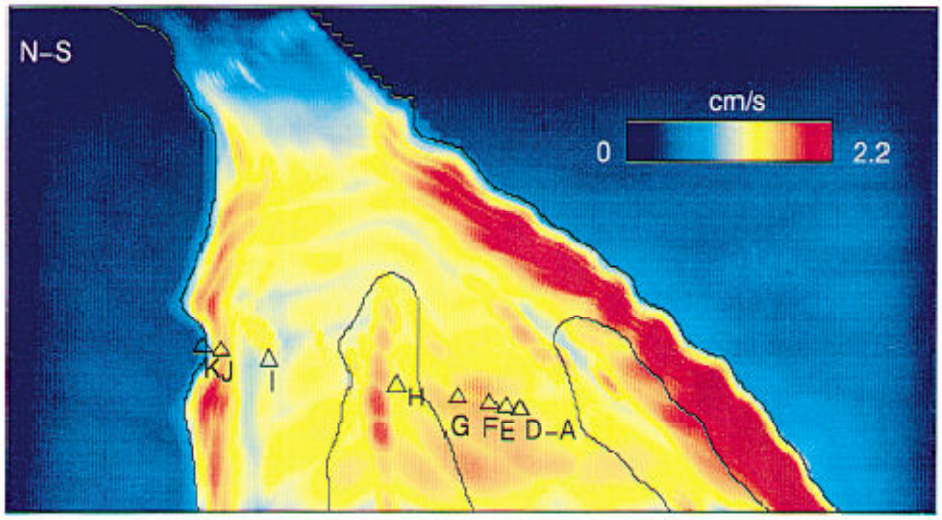

Figure 1.67: Maps of peak velocities in the Borrego Valley for a simulation of the **M** 4.9 earthquake, superimposed with the depth contours of 0.05 km and 0.3 km for the iso-surface of *V*s =1 km/sec *(after Olsen et al, 2000)*

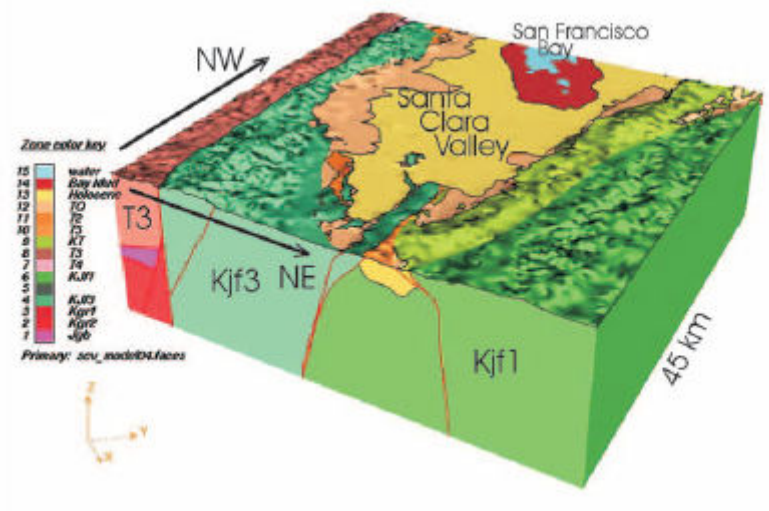

Figure 1.68: (a) Three-dimensional geologic/structural model of the Santa Clara Valley that forms the basis for the 3D seismic-velocity and attenuation model utilized in *Hartzell et al (2003)* study.

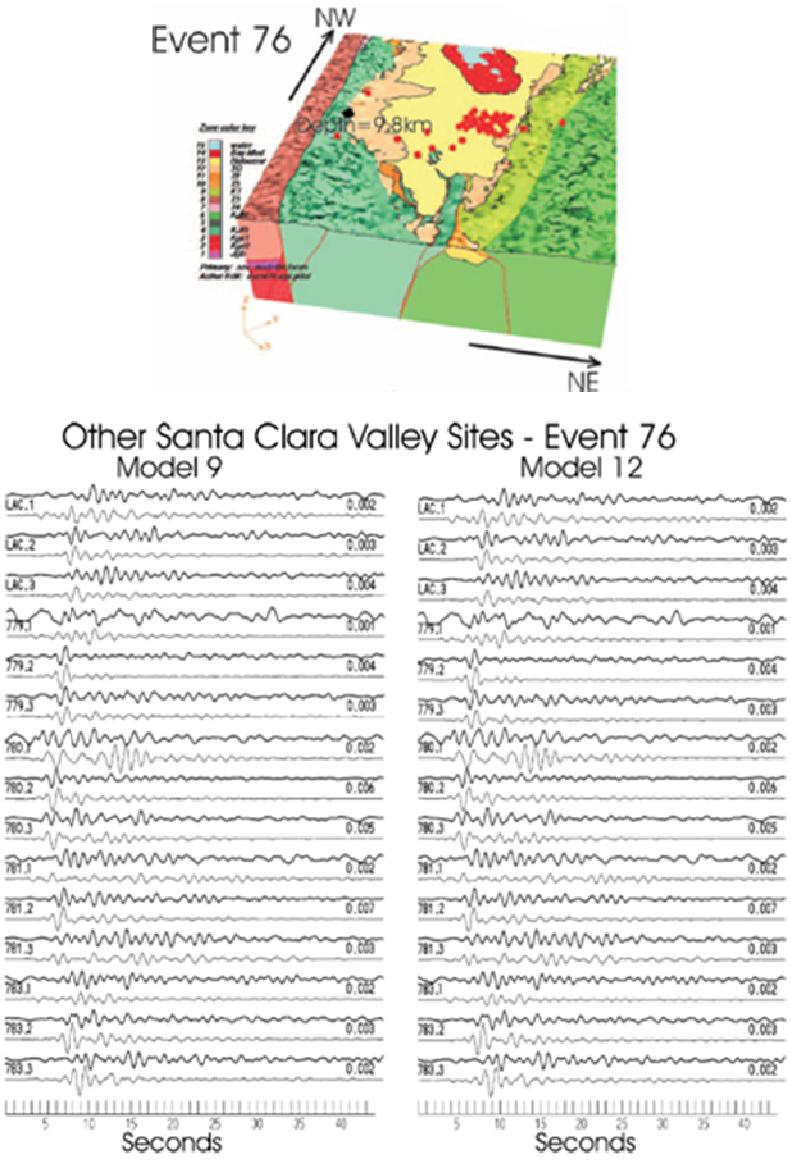

Figure 1.69: Simulation of event 76: black square denotes for the epicenter, while red squares stands for the locations of recording stations. The bottom figure compares data (heavy trace) with the synthetic (lighter trace) velocities for stations along the eastern side of the Evergreen Basin for the specific 76 (after: *Hartzell et al, 2003)*.

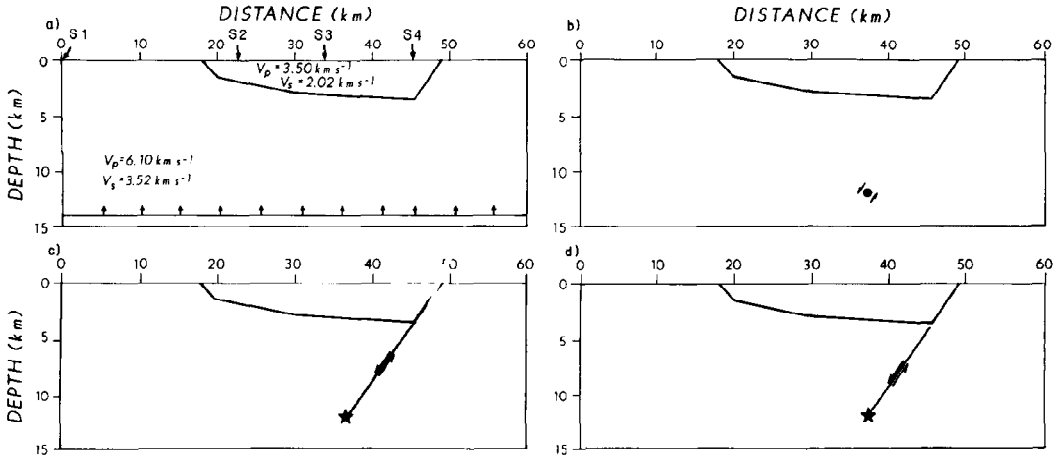

Figure 1.70: Cross sections of the simplified Salt Lakevalley velocity model showing the four kinematic source simulations modeled. The Salt Lake basin is modeled as homogeneous with a P- and S-wave velocity of 3.50 km/sec and 2.02 km/sec, respectively, while the basement is homogeneous with a P- and S-wave velocity of 6.10 km/sec and 3.52 km/sec, respectively. The four source simulations are: (a) a vertically incident plane wave, (b) a buried double-couple, (c) a normal faulting earthquake that ruptures the surface, and (d) a buried normal faulting earthquake.

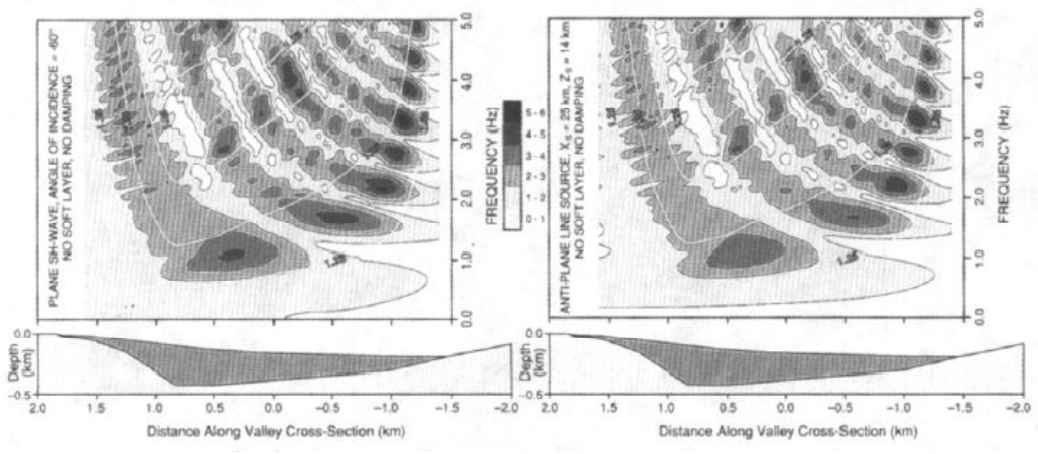

Figure 1.71: Amplification ratios (AR) of valley-model A (a) for plane *SH* waves incident from the north with an incidence angle i = - 60 ° and (b) for the line source located to the north of the valley. On the AR obtained from the 2-D model are superimposed the AR of the corresponding 1-D model of each site across the valley (after *Papageorgiou and Kim, 1991*).

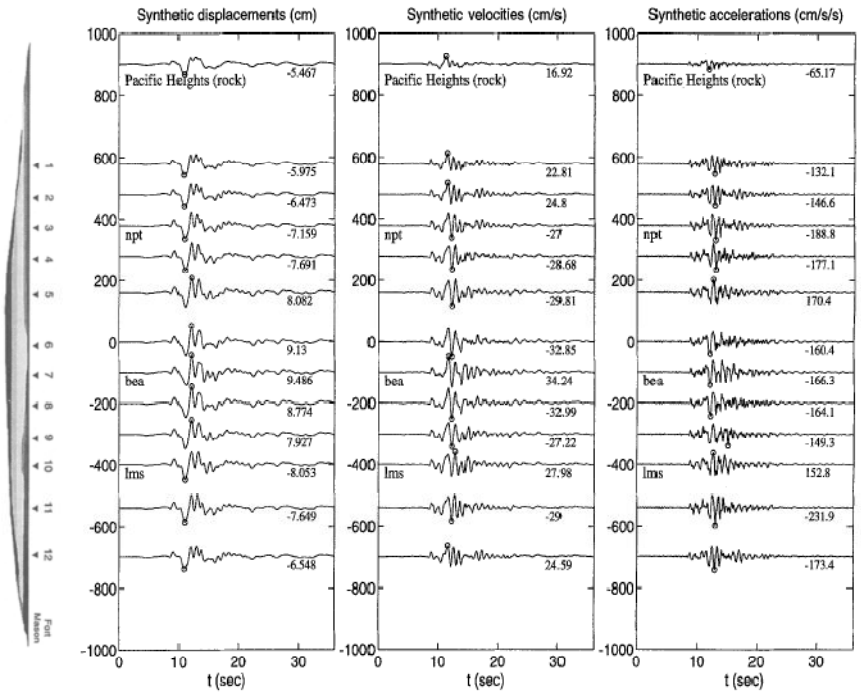

Figure 1.72: Acceleration, velocity, and displacement response for 12 stations along the cross section of the Marina District under investigation, to input motions recorded at the rock site PAC. (*after Zhang and Papageorgiou, 1996*)

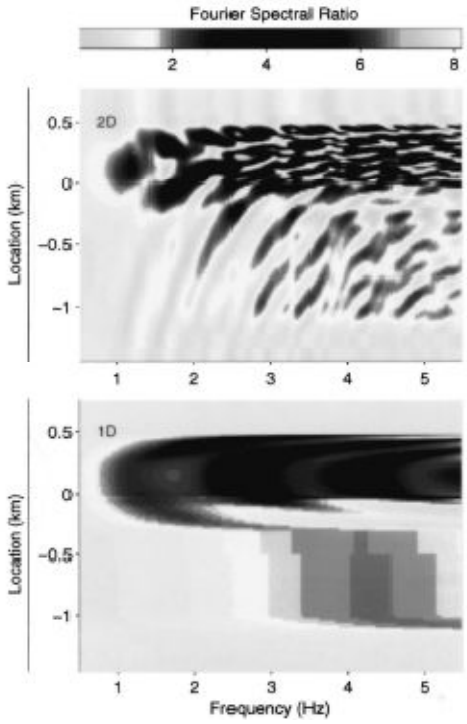

Figure 1.73: Fourier Spectral Ratio as a function of the input frequency along the valley surface. Top: 2D simulation; Bottom: 1D simulation (after: Bielak and Ghattas, 1999)

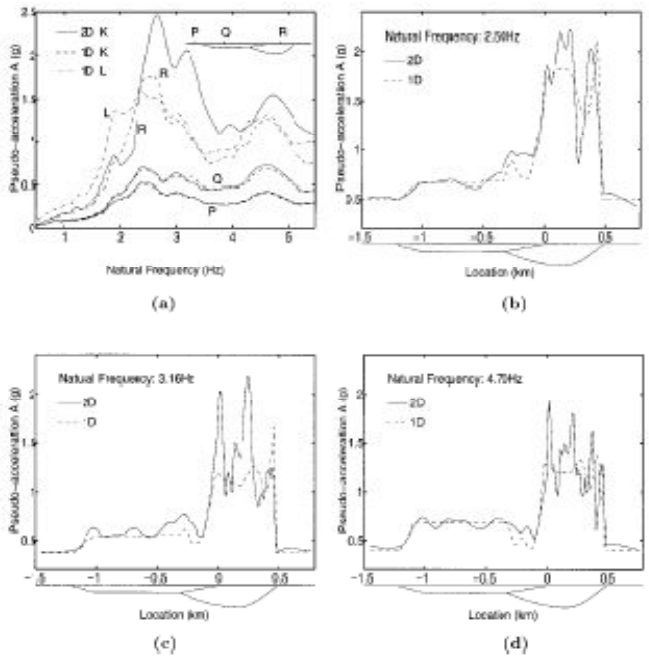

Figure 1.74: Pseudo acceleration Structural Response Spectra for 5% Critical Damping Using Ground Motion Synthetics from 1D and 2D Simulations: (a) Response Spectra for Three Sites in Kirovakan and One in Leninakan, Denoted by K and L, Respectively; (b)–(d) Response along Entire Valley of Kirovakan, for Three Different Natural Frequencies (after: Bielak and Ghattas, 1999)

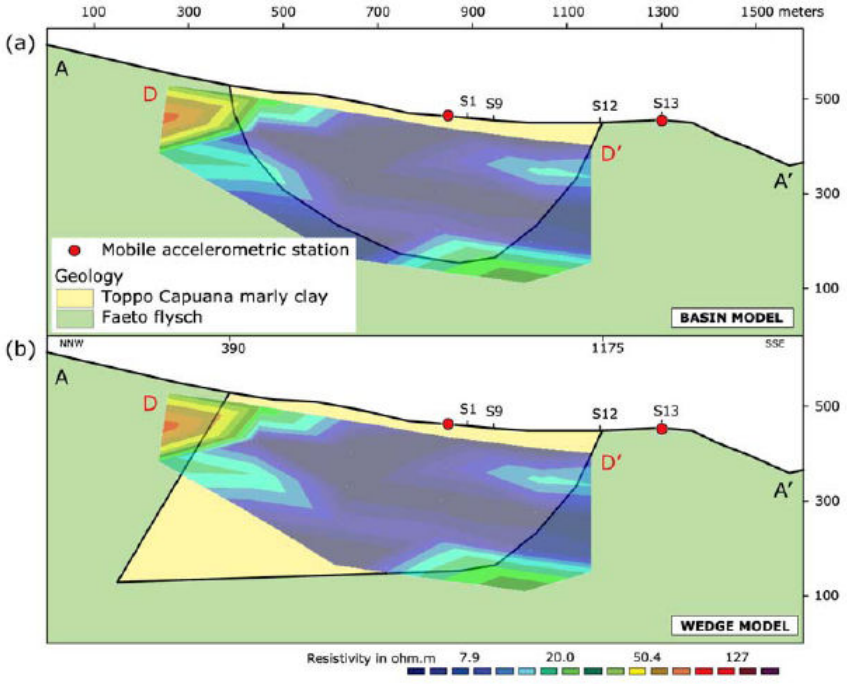

Figure 1.75: Working hypotheses for (a) basin and (b) wedge structures underneath the town of Puglia (after *Puglia et al, 2007*)

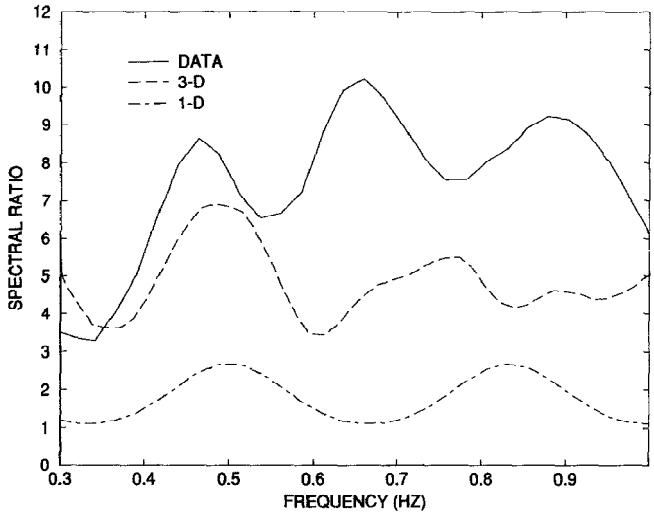

Figure 1.76: (Solid) Observed spectral ratio between transverse components at NA2 and SBE for event 3. (Dashed) Spectral ratio determined from synthetics from 3D simulation. (Dot-dashed) Spectral ratio determined from flat-layered (1D) model with vertically incident S wave. (after *Frankel, 1994*)

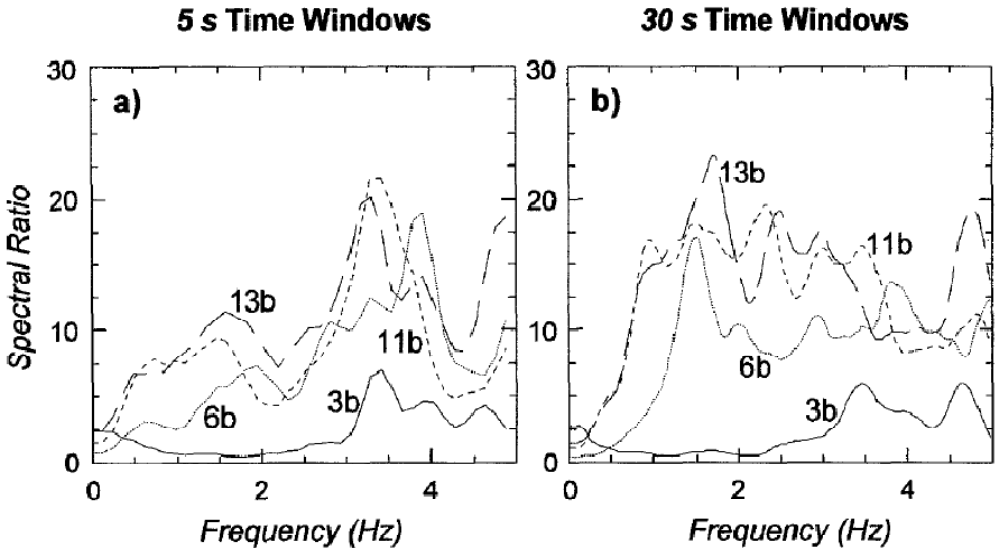

Figure 1.77: Spectral ratios obtained from the shot data for stations on Pliocene sediments, using the hard rock site as a reference station. Spectra were computed over (a) a 5.0 sec time interval windowing the direct S waves and (b) a time interval including the entire S-wave trains and late arrivals (source: *Malagnini et al, 1996*)

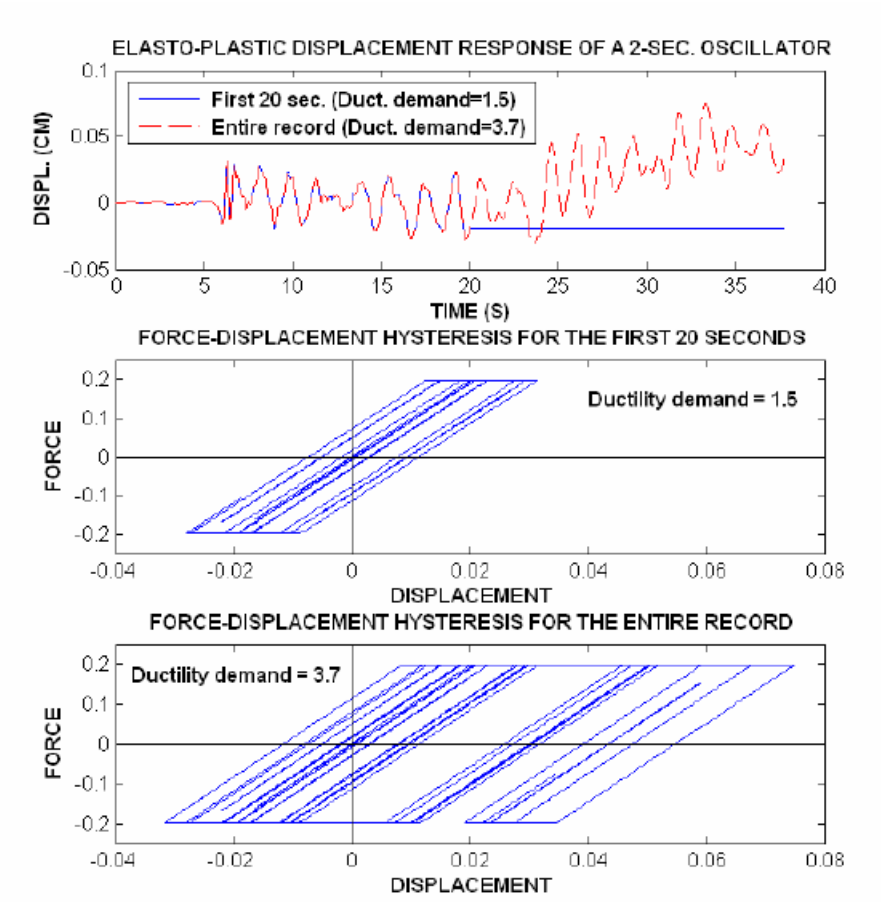

Figure 1.78: Comparison of elasto-plastic responses, ductility demands, and force-deformation hysteresis loops of a 2-second elasto-plastic oscillator corresponding to the first 20 seconds and the entire record *(after Safak, 2007)*

2

Simplified Constitutive Model for Simulation of Cyclic Response of Shallow Foundations : Validation against Laboratory Tests

2.1. Introduction

The fundamental problem that has motivated this study is the seismic response of slender foundation–structure systems, for which P–Δ effects play a significant role. Under severe seismic shaking, the shallow foundations of these systems may experience detachment from the supporting soil due to the large overturning moments (arising from inertial and gravitational forces). The ensuing rotational uplift will, in most cases, lead to a large increase of the imposed stresses on the soil under the edge of the footing. Mobilization of bearing

capacity failure mechanism under the action of combined moment–shear–vertical, *M*–*Q*–*N*, loading is a possible outcome.

But the occurrence of such an event does not necessarily imply failure — thanks to the *cyclic* and *kinematic* nature of the seismic excitation. As a result of the *cyclic* character of the motion, a bearing capacity "failure" mechanism may lead to only a small rotation before the direction of motion is reversed. If the next "pulse" of the ground motion is also strong, another bearing capacity "failure" mechanism will develop on the opposite side of the foundation. And so on, until the end of shaking.

The *kinematic* character of seismic shaking (i.e. the loading in the form of dynamic displacement imposed at the base) distinguishes it from external loading in the form of *force* applied to the mass. Even if the base acceleration is larger than the critical (yield) acceleration A_c , the acceleration that develops in the mass can not exceed A_c , and failure is not necessarily the consequence.

Performance-based design in earthquake geotechnics (i.e., design on the basis of limiting the maximum and permanent displacements and rotations of facilities during the design earthquake) has its justification on the above consequences of the cyclic and kinematic character of motion. Thus, the concept of allowing significant *foundation uplifting* (implying a geometric nonlinearity) and mobilization of ultimate bearing capacity (implying material inelasticity) during strong shaking (**Figure 2.1**) has been suggested in recent years as a change from the prevailing conventional design philosophy [e.g., FEMA-356, 2000]. In fact, a growing body of evidence suggests that allowing such nonlinear-inelastic foundation response is not only unavoidable, but may even be beneficial [Paolucci, 1997; Pecker, 1998,

2003; Martin & Lam, 2000; Makris & Roussos, 2000; Comartin et al., 2000; Pecker & Pender, 2000; Faccioli et al., 2001; Kutter et al., 2003; Gazetas et al., 2003; 2007; Gajan et al., 2005; Paolucci et al., 2008; Kawashima et al., 2007; Gajan & Kutter, 2008; Chatzigogos et al., 2009 ; Anastasopoulos et al., 2009].

Despite the fact that the nonlinear load-displacement response of shallow foundations has been extensively studied [e.g. Bartlett, 1976; Taylor et al., 1981; Georgiadis & Butterfield 1988; Butterfield & Gottardi, 1994; Faccioli et al. 2001; Gajan et al., 2005; Kutter, 1995; Houlsby & Puzrin, 1999; Allotey & El Naggar, 2003; 2008; Pecker, 2005; Harden et al., 2005; Pender, 2007; Gajan & Kutter 2008; Harden & Hutchinson, 2009], there is still quite a long way before such a *major* change in seismic design philosophy could be applicable in practice. Aside from reliability issues, a *key prerequisite* to render such concepts more attractive to engineers is the capability to realistically model the inelastic response of foundations.

Although several advanced and sophisticated constitutive models have appeared in the literature [e.g., Prevost, 1981; Dafalias, 1986; Houlsby, 1986; Jefferies, 1993; Gajo & Wood, 1999; Pestana, 1994; Pestana & Whittle, 1995; 1999; Jeremic et al., 1999; Puzrin & Houlsby, 2001a; 2001b; 2001c; Einav et al., 2003; Dafalias & Manzari, 2004; Houlsby & Puzrin, 2006], the current state–of–the art in nonlinear analysis of foundations emphasizes the development of macro-element models [Paolucci, 1997; Cremer et al., 2001; 2002; Le Pape & Sieffert, 2001; Pecker, 2002; Paolucci et al., 2008]. This is not only because sophisticated constitutive models typically require extensive calibration of their numerous parameters. Being usually implemented in highly specialized finite element (FE) or finite differences (FD) codes, their use is also restricted to simple superstructures. Additionally, in most cases, such

models can only be applied by numerical analysis specialists, prohibiting their use in practice. On the other hand, *macro-elements* constitute a valid solution, but are also usually restricted (at least until today) to simple superstructures.

In an attempt to overcome some of the above difficulties, this Chapter presents a simplified constitutive model for analysis of the cyclic response of shallow foundations. The model is based on a simple kinematic hardening constitutive model with Von Mises failure criterion, available in commercial FE codes. As it will be discussed in the sequel, the model is modified to be applicable for sand, following a simplified procedure, and is encoded in the FE code ABAQUS through a simple user subroutine, hence formulating a numerical tool able to provide fully coupled solution to soil-structure interaction problems such as the ones examined herein. The model is validated against centrifuge tests performed at UC Davis and large-scale 1-g experiments under the EU program TRISEE. Despite its simplicity and lack of generality and rigor, for the particular type of problem investigated herein such a constitutive model yields quite reasonable results. Requiring calibration of two parameters only, and being (relatively) easy to implement in a commercial FE code, the developed model is believed to provide a practically applicable solution. By no means should this model be considered as a general purpose model, able to reproduce all aspects of complex soil behavior under static and dynamic loading. However, despite its limitations (discussed in the sequel), it may be utilizable to model different aspects of dynamic soil response.

2.2. Constitutive Relations

As previously discussed, the constitutive model presented herein is based on a rather simple kinematic hardening model with Von Mises failure criterion, which is available in ABAQUS [2008]. Based on the work of Armstrong & Frederick [1966], the original model [Lemaitre & Chaboche, 1990] may be considered appropriate for clay, the behavior of which under undrained conditions is considered as normal-pressure-independent. Of course, phenomena such as pore-pressure buildup and dissipation cannot possibly be captured. However, for the key aspects of the investigated problem, given the rapid application of seismic loading the undrained behavior is considered as a reasonable simplification of reality. The model is modified, as described in the sequel, to be applicable for sands, as well. To provide a more concise presentation, the relevant constitutive relations for clay and sand are discussed together.

An extended pressure-dependent Von Mises failure criterion (**Figure 2.2a**) is combined with nonlinear kinematic hardening and associated plastic flow rule. It is noted that this assumption is not valid for sand, the volumetric behavior of which largely depends on dilation. The evolution of stresses is defined as :

$$\sigma = \sigma_o + \alpha \tag{2.1}$$

where σ_o corresponds to the stress at zero plastic strain, and α is the "backstress". The latter determines the kinematic evolution of the yield surface in the stress space. This is performed through a function F which defines the yield surface :

$$F = f(\sigma - \alpha) - \sigma_o \tag{2.2}$$

where $f(\sigma - \alpha)$ is the equivalent Mises stress with respect to the backstress α :

Given the associated plastic flow, the plastic flow rate $\dot{\varepsilon}^{pl}$ is :

$$\dot{\varepsilon}^{\mathrm{pl}} = \dot{\bar{\varepsilon}}^{\mathrm{pl}} \frac{\partial F}{\partial \sigma} \tag{2.3}$$

where $\dot{\bar{\varepsilon}}^{pl}$ the equivalent plastic strain rate.

The evolution of stress is composed of two components :

(a) an isotropic hardening component, which describes the change of the equivalent stress defining the size of the yield surface σ_o as a function of plastic deformation, and

(b) a nonlinear kinematic hardening component, which describes the translation of the yield surface in the stress space, and is defined by the superposition of a purely kinematic term and a relaxation term (which introduces the nonlinear behavior).

The isotropic hardening component defines the evolution of the size of the yield surface as a function of the equivalent plastic strain $\bar{\varepsilon}^{\mathrm{pl}}$:

$$\sigma_o = \sigma_0 + Q_\infty \left(1 - e^{-b\bar{\varepsilon}^{\mathrm{pl}}}\right) \tag{2.4}$$

where Q_∞ and *b* are model parameters, defining the maximum change of the size of the yield surface, and the rate of this change with $\bar{\varepsilon}^{\mathrm{pl}}$, respectively. For Q_∞ = 0 the size of the yield surface remains constant and the model reduces to a nonlinear kinematic hardening model.

The evolution of the kinematic component of the yield stress is described by the expression :

$$\dot{\alpha} = C \frac{1}{\sigma_o} (\sigma - \alpha) \dot{\bar{\varepsilon}}^{\mathrm{pl}} - \gamma \alpha \dot{\bar{\varepsilon}}^{\mathrm{pl}} \tag{2.5}$$

where *C* is the initial kinematic hardening modulus [$C = \sigma_y / \varepsilon_y = E = 2(1+\nu)G_o$] and *γ is* a parameter determining the rate of decrease of the kinematic hardening with increasing plastic deformation. The above equation is based on Ziegler's [1959] kinematic hardening law, in which the "recall" term $\gamma\alpha\dot{\bar{\varepsilon}}^{pl}$ has been added to introduce the non-linearity in the evolution law [Lemaitre & Chaboche, 1990]. **Figure 2.2b** illustrates the evolution of the two hardening components (kinematic and isotropic) for multi-axial loading. According to the evolution law governing the kinematic hardening component, the "backstress" *α* must be contained within a cylinder of radius $\sqrt{2/3}\,C/\gamma$. The bounding of the yield surface demands that all stress points lie within a cylinder of radius $\sqrt{2/3}\,\sigma_y$, where σ_y is the maximum yield stress at saturation. At large plastic strains, when *σ* approaches σ_y , the magnitude of *α* becomes equal to $\alpha_s = C/\gamma$ and ($\sigma - \alpha$) tends to σ_o (**Figure 2.3a**), which means that $\dot{\alpha}$ (Eq. 5) tends to zero.

For the case of clays, the undrained strength of which is not pressure dependent, the maximum yield stress can be defined as :

$$\sigma_y = \sqrt{3}S_u \tag{2.6}$$

Since $\sigma_y = C/\gamma + \sigma_0$, parameter γ can be expressed as [Gerolymos et al., 2005] :

$$\gamma = \frac{C}{\sqrt{3}S_u - \sigma_0} \tag{2.7}$$

In the case of sand, the shear strength depends on the confining pressure and the friction angle *φ*. This pressure-dependency is incorporated in the model by defining the yield stress at saturation as a function of octahedral stress and the friction angle, as follows :

$$\sigma_{\mathrm{y}} = \sqrt{3}\left(\frac{\sigma_1 + \sigma_2 + \sigma_3}{3}\right)\sin\varphi \qquad (2.8)$$

where σ_1 , σ_2 , and σ_3 the principal stresses. Accordingly, parameter γ can be expressed as :

$$\gamma = \frac{\mathrm{C}}{\sqrt{3}\left(\frac{\sigma_1 + \sigma_2 + \sigma_3}{3}\right)\sin\varphi - \sigma_0} \qquad (2.9)$$

Parameter σ_0 , which controls the initiation of the non-linear behaviour is defined as a fraction λ (typically ranging from 0.1 to 0.3) of the yield stress σ_y :

$$\sigma_0 = \lambda\, \sigma_y \qquad (2.10)$$

Figure 2.3a summarizes the parameters that are incorporated in the formulation of the proposed model, while **Figure 2.3b** vividly illustrates the effect of σ_o on material behavior (in terms of shear stress –shear strain loops) for two extremes. For σ_o = 0.1 σ_{y} , the material exhibits non-linear behavior even for very low amplitude strains. In contrast, for σ_o = 0.3 σ_y a considerable amount of shear strain is necessary to enter the non-linear regime. It should be clarified that the model, as presented herein, does not account for strain softening. Yet, in **Figure 2.3a** the more general case of strain softening soil is schematically illustrated just to define model parameters.

Parameter *C* is the Young's modulus for very small strains ; it determines the initial "elastic" stiffness at low strain amplitudes (**Figure 2.3c**). It can be directly computed on the basis of the measured shear wave velocity V_s , or estimated from empirical correlations [e.g. Hardin & Richart, 1963; Robertson & Campanella, 1983; 1983b; Seed et al., 1986; Mayne & Rix, 1993] and expressed as a function of the overburden stress σ_y :

$$\mathrm{C} = \mathrm{a}\, \sigma_y \qquad (2.11)$$

Based on such empirical correlations, the ratio a typically ranges from 150 to 1000 (i.e. E = 300S_u to 1800S_u) for clays, and from 1000 to 10000 for sands.

The modified kinematic hardening constitutive model is encoded in the ABAQUS [2008] finite element environment through a user-defined subroutine. As already alluded, model parameters can be easily calibrated, even with limited experimental or field data. In summary, the calibration requires the following data : (i) soil strength : S_u for clay, φ for sand ; (ii) small-strain stiffness : G_o or V_s (if measurement is not available, the aforementioned empirical correlations can be utilized) ; and (iii) G–γ curves : to calibrate parameter λ and the ratio a.

For the purposes of the present study, model parameters were systematically calibrated for various levels of the overburden stress (for sands) and PI ratios (for clays), according to the experimental G–γ curves of Ishibashi & Zhang [1993] (see also Vucetic & Dobry, 1991). To this end, a numerical simulation of the cyclic simple shear test was conducted. Typical comparisons between experimental and computed G–γ and ξ–γ curves for sand are portrayed in **Figure 2.4**. For the soil materials investigated herein, λ = 0.1 was found to provide a reasonable fit to G–γ curves. For lower confining pressures (**Figure 2.4a**), the model slightly under-predicts the strength reduction at low to intermediate strains. The agreement is improved with increasing σ_{vo} (**Figure 2.4b**). As also seen in the FE computed τ–γ (shear stress–shear strain) hysteresis loops of **Figure 2.5** (corresponding to a typical sand), due to the adoption of the Masing criterion for loading-unloading, the model over-estimates the hysteretic damping for large shear strain amplitudes ($\gamma \approx 10^{-2}$). As expected, the reduction of λ leads to improvement of model accuracy. However, since σ_0 essentially

defines the initiation of non-linear soil behavior, a great reduction of λ unavoidably leads to an increase of computational cost. Therefore, an initial sensitivity analysis was performed to estimate the optimum range of λ, which was found to range between 0.1 and 0.3. The results presented herein refer to λ = 0.1 (or $\sigma_0 = 0.1\sigma_y$). Increasing λ to 0.3 leads to a 10% deviation from the presented results. Similarly, the value of a was calibrated so as to more effectively capture the initial part of the stress-strain curve.

2.3. Model Validation for Clay

The original constitutive model for clay will be validated first, making use of published UC Davis experimental results.

2.3.1. Description of Tests

Gajan et al. [2005] conducted experiments in the 9.1 m radius beam centrifuge at the Center of Geotechnical Modeling of the University of California, Davis. The tests were conducted at 20 g centrifugal acceleration, comprising 40 models of shear wall footings imposed to cyclic and dynamic loading. A comprehensive set of footing dimensions, depths of embedment, dead load, initial factor of safety against static bearing capacity failure, soil density, and soil types (dry sand and saturated clay) were parametrically investigated with respect to the nonlinear load-deformation foundation response. Four series of tests were conducted on dry sand ($D_r \approx$ 80 % and 60%) and one on saturated clay of $S_u \approx$ 100 kPa. The latter is selected for model validation.

The structure had a weight of 364.8 kN, corresponding to an initial vertical factor of safety FS_V = 2.8. The footing length was L = 2.672 m and its width B = 0.686 m (all dimensions

in prototype scale). The footing models were tested on a soil bed prepared in a rigid container. The material composing the clay layer consisted of remolded San Francisco Bay Mud, with Atterberg limits : *LL* = 90 and *PL* = 38. Before spinning, the mud was consolidated on top of a dense sand layer. The final thickness of the consolidated clay layer was 1.7 m.

The centrifuge model setup and the relevant instrumentation (for the tests investigated here : vertical push and slow cyclic lateral push) are displayed in **Figure 2.6**. Each test series included at least one concentric vertical push test to measure the bearing capacity of the soil and to confirm the undrained shear strength of the clay. This initial test was displacement controlled in order to mobilize the foundation capacity without developing excessive movement.

The vertical push was followed by slow cyclic lateral push tests, during which displacement was applied through an actuator at a height of 4.75 m from the footing (which is close to the height of the center of gravity of the structure). The height of the structure tested was 10 m. Displacement was applied in packets of increasing amplitude, each one including three cycles of constant amplitude. Horizontal and vertical linear potentiometers were mounted at different positions on the wall and the footings to measure the displacements of the structure ; a load-cell attached on the actuator was measuring the force acting upon the wall. Detailed description of the experiments and the procedures followed are documented in Rosebrook & Kutter [2001a; 2001b; 2001c], Gajan et al. [2003a ; 2003b], Kutter et al. [2003], and Phalen [2003].

2.3.2. Methodology of Numerical Analysis

The problem is analyzed through 3-D finite element (FE) analysis. The developed 3D FE model, taking advantage of centrifuge model symmetry, is displayed in **Figure 2.7**. The soil is modeled with 8-noded hexahedral continuum elements. The same elements are used for the foundation. In contrast to the soil, their behavior is assumed linear elastic, and they are given the Young's modulus of aluminum (which was used in the centrifuge model tests). An initial sensitivity analysis revealed that the footing has to be discretized into at least 10 elements to reproduce the mechanism of bearing capacity failure (for the vertical loading test) and the rocking behavior (for the lateral cyclic pushover test). The soil-foundation interface is modeled using special "gap" elements [ABAQUS, 2008], which allow the structure to slide on, or detach from the soil depending on the loading. These elements connect the nodes of the soil with the corresponding nodes (i.e. having the same coordinates) of the foundation, which are initially in contact but are allowed to separate when uplifting takes place. While being "infinitely" stiff in compression, the gap elements are tensionless allowing separation. In the horizontal direction, they follow Coulomb's friction law, allowing for sliding when the friction force is exceeded. In the analyses presented herein, the friction coefficient was set equal to 0.7. The shear wall was modeled with practically rigid 3-dimensional beam elements. Since the response is governed by foundation rocking, the flexural deformation of the shear wall may be assumed to be negligible. Hence, no attempt was made to model accurately the shear wall. Non-linear $P-\delta$ geometry effects were also taken into account.

Soil stiffness has been assumed to be constant with depth, which is a fair assumption for OC clays. In the absence of V_s or G_o measurements, parameter C (i.e. the initial stiffness) of the constitutive model was calibrated exploiting the results of vertical push tests. Keeping all other parameters constant (S_u = 100 kPa, Poisson's ratio v = 0.3), C was parametrically varied from $300S_u$ to $1800S_u$. The best fit was achieved for $C = E = 600S_u$, which was adopted for the analysis of the slow cyclic lateral push sequence. No further calibration was conducted with respect to parameters λ and α : the already conducted calibration results for PI = 50 clay were utilized (**Table 2.1**). The comparison between the FE-computed ultimate vertical load and the experimental load-displacement curves (as measured by the two potentiometers on the footing) for the vertical loading is illustrated in **Figure 2.8**.

The FE computed bearing capacity under undrained conditions was p_{ult} = 560 kPa, which corresponds to a static factor of safety FS_v = 2.87. This compares satisfactorily with the experimentally measured bearing capacity p'_{ult} = 546 kPa (i.e. FS_v = 2.8), and is, understandably, slightly higher than the theoretical Prandtl [1921] solution for plane-strain :

$$p'_{ult} = (\pi+2)S_u = 514 \text{ kPa} \qquad (2.11)$$

Having partially calibrated the model using the results of the vertical push test (parameter C only), we now proceed to the simulation of the slow cyclic lateral pushover sequence. The FE model was subjected to 3 displacement-controlled loading packets (each one consisting of three load cycles) of increasing amplitude. Loading during the experiment was applied slowly, with the period of each cycle being equal to 200 seconds. In the numerical simulation, the displacement was applied quasi-statically.

Figures 2.9 to **2.11** compare the FE computed with the measured results in terms of : (a) moment–rotation response, and (b) settlement–rotation response of the foundation. More specifically :

First Loading Packet

Some uplifting can be traced in the moment-rotation loops predicted by the numerical model during the first loading packet (**Figure 2.9a**), something which is not observed to the same extent in the experiment. The latter are indicative of increased plastic straining of the soil underneath the footing, hence resulting to higher dissipation of energy as elucidated by the area included within the experimental hysteresis loops. The analysis slightly *over-predicts* the maximum moment of the system during loading to the east direction (negative values in the diagram), while the discrepancy becomes larger to the opposite direction.

The experimentally measured hysteresis loops systematically reveal a rather rapid decrease of the moment (by about 30%) at every maximum moment attainment, which is not followed by a respective decrease in footing rotation (in both loading directions). This is clearly demonstrated by the almost vertical segments of the loop immediately upon initiation of unloading and, in turn, results in substantial growth of the area of the M–ϑ loop. This may be the product of localized plastification underneath the footing edges, which could be attributed to reduced strength of the soil in these areas (due either to earlier cycles of shearing, or to soil inhomogeneities, or to details of the experimental procedure, which are not precisely known and/or cannot be reproduced with the numerical model).

The model reliably reproduces the experimental settlement-rotation curve (**Figure 2.9b**) both in terms of settlement per cycle and total settlement. Admittedly, however, apart

from the general agreement, it is worth noting that the numerical analysis predicts an uplifting–dominated response (indicated by the steep edges of the settlement–rotation plot) as opposed to the sinking–dominated response observed in the experiment. This discrepancy could also be attributed to localized plastification underneath the footing edges.

Second Loading Packet

During the 2nd loading-unloading packet, both the experiment and the analysis show that a large area is enclosed within the hysteresis loops (**Figure 2.10a**), revealing the dissipation of a substantial amount of energy at the footing–soil interface. Experimental measurement and model prediction show that the ultimate moment capacity M_{ult} of the system has been attained. Its value is of the order of 300kNm. The deviation of the experimental measurement from this value when the footing is loaded to the east (negative values) is tentatively attributed to some experimental asymmetry, or, as before, soil inhomogeneity.

As shown in **Figure 2.10b**, with the exception of a slight underprediction of the settlement by the numerical analysis, the comparison in terms of settlement–rotation response is quite satisfactory.

Third Loading Packet

Excessive plastification is evident in both the experimental results and the numerical prediction (**Figure 2.11a**). The hysteresis loops reveal a highly non-linear response of the system. The curve now conspicuously manifests the mobilization of the ultimate capacity ($M_{ult} \approx 300$ kNm) : increase of rotation for constant moment. Still though, the non-symmetric behavior (different values of the ultimate moments in the east and west direction)

demonstrated by the experimental curve cannot be precisely captured with the numerical analysis.

The numerical prediction is quite successful in terms of the settlement–rotation response (**Figure 2.11b**). According to Gajan et al. [2005], foundation rocking during large amplitude lateral loading leads to (permanent) loss of contact between the soil and the footing. The generated gap at the uplifted side is associated with a drastic reduction of the effective width of the foundation, leading to extensive soil yielding at the opposite side, further increasing the detached area of the foundation (see also **Figure 2.7b**). This is clearly betrayed by the sharp edges of the settlement–rotation curves.

Generally, it is concluded that experiment and analysis confirm that the moment–rotation plot does not reveal any appreciable reduction in *moment capacity* with increasing number of cycles, or rotation amplitude ; but it does demonstrate a degradation of rotational *stiffness* with increasing rotation amplitude. Moreover, the model realistically reproduces the accumulation of permanent settlement underneath the footing. The analysis confirms the experimental conclusion that, as the number of cycles increases, the rate of increase in settlement per cycle of rotation decreases. This is normally attributed to the increase of soil vertical stiffness due to soil densification. However, as seen in the model description (Eq. 4-10), the model is not capable of reproducing such increase of soil stiffness with settlement (i.e. the effect of soil densification). Nevertheless, as evidenced by the results, the systemic behavior is captured within acceptable engineering accuracy. This is attributed to the fact that as the footing settlement increases, soil plastification has to propagate deeper into the soil, and hence an increasing number of elements must be

contained within the failure mass. As the number of elements that must reach failure for the footing to settle increases, the rate of settlement will unavoidably decrease. Hence, although at the element level the model is not capable of capturing dynamic densification effects, the systemic behavior is captured correctly. At least for the specific problem, it seems that such systemic effects are probably more important.

It is noteworthy that although the model predicts the settlement quite accurately, the energy dissipation prediction is not as successful. As can be seen in the rotation-settlement plots of **Fig. 2.9** to 2.**11**, the model tends to underpredict foundation uplifting as the loading packets increase. Although the total settlement is predicted with reasonable engineering accuracy, the settlement per loading cycle is underpredicted. For example (**Figure 2.11b**), during the first cycle of the third packet the measured settlement (at the center of the footing) reduces from its initial value of -52 mm to about -28 mm, due to uplifting. The numerical prediction is a mere -40 mm, which means that foundation uplifting is substantially underpredicted. The same observation applies to all subsequent loading cycles. This underprediction of uplifting, which is the main mechanism of energy dissipation in such systems [e.g. Housner, 1963; Gottardi and Butterfield, 1995; Gajan et al, 2003; Gajan & Kutter, 2008] apparently leads to the observed underprediction of energy dissipation. On the other hand, as the model is able to correctly predict the soil ultimate strength (**Figure 2.11a**), the total soil settlement is correctly predicted. Naturally, such effects are more obvious in the third loading packet, during which the uplifting is more intense.

2.4. Model Validation for Sand

The model for sand will be validated making use of the TRISEE large-scale (*1g*) geotechnical experiments, conducted in ELSA facility in ISPRA, Italy.

2.4.1. Description of Tests

A series of slow cyclic and dynamic tests were performed on an isolated footing resting on saturated sand. Loading of the structure was stemming from the application of cycles of horizontal (shear) force and (overturning) moment simulating the inertial loading transmitted onto the foundation from the superstructure. The soil properties were varied to model a high Density (*HD*) and a Low Density (*LD*) sand. The measured relative densities were D_r = 85% for the HD tests, and D_r = 45% for the LD tests.

As schematically illustrated in **Figure 2.12** [after Faccioli et al., 1999], the experimental prototype consisted of a concrete caisson, filled with coarse-to-medium Ticino sand [Bellotti et al., 1996], and a rigid slab, representative of a typical concrete shallow footing. The sand-box dimensions were 4.6 m by 4.6 m in plan and 4 m in height. The foundation was 1 m by 1m in plan. The sand-box lateral boundaries were rigid and impermeable. It must be noted that the response of the foundation may have been influenced by its proximity to the caisson lateral boundaries. The interface of the slab with the soil was made of concrete in order to achieve a high friction coefficient. The foundation was placed at 1 m depth in a trench of sand, to obtain an overburden pressure of about 20 kPa ; a 1 m high steel formwork was placed around the foundation to retain the sand.

An air cushion system was transmitting a constant vertical load throughout the test. The design values for the vertical load were 300 kN and 100 kN for the High Density (HD) and Low Density (LD) sand specimens, respectively (typical values of current design pressure levels for shallow foundations). In both cases, the design vertical load was considerably lower than the system's bearing capacity. A hydraulic actuator set at 0.9 m above the foundation level for the HD case and at 0.935 m for the LD case, was used to impose to the foundation the prescribed horizontal displacement time history.

Before initiation of the slow cyclic tests, a vertical load (which was simulating the structure load and hence was maintained throughout the test) was applied on the foundation. This was followed by three series of horizontal slow cyclic loading (slow application of horizontal displacements), of which only the third one is being modeled here. During the *first phase*, small-amplitude force-controlled cycles were applied to the structure. *Phase II* consisted of the application of a typical earthquake time-history providing a base shear similar to that of a four-storey reinforced concrete building designed according to Eurocode 8.

During the *third phase* (which constitutes the validation target), the top of the structure was subjected to sine-shaped displacement cycles of increasing amplitude, until mobilization of the ultimate lateral foundation capacity. To achieve this capacity while avoiding excessive displacements, the test was displacement-controlled. The time history of the applied horizontal displacement is displayed in **Figure 2.13** for the HD (*high density*) and the LD (*high density*) test. After application of the initial vertical loading, the settlement experienced by the foundation was around 7 mm for dense sand, and 16 mm for loose sand.

2.4.2. Methodology of Numerical Analysis

The 3-D FE model shown in **Figure 2.14** was developed to analyze the TRISEE experiment. The adopted numerical analysis methodology is the same with the one discussed in the previous section. The prescribed displacement was applied at the beam node at a height of 0.9 m and 0.935 m above the foundation level for the HD and the LD tests, respectively. The part of the soil below the foundation level was saturated (degree of saturation ranging from 80 to 90%) while the overburden soil layers were dry. The two soil states were modeled assuming a different unit weight : while the overlying dry sand was modeled with its dry unit weight γ_{dry} , the saturated unit weight γ_{sat} was assumed for the saturated sand layer. This way, the effective stresses were taken into account in the analysis. It is noted that such analysis cannot possibly capture the development of transient pore pressure and its effect on soil response.

Similarly with the tests on clay, initial sensitivity analyses were performed to calibrate the initial stiffness (parameter *C* of the constitutive model). The best match was achieved for $C = 8500\sigma_y$ and $6000\sigma_y$ for the HD and the LD tests, respectively (**Table 2.1**). A parabolic distribution of *C* with depth was assumed –a reasonable (but certainly not accurate) assumption for sand deposits. The initial static Factor of Safety (FS_v) was not directly measured but has been calculated by various researchers [Negro et al., 2000; Faccioli et al., 2001; Kutter et al., 2003; Gajan et al., 2005]. All researchers agree that the FS_v for the HD tests was about 5. This is consistent with the *S*–shaped M–ϑ curve of the HD test : such a shape has been linked to intense uplifting of foundations (a characteristic of relatively high FS_v). Utilizing the strength parameters proposed by Belloti et al. [1998] and Ahmadi et al.

[2005], for Ticino sand of D_r = 85% (peak friction angle $\varphi_p = 43^o$; constant volume friction angle $\varphi_{cv} = 35^o$), the analysis also produced an initial factor of Safety $FS_v^{anal} \approx 5$. For the LD case however, the FSv as calculated by the aforementioned researchers ranges (astonishingly) from 2 to 7 ! Negro et al. [2000] report $FS_v = 5$, and Faccioli et al. [2001] estimated an $FS_v = 7$ based on bearing capacity formulae, with the theoretical strength of the Ticino Sand. However the oval shape of the LD M–ϑ curves is indeed a feature of low FS_v conditions (i.e. lower than 5). Allottey & El Naggar [2008] after back calculations of the FS_v based on (a) moment capacity equations and (b) the Butterfield & Gottardi [1994] bounding surface, recommend that the actual factor of safety for the specific LD tests ranges between 2 and 2.85. Therefore, two strength scenaria are considered in the calculations, taking account of the Allottey & El Naggar [2008] recommendation that the peak friction angle of the Ticino sand achieved in the LD experiment ranges between 30^o and 35^o. :

(a) the $FS_v \approx 5$ scenario, assuming $\varphi_p = 35^o$, and

(b) the $FS_v \approx 3$ scenario, assuming $\varphi_p = 30^o$.

2.4.3. Comparison of Numerical Prediction with Experimental Results

Dense Sand (HD Test)

A remarkable agreement is observed between the measured and the calculated hysteresis loops produced during slow cyclic tests (**Figure 2.15a**). Both loops evolve quite symmetrically. The numerical analysis effectively reproduces the lateral capacity of the system : $M_{ult} \approx 100$ kNm. The analysis captures with sufficient accuracy both the initial stiffness of the system, and the gradual degradation of rotational stiffness with increasing

rotation amplitude. Analysis and experiment produce an *S*-shaped moment−rotation curve, which clearly manifests an uplifting–dominated response. As the amplitude of imposed rotation increases, the numerical model slightly *overpredicts* the dissipation of energy during cyclic loading.

A relatively good agreement between the numerical prediction and the experiment is also achieved in terms of horizontal force versus horizontal displacement of the footing (**Figure 2.15b**). The experimental loop (dashed line) is slightly asymmetric, in that the maximum horizontal displacement is rather higher in the negative direction (6 mm) compared to that in the positive direction (5 mm). The numerically calculated loop (solid line), despite capturing the observed behaviour does not accurately predict the higher displacement in the negative direction (δ^{anal} = 5.5 cm).

Loose Sand (LD Test)

Contrary to the uplifting behavior of the footing on *HD* sand, the foundation on loose sand is obviously subjected to substantial irrecoverable sinking within the soil. This is justified by both the numerical model *and* the experimental results, which show clearly larger energy dissipation in the loose sand for both FS_v scenarios (**Figure 2.16** for the $FS_v \approx 3$ scenario and **Figure 2.17** for the $FS_v \approx 5$ scenario). The loops produced during the LD tests are obviously asymmetric due to the irregularity of the input displacement time-history which contained a permanent negative horizontal displacement. This intense irregularity has not been captured by the analysis. Still though, a very good agreement is observed between the measured and the calculated hysteresis loops for the low $FS_v \approx 3$ scenario, while in the high $FS_v \approx 5$ case the

hysteresis exhibits moderately *S*-shaped loops, which are (as already discussed) indicative of uplifting. Both the initial stiffness of the system, as well as its stiffness during loading are successfully predicted. For the higher amplitudes of rotation though, both scenarios predict a stiffer behavior.

The analysis has been successful in simulating the experimentally observed mobilization of the foundation capacity. In very good accord with the measured value, the predicted ultimate moment of the system is $M_{ult} \approx 40$ kNm in the negative loading direction. However, the $\varphi = 35^{o}$ scenario leads to *overestimation* of the calculated moment capacity, while for the $\varphi = 30^{o}$ case the capacity is rather accurately predicted.

In terms of horizontal force versus horizontal displacement, the $\varphi = 30^{o}$ scenario predicts lager displacements than the $\varphi = 35^{o}$ case. Admittedly, however, none of the two scenarios are capable to capture the intensity of asymmetric sliding (towards the negative x-axis direction).

Cyclic Foundation Settlement (HD and LD Test)

The comparison of the evolution of vertical displacements for the HD and LD tests is displayed in **Figure 2.18**. *The recorded trend is almost linear in both cases, probably due to the progressive squeezing of sand underneath the plate toward the sides during the sinking of the foundation* [as suggested by Faccioli et al., 2001].

In all cases, settlements are accumulated underneath the footing, reaching ultimate values of about 20 mm and 70 mm for dense and loose sand respectively. These values are slightly *overpredicted* by the analysis for the HD test : $s^{anal} = 25$ mm. While a cumulative

settlement trend is macroscopically obvious in the HD case, the footing undergoes reversible settlement-uplifting cycles within each set of loading-unloading series. The numerical model indeed predicts the general trend, while it matches the seesawing shape of settlement-uplifting cycles during each series (**Figure 2.18b**), but results in (slightly) higher settlement.

For the LD case (**Figure 2.18c**) both scenarios lead to reasonable predictions of the settlement : *59 mm* for the $FS_v \approx 5$ scenario ; *84 mm* for the $FS_v \approx 3$ scenario. The predicted evolution of cyclic foundation settlement agrees reasonably with the experimental measurements. Observe that during the final stages of the LD test, the vertical displacements reveal some uplifting of the foundation : this is effectively captured by the numerical model when the $FS_v \approx 5$ scenario is considered ($\varphi = 35^o$).

2.5. Summary and Conclusions

This chapter has dealt with the presentation of a simplified but fairly comprehensive constitutive model of clays and sands for analysing the cyclic response of shallow foundations undergoing strong rocking oscillations, involving uplifting and mobilization of bearing-capacity “failure” mechanisms. Having as basis a simple kinematic hardening constitutive model, readily available in commercial FE codes, a simple modification was implemented to render the model applicable for sand. The model was encoded in ABAQUS through a rather simple user subroutine, and thoroughly validated against centrifuge (UC Davis) and large scale 1-g (TRISEE) experimental results.

The key conclusions *and* limitations can be summarized as follows :

(1) The Von Mises failure criterion of the constitutive model can be considered appropriate for clay under undrained conditions. Phenomena such as pore-pressure buildup and dissipation cannot be captured. For the key aspects of the problem investigated herein, given the rapid application of seismic loading, undrained behavior is considered as a reasonable simplification of reality.

(2) The extended normal-pressure-dependent Von Mises failure criterion, employed to render the model applicable to sand, constitutes a simplified approximation of real sand behavior. By no means, can it be considered as accurate or rigorous. The assumption of an associated plastic flow rule is also a "gross" simplification, not valid for sand, the volumetric behavior of which largely depends on dilation. Hence, the volumetric behavior of sand cannot be reproduced.

(3) Despite the above drawbacks, for the problem of interest (i.e. the nonlinear response of shallow foundations) the proposed simplified model has been shown to yield quite reasonable results. Through the validation presented herein, the model was found capable of capturing with reasonable engineering accuracy :

- the response of shallow foundations subjected to *vertical loading*, both in terms of FS_v and load-settlement response ;
- the *lateral capacity* of the shallow foundations, as expressed through M_{ult} ;
- the *lateral cyclic performance* of the foundation, both in terms of moment−rotation and load−displacement response ; and
- the *accumulation of foundation settlement* due to lateral cyclic loading.

(4) Some discrepancies (small in general) between numerical predictions and experimental results can be attributed to the approximate nature of the model, and several experimental details (such as the exact strength and stiffness profiles, soil inhomogeneities, slight but possibly important asymmetries, etc.) that are either unknown or cannot be captured numerically.

(5) Having knowledge of *soil strength* (S_u for clays and φ for sand) and small-strain stiffness (G_o or V_s), the model requires calibration of two parameters only (λ and ratio a), which has been shown to be simple and straightforward : it is conducted on the basis of G–γ curves.

(6) Easily implemented in commercial FE codes (as done here through a simple user subroutine in ABAQUS), the model is believed to provide a practically applicable solution, not restricted to simple superstructures, and not to be solely used by numerical analysis specialists.

Figures of Chapter 2

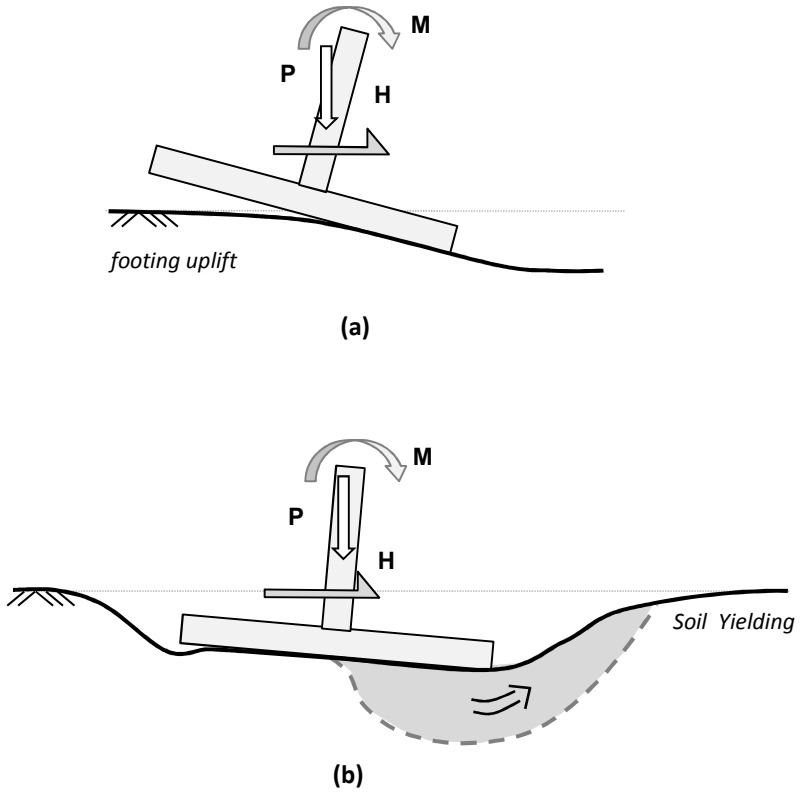

Figure 2.1. Mobilization of the ultimate capacity of the soil–foundation system. Schematic of a foundation subjected to combined horizontal and vertical loading, and bending moment : (a) when uplifting is critical ($SF_v \geq 2$) ; (b) when the bearing capacity failure mechanism is prevailing ($SF_v < 2$).

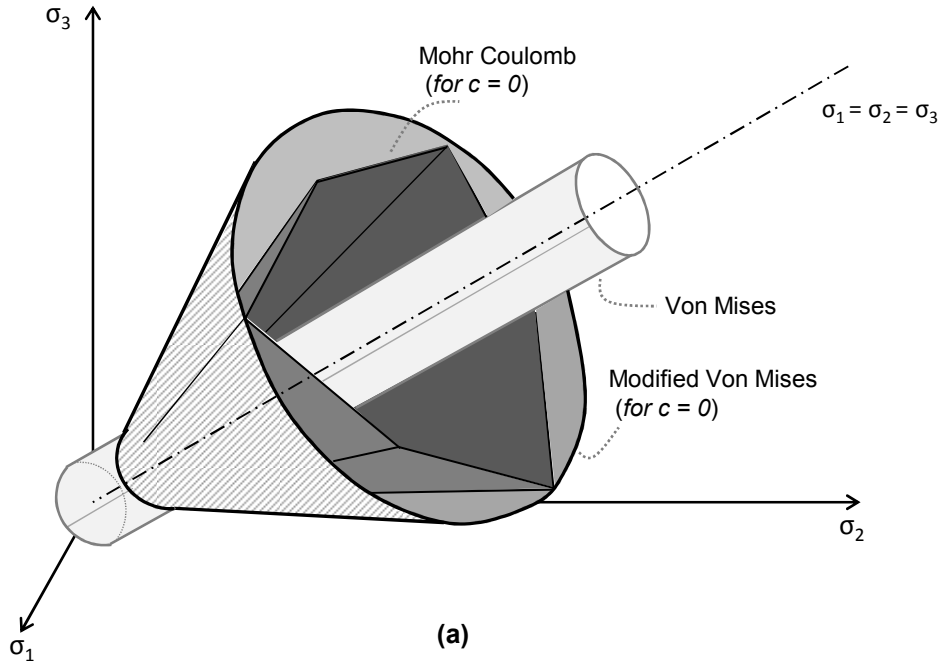

Figure 2.2. Simplified constitutive model : (a) representation of the extended pressure-dependent Von Mises failure criterion in the principal stress space (hashed shape) together with the Von-Mises (light grey shape) and the Mohr Coulomb failure criterion (dark grey shape), (b) projection of the failure surface at pressure $p = (\sigma_1 + \sigma_2 + \sigma_3)/3$ on the π-plane.

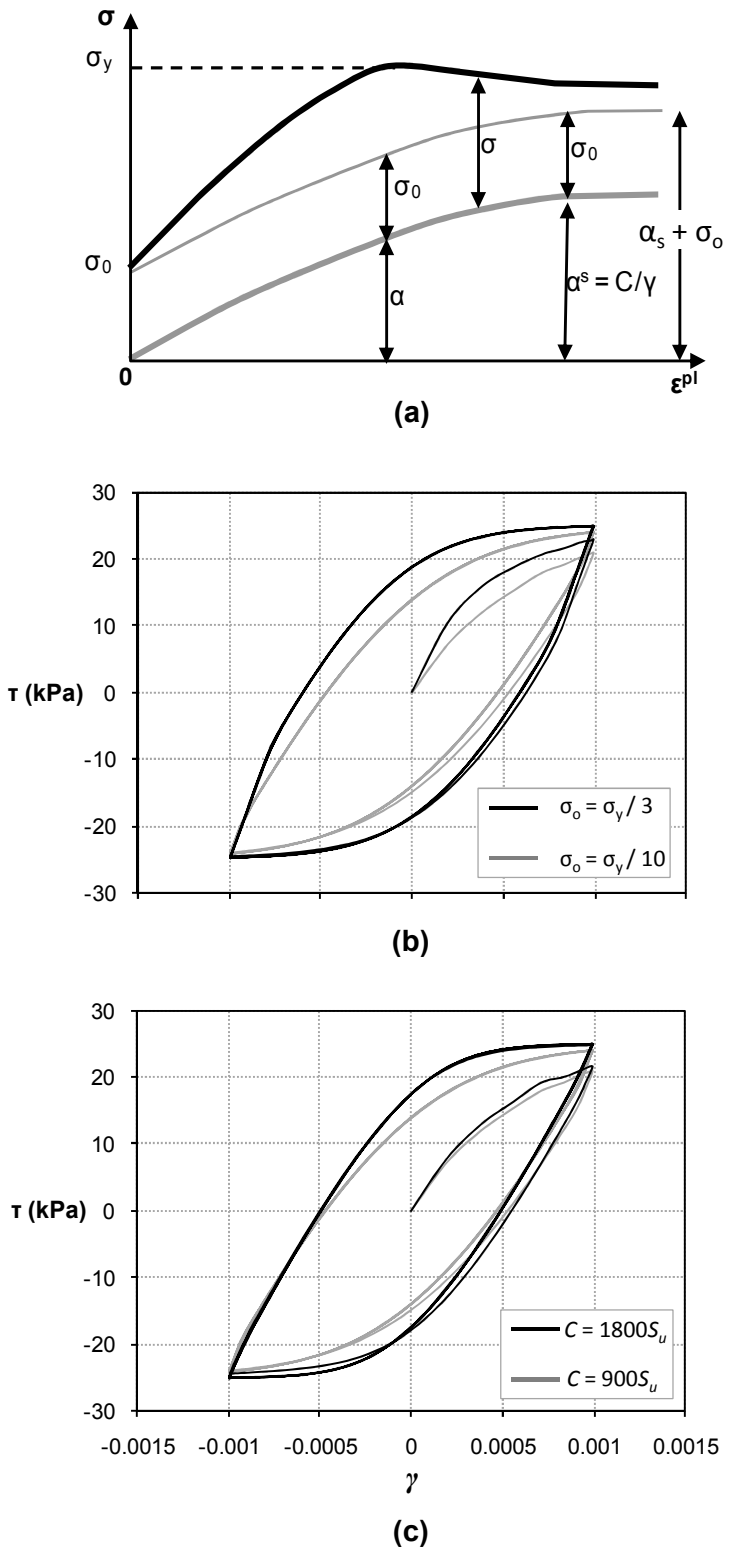

Figure 2.3. (a) Parameters incorporated into the formulation of the constitutive model, and example illustration of model sensitivity to (b) parameter σ_o (which controls the onset of inelasticity), and (c) parameter C (i.e. the initial Young's modulus, which controls the initial stiffness).

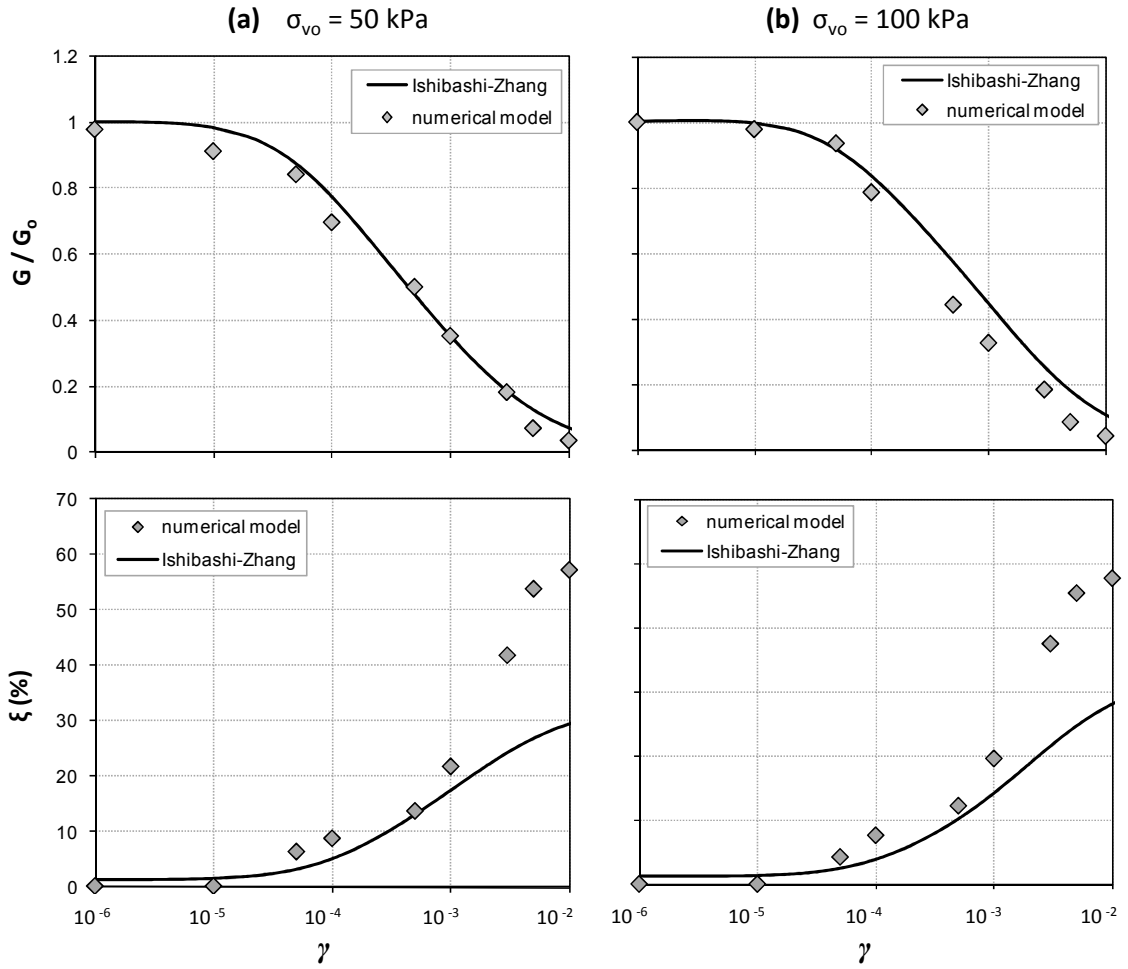

Figure 2.4. Constitutive model calibration for sand. Comparison of FE computed G–γ and ξ–γ curves with published curves of Ishibashi and Zhang [1993] for three levels of confining pressure : (a) σ_{vo} = 50 kPa ; and (b) σ_{vo} = 100 kPa.

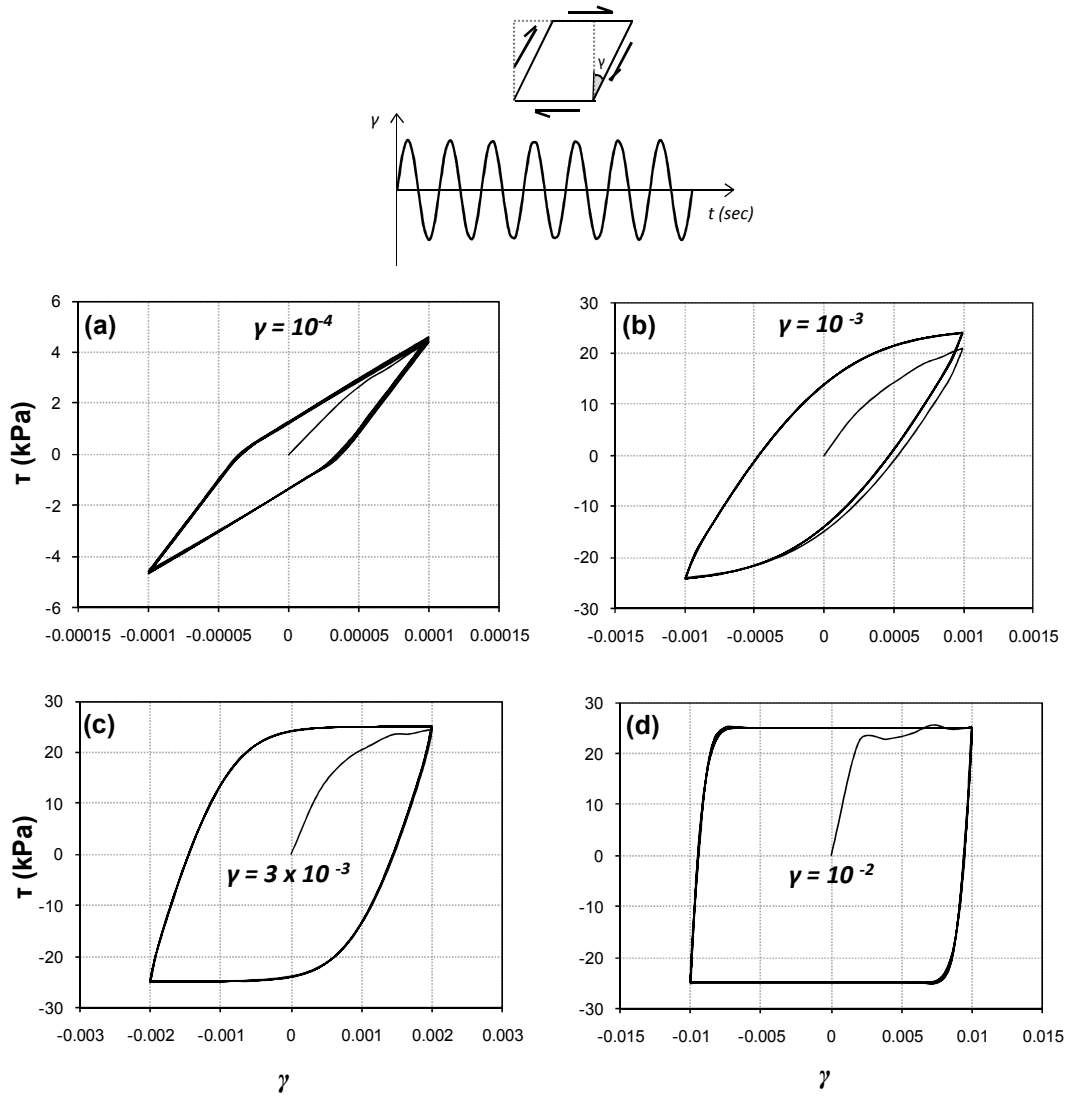

Figure 2.5. FE simulation of simple shear test in sand (φ = 30°, G_o = 65 MPa, σ_{vo} =50 kPa). τ-γ hysteresis loops for different stain levels : (a) $\gamma = 10^{-4}$; (b) $\gamma = 10^{-3}$; (c) $\gamma = 3 \times 10^{-3}$; and (d) $\gamma = 10^{-2}$.

(a) Vertical Push

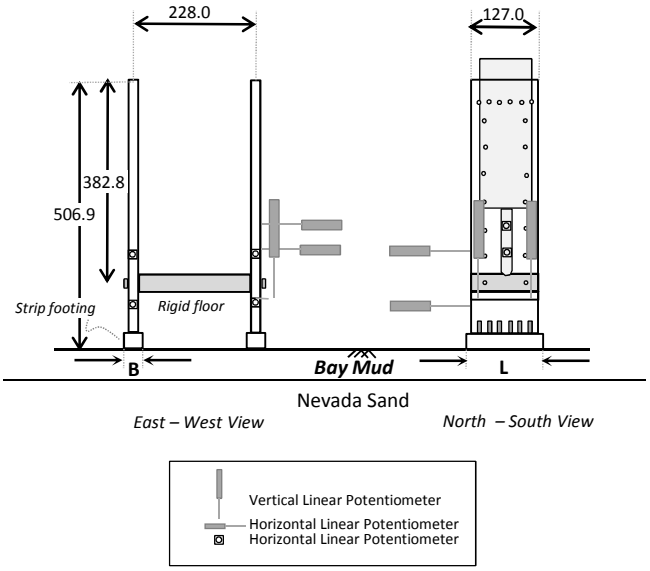

(b) Slow Cyclic Lateral Tests

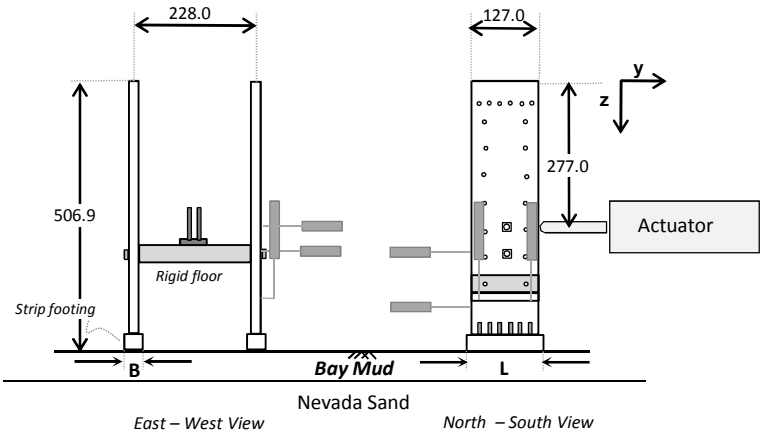

Figure 2.6. Schematic of the general setup of the Centrifuge Experiments conducted at UC Davies [after Gajan et al., 2005] : **(a)** Vertical Push (test KRR03 – AW) configuration ; and **(b)** Slow Cyclic Lateral Push (test KRR03 –AE). All units are in millimeters (model scale).

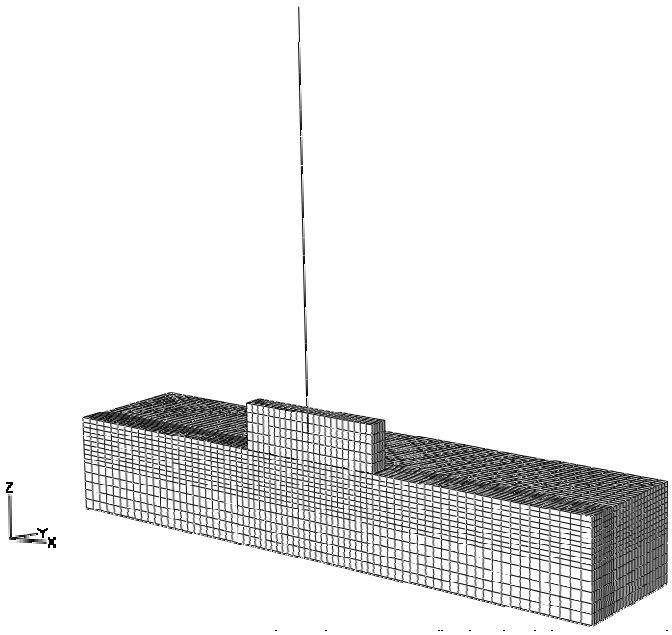

(a)

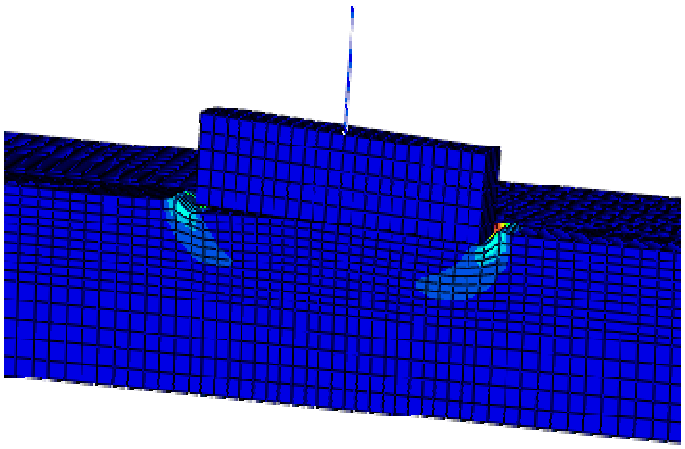

(b)

Figure 2.7. (a) The 3D finite element half-model utilized for the numerical analyses of the UC Davis centrifuge experiments ; (b) snapshot of deformed mesh with superimposed plastic strain contours. Note the gap formulation on the left side of the footing where it detaches from the underlying ground, and the plastic strain concentration at both edges.

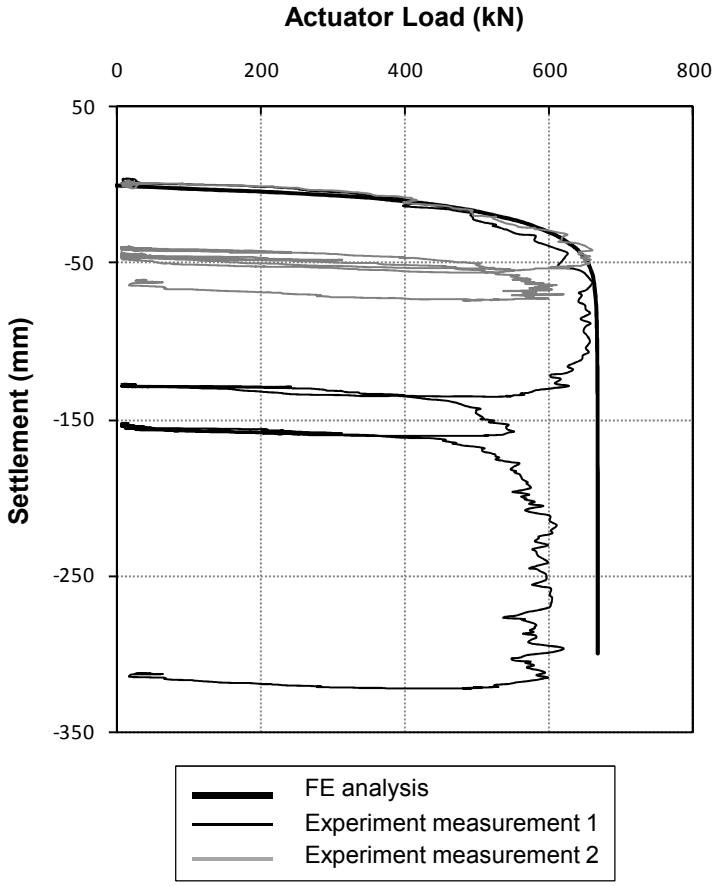

Figure 2.8. Model validation against UC Davis Centrifuge Tests : comparison of FE computed with experimental load-displacement response for the vertical push test.

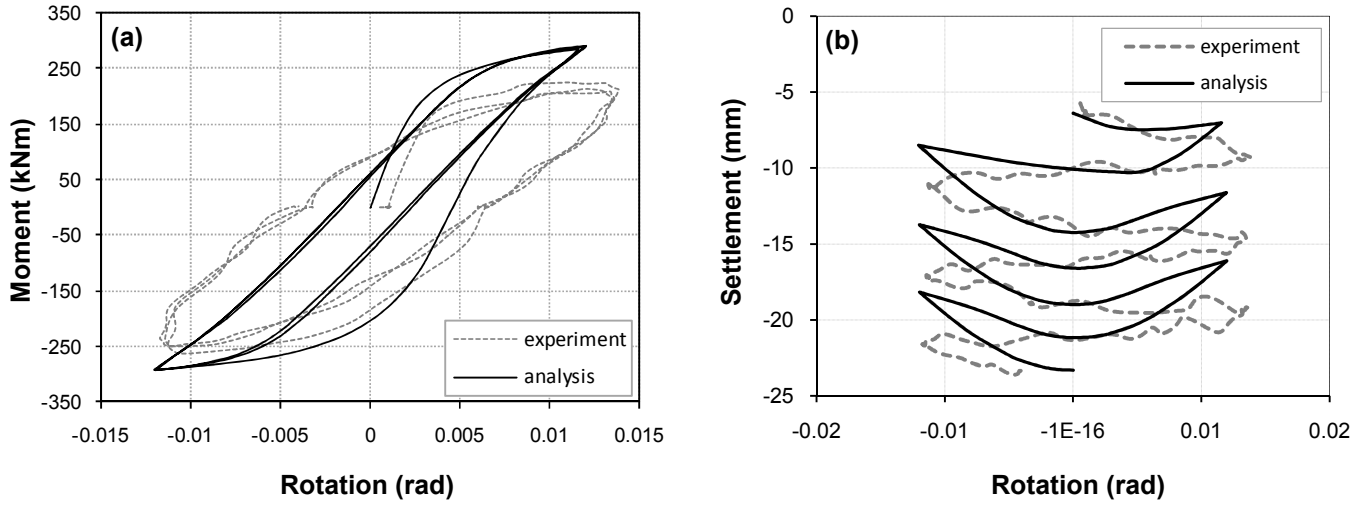

Figure 2.9. Model validation against UC Davis Centrifuge Tests – *first packet of loading*. Comparison of FE computed with experimental : (a) moment–rotation response, and (b) settlement–rotation response.

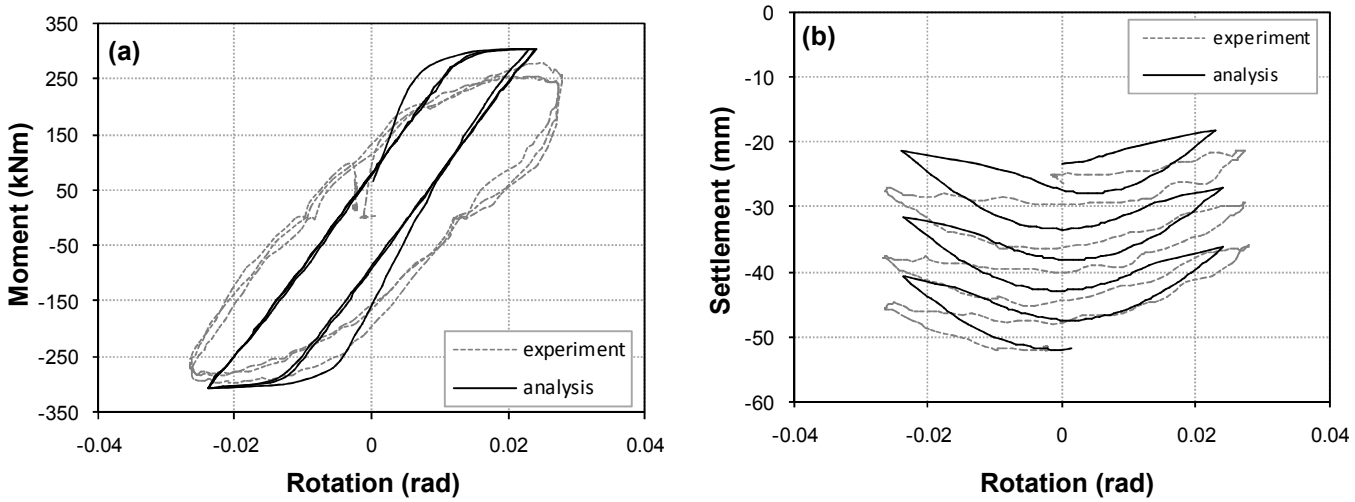

Figure 2.10. Model validation against UC Davis Centrifuge Tests – *second packet of loading*. Comparison of FE computed with experimental : (a) moment–rotation response, and (b) settlement–rotation response.

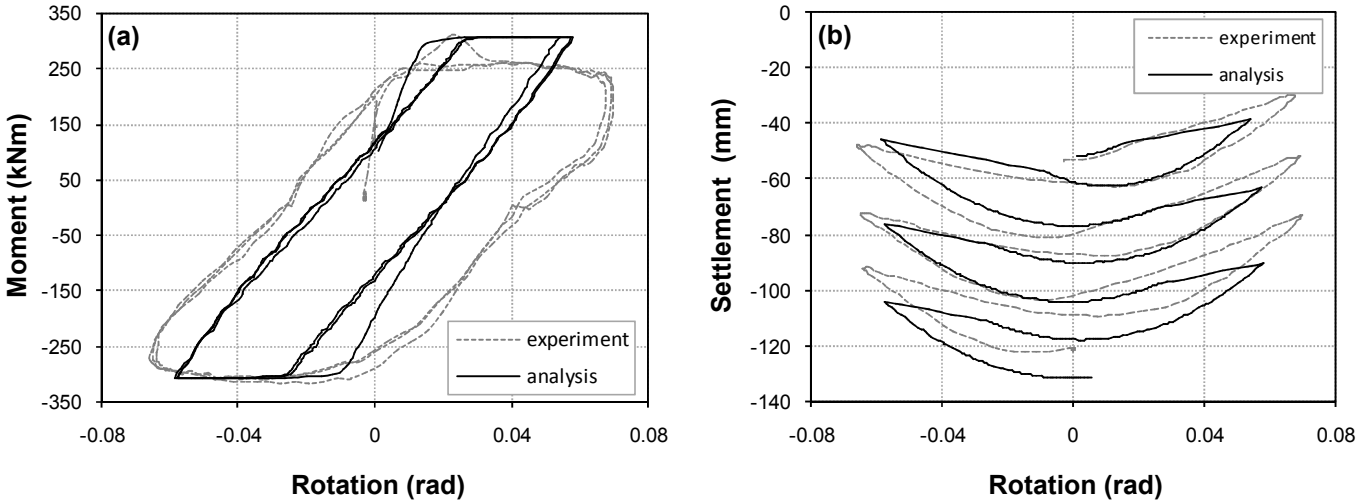

Figure 2.11. Model validation against UC Davis Centrifuge Tests – *third packet of loading*. Comparison of FE computed with experimental : (a) moment–rotation response, and (b) settlement–rotation response.

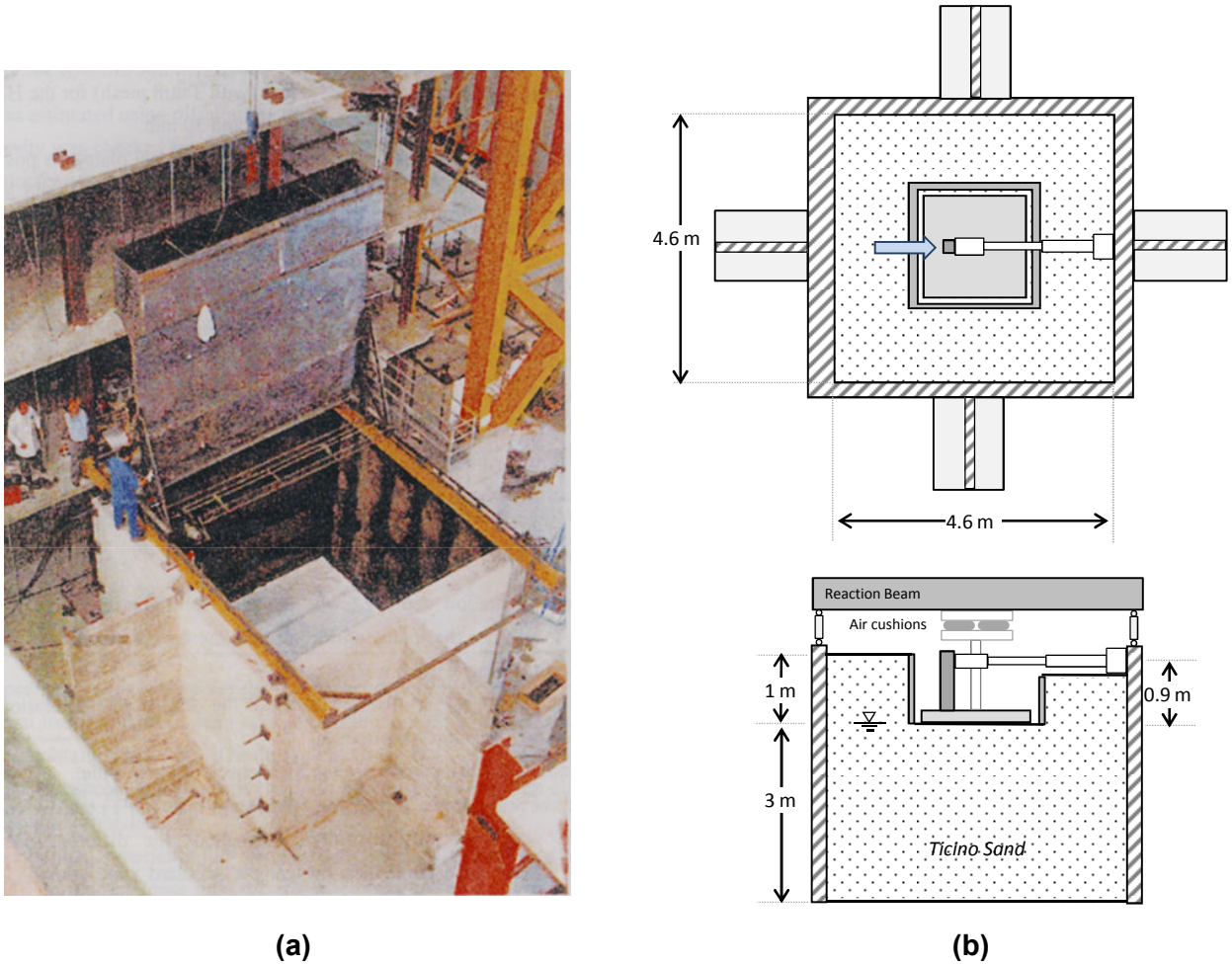

(a) **(b)**

Figure 2.12. The TRISEE large scale (1g) experiment : (a) Photo of the model and the sand spreader, and (b) Schematic of the general experimental setup [after Faccioli et al., 1999]

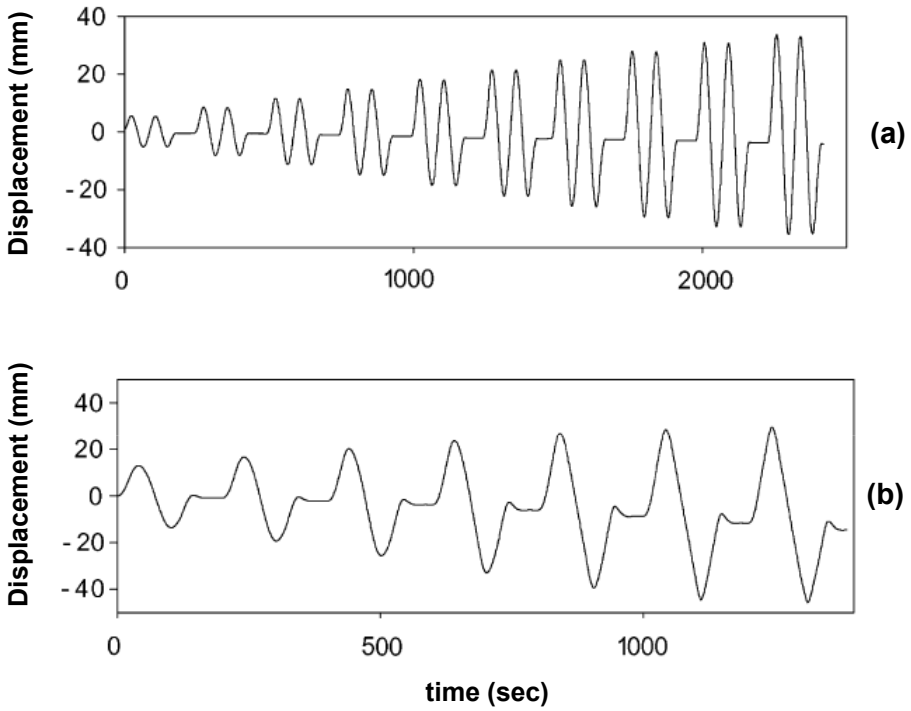

Figure 2.13. The TRISEE large scale (1g) experiment : time histories of imposed lateral displacement for : (a) the HD (*high density*) test, and (b) the LD (*low density*) test.

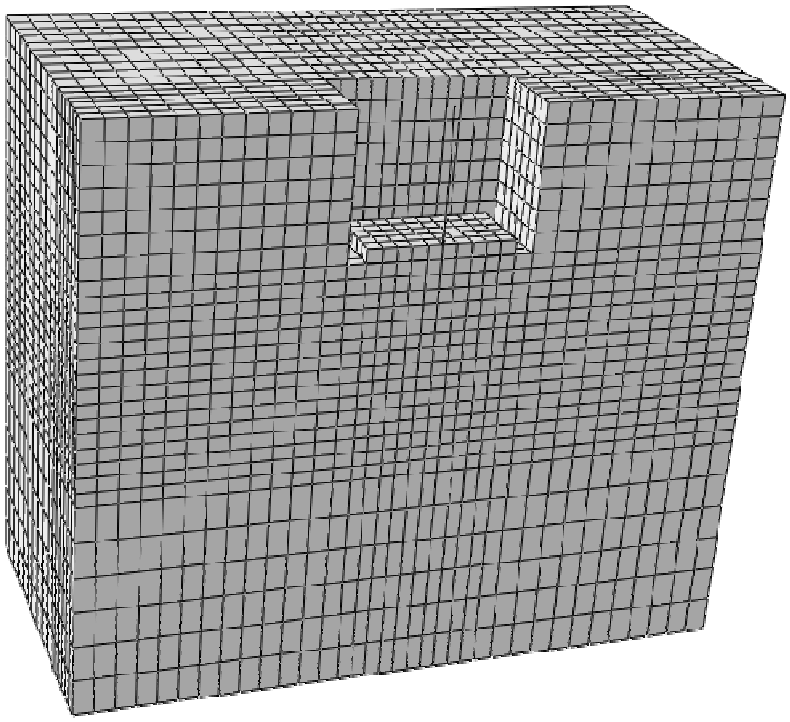

Figure 2.14. The 3D finite element half-model utilized for the numerical analyses of the TRISEE large scale tests.

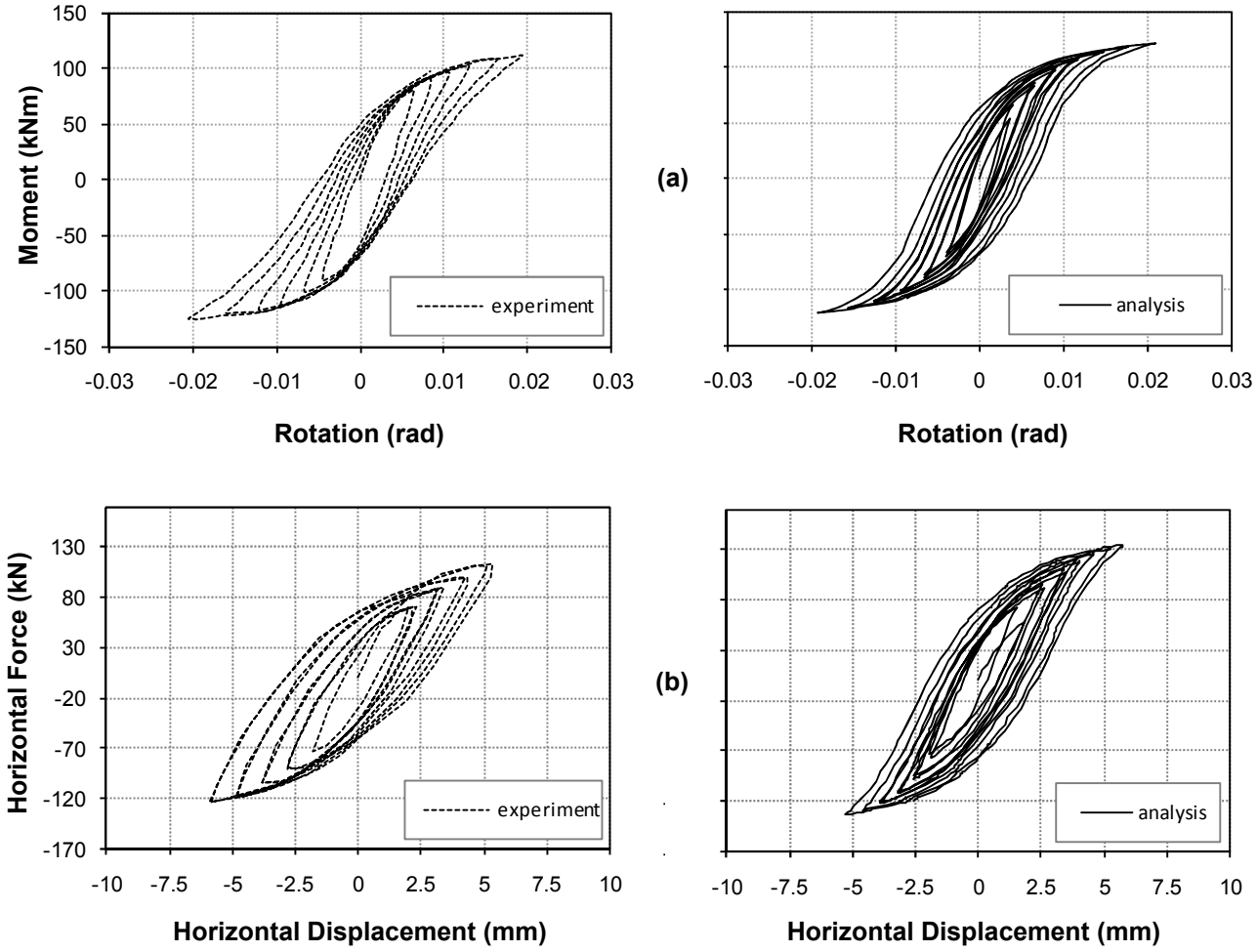

Figure 2.15. Model validation against the TRISEE Large Scale Tests. Comparison of numerical analysis prediction (solid black line) with experimental result (dashed line) for the HD (high density) test : (a) Moment-Rotation response, and (b) lateral force-displacement response

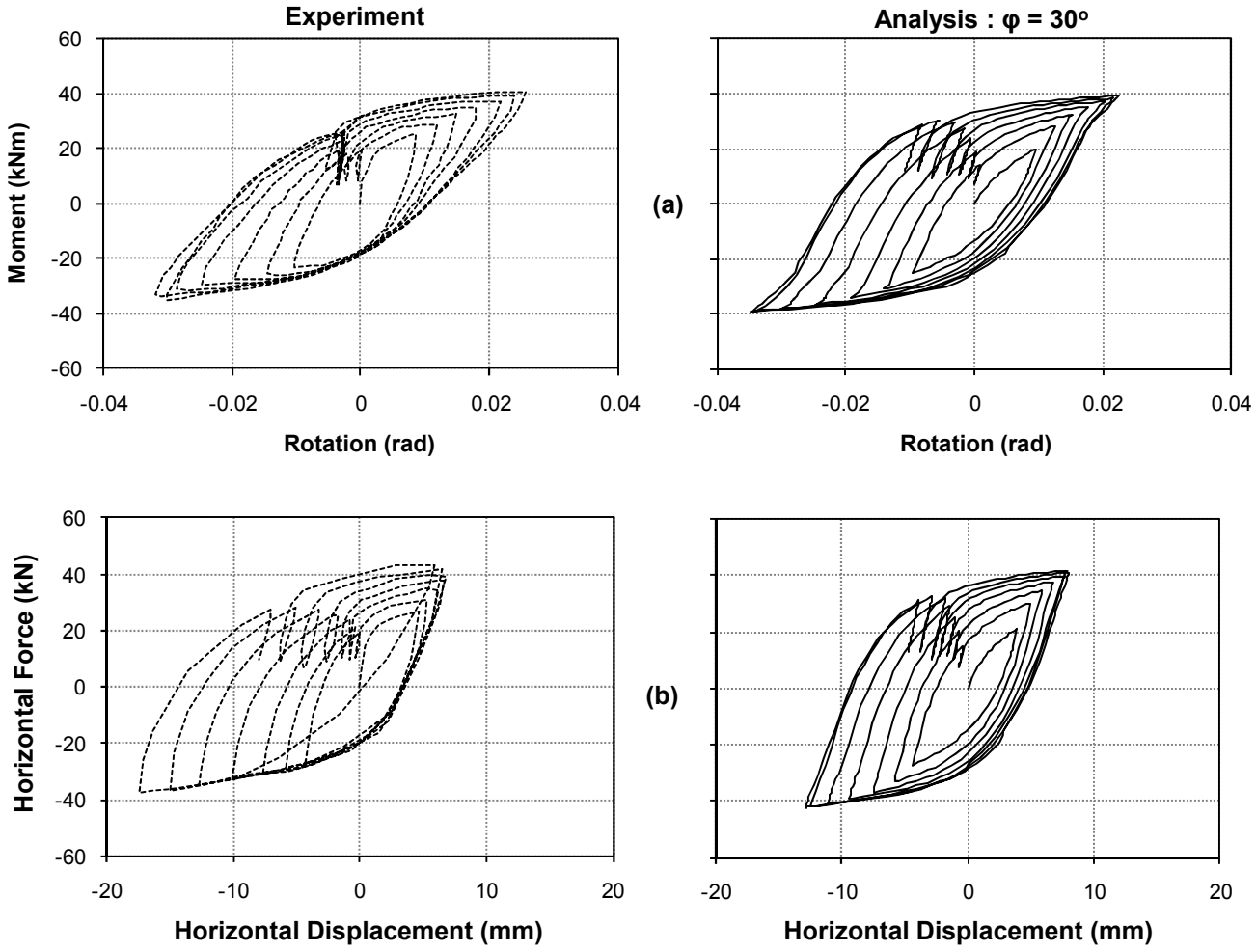

Figure 2.16. Model validation against the TRISEE Large Scale Tests. Comparison of numerical analysis prediction (solid black line) with experimental results (dashed line) for the LD test for the *FSv* ≈ 3 – φ = 30° scenario : (a) moment-rotation response, and (b) lateral force-displacement response.

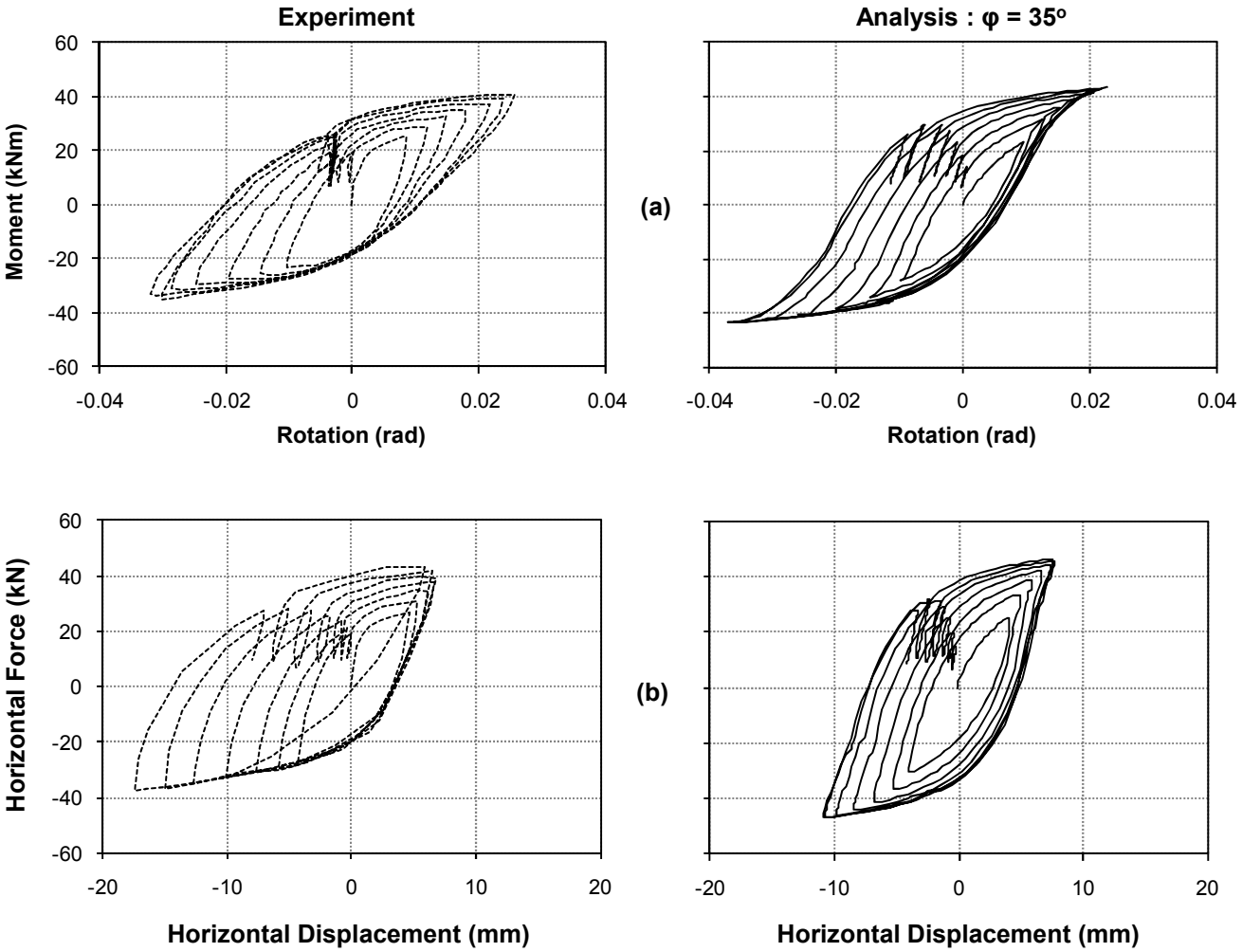

Figure 2.17. Model validation against the TRISEE Large Scale Tests. Comparison of numerical analysis prediction (solid black line) with experimental results (dashed line) for the LD test for the $FSv \approx 5 - \varphi = 35^{o}$ scenario : (a) moment-rotation response, and (b) lateral force-displacement response.

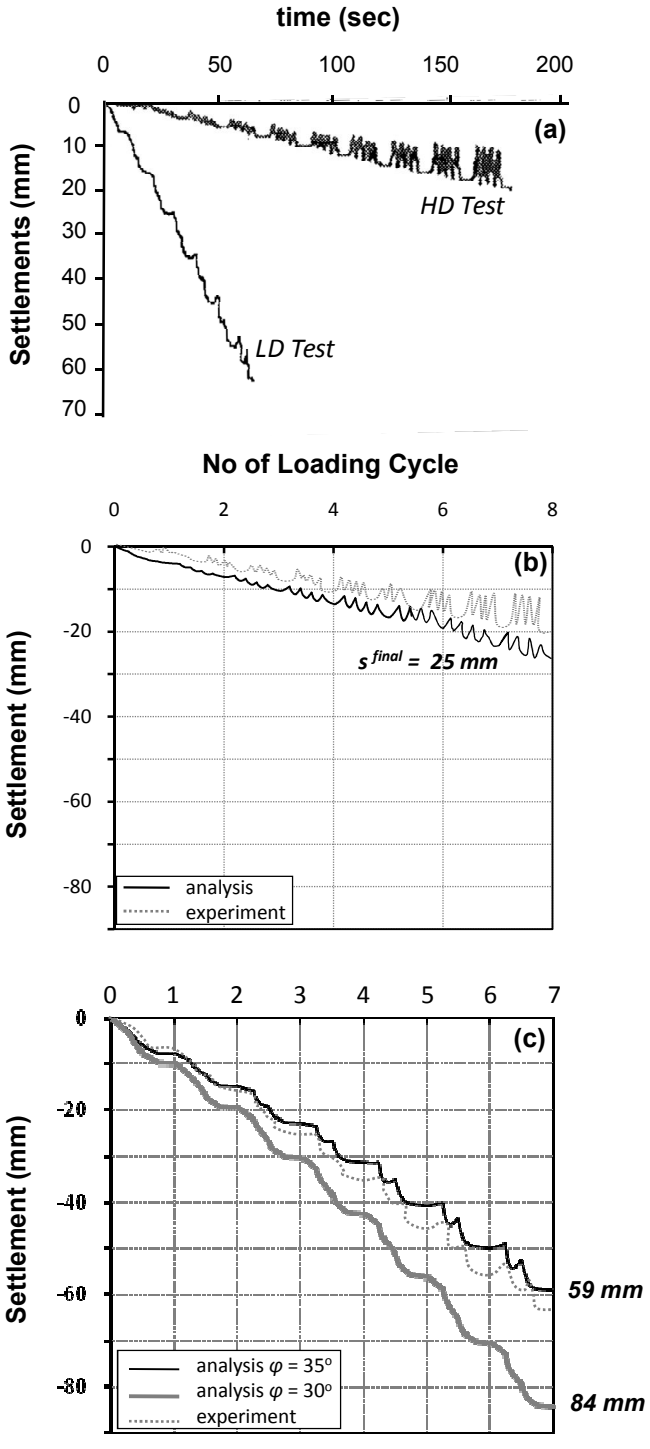

Figure 2.18. Model validation against the TRISEE Large Scale Tests : (a) experimentally measured evolution of foundation cyclic settlement ; comparison of numerical prediction with experimental results for (b) the HD test, and (c) the LD test (for both scenarios).

3

Rocking Isolation of Frame Structures Founded on Separate Footings

3.1. Introduction

Seismic design of structures has recognised that inelastic material response is unavoidable under the strongest probable earthquake. Thus, ductility levels of the order of 3 or more are allowed to develop under strong seismic shaking, implying that the strength of a number of structural elements will be fully mobilized. In the prevailing structural terminology, *plastic hinging* is allowed as long as the overall stability is maintained. Accepting that a limited amount of structural damage is unavoidable and realizing that increasing structural strength is not always associated with enhanced safety levels, lead to the development of modern

seismic design principles, which aim to *control* damage rather than attempting to avoid it—*ductility* and *capacity* design. While ductility design ensures (through proper reinforcement detailing) that critical structural members can sustain loads that reach their capacity without collapsing, capacity design focuses on *"guiding"* failure to structural members that are not crucial for safety (beams instead of columns) and to non-brittle mechanisms (bending instead of shearing) [Park & Paulay, 1976].

In marked contrast, a crucial goal of current seismic *foundation* design, particularly as entrenched in codes, is to *avoid full mobilisation of strength* in the foundation. In other words, capacity design applied to foundations *guides* plastification and failure to the superstructure. In *structural* terminology, plastic "hinging" is restricted to the superstructure, and is not allowed to develop in the foundation soil. In simple *geotechnical* terms, the designer must ensure that the below-ground (difficult to inspect) support system will not even reach a number of "thresholds" that would statically imply failure. Thus, mobilisation of the *bearing-capacity failure* mechanism, severe foundation uplifting sliding, or any relevant combination are prohibited. To ensure that such mechanisms will not develop, *over-strength* factors and (explicit or implicit) factors of safety larger than 1 are introduced against each of those "failure" modes.

However, thanks to the *cyclic* and *kinematic* nature of the seismic excitation, mobilization of the bearing capacity failure mechanism under severe seismic shaking does not necessarily imply failure. In fact, recent research suggests that soil–foundation plastic yielding under seismic excitation may be advantageous, and should be seriously considered in analysis and perhaps allowed in design [Paolucci, 1997; Pecker, 1998, 2003; FEMA-356,

2000; Martin & Lam, 2000; Makris & Roussos, 2000; Comartin et al., 2000; Pecker & Pender, 2000; Kutter et al., 2001, Faccioli et al., 2001; Kutter et al., 2003; Gazetas et al., 2003; 2007; Gajan et al., 2005; Harden et al., 2006; Hutchinson et al., 2006; Paolucci et al., 2008; Kawashima et al., 2007; Gajan & Kutter, 2008; Chatzigogos et al., 2009]. It should be noted that several critically–important structures could not have been designed against severe ground motions if "plastic hinging" was not allowed in the foundation. The 2.5 km long Rion-Antirrion cable-stayed bridge in Greece constitutes one of the best such examples : its 90 m in diameter and 80 m in height foundation piers, have been designed allowing for full mobilisation of foundation bearing capacity mainly in the form of sliding [Pecker, 2005].

The time is therefore ripe for soil–foundation–structure interaction (SFSI) philosophy to also move from imposing "safe" limits on forces and moments acting on the foundation (aiming at avoid pseudo-static "failure") to performance–based design in which all possible conventional "failure" mechanisms are allowed to develop, to the extent that maximum and permanent displacements and rotations are kept within acceptable limits. Such a new seismic design philosophy, in which soil failure is used as a safety fuse for the superstructure (i.e. plastic "hinging" is moved from the superstructure to the foundation soil, exactly the opposite of conventional capacity design) has been developed by Anastasopoulos et al. [2010a]. Using a simple 1-dof bridge structure as an example, it was shown that such new design philosophy may provide substantially larger safety margins (i.e. avoidance of collapse) for seismic motions that exceed the design limits, at the cost of increased foundation settlement (mainly).

This paper investigates the potential effectiveness of such new design philosophy for the case of frame structures, which are more representative for buildings. Since foundation plastic "hinging" is mainly in the form of foundation rocking and uplifting, the new design concept is termed *rocking isolation*. The idea of isolation through rocking is not a novelty to structural engineers. However, in the framework of the idea proposed herein rocking-isolation refers to foundation rather than structural members rocking. It is defined as the intentional *under-design* of the footings of the frame so that they will respond to ground shaking by uplifting and mobilization of soil-failure mechanisms, thereby limiting the acceleration transmitted onto the superstructure. To illuminate the potential effectiveness of the *rocking isolation* concept to frame structures, an idealized simple but realistic 2-storey building is used herein.

3.2. Problem Statement and Design Considerations

The problem analyzed herein is depicted in **Figure 3.1**. It refers to a fairly typical urban residential structure founded on a stiff clay layer (of S_u = 150 kPa). This is a simple 1-bay 2-storey reinforced concrete frame with a span of 5 m, ground floor height of 4 m, and first floor height of 3m. The dimensions of structural members of the frame are summarized in **Table 3.1**.

Figures 3.1a and **3.1b** compare schematically the differences between conventional *capacity design* and *rocking isolation* design. In the first case, the design dictates that the footings are large enough to ensure sufficient fixity of the columns at their base (i.e. their

ultimate moment capacity is larger than that of the columns). Hence, the structure will respond to seismic loading through flexural distortion. Whenever the earthquake demand tends to be larger than the bending moment capacity of the column, a plastic hinge develops at the base of the column. **Figure 3.1c** illustrates the moment-curvature curve of the reinforced concrete column, designed according to EC8 (ductile design). The curvature ductility of the column is defined as [Priestley et al., 2007] :

$$\mu_\varphi = C_u / C_y \tag{3.1}$$

where C_y is the yield curvature of the reinforced concrete section (corresponding to the development of the maximum bending moment and the initiation of plastic hinging) and C_u its ultimate curvature (corresponding to initiation of failure). For the well-reinforced column of the frame investigated herein, $\mu_\varphi \approx 10$.

In the case of rocking isolation, the design of the superstructure follows exactly the same principles, but the capacity design for the foundation is reversed : the footings are *under-designed* to have a lower moment capacity than that of the corresponding column. Therefore, whenever the earthquake demand tends to exceed the capacity of the foundation, the latter "yields" through a combination of uplifting and soil failure mechanisms, thus limiting the inertia transmitted onto the superstructure. The moment–rotation response of the footing (for combined axial and shear force at a constant lever arm) resting on a stiff clay layer (of S_u = 150 kPa) is depicted in **Figure 3.1d**, demonstrating the effect of reduction of its width b. In accord with theoretical expectations, the decrease of the footing width leads to reduced moment capacity M_u and ultimate toppling rotation ϑ_u.

Since the ductility of the system is now more directly associated with foundation *rotation* rather than superstructure plastic hinging, a *rotational ductility* μ_ϑ can be defined :

$$\mu_\vartheta = \vartheta_u / \vartheta_y \tag{3.2}$$

where ϑ_u the ultimate toppling rotation of the footing, and ϑ_y the yield rotation at the initiation of uplifting. For both foundations, μ_ϑ is of the order of 50. Note that since μ_ϑ is defined on the basis of rotation, it may be qualitatively similar to μ_φ , but it is not equivalent. The two ductilities can be rendered equivalent if converted to displacement ductilities, following the definition of Priestley et al. [1996; 2000]. However, as will be shown in the sequel, the overall response and ductility of the soil–foundation–structure system is quite complicated, and cannot be analyzed just with reference to the ductility of one member.

Before proceeding, note that the effectiveness of rocking isolation concept depends on the nature of the system. While it may be effective for relatively slender systems the response of which is rocking-dominated (such as the one analyzed herein), it may not be as effective for squatty structures the response of which is dominated by shear. Hence, 1-storey frames are not examined herein, although if they are unusually tall they experience bending-dominated response (e.g. industrial buildings, airport hangars, etc.). On the other hand, multi-storey frames are likely to conspicuously demonstrate the effectiveness of this approach.

Conventional Design

Geometry and member properties of the frame structure are shown in **Figure 3.2**. The structure is designed in accordance to the Seismic Eurocode EC8 [2000] and the Greek

Reinforced Concrete Code (EKOS 2000), for a design acceleration A_d = 0.36 g, and a behavior factor q = 3.5. The adopted dead and live loads (g = 1.3 kN/m^2 and q = 2 kN/m^2) are typical values for residential buildings. The structure was analysed and designed with a conventional structural analysis software. **Table 3.1** summarizes the computed internal forces of all members of the frame. The resulting reinforcement (applying capacity design), along with the bending moment capacities M^{RD} of the structural members, are outlined in **Table 3.2**.

The footings are designed according to current Seismic Codes. Obeying the principle of capacity design, the moment capacity of the foundation is calculated as :

$$M_{Fd} = M_V + a_{CD}\, M_E \qquad (3.3)$$

where M_{FD} is the foundation moment capacity ; M_V and M_E the moment due to *non-seismic* (G + 0.3Q) and *seismic* (E) loads (of the seismic load combination), respectively ; and a_{CD} an *over-strength* factor, defined as follows :

$$a_{CD} = 1.20\, M_R/M^C_E - M_V/M_E \qquad (3.4)$$

where M_R is the actual (as designed) moment capacity of the column ; and M^C_E the moment due to the seismic loads (always for the seismic load combination). The same calculations are performed for the design shear and axial forces on the footings (**Table 3.3a**).

Most codes (*and* the current state of practice) require that the eccentricity e (due to the combined action of bending moment M and axial force N) does not exceed one third of te footing width, $B/3$. The minimum allowable safety factors for static and seismic loading are $SF^S \geq 3$ and $SF^E \geq 1$, respectively. Taking account of the above provisions, the width of the square footing is conventionally computed as B = 1.7 m. As summarized in **Table 3.4**, with

the limitation on eccentricity being the controlling factor, the resulting safety factors for static and seismic loading turn out to be quite large: SF^S = 8 and SF^E = 1.93, respectively.

Rocking-isolation Design

In the spirit of rocking isolation design, by relaxing the eccentricity criterion the footing can be intentionally under-designed to be allowed to uplift, "guiding" the plastic hinge below the foundation base (instead of the base of the column). When the earthquake demand on the footing exceeds its capacity the soil ultimate resistance is fully mobilized and the response is dominated either by uplifting or sinking. To reduce settlement and foundation rotation, SF^S has to be greater than 3 [Kutter et al., 2001 ; Faccioli et al., 2001; Gajan et al., 2005 ; Pecker & Pender, 2005; Paolucci et al., 2007 ; Kawashima et al., 2007 ; Gajan & Kutter, 2008 ; Chatzigogos et al., 2009]. Based on this criterion, **Table 3.4** summarizes the acceptable footing widths, along with their corresponding moment capacities M_{ult} [calculated according to Gourvenec, 2007], the safety factors SF^S and SF^E, and the *Capacity Reduction Factor (CRF).* The latter is defined as :

$$CRF = M^{RD}/M_{ult} \qquad (3.5)$$

and represents the *under-strength* of the foundation relative to the capacity of the column.

Large values of *CRF* imply reduced foundation capacity, and hence more substantial rocking (which will hopefully result in more drastic cutoff of inertia forces transmitted onto the superstructure). For *B* = 1.0 m, *CRF* = 2.7, which is still acceptable in terms of SF^S and SF^E. Still, increased rocking is unavoidably associated with increased foundation rotation, and hence rotation-induced drift. On the other hand, when *CRF* tends to 1.0 (as for *B* = 1.6 m),

not only the effectiveness of rocking isolation is expected to be diminished, but the risk (due to the unavoidable uncertainties in the estimation of soil *and* superstructure properties) of M_{ult} becoming larger than M^{RD}, is also augmented substantially. In other words, a trade-off exists between isolation effectiveness and rotation-induced drift.

Before proceeding, it should be noted that the whole rocking-isolation concept relies on foundation under-design, i.e. reduction of its width B. As previously discussed, this is feasible for the typical frame analyzed simply because the eccentricity criterion is critical. For a short structure (such as a 1-storey frame), the response of which is shear-dominated, in the absence of substantial moment M acting on the footing, the $e \leq B/3$ criterion may not be the one controlling foundation design. In such cases, the safety factor may be critical and the rocking-isolation concept might be less applicable.

3.3. Analysis Methodology

Assuming plane-strain soil conditions, a representative equivalent (as described in detail in the sequel) plane-strain "slice" (**Figure 3.2a**) of the soil–structure system is analyzed employing the finite element (FE) method, taking account of material (soil and superstructure) and geometric (uplifting and P-Δ effects) nonlinearities. As shown in **Figure 3.3**, while the soil and footings are modeled with nonlinear quadrilateral plane strain continuum elements, nonlinear beam elements are used for superstructure members. The soil-foundation interface is modeled using special interface elements which allow both detachment and sliding. The latter obeys Coulomb's friction law, with detachment and uplifting arising from the tensionless interface behavior. Free-field boundaries are used at

the two lateral boundaries of the model, and the dynamic response of the system is analyzed through nonlinear dynamic time history analysis, applying the seismic excitation (i.e. acceleration time history) at the base of the model. The left and right side nodes of the model (on the same height) are connected by means of kinematic horizontal constraints, while vertical boundaries are imposed on all the bottom and side nodes of the model.

Soil Modeling

Nonlinear soil behavior is modeled through a simple kinematic hardening model with Von Mises failure criterion, and associated flow rule. The model can be considered appropriate for clay under undrained conditions. Although phenomena such as pore-pressure buildup and dissipation cannot be captured, for the key aspects of the problem analyzed herein, undrained behavior may be considered a reasonable simplification. The model has been validated against centrifuge model tests in Anastasopoulos et al. [2010b], and modified to be also applicable for sands (extended pressure-dependent Von Mises). Although the associated flow rule is not valid for sand, the model was shown to predict with adequate realism the cyclic response of footings in sand, as well. The model is briefly described in the sequel, focusing on clay. More detailed model description and calibration can be found in Anastasopoulos et al. [2010b].

According to the Von Mises failure criterion, the pressure-independent yield surface of the model is defined through the following function F :

$$F = f(\sigma - \alpha) - \sigma_0 \tag{3.6}$$

where σ_o is the stress at zero plastic strain, and α the *backstress*, which defines the

kinematic evolution of the yield surface in the stress space. Parameter σ_o controls the initiation of non-linear behaviour, and is defined as a fraction λ (typically ranging from 0.1 to 0.3) of the yield stress σ_y :

$$\sigma_o = \lambda \sigma_y \tag{3.7}$$

For clay under undrained conditions, the yield stress σ_y is defined as :

$$\sigma_y = \sqrt{3} S_u \tag{3.8}$$

The associated plastic flow rule of the model is defined as follows :

$$\dot{\varepsilon}^{pl} = \dot{\bar{\varepsilon}}^{pl} \frac{\partial F}{\partial \sigma} \tag{3.9}$$

where $\dot{\varepsilon}^{pl}$ is the plastic flow rate, and $\dot{\bar{\varepsilon}}^{pl}$ the equivalent plastic strain rate. The evolution law of the model consists of a *nonlinear kinematic* and an *isotropic* hardening component. The evolution of the kinematic component of the yield stress is described as follows :

$$\dot{\alpha} = C \frac{1}{\sigma_0} (\sigma - \alpha) \dot{\bar{\varepsilon}}^{pl} - \gamma \alpha \dot{\bar{\varepsilon}}^{pl} \tag{3.10}$$

where $C = \sigma_y / \varepsilon_y$ is the Young's modulus for very small strains, and γ a parameter that determines the rate of decrease of the kinematic hardening with the increase of plastic strain.

C can be directly computed from shear wave velocity V_s (if measured), or estimated through empirical correlations [e.g. Hardin & Richart, 1963; Robertson & Campanella, 1983; 1983b; Seed et al., 1986; Mayne & Rix, 1993] as a function of σ_y :

$$C = \alpha \sigma_y \tag{3.11}$$

where a ranges from 150 to 1000 for clays (i.e. $E = 300S_u$ to $1800S_u$). Since $\sigma_y = C/\gamma + \sigma_o$, parameter γ can be expressed as [Gerolymos et al., 2005] :

$$\gamma = \frac{C}{\sqrt{3}S_u - \sigma_0} \tag{3.12}$$

In summary, and as described in mire detail in the aforementioned publication, model calibration is quite simple, requiring the following data : (a) S_u to compute the yield stress σ_y ; (b) G_o or V_s to estimate the small-strain stiffness C ; and (c) G–γ curves to calibrate parameters λ and α. In this study, published G–γ curves [Vucetic & Dobry, 1991; Ishibashi & Zhang, 1993] we utilized to calibrate model parameters. Detailed results can be found in Anastasopoulos et al. [2010b].

Superstructure Modeling

The same constitutive model is used, after proper adaptation [Gerolymos et al., 2005], to simulate the nonlinear moment–curvature response of the superstructure reinforced concrete (RC) members. For each member, the moment–curvature relationship is computed through static section analysis employing the X-tract 2000 [Imbsen Assoc. & Chadwell, 2004] software. Then, model parameters are calibrated against these target moment–curvature relationships. For a rectangular RC member of width d_b and height d_h , the yield stress σ_y can be defined as :

$$\sigma_y = \frac{4M_y}{d_b d_h^2} \tag{3.13}$$

The small strain modulus *C* is equal to the Young's modulus of reinforced concrete. The residual bending moment of each RC section is assumed equal to 30% of the bending moment capacity [Vintzilaiou et al., 2007], and is attained for a curvature 3 times larger than the ultimate curvature c_u . To capture such softening response, a user subroutine is encoded in the finite element code ABAQUS. Since the structure was designed following the provisions of modern seismic codes, the hoop reinforcement justifiably presumed to prevent strength degradation due to cyclic loading [Vintzileou et al., 2007]. Therefore, this effect has been neglected in the concrete modeling. Parameters λ and α of the model are calibrated through numerical simulation of the static pushover test.

Figure 3.4 portrays the results of model calibration against monotonic moment-curvature response calculated through RC section analysis, and FE results for cyclic loading of gradually increasing amplitude. As expected, and according to the principles of capacity design, the strength of the columns is larger than that of the corresponding beam members. The column curvature ductility, μ_φ = 10, corresponds to medium ductility class according to Eurocode EC8 for moment resisting frames.

Equivalence of 2D with 3D analysis

As previously discussed, the analysis is conducted under plane-strain conditions, considering a representative *equivalent* "slice" of the soil−structure system. Although the real problem is definitely 3 dimensional, modeling the whole system in 3D is computationally too demanding for a parametric study, especially considering the severe constraints with respect to mesh refinement. To render the 2D numerical model equivalent to the 3D problem, the

Meyerhof 1967 shape factor of 1.2 (square foundation) was employed to the soil "slice" of the model (i.e the out of plane dimension of foundation elements was 1.2 times higher than that of the underlying soil elements). To verify the validity of such equivalence, two smaller FE models were developed focusing on one footing only : a 3D and an equivalent 2D model, employing the 1.2 shape factor.

Typical results are presented for the B = 1.7 m footing bearing a vertical load N = 200 kN, subjected to cyclic loading. **Figure 3.5** compares the results of the two models (equivalent 2D vs. 3D) in terms of moment−rotation and settlement−rotation response of the footing, for two idealized soils : a stiff clay of S_u = 150 kPa, and a soft clay of S_u = 50kPa. In accord with experimental evidence [Allotey & El Naggar, 2003; Kutter et al, 2003; Gajan et. al., 2005; Paolucci et al., 2008; Gajan & Kutter, 2008], when the static safety factor is relatively large (as with the stiff clay of S_u = 150 kPa where SF^s > 3) the response of the footing is uplifting−dominated (**Figure 3.5a**) ; for relatively small safety factors (as with the soft clay of S_u = 50 kPa where SF^s < 2) the response is dominated by accumulating settlement (**Figure 3.5b**). In the first case (stiff soil), the equivalent 2D model reproduces with reasonable accuracy the results of the 3D FE model; the latter has been thoroughly validated in Anastasopoulos et al. [2010b]. In the case of soft soil, the equivalent 2D model barely under-predicts (by less than 10%) the cyclic loading induced settlement, while the ultimate moment M_{ult} is slightly over-predicted (by less than 5%). The overall hysteretic damping is captured quite effectively in both cases. The same result holds true for the footing rotations. Overall, it may be concluded that the equivalent 2D approach reproduces the key aspects of

the 3D problem very effectively, and may thus be adopted for the parametric dynamic analyses in the sequel, which refer to the case of the stiff soil layer (S_u = 150kPa).

3.4. Static Pushover Analysis : Insights on the Rocking Behavior of Frames

The rocking response of frame structures deviates substantially from that of 1-dof systems, such as the one discussed in the previous section. To gain insights on the mechanisms controlling the response of frame structures, the model frame is first subjected to static displacement−controlled pushover loading. The analysis is conducted by imposing onto the frame a monotonically increasing lateral displacement, taking P–δ effects into account. **Figure 3.6** compares the response of the conventional system (with over-designed B = 1.7 m footings), with two rocking-isolation alternatives (under-designed, B = 1.4 m and 1.2 m footings). System response can be divided into three characteristic phases : (a) an *initial phase*, in which column bending dominates ; (b) an *intermediate phase*, in which both column bending and foundation rocking take place, and (c) the *ultimate phase*, which is dominated by foundation rocking.

In the *initial phase*, the frame responds to the imposed lateral loading mainly through flexural deformation (bending). The conventional system (with larger capacity footings) develops slightly larger resisting force P compared to the two rocking-isolation alternatives. Hence, decreasing B leads to a decrease of the capacity of the system. The maximum lateral force takes place when the beams reach their bending moment capacity M^{RD} (or equivalently their yield curvature c_y —Point A in the diagram). With increasing displacement δ the beams finally reach their ultimate curvature c_u (when their ductility capacity has just

been consumed). This behavior clearly mirrors the capacity design principles, according to which the beams should fail before the columns (weak beam−strong column design).

During the *intermediate phase*, the columns of the conventional design (B = 1.7 m) are pushed beyond their yield curvature c_y (point A' in the diagram), and continue being subjected to inelastic deformation until reaching c_u when their ductility capacity is completely expended (point B in the diagram). After this point, all structural members of the conventionally designed system have exhausted their ductility capacity and collapse is imminent. On the other hand, the rocking−isolation alternatives (B = 1.4 and 1.2 m) respond to increasing δ with footing detachment, uplifting and substantial rotation : since the moment capacity M_{ult} of the foundations is lower than the M^{RD} of the columns, the plastic "hinge" develops in the foundation-soil system, thereby providing a "shield" to the columns. But, although the columns are protected, the beams keep accumulating plastic deformation until reaching their residual strength (point C in the diagram).

Finally, in the *ultimate phase*, since the beams have already reached their residual strength (assumed to be constant –an unavoidable at this stage of analysis but not necessarily realistically safe simplification), the rocking−isolated system reduces from its initial state (frame structure) to two idealized 1-dof systems connected with each other through the 2 hinged beams. Further increase of the imposed displacement δ leads to a decrease of P (due to P−δ effects), until it reaches zero and the structure topples. Observe that the displacement δ (which is directly related to footing rotation) that leads to toppling of the system is larger for the B = 1.4 m footing (point D in the diagram), compared to the even smaller one (B = 1.2 m, point D'). This observation is of the utmost importance for the

design of the rocking–isolation concept : increasing *B* does not only increase the footing moment capacity M_{ult}, but also – and most importantly – the ultimate footing rotation ϑ_{ult} . In other words, the increase of *CRF* may lead to more effective rocking isolation (in terms of limitation of the transmitted inertia forces), but reduces the ductility of the system. However, as it will be shown in the sequel, ϑ_{ult} is not only a function of *B*, but also depends on the combination of the axial load *N* acting on the footing, and the *M/Q* (moment-shear force) ratio, which fluctuate substantially during seismic loading and pushover loading. The influence of such effects on system performance is elucidated in the following sections, making use of the results of static pushover analysis.

The effect of Axial Load Fluctuation on Footing Response

Figure 3.7a displays the evolution of the axial loads *N* of the two frame columns with imposed displacement δ, with due reference to the three previously identified phases of system response. During the *initial phase*, the increase of δ leads to increase of *N* on the right column and an equal decrease on the left, while of course their sum is maintained constant and equal to the total vertical load of the superstructure. This reflects the frame reaction to the imposed lateral loading through development of a pair of axial forces on the columns, in addition to bending moments *M* and shear forces *Q*. In the subsequent *intermediate phase*, during development of plastic hinging in the beams, frame action is gradually reduced and both columns tend to "retreat" towards their initial static N value of 150 kN. In fact, the assumption of a non-zero and constant residual moment capacity of beams is the only reason why N is not becoming exactly equal to its original value : since a

small bending moment will still be transmitted, some frame action keeps taking place. The axial column load is maintained constant throughout the *ultimate phase*, during which no change in system response takes place.

Figure 3.7b illustrates the effect of N on the $M-\vartheta$ (moment−rotation) response of the B = 1.4 m footing (rocking-isolation alternative). As expected [Houlsby & Puzrin, 1999; Bransby, 2001; Taiebat & Carter, 2002; Gourvenec, 2007], since the static safety factor SF^S of the footing is substantially larger than 2, M_{ult} increases with increasing N. Yet, however paradox it may appear, in the context of rocking−isolation design such an increase of M_{ult} is not desirable as it amplifies the risk of increasing the amount of bending moment that may be transmitted by the footing onto the column hence jeopardizing the structural integrity of the latter. Therefore, in the process of the previously discussed selection of the optimum *CRF*, such effects must be carefully investigated.

Effect of M/Q Fluctuation on Foundation Response

Figure 3.8a displays the evolution of the M/Q ratio versus the imposed lateral displacement δ, with reference again to the three phases of system response. In the initial phase, as the frame is still "undamaged" (no plastic hinging has yet developed), M/Q varies between about 1.9 and 2.5—quite a similar result to that of a conventional pseudostatic analysis of the frame (**Table 3.1**, seismic load combination, ground floor columns : M^E = 101 kNm, Q^E = 41 kN).

During the *intermediate phase*, as already discussed the system tends to reduce from its initial state (frame structure) to two idealized 1-dof oscillators interconnected with the 2

hinged beams. The center of mass of these equivalent 1-dof systems will naturally coincide with the center of mass of the whole structure, i.e. at an elevation of 4.82 m. Quite interestingly, during this phase and as the beams gradually reach their residual moment capacity, *M/Q* is asymptotically approaching this value (of 4.82m), but without actually reaching it. This is endorsed to the fact that the column-beam connection never actually reduces to an ideal hinge, since the residual strength of the beam does not vanish.

In the *ultimate phase* the *M/Q* ratio diminishes again. At this stage, the footing has reached its moment capacity M_{ult} and the corresponding column bending moment cannot possibly further enlarge. But this is hardly the case with the shear force: since the lateral horizontal capacity of the footing has not yet been reached, the column base shear may increase further to undertake the additional imposed lateral loading. Therefore, since the moment acting on the footing remains constant (M_{ult}) while the shear force keeps increasing, the *M/Q* ratio unavoidably recedes. Note that the rate of decrease is steeper for the left column (Column 1), whose shear force *Q* increases more rapidly than that of the right column.

The effect of the *M/Q* ratio is of particular significance for rocking−isolation design: it affects the rotation capacity ϑ_{ult} of the footing and consequently the overall ductility of the system. As depicted in **Figure 3.8b** for the *B* = 1.4 m alternative and assuming constant *N* = 150 kN (equal to the initial static value), ϑ_{ult} (and, hence, system ductility) decreases substantially with increasing *M/Q* : while for *M/Q* = 2.5 (*initial phase*, frame still undamaged) $\vartheta_{ult} \approx 0.25$, with *M/Q* = 4.5 (ultimate phase, fully developed plastic hinges in the beams) $\vartheta_{ult} \approx 0.13$ (i.e. an almost 50% decrease). On the other hand, at least for the cases examined

herein, the capacity of the footing, M_{ult}, is quite insensitive to *M/Q*. This is in contrast to the previously discussed high sensitivity of M_{ult} to the variations in N.

3.5. Existence of Response Envelope : Equivalent 1-dof Systems

The two mechanisms presented and extensively analysed in the previous section take place simultaneously and interactively during lateral loading (static or dynamic), further complicating the behavior of the frame. **Figure 3.9** compares the $M–\vartheta$ response of the two *B* = 1.4 m footings (left and right) in static pushover analysis of the frame. During the *initial phase*, *M* increases with ϑ for both footings. However, as the frame develops the previously discussed pair of axial forces, *M* on the left footing is subjected to a rather pronounced decrease as *N* drops from 150 kN to 70 kN (see also **Figure 3.7**). At the same time, *M* on the right footing manifests an increased rate of augmentation as *N* rises from 150 kN to 230 kN. Subsequently, in the *intermediate phase*, as *N* on both footings tends to "retreat" to the initial static value, *M* of the left footing rises (as *N* increases form 70 kN to 125 kN, recall **Figure 3.7**), while that of the right footing is reduced (as *N* decreases form 230 kN to 175 kN). During the *ultimate phase*, the response of both footings is affected by the transition of *M/Q* from 2.5 (intact frame) to 4.5 (behavior as a 1-dof system).

In an attempt to further clarify the response of the system, two roughly equivalent 1-dof systems are perceived, each one of them representing two extreme phases of system response (**Figure 3.9**) :

(a) **Type A :** a 1-dof system with mass $m = N_{max}/g \approx 2.3$ Mg, (corresponding to $N_{max} = 230$ kN) at height $h = 2.4$ m (which is the average lever arm, or M/Q ratio, observed during the *initial* phase), and

(b) **Type B :** a 1-dof system with mass $m = N^{G+0.3Q}/g \approx 1.5$ Mg, (corresponding to $N^{G+0.3Q} = 150$ kN, as computed for the seismic load combination) at height $h = 4.6$ m (which corresponds the average M/Q ratio observed during the *ultimate* rocking-dominated phase).

As illustrated in the figure, the behavior of the two footings of the frame is successfully enveloped by the two idealized 1-dof systems. The first one, *Type A*, provides a conservative (upper bound) estimate of M_{ult} , but yields an unconservative estimate ϑ_{ult} (which is directly associated with system ductility). In contrast, *Type B* provides a conservative estimate of ϑ_{ult}, but is un-conservative in terms of M_{ult} .

The two "equivalent" 1-dof systems are equally successful in capturing the $M-\vartheta$ response of the two frame footings under seismic shaking. As shown in **Figure 3.10**, the $M-\vartheta$ response of the frame (from dynamic time history analysis (under moderately strong and very strong seismic shaking) is bounded between the monotonic $M-\vartheta$ curves of the two idealized 1-dof systems. Hence, although none of the two 1-dof systems constitutes an accurate representation of the frame, their combination provides a useful interpretation of the nature of the response.

3.6. Dynamic Analysis : Comparison of Conventional with Rocking-Isolated System

The seismic performance of the two design alternatives (conventional, B = 1.7 m ; rocking–isolated, B = 1.4 m) is further elucidated through a series of nonlinear dynamic time history analyses in which the FE model is subjected to a wide range of seismic motions: 24 earthquake records of worldwide historic events. Given in **Figure 3.11** along with their acceleration (*SA*) and velocity (*SV*) elastic response spectra, these selected records can broadly be categorized into moderately strong and very strong seismic motions. They cover a wide range of strong-motion parameters such as *PGA*, *PGV*, *SA*, *SV*, frequency range, number of strong-motion cycles, duration; near source (directivity and fling-step) effects are embodied in many of these records.

The seismic performance of the two alternatives is first compared in detail for two characteristic cases : (a) moderately strong seismic shaking, utilizing the El Centro 1940 record, which is close to but always less than the frame design spectrum; and (b) very strong seismic shaking, utilizing the Takatori (Kobe 1995) record, which substantially exceeds the design spectrum of the frame. In the first case, the objective is to explore the performance of the two alternatives, mainly in terms of *serviceability* after a design level seismic shaking. In the latter case, the focus is on safety in case of an “unanticipated” event that substantially exceeds the design. Results for the complete set of motions are then shown in summary for each alternative.

Performance in Moderately Strong Seismic Shaking

The two design alternatives are subjected to the El Centro record of the M_s 7.2 Imperial Valley 1940 earthquake [Trifunac, 1972]. As illustrated in **Figure 3.11**, this seismic motion may be considered roughly equivalent to the "*design earthquake*". The comparison of the two alternatives is portrayed in **Figure 3.12** in terms of : (a) column bending moment–curvature (M–c) response (revealing the "consumption" of superstructure ductility); (b) foundation moment–rotation (M–ϑ) response (revealing the "consumption" of foundation ductility); (c) foundation settlement–rotation (w–ϑ) response; and (d) time history of ground floor drift δ. The latter, as sketched at the top of the figure, consists of two components: (i) the *"flexural drift"* δ_c (i.e. the lateral displacement of the structure due to flexural distortion of its structural members), and (ii) the *"rocking drift"* $\delta_R = \vartheta h$ (i.e. the lateral displacement at height h due to foundation rocking of angle ϑ_R). The flexural drift δ_c is obviously a direct indicator of damage inflicted on reinforced concrete frame elements (i.e. columns and beams). On the other hand, the overall differential (top-to-base) displacement of the structure (and, hence, the damage of non-structural members) is more directly related to the total drift δ.

As revealed by the column M–c response (**Figure 3.12a**), both structures react almost elastically. Also (essentially) elastic is the response of the foundations of both alternatives (**Figure 3.12b**). The B = 1.4 m footings of the rocking-isolated alternative experience slightly more intense uplifting than those of the conventional system, but the rotation ϑ is maintained at essentially the same (very low) levels. The same applies to the shaking-induced settlement w, which in both cases remains well within serviceability limits (**Figure**

3.12c). Nevertheless, the unconventionally designed footing responds mostly by uplifting, contrary to the bending–dominated behavior of the conventional frame. This can me appreciated in **Fig. 3.12d**: although the maximum total drift δ is practically the same for the two alternatives, a significant discrepancy may be observed in the contribution of the two drift-generating mechanisms (i.e. *flexural distortion* and *rocking*). In the conventional system, the response is dominated by flexural distortion, with δ being predominantly related to δ_C; in the rocking-isolated alternative δ_R contributes much more than δ_C in the development of the total drift δ.

Performance in Very Strong Seismic Shaking

The Takatori record [Fukushima et al., 2000] of the M_s 7.2 Kobe 1995 earthquake is utilized to explore the performance of the two alternatives well beyond the limits of the design. As shown in **Figure 3.11**, with a *PGA* of 0.70 g, *PGV* of 169 cm/s, and encompassing the effect of forward rupture directivity and soil amplification, this record is considered as one of the worst seismic motions ever recorded. In terms of SA, it exceeds the design by a factor of at least 2 over the whole period range.

As depicted in **Figure 3.13a**, the conventionally designed system cannot withstand this level of ground shaking. Plastic hinges first develop at the beams, and later in the two columns. The ensuing sever accumulation of plastic curvatures, expends the available column ductility (**Figure 3.13b**), and the frame is unavoidably led to collapse. In stark contrast, the rocking–isolated alternative succeeds in surviving such tremendous seismic shaking, with its columns behaving almost elastically : since the moment capacity of the

footing is lower than the bending moment capacity of the column, foundation yielding (mainly through uplifting and some very limited mobilization of soil failure mechanisms) protects the column from failing.

Naturally, in terms of foundation $M-\vartheta$ response the picture is reversed (**Figure 3.13c**) : in the conventional system, the large B = 1.7 m footing never reaches its ultimate capacity as it is "protected" by column plastic hinging ; after the columns have failed (i.e. their ductility capacity has been reached), ϑ increases "infinitely" due to the collapse of the structure. In contrast, in the case of the rocking−isolated alternative the smaller (B = 1.4 m) footing reaches its moment capacity several times during seismic shaking, being subjected to intense uplifting and rocking. But its rotation ϑ remains well below its ultimate capacity ϑ_{ult} and toppling is avoided. While the large footings of the conventional alternative are subjected to limited rocking oscillation and uplifting, the smaller footings of the rocking−isolated structure develop larger rotations and are subjected to noticeable uplifting (**Figure 3.13d**). The seismic settlement w is large for the rocking-isolated alternative, but should not be of concern since it does not exceed 0.5 cm.

Although thanks to rocking isolation, column failure and subsequent frame collapse may be avoided, structural damage is inevitable. As shown in **Figure 3.13e**, footing rotation results in quite substantial interstorey drift : during rocking δ reaches 50 cm, implicating very intense distortion of the superstructure. Yet, the residual δ of the ground floor is limited to no more than 5 cm, corresponding to a drift ratio $\delta/h \approx 2\%$ (where h is the height of the storey). It should be noted though that the aforementioned drift is mainly due to rocking drift δ_R (i.e. due to foundation rotation) rather than flexural δ_C. Hence, the structural

integrity of frame columns (which is associated with δ_C) is not jeopardized (as for the conventionally designed system), but severe damage to beams (which consume all their ductility capacity) and to non-structural elements (such as infill walls, etc.) cannot be avoided.

3.7. Rocking Isolation of 1-bay Frames: Synopsis and Conclusions

The performance of the two design alternatives is summarized in **Figure 3.14** for all investigated earthquake scenarios (24 seismic excitations). Key performance indicators are plotted against the peak spectral pseudo-velocity, max*PSV* of the seismic excitation (undoubtedly far more representative than *PGA* or *PSA* for inelastic systems). Following Priestley et al. (2007), three limit states may be defined regarding the performance of the frame, related to the flexural drift ratio (δ_c / h) :

(a) The *Serviceability Limit State*, for $\delta_c / h \leq 1\%$, in which the structure can be fully functional after the earthquake, without the need for significant remedial measures ;

(b) The *Damage Control Limit State*, for $1\% < \delta_c/h \leq 2\%$, in which the structure is expected to sustain repairable damage, but the cost of repair should be substantially lower than the cost of replacement ; and

(c) The *Survival Limit State*, for larger δ_c / h, in which the collapse of the structure may be marginally avoided, although structural damage will be excessive and replacement will be unavoidable.

Figures 3.14a and b outlines the performance of the two systems in terms of ground floor column "*ductility consumption*" ratio $\mu_{demand}/\mu_{capacity}$ and the flexural drift ratio δ_c / h. As

previously discussed, the available ductility of the RC column is $c_u/c_y \approx 10$ (see also **Figure 3.1b**). Naturally, the damage to columns of the conventional system lies within the *serviceability limits* only for moderately strong seismic motions that do *not exceed the design limits* (e.g. El Centro). As seismic shaking gets stronger, column damage falls within *damage control* (e.g. Lefkada 2003, Erzincan), or *survival* (e.g. JMA, Tabas) limit states. For even stronger seismic shaking, *clearly in excess of the design* (such as Takatori-000, Jensen-292) column *failure* is inevitable and frame collapse almost certain. In such cases, μ_{demand} may be even an order of magnitude larger than $\mu_{capacity}$.

The performance of the rocking−isolated alternative is definitely superior, with column damage being within the *serviceability limit state* for almost 50% of the seismic excitations investigated herein, and within *damage control* for the rest. In other words, for the 24 seismic excitations examined, the vast majority of which exceeds the design, the column damage is maintained within repairable limits. In contrast, for the conventional design, although collapse takes place in only 3 out of 24 cases examined (admittedly for extreme seismic motions, substantially in excess of design), column damage is practically irreparable in most cases (even for some motions that fall within the limits of design). By no means should such performance be interpreted as a shortcoming of conventional capacity design. In fact, this is totally consistent with the whole philosophy of current seismic design, according to which the superstructure is designed to sustain extensive plastic hinging, possibly leading to irreparable damage, but avoiding collapse and serious foundation damage.

Figures 3.14b and **3.14c** compare the performance of the two design alternatives in terms of total δ/h and flexural δ_c/h ground floor drift ratios. In all cases, the two design schemes display similar behavior in terms of total δ/h, with the rocking–isolated system performing marginally better and with less scatter about a mean line. The picture is conspicuously different in terms of δ_c/h: while the drift of the rocking–isolated structure is mainly due to foundation rotation and flexural drift δ_c / h is limited, the conventional behavior is diametrically different. However, since the total drift ratio δ/h is practically the same, damage of beams and of non-structural elements is practically similar for the two structures.

In terms of settlement (**Figure 3.14d**), the performance of the two design alternatives is quite similar, with the rocking–isolated system performing marginally worse. This differs substantially from what was concluded for 1-dof systems [Anastasopoulos et al., 2010a], in which case the rocking–isolated system was found to sustain substantially increased foundation settlement. This key difference is attributable to the relatively large static safety factor (SF^s = 5.3, for B = 1.4 m) of the system examined herein, which promotes uplifting rather than "sinking" behavior of the footing.

In conclusion :

- *For moderately strong seismic excitations, within the design limits*, the performance of both design alternatives is acceptable : they would both survive the earthquake, sustaining acceptable structural damage. With conventional design, structural damage would be repairable (flexural cracking of beams and columns), but not necessarily within the serviceability limits (i.e. the structure may not be utilizable after the earthquake). In

contrast, the rocking−isolated structure would suffer rather minor structural damage (flexural cracking of beams), and could −most probably− be utilizable immediately after the earthquake.

- *For very strong seismic shaking, well in excess of the design limits*, the performance of the rocking−isolated system is quite advantageous. While the conventionally designed frame may collapse (in roughly 13% of the seismic scenarios examined) or sustain non-repairable damage (to its beams *and* columns). By contrast, the rocking−isolated frame would survive, sustaining repairable but non-negligible damage to its beams and non-structural elements (infill walls, etc.). In any case, for such extreme seismic shaking, for which avoidance of collapse is the main objective, the rocking−isolation philosophy seems to lead to a robust design. For the studied cases in particular, in which the static bearing capacity safety factor of even the under-designed footings is quite large ($SF^s > 5$), seismic settlements are hardly a serious issue.

3.8. Insights into the applicability of the Rocking-Isolation Concept

3.8.1. The effect of Safety Factor

The previous chapter investigated the validity of the proposed concept for the case of under-designed footings of width B=1.40 m, yielding a static Safety Factor SF_V = 5.31 (**Table 3.4**). The analysis revealed that the proposed concept constitutes a fail-safe design in case of extreme earthquake events exceeding the design strength of the structure by ensuring that the latter responds to the strong shaking through increased footing rotation, thus avoiding intense flexural deformation. It has been implied that decreasing the footing Safety Factor, a

larger rotation (and subsequently enhanced distortion) will be developed by the footing in order to sustain the imposed loading. In order to quantify the consequences of adopting an increased safety factor, the analyses have been repeated using footings of dimensions B= 1.20 m instead of 1.4 m, i.e. adopting an SF_V = 3.84. The results of the two alternatives are compared in detail in **Figures 3.15-3.18** for the lower intensity El Centro record and in **Figures 3.19-3.22** for the very devastating Takatori record, while the collective plots for both Safety Factors are plotted in **Figure 3.23**. As can be verified by the settlement - rotation plot of **Figure 3.20** for the case of the intense Takatori record, the B=1.20m footing is subjected to several cycles of uplifting (due to its lower moment capacity) thus further reducing the amount of inertia transmitted to the column **(Fig. 3.19)**. Indeed, the analyses revealed the very beneficial effect of the further reduction of the footings dimensions in terms of column stressing as expressed by the $\mu_{demand}/\mu_{available}$ ratio (**Fig. 3.23**). It is worthy of notice that the lower values of the ductility consumption ratio are only accompanied by minor increase of the total drift ratio of the frames (in a limited number of cases), while the flexural part of the observed drift ratio is maintained lower for the B = 1.20m alternative than for the B = 1.40m case.

Limiting Condition: Footings with $SF_V \approx 3$

A further investigation of the validity of the concept has been attempted in this final paragraph of the Section, driving the Safety Factor of the frame footings to the limiting condition of $SF_V \approx 3$. It is reminded that this is practically the lower bound value of the Static Safety Factor; SF_V values of lower than 3 are hardly ever applicable in practice.

This value of SF_V is being implemented rather by reducing the undrained soil strength to S_u=85 than through a further reduction of the footing dimension which is maintained at B=1.4 m, in order to explore whether the decreased soil strength could provoke soil failure underneath the foundation. Results between SF_V = 5.31 and SF_V = 3 are compared in detail for the Takatori record in **Figures 3.24-3.25.** Once more, it is shown that the rocking isolation concept prevents the consumption of available column ductility even for the limiting condition of the lowest acceptable value of SF_V . Of course, as anticipated even instinctively, the non structural distortion of the frame members is augmented as the Factor of Safety reduces but interestingly, the latter is not only the consequence of footing rotation due to intense uplifiting but rather that of considerable soil plastification underneath it, (due to the lower soil strength). Therefore, the footing clearly manifests a sinking dominated response with significant uplifting experienced only during the main pulse of the time history. This results to an accumulation of soil plastification-induced rotation of the footing which subsequently brings about irrecoverable permanent rotational drift of the order of 15 cm as opposed to 10cm when SF_V = 5.31 (**Fig.3.25a**). The flexural drift however remains practically unchanged (i.e. less than 2%). This valuable finding further corroborates similar observations of Kutter et al. 2003, who have correlated the uplifting potential of a footing with maintaining its Factor of Safety above the value of 3. Conclusively, it may be noted that although the collapse is avoided through either of the two identified mechanisms, uplifting is definitely preferable than soil yielding since the latter may result in unacceptable residual deformation of the structure. Comparative collective results for both foundation scenario analyzed (SF_V = 5.31 and SF_V = 3) are displayed in **Figure 3.26.**

3.8.2. The effect of Soil Strength

Frames with footings of the Same FS but different Moment Capacity

The aforementioned analyses have attempted to shed light on the effect of the Safety Factor (SF_v) value on the applicability of the proposed concept. Yet, a reduced SF value may be the outcome of either decreased footing dimensions or lower undrained soil strength S_u. In an attempt to manifest the extent to which the soil strength modifies the response of footings of equal Safety Factors, this section investigates the dynamic response of the frame when $SF_v = 4$. The latter is implemented via the following two alternatives:

a. Footings of B=1.20 m, when the soil is characterized by strength Su = 150 kPa
b. Footings of B=1.60 m, with soil strength Su = 85 kPa

The frames are initially subjected to the two extreme earthquake scenaria presented during the previous discussion (Intense Takatori record (Kobe, 1995) and moderate El Centro record (1940).

When shaken by the moderate earthquake scenario, the discrepancies in the behavior of the two alternatives are practically negligible (**Figures 3.27-3.28**). Therefore, the following argumentation focuses on the results of the extreme event, where, in accord with the above expectation, the lower $SF^S = 4$ scenario produces higher displacement demand in both frames than the previously examined $SF^S = 5.31$. Both the B=1.2 m and the B=1.6m frame develop maximum footing rotations (**Fig.3.30b**) of practically the same magnitude: $\theta_{1.2} = 0.07$ rad, $\theta_{1.6} = 0.08$ rad. Yet, the increased value of rotation in case of B=1.6m, is not just the pure consequence of uplifting but also owes to the contribution of footing settlement and subsequent rotation due to soil plastification.

Similarly, the maximum total ground floor drift ratios reach the values of δ = 9.35% for B=1.2 m and δ = 10% for the B=1.6 m footing respectively (**Fig. 3.29a**) Although both values are extreme and indicative of significant distortion it is reminded that the latter is expected to be focused to non-structural members of the structure in case of rocking isolated frames. Indeed, the flexural drift ratio (i.e. due purely to bending of the columns) is maintained at δ_c = 2% for B=1.6m and merely δc = 0.85% when B=1.2m (**Fig. 3.29a**), demonstrating a clearly superior behavior for the B=1.2m footing. This conclusion is also evident in terms of residual flexural drift ratios (thin black line in the Fig 3.30a plots). Although the total drift ratios in both rocking-isolated systems are comparable, the B=1.6m footing allows a larger inertial loading to be transmitted to the column (**Fig. 3.30a**) a fact definitely attributable to its higher Moment Capacity compared to B=1.2m. Indeed as evidenced by the overturning moment-rotation curves of the two systems, the ultimate moment reaches $M_{ult}^{B=1.6} \approx$ 110 kNm for B=1.6m compared to a mere $M_{ult}^{B=1.2}$ = 75 kNm for B=1.2; a noteworthy discrepancy certainly, which undeniably justifies the results.

Detailed results for all cases analyzed are displayed in the Appendix.

3.9. Application of the Rocking–Isolation Approach in case of 2-bay Frames

Following the preceding investigation of the dependence of the effectiveness of the proposed technique on the Safety Factor, this section explores the applicability of the unconventional foundation design approach on a slightly more complex 2 bay 2-storey frame structure. The foundation is accomplished by means of isolated square footings. The geometry of the structure under study is displayed on **Figure 3.31.**

The superstructure conventional design followed exactly the same procedure described in the previous, utilizing the computer code ETABS. The design ground acceleration a^E and the behavior coefficient q have maintained their values of 0.36g and 3.5 respectively.

According to the Greek Code, the minimum acceptable footing dimension is B^C = 1.80 m, while the unconventional design (naturally neglecting the eccentricity criterion), implements footings of dimensions B = 1.30 m.

Initially, the 2-bay frame behavior is compared to that of the 1-bay frame while the effectiveness of the new design approach is then evaluated through comparison of the conventionally and the unconventionally designed frame behavior to dynamic loading.

3.9.1. Response to Push-Over and Dynamic Loading: 2-bay vs 1 bay Frames

The response to Push-Over Loading is illustrated in **Figure 3.32** for both the conventionally and the unconventionally designed frames. Naturally, the reaction force P developed in the 2-bay frame is substantially higher than the corresponding 1-bay (although a minimal portion of this difference can be attributed to the slightly bigger footing dimension): 165 kN instead of 90 kN, at the same level of imposed displacement for the conventional solution. In

the unconventional systems, the difference in the ultimate displacement (δ^{topl}) value is only owing to the lower footing dimension (1.30m instead of 1.40 m). Likewise, the divergence between the peak reaction force developed in the conventionally and the unconventionally designed systems is higher for the 2-bay frame than for the 1-bay case since the difference between the respective footings dimensions is increased in the 2-bay case. The previously identified fluctuation of the axial load and the M/Q ratio is also identifiable in case of the 2-bay frame (**Fig. 3.33b,c**), while their effect on the M-θ response of the footings are evident in **Figure 3.33a.** Note that although the two side columns demonstrate exactly the same behavior for both frame types in terms of axial load fluctuation, the middle column maintains a constant N ≈ 280 kN throughout the duration of the push-over test. Other than these minor observations, the two frames response to push-over loading is similar.

On the other hand, the comparison of the response to dynamic loading between the 1-bay and the 2-bay frames has highlighted a number of discrepancies summarized in **Figures 3.34-3.37**. The main difference is, as expected, due to the existence of the middle column which, bearing a substantially higher axial load than the two lateral ones, encompasses increased bending moment capacity. Therefore, the central column is stressed more than the columns of the 1-bay structure, while the side columns less in both alternatives (**Figures 3.34 and 3.36**). The total drift is lower for the 2-bay frame in both design alternatives; this is definitely attributed to the limited flexibility of the 2-bay frame (see also **Fig. 3.32**). The flexural drift however is of the same order of magnitude in both alternatives. The slightly higher settlements generally observed in the 2-bay frame is the effect of increased axial load in the middle column reduced rather than of the structural system.

3.9.2. Effectiveness of Rocking isolation in 2-bay frames

Figures 3.38 and 3.39 compare the response of the conventionally versus the unconventionally designed 2-bay frame systems subjected to the recorded time-histories database referred to in the previous sections. In terms of μ_{demand} /$\mu_{capacity}$ ratio apparently the unconventional alternative has safely sustained all examined earthquake scenaria. In both cases the central column experiences more intense loading but the ratio fluctuates around only 0.1 (i.e a safety factor of about 10 may be assumed), while for the conventional system the ratio averages around 0.5 (**Fig. 3.38**). Note that ratios exceeding the value of 1 are indicative of failure. The lateral columns are generally less distorted even in the conventionally designed frame, but still, a substantial portion of their available ductility is consumed during strong earthquake scenaria. In stark contrast, for the case of the under-designed foundation the μ_{demand} /$\mu_{capacity}$ ratio never exceeds 0.1 for the side columns. A similar conclusion may be drawn by comparison of the drift ratios examined. The flexural portion of the drift ratio is systematically lower for the under-designed alternative both in terms of maximum and residual value (**Fig.3.39**). As seen before, the total drift ratios are comparable for the two cases and therefore the non-structural distortion should not be considered as avoidable. Similarly, both alternatives develop comparable settlements, with the under-designed alternative demonstrating a marginally inferior behavior (**Fig. 3.39**). Still though, the settlements magnitude is of minor importance for the structural integrity of the frame.

Figures of Chapter 3

Table 3.1. Structural member dimensions of the idealized typical frame, and synopsis of computed internal forces for static and seismic load combinations.

Structural Member	***Dimensions (cm)***	***Static Combination***			***Seismic Combination***					
		1.35G + 1.5Q			Vertical Loading : **G+0.3Q**			Earthquake Loading : **± E**		
		M^{st} : kNm	Q^{st} : kN	N^{st} : kN	M : kNm	Q : kN	N : kN	M^{E} : kNm	Q^{E} : kN	N^{E} : kN
Ground floor Columns – base	40 x 40	13	10	243	8	6	150	101	41	54
1^{st} floor Columns – base	40 x 40	68	51	153	40	30	96	26	25	19
Ground floor Beam – edges	20 x 50	71	117	0	41	68	0	80	35	0
1^{st} floor Beam – edges	20 x 50	61	117	0	35	68	0	45	19	0

Table 3.2. Seismic capacity design of the superstructure : target moment capacity (M^{target}) of structural members, resulting longitudinal reinforcement, and final (achieved) Moment Capacity (M^{RD}).

Structural Member	***Location***	***M^{target}: kNm***	***Reinforcement***	***M^{RD} : kNm***
Ground floor Columns	*top*	119	8Ø20	165
	bottom	146	8Ø20	165
1st floor Columns	*top*	104	8Ø20	165
	bottom	105	8Ø20	165
Ground floor Beam	*edges*	119	5Ø16	120
	middle	64	3Ø14	67
1st floor Beam	*edges*	79	4Ø14	80
	middle	74	4Ø14	80

Table 3.3. Forces acting on the footing for Static and Seismic load combinations.

	Static Combination	***Seismic Combination***		
	1.35G + 1.5Q	**G + 0.3Q**	**± E**	**EAK 2000*** (a_{CD} = 1.78)
M : kNm	13	8	100	186
Q : kN	10	6	41	78
N : kN	322	151	54	247

* : according to conventional capacity design, following

Table 3.4. Alternative footing configurations : footing width *B*, resulting safety factor for static SF^S and seismic SF^E loading, eccentricity *e/B,* moment capacity (computed analytically according to Gourvenec, 2007), and corresponding *Capacity Reduction Factor* (ratio of footing capacity M_{ult} to the column capacity M^{RD}). Observe that according to conventional capacity design, *B* = 1.7 m is the minimum acceptable square footing (to comply with code provisions relevant to the maximum allowable eccentricity of *B*/3).

Footing width B (m)	SF^S	SF^E	Eccentricity e/B	M_{ult} for N=151 kN (G + 0.3 Q)	M_{ult} for N=247 kN (EAK 2000)	Capacity Reduction Factor
1.7	7.96	1.93	**0.34**	136	197	**N.A.**
1.6	7.01	*Not Applicable for Conventional Foundation Capacity Design*		125	180	1.32
1.5	6.13			113	163	1.46
1.4	5.31			101	147	***1.63***
1.3	4.54			91	131	1.81
1.2	3.84			81	115	***2.04***
1.1	3.19			71	100	2.32
1.0	2.6			61	84	2.70

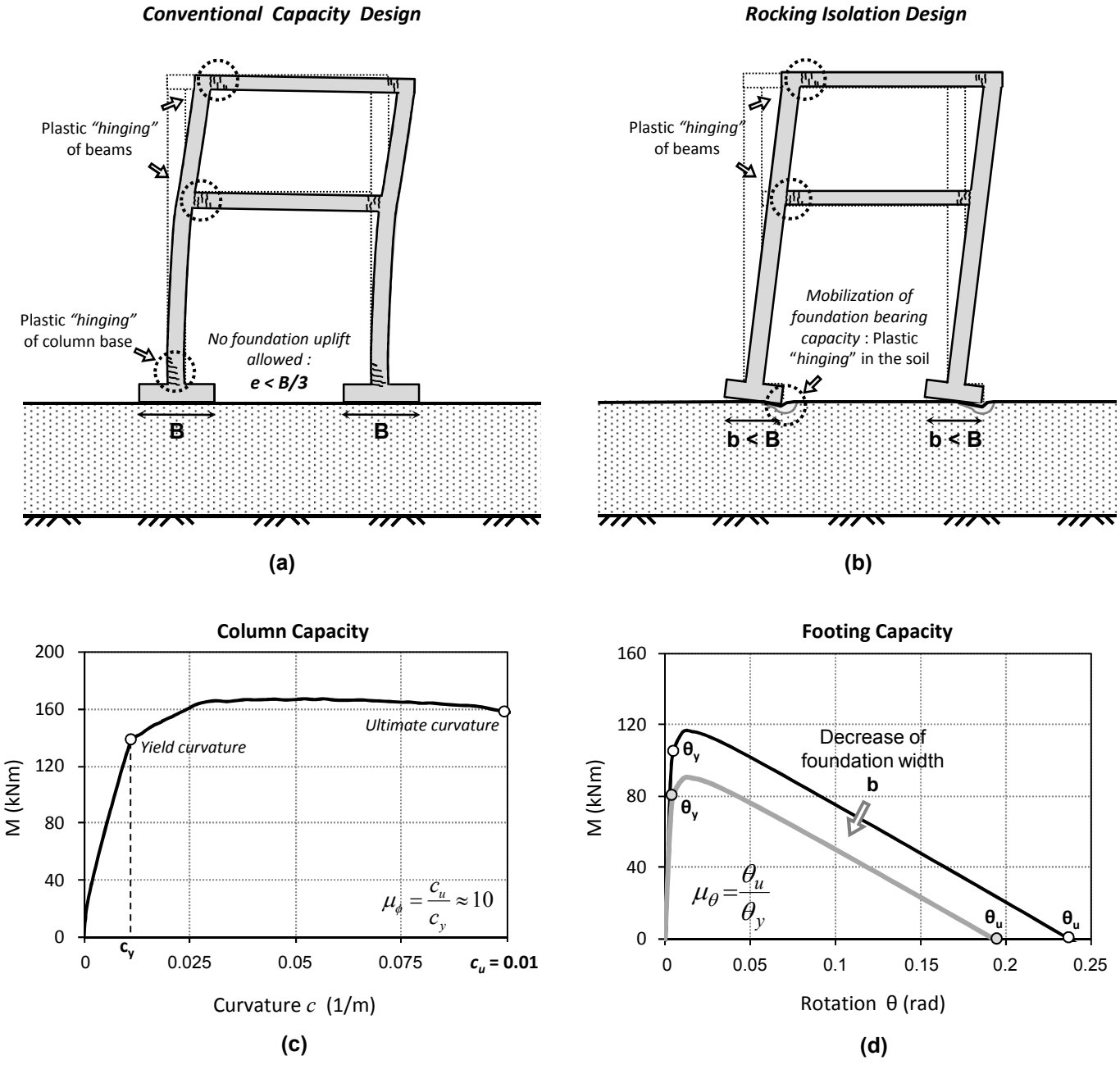

Figure 3.1. (a) Conventional Capacity Design compared with (b) Rocking–Isolation Design. (c) Conventional Capacity Design : moment–curvature curve of the reinforced concrete column (ductile design, according to EC8). (d) Rocking–Isolation Design : moment–rotation curve (for combined axial and shear force at a constant lever arm) of the under-designed square footing, illustrating the effect of the reduction of width b.

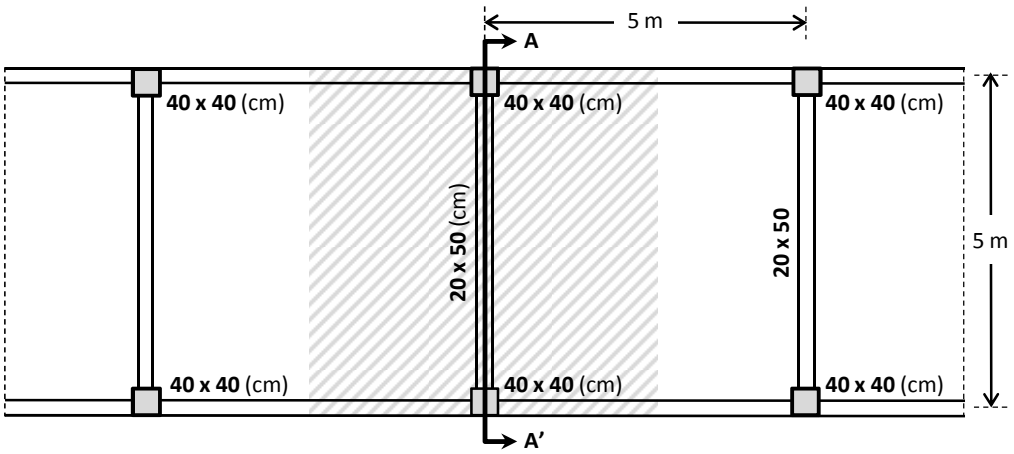

(a)

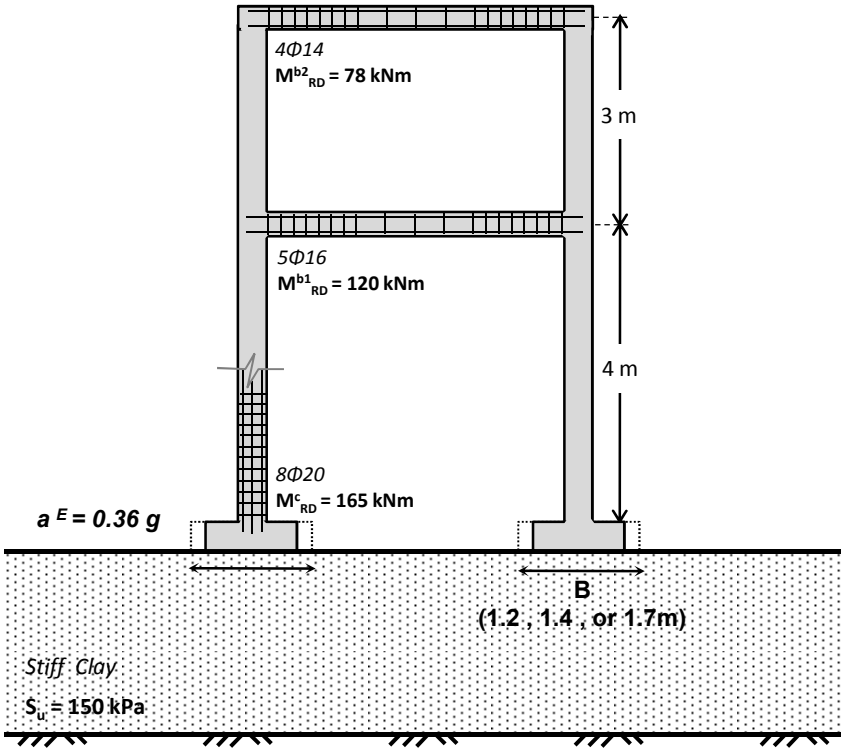

(b)

Figure 3.2. Geometry and member properties of the idealized typical frame structure analyzed : (a) plan view, and (b) cross-section A-A'.

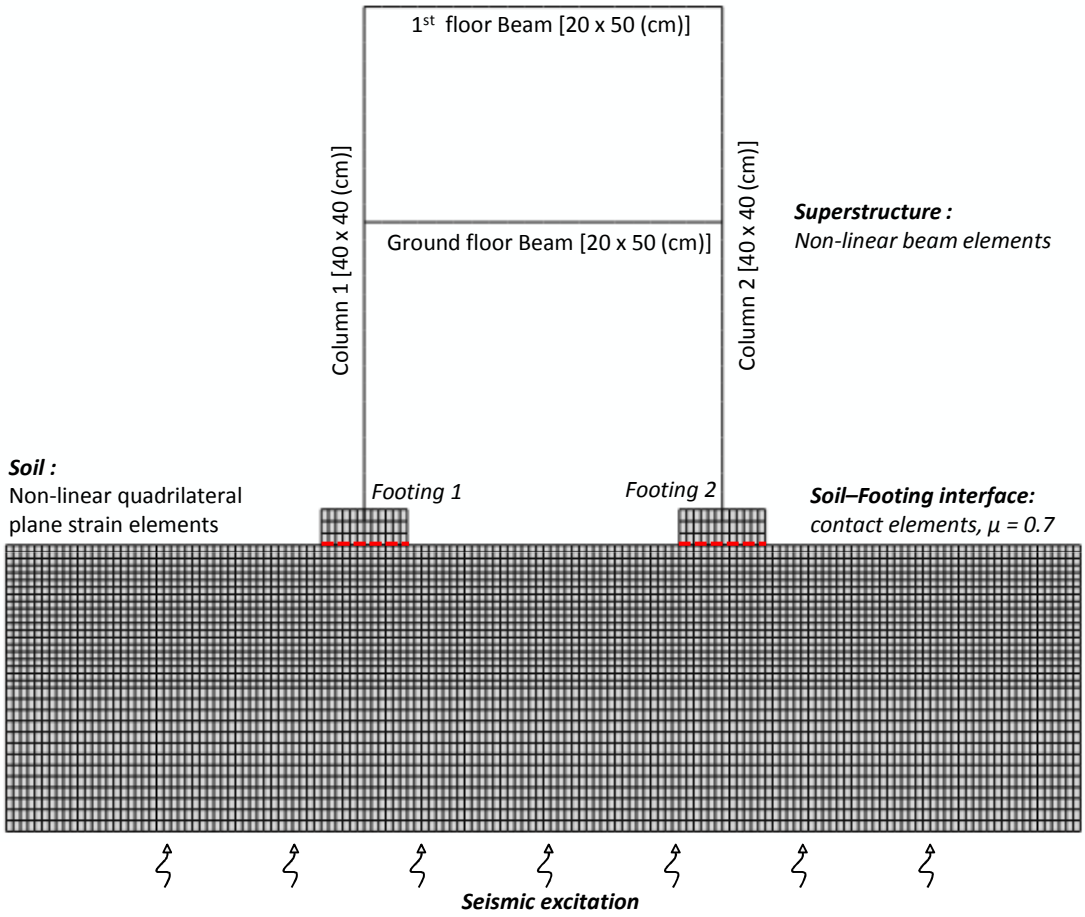

Figure 3.3. Finite element model : assuming plane-strain conditions, the soil-structure system is modeled with due consideration to material (soil *and* superstructure) and geometric (uplifting and P-δ effects) nonlinearities.

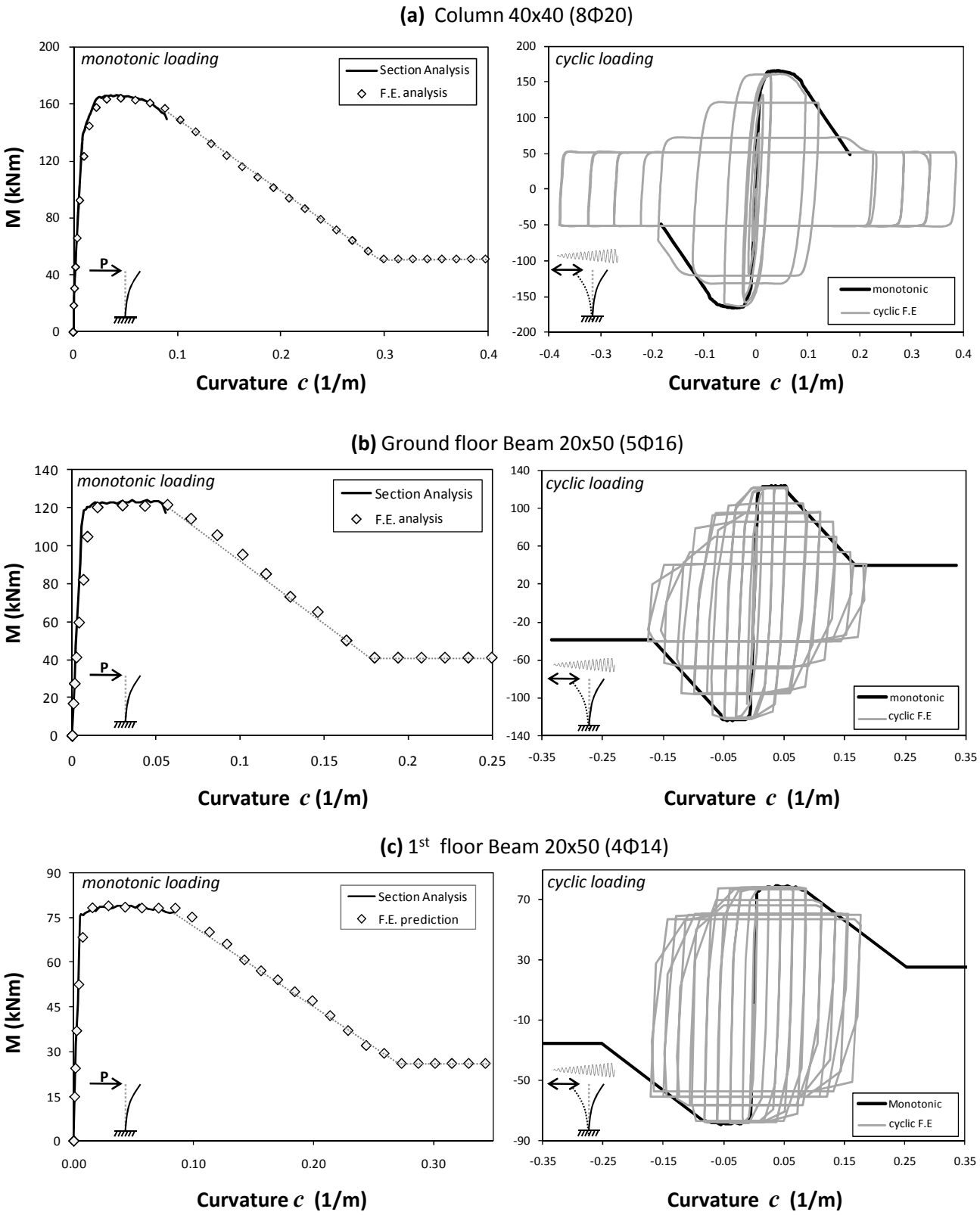

Figure 3.4. Calibration of the superstructure F.E. model against moment–curvature response calculated through reinforced–concrete section analysis under monotonic loading (left column), and FE model response under cyclic loading (right column) : (a) columns (40x40, 8Φ20), (b) ground floor beam (20x50, 5Φ16), and (c) 1st floor beam (20x50, 4Φ14).

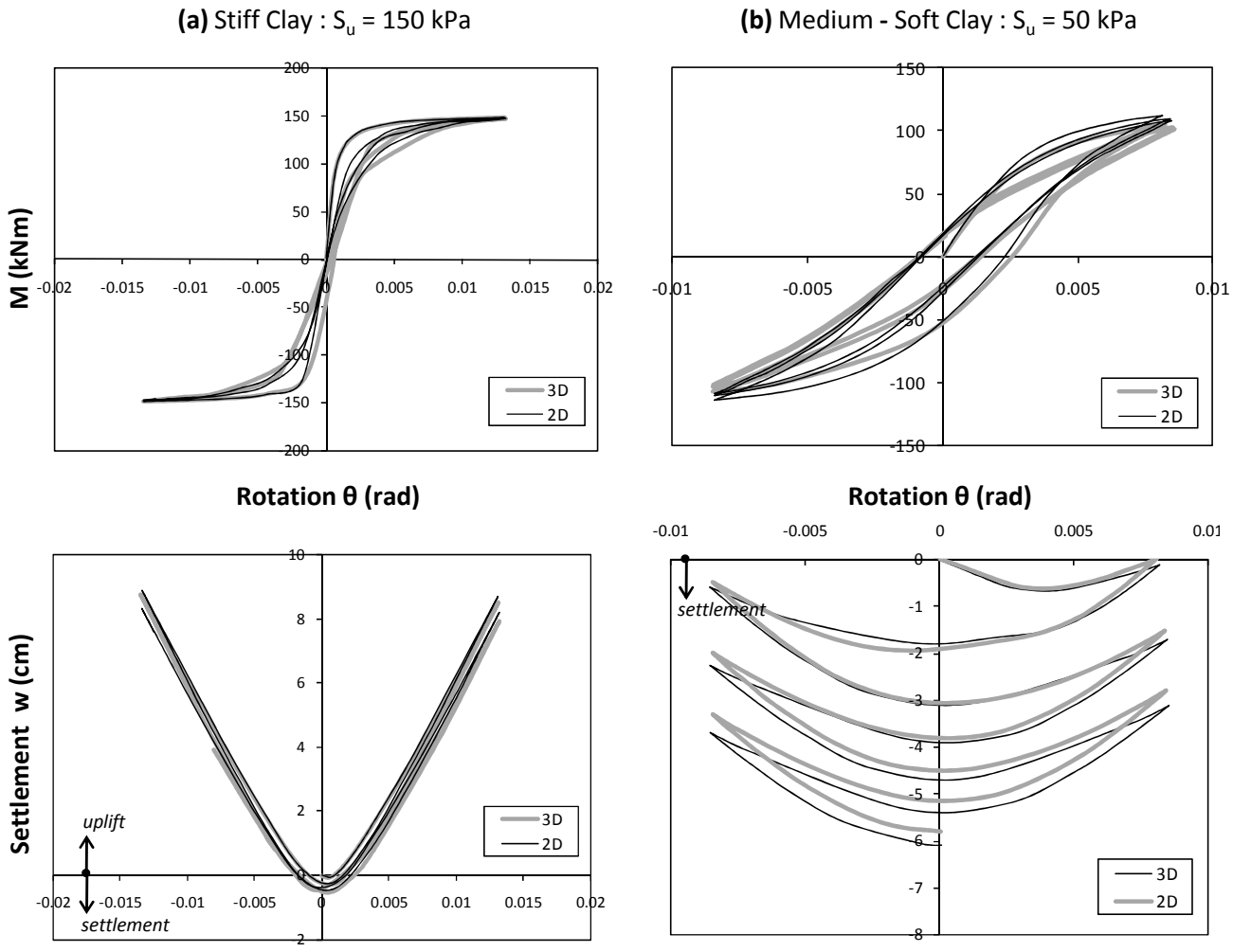

Figure 3.5. Comparison of "equivalent-2D" with 3D F.E. results in terms of moment–rotation (M–ϑ) and settlement–rotation (w–ϑ) response of B = 1.7 m square footing founded on : (a) a S_u = 150 kPa stiff clay, and (b) a S_u = 50 kPa medium-soft clay.

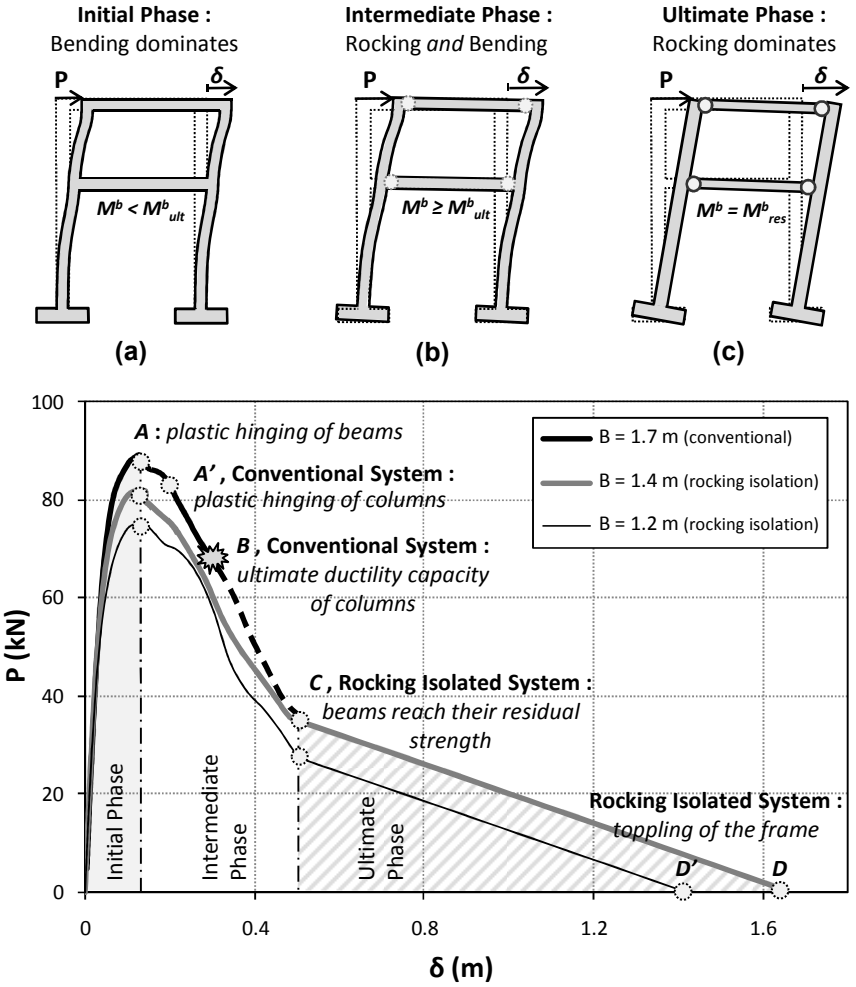

Figure 3.6. Static pushover response of three design alternatives : conventional system with large (over-designed) *B* = 1.7 m footings, compared to rocking-isolation design with smaller (under-designed) *B* = 1.4 m and B = 1.2 m footings (corresponding to capacity reduction factors of 1.6 and 2.0, respectively). System response can be divided into three characteristic phases : (a) an initial phase, in which bending dominates ; (b) an intermediate phase, in which both bending and rocking take place, and (c) the ultimate phase, which is dominated by rocking.

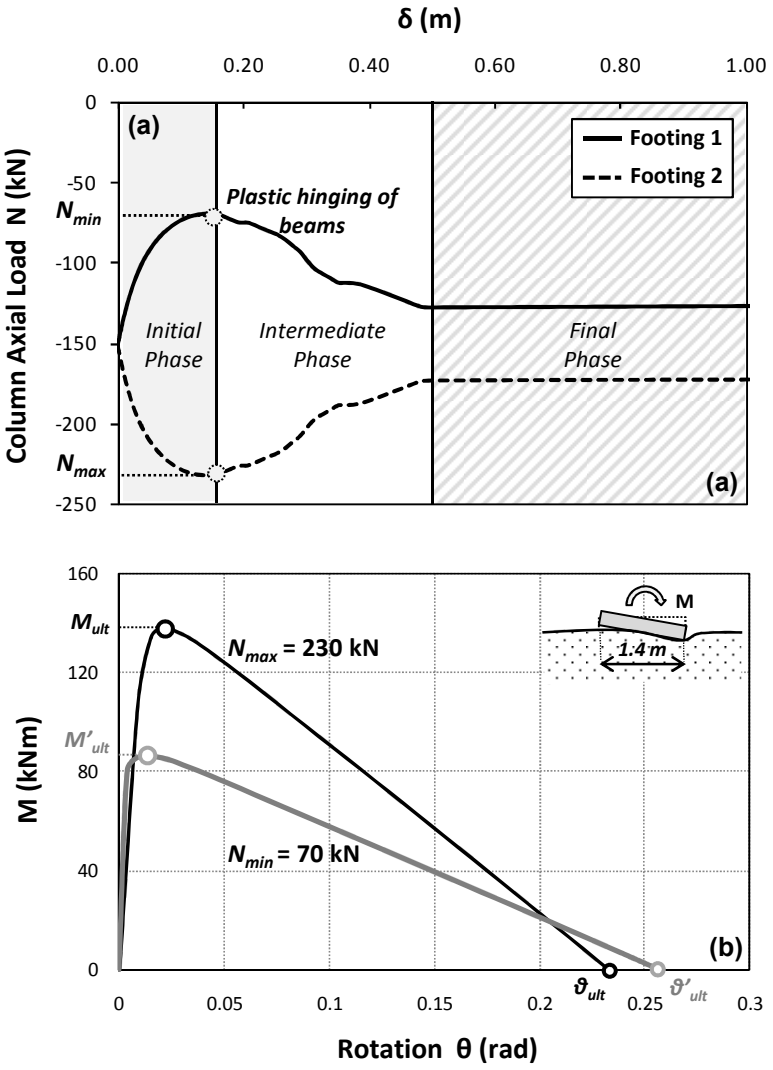

Figure 3.7. Static pushover analysis : (a) evolution of column axial load *N* with increasing imposed lateral displacement *δ* ; and (b) illustration of the effect of *N* on the moment capacity of the footing. (Results shown for the *B* = 1.4 m alternative, as if N_{min} and N_{max} were permanently applied).

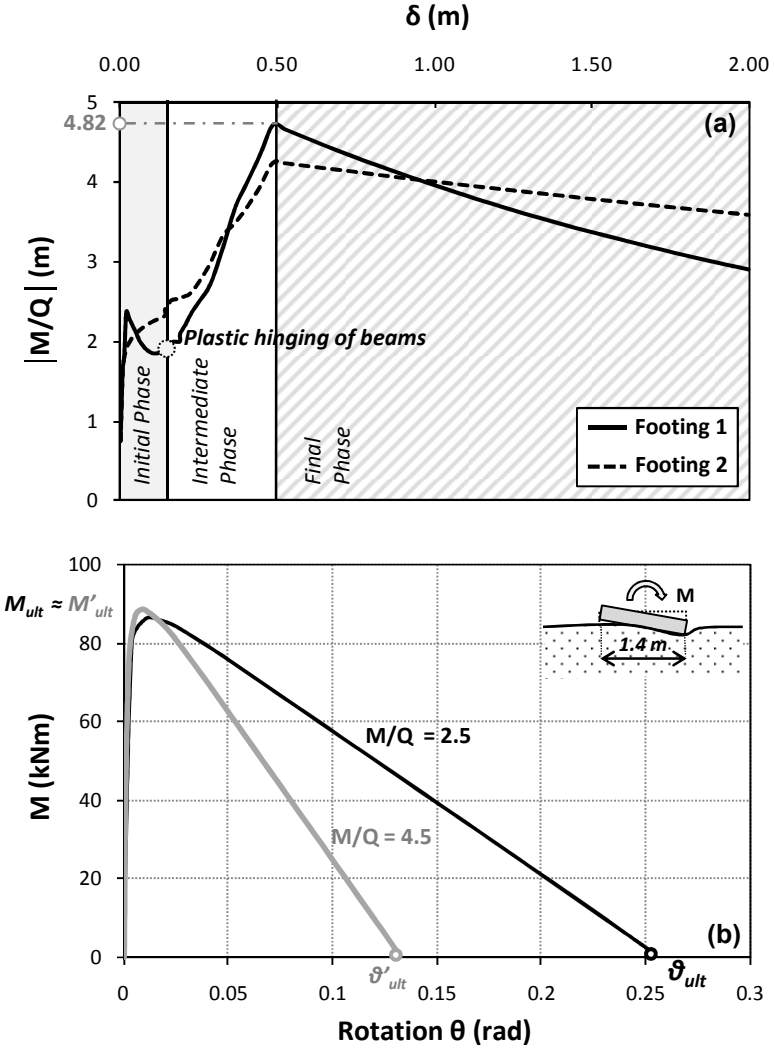

Figure 3.8. Static pushover analysis : (a) evolution of the *M/Q* ratio with increasing imposed lateral displacement *δ.* During the initial phase, no plastic hinging has yet developed and *M/Q* fluctuates between 1.8 and 2.4. During the intermediate phase, and as plastic hinging develops, the *M/Q* ratio increases to 4.5 (corresponding to the center of mass of the rocking system). In the final phase, *M/Q* decreases again. (b) The effect of *M/Q* on the moment–rotation response of the footing (results shown for the *B* = 1.4 m alternative, assuming N = 150 kN).

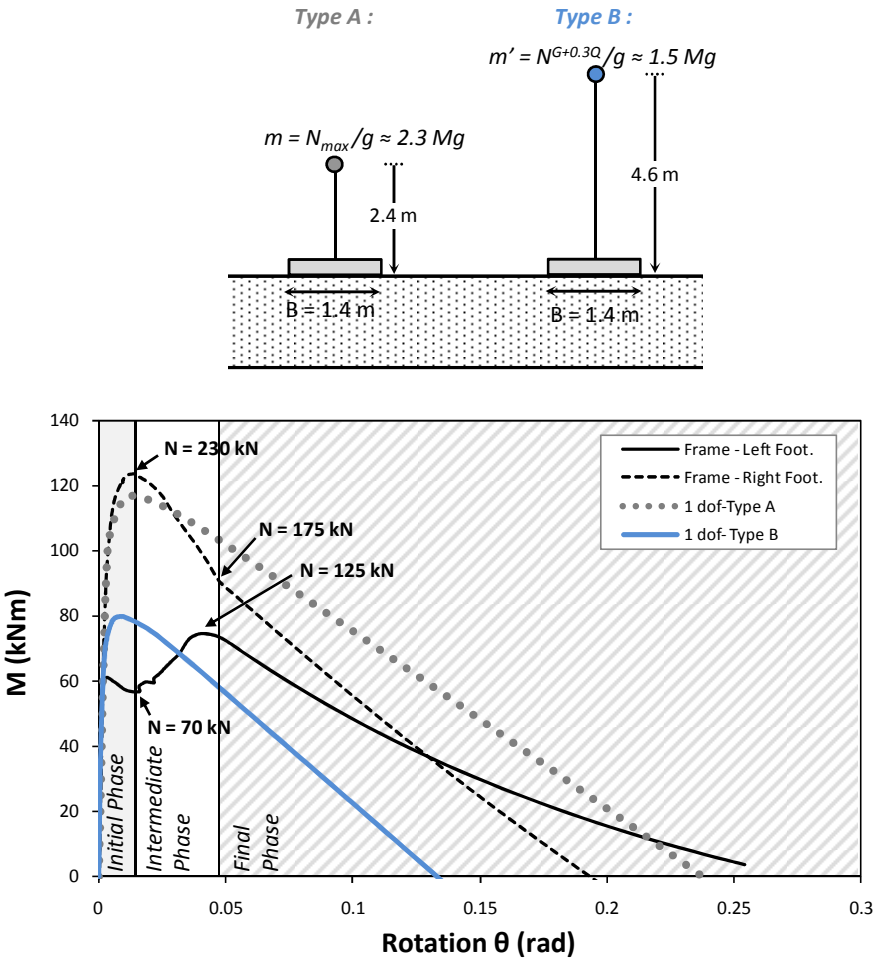

Figure 3.9. Static pushover analysis : moment-rotation (M–ϑ) response of the two frame footings, compared with the response of the footings of the two simplified "equivalent" 1-dof systems (Type A and Type B).

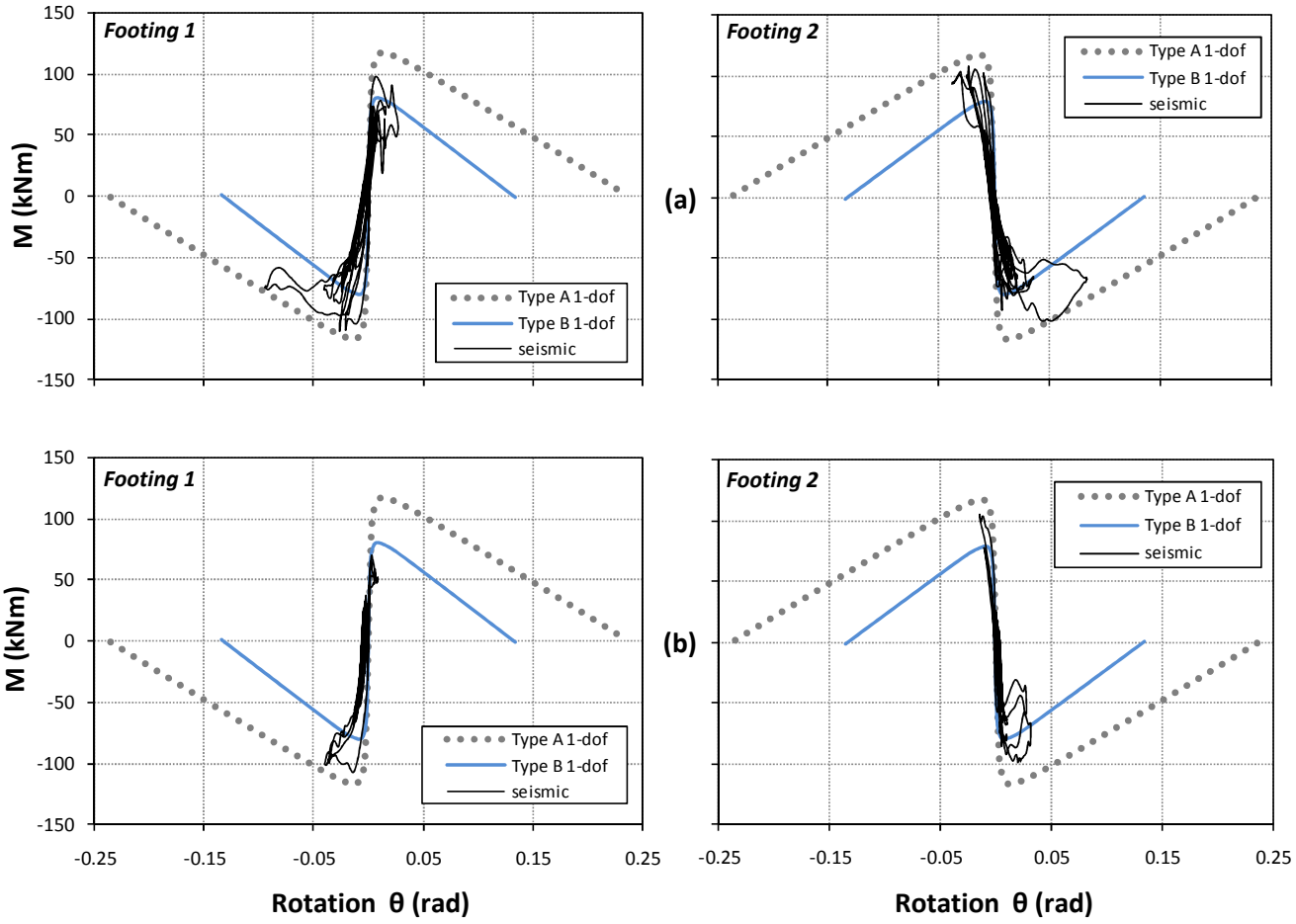

Figure 3.10. Seismic (computed through dynamic time-history analysis) moment–rotation (M–ϑ) response of the two frame footings, compared with the monotonic response of two simplified equivalent 1-dof systems (Type A and Type B), for two seismic excitations : (a) Takatori (000) record, Kobe 1995 ; and **(b)** Jensen (022), Northridge 1994. The monotonic response is also plotted for comparison.

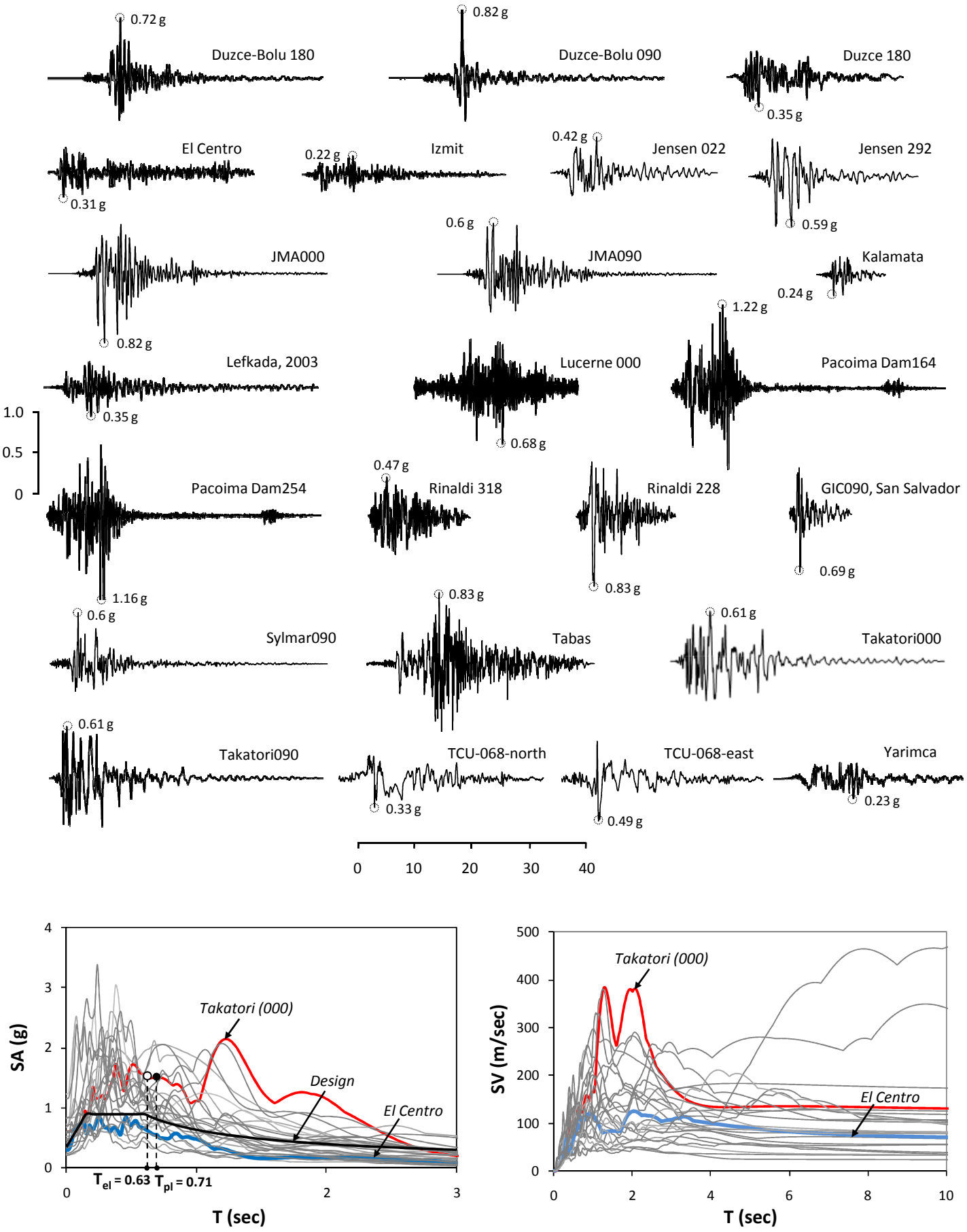

Figure 3.11. The 24 earthquake records used as excitation for the dynamic analysis of the three design alternatives, along with their acceleration and velocity response spectra. The selected records cover a wide range of seismic motions produced from medium to very strong seismic events collectively encompassing forward-rupture directivity, multiple strong-motion cycles, and/or fling-step effects.

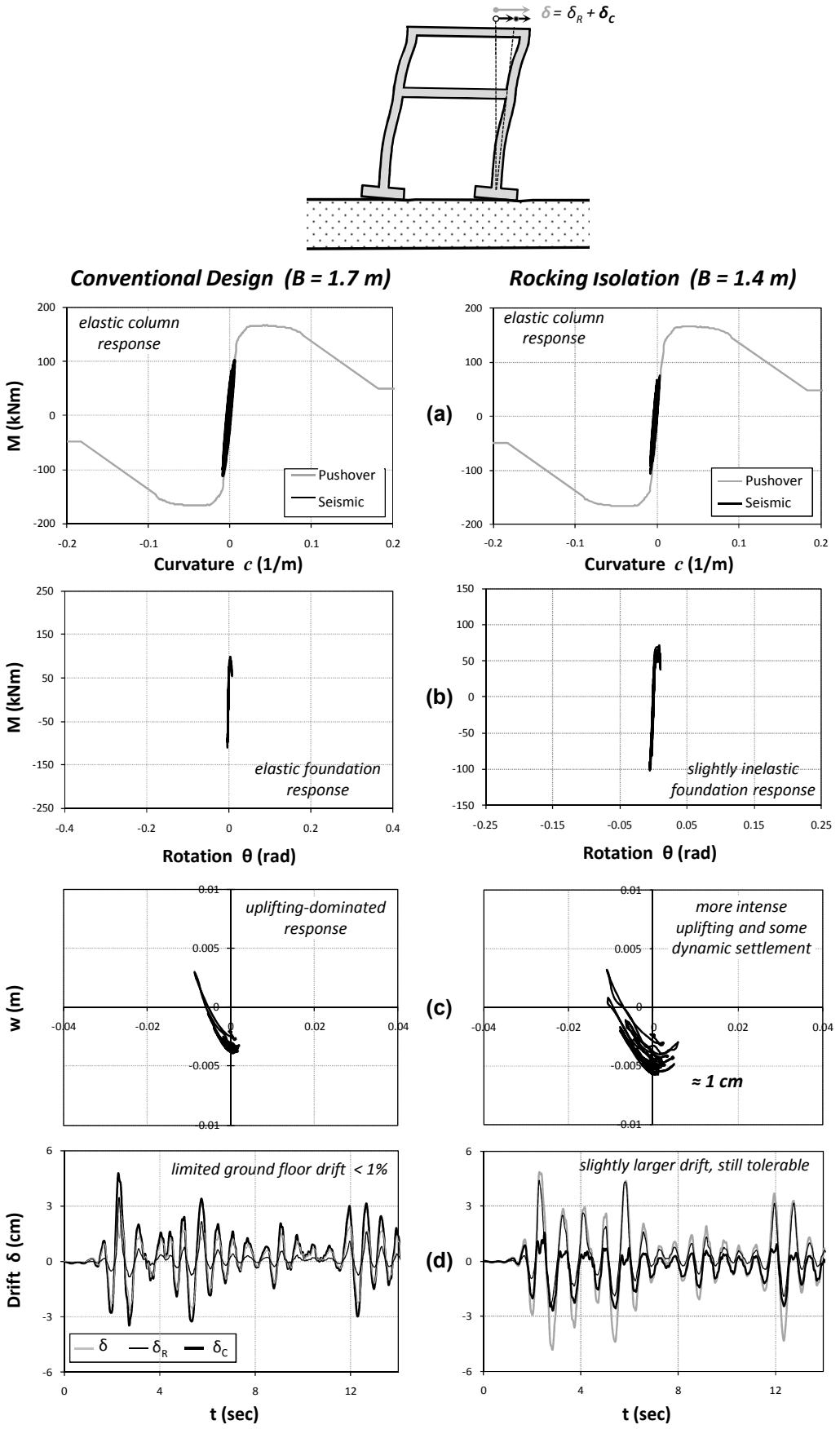

Figure 3.12. Performance of the two design alternatives (conventional, B = 1.7 m ; rocking isolation, B = 1.4 m) subjected to a moderately–strong seismic shaking (El Centro record), in terms of : (a) Column bending moment–curvature (M–c) response ; (b) foundation moment–rotation (M–ϑ) response (compared to the corresponding static pushover of the two equivalent 1-dof systems) ; (c) foundation settlement–rotation (w–ϑ) response ; and (d) time history of ground floor drift δ.

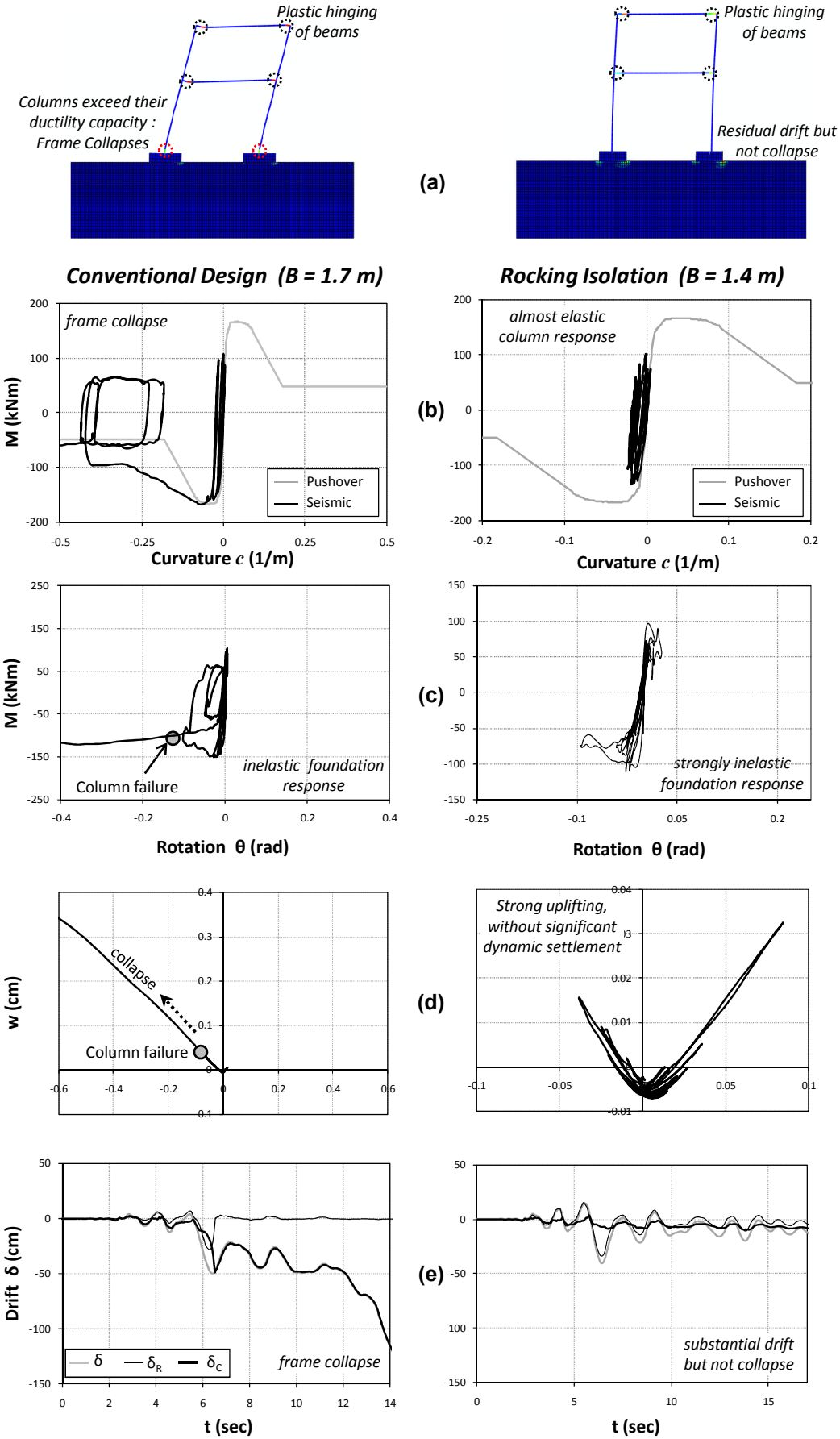

Figure 3.13. Performance of the two design alternatives (conventional, B = 1.7 m ; rocking isolation, B = 1.4 m) subjected to very strong seismic shaking (Takatori record). (a) Deformed FE mesh with superimposed plastic deformation ; (b) column bending moment–curvature (M–c) response ; (c) foundation moment–rotation (M–ϑ) response (compared to the corresponding static pushover of the two equivalent 1-dof systems) ; (d) foundation settlement–rotation (w–ϑ) response ; and (e) time history of ground floor drift δ.

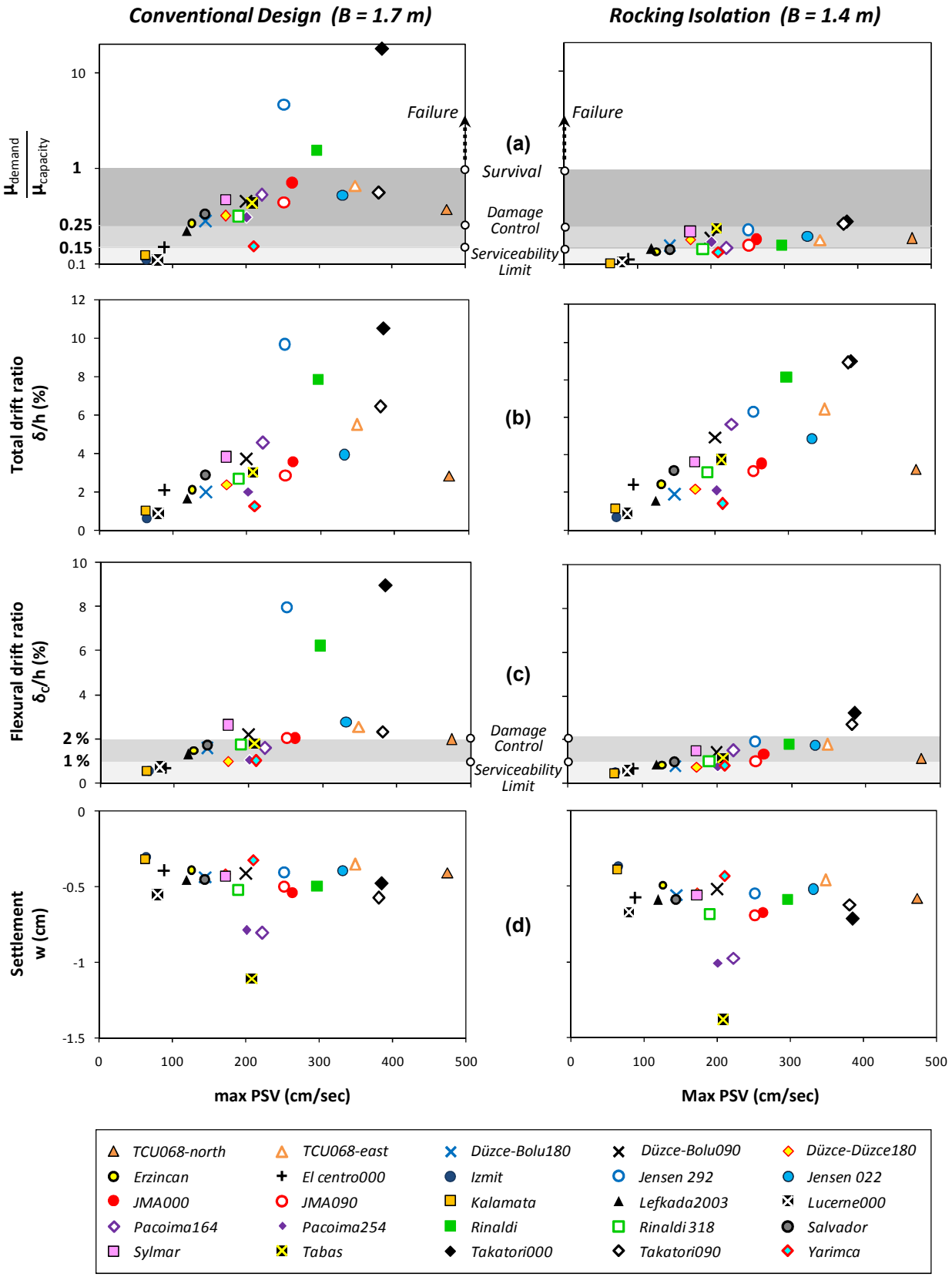

Figure 3.14. Summary of the response of the two design alternatives as a function of the maximum spectral velocity *SV*: (**a**) Column curvature ductility ratio (i.e. ductility *demand* over ductility *capacity).* Damage level is indicated with reference to *Response Limit States* (Priestley et al., 1996) , (b) Total drift ratio for the ground floor δ/h (where h is the height of the ground floor) ; (c) Flexural drift ratio δ_c / h ; and (d) Settlement w.

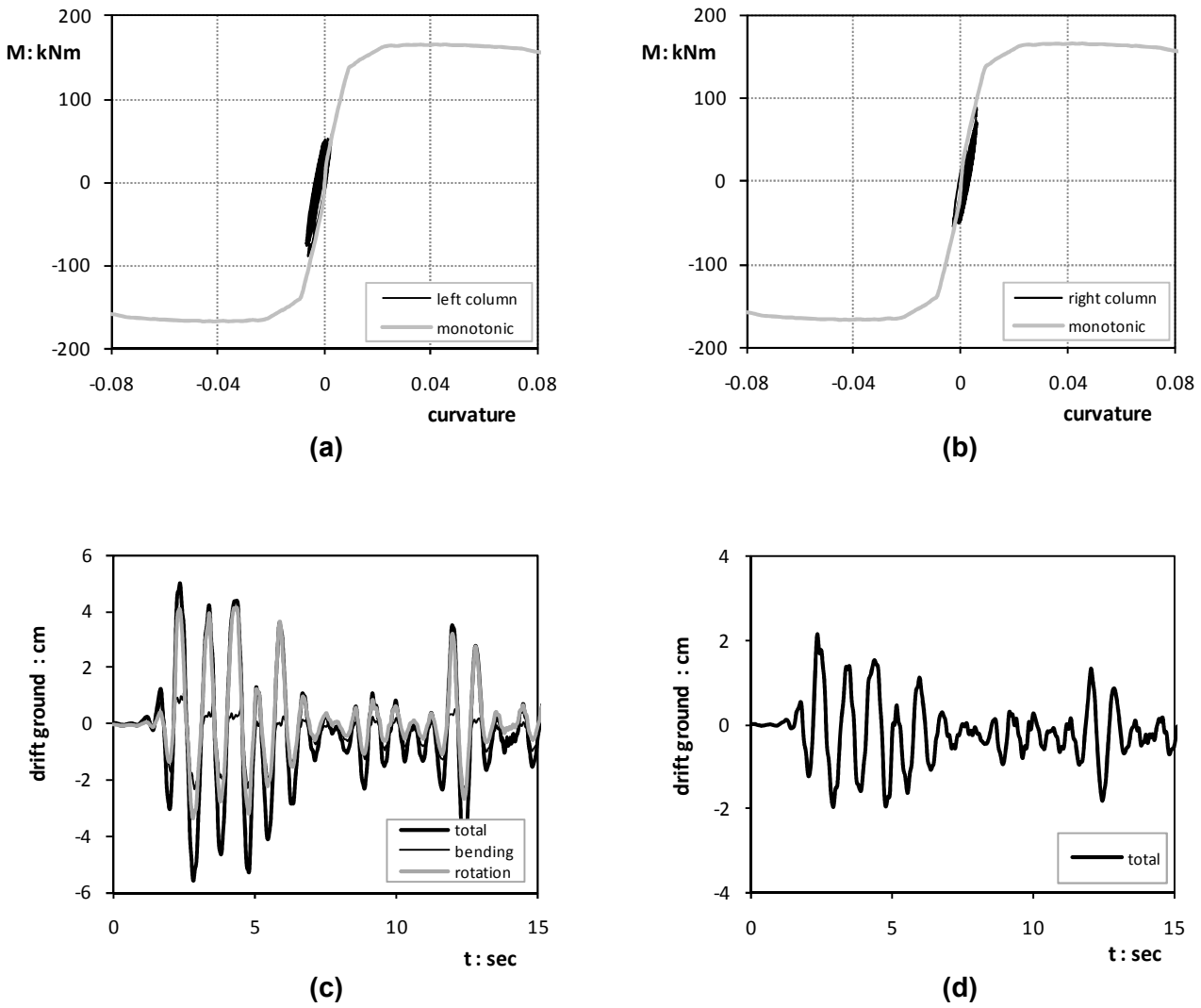

Figure 3.15. Performance of the unconventional foundation system **(*B* = 1.2 m)** that corresponds to $SF_V = 3.84$ when subjected to a *moderately strong earthquake scenario* (El Centro record) : (a), (b) column bending moment–curvature (*M*–*c*) response of both columns ; (c), (d) time history of ground floor and 1st floor drift *δ*. Bold black line stands for the total drift, thin black line for the flexural and grey line for the rotational drift.

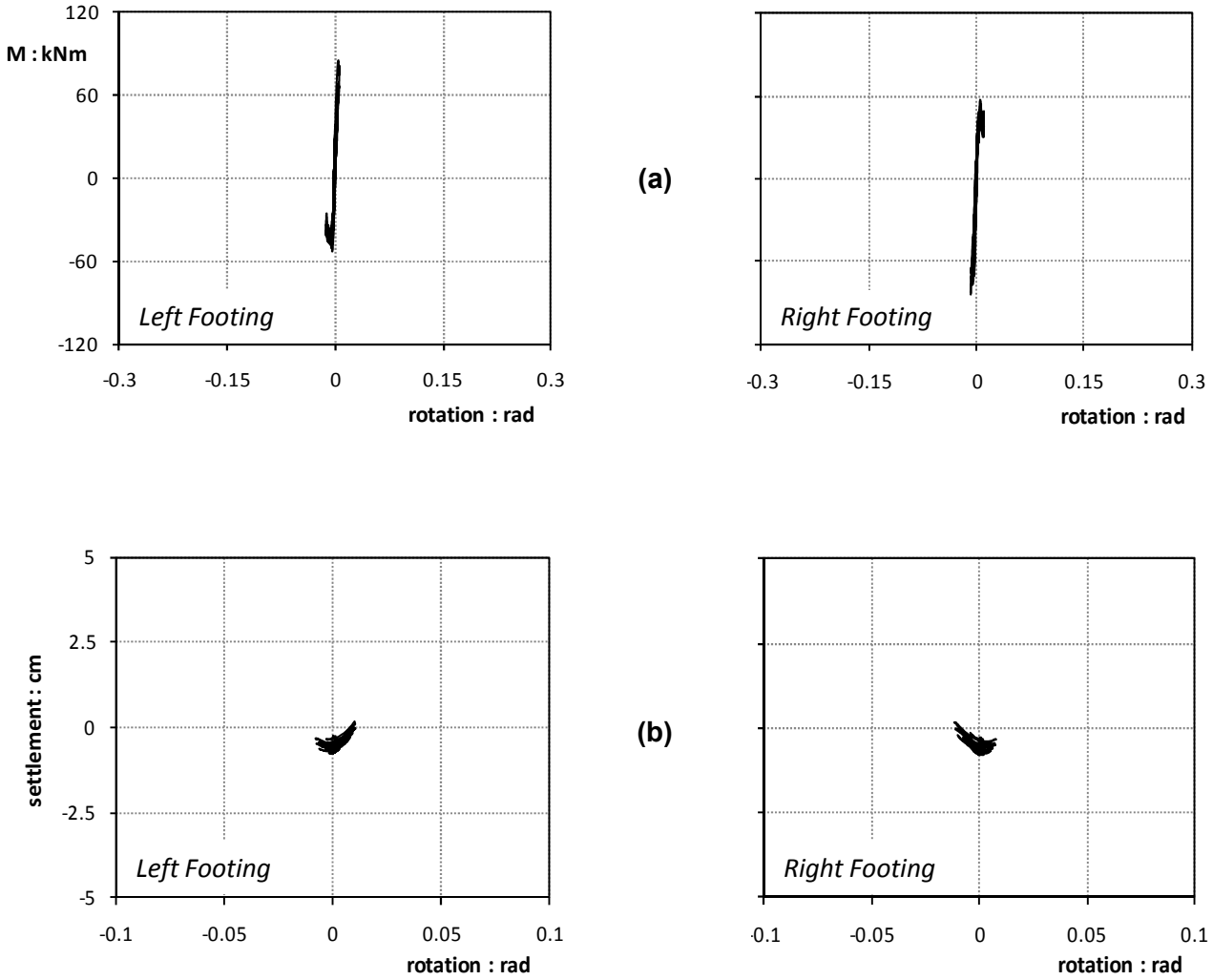

Figure 3.16. Performance of the unconventional foundation system **(*B* = 1.2 m)** that corresponds to $SF_V = 3.84$ when subjected to a *moderately strong earthquake scenario* (El Centro record) : (a) Overturning Moment – rotation loops and (b) settlement – rotation loops for both footings.

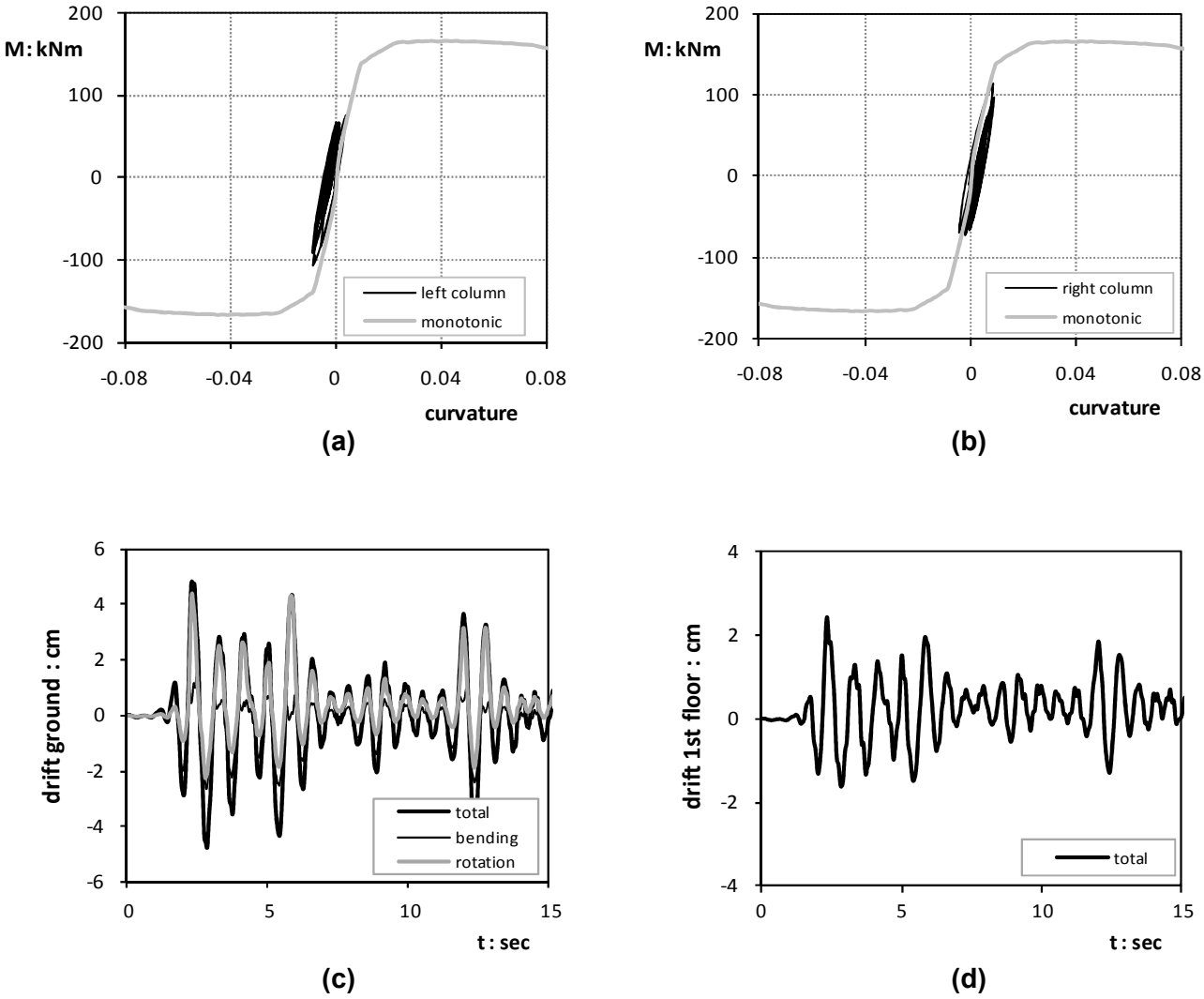

Figure 3.17. Performance of the unconventional foundation system **(*B* = 1.4 m)** that corresponds to $SF_V = 5.31$ when subjected to a *moderately strong earthquake scenario* (El Centro record) : (a), (b) column bending moment–curvature (*M*–*c*) response of both columns ; (c), (d) time history of ground floor and 1st floor drift *δ*. Bold black line stands for the total drift, thin black line for the flexural and grey line for the rotational drift.

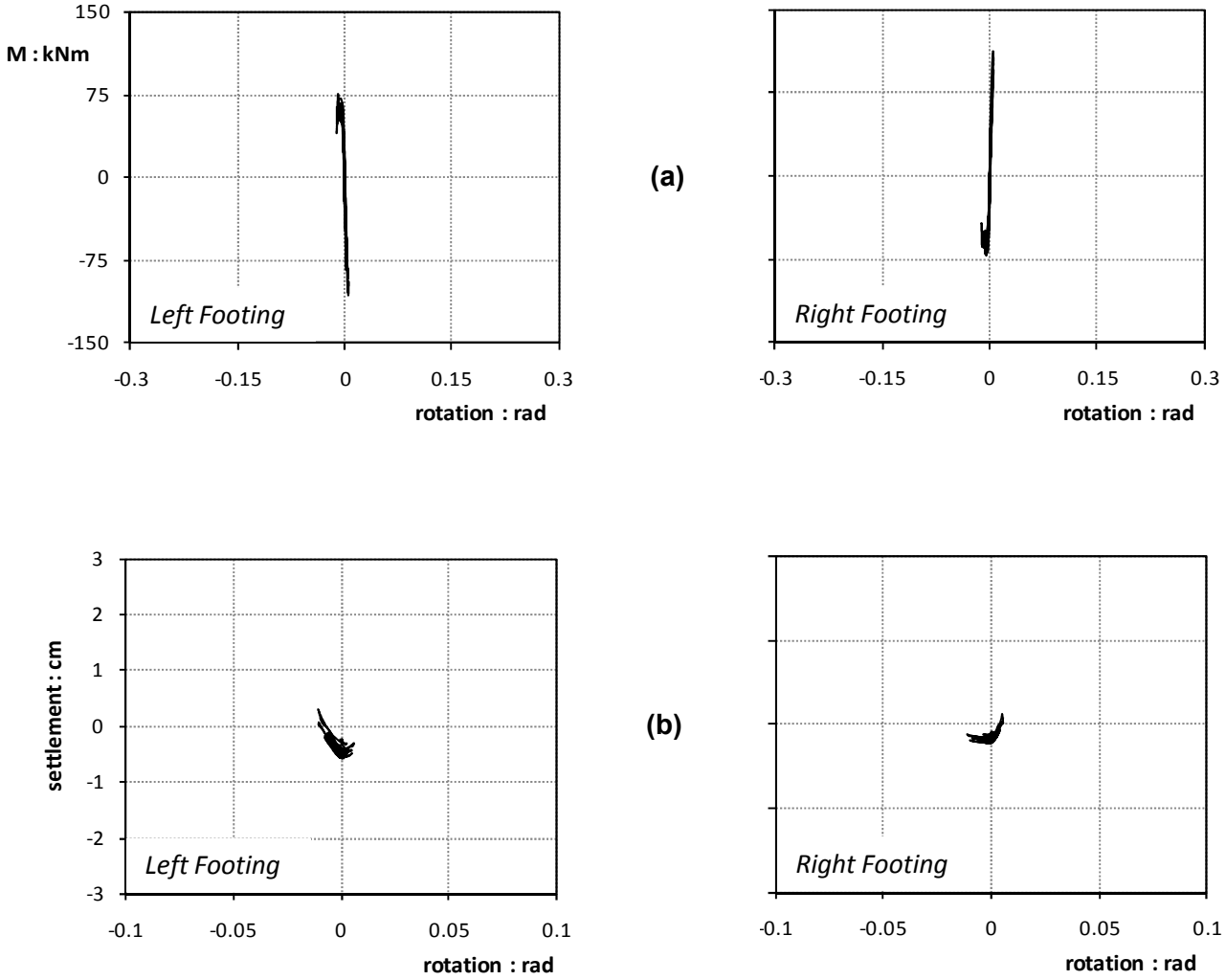

Figure 3.18. Performance of the unconventional foundation system **(*B* = 1.4 m)** that corresponds to $SF_V = 5.31$ when subjected to a *moderately strong earthquake scenario* (El Centro record) : (a) Overturning Moment – rotation loops and (b) settlement – rotation loops for both footings.

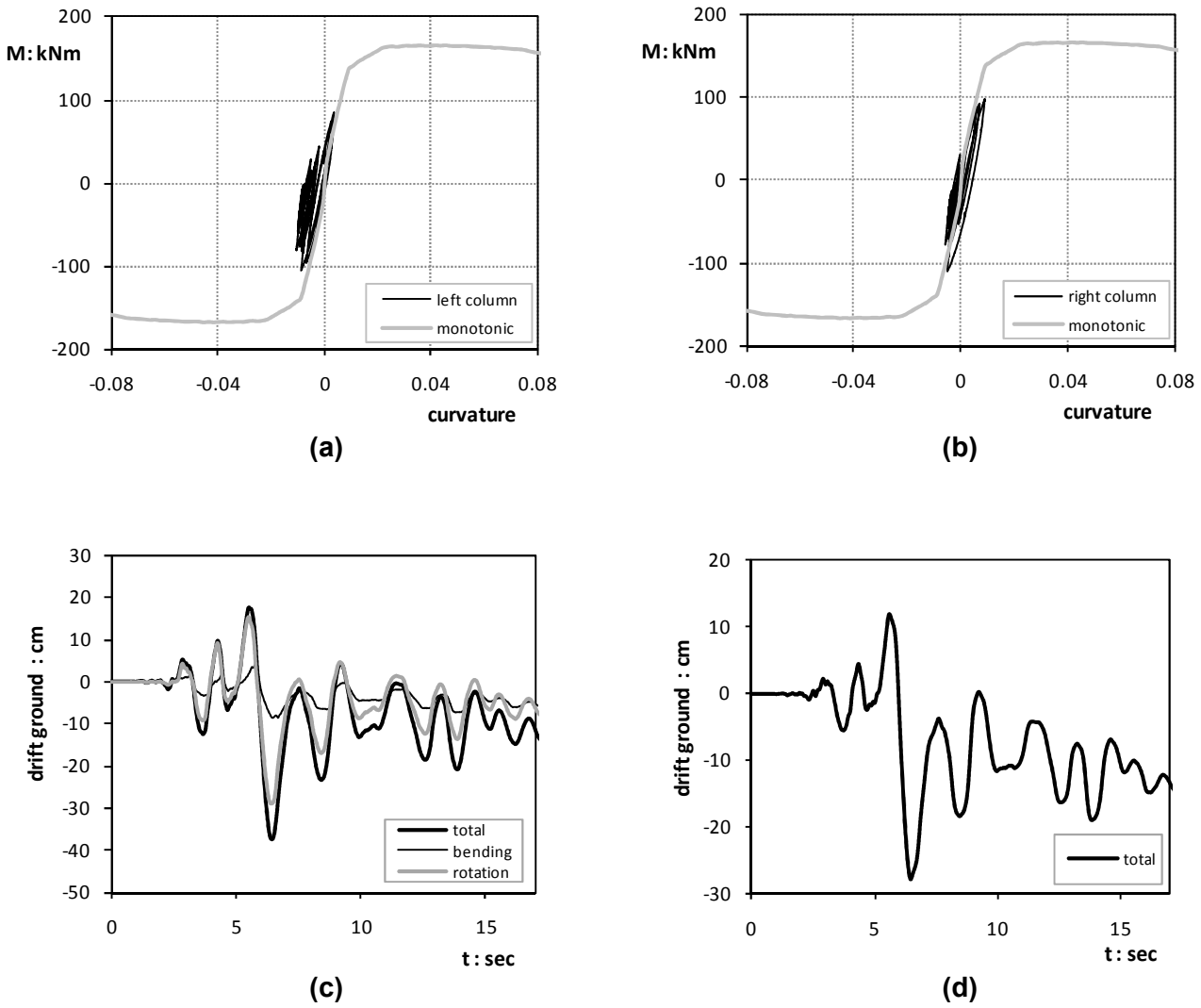

Figure 3.19. Performance of the unconventional foundation system **(*B* = 1.2 m)** that corresponds to SF_V = *3.84* when subjected to a *very strong earthquake scenario* (Takatori000 record) : (a), (b) column bending moment–curvature (*M*–*c*) response of both columns ; (c), (d) time history of ground floor and 1st floor drift *δ*. Bold black line stands for the total drift, thin black line for the flexural and grey line for the rotational drift.

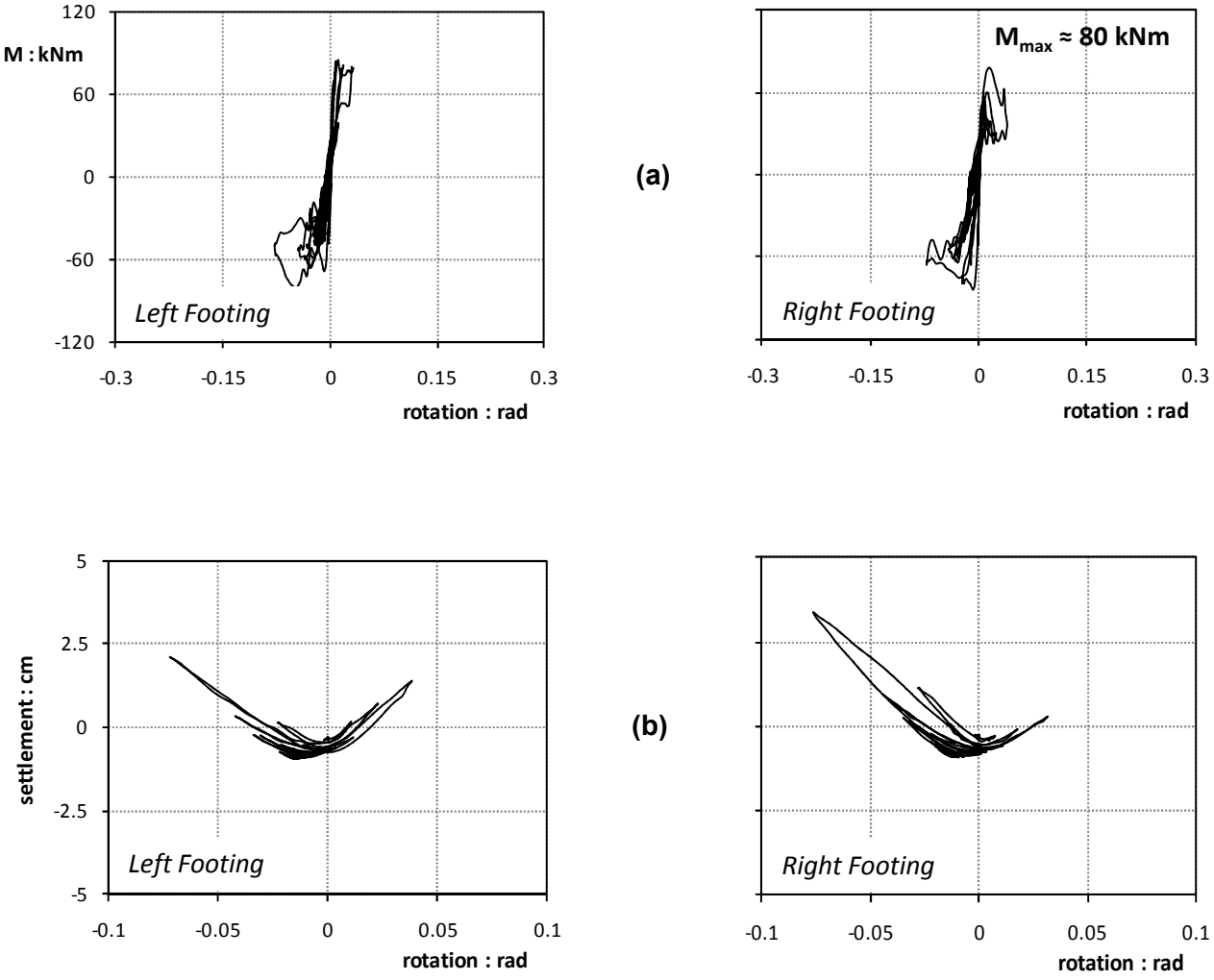

Figure 3.20. Performance of the unconventional foundation system **(*B* = 1.2 m)** that corresponds to SF_V = *3.84* when subjected to a *very strong earthquake scenario* (Takatori000 record) : (a) Overturning Moment – rotation loops and (b) settlement – rotation loops for both footings.

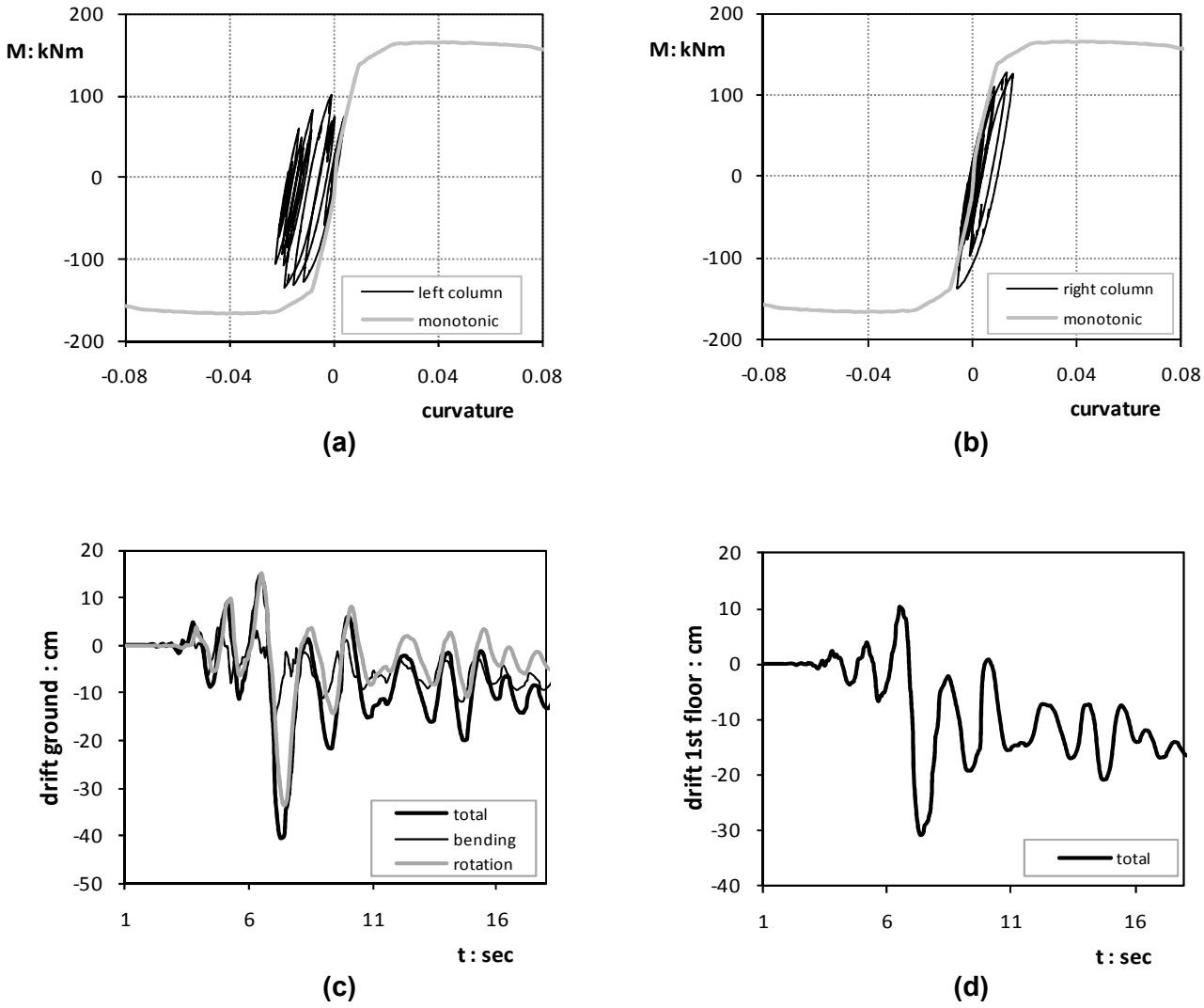

Figure 3.21. Performance of the unconventional foundation system **(*B* = 1.4 m)** that corresponds to SF_V = *5.31* when subjected to a *very strong earthquake scenario* (Takatori000 record) : (a), (b) column bending moment–curvature (*M*–*c*) response of both columns ; (c), (d) time history of ground floor and 1st floor drift *δ*. Bold black line stands for the total drift, thin black line for the flexural and grey line for the rotational drift.

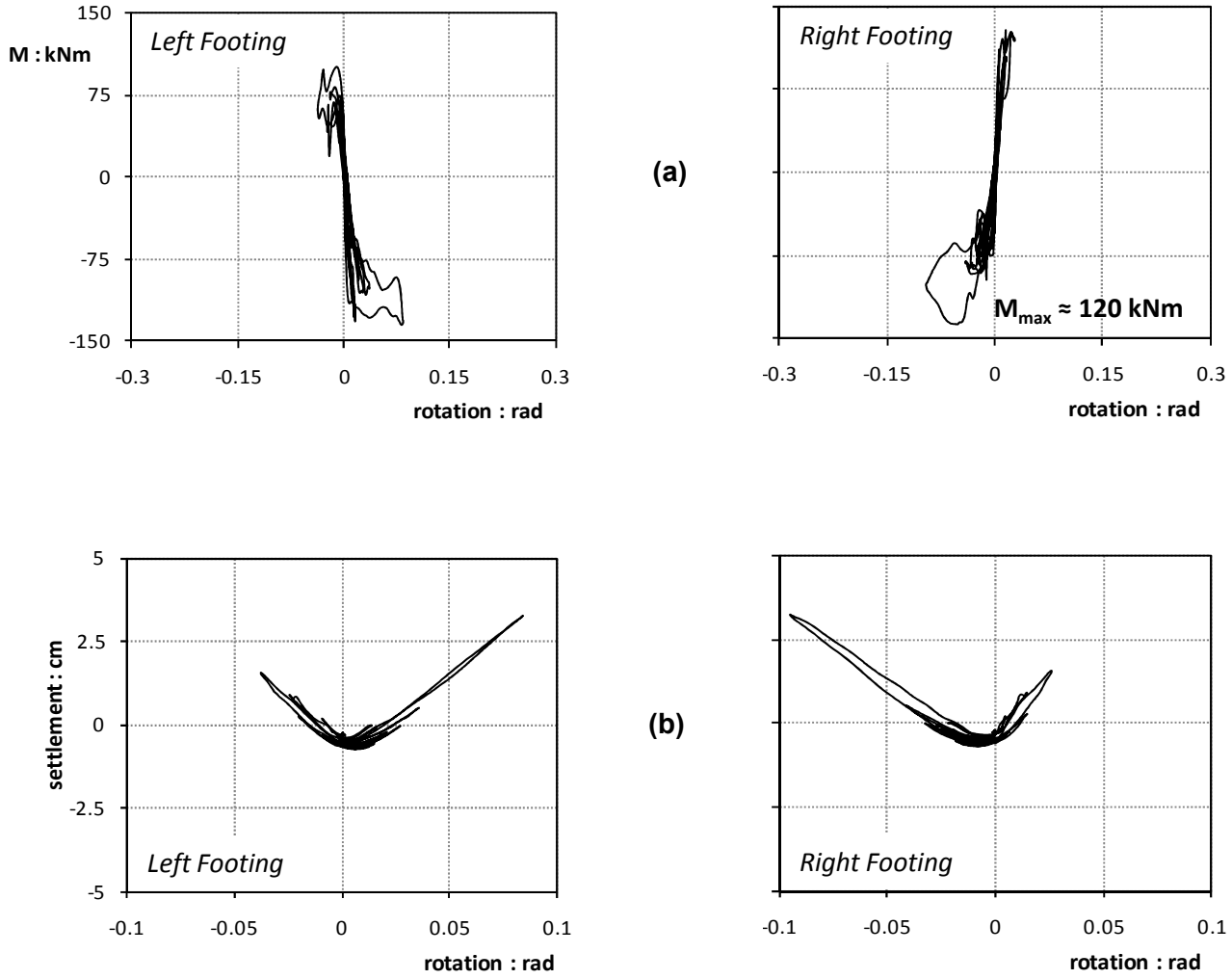

Figure 3.22. Performance of the unconventional foundation system **(*B* = 1.4 m)** that corresponds to SF_V = *5.31* when subjected to a *very strong earthquake scenario* (Takatori000 record) : (a) Overturning Moment – rotation loops and (b) settlement – rotation loops for both footings.

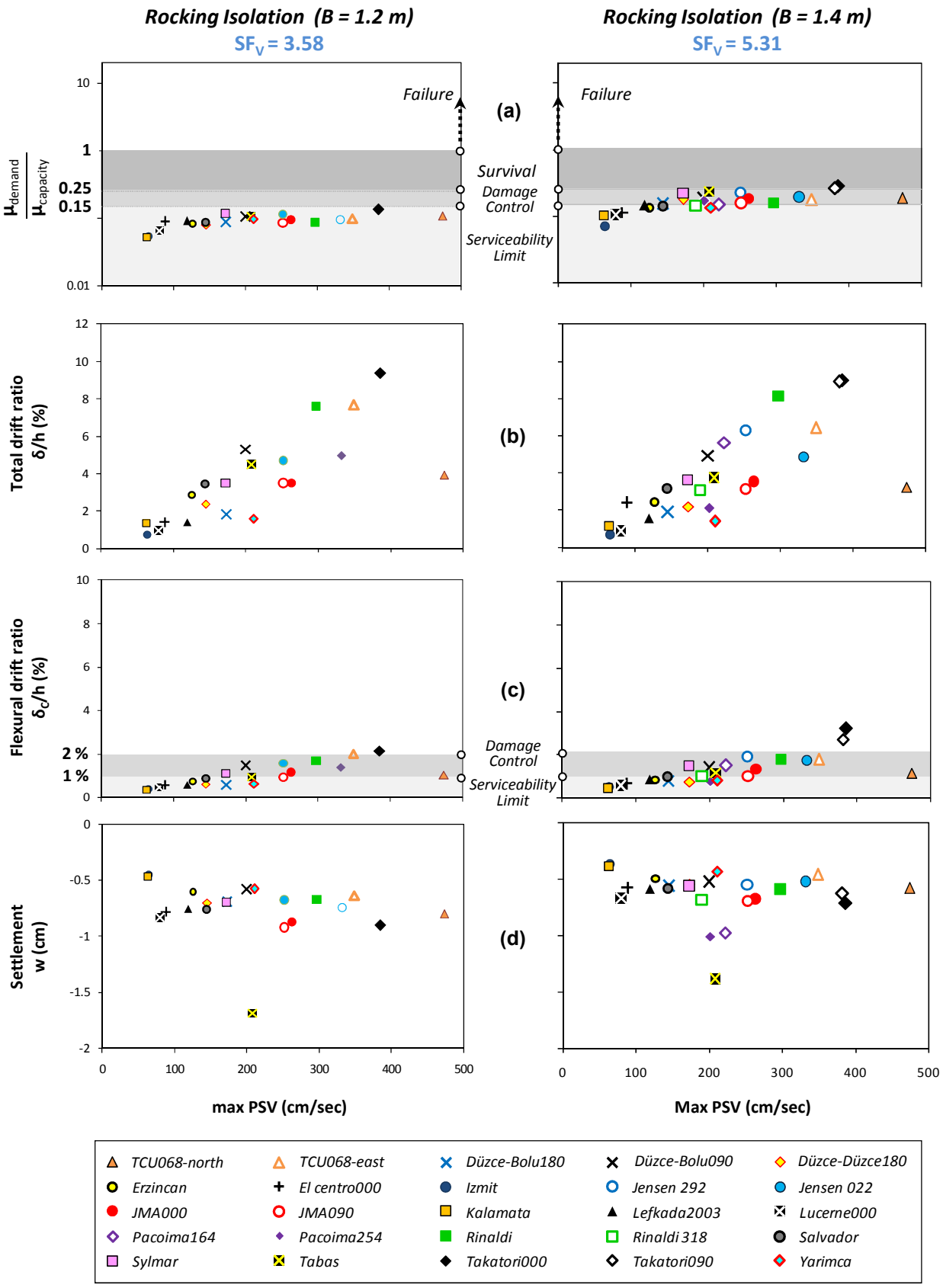

Figure 3.23. Summary of the response of the two un-conservative alternatives (B=1.20 m and B=1.40 m that correspond to SF_V = 3.84 and 5.31 respectively) as a function of the maximum spectral velocity *SV*: (**a**) Column curvature ductility ratio (i.e. ductility *demand* over ductility *capacity).* Damage level is indicated with reference to *Response Limit States* (Priestley et al., 1996) , (b) Total drift ratio for the ground floor δ/h (where h is the height of the ground floor) ; (c) Flexural drift ratio δ_c / h ; and (d) Settlement w.

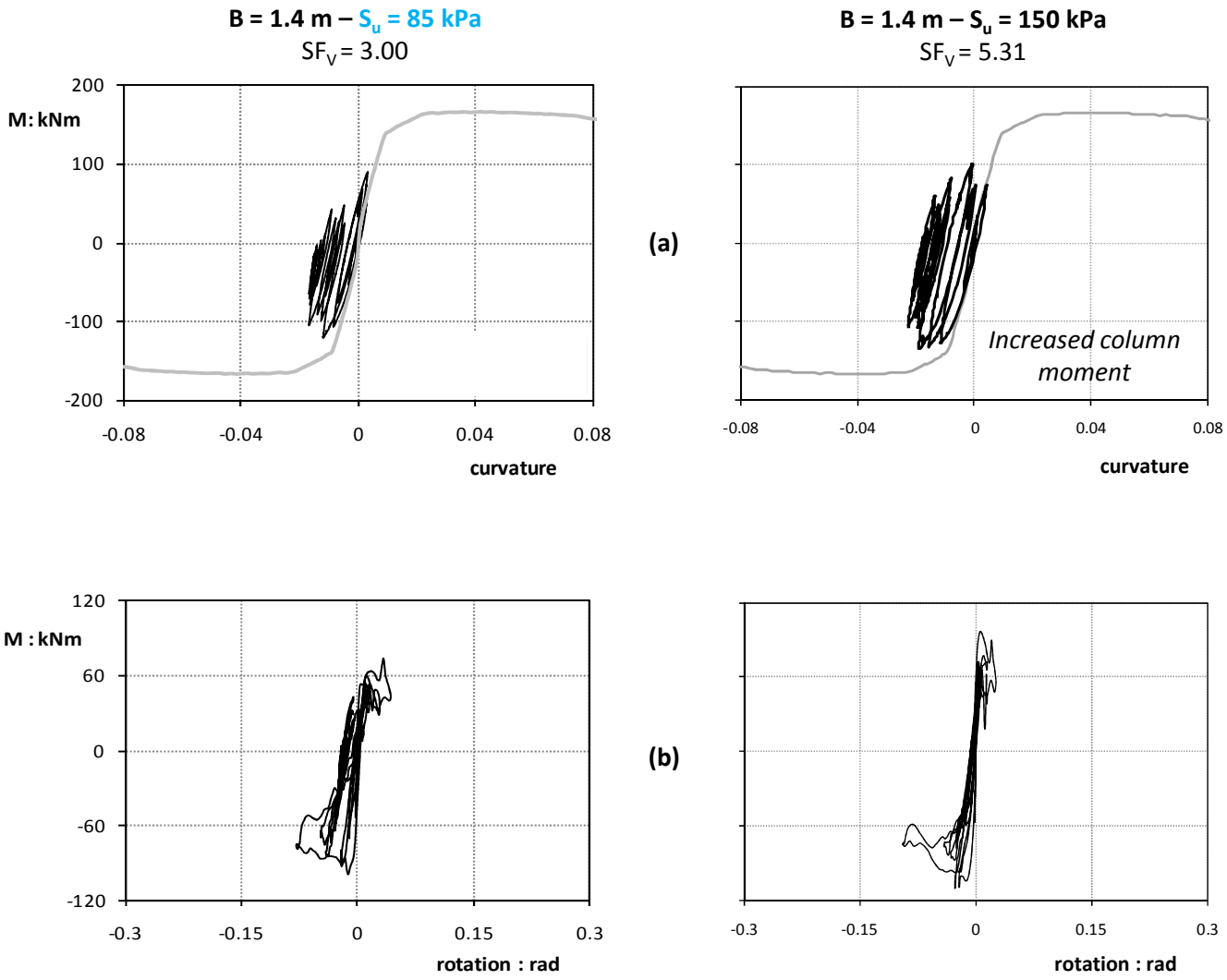

Figure 3.24: Effect of Factor of Safety in the applicability of the rocking isolation concept. Two solutions are compared with FSv = 3.00 (left column) and FSv = 5.31 (right column): (a) Moment – curvature loops and (b) Overturning Moment - footing rotation loops.

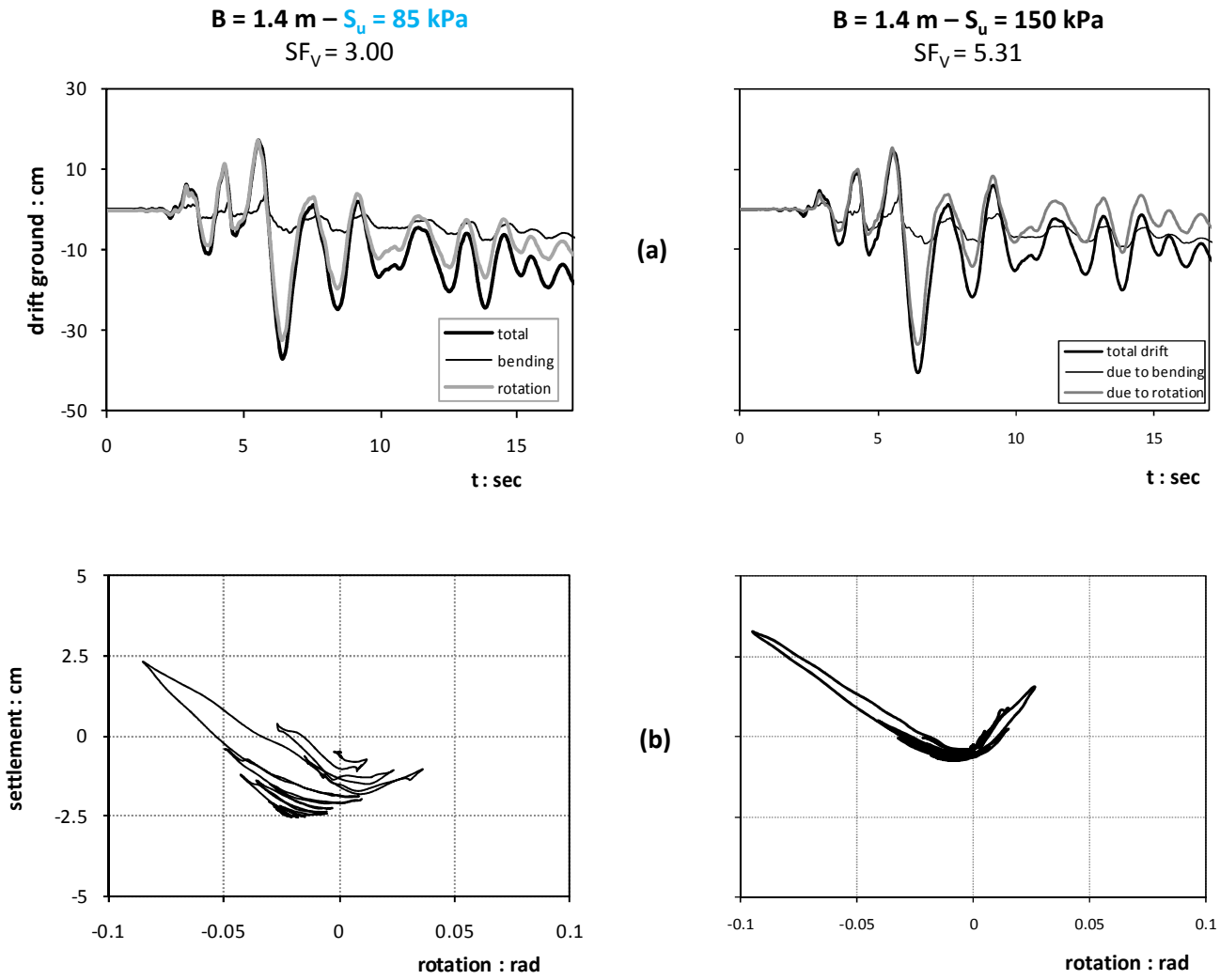

Figure 3.25: Effect of Factor of Safety in the applicability of the rocking isolation concept. Two solutions are compared with FSv = 3.00 (left column) and FSv = 5.31 (right column): (a) time history of ground floor drift and (b) settlement-footing rotation loops.

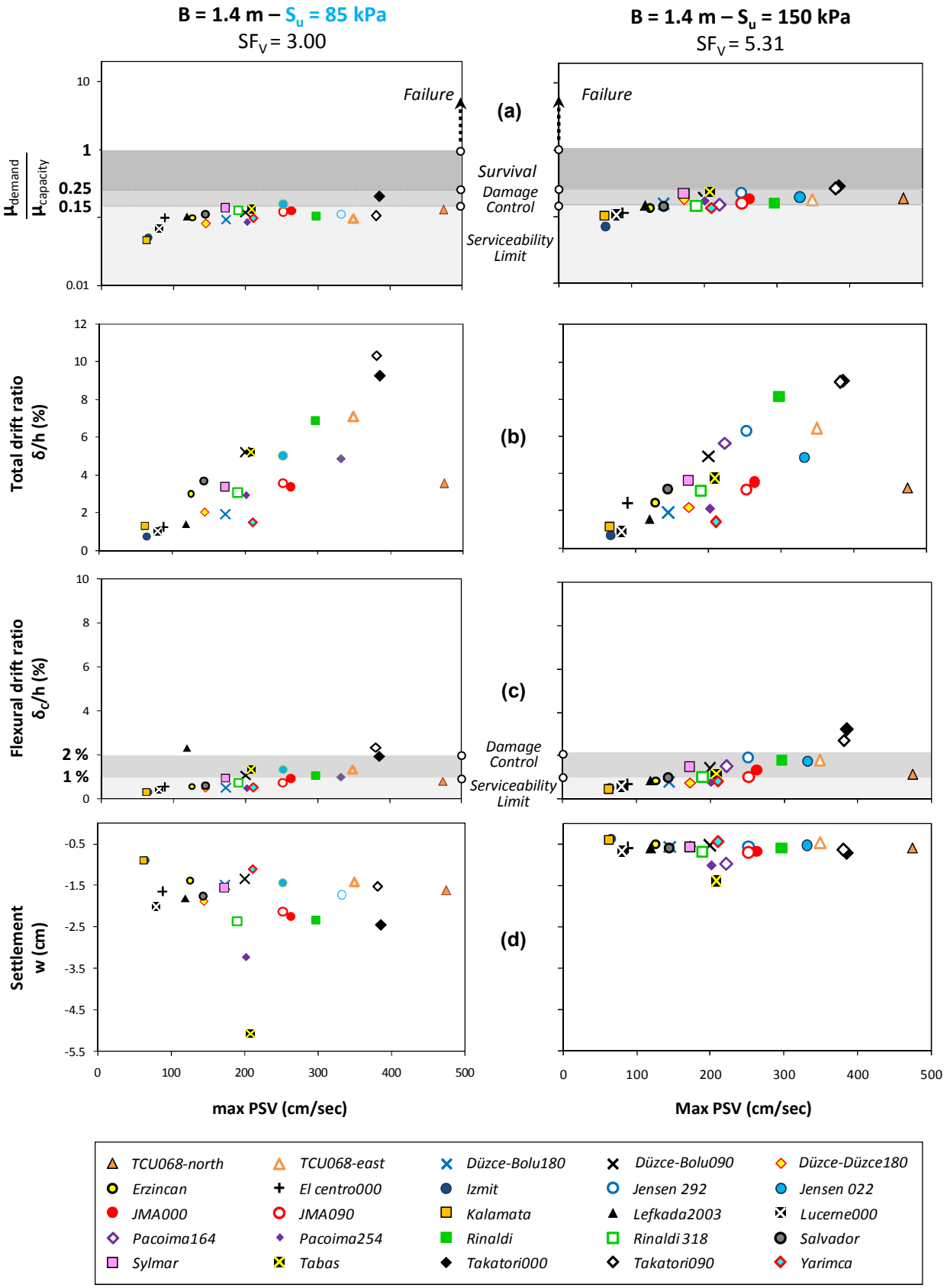

Figure 3.26. Effect of Factor of Safety in the applicability of the rocking isolation concept. Collective results fot two solutions with FS_v = 3.00 (left column) and FSv = 5.31 (right column) respectively as a function of the maximum spectral velocity *SV*: (a) Column curvature ductility ratio (i.e. ductility *demand* over ductility *capacity).* Damage level is indicated with reference to *Response Limit States* (Priestley et al., 1996) , (b) Total drift ratio for the ground floor δ/h (where h is the height of the ground floor) ; (c) Flexural drift ratio δ_c / h ; and (d) Settlement w.

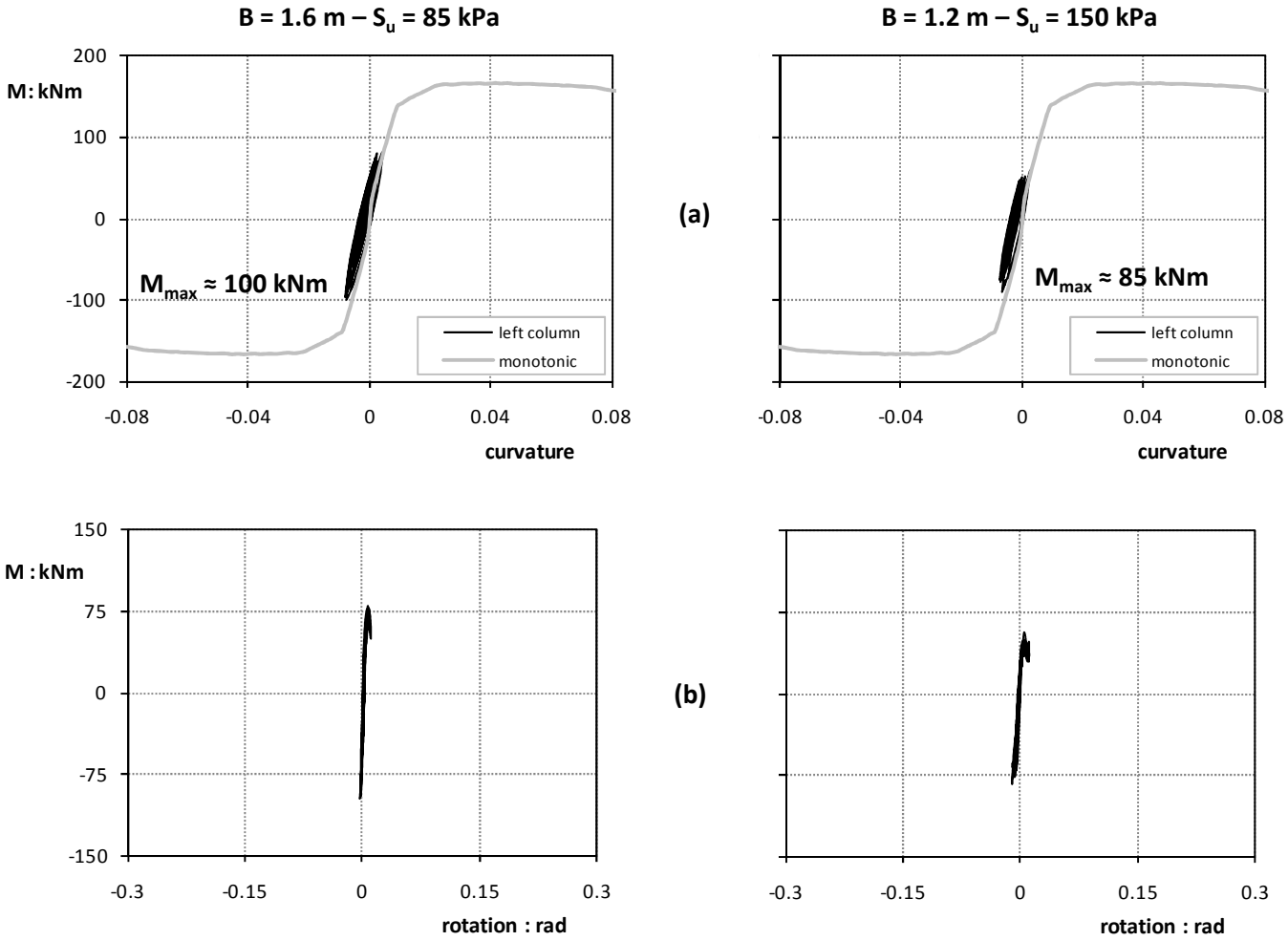

Figure 3.27: The effect of soil strength. Two footing alternatives both of FS_v = 4.0 are compared : Footings of B=1.6 m on a Su = 85 kPa ground (left column) and footings of B=1.2 m on a Su = 150 kPa ground (right column). Results are presented in terms of (a) Moment – curvature loops and (b) Overturning Moment - footing rotation loops when the frames are subjected to the moderate *El Centro recor*d (1940).

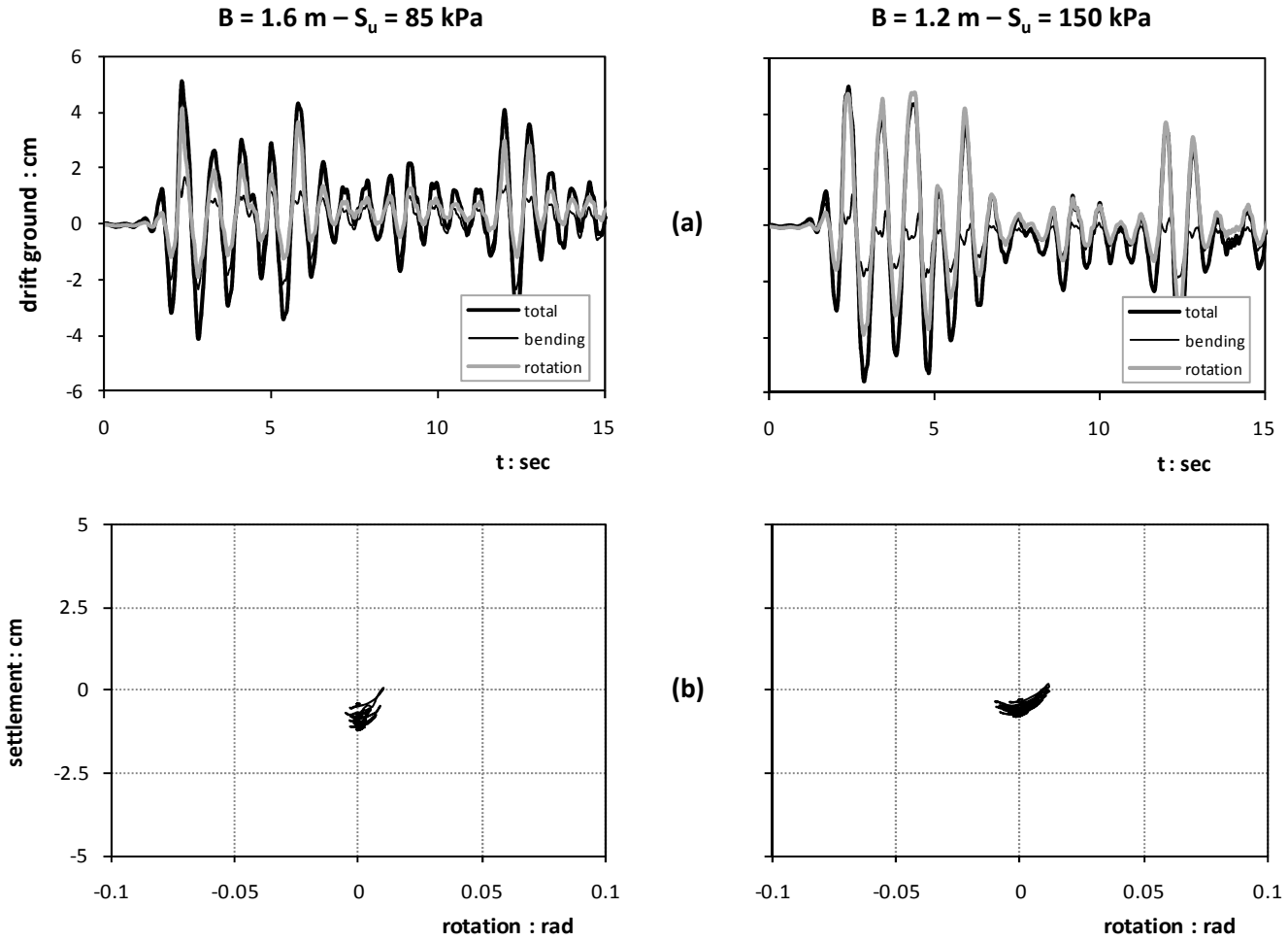

Figure 3.28: The effect of soil strength. Two footing alternatives both of FS_v = 4.0 are compared : Footings of B=1.6 m on a Su = 85 kPa ground (left column) and footings of B=1.2 m on a Su = 150 kPa ground (right column). Results are presented in terms of (a) time history og ground floor drift and (b) settlement-footing rotation loops when the frames are subjected to the moderate *El Centro record* (1940).

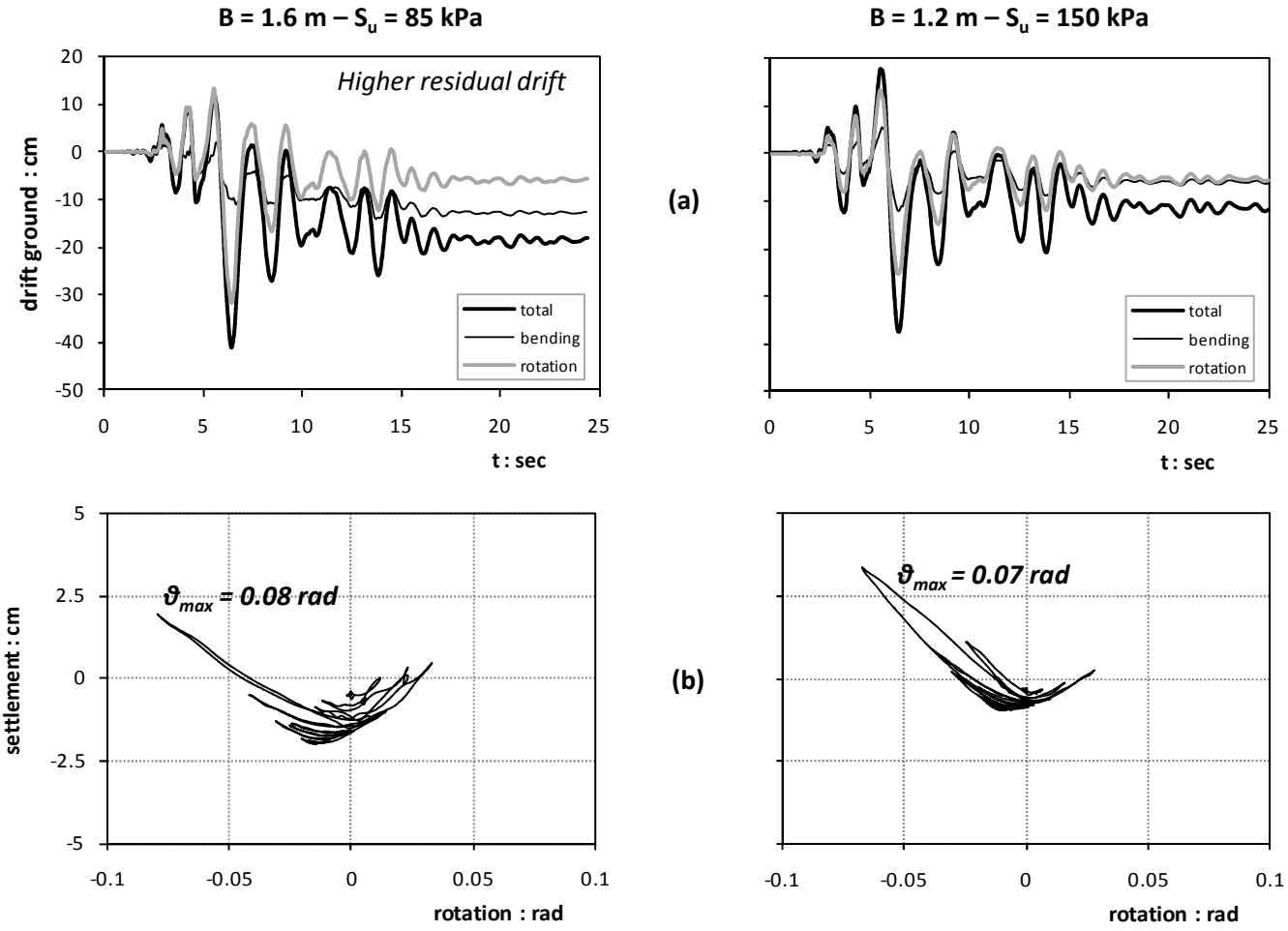

Figure 3.29: The effect of soil strength. Two footing alternatives both of FS_v = 4.0 are compared : Footings of B=1.6 m on a Su = 85 kPa ground (left column) and footings of B=1.2 m on a Su = 150 kPa ground (right column). Results are presented in terms of (a) time history og ground floor drift and (b) settlement-footing rotation loops when the frames are subjected to the moderate *El Centro record* (1940).

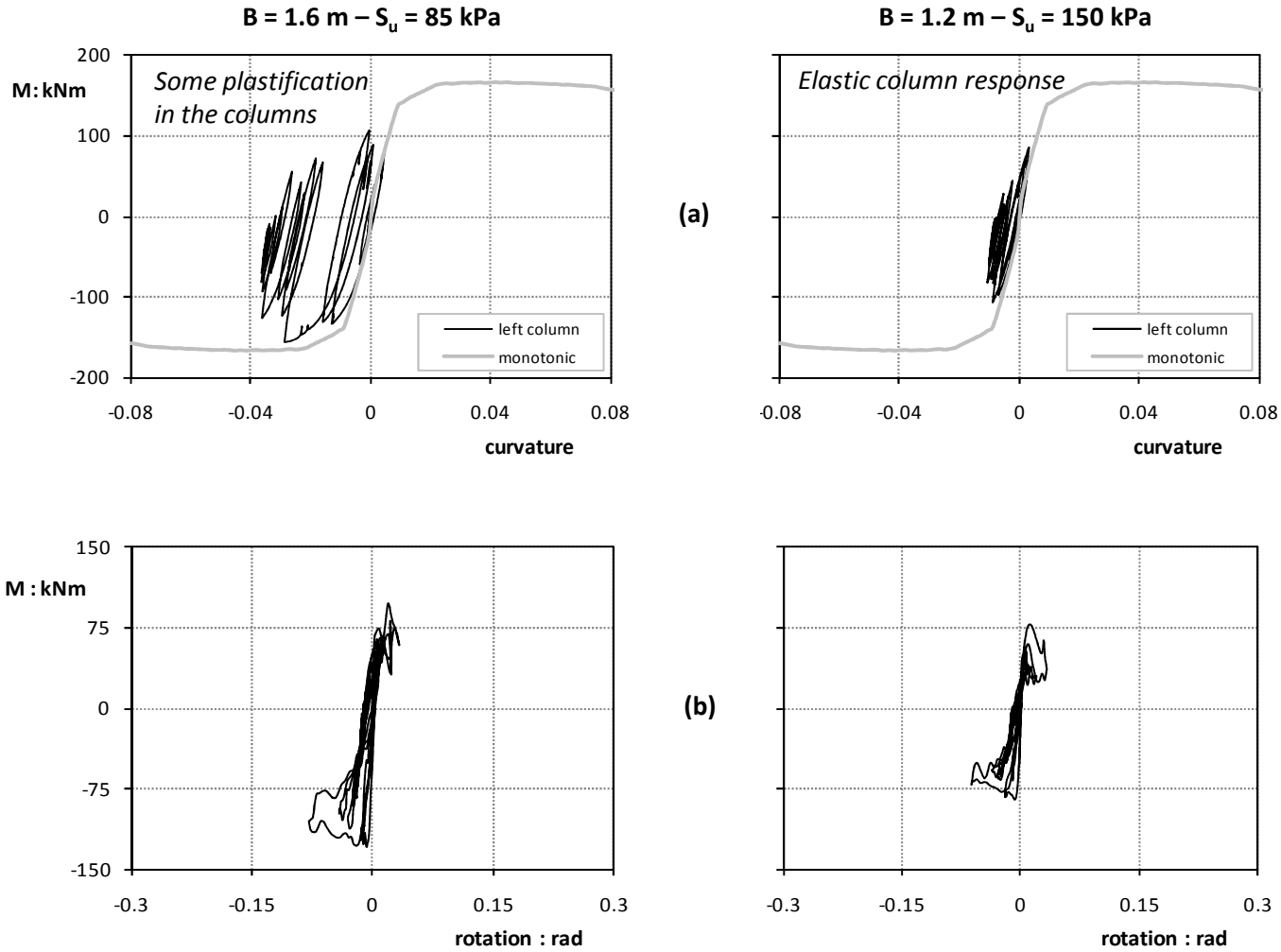

Figure 3.30: The effect of soil strength. Two footing alternatives both of FS_v = 4.0 are compared : Footings of B=1.6 m on a Su = 85 kPa ground (left column) and footings of B=1.2 m on a Su = 150 kPa ground (right column). Results are presented in terms of (a) Moment – curvature loops and (b) Overturning Moment - footing rotation loops when the frames are subjected to the very strong *Takatori000 record* (Kobe, 1995).

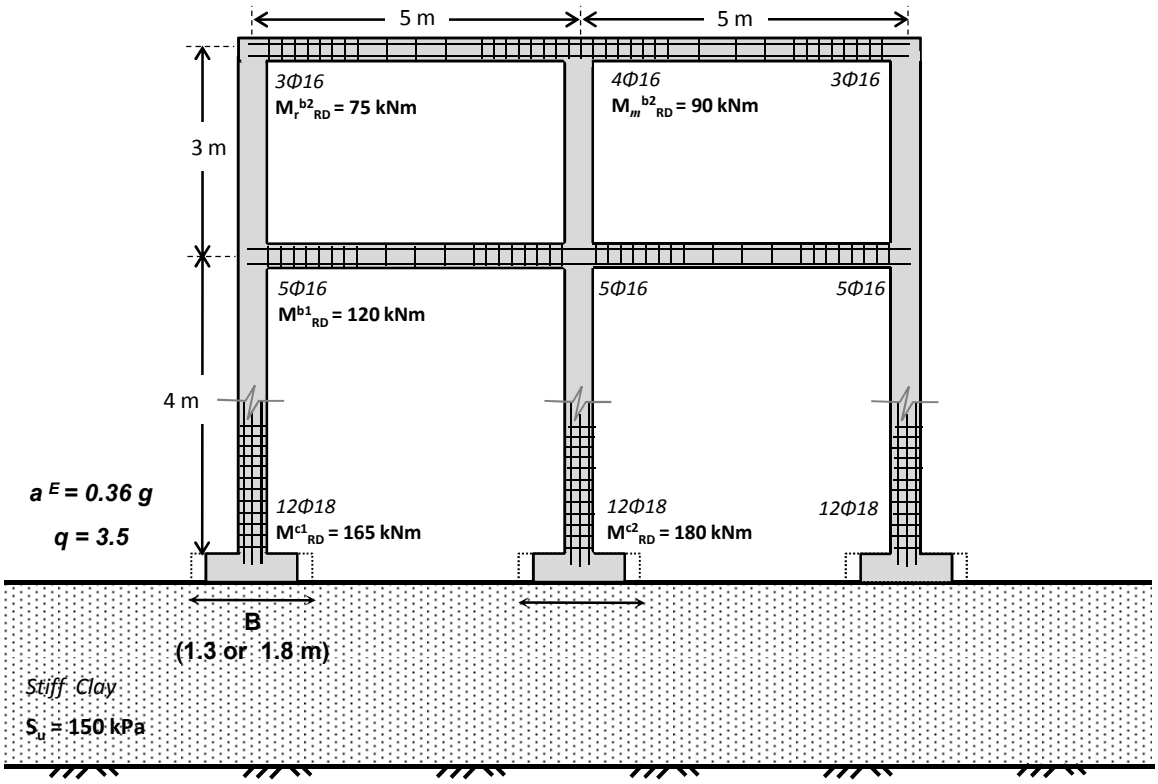

Figure 3.31. Geometry and member properties of the idealized 2-bay 2-storey frame structure analyzed

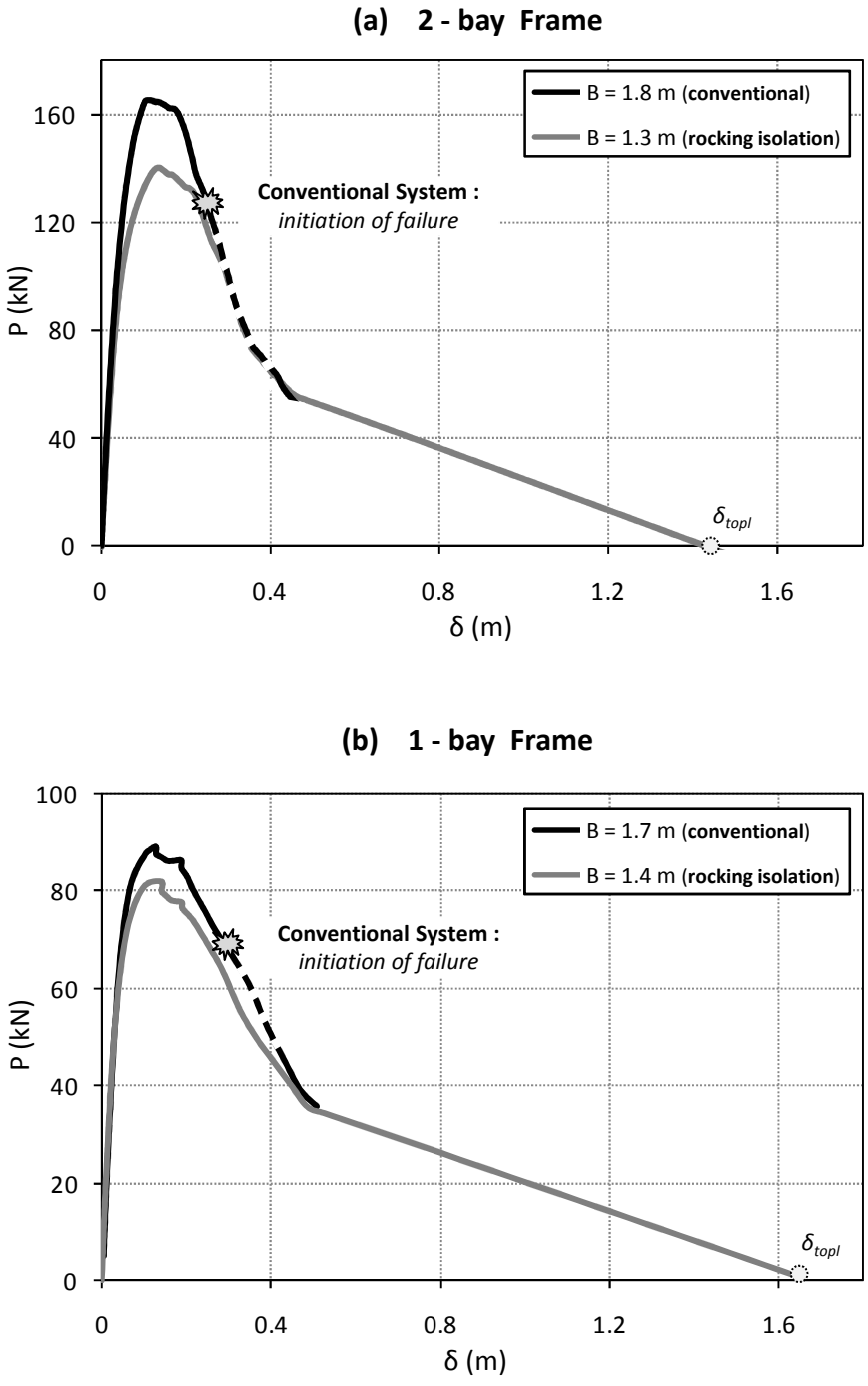

Figure 3.32: 2-bay vs 1-bay Frame: Response to Push-over tests for both conventional (black line) and unconventional (grey line) foundation design.

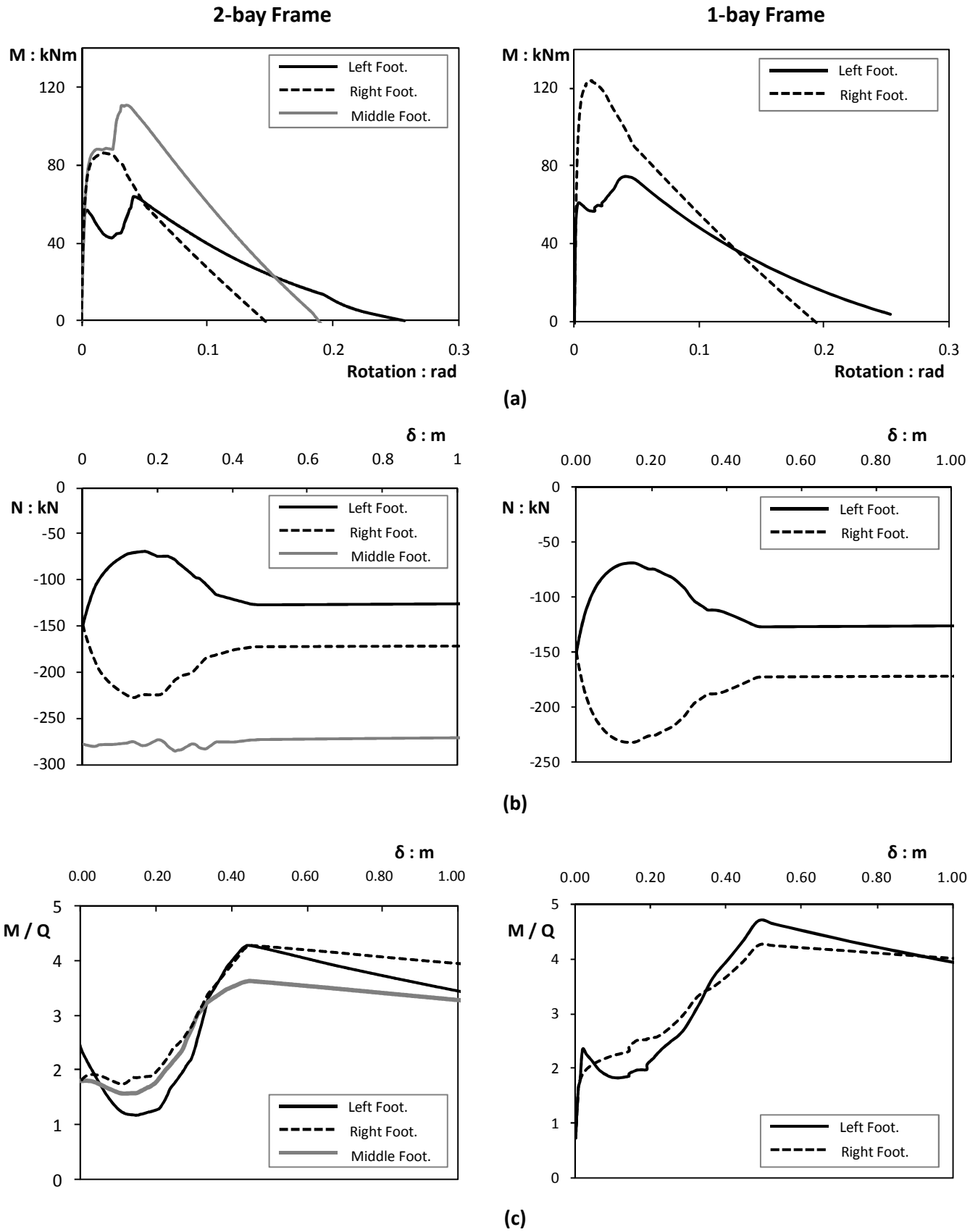

Figure 3.33: Comparative response of 2-bay (left column) and 1-bay frames (right column) under static pushover analysis: (a) Overturning Moment – rotation curves for all footings; (b) evolution of column axial load *N* and (c) M/Q ratio with increasing imposed lateral displacement *δ.*

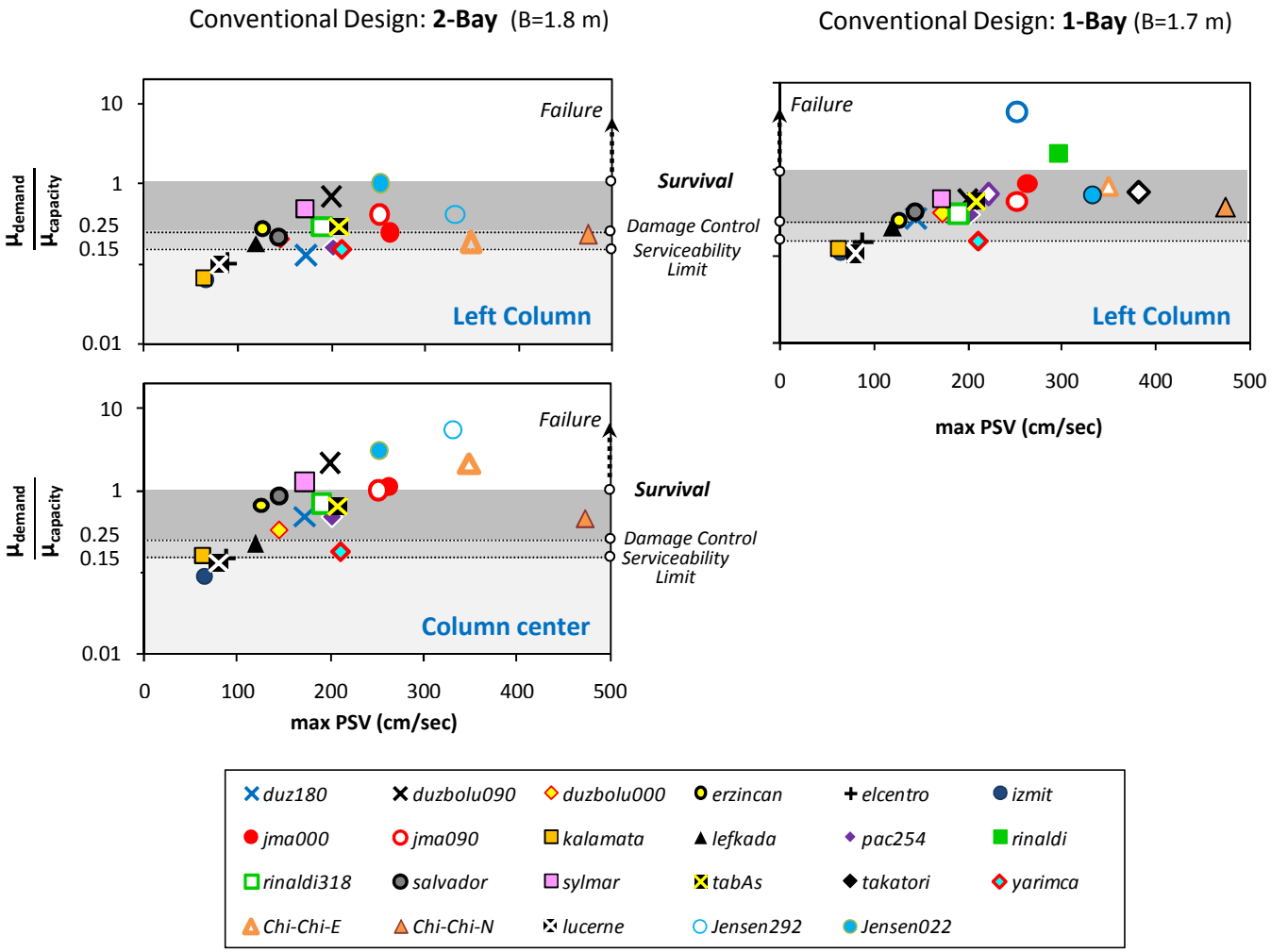

Figure 3.34: Comparative response of 2-bay (left column) and 1-bay frames (right column) both designed conventionally under earthquake loading in terms of column curvature ductility ratio (i.e. ductility *demand* over ductility *capacity).* Damage level is indicated with reference to *Response Limit States* (Priestley et al., 1996).

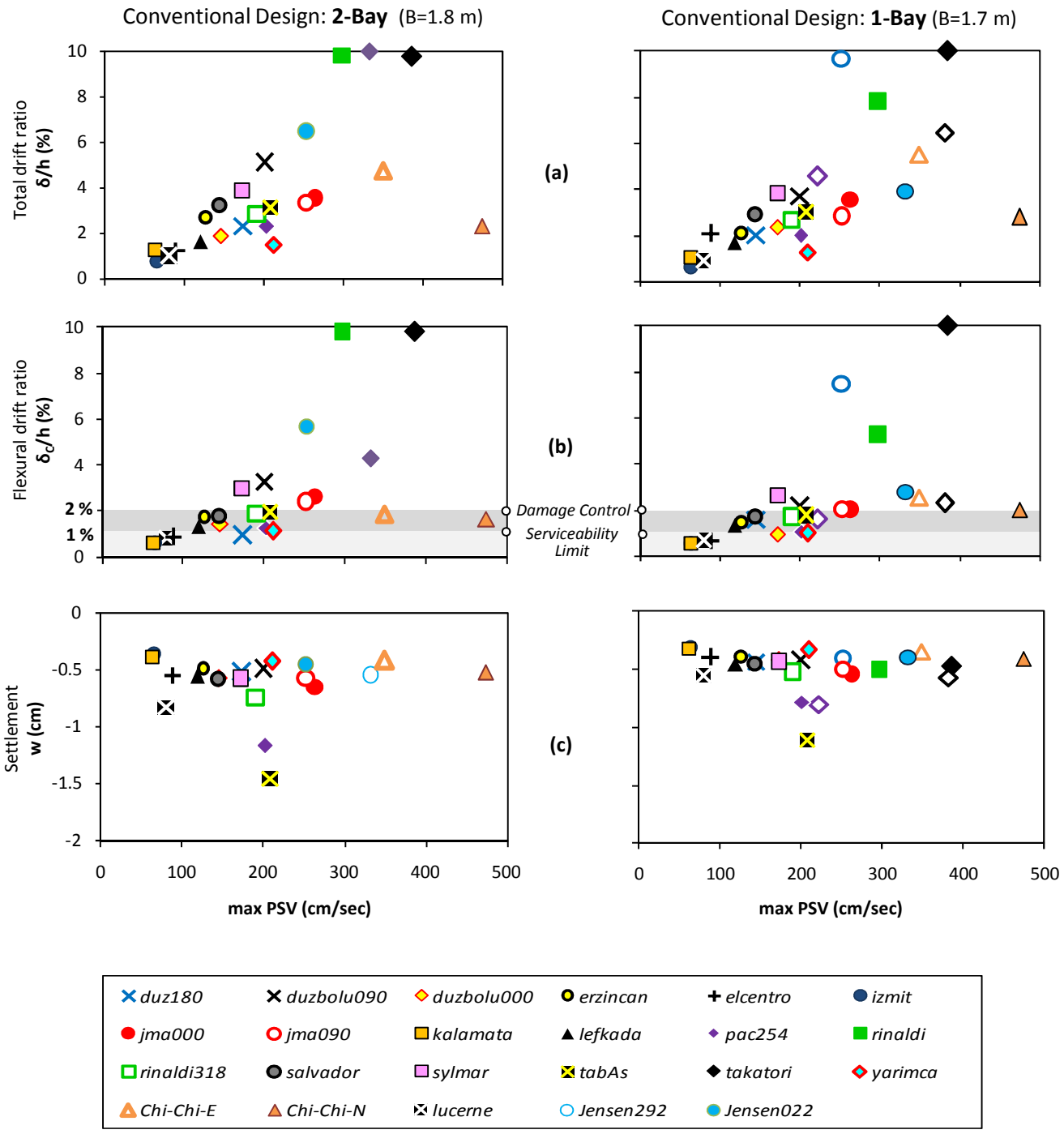

Figure 3.35: Comparative response of 2-bay (left column) and 1-bay frames (right column) both designed conventionally under earthquake loading in terms of (a) Total drift ratio for the ground floor δ/h (where h is the height of the ground floor), (b) Flexural drift ratio δ_c / h , and (c) Settlement w.

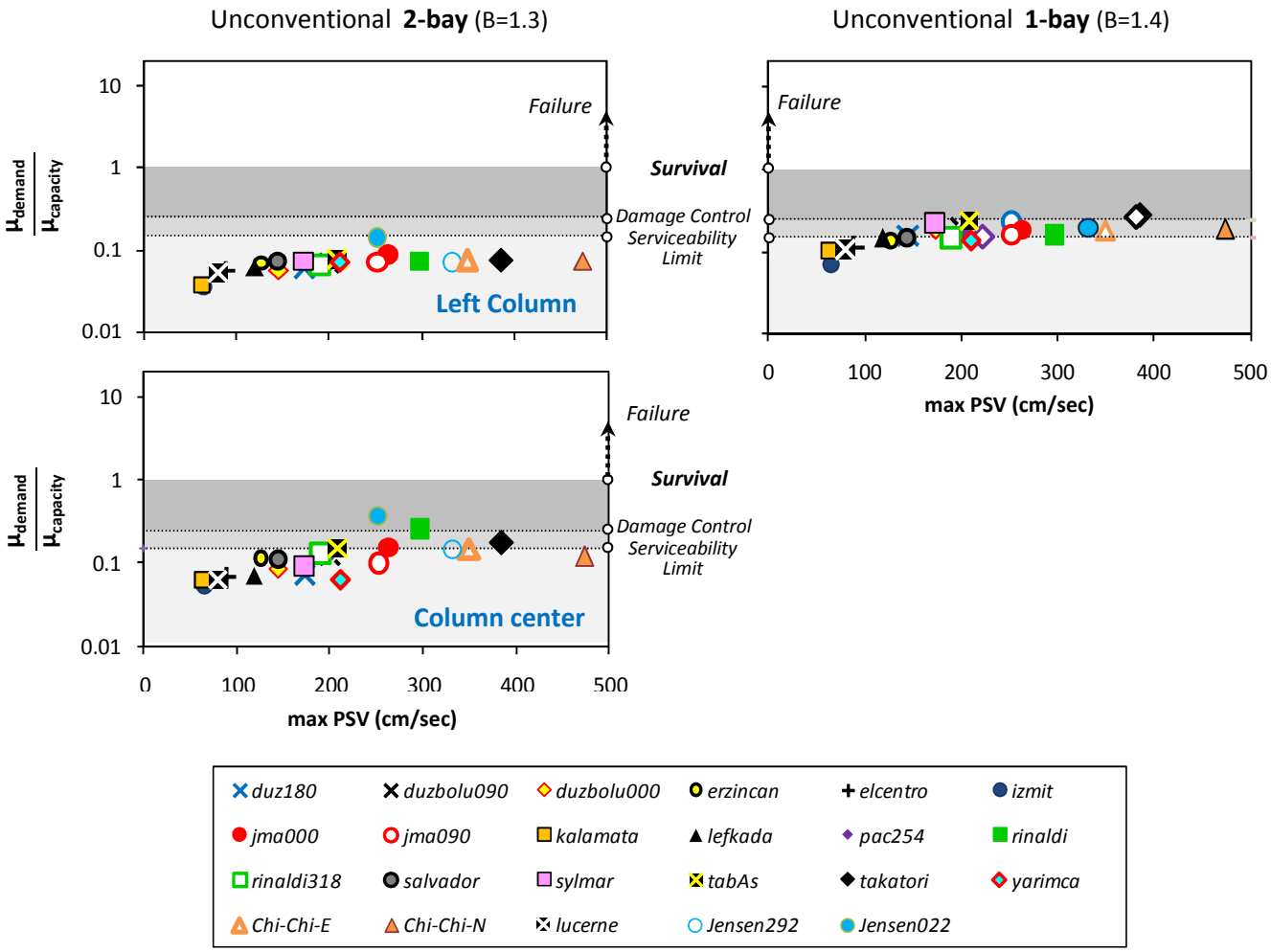

Figure 3.36: Comparative response of 2-bay (left column) and 1-bay frames (right column) both designed following the rocking isolation concept under earthquake loading in terms of column curvature ductility ratio (i.e. ductility *demand* over ductility *capacity).* Damage level is indicated with reference to *Response Limit States* (Priestley et al., 1996).

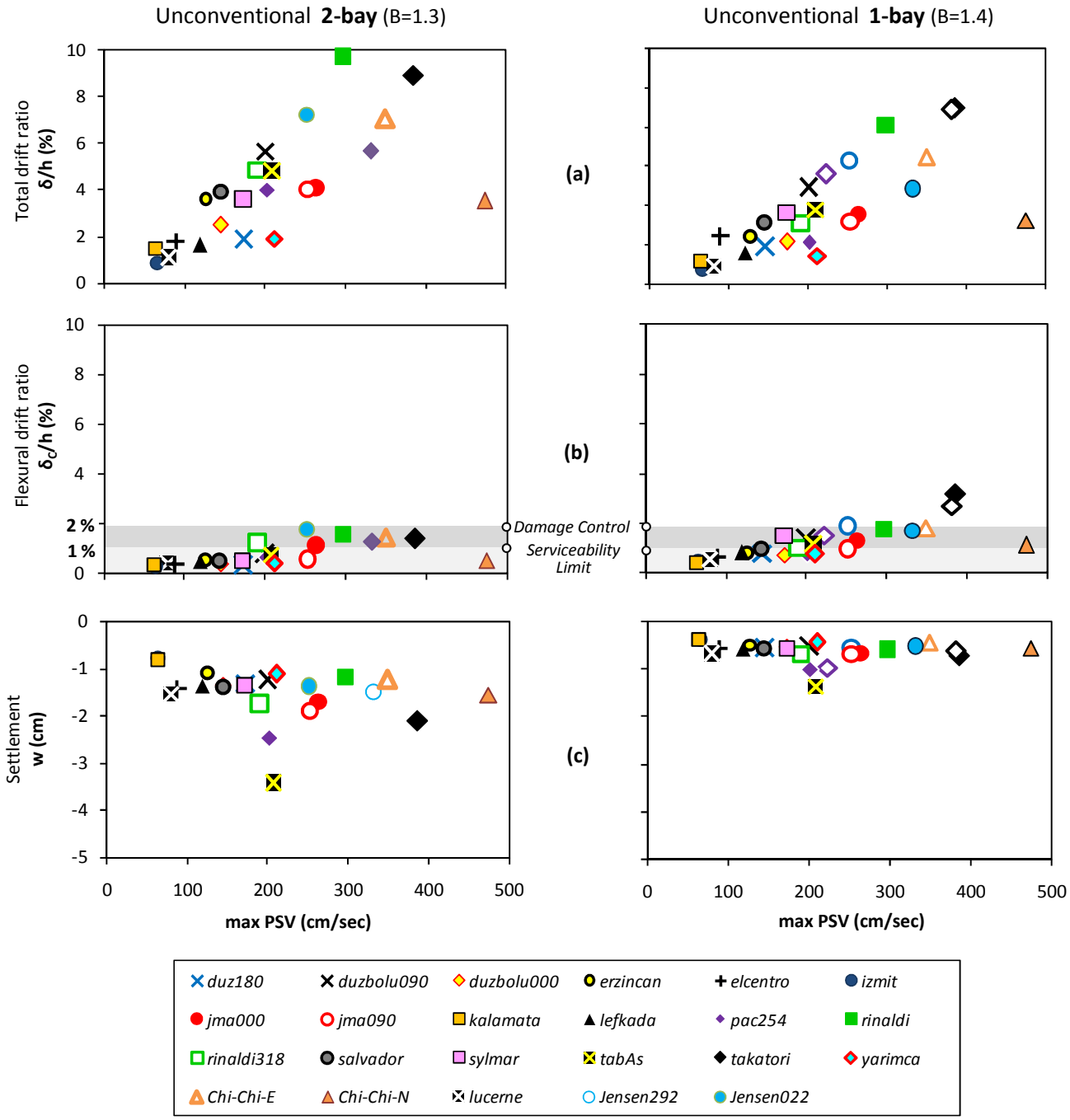

Figure 3.37: Comparative response of 2-bay (left column) and 1-bay frames (right column) both designed following the rocking isolation concept under earthquake loading in terms of (a) Total drift ratio for the ground floor δ/h (where h is the height of the ground floor), (b) Flexural drift ratio δ_c / h , and (c) Settlement w.

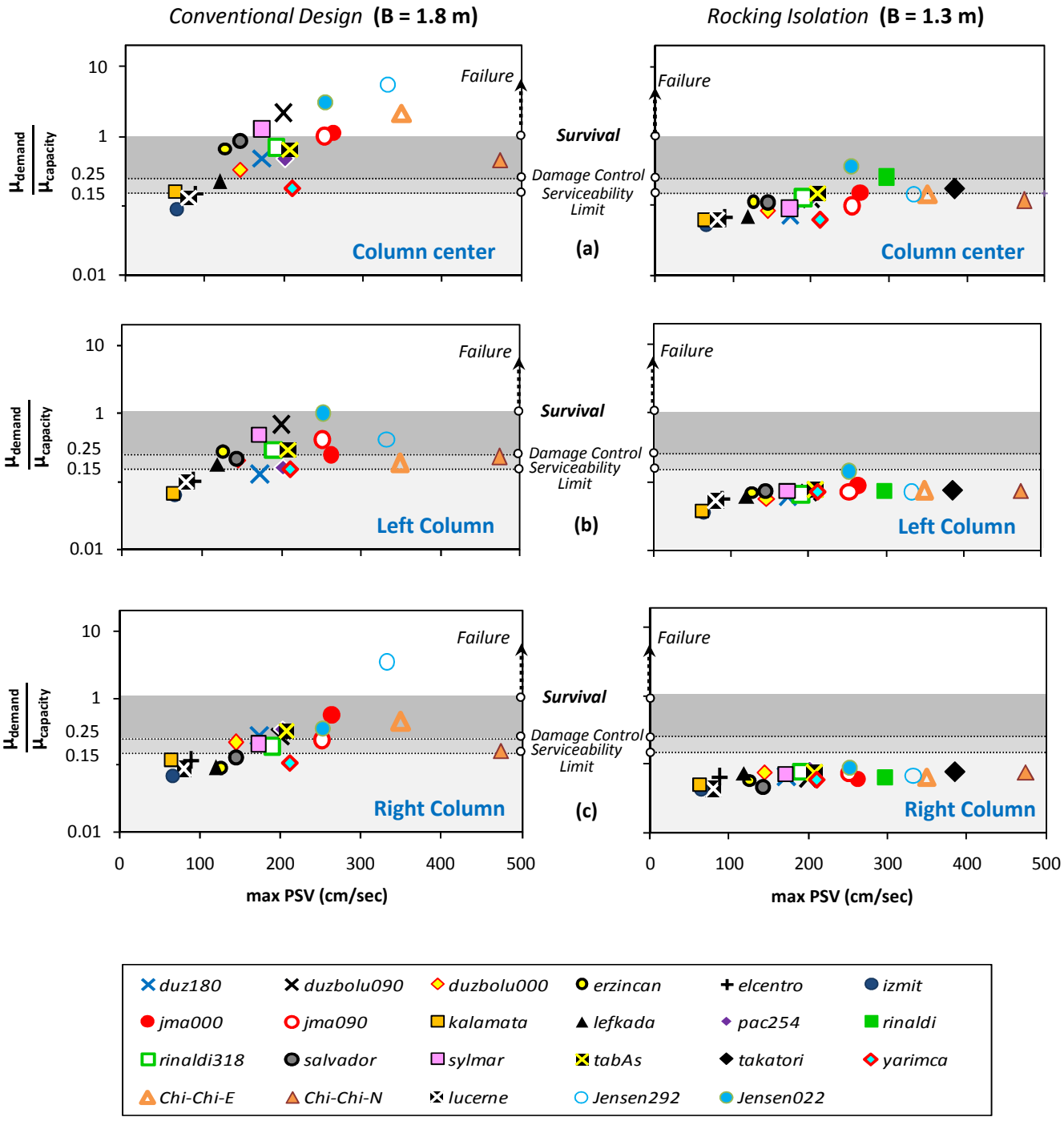

Figure 3.38. Summary of the response of the two design alternatives when applied to 2-bay frames as a function of Column curvature ductility ratio (i.e. ductility *demand* over ductility *capacity).* Damage level is indicated with reference to *Response Limit States* (Priestley et al., 1996)

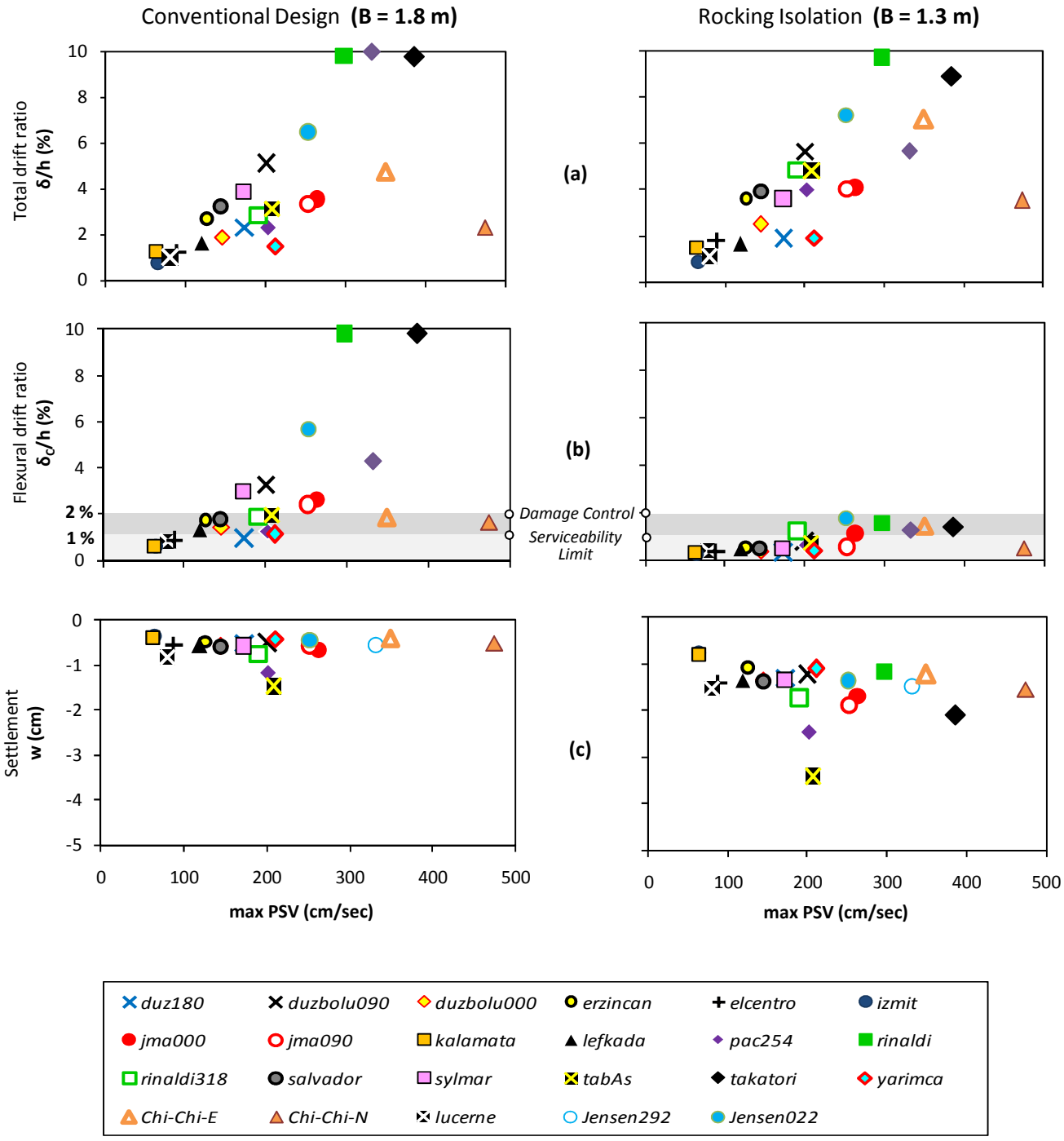

Figure 3.39. Summary of the response of the two design alternatives when applied to 2-bay frames as a function of : (a) Total drift ratio for the ground floor δ/h (where h is the height of the ground floor) ; (b) Flexural drift ratio δ_c / h ; and (c) Settlement w.

4

Simplified Method for Foundation Design of Rocking–isolated Frames

4.1. Introduction

Due to the *kinematic* and *cyclic* nature of earthquake loading, uplifting and mobilization of foundation bearing capacity under severe seismic shaking do not necessarily lead to failure [Pecker, 1998; Makris & Roussos, 2000; Pecker & Pender, 2000; Kutter et al., 2003; Gajan et al., 2005; Harden & Hutchinson, 2006; Paolucci et al., 2008; Kawashima et al., 2007]. In fact, recent research suggests that such strongly nonlinear mechanisms may be beneficial and should be taken into account for the seismic design and retrofit of structures [Martin & Lam,

2000; Pecker, 2003; FEMA-356, 2000; Kutter et al. 2001; Gazetas et al., 2003; Gajan et al., 2005; Mergos & Kawashima, 2005; Gajan & Kutter, 2008; Gajan et al., 2008].

Taking advantage of the above, a new seismic design philosophy was introduced in Anastasopoulos et al. [2010a], guiding the plastic "hinge" from the superstructure to the soil-foundation interface (i.e., exactly the opposite of conventional capacity design). This way, instead of over-designing the foundation to ensure that inertia forces can be transmitted to the superstructure, the foundation is intentionally under-designed to yield, *mainly in the form of foundation rocking and uplifting*, acting as “rocking isolation”. Using a simplified bridge structure as an illustrative example, it was shown that such design philosophy may provide increased safety levels (i.e. avoidance of collapse), with the price to pay being mainly in the form of increased dynamic settlement.

The effectiveness of such *rocking isolation* design philosophy was further investigated in the previous Chapter for a simplified 2-storey 1-bay frame (**Figure 4.1**). The seismic performance of a conventionally designed structure (with larger over-designed footings, **Figure 4.1a**) was compared to a rocking-isolation alternative (with smaller under-designed footings, **Figure 4.1b**). Through static pushover and nonlinear dynamic time-history analysis (using an ensemble of 24 strong motion records), the performance of the rocking−isolated alternative was found to be advantageous for very strong seismic shaking, well in excess of the design limits. In contrast to the conventionally designed structure, which collapsed in 3 out of 24 earthquake scenarios and sustained irreparable damage in all other cases, the rocking−isolated structure survived all seismic excitations sustaining minor to repairable column damage, but non-negligible damage to its beams and non-structural elements (infill

walls, etc.). Interestingly, (at least for the cases examined) dynamic settlement was shown not to be an issue, provided that the static safety factor of the under-designed footing is adequately large : $SF^s > 5$.

While in conventional capacity design (**Figure 4.1a**) the footings have to be large enough so that their moment capacity M_{ult} is larger than that of the columns M^{RD}, in the case of rocking isolation (**Figure 4.1b**) they are *under-designed* so that $M_{ult} < M^{RD}$. The under-strength of the foundation will depend on the *Capacity Reduction Factor (CRF)*, which is defined as :

$$CRF = M_{ult}/M^{RD} \tag{4.1}$$

For a given structure, the increase of *CRF* leads to a reduction of M_{ult}, and hence, more effective rocking isolation. But, unfortunately, such increased isolation effectiveness is directly associated with a decrease of the static safety factor SF^s , thus leading to increased foundation rotation and risk of toppling. On the other hand, the decrease of *CRF* is not only reducing the effectiveness of rocking isolation, but also increases the risk of M_{ult} actually becoming larger than M^{RD}. Such risk is not only associated with the uncertainties in the estimation of soil and superstructure strength, but also with dynamic footing overstregths [Gelagoti et al., 2010]. Hence, the optimum footing width will have to ensure an adequately large *CRF* (i.e. adequately reduced foundation capacity) so that $M_{ult} < M^{RD}$, while maintaining an adequate margin of safety against toppling.

To this end, this section develops a simplified procedure to estimate the range of optimum (or acceptable) footing width.

4.2. Problem Definition and Analysis Methodology

As depicted in **Figure 4.2a**, the problem investigated herein refers to an idealized 5 m wide and 7 m high 2-storey reinforced concrete building. The structure was designed with a conventional structural analysis software, in accordance with EC8 [2000] and the Greek Seismic code [EAK 2000], for design acceleration a_d = 0.36 g and behavior factor q = 3.5. The geometric characteristics and main member properties are shown in **Figure 4.2a**. More details can be found in the previous chapter discussion.

For conventional capacity design, the footings would have to be over-designed so that $M_{ult} > M^{RD}$, achieving safety factors for static and seismic loading $SF^S \geq 3$ and $SF^E \geq 1$, respectively, and eccentricity $e < B/3$ (where B is the footing width). As already discussed, with e being critical, the conventionally required footing width is B = 1.7 m and the resulting safety factors SF^S = 8 and SF^E = 1.93. In the case of rocking isolation design, the footing is intentionally under-designed to uplift, "guiding" the plastic hinge from the base of the column to the soil–foundation interface. While the eccentricity criterion is relaxed (i.e. $e > B/3$ is allowed) and $SF^E < 1$ is pursued, the static factor SF^S has to be greater than 3 so that the footing is not subjected to sinking but uplifting response. The latter is definitely preferable, since the dynamic settlement is substantially reduced [Kutter et al., 2001; Pecker & Pender, 2005; Chatzigogos et al., 2009].

Based on the above design criteria, **Table 4.1** summarizes the allowable footing widths, along with their corresponding moment capacities M_{ult} [calculated according to Gourvenec, 2007], static safety factor SF^S, and capacity reduction factor CRF. Since the column axial load N fluctuates substantially during seismic loading due to frame action [Gelagoti et al., 2010],

all of the above are computed for the static column axial load N = 151 kN, and its maximum value (computed through static pushover analysis) N_{max} = 232 kN. According to the above, the allowable footing width B ranges from 1.6 m (with SF^S = 7 and CRF ranging from 1.2 to 1.6) to 1.1 m (with SF^S = 3.2 and CRF ranging from 2.4 to 3.3).

Before proceeding, it should be noted that the whole rocking-isolation concept relies on foundation under-design, i.e. reduction of its width B. As previously discussed, this is feasible for the typical frame analyzed simply because the eccentricity criterion is critical. For a short structure (such as a 1-storey frame), the response of which is shear-dominated, in the absence of substantial moment M acting on the footing, the $e \leq B/3$ criterion may not be the one controlling foundation design. In such cases, the safety factor may be critical and the rocking-isolation concept will not be applicable.

The problem is analyzed through the finite element (FE) method. Assuming plane-strain conditions, a representative equivalent "slice" of the soil−structure system is analyzed, with due consideration to material (soil *and* superstructure) and geometric (*uplifting* and *P-Δ effects*) nonlinearities. Although the problem is definitely 3 dimensional, 3D modeling would be computationally inefficient. Hence, the 2D numerical model is rendered equivalent to the 3D problem through application of a shape factor of 1.2 (square foundation) to the soil "slice" of the model. The validity of such equivalence has been demonstrated in the preceding. Soil and footings are modeled with quadrilateral plane strain continuum elements, nonlinear and elastic, respectively. Nonlinear beam elements are used for the superstructure, which is connected to the soil through an interface, which allows detachment and sliding. Free-field boundaries are used at the two lateral boundaries of the

model, allowing for realistic kinematic soil response. The dynamic response of the system is analyzed through nonlinear dynamic time history analysis, applying the seismic excitation at the base of the model.

Soil behavior is modeled through a kinematic hardening model with Von Mises failure criterion and associated flow rule. In Anastasopoulos et al. [2010b], the model was modified to be applicable for sands (extended pressure-dependent Von Mises), and validated against centrifuge and large scale tests. Despite its simplicity, the model was shown to predict well the cyclic response of footings in clay and sand. The model is breifly described in the sequel, while more details can be found in Anastasopoulos et al. [2010b].

The pressure-independent yield surface of the model is defined through the following function F :

$$F = f(\sigma - \alpha) - \sigma_0 \tag{4.2}$$

where σ_o is the stress at zero plastic strain, and α the *backstress*, which defines the kinematic evolution of the yield surface in the stress space. σ_o controls the initiation of non-linear behaviour, and is defined as a fraction λ of the yield stress σ_y :

$$\sigma_o = \lambda \sigma_y \tag{4.3}$$

For clay under undrained conditions, σ_y can be defined as follows :

$$\sigma_y = \sqrt{3} S_u \tag{4.4}$$

The evolution law of the model consists of a *nonlinear kinematic* and an *isotropic* hardening component. The evolution of the kinematic component is described as :

$$\dot{\alpha} = C \frac{1}{\sigma_0} (\sigma - \alpha) \dot{\varepsilon}^{pl} - \gamma \alpha \dot{\varepsilon}^{pl} \tag{4.5}$$

where $\dot{\bar{\varepsilon}}^{pl}$ the equivalent plastic strain rate, $C = \sigma_y / \varepsilon_y$ is the small strain Young's modulus, and γ a parameter that determines the rate of decrease of the kinematic hardening with the increase of plastic strain.

The small strain Young's modulus C can be directly computed from shear wave velocity V_s , or estimated through empirical correlations [e.g. Hardin & Richart, 1963; Seed et al., 1986; Mayne & Rix, 1993] as a function of σ_y :

$$C = \alpha \, \sigma_y \tag{4.6}$$

where a ranges from 150 to 1000 for clays (i.e. E = 300S_u to 1800S_u). Since $\sigma_y = C/\gamma + \sigma_o$, parameter γ can be expressed as [Gerolymos et al., 2005a] :

$$\gamma = \frac{C}{\sqrt{3} S_u - \sigma_0} \tag{4.7}$$

The nonlinear moment–curvature response of reinforced concrete (RC) members is modeled employing the same constitutive model, after proper adaptation [Gerolymos et al., 2005a]. To this end, the moment–curvature response of superstructure members is first computed through static section analysis employing the X-tract 2000 software [Imbsen Assoc. & Chadwell, 2004]. Then model parameters are calibrated to match the target moment–curvature response. For a rectangular RC member of width d_b and height d_h , the yield stress σ_y can be defined as :

$$\sigma_y = \frac{4 M_y}{d_b \, d_h^2} \tag{4.8}$$

The residual bending moment is assumed equal to 30% of the bending moment capacity [Vintzilaiou et al., 2007]. To capture this softening response, a user subroutine was encoded

in ABAQUS. Parameters λ and α of the model are calibrated through numerical simulation of the static push-over test. **Figure 4.2b** illustrates the monotonic and dynamic pushover response of ground floor columns and beams. Evidently, according to the principles of capacity design, column strength is larger than that of beams. The column curvature ductility μ_φ = 10, corresponds to the medium ductility class according to the EC8, as shown in the previous Chapter.

4.3. Insight on the Seismic Behavior of the Rocking-Isolated Structure

As summarized in **Table 4.1**, taking into account of the necessity for $SF_S \geq 3$ (to ensure uplifting−dominated response), the footing width B may range from 1.6 m to 1.1 m (further reduction will result in unacceptable SF_S). However, as previously discussed, two contradicting criteria need to be simultaneously satisfied : (i) the footing width B needs to be *small enough*, so that its moment capacity M_{ult} is adequately smaller than the corresponding capacity of the column M^{RD} (taking account of uncertainties in estimation of soil and superstructure strength, and dynamic footing overstregths) ; and (ii) the footing width B has to be *large enough*, so that an adequate margin of safety against toppling is achieved. In other words, there exists a *lower-bound* and an *upper-bound* of footing width B, which will be critical to satisfy the aforementioned criteria. This is further elaborated in the ensuing.

4.3.1. Estimation of the Upper-Bound of the Footing Width

The *upper-bound* refers to the larger possible B that satisfies the criterion of the footing moment capacity M_{ult} being adequately smaller than the column capacity M^{RD}. As

investigated in detail already, M_{ult} and the whole M–ϑ (moment-rotation) response largely depend on dynamic fluctuations of the axial force N and the M/Q (moment to shear) ratio acting on the footings. Such fluctuations are related to the dynamic frame response, and have to be taken carefully into account to define the *upper-bound* of the width B.

Figure 4.3 illustrates the effect of such fluctuations on foundation M–ϑ response (for the frame with B = 1.4 m footings). As shown in **Figure 4.3a**, initially both footings experience equal vertical loads N_o = 151 kN, due to the dead load of the superstructure. As the imposed lateral displacement δ increases, due to the developing frame response, the axial force N acting on footing 1 (left) decreases to N_{min} = 70 kN, while the one acting on footing 2 (right) increases to N_{max} = 231 kN. As illustrated in **Figure 4.3b**, this fluctuation of N has a significant effect in enhancing the moment capacity of footing 2 from its theoretical (i.e. static) value of 101 kNm (for N_o = 150 kN) to $M_{ult,max}$ = 147 KNm (for N_{max} = 231 kN), while it tends to slightly reduce its ultimate rotation ϑ_{ult} ; at the same time, the moment capacity of footing 1 is reduced to $M_{ult,min}$ = 90 KNm due to the decrease of the corresponding axial load (to N_{min} = 70 kN). However paradox as it may appear, the enhancement of M_{ult} is *detrimental* in the context of rocking isolation, since it increases the amount of bending moment that may be transmitted to the superstructure.

As summarized in **Table 4.1**, due to the developing frame response and the associated increase of N, for the investigated frame the maximum moment capacity $M_{ult,max}$ of the footing may exceed by up to 40% the moment capacity M_{ult} calculated considering the initial axial load N_o. Hence, the upper bound B should be estimated on the basis of $M_{ult,max}$ (i.e. for

N_{max}) and not assuming M_{ult} (i.e. for N_o , ignoring frame response), something that can be achieved through static pushover analysis of the structure. In other words, to ensure rocking-isolation effectiveness, the footing has to be small enough so that its $M_{ult,max}$ is *adequately lower* than the moment capacity M^{RD} of the corresponding column. This means (at least for the frame investigated herein) that the capacity reduction factor *CRF* should be at least equal to 2 (see also **Table 4.1**), so that the actual CRF_{max} (i.e. the capacity reduction factor computed on the basis of $M_{ult,max}$) is at least equal to 1.4, a value which allows a reasonable safety margin for the aforementioned uncertainties.

An additional complication may arise from the fluctuation of the *M/Q* ratio with imposed lateral displacement δ (**Figure 4.3c**). Initially, before the development of plastic hinging, *M/Q* ≈ 2.4 being roughly equivalent to what would be computed on the basis of conventional elastic pseudostatic analysis of the frame. Then, with the increase of δ and plastic hinging taking place at the two beams, *M/Q* asymptotically approaches 4.8, and then (for δ > 0.5 m) it decreases again. As depicted in **Figure 4.3d**, while foundation moment capacity is practically insensitive to the increase of *M/Q* from 2.4 to 4.8 (in accord with foundation failure envelopes, see Gourvenec [2007]), a rather dramatic effect may be observed for the rotation capacity ϑ_{ult} of the foundation, which is reduced from 0.25 (for *M/Q* = 2.4) to 0.13 (for *M/Q* = 4.5). While this may be of particular significance for the overall ductility of the system, it may be concluded that fluctuation of *M/Q* is of trivial importance to the determination of the upper bound of the footing width *B*.

4.3.2. Estimation of the Lower-Bound of the Footing Width

Based on the previous discussion, a straight-forward procedure can be developed to estimate the *upper-bound* of the footing width B (i.e. the larger footing B that satisfies the design criteria). Notice that in conventional design no such upper-bound exists. On the other hand, the *lower-bound* refers to the smallest possible footing width B that provides an adequate margin of safety against toppling. As it can be seen in **Table 4.1**, in terms of SF_s the footing width could be reduced to B = 1.0 m, a solution that would yield a CRF of the order of 3 (i.e. M_{ult} roughly 3 times lower than M^{RD}. However, as M_{ult} reduces, the rotation it develops to sustain the same amount of earthquake demand will unavoidably increase. In addition, the decrease of B and consequently of M_{ult} is unavoidably associated with a reduction of ϑ_{ult} , meaning that system ductility will also be reduced. Naturally, the *lower bound* of B is not only associated with strength (as was the case for its *upper bound*), but is also a function of earthquake demand.

Figure 4.4a depicts the M–ϑ response of the two (B = 1.4 m) frame footings subjected to pushover analysis. The response of the system can be broadly categorized in two distinct phases :

1) Frame−dominated Response ($\vartheta \leq 0.05$ rad)

During this first phase, the response of the system is dominated by frame action. Initially (for $\vartheta < 0.005$ rad), M increases with ϑ for both footings. As the imposed lateral displacement δ increases (for $0.005 < \vartheta \leq 0.02$ rad), the frame develops column axial forces leading to a *decrease* of M on footing 1 (due to a corresponding *decrease* of N) and an *increase* of M on footing 2 (due to a corresponding *increase* of N). Then, during an *intermediate phase* (for

$0.02 < \vartheta \leq 0.05$ rad), with the development of plastic hinges on beams and the consequent reduction of N to its initial static value N_o (due to beam plastic hinging, frame action is practically cancelled), M on footing 1 rises again (because N increases, going back to N_o) and M on footing 2 is reduced (because N decreases, going back to N_o) : the previously discussed effect of the fluctuation of N. At this stage, since $M_{ult} < M^{RD}$ frame response is governed by footing uplifting. The beams experience extensive plastic hinging and finally reach their ductility capacity. During this *frame–dominated* phase, $M/Q \approx 2.4$ (see also **Figure 4.3c**) and the response of each footing can be approximated with an equivalent 1-dof system, of mass $m_f/2$ (i.e. half of the total frame mass) at height $h_1^m = 2.4$ m (**Figure 4.4b**).

2) Rocking–dominated Response ($\vartheta > 0.05$ rad)

During this *ultimate phase* (for $\vartheta > 0.05$ rad), the beams have failed and the response of the system is dominated by rocking. The response of the two footings is mainly affected by the aforementioned increase of M/Q from 2.5 for the intact frame (see frame-dominated response) to 4.5. At this phase, with frame beams having reached their residual strength (assumed equal to 30% of their M^{RD}), the system can be seen to reduce from a frame to two idealized 1-dof systems connected with each other with the 2 hinged beams. Hence, the response of each footing can be approximated with an equivalent 1-dof system, of mass $m_f/2$ (i.e. half of the total frame mass) at height $h_2^m = 4.5$ m (**Figure 4.4b**).

The two equivalent 1-dof systems, each one of them representing two extreme phases of system response, can be seen to provide a response envelope for the pushover response of the studied frame (**Figure 4.4a**). Evidently, the ultimate rotation ϑ_{ult} is a function of the footing width B and the lever arm (i.e. M/Q) : observe in **Figure 4.4a** the difference in ϑ_{ult}

between the two idealized 1-dof systems. Hence, the estimation of the *lower bound* footing width requires combined knowledge of : (a) footing *M-ϑ* response (for a specific *M/Q*), which determines its rotation capacity ϑ_{ult} ; and (b) earthquake demand in terms of footing rotation ϑ_{dem} , which can be expressed directly through the earthquake displacement demand δ_{dem}. Since δ_{dem} is impossible to be known a priori and the exact *M-ϑ* footing response greatly depends on the active lever arm, which constantly fluctuates during shaking as elucidated earlier (see the effect of *M/Q*), a simplified approach is sought for to facilitate the estimation of the lower bound footing width in a conservative though practically applicable manner.

4.4. Simplified Method to Estimate the Lower-bound of the Footing Width

The methodology presented herein focuses on the state of the frame during the ultimate phase described above, when toppling is incipient. During that stage, frame behavior may be enveloped by the two previously discussed idealized 1-dof systems (**Figure 4.4**). Apparently, both idealized systems are intrinsically incapable to predict with accuracy the response of the structure, since they both refer to a hinged system rather than a frame. Moreover, neither of them is able to accurately capture the observed critical toppling rotation ϑ_{ult}. Yet, notwithstanding these significant limitations, as shown in **Figure 4.4b** such simplified approximation may indeed provide a rational estimate for the upper and lower bounds of ϑ_{ult}. The validity of such an approach is examined in the sequel.

4.4.1. Rigid–Block on Rigid–Base Approximation

As already shown, at this *ultimate phase* the response of the structure is dominated by rocking, and the *flexural drift* δ_c (i.e. the lateral displacement of the structure due to flexural distortion of its structural members) may be considered negligible compared to the *rocking drift* δ_r (i.e. the lateral displacement due to foundation rocking). Hence, it is considered reasonable to approximate the response of the equivalent 1-dof system to that of a *rigid-block* of the same geometric characteristics (i.e., same width and center of mass). Moreover, since the footings of the frame are designed for uplifting-dominated response ($SF_s \geq 3$), the approximation of the foundation soil with a *rigid-base* could may also be considered reasonable.

The validity of such *rigid-block on rigid-base* approximation is verified through static pushover analysis of the two systems: (i) the equivalent 1-dof system lying on a homogenous clayey soil of undrained shear strength S_u , and (ii) the equivalent *rigid-block* resting on a *rigid-base*. For this purpose, the two systems are analyzed in 3D, taking account of material (for the first case only) and geometric (i.e., uplifting and $P–\delta$ effects) nonlinearities. Besides from the three-dimensional nature of this simulation (8-noded hexahedral brick elements, instead of 4-noded quadrilateral plane strain elements), the analysis methodology is in accordance with the one previously discussed.

Comparative results are presented in **Figure 4.5** for a 1-dof system with B = 1.4 m and h_1^m = 2.4 m and its equivalent *rigid-block on rigid-base.* To investigate the effect of SF_s, two cases are examined varying the undrained shear strength S_u from 80 kPa (yielding SF_s = 2.0) to 150 kPa (yielding SF_s = 4.5). Evidently, the $M–\vartheta$ (moment−rotation) response of the *rigid-*

block on rigid-base reasonably approximates that of the 1-dof system with SF_s = 4.5 (in which case the response is clearly uplifting-dominated). Naturally, the approximation is invalidated as the safety factor reduces (see results for SF_s = 2.0), and the response becomes less dominated by uplifting. In general, and based on additional results not shown herein, the *rigid-block on rigid-base* approximation may be considered reasonable for $SF_s \geq 3$, which is in any case the lower allowable limit for all practical purposes.

4.4.2. Conservative Estimate of the Toppling Potential of a Seismic Motion

As previously discussed, the estimation of the *lower bound* footing width requires combined knowledge of its rotation capacity ϑ_{ult} *and* earthquake demand, i.e. the amount of rotation or displacement it will have to undertake. Assuming that ϑ_{ult} can be estimated on the basis of the *rigid-block on rigid-base* approximation, the problem reduces to establishing a procedure to obtain a conservative estimate of the maximum rotation demand ϑ_{dem} of a seismic motion.

For a *rigid-block* of width $B = 2b$ and height $H = 2h$ (**Figure 4.6**), toppling will take place when the imposed rotation exceeds a critical value ϑ_{ult} (**Figures 4.6a** and **4.6b**):

$$\vartheta_{ult} = tan^{-1}(b/h) \approx b/h \qquad (4.9)$$

The critical toppling rotation ϑ_{ult} may be converted to critical toppling displacement δ_{ult} (imposed at the center of mass of the *rigid-block*) as follows :

$$\delta_{ult} \approx b = B/2 \qquad (4.10)$$

Observe that the effective period T of the system changes continuously with the imposed displacement δ, asymptotically tending to infinity when δ approaches δ_{ult} (**Figure 4.6c**). For the specific example (B = 1.4 m, H = 4.8 m), this is observed for $\delta \rightarrow \delta_{ult} \approx 0.7$ m.

The issue of earthquake-induced rocking of *rigid blocks* on *rigid base* has been studied very thoroughly over the last decades [Housner, 1963; Ishiyama, 1980; Psycharis & Jennings, 1983; Koh et al., 1986; Makris & Roussos, 2000; Zhang & Makris, 2001; Gazetas et al., 2003; Gerolymos et al., 2005b; Apostolou et al. 2007], revealing the sensitive nonlinear nature of the problem. Most researchers [e.g. Zhang & Makris, 2001; Apostolou et al., 2007] conclude that the overturning (or toppling) of such structures is quite unpredictable − *if not chaotic* − even for simplified cycloidal pulses. Hence, attempting to accurately quantify the toppling potential of a seismic motion (for a given *rigid block*) within the framework of the present study would be overly optimistic. Instead, the present study seeks for a *conservative upper-bound* of earthquake displacement demand δ_{dem}, for which toppling will not take place. This conservative estimate, in combination with the capacity of the footing δ_{ult} (Eq. 10), may provide the criterion to define the lower-bound of the footing width B.

Taking account of the above limitations, the peak spectral displacement SD_{max} is proposed as a conservative measure of the *upper bound* displacement demand. Although the spectral displacement may appear as a reasonable measure, it is well known that response spectra are applicable to 1-dof oscillators of a specific period T. So, it would probably be more straight-forward to set as measure the spectral displacement $SD(T_{eff})$ for the effective period T_{eff} of the system, and not the peak SD_{max}. However, as previously discussed (see **Figure 4.6c**), and in accord with the relevant bibliography [e.g. Makris &

Roussos, 2000; Apostolou et al., 2007], T_{eff} of a rocking system constantly changes during shaking, rising from zero (in the case of a rigid block) to infinity once the toppling condition has been met. Hence, T_{eff} cannot be known a-priori and consequently $SD(T_{eff})$ cannot be easily defined. Although Priestley et al. [1978] had proposed an iterative simplified method to compute T_{eff} and estimate the rotation ϑ of a rocking system on the basis of *SD*, Makris & Konstantinidis [2003] have shown that rocking response cannot be approximated by 1-dof oscillator−based methodologies, as the two systems are fundamentally different (stiffness, damping, and restoring mechanisms).

No such attempt is made here. SD_{max} is simply treated as a conservative index of seismic displacement demand. The aforementioned T_{eff} , for which $SD(T_{eff}) = SD_{max}$, *may* or *may not* be approached during seismic shaking, depending on the characteristics of the seismic motion *and* the response of the system. And even if it did, it would only be momentary. Hence, SD_{max} will not necessarily develop during seismic shaking, and can only be seen as the worst-case scenario. The validity and limitations of such approximation are investigated in the following sections : (i) for a rigid-block on a rigid-base, and (ii) for the frame structure on nonlinear soil.

4.5. Validation of the Simplified Approach for a Rigid block on Rigid Base

With reference to the case of a rigid-block on a rigid-base, the validity of SD_{max} as a conservative upper-bound estimate of earthquake demand is investigated : (a) for cycloidal (sinus and cosine) pulses, and (b) for Ricker wavelets.

4.5.1. Rigid block subjected to sinus and cosine pulses

Zhang & Makris [2001] investigated the transient rocking response of free-standing rigid blocks subjected to trigonometric (sine and cosine pulses) base excitation. Having derived analytical expressions for the dynamic horizontal and vertical reactions at the pivot point of a rocking block, they showed that under one-cycle cycloidal excitation the block may topple either after one impact (mode 1), or without impacts at all (mode 2). As a consequence, a ''safe region'' exists between the two modes, implying that while the block may topple after one impact (mode 1) for a certain level of shaking, it may remain standing for a larger amplitude, and finally topple without impact (mode 2) for even higher levels of shaking. These rigorous analytical results are used herein as a yardstick to investigate the validity of the previously discussed simplified methodology.

A rigid block of width $B = 2b$ and height $H = 2h$ (**Figure 4.6a**) is characterized by its slenderness ratio $\alpha = tan^{-1}(b/h)$ and the frequency parameter p :

$$p = \sqrt{3g/4R} \tag{4.11}$$

The latter can be seen as a measure of the dynamic characteristics of the block, decreasing with the size of the block (i.e. a larger structure will have a smaller characteristic frequency). Two rigid blocks are studied, following Zhang & Makris [2001] : a larger block of p = 2.0 rad/s and α = 0.35 rad, and a smaller one of p = 2.14 rad/s and α = 0.25 rad. Both are subjected to one-cycle sinus and cosine pulses of amplitude a and cyclic frequency ω_p . The acceleration amplitude required to cause overturning of the block is defined as the toppling acceleration a_p.

Figure 4.7 compares the simplified SD_{max} approach with the rigorous analytical solution of Zhang & Makris [2001]. The non-dimensional toppling acceleration $a_p/\alpha g$ is plotted as a function of non-dimensional excitation frequency ω_p/p for sinus (left column) and cosine pulses (right column). The shaded areas in **Figures 4.7a** and **4.7b** depict the overturning areas of the two rigid blocks. Evidently, the non-dimensional toppling acceleration $a_p/\alpha g$ increases exponentially with the increase of ω_p/p, and with the size of the block (expressed through the frequency parameter p). The simplified approach is employed to compute the pulse acceleration amplitude a_p^{SD} (for a given frequency ω_p) required to produce a displacement spectrum with SD_{max} equal to the toppling displacement δ_{ult} of each block : $\delta_{ult} = 40\ cm$ for the large block ($p = 2.0$ rad/s) ; $\delta_{ult} = 63\ cm$ for the smaller one ($p = 2.14\ rad/s$). By no means, should this be viewed as an attempt of capturing such complex phenomena. For the sinus pulse, the simplified approach provides a conservative estimate of a_p for the whole frequency range. However, for the cosine pulse it can be seen to provide a conservative estimate for lower ($\omega_p/p \leq 1.8$) and higher ($\omega_p/p \geq 4.3$) values of ω_p/p, becoming marginally unconservative for intermediate frequencies ($1.8 < \omega_p/p < 4.3$).

The effectiveness of the simplified approach is better quantified in **Figure 4.7c**, where the *Safety Factor SF,* defined as the ratio of the rigorous toppling acceleration $a_p^{rigorous}$ over the predicted toppling acceleration a_p^{SD} ($SF = a_p^{rigorous}/a_p^{SD}$), is plotted as a function of the dimensionless frequency ω_p/p. While for the sinus pulse SF is always greater than or equal to 1.0 (which means that it is always on the conservative side), for the cosine pulse SF may be as low as 0.76 (for $1.8 < \omega_p/p < 4.3$), which means that the simplified approach may under-predict a_p by as much as 26%. For practical purposes, a *Factor of Safety* of the order of 1.5

should be applied on SD_{max}-based estimates to wipe out such discrepancies. Going back to Eq. 10, this suggests that the lower-bound footing width should be increased accordingly, so that $b = B/2 = 1.5\ SD_{max}$ (for the design seismic motion).

4.5.2. Rigid block subjected to Ricker pulses

Although the preceding analysis has yielded quite encouraging results, the simplified SD_{max} approach needs to be further validated against more realistic – yet still idealized – pulses. To this end, SD_{max} predictions are compared to rigorous numerical analysis results, referring to the overturning of rigid blocks subjected to Ricker pulses. Gerolymos et al., [2005], based on validated numerical analysis results, employed artificial neural networks to derive closed-form analytical expressions for predicting the overturning acceleration a_p of a rigid block, as a function of its geometric properties and excitation characteristics. The present study utilizes three characteristic example cases in order to explore the applicability of the proposed simplified method : (i) a small-size block of p = 3.38 rad/s and α = 0.16 rad, simulating a *cemetery tomb* ; (ii) a medium-size block of p = 3.14 rad/s and α = 0.25 rad, simulating an *electrical transformer* ; and (iii) a large-size block of p = 0.76 rad/s and α = 0.30 rad, simulating a *slender building*.

Figure 4.8 depicts the comparison of the simplified SD_{max}-based prediction with the more rigorous analytical solution of Gerolymos et al., [2005]. The toppling acceleration a_p is plotted as a function of excitation frequency f_E (i.e., the characteristic frequency of the Ricker pulse). The shaded areas represent the overturning regions of the three rigid blocks, according to the aforementioned rigorous solution. As for the cycloidal (sinus and cosine) pulses, the toppling acceleration a_p increases exponentially with the increase of the

frequency (f_E in this case), and with the size of the rigid block. As for the previous case, the simplified approach is employed to compute the Ricker pulse acceleration amplitude a_p^{SD} (for a given frequency f_E) required to produce a displacement spectrum with SD_{max} equal to the toppling displacement δ_{ult} of each block. Interestingly, for this more realistic pulse type, the prediction of the simplified approach is nearly always conservative. In this case, although not necessary, the application of a factor of safety (as described in the previous section) would still be recommended for design purposes.

4.6. Validation of Simplified Approach for the 2-Storey Frame on Inelastic Soil

In the previous sections, the SD_{max} approach was validated for rigid blocks on a rigid base, subjected to idealized pulses. Although the *rigid-block* on *rigid-base* has been shown to be a reasonable approximation of the more complex reality, the effectiveness of the simplified approach needs to be verified for the actual problem. For this purpose, the SD_{max} approach is employed for the 2-storey frame structure resting on nonlinear soil, subjected to Ricker pulses and real seismic records. SD_{max} predictions are compared with numerical analysis results of the investigated frame structure.

The analysis is conducted for the frame with B = 1.10 m footings : the minimum allowable footing dimension based on the SF_s > 3 criterion (**Table 4.1**). As previously discussed, at the stage of incipient toppling the frame has been reduced to two 1-dof structures connected with each through the hinged beams (**Figure 4.10a**), something which is clearly evidenced by the numerical analysis of the frame subjected to static pushover (**Figure 4.10b**). According to the M–ϑ response of the two frame footings (**Figure 4.10c**), the

most conservative estimate of the toppling rotation would be that of footing 1 (left), which yields ϑ_{ult} = 0.143 rad. This corresponds to δ_{ult} = 71 cm (at the center of mass of the frame), which, according to the simplified approach should be equal to the peak spectral displacement SD_{max} of the design ground motion. Hence, the validation of the simplified approach will consist of applying to the frame (i.e., at the base of the finite element model) seismic excitations whose SD_{max} is equal to the toppling displacement δ_{ult} of the frame.

In order to investigate the safety margins provided by the SD_{max} approach, the applied seismic excitations are scaled in such a way so that their SD_{max} is equal to : (a) $1.1\delta_{ult}$ = 78 cm, denoted SD^{+} (i.e. 10% larger than the toppling displacement δ_{ult}) ; and (b) $0.9\delta_{ult}$ = 63 cm, denoted SD^{-} (i.e. 10% lower than δ_{ult}).

4.6.1. Ricker Pulses

Ricker pulses of seven different characteristic frequencies f_E = 0.4, 0.5, 0.65, 0.85, 1.0, 1.25, and 1.5 Hz are utilized to investigate the effectiveness of the simplified approach. According to the simplified SD_{max} approach, all pulses are scaled so that their SD_{max} is equal to SD^{+} = $1.1\delta_{ult}$ = 78 cm, or SD^{-} = $0.9\delta_{ult}$ = 63 cm (**Figure 4.11a**). This way, their scaled (to yield SD_{max}) acceleration amplitude (which ranges from 0.34 g for f_E = 0.4 Hz, to 4.83 g for f_E = 1.5 Hz) is equal to the predicted toppling acceleration a_p^{SD} of the system.

The validity of this prediction is verified through dynamic nonlinear time-history analysis of the frame, employing the previously described FE analysis methodology. The system is subjected to the seven Ricker pulses, their amplitude being progressively increased until failure (i.e. toppling of the frame structure). The minimum acceleration amplitude of each pulse which provokes failure constitutes the actual (rigorously computed) toppling

acceleration a_p of the frame. In **Figure 4.11b**, a_p (isolated markers) is plotted as a function of non-dimensional frequency ω_p/p of the system, and compared to the predicted a_p^{SD} toppling acceleration (solid lines). Evidently, throughout the whole frequency, the simplified approach yields a reasonably conservative prediction. For such pulse-type seismic excitations, it provides a substantial margin of safety in the estimation of a_p . This margin of safety increases with the increase of the non-dimensional frequency ω_p/p, in accord with what was previously discussed for the *rigid−block* on *rigid−base*.

4.6.2. Real Records

Although the simplified SD_{max} approach has been shown to yield conservative estimates of a_p for idealized pulse-type excitations, it needs to be further verified for real seismic excitations. To this end, an ensemble of 18 recorded earthquake time histories (from the US, Europe, and Asia) are utilized as seismic excitation. During their selection, emphasis was given in creating a collection of records covering a wide range of periods, and enabling us to capture the consequences of various characteristics of real seismic motions, such as PGA and PGV, SA and SD, frequency content, duration, number of strong motion cycles, and directivity effects.

As for the Ricker pulses, to apply the simplified SD_{max} approach all records are scaled to SD^+ = 78 cm, or SD^- = 63 cm. The resulting, scaled to SD^+ = 78 cm, time histories are shown in **Figure 4.12**. In most cases (**Figure 4.12a**), the original records had to be scaled *up* substantially to yield SD^+ = 78 cm. Only in a few exceptions, were they scaled *down* to match the required SD^+ (**Figure 4.12b**). The resulting displacement *SD* and acceleration *SA* response spectra are displayed in **Figures 4.12c** and **4.12d**. In most cases, the resulting *SA* of the scaled

accelerograms overly exceeds the design spectrum of the frame. The scaled (to yield SD_{max}) acceleration amplitude of the records constitutes the predicted toppling acceleration a_p^{SD} of the system.

The validity of the prediction is verified through dynamic nonlinear time-history analysis of the frame, subjected to the records scaled at : (i) SD^+ = 78 cm, and (ii) SD^- = 63 cm. For all cases examined, toppling is avoided for the SD^- scaled records. In other words, for a value just 10% lower ($SD^- = 0.9\delta_{ult}$) than the toppling displacement of the B = 1.1 m footings (δ_{ult} = 71 cm), the frame will not overturn. Hence, in contrast to what was previously concluded for the *rigid−block* on *rigid−base* subjected to cosine excitation, a *Factor of Safety* of the order of 1.1 may be considered adequate for real seismic motions, suggesting that the lower-bound footing width does not have to be increased to $b = B/2 = 1.5\ SD_{max}$, but to merely $1.1SD_{max}$. This marked difference between real seismic motions and the cosine pulse may be attributed to the unrealistic (for a seismic motion) nature of the latter (which is initiating and ending with maximum acceleration). Quite encouragingly, even for the SD^+ scaled seismic motions ($SD^+ = 1.1\delta_{ult}$), in most cases the frame does not topple (experiencing quite an increased distortion though). Yet, in 2 cases (bold in **Table 4.2**) out of the 18 records examined, the SD^+ scaled ground motion results to toppling of the frame. Although this observation does not question the applicability of the simplified approach (since the imposed SD is 10% higher than the toppling displacement δ_{ult}) a more detailed insight into the factors affecting the toppling potential of a seismic excitation is attempted in the following sections.

4.7. Insight on Ground Motion Toppling Potential

The most fundamental condition that needs to be met for a seismic motion to have the potential of provoking overturning, is that it exceeds the yield acceleration a_{yield} of the system. In the context of rocking isolation, a_{yield} is a function of the capacity of the under-designed footings, and can thus be computed by dividing the design spectral acceleration SA^D of the frame (computed according to EC8 or the corresponding seismic code) with the capacity reduction factor *CRF* of its foundation system :

$$a_{yield} = SA^D/CRF \quad (4.12)$$

Obviously, the above consideration intrinsically assumes that once the capacity of the system is exceeded (in terms of imposed acceleration), its foundation will yield (mainly through uplifting) and will be subjected to inelastic rotation. Consequently, increasing the acceleration amplitude (i.e. the PGA) of the seismic excitation is expected to lead to increased foundation rotation, thus augmenting the risk of toppling. Naturally, PGA is not the only factor determining the toppling potential of a ground motion : observe, for example, in **Table 4.2** that while the scaled Lucerne-000 record with a *PGA* of 1.48 g does not lead to toppling, the scaled JMA-000 with a *PGA* of 1.4 g does.

A number of factors affect the toppling potential of a seismic motion. While its dominant frequency has been shown to play a crucial role [e.g. Zhang & Makris, 2001], its kinematic characteristics (asymmetry, existence of large velocity directivity pulses, and sequence of strong motion cycles) are equivalently important [e.g. Makris & Roussos, 2000; Apostolou et al., 2007]. Aiming to better quantify the toppling potential of a ground motion, a destructiveness measure is defined, termed as the *maximum impact pulse velocity* :

$$V_{imp,\max} = \max\left|V_{imp}\right| = \max\left|\int_0^{t_{tot}} \left(a - a_{yield}\right) dt\right| \qquad (4.13)$$

where t_{tot} is the total duration of the ground motion, and a the acceleration. This measure is believed to provide a more accurate measure of the toppling potential of strong motions containing large velocity pulses. The role of the aforementioned parameters and the applicability of $V_{imp,max}$ is investigated in the sequel.

Figure 4.13 compares the Lucerne-000 record (Landers, 1992) with the GIC-090 record (San Salvador, 1986), both scaled at SD^{+} = 78 cm. Although the Lucerne record contains a tremendous number of strong motion cycles that exceed the yield acceleration a_{yield} (**Figure 4.13a**), it does not contain a large impact velocity pulse $V_{imp,max}$ (**Figure 4.13b**), and is therefore not leading to appreciable foundation rotation (**Figure 4.13c**). In stark contrast, despite having a significantly smaller number of strong motion cycles (and duration), the San Salvador record is characterized by a substantially larger $V_{imp,max}$ (2.04 m/s compared to 0.78 m/s of Lucerne), thus leading to large foundation rotation and finally inciting toppling of the structure. The time histories of V_{imp} can be seen to reveal the key disparity between the two records. A well distinguished pulse produces a pronounced *"impact"* on the structure, forcing it out of its equilibrium position. Depending on the intensity of this *velocity impact pulse*, this instability may become irrecoverable, leading to toppling of the structure. This effect is brightly reflected on the time history of footing rotation ϑ for the San Salvador record : the large *impact velocity pulse* at t = 1.4 s leads to a rather pronounced ϑ of the order of 0.08 rad. Although this rotation is substantially lower than the toppling rotation ϑ_{ult} = 0.186 rad, the deviation from the equilibrium position is irrecoverable, with subsequent

strong motion cycles generating further accumulation of ϑ and finally leading to toppling. The Lucerne record is dramatically different. Despite containing a multitude of strong motion cycles substantially exceeding a_{yield}, none of them has the kinematic characteristics (asymmetry *and* low frequency, i.e. large duration) to produce a large enough V_{imp}. As a result, the produced footing rotation ϑ fluctuates around the zero axis, while the residual rotation remains relatively small.

The previous comparative example suggests that $V_{imp,max}$ may reveal certain characteristics of a seismic motion, mainly related to the existence of impact velocity pulses. However, as it will be shown in the sequel through a different example, $V_{imp,max}$ alone is not sufficient to describe the toppling potential of a strong motion. For this purpose, the JMA-000 record (Kobe, 1995) is compared with a Ricker 1 pulse (i.e. f_E = 1 Hz). As shown in **Figure 4.14a**, the Ricker 1 pulse (scaled with respect to *PGA*) matches quite well with the prevailing strong motion pulse of the JMA record. Quite interestingly, the two motions also match very well in terms of acceleration response spectra (**Figure 4.14b**), despite the obvious differences of their time histories (the JMA record contains a substantial number of strong motion cycles, and much larger duration).

In the context of the SD_{max} approach, the two ground motions are scaled to SD^+ = 78 cm. As shown in **Figure 4.15a**, Ricker 1 needs larger PGA (2.2 g) to achieve the same *SD* with the JMA record (1.4 g). Despite containing a substantially larger *impact pulse velocity* $V_{imp,max}$ = 2.1 m/s (**Figure 4.15b**), in contrast to the SD^+ scaled JMA record (of $V_{imp,max}$ = 1.87 m/s) which leads to toppling of the structure, Ricker 1 is clearly inadequate to provoke toppling. As shown in **Figure 15c**, the first pulse of Ricker 1 generates a rotation ϑ of the order of 0.09

rad, which is, however, recovered during the next (of opposite direction) cycle of motion. Due to the lack of subsequent strong motion pulses, the generated instability does not lead to toppling. Dramatically different is the observed system response for the JMA record. While its prevailing strong motion cycle (at t = 8 s) generates footing rotation ϑ of similar magnitude to Ricker 1, its subsequent strong motion cycles which exceed a_{yield} produce gradual accumulation of ϑ ultimately resulting to toppling.

This implies that the number of strong motion cycles that exceed a_{yield}, or equivalently the total duration of the record t_{yield} for which a_{yield} is exceeded, should also be taken into account to estimate the toppling potential of a seismic motion. However, the JMA record is substantially different than the previously discussed case of the Lucerne record (**Figure 4.13**). While both contain several strong motion cycles clearly exceeding a_{yield}, the one (JMA) leads to toppling and the other (Lucerne) does not. Quite interestingly, Lucerne contains a substantially larger amount of strong motion cycles than JMA. The key difference between the two lies in their *impact pulse velocity* : $V_{imp,max}$ = 1.87 m/s for JMA, compared to merely 0.78 m/s for Lucerne. This implies that both factors (i.e. $V_{imp,max}$ and t_{yield}) are important and should be combined to assess the toppling potential of a seismic motion.

Based on the above, a destructiveness index in terms of toppling potential of a ground motion may be defined :

$$TPi = V_{imp,max} \times t_{yield} \qquad (4.14)$$

Table 4.3 summarizes the two factors ($V_{imp,max}$ and t_{yield}) affecting the toppling potential of a record, along with their product (i.e. *TPi*), for the frame structure under study subjected to the 18 SD^{+} scaled records. Toppling occurs for two records only (GIC-090, San Salvador 1986 ;

and JMA-000, Kobe 1995), for which *TPi* > 15. Although no correlation has been attempted between *TPi* and footing rotation ϑ or superstructure displacement δ, for the cases examined herein such an index yields reasonable results, at least qualitatively.

4.7.1. The Paradox of the Chi-Chi Record

The preceding discussion focused on the safety margin provided by the simplified SD_{max} approach, revealing that a *Factor of Safety* of the order of 1.1 may be considered adequate for real seismic motions, and suggesting that a lower-bound footing $b = B/2 = 1.1SD_{max}$ may be adequate for the design of rocking-isolated systems. For this purpose, all seismic motions were scaled to a specific value of SD_{max} (= $1.1\delta_{ult}$). Yet, to achieve such SD_{max} some of the records had to be un-realistically scaled by factors as high as 7 (**Table 4.2**). In reality, however, such *tremendous* seismic motions (e.g. the devastating JMA record scaled up at 1.4 g) have never been recorded and cannot possibly be considered realistic, especially for design purposes. **Figure 4.16a** depicts the original displacement spectra of all ground motions examined, aiming to reveal their real toppling potential. Observe that despite the fact that all ground motions have been recorded during devastating seismic events, in most cases their SD_{max} lies well below the toppling displacement δ_{ult} = 71 cm of the B = 1.1 m footings. In fact, only three records (Takatori-000, Jensen-292, and Tabas) exceed δ_{ult} and had to be scaled-down. This observation is of particular importance, since it implies that toppling can be quite *improbable* for real seismic motions, even in case of occurrence of *extremely strong earthquakes* (such as the ones deliberately selected for analysis), and even for *extremely under-designed* footings (B = 1.1 m).

Although the selected records cover a wide range of seismic motions, none of them is characterized by fling-step effects — a different category of near-source effects, associated with large permanent displacement rather than a large velocity pulse. As shown in the examples of **Figure 4.16b**, such ground motions are characterized by excessively large spectral displacements. For example, the TCU-068 records (Chi-Chi, Taiwan 1999) yield SD_{max} of the order of several meters, i.e. almost an order of magnitude larger than δ_{ult} . With such large SD_{max} , it would be expected that the structure would easily be lead to toppling. To unravel the response of the system when subjected to this special category of near-source seismic motions, additional analyses are conducted utilizing the original records of **Figure 4.16b** (without any scaling). Quite remarkably, even for the very extreme case of the TCU-068(NS) record (**Figure 4.17a**), the footing experiences almost negligible rotation ϑ (**Figure 4.17b**), and the structure is not toppling.

As paradox as this may appear, it is explainable on the basis of the acceleration time history. Despite the large SD_{max}, the yield acceleration a_{yield} is only slightly exceeded, and not for a long duration. This means that both V_{imp} and t_{yield} , and consequently TPi , are not large enough to provoke toppling. This implies that the long-period (almost quasi-static) component of the seismic motion, which is responsible for the excessive SD_{max} , is not really exceeding a_{yield} and, therefore, cannot lead to toppling. As clearly seen in **Figure 4.17a**, the acceleration pulses that do exceed a_{yield} are of much higher frequency, and are not associated with the large SD_{max} of the record. This example reveals the notable conservatism of the simplified approach, for such special cases of near source seismic motions characterized by fling-step effects.

4.8. Summary and Conclusions

The present study has investigated the applicability of a simplified procedure to estimate the range of acceptable footing width B for rocking–isolated frame structures. In this context, the foundation is *under-designed* so that its moment capacity M_{ult} is lower than the corresponding column capacity M^{RD}. Two contradicting criteria need to be simultaneously satisfied : (i) B needs to be *small enough*, so that M_{ult} is adequately smaller than M^{RD} ; and (ii) B has to be *large enough*, so that an adequate margin of safety against toppling is achieved. In other words, there exists an *upper-bound* (B_{max}) and a *lower-bound* (B_{min}) footing width, which will define the range of allowable footing width $B_{min} \leq B < B_{max}$ to simultaneously satisfy the aforementioned criteria.

With respect to the *upper-bound*, B_{max} should be small enough so that the footing capacity is at least 40% lower than the corresponding column capacity M^{RD}. In exactly the opposite sense to conventional capacity design (where an over-strength factor of 1.4 is typically applied), an under-strength factor of the same magnitude is required to account for uncertainties related to soil and superstructure strength. B_{max} should be estimated on the basis of $M_{ult,max}$ (i.e. for the maximum axial force N_{max} that may develop during seismic shaking) and not assuming M_{ult} (i.e. for the initial axial load N_o). N_{max} can be computed through conventional static pushover analysis, rendering the proposed procedure straight-forward to apply. For the 2-storey frame investigated herein, $M_{ult,max}$ was found to exceed M_{ult} by up to 40%, implying that the capacity reduction factor ***CRF*** **(= M_{ult}/M^{RD}) should be at**

least equal to 2, to have a reasonable safety margin for the aforementioned uncertainties *and* the dynamic footing overstrength (due to generation of N_{max}).

On the other hand, the estimation of the lower-bound B_{min}, required to achieve acceptable safety against toppling, is not equally straight-forward. A simplified approach was developed, according to which B_{min} is estimated on the basis of the displacement spectrum. The peak spectral displacement SD_{max} is proposed as a conservative measure of the *upper bound* of displacement demand. The validity and limitations of such approximation were investigated for a *rigid-block* on *rigid-base*, utilizing rigorous solutions from the bibliography ; and for the frame structure on nonlinear soil, by conducting nonlinear dynamic time history analysis. While in the first case the seismic excitation consisted of cycloidal and Ricker pulses, in the latter case an ensemble of 18 records (covering a wide range of devastating seismic motions), was utilized. With the exception of the unrealistic (for a seismic motion) cosine pulse, the simplified SD_{max} approach was shown to provide reasonably conservative estimates of the toppling acceleration a_p . Based on the results of the conducted analyses, and at least for the cases examined herein, it is concluded that $\boldsymbol{B_{min} = 2.5SD_{max}}$ may provide adequate margins of safety against toppling.

In an attempt to gain insight on the toppling potential of a ground motion, a destructiveness index $\boldsymbol{TPi = V_{imp,max} \times t_{yield}}$ was defined, combining the effects of the *"maximum impact pulse velocity"* $V_{imp,max}$ (see Eq. 13), with the total duration t_{yield} of the record for which the yield acceleration of the system a_{yield} is exceeded. While $V_{imp,max}$ is characteristic of strong motions containing large velocity pulses, t_{yield} can be seen to capture

the effects of the number of strong motion cycles. It was shown, that for the (admittedly limited) cases examined herein, such an index may yield qualitatively reasonable results.

Figures of Chapter 4

Table 4.1. Alternative footing configurations : footing width *B*, resulting safety factor SF^S for static loading, moment capacity (computed analytically according to Gourvenec, 2007) for the initial (N = 151 kN) and the maximum value of column axial load (N_{max} = 232 kN), and corresponding *Capacity Reduction Factor* (*CRF* : ratio of footing capacity M_{ult} to column capacity M^{RD}).

Footing width B (m)	**SF^S**	**M_{ult}** *for N = 151 kN*	**$M_{ult,max}$** *for N_{max} = 231 kN*	**CRF** *for N = 151 kN*	**CRF_{max}** *for N_{max} = 231 kN*
1.6	7.01	125	180	1.60	1.17
1.5	6.13	113	163	1.76	1.29
1.4	5.31	101	147	1.97	1.42
1.3	4.54	91	131	2.19	1.60
1.2	3.84	81	115	2.46	1.81
1.1	3.19	71	100	2.81	2.03
1.0	2.6	61	84	3.27	2.43

Table 4.2. Scale factors applied to each record to achieve the required peak spectral displacement *SD*, and summary of analysis results (toppling or not).

Record	Earthquake	Original PGA (g)	for SD^{-} = 63 cm			for SD^{+} = 78 cm		
			Scale Factor	Scaled PGA (g)	Toppling	Scale Factor	Scaled PGA (g)	Toppling
Treasure-Island	Loma Prieta, 1989	0.08	5.47	0.44	NO	7.00	0.56	NO
Kalamata	Kalamata, Greece, 1986	0.25	3.50	0.88	NO	4.48	1.12	NO
ElCentro000	ElCentro, 1940	0.31	2.35	0.73	NO	3.00	0.93	NO
GIC090	**San Sanvaldor, 1986**	**0.69**	**1.99**	**1.38**	**NO**	**2.55**	**1.76**	**YES**
Lucerne000	Landers, 1992	0.68	1.70	1.16	NO	2.18	1.48	NO
Izmit	Kocaeli, 1999	0.22	1.42	0.31	NO	1.82	0.40	NO
JMA000	**Kobe, 1995**	**0.82**	**1.34**	**1.09**	**NO**	**1.71**	**1.40**	**YES**
Duzce-Bolu000	Duzce, 1999	0.73	1.22	0.89	NO	1.56	1.14	NO
Erzincan-ew	Erzincan, 1992	0.49	1.09	0.53	NO	1.39	0.68	NO
Rinaldi218	Northridge, 1994	0.83	1.02	0.84	NO	1.30	1.08	NO
Sylmar Olive view-090	Northridge, 1994	0.6	1.02	0.61	NO	1.30	0.78	NO
Jensen Filtration Plant-292	Northridge, 1994	0.59	0.80	0.47	NO	1.02	0.60	NO
Pacoima Dam254	San Fernado, 1971	1.22	0.78	0.95	NO	1.00	1.22	NO
Takatori000	Kobe, 1995	0.61	0.53	0.32	NO	0.67	0.41	NO
Tabas-LN	Iran, 1978	0.84	0.47	0.39	NO	0.60	0.50	NO
Duzce000	Duzce, 1999	0.35	0.42	0.15	NO	0.54	0.19	NO
Lucerne275	Landers, 1992	0.7	0.38	0.27	NO	0.49	0.34	NO
Duzce270	Duzce, 1999	0.54	0.38	0.20	NO	0.48	0.26	NO

Table 4.3. Summary of analysis results : toppling potential with respect to the impact pulse velocity $V_{imp,\,max}$, the total duration t_{yield} for which a_{yield} is exceeded, and the toppling index *TPi*.

Record	**Scaled PGA** (g)	$\mathbf{V_{imp,\,max}}$ (m/s)	$\mathbf{t_{yield}}$ (s)	$\mathbf{TPi = V_{imp,\,max} \times t_{yield}}$ (m)
No toppling				
Jensen Filtration Plant-292	0.6	0.71	1.1	0.78
Duzce000	0.19	0.036	0.84	0.03
Duzce270	0.26	0.16	1.28	0.20
Tabas-LN	0.5	0.32	1.125	0.36
Lucerne275	0.34	0.147	2.66	0.39
Izmit	0.4	0.2	6.09	1.22
Erzincan-ew	0.68	0.62	3.96	2.46
Sylmar Olive view-090	0.78	0.7	4.86	3.40
Takatori000	0.41	0.61	7.96	4.86
Kalamata	1.12	0.8	6.11	4.89
Duzce-Bolu000	1.14	0.66	8.33	5.50
Pacoima Dam254	1.22	0.78	7.08	5.52
Treasure-Island	0.56	1.18	5.75	6.79
ElCentro000	0.93	0.63	17.12	10.79
Lucerne000	1.48	0.78	15.92	12.42
Rinaldi218	1.08	1.608	8.2	13.19
Toppling				
GIC090	1.76	2.04	7.56	15.42
JMA000	1.4	1.87	10.58	19.78

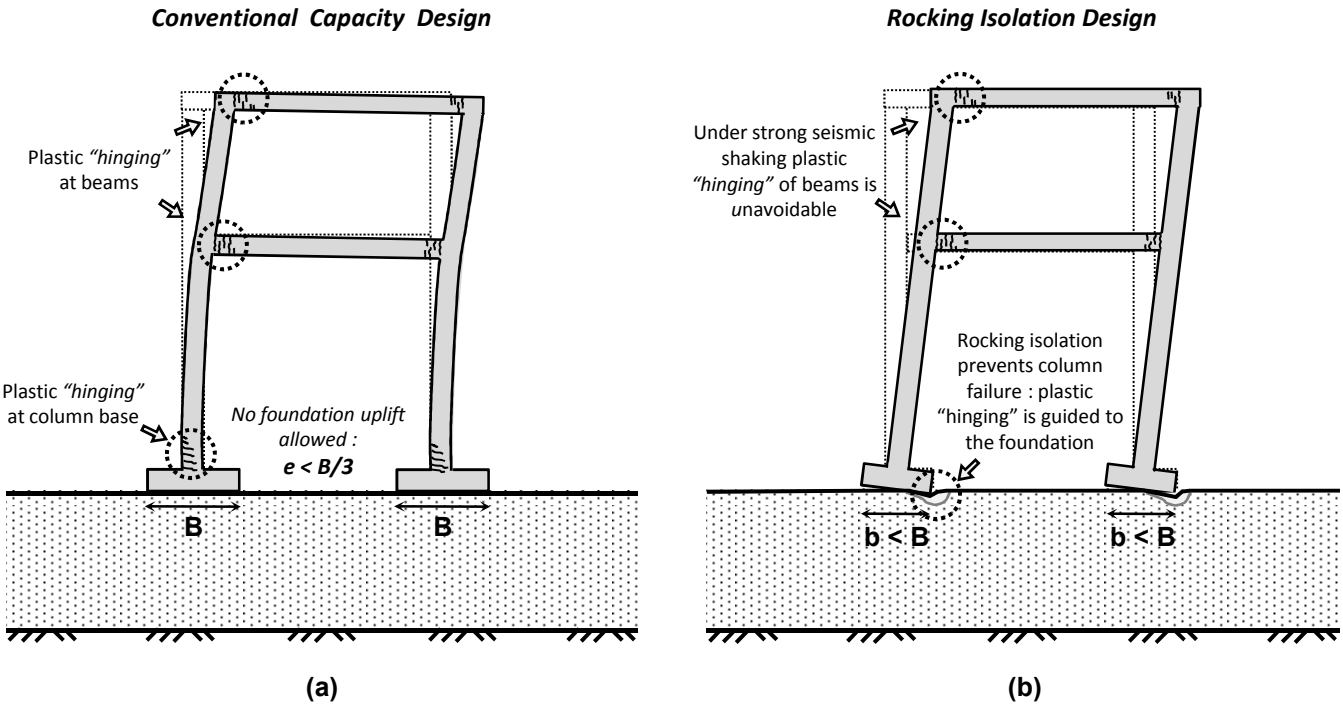

Figure 4.1. (a) Conventional Capacity Design compared with (b) Rocking–Isolation Design.

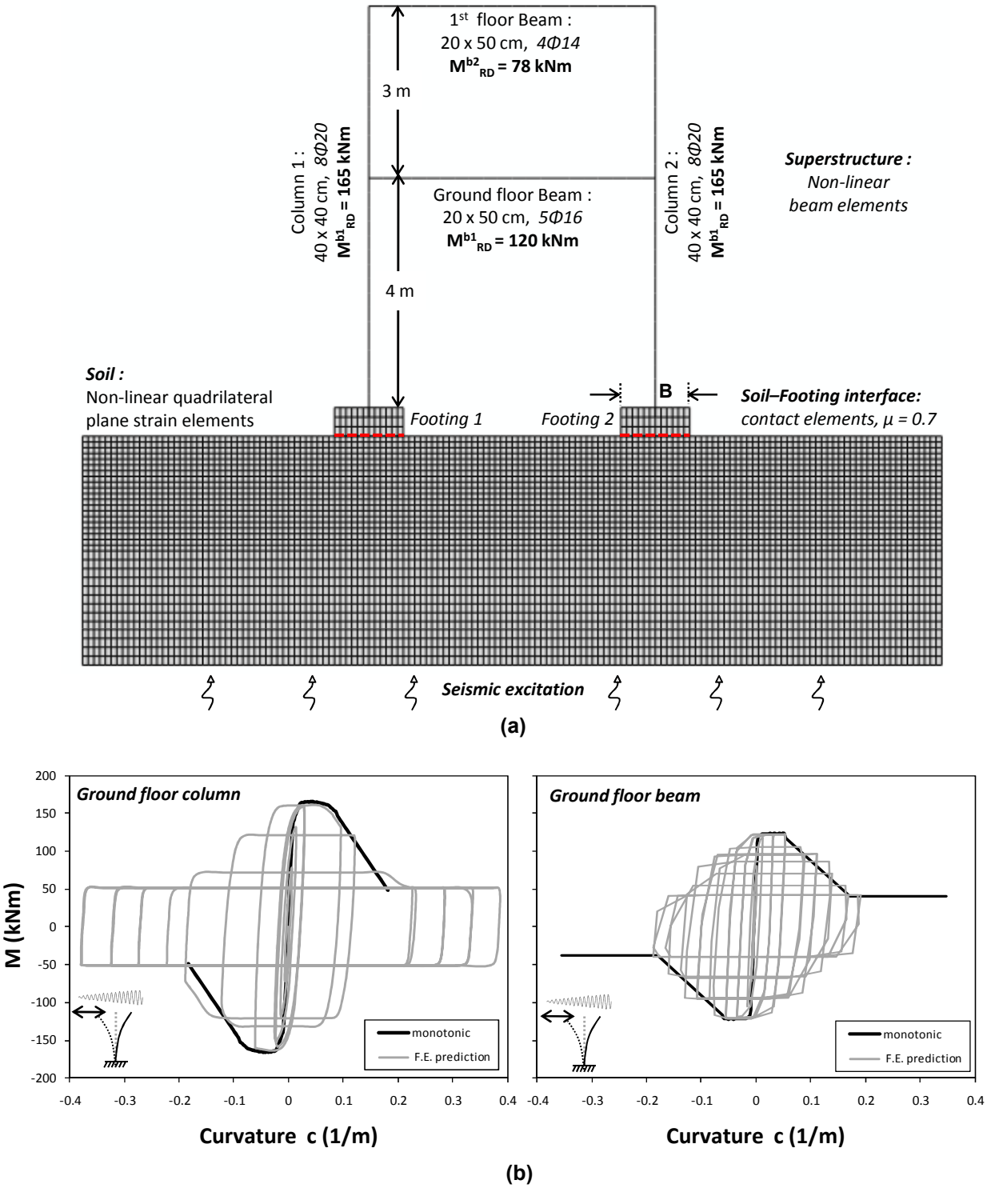

Figure 4.2. (a) Geometry, member properties, and outline of finite element (FE) model. A typical "slice" of the frame is analyzed in plane-strain, taking account of material (soil *and* superstructure) and geometric (uplifting and P-δ effects) nonlinearities. (b) FE model response under dynamic loading for ground floor columns (left) and beam (right).

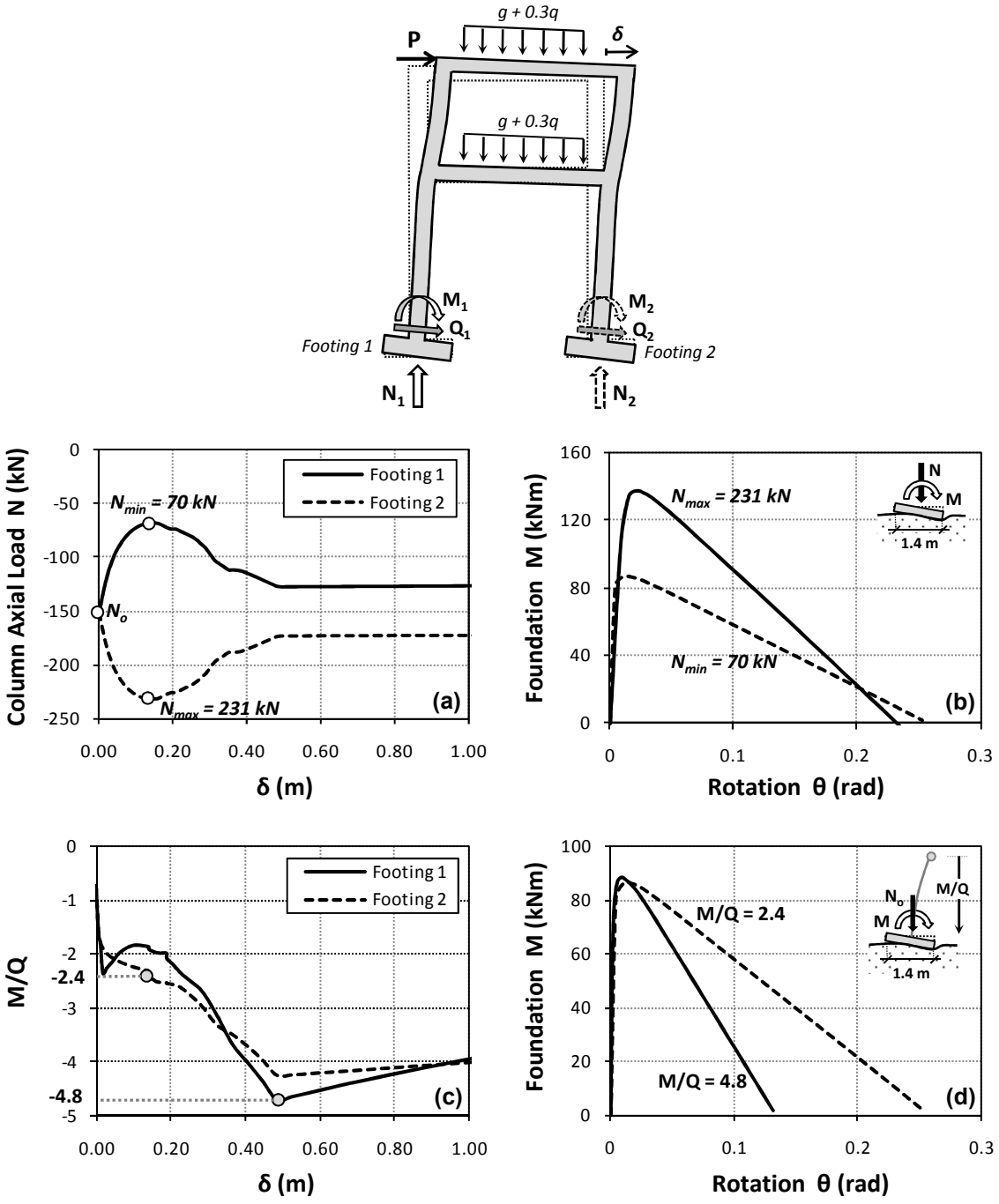

Figure 4.3. Illustration, through static pushover analysis, of the effect of fluctuation of column axial load *N* and *M/Q* ratio on foundation moment–rotation (*M*–*ϑ*) response : (a) evolution of column axial load *N* with imposed lateral displacement *δ,* and (b) its effect on foundation *M*–*ϑ* response ; (c) evolution of *M/Q* with *δ*, and (d) its effect on foundation *M*–*ϑ* response (results shown for *B* = 1.4 m).

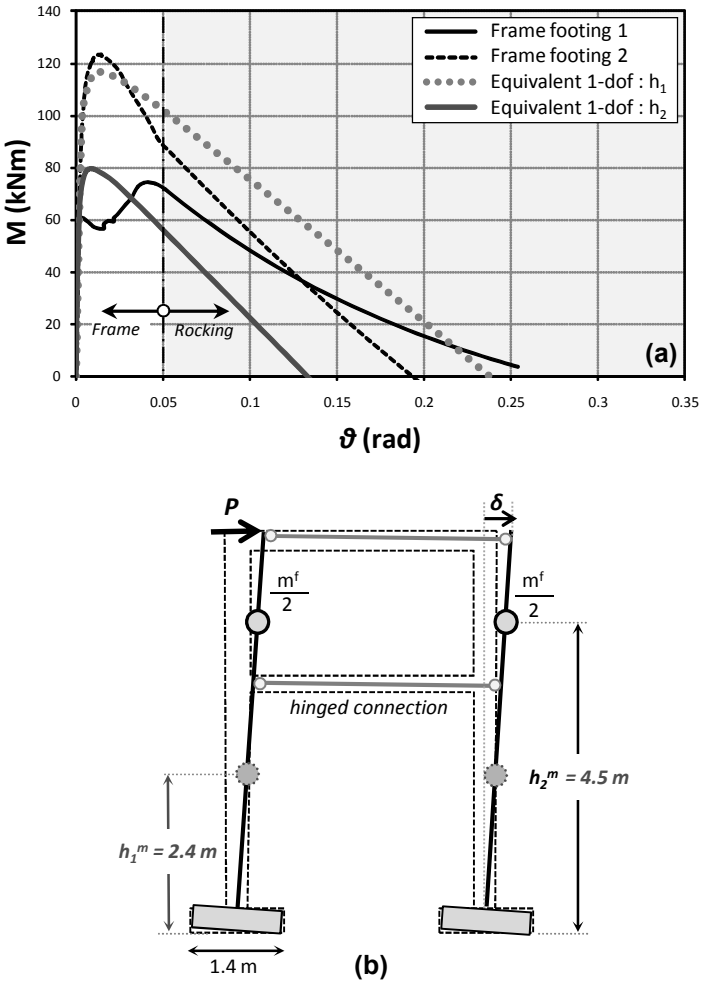

Figure 4.4. (a) Static pushover *M–ϑ* (*moment–rotation*) response of the two frame footings compared with the two simplified equivalent 1-dof systems. Frame response can be seen to be roughly bounded between the two simplified 1-dof systems ; (b) Simplified sketch of the ultimate state of the frame : after the beams have failed, the system is roughly reduced to two 1-dof systems joined together through the two hinged beams.

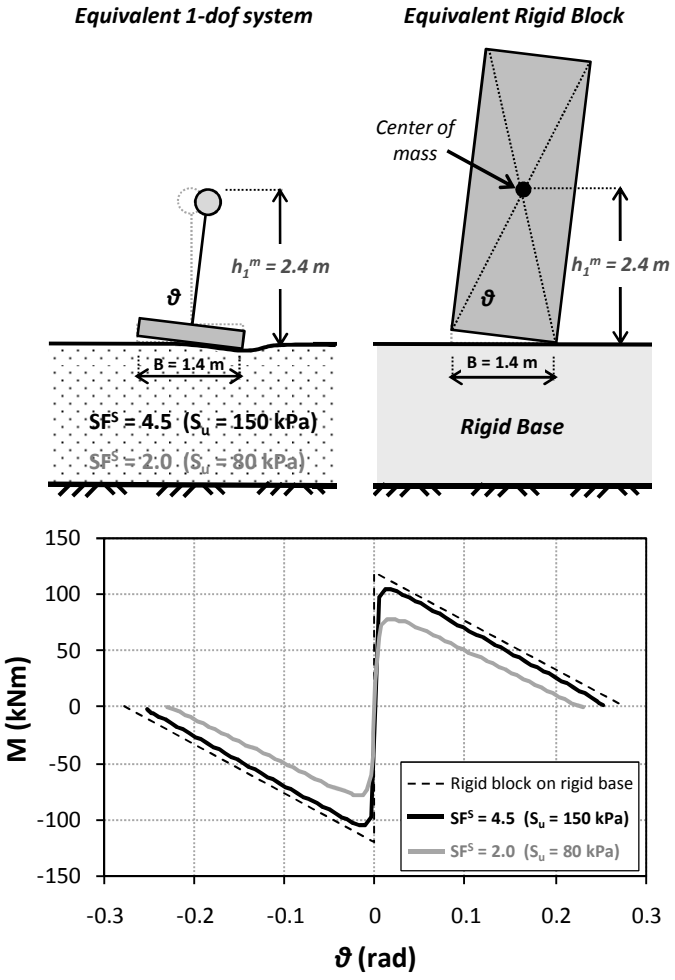

Figure 4.5. Comparison of static pushover M–ϑ (moment–rotation) response of simplified equivalent 1-dof system (with h_1^m = 2.4 m) with that of an equivalent rigid block lying on a rigid base. For large static safety factors (SF^S > 4), the response of the 1-dof system is roughly equivalent to that of the rigid block.

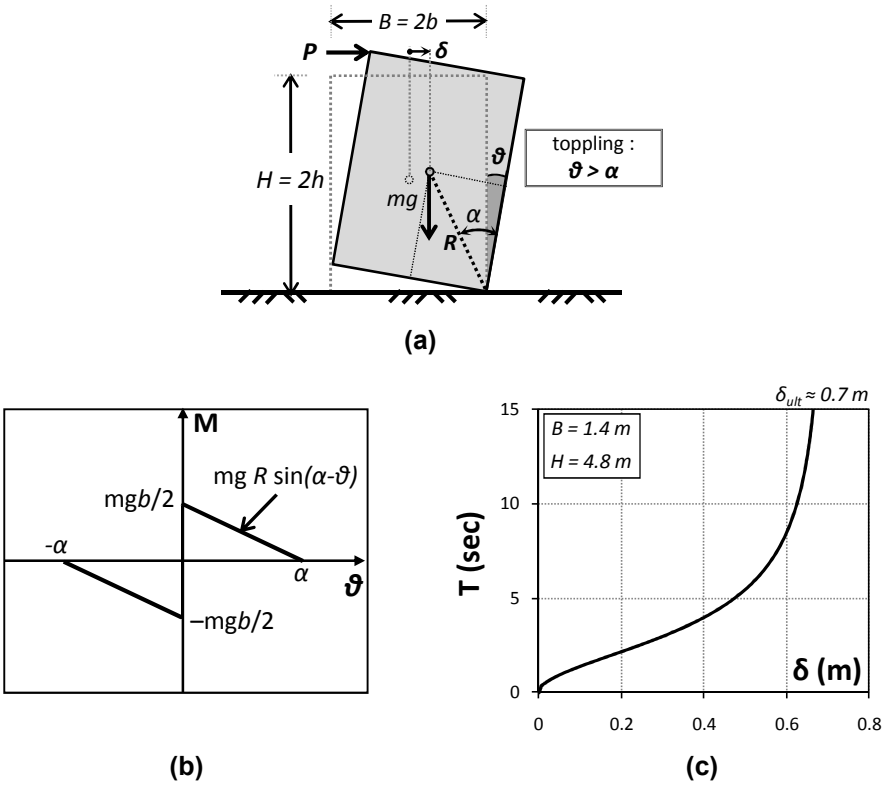

Figure 4.6. Rigid block lying on a rigid base : (a) problem geometry ; (b) M–ϑ (moment-rotation) response (the critical toppling rotation α of the block is roughly equal to b/h) ; (c) evolution of the period T with displacement δ (at the state of incipient toppling, T tends to infinity).

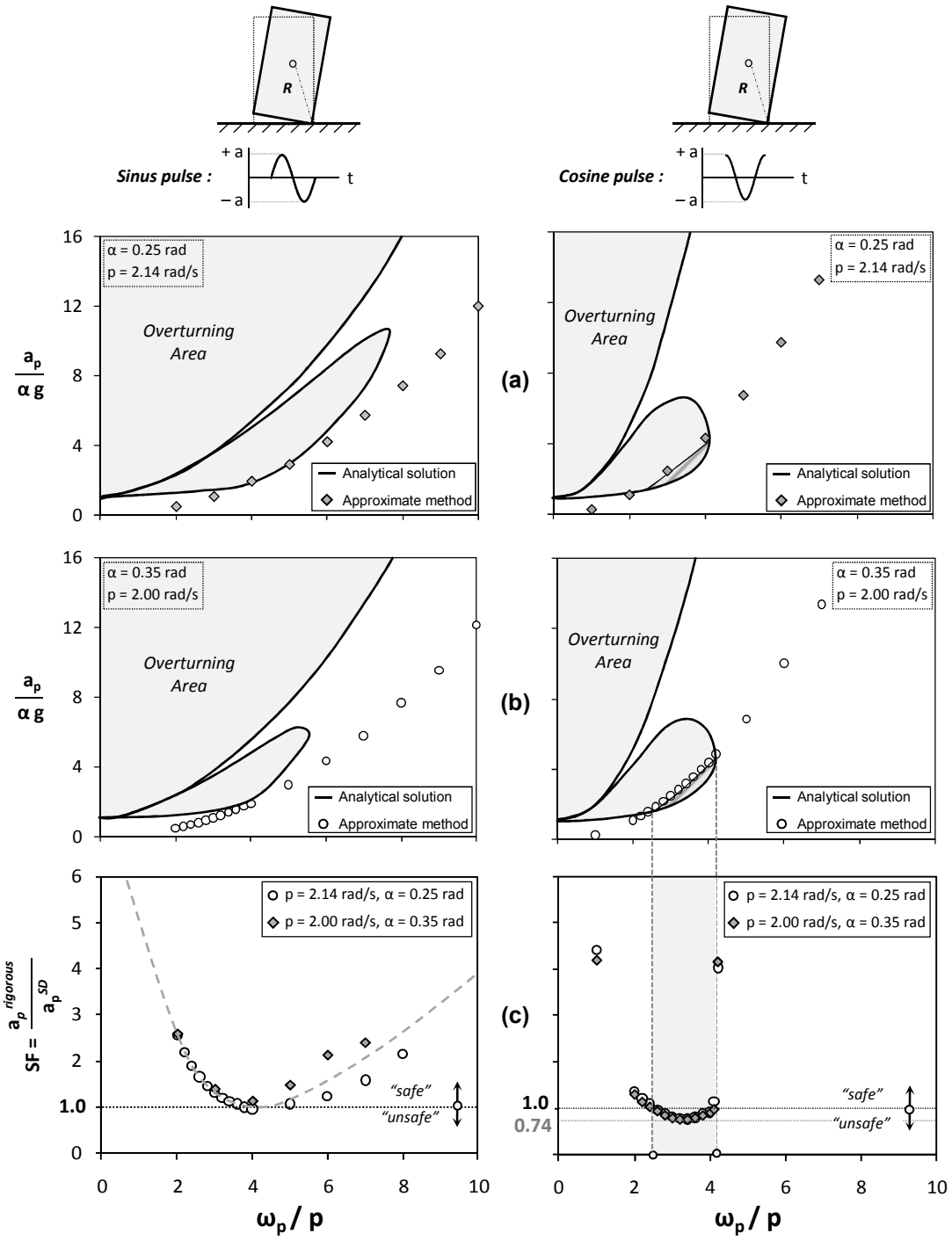

Figure 4.7. Comparison of simplified method (based on the maximum spectral displacement SD_{max}) with the rigorous analytical solution of Zhang & Makris [2001]. Non-dimensional toppling acceleration of a rigid body rocking on a rigid base subjected to sinus (left column) and cosine pulses (right column) as a function of non-dimensional excitation frequency ω_p/p , for : (a) a smaller block of p = 2.14 rad/s and α = 0.25 rad, and (b) a larger block of p = 2.0 rad/s and α = 0.349 rad. (c) Safety Factor SF of the simplified method with respect to the rigorous analytical solution ($SF = a_p^{rigorous}/a_p^{SD}$).

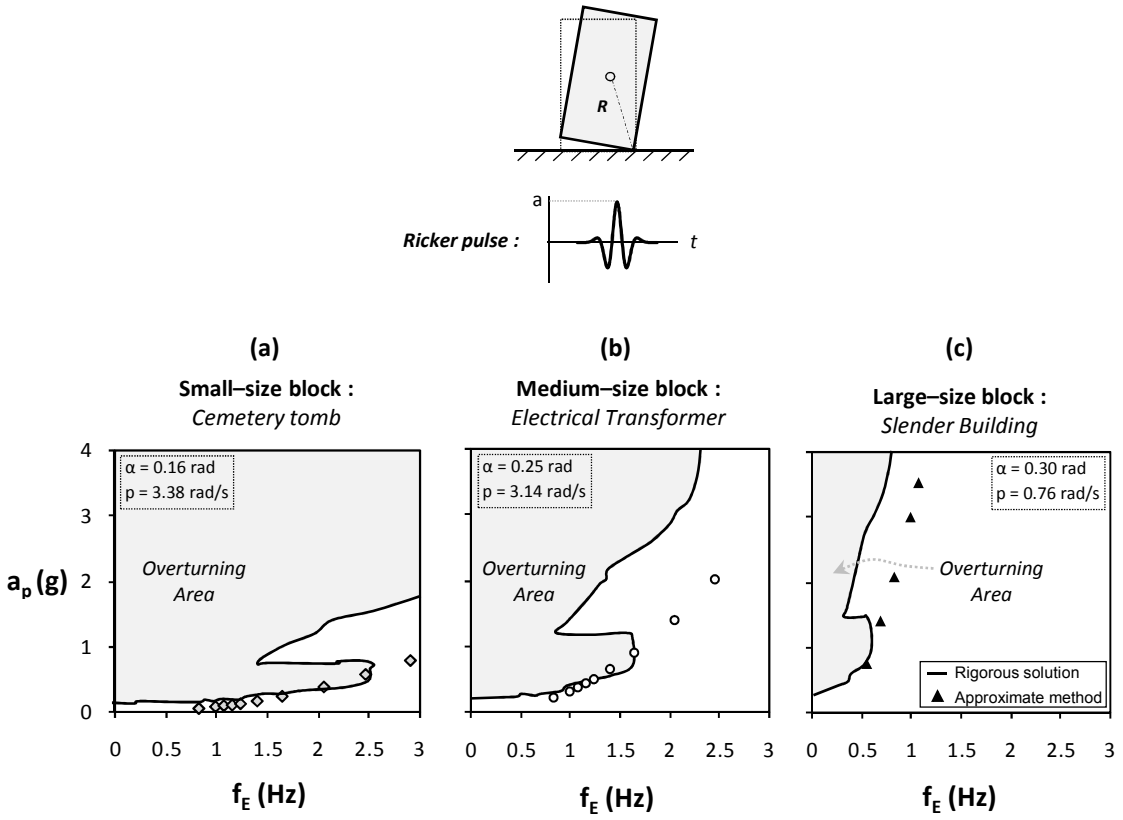

Figure 4.8. Comparison of simplified method (based on the maximum spectral displacement SD_{max}) with the more rigorous solution of Gerolymos et al. [2005]. Toppling acceleration a_p of a rigid body rocking on a rigid base subjected to Ricker pulses, as a function of excitation frequency f_E for : (a) a small–size block (cemetery tomb) of p = 3.38 rad/s and α = 0.16 rad, (b) a medium–size block (electrical transformer) of p = 3.14 rad/s and α = 0.25 rad, and (c) a large–size block (slender building) of p = 0.76 rad/s and α = 0.30 rad.

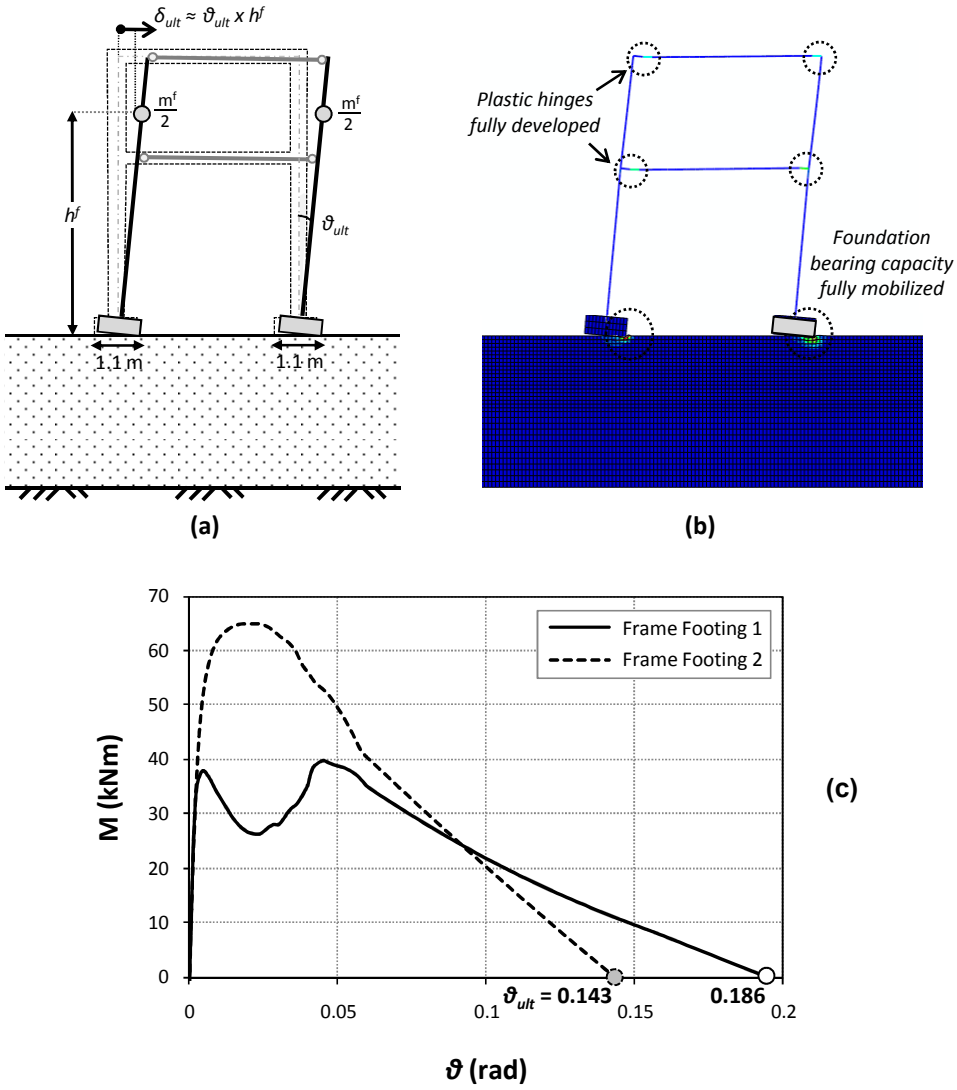

Figure 4.9. Static pushover analysis of the frame with B = 1.1 m footings : (a) sketch of the frame and of its equivalent 1-dof system just before toppling (the toppling displacement $\delta_{ult} = \vartheta_{ult} h^f$) ; (b) deformed mesh with superimposed plastic strain contours just before toppling ; and (c) M–ϑ response of of the two frame footings. The moment capacity and the ultimate rotation ϑ_{ult} of the footing are affected by the fluctuation of the axial load N and the M/Q ratio.

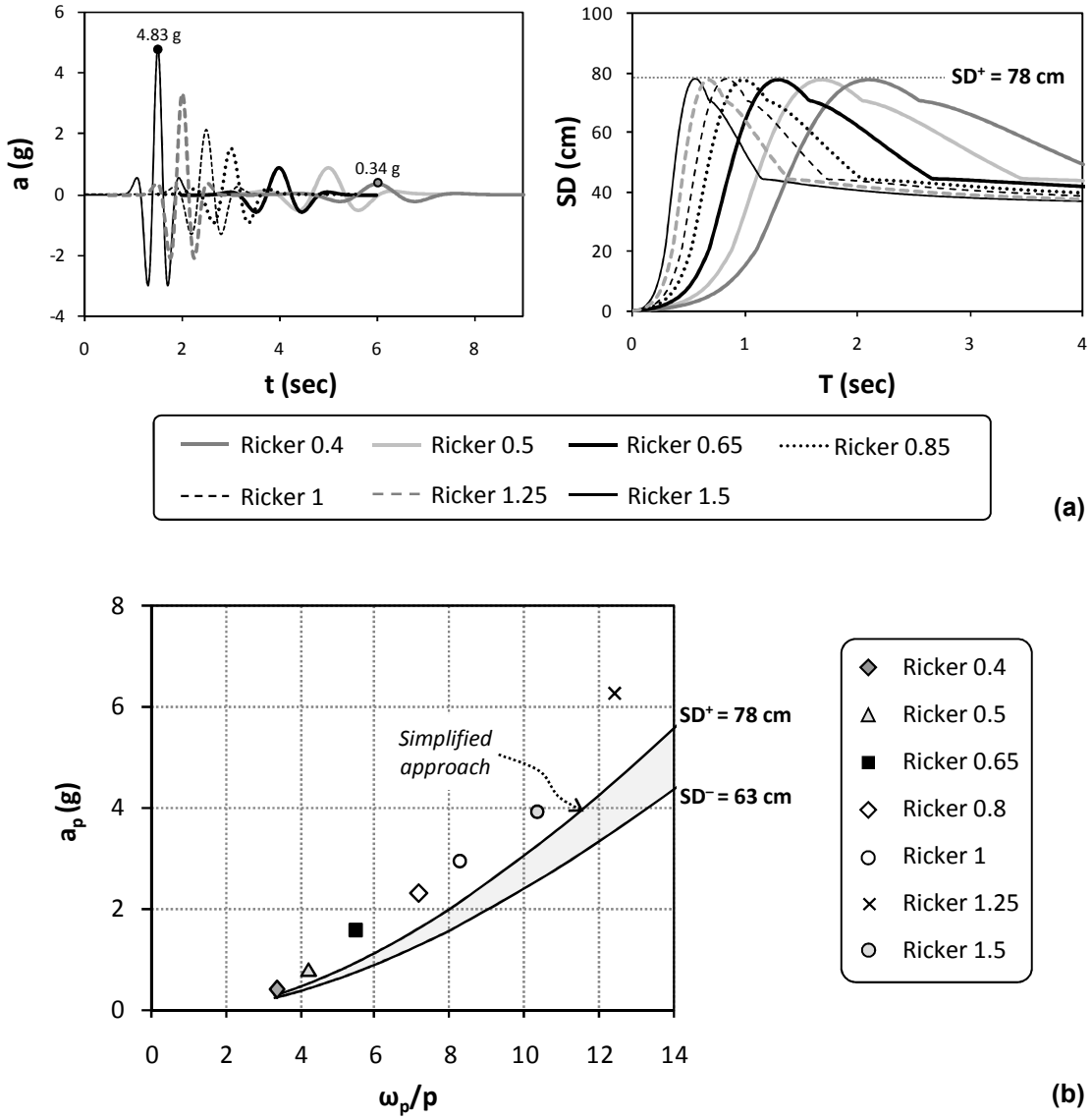

Figure 4.11. Comparison of simplified method (based on the maximum spectral displacement SD_{max}) with dynamic time history analysis of the frame on nonliear soil subjected to Ricker pulses of various dominant frequencies f_E : (a) Acceleration time histories and displacement response spectra *SD* of scaled (to produce SD^+ = 78 cm) Ricker pulses ; (b) comparison of FE computed toppling acceleration a_p with the predicted (employing the simplified SD_{max} approach) a_p^{SD} , as a function of non-dimensional excitation frequency ω_p/p .

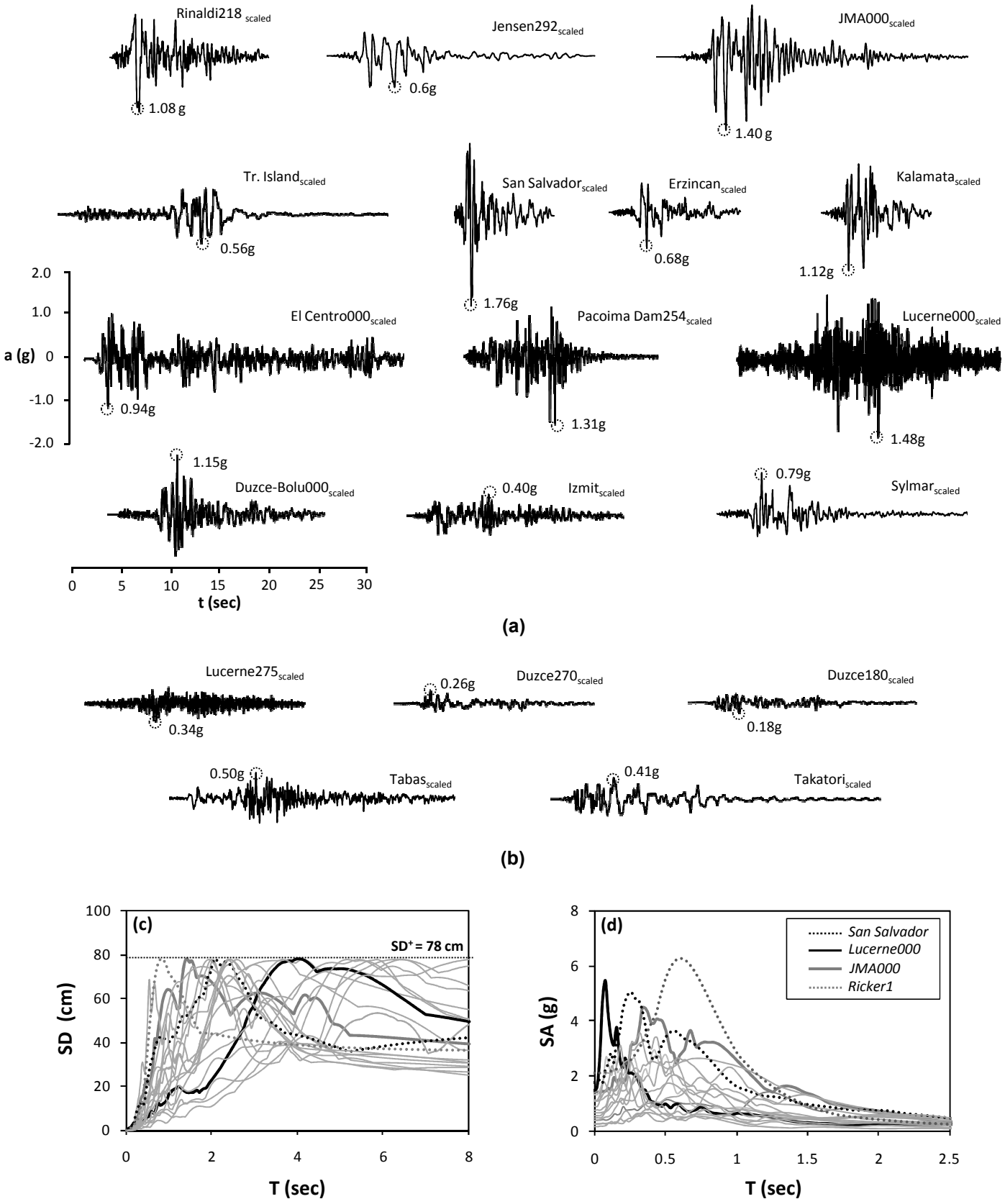

Figure 4.12. Acceleration time histories recorded during devastating earthquakes : (a) scaled *up* to achieve SD^+ = 78 cm, and (b) scaled *down* to achieve SD^+ = 78 cm ; (c) corresponding spectral displacement *SD* response spectra of the scaled seismic motions, and (d) acceleration *SA* elastic response spectra.

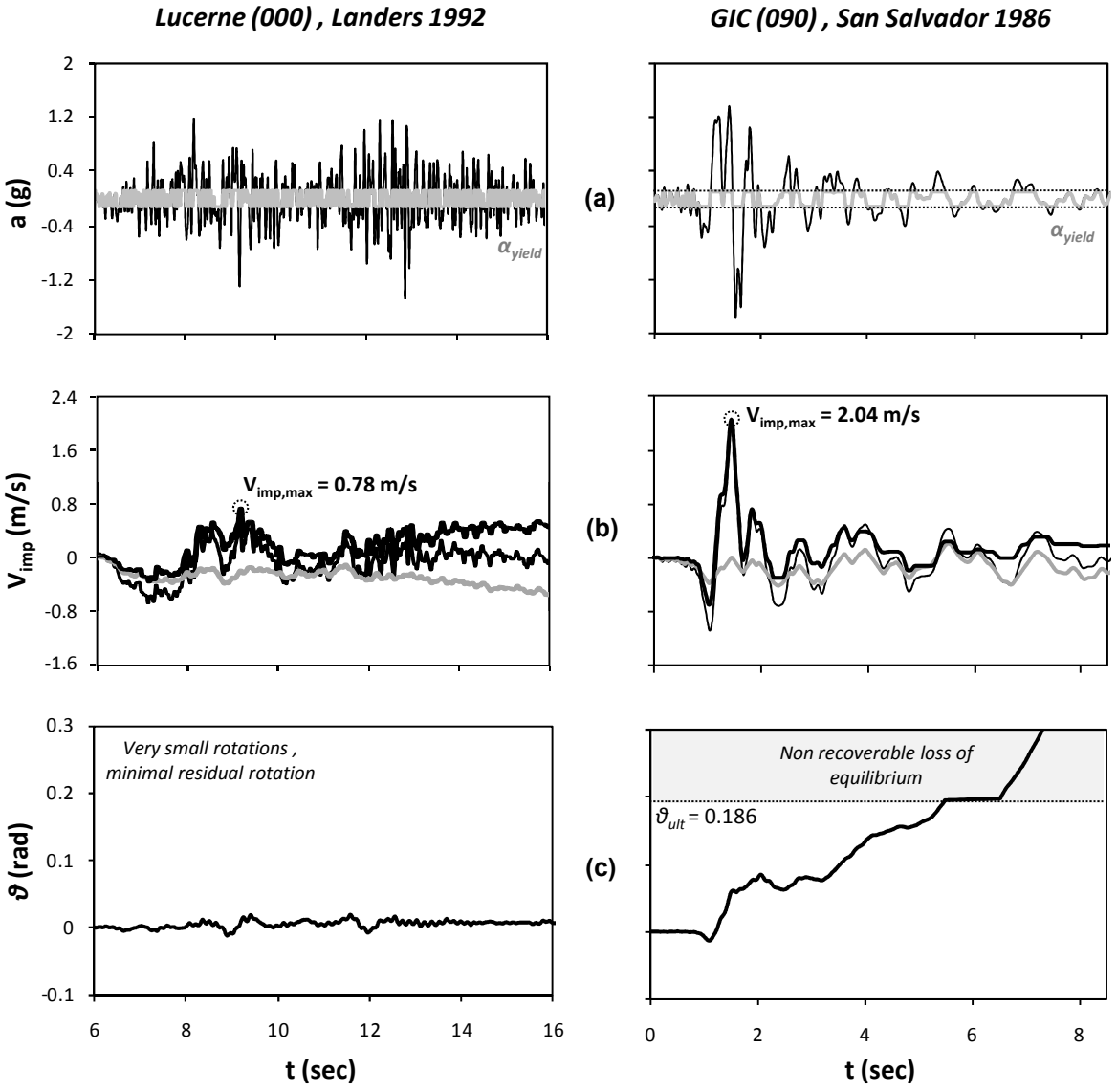

Figure 4.13. Nonlinear dynamic time history analysis – comparison of Lucerne-000 (left column) with GIC-090 record (right column), both scaled at SD^{+} = 78 cm : (a) acceleration time histories (the grey-shaded lines represent the portion of the acceleration time history which lies below the critical uplift acceleration α_{uplift}) ; (b) time histories of "*impact velocity*" V_{imp} (bold black line), calculated by subtracting the integral of the acceleration that is lower than α_{yield} (bold grey line) from the integral of the total acceleration (thin black line) ; and (c) time histories of footing rotation ϑ.

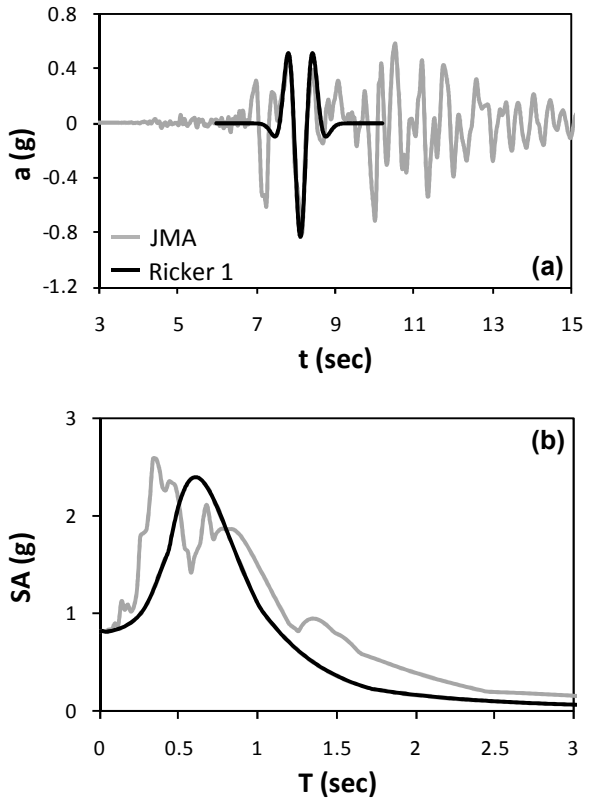

Figure 4.14. Comparison of JMA(000) record with Ricker 1 pulse (scaled in terms of PGA) : (a) acceleration time histories, and (b) elastic acceleration response spectra *SA*.

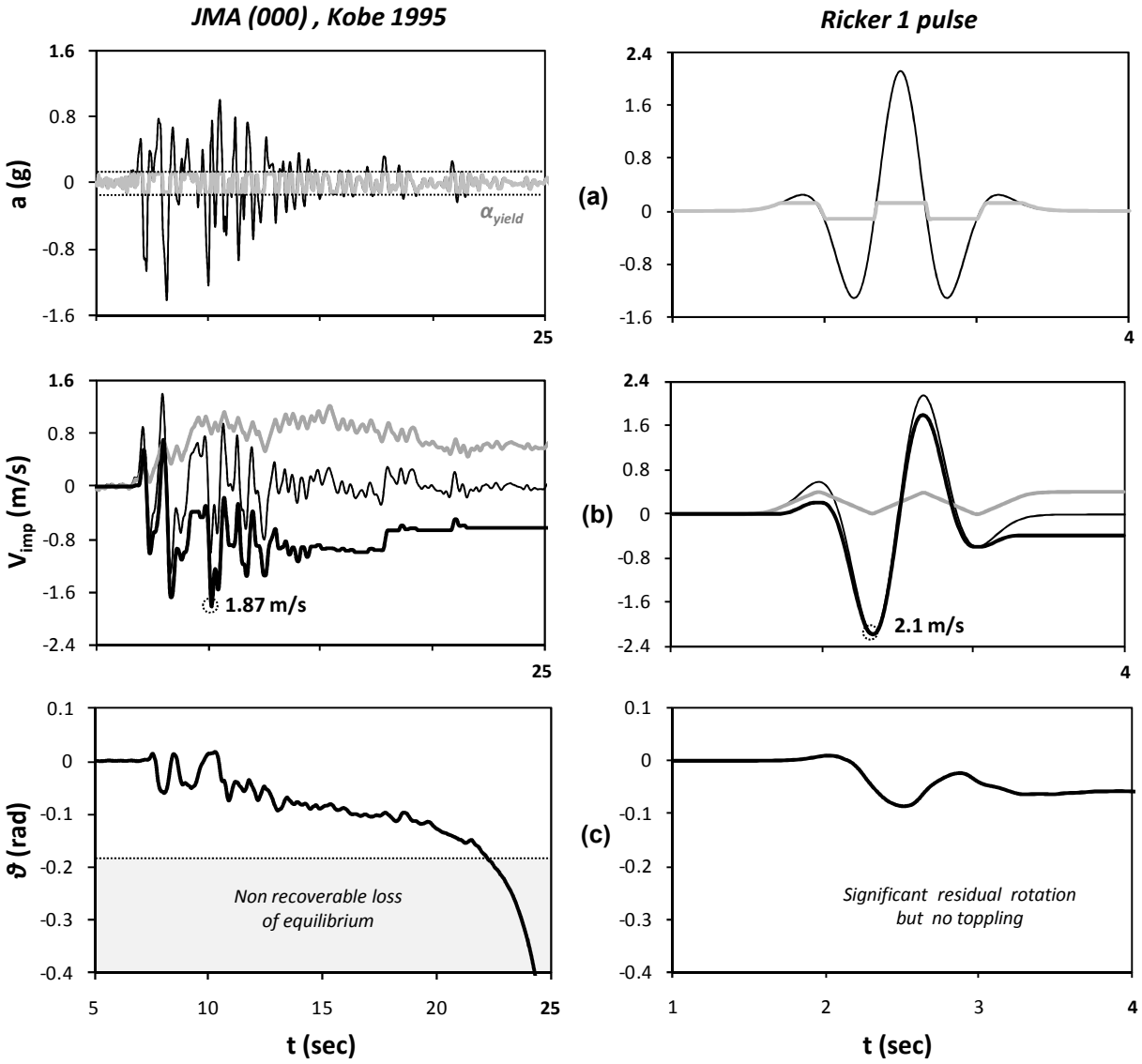

Figure 4.15. Nonlinear dynamic time history analysis – comparison of JMA-000 record (left column) with Ricker 1 pulse (right column), both scaled at SD^{+} = 78 cm : (a) acceleration time histories (the grey-shaded lines represent the portion of the acceleration time history which lies below the critical uplift acceleration α_{uplift}) ; (b) time histories of "*impact velocity*" V_{imp} (bold black line), calculated by subtracting the integral of the acceleration that is lower than α_{yield} (bold grey line) from the integral of the total acceleration (thin black line) ; and (c) time histories of footing rotation ϑ.

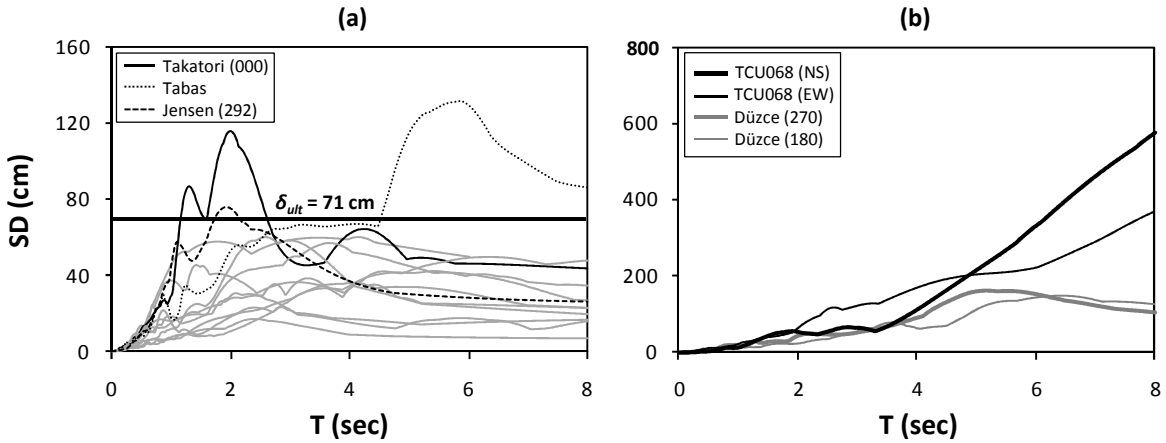

Figure 4.16. Displacement response spectra of *original records* used for the analyses of the present study : (a) all records, and (b) special cases of near-source motions characterized by fling-step effects.

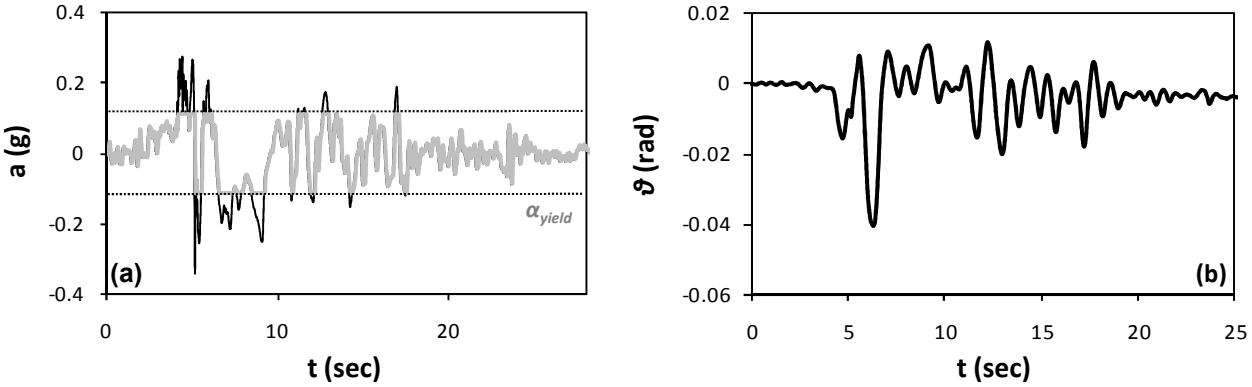

Figure 4.17. Nonlinear dynamic time history analysis of the frame subjected to seismic excitation with the TCU-068 (NS) record (Chi-Chi, Taiwan 1999) : (a) acceleration time history (the grey-shaded line represents the portion of the acceleration time history which lies below the yield acceleration α_{yield} – only a very small portion of the record exceeds α_{uplift} ; (b) time history of footing rotation ϑ.

5

Seismic Wave Propagation in a Very Soft Alluvial Valley : Sensitivity to Soil Nonlinearity, Generation of Parasitic Vertical Component

5.1 Introduction

Although the surface response of 2D alluvial valley formations has been extensively investigated in the literature, research interest has mostly focused on valleys of *idealized geometry* (cosine-shaped, circular, elliptical, trapezoidal, etc.) subjected to *idealized seismic motions* (e.g., harmonic excitation or to simple wavelets), assuming *elastic soil response*. Such analyses have provided deep understanding of the complicated wave propagation phenomena. Among various valuable insights and findings, it was concluded that surface waves generated at the valley boundaries (Love waves when the excitation is SH waves ; Rayleigh waves in case of SV and P waves) propagate back and forth along the valley surface resulting to significant amplifications [Trifunac, 1971; Wong & Trifunac, 1974; Bard & Bouchon, 1980; Harmsen & Harding, 1981; Othuki & Harumi, 1983; Aki, 1988; Todorovska & Lee, 1991; Fishman & Ahmad, 1995]. Hereafter, the term

aggravation will be used to indicate the severity of amplification of the motion above what the 1D theory would predict.

Although the research on the subject has been extended to 3D valley response [Sánchez-Sesma et al., 1989; Sánchez-Sesma & Luzón, 1995; Bao et al., 1996; Bielak et al., 1999; 2000], the effects of soil nonlinearity have received limited attention. In a pioneering study, Zhang & Papageorgiou [1996] studied with the non-linear response of the Marina District during the Loma Prieta earthquake, and showed that wave focusing effects and lateral interferences gradually diminish with increasing soil nonlinearity.

Lately, the critical issue of capturing the real aggravation mechanisms and the necessity to confirm the theoretical results has led to the development of fully instrumented test-sites, which serve as large scale natural laboratories. The Euroseistest in the Volvi basin in Greece [Pitilakis, 2004; Chavez-Garcia et al., 2000; Raptakis et al., 2000; Makra et al., 2001; 2005], the Japanese seismograph arrays in Ashighara Valley [Ohtsuki & Harumi, 1983; Ohtsuki et al., 1984] and Ohba Valley [Tazoh et al., 1988; Gazetas et al., 1993], the alluvial Valley of Parkway in New Zealand [Chavez-Garcia et al., 1998], the Coachella Valley in California [Field, 1996], and the Valley of Nice in France [Sanchez-Sesma et al., 1988], are some of the best known test sites. Their merits include : (i) the high density of the installed accelerograph arrays, (ii) the detailed knowledge of subsoil geometry and soil mechanical properties, and (iii) the accumulation of records. Site response analysis confirmed the importance of 2D geometry effects, clearly suggesting that 1D soil amplification phenomena may be significantly contaminated (*aggravated*) by laterally propagating surface waves. Although such studies have offered valuable insights, in most cases only weak ground motions have been recorded so far.

Despite the extensive bibliography on the subject, most of the research conducted until now has focused on elastic soil response and idealized input motions. The scope of this chapter is to gain further insight on the sensitivity of 2D wave effects to crucial parameters, such as : (a) the frequency content of the input motion, (b) the details of the input motion (duration, number of cycles, frequency content, etc.), and (c) soil non-linearity. A numerical study is conducted, utilizing the Ohba Valley (Japan) as an illustrative example. In addition, emphasis is given to the generation of parasitic vertical component, the effects of which may be detrimental for overlying structures, a phenomenon which has so far received scarce attention.

5.2 Problem Definition and Analysis Methodology

5.2.1 The Ohba Valley

Situated close to Fujisawa City in Japan, the Ohba Valley is an extremely–soft alluvial basin. The valley is crossed by a 600 m – long road bridge: Ohba Ohashi. The geometry of the valley and the soil profile are shown in **Fig. 5.1** [adapted from Tazoh et al., 1984]. The top layers (20 to 25 meters) consist of extremely soft Holocene alluvium (organic layers of humus and clay). Despite the extensive soil improvement that was conducted for the construction of the bridge, the N_{SPT} values of the standard penetration test are very close to zero, while the shear wave velocity, V_S, measured through down-hole tests, ranges between 40 and 65 m/s.

The underlying substratum consists of Pleistocene diluvial deposits with N_{SPT} values greater than 50 and V_S around 400 m/s. The ground water table is almost at the ground surface, while the water content of the top layers by far exceeds 100 %. The latter are

also characterized by large plasticity index (*PI* in excess of 150), and therefore it is likely to exhibit elastic behaviour even under strong seismic shaking [Vucetic & Dobry, 1991]. For more details see Tazoh et al. [1984].

5.2.2 Numerical Analysis Method

The problem is analyzed in the time domain employing the finite element (FE) method, assuming plane-strain conditions. The idealized geometry of the valley and the associated configuration of the FE model are depicted in **Figure 5.2**. The soil is modeled with quadrilateral continuum elements, with a very fine discretization to ensure realistic representation of the propagating waves. The valley deposit is assumed homogeneous with V_S = 60 m/s, while the shear wave velocity of the substratum is significantly higher : V_S = 400 m/s. With mass densities of 1.4 and 1.9 Mg/m^3, respectively, the impedance contrast between soil and base, $\rho_2 V_{S2} / \rho_1 V_{S1}$ is about 10).

Reflections at the base of the formation are avoided by utilizing absorbing boundaries. *Free-field* boundaries responding as shear beams are placed at each lateral boundary of the model, to simulate the motion produced by in–plane vertically incident SV waves.

Three different types of analysis are conducted : (i) visco-elastic analysis, utilizing the finite element code ABAQUS [2008]; (ii) equivalent-linear analysis, utilizing the code QUAD4M [Idriss et al, 1993; Hudson et al., 1994]; and (iii) nonlinear analysis with ABAQUS, employing a kinematic hardening constitutive model. By comparing the results of visco-elastic with nonlinear (equivalent linear and fully nonlinear) analyses, the effects of soil nonlinearity can be quantified.

5.2.3 Soil Constitutive Modeling

For the nonlinear analyses, a nonlinear kinematic hardening constitutive model is employed. The evolution law of the model consists of two components : a nonlinear kinematic hardening component, which describes the translation of the yield surface in the stress space (defined through the backstress *α,* a parameter which describes the kinematic evolution of the yield surface in the stress space), and an isotropic hardening component, which describes the change of the equivalent stress controlling the size of the yield surface σ_o as a function of plastic deformation.

The model incorporates a Von Mises failure criterion, considered adequate to simulate the undrained response of clayey materials, with an associative plastic flow rule [Anastasopoulos et al., 2009]. The evolution of stresses is described by the relation :

$$\sigma = \sigma_o + \alpha \tag{5.1}$$

The evolution of the kinematic component of the yield stress is described as follows :

$$\dot{\alpha} = C\frac{1}{\sigma_0}(\sigma - \alpha)\dot{\bar{\varepsilon}}^{\mathrm{pl}} - \gamma\alpha\dot{\bar{\varepsilon}}^{\mathrm{pl}} \tag{5.2}$$

where *C* the initial kinematic hardening modulus ($C = \sigma_{\mathrm{y}} / \varepsilon_{\mathrm{y}} = E$) and *γ* a parameter that determines the rate of kinematic hardening decrease with increasing plastic deformation.

Model parameters are calibrated against *G–γ* curves of the literature, as described in Gerolymos et al. [2005]. **Figure 5.3** illustrates the results of one such calibration (through finite element simulation of the simple shear test) against the *G–γ* curves of Ishibashi and Zhang [1993].

5.2.4 Validation against Recorded Response

The numerical analysis methodology employed herein has been extensively validated against recorded seismic response in Tazoh et al. [1988], Fan et al. [1994] and Psarropoulos et al. [2007]. Among a number of recorded seismic events, two earthquakes were selected for analysis : (a) an earthquake of M_{JMA} = 6.0 at 81 km epicentral distance, with recorded *PGA* = 0.03 g at the ground surface, referred to as *earthquake A* ; and (b) the M_{JMA} = 6.0 earthquake at 42 km epicentral distance, with recorded *PGA* = 0.12 g at the ground surface, referred to as *earthquake B.*

A comparison between the FE computed ground motion at the valley surface with the recorded is reproduced in **Figure 5.4**, in terms of elastic acceleration response spectra *SA*. Given the relatively small acceleration amplitude of both earthquakes (0.029 to 0.114 g), the shaking-induced shear strains within the soil will not be large enough to generate any substantial soil nonlinearity. In fact, the alluvial layers of the valley are characterized by large *plasticity indexes* (in excess of 100), and are thus expected to behave almost linearly, even for larger imposed strains. Hence, the problem was analyzed assuming elastic soil response with damping ratio ξ = 1 % and ξ = 3%, respectively. Evidently, for both earthquakes the comparison is quite satisfactory, capturing most of the features of valley response. Note that these features could not possibly be captured through 1-D soil response analysis (i.e. ignoring 2-D wave effects).

5.3 The Effect of Frequency Content

To investigate the frequency-dependent scattering phenomena, Ricker wavelets are first utilized as seismic excitations [Ricker, 1960]. The displacement time history of these wavelets is given by :

$$u(t) = \left[1 - 2b\left(t - t_o\right)^2\right] e^{-b(t-t_o)^2} \quad (5.3)$$

where the parameter b is defined as : $b = \pi f_o^2$, f_o the *characteristic* frequency of the pulse, and t_o the time for which $u(t)$ is maximized. In the sequel, three characteristic frequencies are used to illuminate the effects of frequency content on the dynamic response of the valley:

- a high-frequency Ricker 3 (with f_o = 3 Hz),
- a low-frequency Ricker 0.5 (with f_o = 0.5 Hz), and
- an intermediate Ricker 1 (with f_o = 1 Hz) .

Fig. 5.5 depicts the acceleration time histories of the three idealized wavelets (all scaled to 0.20 g), along with their corresponding response spectra.

The following sections go through the key findings of this analysis. Results are shown in terms of peak ground acceleration (PGA) and wavefield patterns.

5.3.1 Spatial Distribution of Peak Ground Acceleration (PGA)

Figure 5.6 depicts the spatial distribution of the aggravation factor $AG = A_{2D}/A_{1D}$ (defined as the ratio of peak ground accelerations from the 2-D and 1-D analyses) along the valley surface for the three Ricker wavelets. All results refer to elastic analysis with a damping ratio ξ = 2 %.

In the case of the high-frequency Ricker 3 wavelet (**Fig. 5.6a**), 1-D soil amplification is clearly prevailing at the central part of the valley (*AG* ≈ 1), while strongly 2-D phenomena are localized near the edges. At those areas, trapping of obliquely incident body waves tends to amplify the motion experienced near the edges, resulting in appreciable aggravations (*AG* ≈ 1.3). Such *focusing effects* have been addressed, among

others, by Sanchez-Sesma et al. [1988]. This particular aggravation pattern is reminiscent of the distribution of damage observed in several earthquakes : in Caracas, for example, the high concentration of damage in the area of Palos Grandes during the 1967 earthquake was attributed to the steep slope of the underlying bedrock at the northern boundary of the 3 km wide sendimentary valley [Papageorgiou & Kim, 1991], rather than simply to the large thickness of the soil deposit and the ensuing 1-D wave amplification.

As shown in **Fig. 5.6b**, the decrease of the dominant frequency of the input seismic motion (Ricker 1 : f_o = 1 Hz) leads to a different distribution of *AG* along the valley surface, with the maximum *AG* (of the order of 1.7) being observed closer to the center of the valley. Observe also the rapid fluctuations of *AG from point to point along the surface.* Evidently, 2D phenomena associated with multiply reflected waveforms at the slope of the bedrock, which were dominant in the case of the high-frequency Ricker 3 seismic excitation, are now absorbed: the length of the wave has become too large to be affected by the topographic anomaly (i.e., the slope of the supporting bedrock). Hence, such effects are clearly overshadowed by the laterally propagating surface waves, leading to a shift of the location of the maximum *AG* towards the center of the valley. Conversely, the AG factor drops even below 1.0 close to the valley edges.

Figure 5.6c depicts the distribution of *AG* along the valley surface for the low-frequency Ricker 0.5 wavelet. In this case, basin-induced waves strongly contaminate the 1-dimensional valley response triggering a strongly 2-dimensional behaviour along the whole valley length. The maximum observed aggravation reaches 1.4 at the center of the valley. Observe that the distribution of *AG* is quite similar to the previous case (Ricker 1), with the main difference being the absence of the previously discussed fluctuations : the

increase of the wavelength has apparently increased the distance between those anomalies and in effect smoothened them significantly.

It is believed that the maximum aggravation in the middle of the valley is the result of the constructive interference of Rayleigh waves, generated at the valley edges and propagating horizontally along the surface in opposite directions. Furthermore, the interference of the directly arriving vertically propagating SV wave pulse with the horizontally propagating Rayleigh waves is responsible for the observed peak values at $x = \pm$ 130 m. The absence of conspicuous focusing effects is hardly surprising, given the large wavelength of the incident SV waves [of the order of 60 (m/s) / 0.75 (s^{-1}) = 80 m] compared to the dimensions of the bedrock irregularity. The above remarks will be further justified in the sequel by means of seismogram synthetics.

It must be generally noted that the symmetrical shape of the valley undoubtedly plays a significant role, as the diffracted waves reach the middle of the valley in phase. Any potential asymmetry of the valley geometry may significantly modify the aggravation pattern.

5.3.2 Wavefield Patterns : Seismogram Synthetics

To get a deeper insight into the aggravation generation mechanisms, a useful numerical diagnostic tool is the seismogram synthetics. **Figs. 5.7** and **5.8** depict the synthetics of horizontal and vertical acceleration, respectively, along the valley surface.

In the case of the *high-frequency* Ricker 3 seismic excitation (**Figs. 5.7a** and **5.8a**), one can clearly observe the generation of laterally induced Rayleigh waves which propagate towards the middle part of the valley with their amplitude gradually

decreasing due to damping. Recall that in this case the aggravation factor in the central part of the valley, is indeed equal to about 1.0 (no Rayleigh wave interference).

For the *intermediate* Ricker 1 seismic excitation the resulting wavefield patterns are presented in **Figs. 5.7b** and **5.8b**. All the different waveforms are clearly depicted : body waves (*SV*), refracted inclined waves (C_a), and two different modes of Rayleigh waves (*R1* and *R2* respectively). The first mode (denoted *R1* in the figure) travels at 120 m/s and is believed to be the mode with the significant horizontal component. The mode with the prevailing vertical behavior (clearly seen in the seismograph synthetic of the vertical motion **Fig. 5.8b**) propagates with significantly lower velocity (65 m/s); an observation which agrees completely with theoretical expectations. The *refracted inclined waves* propagate along the horizontal *x* axis with an apparent propagation velocity C_a defined as :

$$C_a = {}^{V_s}/_{sin\psi} \approx 60/0.287 \approx 209\ m/s \qquad (5.4)$$

where V_s = 60 m/s and tanψ = 24/80 the slope inclination. This theoretical value of velocity agrees fairly well with the one graphically measured (≈ 200 m/s).

In case of *low-frequency* Ricker 0.5 (**Figs. 5.7c** and **5.8c**), Rayleigh waves generated at both edges of the valley and propagating towards its center are clearly illustrated (denoted *R1* in the figure). Their graphically measured velocity is equal to about 100 m/s, which is in good accord with the theoretical value calculated based on the dispersion curve of Ohtsuki & Harumi [1983]. Only one vibrating mode is stimulated. Note also the collision of the opposite propagating Rayleigh waves at the center of the valley. This fact confirms our former assumption that the high aggravations around the valley center are attributed to Rayleigh wave constructive interference.

5.4 The Effect of the Details of the Seismic Excitation

In the previous section, some insights on the prevailing role of frequency content to the resulting wave scattering phenomena were investigated and discussed. The objective here is to examine whether, and to what extent, the largely unpredictable details of the seismic excitation (duration, number of cycles, frequency content, etc.) influence the 2D valley response.

To this end, the valley is subjected to real earthquake records. It is worth mentioning that in their majority the seismic motions used in the analysis have been recorded at the surface of soil deposits, and therefore do not necessarily constitute realistic bedrock excitations. However, the scope of this analysis is not to predict the surface response of the examined formation for a given seismic motion. Our intention is a systematic investigation of the problem, in order to delineate which input motion characteristics are responsible for the significant aggravation.

Three time histories will be analyzed, each corresponding to a characteristic frequency range : (a) the Kede record of the 1999 M_s 5.9 Athens (Greece) earthquake [Papadopoulos et al., 2000; Gazetas et al., 2002], (b) the record of the 2003 M_s 6.4 Lefkada (Greece) earthquake [Benetatos et al., 2005; Gazetas et al., 2005], and (c) the Yarimca record of the 1999 M_w 7.4 Kocaeli (Turkey) earthquake [Elnashai, 2000]. Because of the complexity of wave scattering phenomena with real records, seismogram synthetics are inadequate for the specific analyses. Therefore the results will be presented solely in terms of peak ground accelerations.

5.4.1 High-frequency Seismic Excitation : Kede, (Greece) 1999

Figure 5.9a compares the time history of acceleration and the elastic response spectra of the Kede record with the Ricker 3 wavelet (both *high frequency* seismic excitations). Evidently, the comparison between the real record and the idealized pulse is quite favorable. Apart from certain *irregularities* observed in the record, the time history and the frequency content (see *SA*) of the two motions are rather similar.

The distribution of the aggravation factor *AG* along the ground surface for the two motions are compared in **Figure 5.9b**. At the valley edges, the agreement between real record and Ricker pulse is quite remarkable. Not only the distribution pattern, but also the peak values of *AG* are practically the same. However, moving towards the center of the valley, the two distributions start exhibiting significant discrepancies: two more peaks of *AG* (at $x \approx \pm 200$ m and ± 150 m) appear with the Kede record ; these are not observed with the Ricker 3 excitation. Still though, the behaviour in the central part of the valley is in both cases practically 1-dimensional, with the maximum AG being about 1.0.

5.4.2 Intermediate Seismic Excitation : Lefkada (Greece) 2003

With a rather large number of strong motion cycles (of the order of 8), it could be argued that the record of the Lefkada 2003 earthquake is one of the worst seismic motions ever recorded in Greece. The acceleration time history of the record (characterized as an *intermediate* seismic excitation) is compared in **Figure 5.10a** with the idealized fitted Ricker 1.5 pulse, which exhibits practically the same frequency content.

The results of the numerical analysis (always in terms of distribution of *AG* along the valley surface) are summarized in **Figure 5.10b**. Observe that the *AG* for the Lefkada 2003 record is significantly higher compared to Ricker 1.5, despite the similarity in frequency

content. Notice also that while the Ricker 1.5 generates a single rather distinct peak of *AG* (at $x \approx \pm 130$ m), the real record is characterized by a large number of fluctuations : peaks at $x \approx \pm 75$ m and ± 20 m.

Interestingly, the response of the real record agrees fairly well with that of the idealized pulse close to the valley edges. The *irregularities* of the record do not affect the response at the valley edges, where focusing effects are dominant, but make an important difference towards the center of the valley, where horizontally propagating Rayleigh waves seem to be in control. While the *single* pulse of the Ricker wavelet creates a *single* Rayleigh wave, the *multiple* strong motion pulses of the record are responsible for the development of a *multitude* of surface waves. Obviously, the increase of the number of such waves, increases the probability of constructive interference at different locations, as they travel towards the center of the valley.

5.4.3 Low-frequency Seismic Excitation : Yarimca (Kocaeli) 1999

At a distance of only 3 km from the North Anatolian fault (responsible for the Kocaeli 1999 earthquake), the Yarimca record is characterized by both forward-rupture directivity and fling-step effects [Garini et al., 2009]. Once the directivity and fling pulses are unveiled, the record (**Fig. 5.11a**) appears to be comparable with the Ricker 0.5 wavelet in terms of frequency content. The comparison is certainly not perfect in terms of *SA*, but Ricker 0.5 can be seen to reasonably fit the (first at least) hidden low-frequency acceleration pulse of the record (see acceleration time histories). Naturally, the record is in addition characterized by subsequent low-frequency pulses and multiple higher-frequency perturbations, which are also evident in the elastic response spectra, (observe the higher-frequency peaks).

As shown in **Fig. 5.11b**, despite the substantial differences between the record and Ricker 0.5, the agreement among the distributions of *AG* is quite remarkable. Some discrepancies between the record and the idealized pulse do exist, but the general trend is quite similar. The record yields slightly higher maximum *AG*, and is characterized by a more irregular distribution. It could be claimed that the aforementioned hidden low-frequency acceleration pulse of the record yields a distribution of *AG* almost identical to that of the Ricker 0.5, while the higher-frequency irregularities are responsible for the observed fluctuations :

- constructive interference of Rayleigh surface waves at the areas of *AG* local peaks ($x \approx \pm$ 200 m and ± 100 m) ;
- destructive interference at the areas of *AG* local troughs ($x \approx \pm$ 250 m and ± 160 m).

At this point, it should be noted that the comparison between Ricker pulses (i.e. narrow band seismic motions) and real records (i.e., broadband seismic motions) would not necessarily be equally acceptable if the soil was not homogeneous.

5.5 The Effect of Soil Nonlinearity

The role of nonlinear soil response is investigated in three different ways : (i) with viscoelastic analyses, in which a small degree of soil nonlinearity is *partially* accounted for through increased damping ξ ; (ii) with equivalent-linear analysis (in which a moderate degree of soil nonlinearity is taken into account through an iterative procedure according to which the soil stiffness *G* and the damping ratio ξ are made consistent with the shear strain level) ; and (iii) with fully nonlinear analysis, in which strongly nonlinear

soil response is taken into account with the aforementioned kinematic hardening constitutive model.

5.5.1 The Influence of Damping Ratio

All of the results shown until now referred to elastic analysis with ξ = 2%, an assumption which can be considered valid for (very) small magnitude seismic excitation and / or very stiff soil. At such low shear strain amplitudes, the secant shear modulus *G* is very close to the initial (elastic) shear modulus G_{max}. However, with stronger seismic motions, the soil will behave nonlinearly: *G* will decrease with increasing amplitude of shear strain, and the damping ratio will increase. The scope of this section is to reveal whether and to what extent material damping influences the dynamic response of the valley. For this purpose, the analyses are repeated, with parametrically varying ξ between 2% and 10%. To keep comparisons simple, results are discussed for the three idealized Ricker pulses only.

Figure 5.12 summarizes the results in terms of *AG* distribution along the valley surface. A general conclusion is that the increase of the damping ratio ξ mainly influences surface wave propagation. Observe that the local peaks towards the center of the valley, which are related to Rayleigh wave interferences, decrease substantially with the increase of ξ. In contrast, the increase of ξ does not appear to have any effect on *AG* at the valley edges. Hence, for the high-frequency Ricker 3 (**Fig. 5.12a**), the increase of ξ does not appear to have any effect on the distribution of *AG*. Recall that in this case the aggravation is purely related to focusing effects, which are the result of multiple wave reflections at the ground surface and the sloping bedrock. This mechanism, the direct result of geometry, is naturally not affected by the damping ratio. On the other hand, the

aggravation due to surface waves requires that these waves, generated at the edges, propagate and reach the center of the valley. Hence, since the increase of ξ tends to substantially dampen their propagation, the related aggravation unavoidably decays as well.

This phenomenon becomes more evident in the case of the intermediate Ricker 1 wavelet (**Fig. 5.12b**), in which case *AG* at x = 0 m (which is clearly related to constructive interference of surface waves) reduces from 1.65 for ξ = 2 % to roughly 1.0 for ξ = 10 %. Observe that the geometry-related AG at the valley edges is again insensitive to increasing ξ. The conclusions are qualitatively similar for the low-frequency Ricker 0.5 (**Fig. 5.12c**). Analyses with real records, not shown here for the shake of brevity, lead practically to the same conclusions.

5.5.2 Equivalent Linear versus fully Nonlinear Analysis

In this section, the results of equivalent linear analysis (using the numerical code QUAD4M) are compared with those of a fully nonlinear analysis employing a kinematic hardening constitutive model (see detailed description above). In the first case, the analysis is practically elastic, but soil nonlinearity is taken into account through an iterative procedure according to which the soil stiffness G and the damping ratio ξ are made consistent with the shear strain level. In the latter case, nonlinear soil response is modeled with an increased degree of realism. For the equivalent linear analysis, the G–γ curves of Ishibashi & Zhang [1993] for PI = 50 have been utilized. For the nonlinear analysis, the same curves are employed for calibration of constitutive model parameters (see **Fig. 5.3**). As in the previous section, results are shown for the three Ricker wavelets, all scaled at PGA = 0.2g.

The comparison is summarized in terms of distribution of *AG* along the valley surface in **Figure 5.13**. Although the general trends can be claimed to be comparable, the generic conclusion is that the two methods may yield different results.

In the case of the high-frequency Ricker 3 (**Figure 5.13a**), although the maximum *AG* (≈ 1.4) predicted by the two methods is quite similar, their distributions have noticeable discrepancies. It is interesting to notice the shift in the location of the maximum *AG* : from $x \approx \pm$ 250 m for the equivalent linear analysis (denoted with the grey line) to $x \approx \pm$ 220 m for the nonlinear analysis. Going back to the elastic analysis (see **Fig. 5.12a**), it becomes clear that both the location and the amplitude of maximum *AG* produced by the equivalent linear analysis is almost the same with that of the elastic analysis. This is attributable to the high frequency of the seismic excitation, due to which the developed shear strain is not enough to mobilize a large degree of nonlinearity.

Conversely, in case of both the intermediate Ricker 1 (**Fig. 5.13b**) and the low-frequency Ricker 0.5 (**Fig. 5.13c**) the induced non-linearity practically eliminates the 2D aggravation phenomena previously attributed to Rayleigh waves. This trend is captured by both the equivalent linear and the fully non-linear model, with the former predicting quite higher values of AG.

Figure 5.14 compares the distribution of peak horizontal accelerations along the valley surface (for the case of Ricker 1 excitation) computed by means of equivalent linear and fully non-linear analysis, in order to demonstrate the very good agreement of the two methods at the central part of the valley, where the response is dominated by 1D soil amplification. Any differences are localized at valley edges, where 2D wave scattering phenomena determine the response. Results are similar for all three Ricker wavelets.

5.5.3 Fully Nonlinear versus Elastic Analysis

Having investigated the differences between equivalent linear and nonlinear analysis, the latter is employed in this section to investigate the role of soil nonlinearity for real seismic excitations.

The comparison of elastic (ξ = 2%) with nonlinear analysis is shown in **Fig. 5.15** in terms of distribution of *AG* along the valley surface. Quite interestingly, and contrary to the common expectation, it appears that soil nonlinearity does not always cause AG to reduce. In fact, for the high-frequency Kede (Athens 1999) seismic excitation (**Fig. 5.15a**), *AG* at the valley edges increases with soil nonlinearity (from roughly 1.25 to 1.6). At the valley center there is practically no difference.

The same observation is valid for the intermediate Lefkada 2003 (**Fig. 5.15b**) and the low-frequency Yarimca (**Fig. 5.15c**): *AG* at the valley edges increases when soil nonlinearity is modeled. To explain this observation, the following hypothesis is made: soil plastification near the soil-rock interface, leads to the formation of a very soft plastified zone. In the case of the single pulse Ricker wavelets, soil plastification acted as a damping mechanism, leading to reduction of *AG*. But in the case of real seismic excitations, which contain a large number of strong motion cycles, the picture is altered : the zone of plastification is generated by the first arriving waves (due to the initial strong motion cycles), and then acts as a trap for forthcoming (due to the subsequent strong motion cycles) inciting waves. The latter are trapped in a narrow band between the plastic zone and the surface, and are thus generating larger *AG*.

If the above hypothesis holds true, then this phenomenon should become more evident with the increase of strong motion cycles. Indeed, the difference between elastic and nonlinear analysis (always referring to valley edges) is larger for the Lefkada 2003

and the Yarimca seismic excitations which contain several strong motion cycles : $AG \approx$ 1.65 for the nonlinear analysis compared to roughly 1 (no amplification) for elastic analysis.

In the case of the intermediate frequency and multi-cycle Lefkada 2003 seismic excitation, the fluctuations of AG towards the valley center practically disappear with soil inelasticity. The nonlinearity increases the effective damping (which is of hysteretic nature in this case), reducing the aggravation related to laterally propagating surface waves (similarly to the previously discussed observations referring to the increase of the damping ratio).

5.6 Generation of Parasitic Vertical Component

In the previous sections, the aggravation due to 2D valley effects has been investigated, focusing on the prevailing horizontal component of the seismic motion. However, due to the geometry of the bedrock slope, a purely horizontal seismic motion will unavoidably generate a parasitic vertical component. A first attempt to address such phenomena is presented in the sequel, focusing on real records.

Figure 5.16 depicts the results for the high-frequency Kede seismic excitation. The analysis is conducted subjecting the valley to the horizontal component of the record *only* (bottom). As revealed by the distribution of the ratio ($\max A_v$ / $\max A_h$) of the valley-generated parasitic vertical component A_v to the horizontal component A_h (middle of the figure), a significant parasitic vertical component is developed which, close to the valley edges may even exceed A_h. Moreover, since the parasitic valley-generated A_v is the result

of geometry, it is totally correlated with A_h (see produced surface acceleration time histories at the top of the figure).

Figure 5.17 compares the natural recorded vertical component time history and spectrum with the parasitically generated ones at the valley surface. Observe that the vertical component of the Kede record (**Fig. 5.17c**), is of higher frequency compared to the horizontal one. As with most real records, such high-frequency vertical component may not really have any substantial effect on the performance of structures, even if completely correlated with the horizontal motion [e.g. Fardis et al., 2003]. On the other hand, the frequency content of the parasitic vertical component (**Fig. 5.17a** and **5.17b**) is practically the same with that of the horizontal component, while its amplitude is dramatically higher than that of the natural component. Hence, in stark contrast to the natural vertical component, which is the result of P-waves, the valley-generated parasitic vertical component can be detrimental for overlying structures.

For the intermediate Lefkada 2003 (**Figs. 5.18** and **5.19**) and the low-frequency Yarimca (**Figs. 5.20** and **5.21**) seismic excitations the results are not as intense (the ratio does not exceed 0.65), but the key conclusion remains. Being mainly the result of geometry (or focusing) effects, the parasitic vertical component almost disappears at the center of the valley.

Figure 5.22 investigates the effect of non-linearity on the generated parasitic vertical component. For the high-frequency Kede seismic excitation (**Fig. 5.22a**), the A_v/A_h ratio remains unaffected by the induced non-linearity. For the intermediate Lefkada 2003 case (**Fig. 5.22b**) and the low-frequency Yarimca (**Fig. 5.22c**), the soil non-linearity, while not altering the general trend, modifies the A_v/A_h ratio especially in the

valley edges. The ratio appears even higher in the non-linear case in these regions. This increase is rather the result of decreased A_h than increased A_v.

5.7 Conclusions

A numerical study has been conducted, utilizing a shallow soft valley as a test case, to gain insights on the sensitivity of 2D valley response on parameters, such as the frequency content of the input motion, its details, and soil non-linearity. The numerical methodology employed herein has been validated against recorded seismic response. The following conclusions have emerged :

1) The dynamic response of the valley was shown to be strongly two-dimensional, and cannot possibly be captured through 1-D soil response analysis.
2) *Wave focusing* at the valley edges and surface waves originating at the corners of the valley are responsible for *substantial aggravation* (*AG*) of the seismic motion.
3) In the case of *high-frequency* seismic excitation, 1D soil amplification is prevailing at the central part of the valley (*AG* ≈ 1), while strongly two–dimensional phenomena are restricted at the corners, where trapping of obliquely incident body waves amplifies the motion, resulting to aggravation of (*AG* ≈ 1.3).
4) For *low-frequency* seismic excitations, the wavelength becomes too large to be affected by the topographic anomaly (i.e. the slope of the supporting bedrock), and focusing effects are overshadowed by the horizontally propagating surface waves, leading to a shift of the location of the maximum *AG* towards the center of the valley.
5) For elastic response, the details of the seismic excitation do make a difference in the development of surface waves, responsible for the aggravation at the valley center

while they do not affect to the same extent focusing effects at valley edges (which are geometry related). The increase of the number of strong motion cycles increases the probability of constructive interference of surface waves traveling towards the center of the valley, thus increasing the resulting *AG*.

6) The increase of damping *ξ* mainly influences surface wave propagation, reducing *AG* towards the center of the valley. Yet, it does not appear to have any effect on *AG* at valley edges.
7) Soil nonlinearity may modify the 2D valley response to a substantial extent. The equivalent linear method can capture parts of the problem, but will not yield the same results as a fully nonlinear analysis.
8) For idealized single-pulse (Ricker) seismic excitations, soil nonlinearity in general reduces *AG*, mainly at the center of the valley (where the role of surface waves is dominant). At the valley edges, where the response is controlled by the geometry, the differences are not as pronounced.
9) The details of real seismic excitations complicate things further, and *quite remarkably* lead to an increase in AG at the valley edges as soil nonlinearity increases. Soil plastification near the soil-rock interface at valley edges, leads to development of a very soft plastified zone : this is generated by the first arriving waves, which act as a trap for incident waves, which are captured between the plastic zone and the surface, thus generating larger *AG*.
10) The 2D geometry of the valley (excited by exclusively-horizontal waves) generates a *parasitic vertical component*. Compared to the natural vertical component of an earthquake, which is the result of P-waves and is usually of very high frequency content to pose a serious threat to structures, this valley-generated parasitic vertical

component *can be detrimental for overlying structures*: being a direct result of geometry, it is fully correlated and of practically the same dominant period as the horizontal component.

Figures of Chapter 5

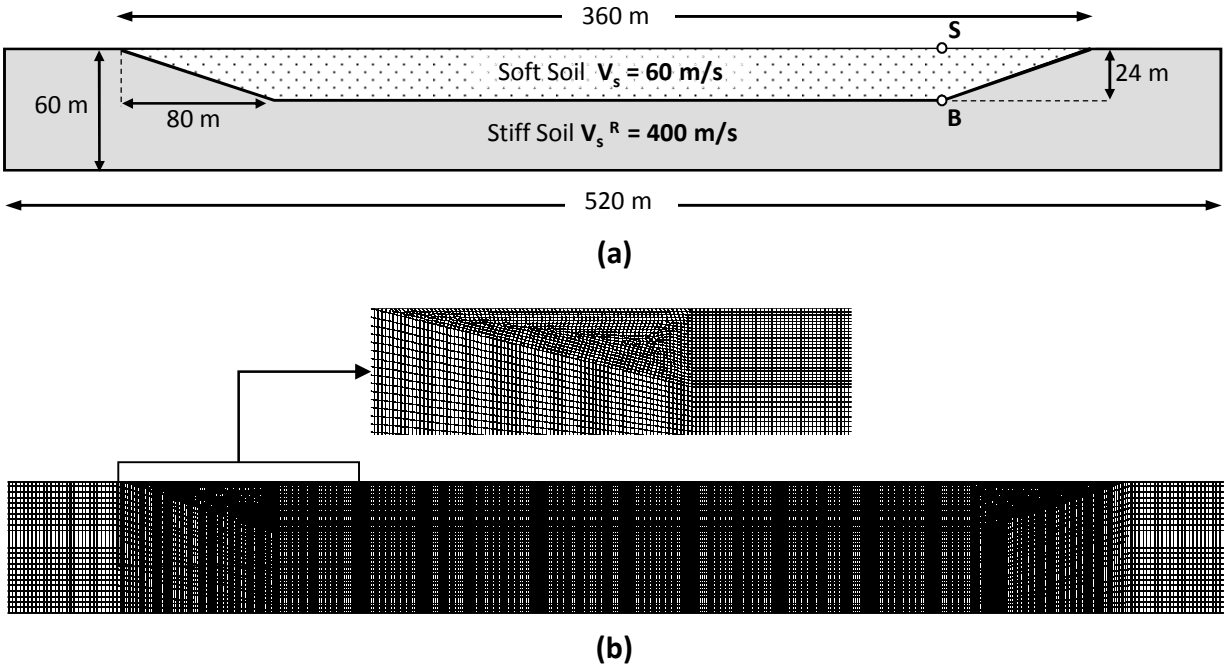

Figure 5.2. (a) Idealized cross-section of the Ohba Valley modeled in the paper; and (b) finite element discretization, along with zoomed view at the edge of the valley.

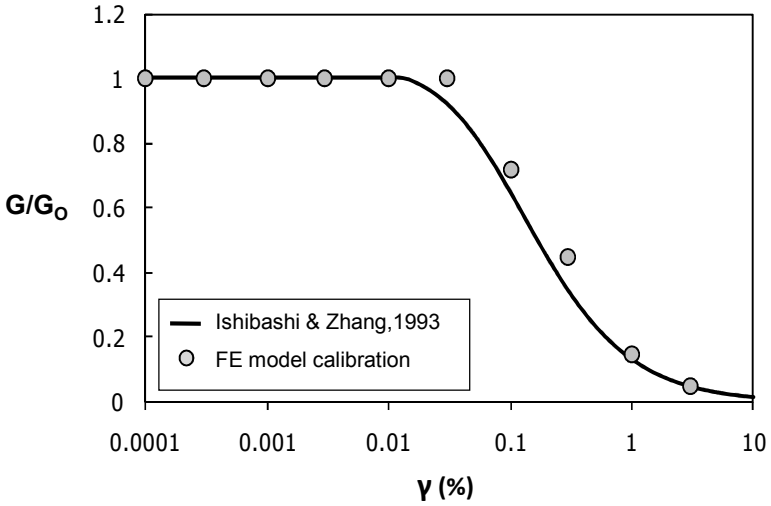

Fig. 5.3. Nonlinear kinematic hardening constitutive soil model calibrated against published G–γ curves from the literature.

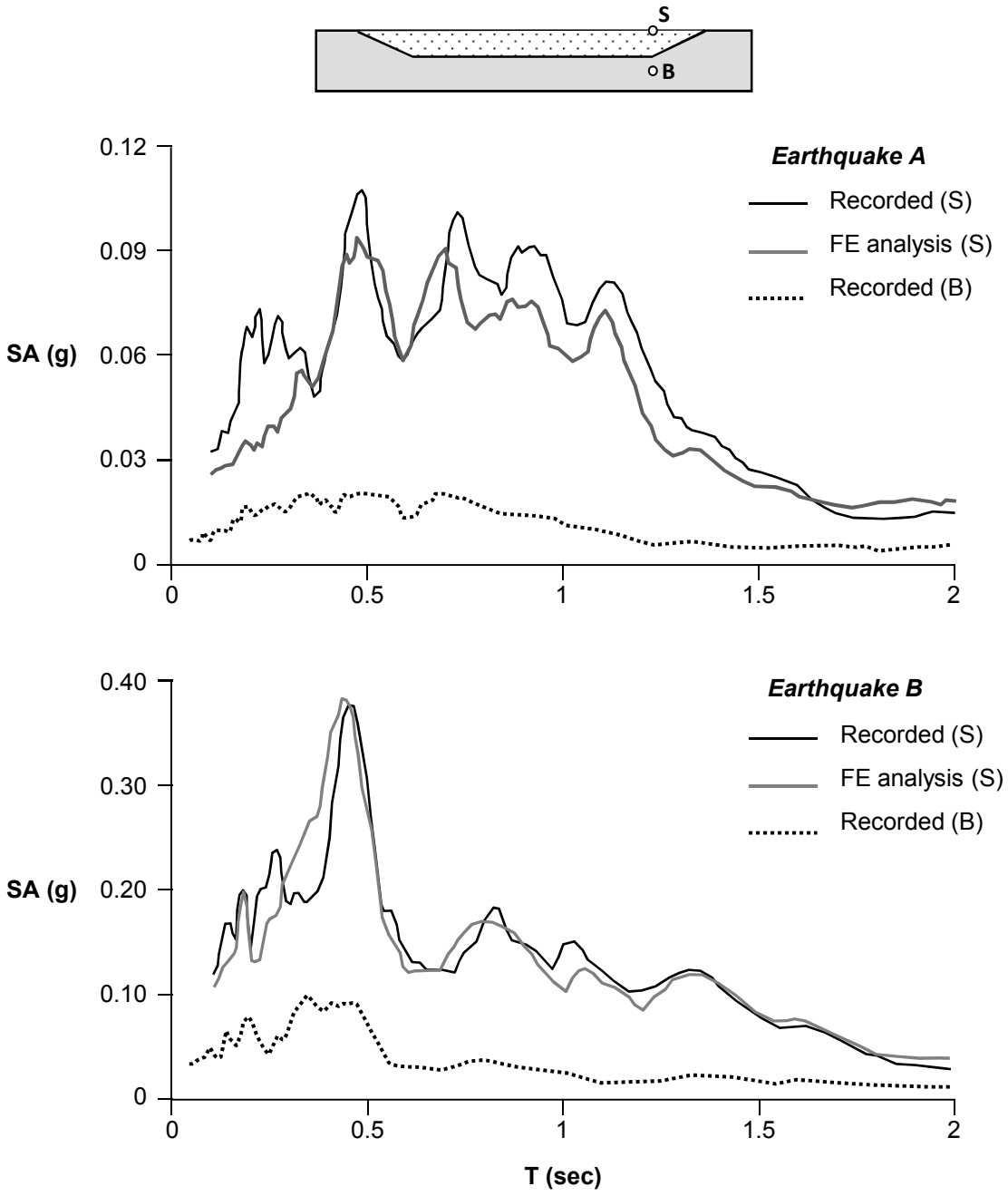

Figure 5.4. Validation of numerical analysis method against observations : comparison of spectral accelerations response SA derived from the accelerograms recorded at the ground surface (point S) and the base stiff soil (point B) with those derived from the FE computation (assuming viscoelastic soil response). Two different earthquake motions (as recorded at B) were used as excitation [Psarropoulos et al., 2007].

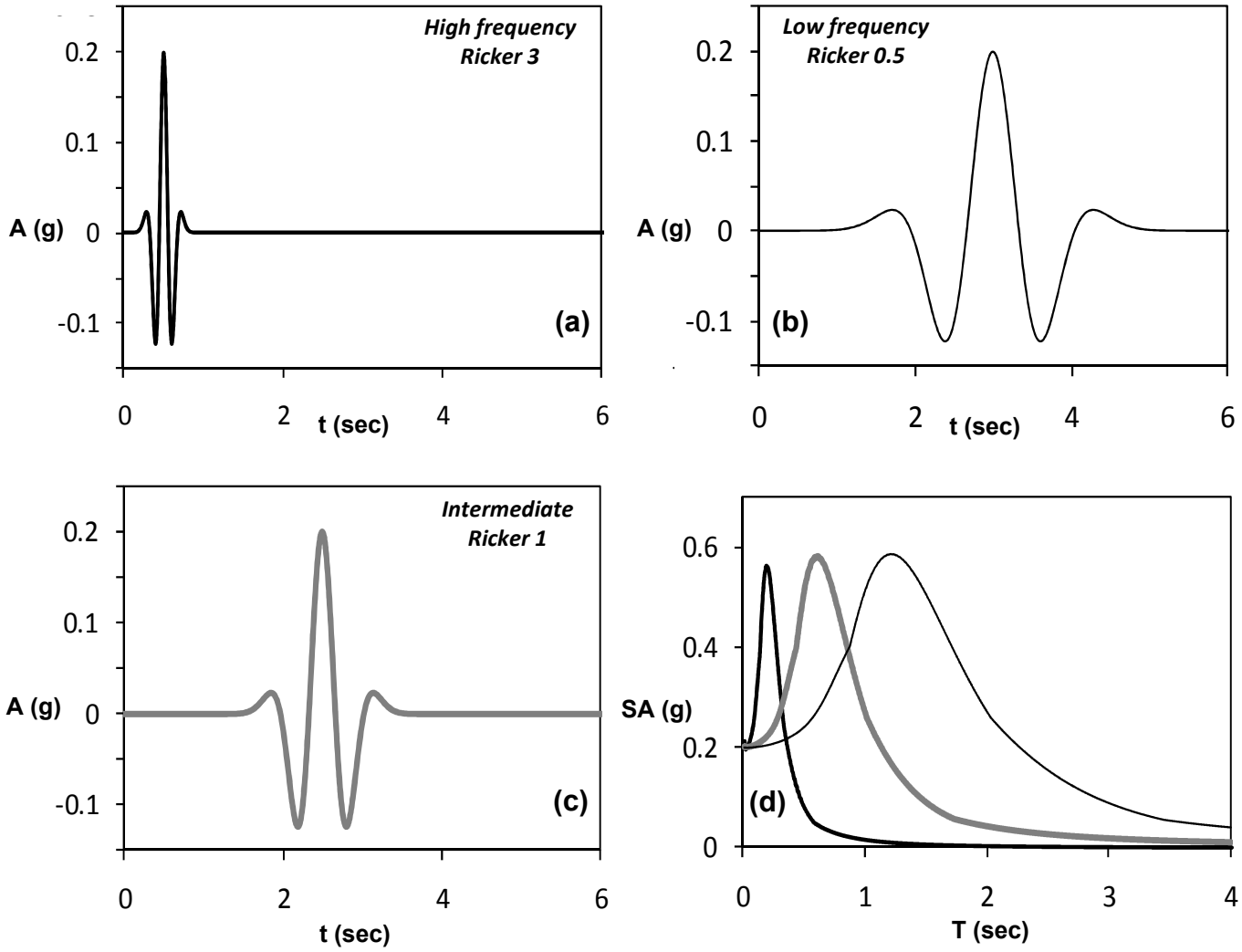

Figure 5.5. The three Ricker wavelets used as seismic excitations : (a) the high-frequency Ricker, f_o = 3 Hz ; (b) the low-frequency Ricker, f_o = 0.5 Hz ; (c) the intermediate Ricker, f_o = 2 Hz ; along with (d) their 5 % damped acceleration elastic response spectra.

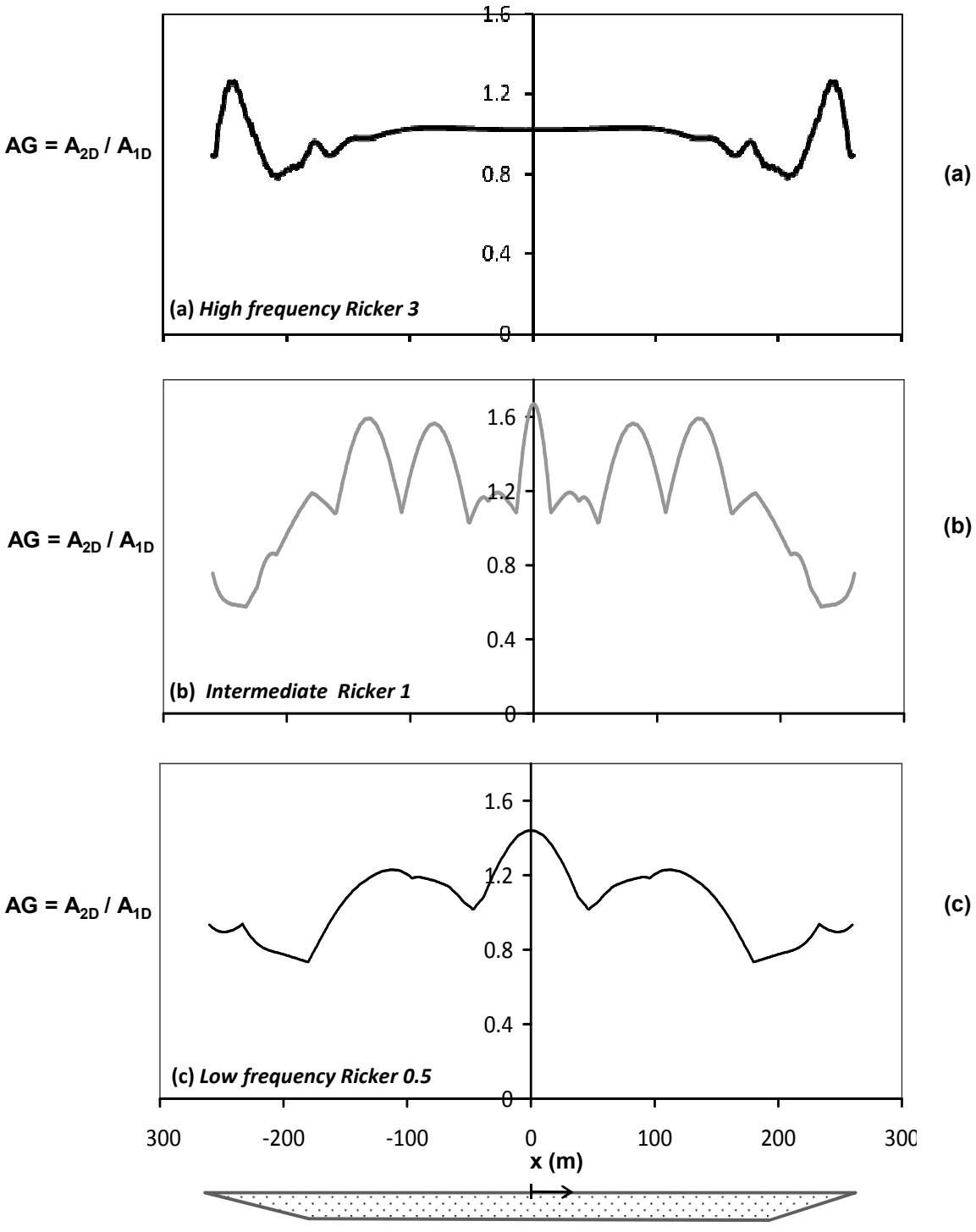

Figure 5.6. The effect of frequency content on the response along the ground surface : elastic analysis with soil hysteretic damping ξ = 2 %. Distribution of the aggravation factor *AG* for : (a) the high frequency Ricker 3 wavelet, (b) the intermediate Ricker 1, and (c) the low frequency Ricker 0.5.

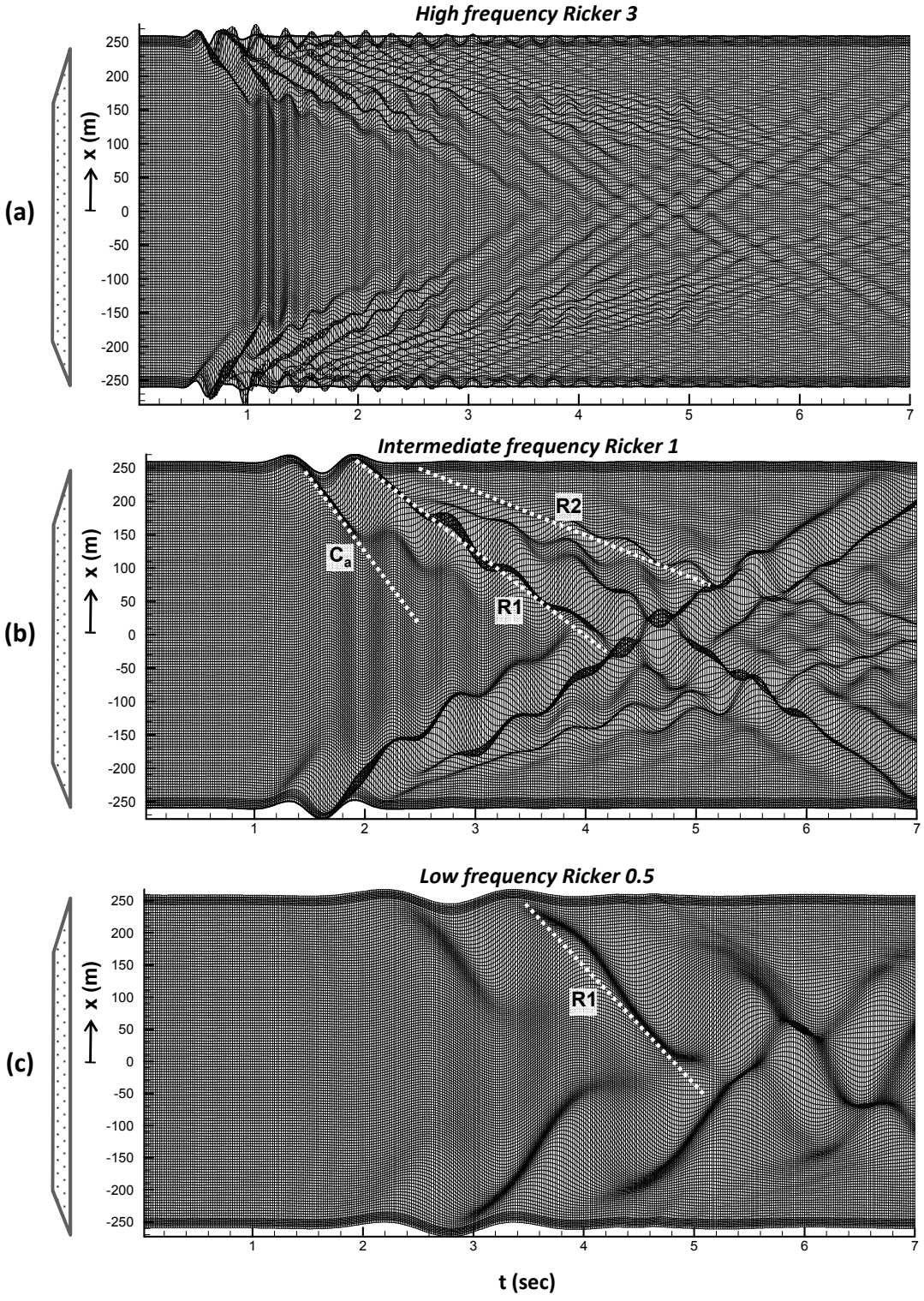

Figure 5.7. The effect of frequency content on ground motion synthetics. Elastic analysis with soil hysteretic damping ξ = 2 %. Wavefields of **horizontal** acceleration at the ground surface of the valley for : (a) the "high frequency" Ricker 3 wavelet, (b) the "intermediate" Ricker 1, and (c) the "low frequency" Ricker 0.5.

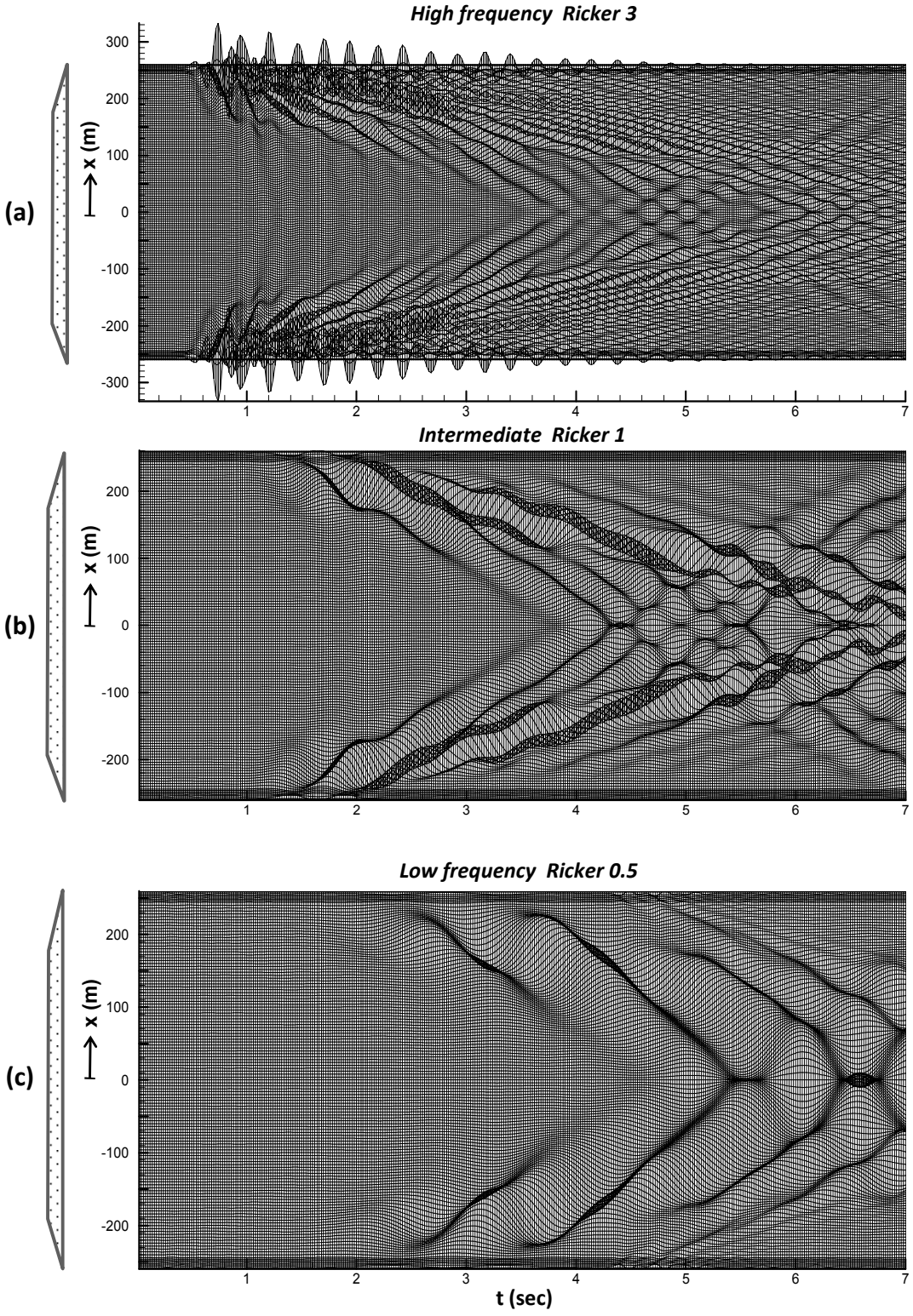

Figure 5.8. The effect of frequency content on ground motion synthetics. Elastic analysis with soil hysteretic damping ξ = 2 %. Wavefields of **vertical** acceleration at the ground surface of the valley for : (a) the "high frequency" Ricker 3 wavelet, (b) the "intermediate" Ricker 1, and (c) the "low frequency" Ricker 0.5.

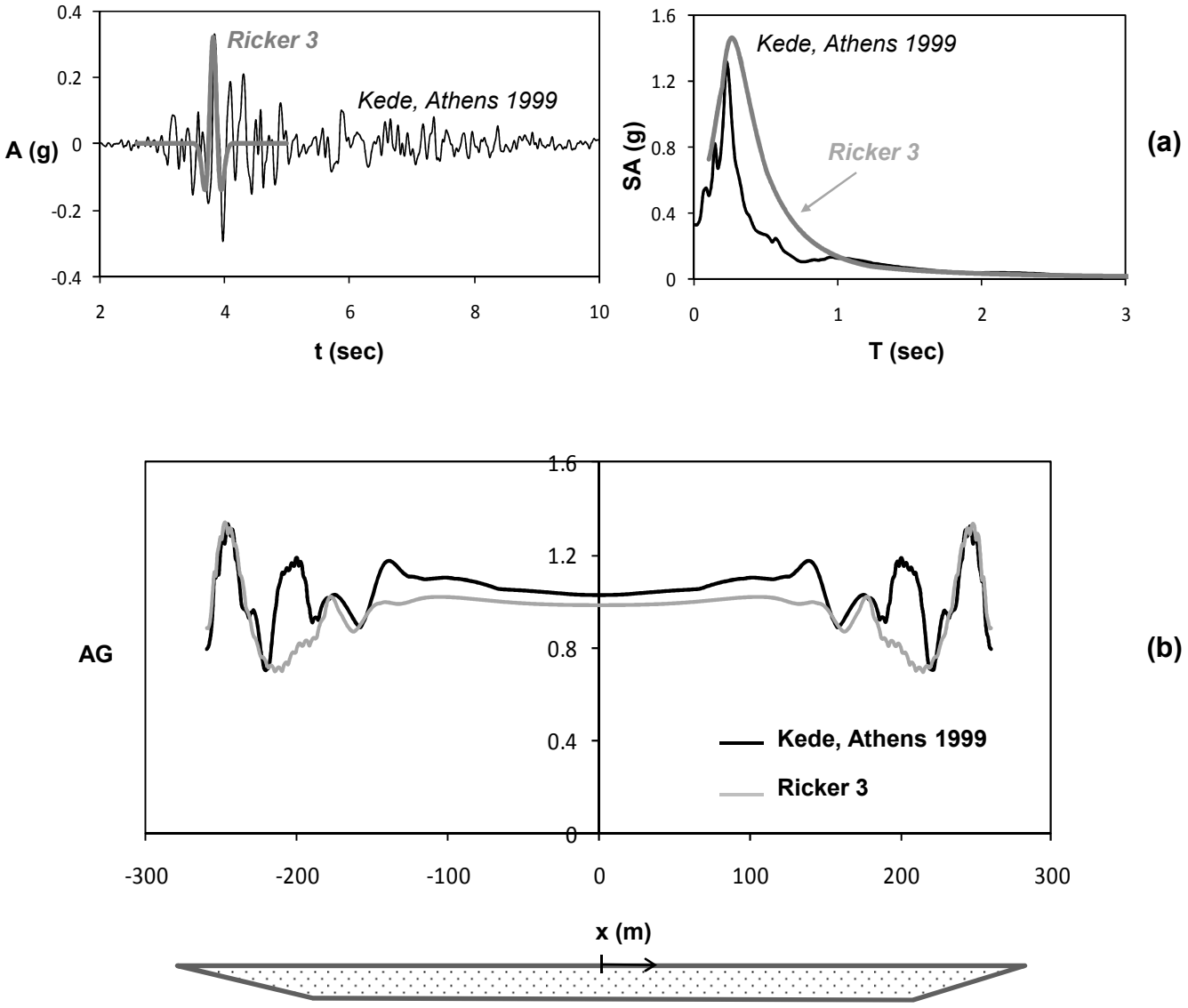

Figure 5.9. The effect of the "details" of the seismic excitation. Elastic analysis with soil hysteretic damping ξ = 2%. (a) Acceleration time histories and elastic response spectra of the Kede (Athens, 1999) record, compared with a "fitted" idealized Ricker wavelet (f_o = 3 Hz) ; (b) comparison of the aggravation factor *AG* along the ground surface of the valley for the Kede (Athens, 1999) record and the idealized Ricker wavelet (Ricker 3).

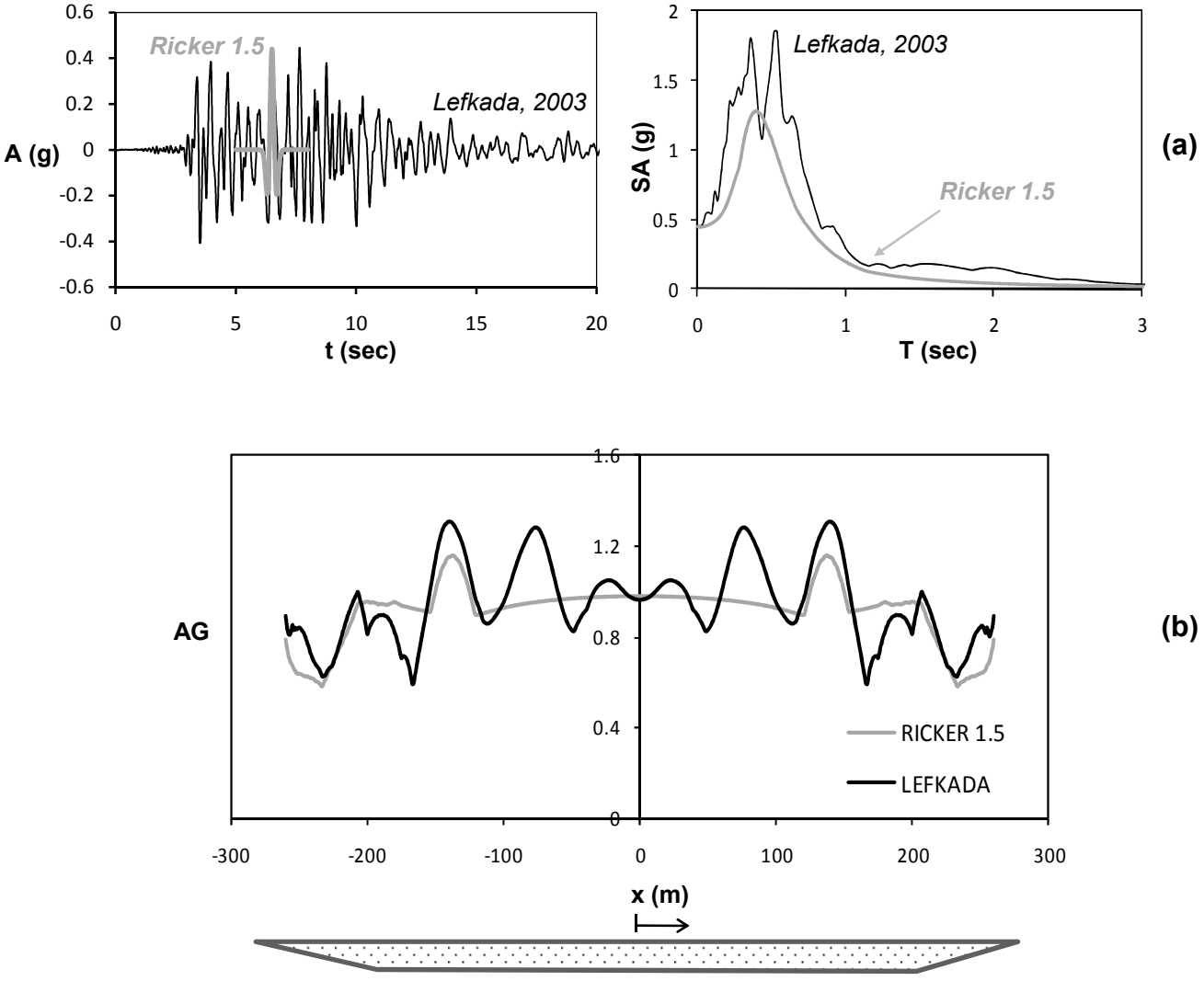

Figure 5.10. The effect of the "details" of the seismic excitation. Elastic analysis with soil hysteretic damping ξ = 2%. (a) Acceleration time histories and elastic response spectra of the Lefkada 2003 record, compared with a "fitted" idealized Ricker pulse (f_o = 1.5 Hz) ; (b) comparison of the aggravation factor *AG* along the ground surface of the valley for the Lefkada, 2003 record and the Ricker1.5 pulse.

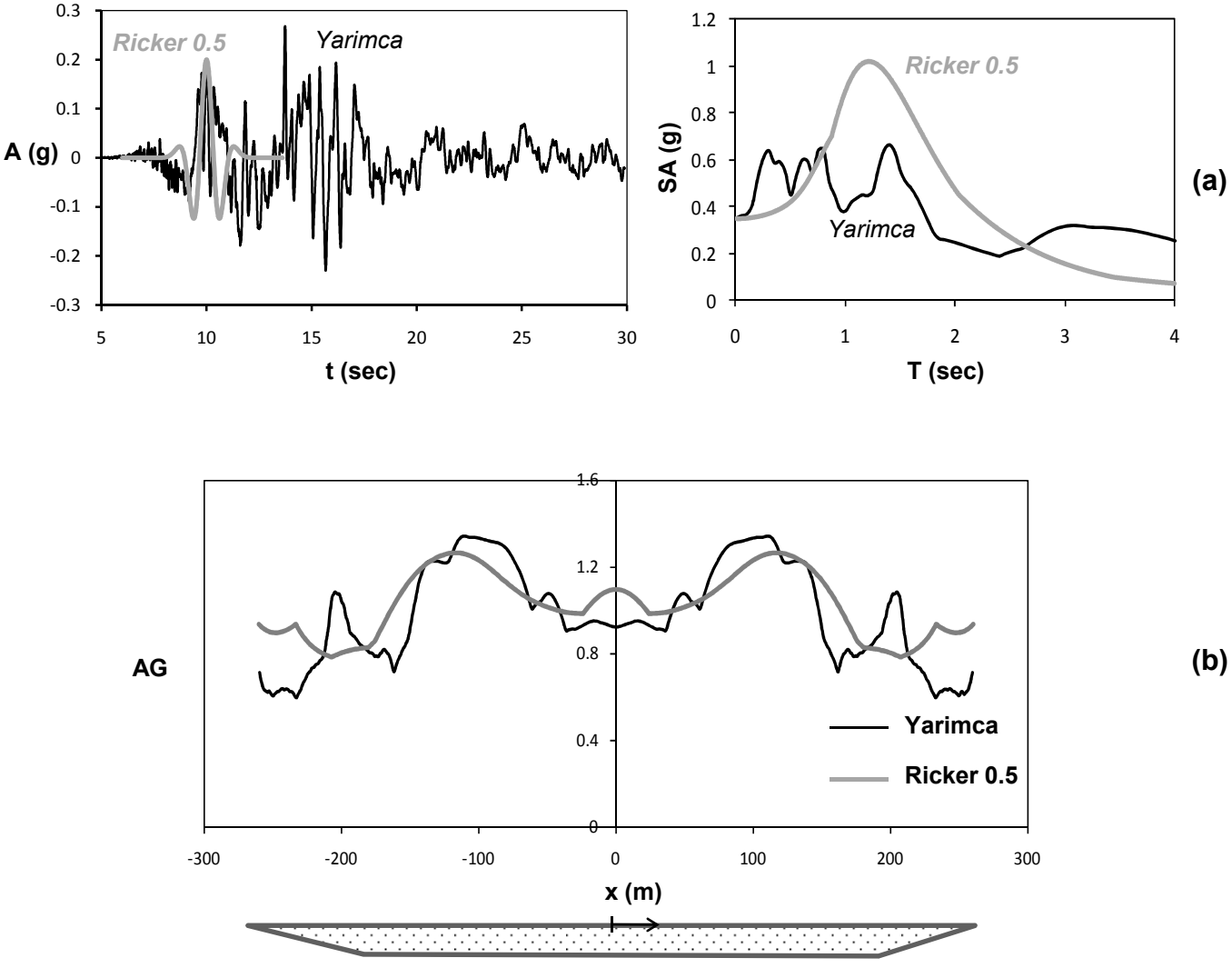

Figure 5.11. The effect of the "details" of the seismic excitation. Elastic analysis with soil hysteretic damping ξ = 2%. (a) Acceleration time histories and elastic response spectra of the Yarimca 1999 record, compared with a "fitted" idealized Ricker wavelet (f_o = 0.5 Hz) ; (b) comparison of the aggravation factor *AG* along the ground surface of the valley for the Yarimca 1999 record and the idealized Ricker wavelet (Ricker 0.5).

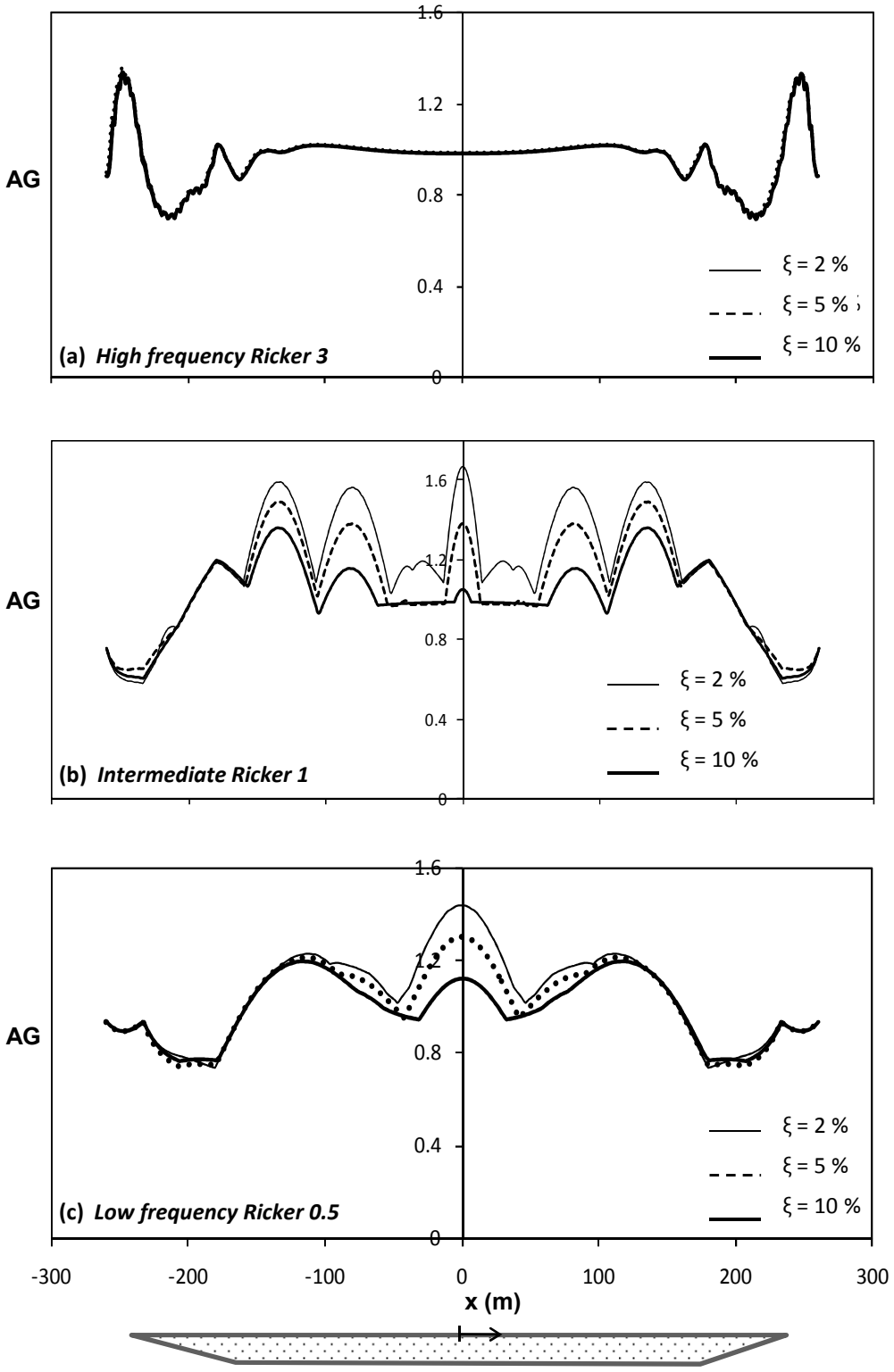

Figure 5.12. The effect of damping ratio – elastic analysis. Distribution of the aggravation factor *AG* along the valley surface for ξ = 2 %, 5 %, and 10% for : (a) the "high frequency" Ricker 3 wavelet, (b) the "intermediate" Ricker 1, and (c) the "low frequency" Ricker 0.5.

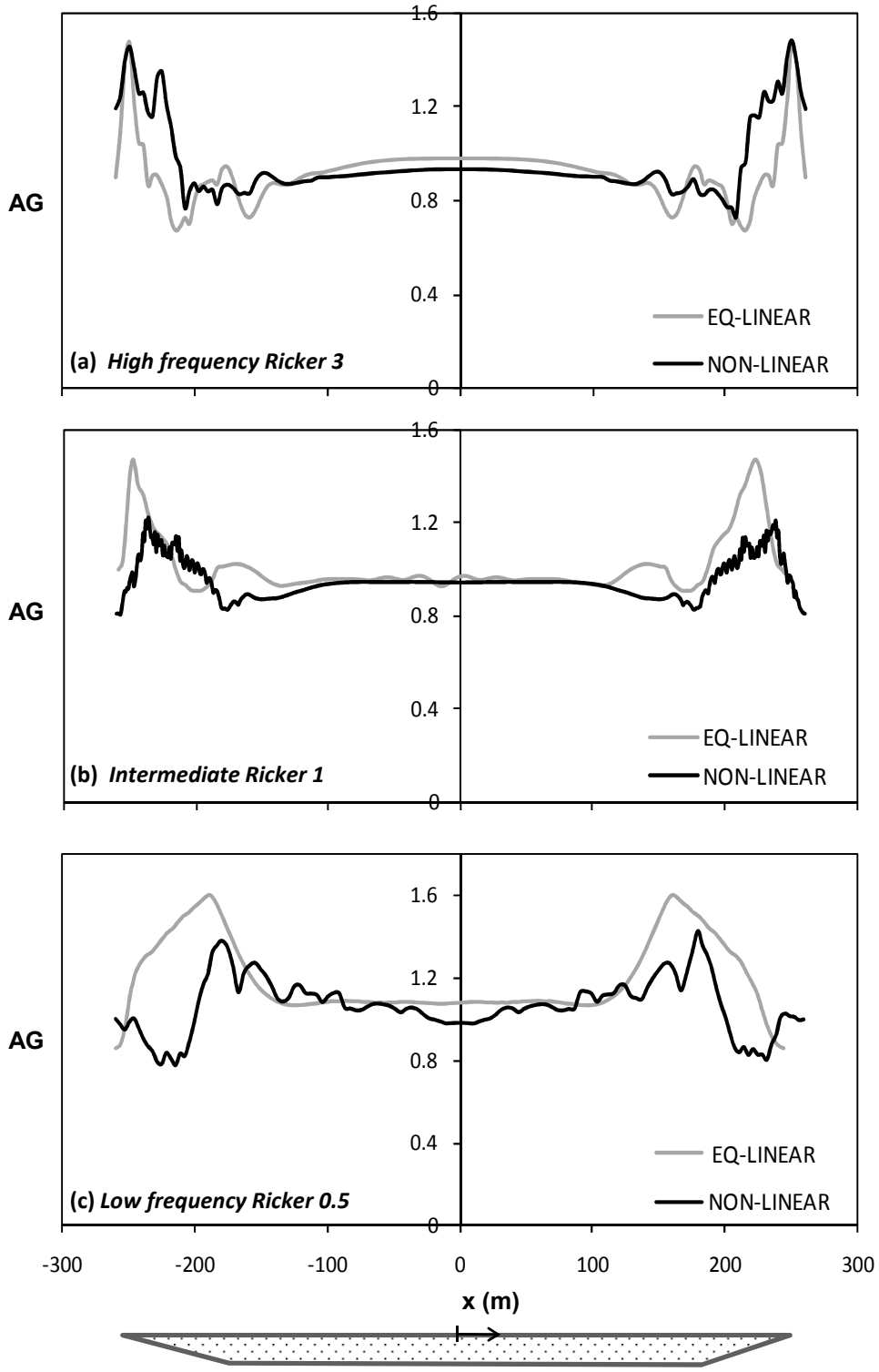

Figure 5.13. The effect of soil non-linearity : comparison of equivalent linear with nonlinear analysis using a kinematic hardening constitutive model. Distributions of the aggravation factor *AG* along the valley surface for : (a) the "high frequency" Ricker 3 wavelet, (b) the "intermediate" Ricker 1, and (c) the "low frequency" Ricker 0.5 [PGA = 0.2g for all input motions].

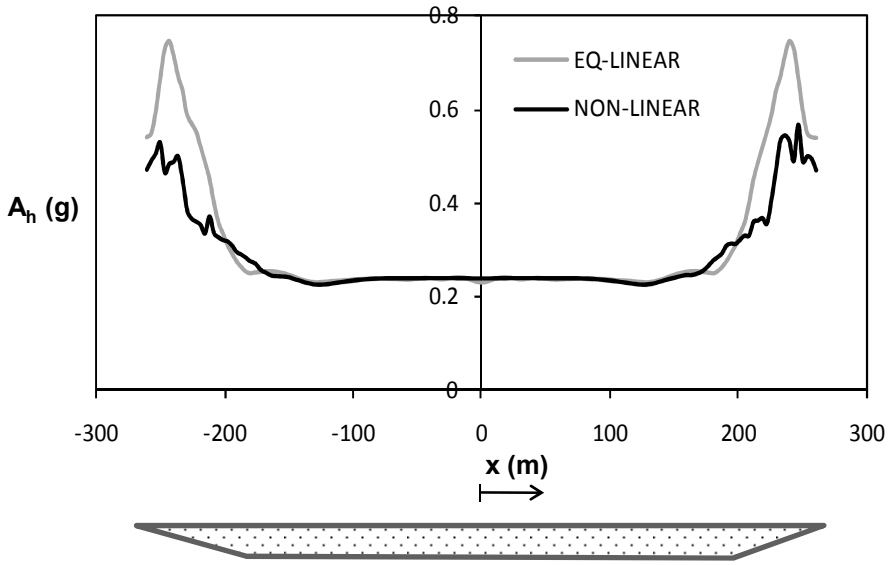

Figure 5.14. Comparison of equivalent linear with fully nonlinear analysis: distributions of horizontal peak ground acceleration for the Ricker 1 wavelet with PGA = 0.2g.

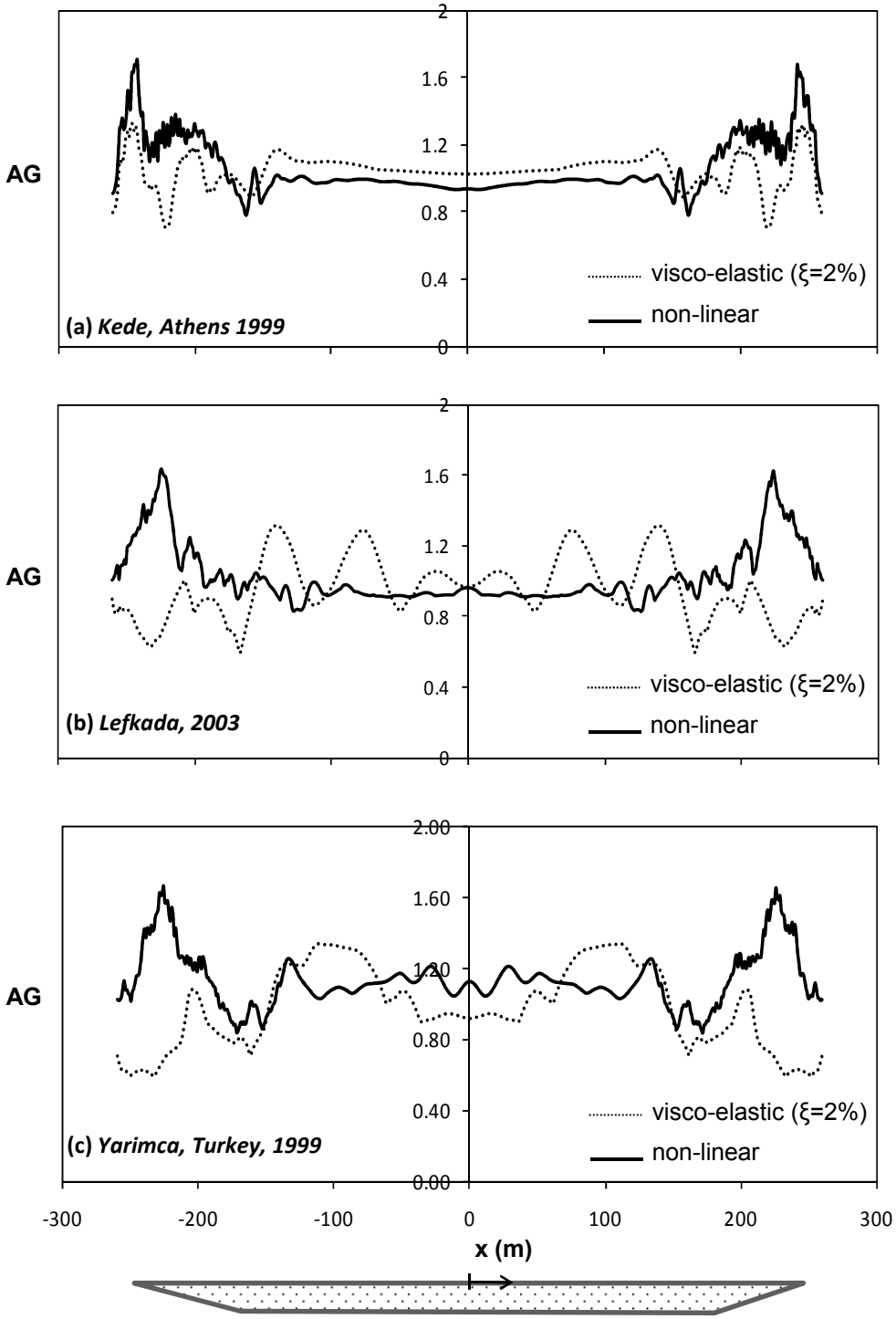

Figure 5.15. The effect of soil non-linearity – comparison of visco-elastic with nonlinear (with the kinematic hardening constitutive model) analyses using real records as seismic excitation. Distributions of the aggravation factor *AG* along the valley surface for : (a) the Kede, Athens 1999 record; (b) the Lefkada 2003 record; and (c) the Yarimca, Kocaeli 1999 record.

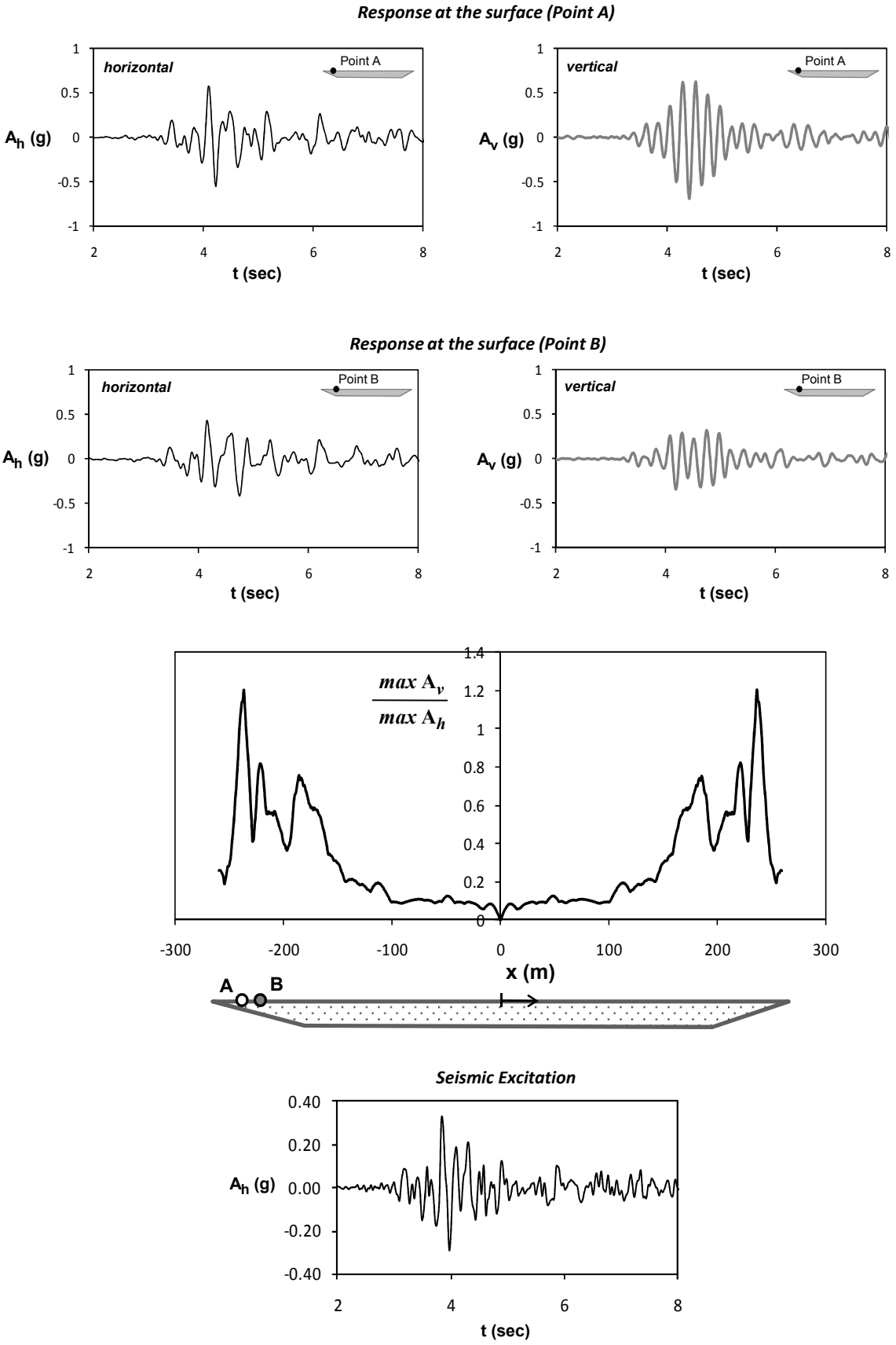

Figure 5.16. Generation of "parasitic" vertical component – elastic analysis (ξ = 2%) using the *horizontal* component of the Kede, Athens 1999 record as the sole seismic excitation (bottom) ; distribution of the ratio of vertical to horizontal acceleration component along the valley surface (middle) ; and horizontal and vertical acceleration time histories at the points A and B of the valley surface (top).

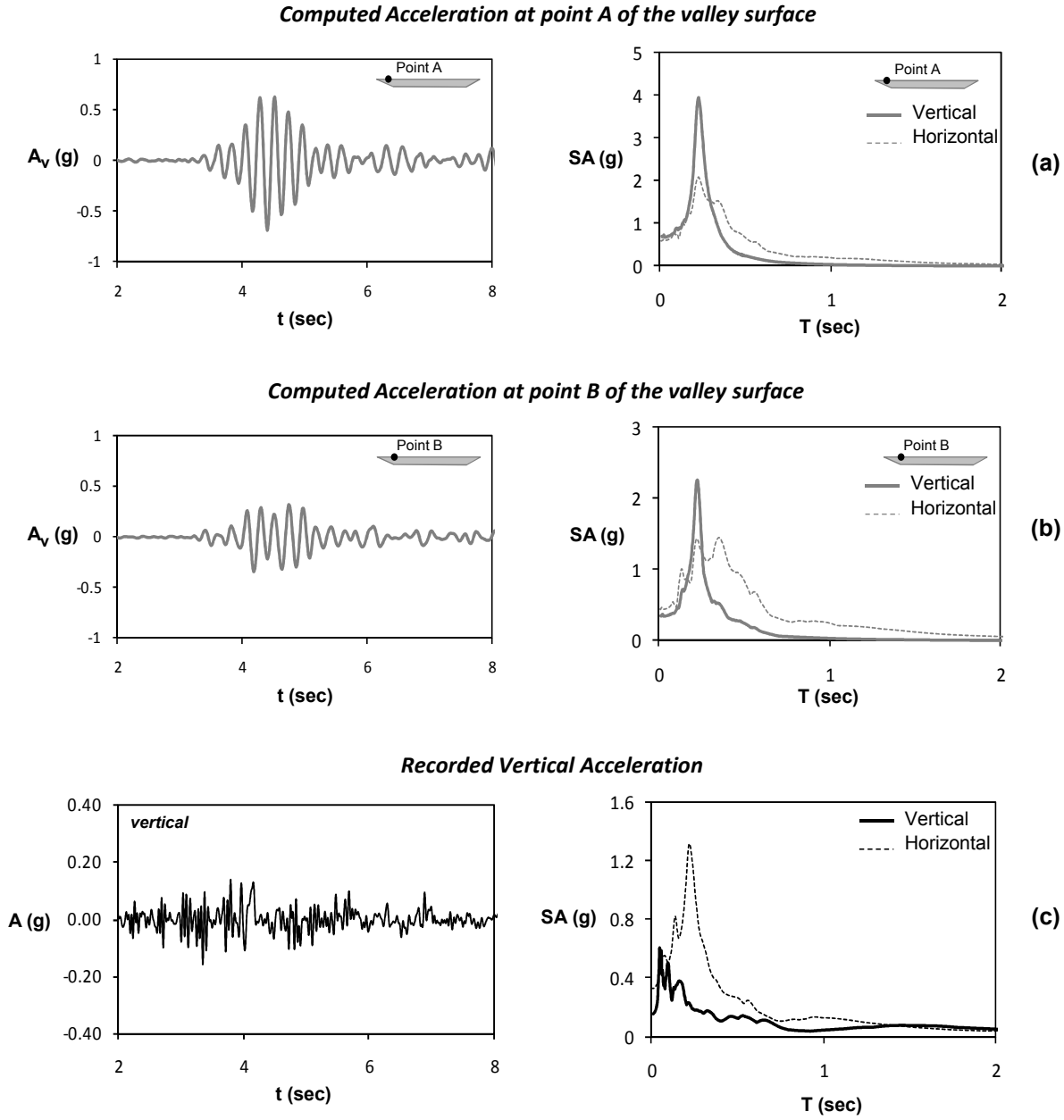

Figure 5.17. Vertical acceleration time histories and elastic response spectra at the valley surface, (a) at point A, and (b) at point B, compared to (c) vertical acceleration time history of the Kede, Athens 1999 record and corresponding elastic response spectra. In the SA diagrams, the respective horizontal acceleration time histories are also plotted (dashed lines) to allow for direct comparison.

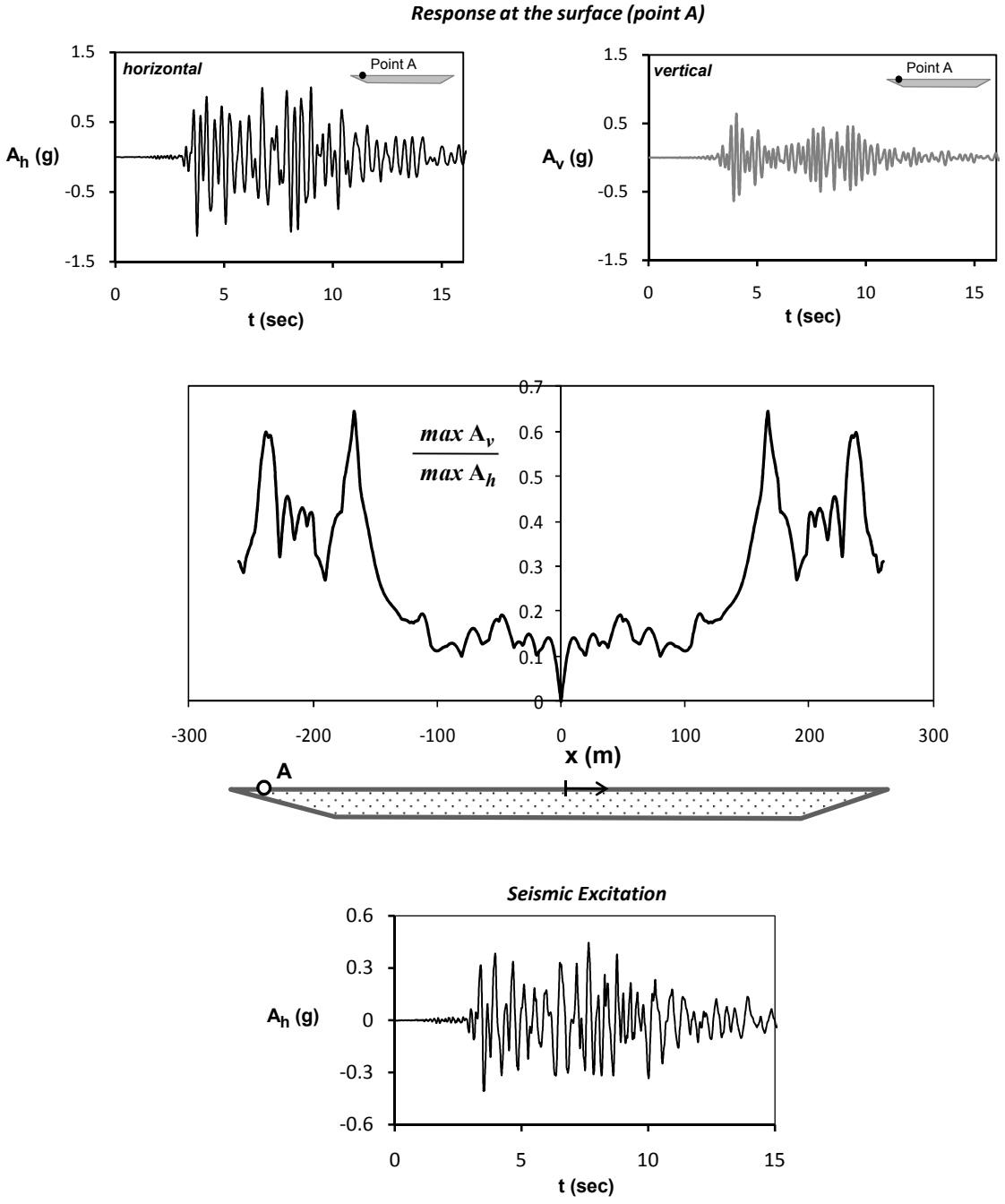

Figure 5.18. Generation of "parasitic" vertical component – elastic analysis (ξ = 2%) using the *horizontal* component of the Lefkada 2003 record as the sole seismic excitation (bottom) ; distribution of the ratio of vertical to horizontal acceleration component along the valley surface (middle) ; and horizontal and vertical acceleration time histories at the ground surface at point A (top).

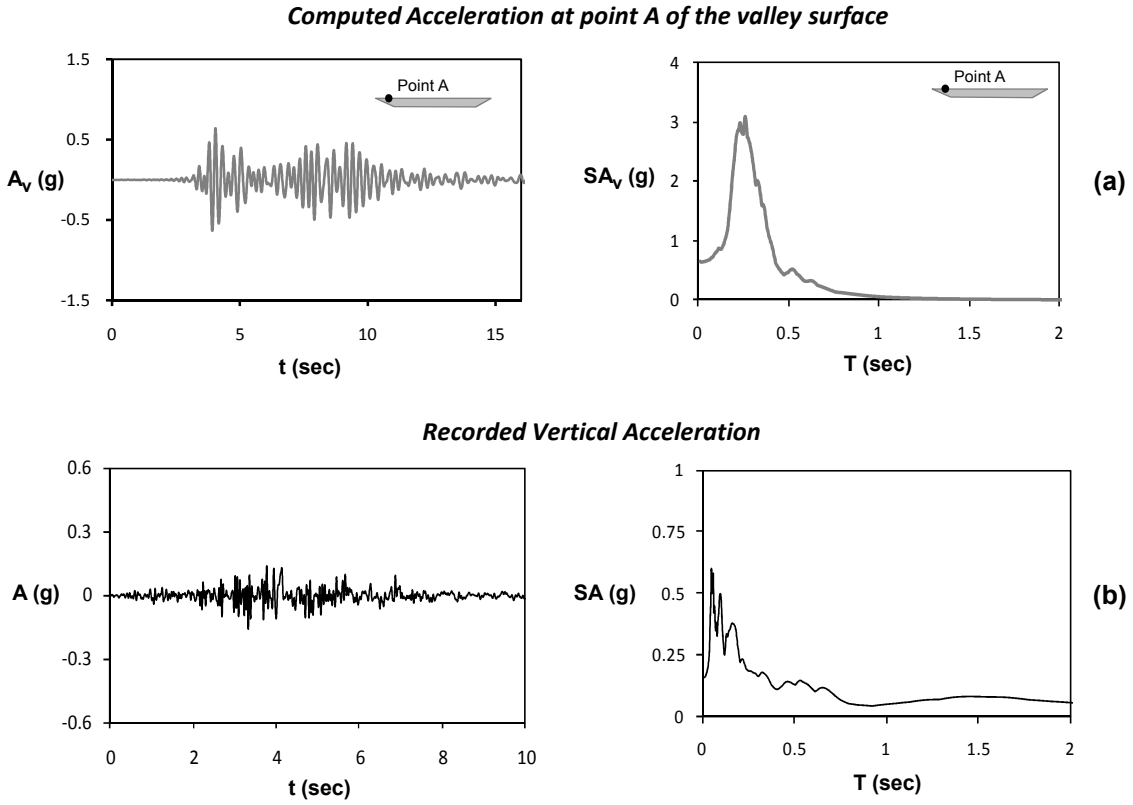

Figure 5.19. (a) Vertical acceleration time history and elastic response spectra at the valley surface (point A), compared to (b) recorded vertical acceleration time history of the Lefkada, 2003 record and the corresponding elastic response spectra.

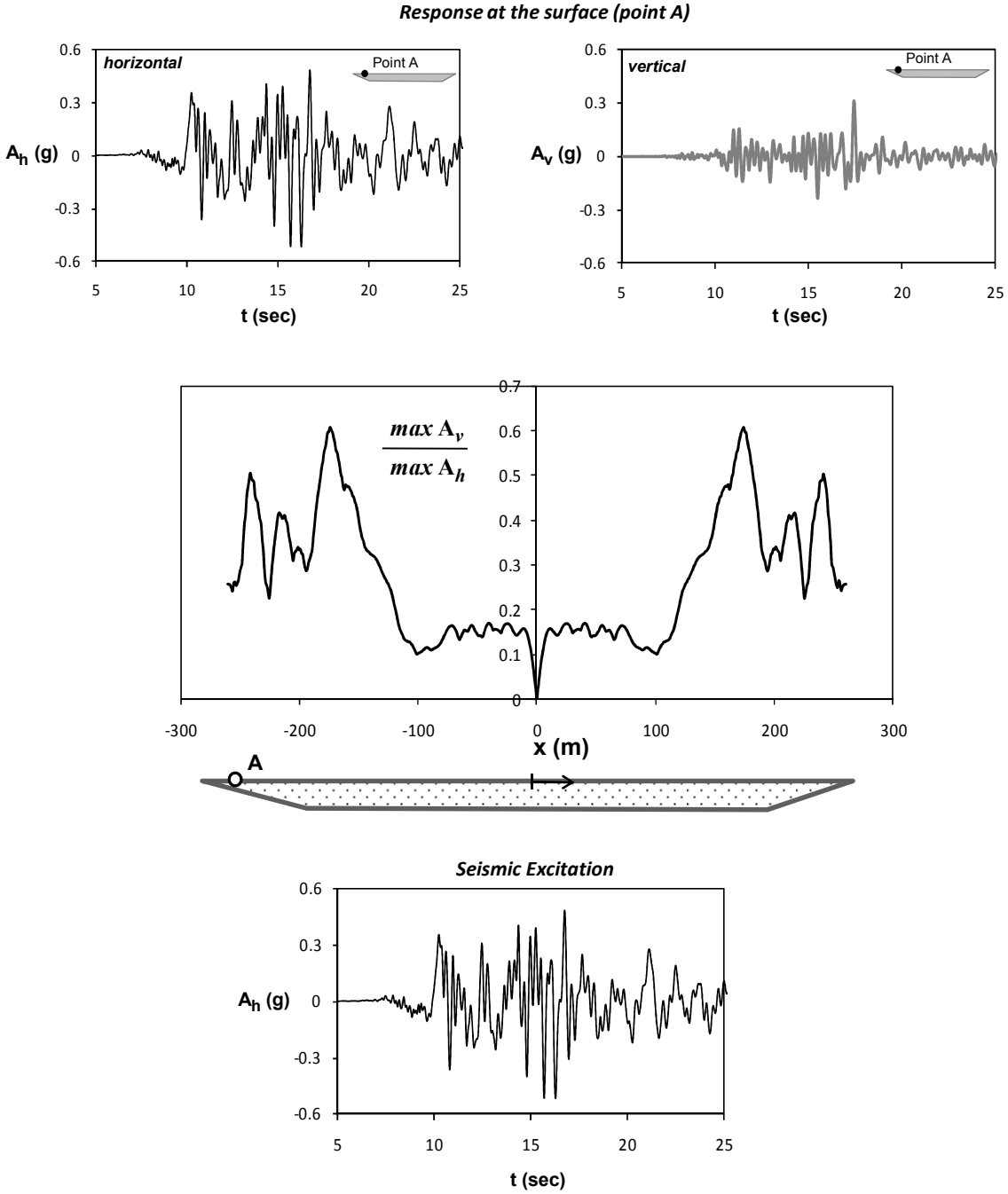

Figure 5.20. Generation of "parasitic" vertical component – elastic analysis (ξ = 2%) using the *horizontal* component of the Yarimca, Kocaeli 1999 record as the sole seismic excitation (bottom) ; distribution of the ratio of vertical to horizontal acceleration component along the valley surface (middle) ; and horizontal and vertical acceleration time histories at the ground surface at point A (top).

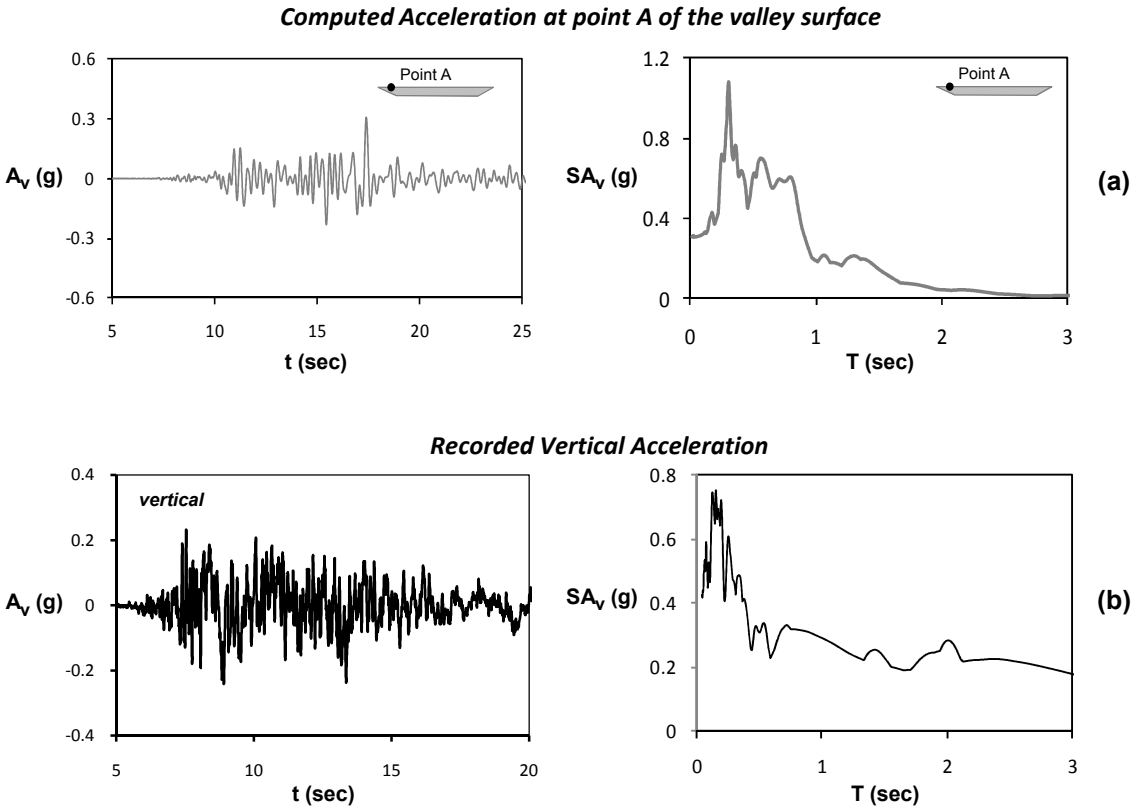

Figure 5.21. (a) Vertical acceleration time history and elastic response spectra at the valley surface (point A), compared to (b) vertical acceleration time history of the Lefkada, 2003 record and the corresponding elastic response spectra.

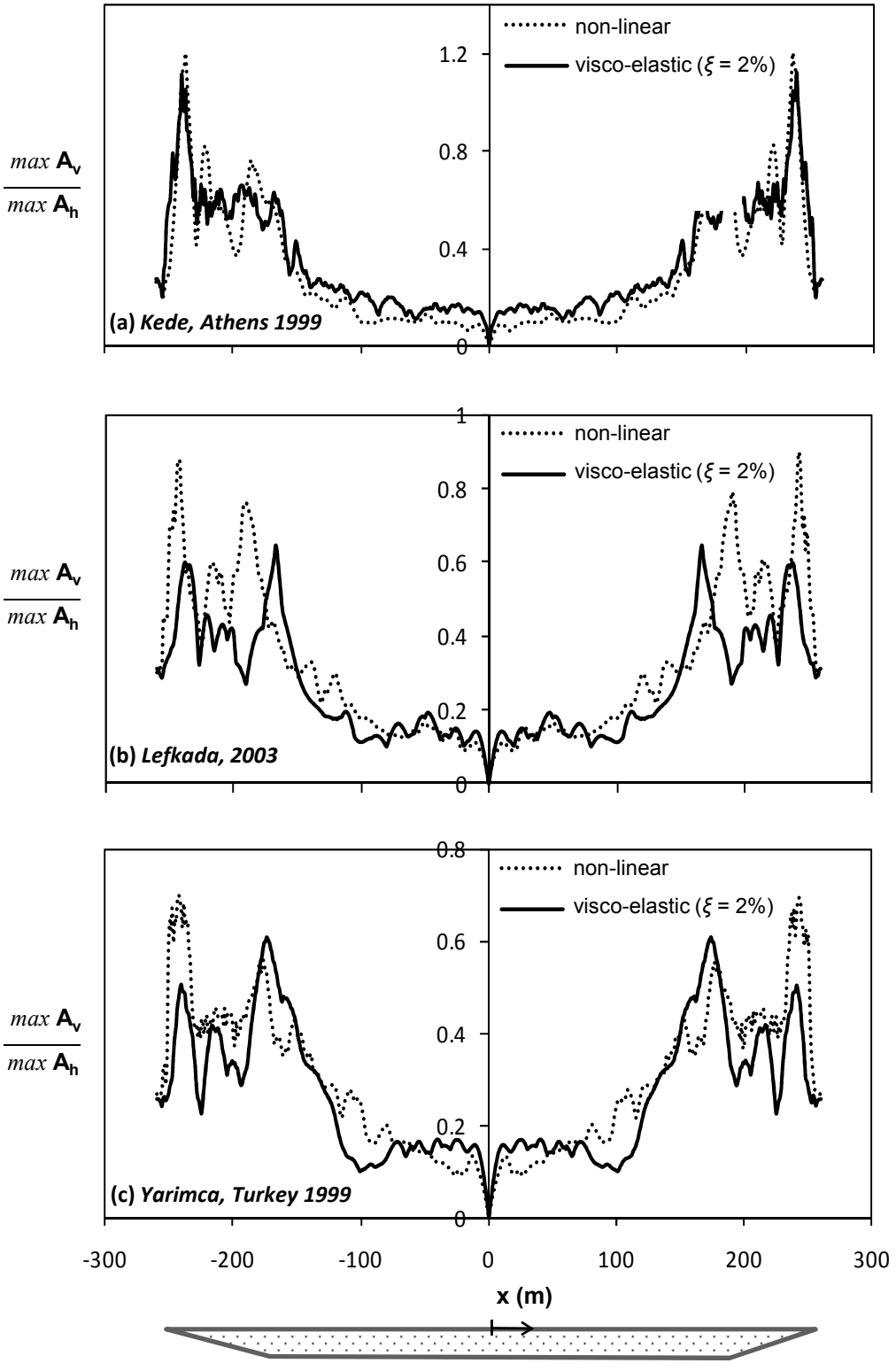

Figure 5.22. The effect of soil-nonlinearity on the parasitic vertical component of motion. Comparison of viscoelastic with nonlinear analysis using only horizontal components of real records as seismic excitation. Distributions of the ratio of vertical to horizontal acceleration along the valley surface for : (a) the Kede, Athens 1999 record; (b) the Lefkada 2003 record; and (c) the Yarimca, Turkey 1999 record.

6

Influence of Valley-Affected Ground Motion on the Seismic Response of Moment-Resisting Frame Structures

6.1. Introduction

The current Chapter attempts to:

a. Generalize the validity of the conclusions drawn during the preceding analysis of the Ohba valley

b. Investigate the response of a simple frame structure subjected to valley contaminated ground motion. Emphasis is given on a realistic modeling of the foundation-structure system which will be able to capture inelastic and non-linear response.

6.2. Generalization of Results and Dimensional Analysis

The previous Chapter presented a study on the sensitivity of 2D wave effects to crucial parameters, such as : (a) the frequency content of the input motion, (b) the “details” of the input motion, and (c) soil non-linearity. A numerical study has been conducted, utilizing the Ohba Valley (Japan) as an illustrative example. In addition, emphasis has been given on the generation of parasitic vertical component, the effects of which may be detrimental for overlying structures. The latter

The main results of the preceding study were that:

- The 2d wave effects are a highly frequency dependant problem and the intensity of the valley effects (i.e. spatial distribution and amplitude of the observed aggravation AG, surface waves generation and propagation towards the valley center, and wave focusing phenomena near its edges) is controlled by the relative ratio of the incoming wavelengths to the dimensions of the valley.
- When the response is elastic, the increase of the number of strong motion cycles increases the probability of constructive interference of surface waves traveling towards the center of the valley, thus increasing the resulting *AG*.
- Soil nonlinearity may modify the 2-D valley response to a substantial extent. For idealized single-pulse monochromatic seismic excitations, soil nonlinearity most often reduces *AG*, mainly at the valley center (where the role of surface waves is dominant), while differences are not as pronounced at the valley edges, where response is controlled by geometry. The details of recorded seismic excitations may further complicate the response, and *quite remarkably* lead to an increase in AG at the valley edges.

- A Parasitic Vertical Acceleration is generated by the refracted waves at the valley inclined boundaries which may be as high as the horizontal component, is in phase and of similar frequency content with it and thus it is believed to be of extreme importance for structures founded at the valley edges [reference to the BSSA paper where results are referred to a specific valley formation of an extremely soft alluvial valley, of high impedance contrast between the soil and the underlying bedrock and thus can by no means be generalized]

In order to increase the generalization potential of the preceding conclusions before examining their effects on the seismic response of a frame structure, the following section attempts to

a. investigate the dependence of the previous outcomes on the soil stiffness and strength while maintaining the valley geometry and,
b. if possible, to perform a dimensional analysis considering both elastic and non-linear soil response in order to take account of the effect of the valley geometry.

6.3. Numerical Analysis Method

The problem is analyzed in the time domain employing the finite element (FE) method, assuming plane-strain conditions. The soil is modeled with quadrilateral continuum elements, with a very fine discretization to ensure realistic representation of the propagating wavelengths.

Reflections at the base of the formation are avoided by utilizing absorbing boundaries. "Free-field" boundaries responding as shear beams are placed at each lateral

boundary of the model, to reproduce the motion produced by in–plane vertically incident SV waves..

Two different types of analysis are conducted : (i) visco-elastic analysis (Rayleigh Damping),; and (ii) nonlinear analysis utilizing the finite element code ABAQUS [2008], employing a kinematic hardening constitutive model. The numerical analysis methodology employed herein has been extensively validated against recorded seismic response in Tazoh et al (1988), Fan et al (1992) and Psarropoulos et al. [2007].

6.4. Soil Constitutive Modeling

For the nonlinear analyses, this study employs the nonlinear kinematic hardening constitutive model described in Chapter 2. The evolution law of the model consists of two components : a nonlinear kinematic hardening component, which describes the translation of the yield surface in the stress space (defined through the "backstress" α, a parameter which defines the kinematic evolution of the yield surface in the stress space), and an isotropic hardening component, which describes the change of the equivalent stress defining the size of the yield surface σ_o as a function of plastic deformation (**Figure 6.1a**).

The model incorporates a Von Mises failure criterion, considered adequate to simulate the undrained response of clayey materials, with an associative plastic flow rule (Anastasopoulos et al 2010). The evolution of stresses is described by the relation :

$$\sigma = \sigma_o + \alpha \tag{6.1}$$

The evolution of the kinematic component of the yield stress is described as follows :

$$\dot{\alpha} = C\frac{1}{\sigma_0}(\sigma - \alpha)\dot{\varepsilon}^{pl} - \gamma\alpha\dot{\varepsilon}^{pl} \quad (6.2)$$

where *C* the initial kinematic hardening modulus ($C = \sigma_y / \varepsilon_y = E$) and *γ* a parameter that determines the rate of kinematic hardening decrease with increasing plastic deformation.

Model parameters are calibrated against G–γ curves of the literature. **Figure 6.1b** illustrates the results of one such calibration (through finite element simulation of the simple shear test) against the G–γ curves of Ishibashi and Zhang [1993].

6.5. Effect of Soil Stiffness and Strength on the Elastic Dynamic Response of a Trapezoidal Valley

In order to highlight the effect of shear wave velocity on the elastic dynamic response of the valley, this section compares the response of three homogeneous valleys of the same geometry but of varying Shear wave velocities V_s so as to model: a very soft valley (V_{s1}=100 m/s), a medium with V_{s2}=150 m/s and a stiff one of V_{s3}=200 m/s while the shear velocity of the substratum is significantly higher : V_S = 400 m/s. The impedance contrast between soil and base, ρ_z, v_{sz}/ρ, V_{s1} ranges between 2 and 4. The idealized geometry of the valley and the associated configuration of the FE model are depicted in **Figure 6.2**. The models have been subjected to Ricker pulses (**Fig.6.3**) of varying frequency, so that the valley response is not biased by the produced wavelengths. The PGA=1g at the bedrock for all cases to ensure that soil non-linear response is mobilized.

Response to Ricker-1 wavelet

As expected, when the stiff valley (V_s=200 m/s) is excited by the relatively low frequency Ricker 1 pulse, the valley response, as revealed by the spatial distribution of peak horizontal acceleration A_H (**Fig.6.4a**) is practically 1 dimensional. Hence, a higher response is observed in the central area of the valley, while a smooth transition occurs towards the valley boundaries due to the contrast between the soil shear wave velocity and that of the outcropping rock. The wavelengths generated in this stiff valley may be assumed to range between roughly λ≈50 and λ≈200 m for the Ricker1 wavelet. It is hence apparent that the valley geometry, whose largest convex dimension is H=24m, is inadequate to cause notable wave refractions, consequently maintaining the produced Aggravation Factors close to unity (**Fig.6.4b**). Correspondingly, as the valley soil stiffness reduces (V_{s2}=150 m/s, V_{s1}=100 m/s), thus generating waves of smaller length, the geometry of the valley becomes more perceptible to the incoming waves and the trapping of waves within the valley wedge now produces multiple reflections, which in turn are mirrored in the increased aggravation factors (**Fig.6.4b).** It is noteworthy, that as the soil formation softens, the 2D effects take place not only in the narrow area of the valley sloping boundary but are indeed detectable along the whole valley surface. The steep peak observed in the very center of the valley should be attributed to the intereference of oppositely propagating Rayeigh waves (Bard and Bouchon, 1980(a,b); Harmsen and Harding*, 1981;* Papageorgiou and Kim, 1991*;* Scrivner & Helmberger, 1999*;* Cornou et al, 2003).

The above phenomena are even more conspicuous in terms of the parasitically generated vertical acceleration (**Fig.6.4c**). Since the parasitic vertical component is the result of refracted waves only, this can practically only appear when the wavelength is

adequately small thus being able to capture the topographic relief which is responsible for the generation of wave refractions. In accord with this theoretical expectation, in the case of the stiff formation (bold black line), the lack of refractions results in negligible "parasitic" vertical acceleration (not exceeding 10% of the input horizontal motion in amplitude). On the other hand, as the soil profile softens, the presence of the parasitic vertical component is ample along even the whole length of the valley surface (**Fig.6.4c).**

As the Ricker3 is a higher frequency wavelet than the previously examined Ricker1, the generated wavelengths are naturally smaller and therefore able to detect an increased amount of relief details. Despite that fact though, for the stiff soil case (V_S=200), the ground motion is de-amplified instead of being enhanced in the area of the valley wedge (**Fig.6.5a**). This should most probably be attributed to the low impedance ratio (King and Tucker, 1984; Olsen et al, 1995*;* Ciliz et al, 2007). As the soil profile softens (V_S=150 m/s) some de-amplification is still present close to the valley edges but the aggravation factor now tends to AG=1.2 within the wedge, mirroring a clear amplification of the ground motion. Likewise, in accord with any potential speculative expectation, a further reduction of the shear wave velocity to the value of V_S=100 m/s will result in enhanced amplification due to multiple wave refractions within the soil wedge, reflected on the increased value of the Aggravation Factor, AG=1.4 (**Fig.6.5a**). Contrary to the horizontal AG distribution, the parasitically generated vertical component reaches surprisingly high values even for the stiffer soil profiles (V_s = 150 and V_s = 200 m/s). Although the horizontal acceleration is slightly de-amplified inside the wedge, the vertical component even exceeds 0.8g at the same area. The amplitude of the vertical motion is further augmented when the profile becomes softer, although it is only detectable in a narrow area close to the valley boundary.

It is noteworthy, that as the shear wave velocity decreases (**Fig.6.5b)** the location of the maximum observed valley-contaminated ground motion gradually shifts towards the valley edges. This shift must again be attributed to the relative dimensions between the valley and the wavelength. As the wavelength decreases (i.e. shear wave velocity decreases), the wave refractions towards the convex borders of the wedges are augmented since their geometry becomes increasingly perceptible by the incoming waves. The entrapment of multiply refracting waves within the wedge naturally amplifies the vertical component in that area hence transferring the location of the peak towards the valley boundaries. Conversely, as the wavelength increases, the refractions mainly materialize away from the valley edge.

6.6. Effect of Soil Non-linearity on the dynamic Response of a trapezoidal Valley

6.6.1. Response to Idealized Pulses

The influence of non-linear soil response on valley effects has been extensively examined in literature utilizing numerous methods of varying degree of sophistication (i.e. elastic analyses with high Rayleigh-type damping values, equivalent linear routines or even complicated non-linear soil constitutive models (Zhang and Papageorgiou, 1996; Olsen et al, 2000; Kamiyama and Matsukawa, 2002; Kamiyama and Fukuchi, 2007; Puglia et al, 2007).

Most of the relevant studies agree that the effect of soil nonlinearity is detrimental for the induced valley phenomena: quite invariably they tend to diminish. In a number of cases some amplification may be apparent close to the valley edges but still the AG values are significantly lower than those observed when neglecting soil inelasticity;

moreover the late arrivals of waves are essentially filtered out. This is certainly true when the valley is excited by motions generating wavelengths that are comparable or smaller than the dimension of the oblique sides of the valley and thus produce significant 2D amplifications in the elastic case. Such a response may be observed in **Figure 6.6**, summarizing the numerical results of the dynamic analysis of a relatively soft valley formation (V_s=100m/s) excited by a high frequency Ricker3 pulse. It is worth mentioning that in terms of AG values, the induced non-linearity results in decreased valley amplification at the valley corners (AG drops from 1.4 to 1.2), while a "shadow area" (**Fig. 6.6a**) is formed where the experienced motion at the valley surface is de-amplified compared to the acceleration values that would take place in the respective 1-d formation (AG values even below unity). As we move to the valley center the response becomes essentially 1-dimensional. In terms of the parasitically generated vertical acceleration, high values are concentrated close to the valley edges in both the elastic and the non-linear case. Certainly, the absolute A_v values in the elastic case are higher than in the non-linear, since the original horizontal acceleration is greater. However, the presence of the parasitic vertical acceleration is constrained in the area of the valley wedge (contrary to the elastic case when a significant vertical acceleration component is evident along an extended area on the valley surface); refracted waves travelling towards the valley center are filtered out resulting in the observed smoothening of the peak vertical acceleration distribution (**Fig. 6.6b**).

The most surprising outcome of the present study though is that soil non-linearity may, under appropriate conditions, even enhance the valley amplification phenomena. **Figure 6.7** demonstrates an example referring to the stiff valley (V_s=200m/s) excited by a relatively low frequency pulse. Observe that when the non-linear soil response is

considered the produced AG is higher than in the elastic case: due to the induced soil softening with increasing strain, the soil stiffness drops from its original G_o value (elastic case) to a lower secant G_{sec} value which in turn corresponds to significantly lower shear wave velocity. For this specific case this decrease in the actual V_s value produces lower wavelengths and, subsequently enhances the 2D valley effects compared to the elastic case (when the produced wavelengths were too high to perceive the bedrock geometric irregularity). These 2D effects are more pronounced for the parasitically produced vertical motion. The latter is systematically higher in the non-linear case along the whole valley length, while its maximum value (A_v=0.5g), acquired close to the valley edges is 5 times higher than the respective elastic value.

6.6.2. Response to Recorded Accelerograms

In order to extend the validity of the previous observations, the medium stiffness valley formation **(Fig.6.1**) has been subjected to an ensemble of quite rich in frequency content recorded acceleration time histories (**Fig. 6.8**). They range in number of important cycles, duration and amplitude so as to avoid the generation of biased conclusions. Results are displayed collectively in the plots of **Figure 6.9** and are briefly outlined below:

- In the elastic soil case, the valley response especially in terms of Aggravation Factors distribution is essentially non-predictable for both the horizontal and the vertical acceleration components. Areas of accumulated amplification are interchanged with areas of unimportant amplification in a totally volatile pattern; a finding consistent with the outcomes of the previous Chapter.
- Soil Non-linearity drastically simplifies the observed response. In all cases examined, valley amplification (if any) is localized within the valley wedges

(shaded areas) i.e. either at x>180 or x<-1480 m. It is noteworthy that very close to the valley edges, the amplification may even be higher than in the elastic case.

- Results are even more interesting when considering the parasitic vertical acceleration. It is clear that even in the non-linear case, the geometry-induced parasitic vertical acceleration component, should not be expected to vanish; on the contrary, it may even exceed the corresponding 1-dimensional horizontal acceleration value!

6.7. Dimensional Analysis

In all the preceding analyses the valley geometry has been kept constant. In order to examine the extent to which the above results may be generalized, this section attempts a dimensional analysis of the valley. The valley geometries and the excitation time histories utilized during the process of this analysis are summarized in **Figure 6.10**. It is expected that when soil non-linearity is neglected, dimensionless results can be produced when the x=λ/D (wavelength over valley depth) ratio is constant, which causes the ratio of the dominant frequency of the soil profile over the excitation frequency to remain constant in turn:

$$\frac{\lambda}{D} = \frac{V_S}{f\ x\ D} = \frac{4\ V_s}{4\ x\ f\ x\ D} = \frac{4\ T_{\delta\iota\varepsilon\rho.}}{T_{\sigma\chi\eta\mu.}} \qquad (6.3)$$

This will enable capturing both the effect of wave propagation (since the produced wavelength depends on the valley length) and the 1-d soil amplification since the $T_{excitation}/T_{profile}$ ratio remains constant. Physically, the dimensionless parameter x is an index of the generated waves "ability" to capture the valley geometry. In this context, lower x values are indicative of low wavelengths compared to the valley dimensions

which in turn results to a more perceptible valley geometry and therefore increased number of wave reflections.

Figures 6.11 and 6.12 display the spatial distribution of peak horizontal accelerations and the horizontal and vertical acceleration time histories respectively in dimensionless terms highlighting the effectiveness of the procedure. Despite the generally excellent coincidence of the analyses results in both terms, some slight discrepancies may be observed as we move to lower x values. These should most probably be attributed to the use of Rayleigh damping during the numerical analyses. The latter drastically increases the numerical stability of the solution but results in a rather "inhomogeneous" damping ratio distribution with frequency. Hence, although the damping ratio around the dominant frequency of the excitation is accurately captured, some high or low frequencies may experience increased damping. Indeed, the higher the excitation frequency the higher the sensitivity of the response to potential discrepancies between the required and the finally achieved damping ratio. Gelagoti et al (2010) have shown that the surface waves responsible for the amplified vertical acceleration component close to the valley center may be too sensitive to damping fluctuations. This observation explains the reason why the most important deviations are concentrated in the central area of the valley (and not at its edges) and are more pronounced for the Type 1 valley geometry which for a given value of the dimensionless ratio x is excited with the highest-frequency-motion. Note, (**Figure 6.12**) that in order to achieve the best match in terms of time histories of the produced ground motion (horizontal and vertical) the time must be divided by the dominant period of the excitation T_E. Naturally, as the time histories refer to valleys of different dimensions, the dimensionless duration of the time history for the

Type-1 valley is longer than that of the Type-3 valley since the former has been excited by the higher frequency Ricker 1 pulse while the latter by the low frequency Ricker 0.5.

When soil non-linearity must be captured, the response is expected to depend not only on the geometric proportionality but must also be taking account of the soil strength. Therefore the S_{u1}/S_{u2} ratio (i.e. the ratio of strength parameters between the two "equivalent" valleys) must be equal to the ratio of their dimensions D_1/D_2. Dimensionless results for the non-linear soil case are plotted in **Figures 6.13** and **6.14** in terms of spatial distribution of peak horizontal accelerations and the horizontal and vertical acceleration time histories respectively, revealing the accuracy of the adopted procedure.

6.8. Free Field Response: Conclusions

The previous analyses have focused on the effects of soil stiffness and non-linearity on the amplification of ground motion due to 2d wave effects, visibly demonstrating that in both the elastic and the non-linear case, valley effects are strongly dependent upon the shear wave velocity, and, maybe more importantly, that the non-linear behavior of soil is not always detrimental for the valley-induced amplification. In most cases though, soil non-linearity causes the 2d-effects to vanish to multiply reflecting waves near the edges of the valley. The most notable conclusion has to do with the generation of the parasitic vertical component of ground motion which, being a result of valley geometry only, has been proven to be less sensitive to soil non-linearity maintaining a rather high amplitude even in positions where the horizontal component is de-amplified. This observation could be of vital importance when designing surface foundations of structures, as the

synchronous vertical acceleration may intensify the footing's seismically-induced distortion. In the process of exploring the validity of this statement, the next sections investigate the seismic response of a frame structure funded on the surface of alluvial valleys near the areas of high-amplitude parasitic vertical component of motion.

6.9. Response of Frames subjected to valley-affected ground motion: Problem Definition

To gain insight into the effect of the parasitic vertical acceleration component on surface foundations of typical structures, a realistically simple frame has been modeled which is assumed to lie on the surface of an alluvial valley close to its edges where the parasitic component has been observed to be maximum (**Fig.6.15a**).

The analysis is conducted in two stages:

(i) The first stage calculates the free field response on the valley surface when subjected to horizontal shaking at the bedrock

(ii) The produced horizontal and parasitic vertical acceleration time histories of the first stage are applied as input excitation of the de-coupled model presented in **Figure 6.15b**.

In order to isolate the effect of each component of the ground motion, the following sets of analyses have been performed:

a. Non-linear dynamic analyses of the decoupled model model subjected to the quasi 1-dimensional ground motion A_{FF} (**Fig. 6.15a**) recorded at the central part of the valley (i.e. not affected by the valley geometry)

b. Non-linear dynamic analyses of the model subjected to the horizontal component only (A_H) of the valley affected ground motion (**Fig. 6.15a**) recorded at the valley model surface (i.e. ignoring the parasitic vertical component of the motion)
c. Non-linear dynamic analyses of the model simultaneously subjected to the horizontal and vertical components (A_H and A_V) of the valley affected ground motion recorded at the valley model surface

6.9.1. Frame Geometry and Modelling

The problem analyzed is displayed in **Figure 6.16.** It consists of a fairly typical 2-storey concrete urban residential structure of 5m span. The ground floor height is 4 m while the first floor has a height of 3m. The dimensions of the structural members of the frame are displayed in **Table 6.1**.

Superstructure Design

The structure has been designed according to the Greek Reinforced Concrete Code (EKOS 2000) and the Greek Aseismic Code (EAK2000). In order to adopt a quite conservative earthquake scenario which would dictate a grave earthquake design strength, the structure's location has been assumed in Seismic Hazard Zone III, i.e. the design earthquake PGA was equal to a_d=0.36g. The behavior factor is q = 3.5. The dead and live loads adopted (g = 1.3 kN/m^2 and q = 2 kN/m^2) are typical values for residential structures provided by EC8 and the Greek Codes.

Finite Element Model Description

The finite element model of the frame structure resting on clay is displayed in **Figure 6.16b**. The soil is modeled with 4-noded quadrilateral plane strain continuum elements. Vertical displacement boundaries have been applied at the bottom nodes of the model.

The acceleration time history is applied at the model base nodes and propagates through the soil layer to its surface. An initial sensitivity analysis revealed that the footing has to be discretized into at least 12 elements to reproduce the mechanism of bearing capacity failure and the rocking behavior. The soil-foundation interface is modeled using special interface elements which allow the structure to slide or detach from the soil depending on the loading. The sliding obeys Coulomb's friction law, with detachment and uplifting arising from the tensionless interface behavior. The structural elements were modeled utilizing nonlinear beam elements whose properties have been calculated as described in the ensuing. Non-linear *P-δ* geometry effects were also taken into account.

As expected, the strength of the columns is larger than that of the corresponding beam members according to the principles of capacity design. The column curvature ductility is μ_ϕ = 10, corresponding to the medium ductility class according to the provisions of EC8 for the case of Moment Resisting Frames.

Concrete Modeling

The constitutive model presented in Chapter 2 after proper adaptation [Gerolymos et al., 2005], is calibrated to match the superstructure reinforced concrete (RC) members response in the macroscopic moment–curvature level.

For each member, the moment–curvature relationship is computed through static section analysis employing the X-tract 2000 [Imbsen Assoc. & Chadwell, 2004] software. Then, model parameters are calibrated against these target moment–curvature relationships. For a rectangular RC member of width d_b and height d_h , the yield stress σ_y can be defined as :

$$\sigma_y = \frac{4M_y}{d_b d_h^2} \tag{6.4}$$

The small strain modulus *C* is equal to the Young's modulus of reinforced concrete. The residual bending moment of each RC section is assumed equal to 30% of the bending moment capacity [Vintzilaiou et al., 2007], and is attained for a curvature 3 times larger than the ultimate curvature c_u . To capture such softening response, a user subroutine is encoded in the finite element code ABAQUS. Since the structure was designed following the provisions of modern seismic codes, the hoop reinforcement justifiably presumed to prevent strength degradation due to cyclic loading. Therefore, this effect has been neglected in the concrete modeling. Parameters λ and α of the model are calibrated through numerical simulation of the static pushover test. **Figure 6.17** depicts the results of model calibration for the pier against moment–curvature relation of the reinforced concrete section calculated through section analysis as stated above.

6.10. Response of Frames subjected to valley-affected ground motion taking account of the parasitic vertical acceleration

As already described, the valley presence has the double effect of amplifying the ground motion (close to its edges) and generating a parasitic vertical acceleration due to the refraction of the incoming waves. The latter may be synchronous with the horizontal acceleration component provided that the incoming wavelength is appropriate. The following paragraphs outline the effect of each component of the excitation to the dynamic response of the frame. Only non-linear soil has been considered in this study since it has been shown [Gelagoti et al, 2010) that ignoring soil non-linearity unrealistically enhances the valley amplification effect.

6.10.1. Effect of the valley-generated parasitic vertical component: Response to the Ricker 1 excitation

This section compares the behavior of the frame when subjected to the horizontal component only to that of the frame under combined horizontal and vertical acceleration action. For the sake of comparison, the results of the analysis of the frame located at "free field" are also presented in selected cases. The pulse-type Ricker1 excitation (PGA = 1g) has been used as input ground motion of the two characteristic valley models displayed in **Figure 6.10**: the shallow valley-1 and the deep valley-3 models. The original base excitation as well as the resulting horizontal and vertical components on the surface (near the edge of the valley) are displayed in **Fig. 6.18** for the shallow valley-1 model. The analyses have revealed two main mechanisms that luminously demonstrate the detrimental effect of the parasitic vertical acceleration. These consist of either increasing or decreasing the vertical load of the footings which is transmitted to them through the axial load of the columns. Both phenomena are expected to only affect the frame response when the vertical component is synchronous with the horizontal one (see previous section Free Field).

6.10.2. Effect of Vertical Acceleration: Increase of Axial Load

Figures 6.19 to 6.21 compare the behavior of the frame when subjected to combined horizontal and vertical acceleration to that of the frame subjected to the horizontal component only. The mechanism is briefly outlined in the contours plot of **Figure 6.19.** In the absence of vertical component, the frame responds to the strong ground shaking through foundation rocking, which restricts the loading that may be transmitted from the ground to the superstructure through the footing. Hence, a strong horizontal

acceleration pulse results in rotation of both footings which, in turn, creates distortion to the superstructure. On the other hand, when the strong horizontal pulse is accompanied by a synchronous vertical acceleration pulse, which substantially increases the vertical load of the foundation, the latter is prevented from uplifting, hence being forced to assume the imposed loading through bending. The above mechanism is clearly mirrored in the moment curvature-plots of the two columns presented in **Figure 6.20** for the shallow-case valley (**Fig. 6.18a**) subjected to the Ricker1 pulse. The figures compare the response of the frame in all three different cases (a,b,c see section 6.9) identified previously. As can be deduced from the figure, the valley amplification effect for this specific case in terms of column stressing is not so important if the parasitic vertical acceleration is ignored. The increase in column curvature because of the horizontal component only is less than 10% for both columns. Hence, the effect of the valley on the frame response would be misleadingly unimportant were the parasitic vertical component totally ignored. The picture as to the valley effect is indeed completely reversed due exactly to that action. Focusing on the right column's curvature time history plots displayed in **Figure 6.20a,** it may be observed that in case of simultaneous horizontal and vertical components the curvature displays a striking increase at time 4.8s. Most of the curvature developed at that instant is irrecoverable afterwards, i.e. the curvature time history during the subsequent cycles of shaking oscillates around the remarkably high value of $c = 4.7$. Note that the residual average curvature on the same column in case of horizontal component only is $c = 1.5$. The mechanism may be further clarified by analyzing the footing rotations time histories (**Fig. 6.21).** As already evidenced by various researchers for foundations with large factors of safety against vertical loads (e.g. Kutter 2003; Pecker 2001; Gelagoti et al 2010b), once the earthquake-induced

bending moment exceeds the footing's moment capacity, the latter is forced to uplift hence limiting the inertia that may be transmitted to the superstructure. Indeed, although the right footing does uplift under the action of the horizontal component only as seen in **Fig. 6.21b** (black line), at the instant t=3.8s the action of the synchronous vertical acceleration produces a dramatic increase in the right column's axial force (compared to that under the horizontal component only) (**Fig. 6.21**), which drastically limits its capacity to uplift. At that very instant, the right footing rotation drops by almost 80% (**Fig. 6.21a**) compared to the no vertical acceleration case, confirming the foundation's inability to uplift. Consequently, the mechanism of uplifting being prevented all the inertial forces on the right column must be undertaken through its bending which, in turn, results to an increase of almost three times of the developed curvature compared to the case when the vertical acceleration is neglected.

6.10.3. Effect of Vertical Acceleration: Decrease of Axial Load

The effect of positive vertical acceleration is better demonstrated in **Figures 6.22 to 6.24** which refer to the deep valley-3 model. They compare the behavior of the frame when subjected to combined horizontal and vertical acceleration to that of the footing subjected to the horizontal component only. The mechanism is briefly outlined in the contours plot of **Fig. 6.22.** The main effect of a synchronous positive vertical acceleration pulse accompanying the strong horizontal pulse is the potential loss of contact between the footing and the ground which, as discussed previously, may result in a kinematically-induced permanent deformation of the column.

During the main horizontal pulse, the left footing whose vertical load is already reduced due to the frame rocking-deformation, (**Fig. 6.23a**) is subjected to a strong

positive vertical acceleration pulse which if only momentarily leads it to loss of contact with the ground. Hence, the new position of the footing upon reattachment with the ground, is slightly translated (to the left) as to its initial position (while the right footing has remained in it) resulting to an irrecoverable deformation of the column (**Fig. 6.23b**), reflected in its residual negative curvature (**Fig. 6.23c**). During the subsequent cycles of shaking the curvature oscillates around that value. The increased stressing of the left column is also confirmed by its moment-curvature plot (**Fig. 6.24a**) and the significantly higher drift ratio produced (**Fig. 6.24b**).

6.10.4. Effect of Frame Positioning along the valley

The previous discussion refers to the frame being positioned on the left edge of the valley (**Fig. 6.25a**) and hence the parasitic vertical component is positive at the instant of peak horizontal displacement (i.e. at the critical instant of maximum inertial force acting on the frame) hence detrimentally increasing the axial load on the column. Were the frame positioned on the opposite end of the valley, geometry dictates that the vertical acceleration time history polarity would be reversed. Indeed, in this case (**Fig 6.25a**) the peak pulse of the vertical acceleration is negative at the instant of maximum inertial demand due to horizontal shaking (t=3s) but is positive during the previous lower pulse, provoking substantial deviations from the response of the no-vertical component scenario in both columns. The effect on the right column (which is subjected to the higher earthquake demand) is not as dramatic as previously in terms of column stressing. The peak curvature (**Fig. 6.25b**) is still increased, yet the instant of peak curvature occurrence does not coincide with the instant of peak horizontal acceleration, as reflected in the substantially reduced footing rotation at t = 3s (**Fig. 6.21a**): the negative

vertical acceleration during the very first (and of lower amplitude) loading cycle augments the column axial load hence limiting its ability to uplift and, in turn, increases its bending-induced deformation which is conspicuously demonstrated by its increased curvature (**Fig. 6.21b).** On the contrary, during the main horizontal shaking pulse, the vertical acceleration component is negative, thus enhancing the right footing's uplifting as mirrored in the rotation time history plot (**Fig. 6.25c).**

6.11. Effect of the valley-generated parasitic vertical component: Response to recorded Earthquake Time Histories

The last section of the investigation of the Frame response subjected to valley-contaminated ground motions explores the effects of recorded accelerograms on the typical structure. Three characteristic time histories have been used as input excitations on the valley bedrock:

a. A moderate earthquake time history recorded during the Kalamata, Greece earthquake. This record may be regarded as corresponding to the "design earthquake" of the structure under study

b. A moderately strong time history recorded during the El Salvador (1985) earthquake.

c. A very strong time history, recorded in the Tabas (Iran, 1981) earthquake.

The non-linear analyses methodology follows the pattern described in the previous sections, comparing the results of the case with and without vertical acceleration component, while in most cases the frame has also been subjected to the free field ground motion in order to quantify the valley effect on its behavior.

6.11.1. Response to Moderate Time History

Figure 6.26 plots the spatial distribution of peak accelerartion values and the recorded time histories on the valley surface when the model is subjected to the mild Kalamata (Greece 1986) record. The horizontal acceleration is maintained within the frame design limits (**Fig 6.26c**) and is therefore not expected to pose a serious threat to the structure, while the amplitude of the vertical acceleration is lower (of the order of 50% of that of the horizontal). By comparison of the response of the two columns (**Fig. 6.27a**) it becomes evident that the frame has behaved practically elastically (as expected) and that the presence of the mild although synchronous with the horizontal, vertical component has not modified its response. The produced ground floor drift ratios (**Fig. 6.27b**) are acceptable.

6.11.2. Response to Strong Earthquake Scenario

When the input excitation is the devastating GIC-090 record (San Salvador 1986), the produced surface acceleration time histories are remarkably more intense both in terms of peak values and time histories (**Figure 6.28).** The consequence of the high horizontal accelerations is more pronounced on the Moment-Curvature plots of the two columns (**Fig. 6.29a**-black line) which develop substantially high curvature, although foundation uplifting protects them from failure. The presence of the synchronous vertical acceleration however although barely affecting the observed footings uplifting (**Fig. 6.29b– grey lines**), does produce a significant increase in the curvature developed in both columns (**Fig. 6.29a**). Observe (**Fig. 6.30**) that the valley-contaminated horizontal component brings about insignificant discrepancies in the frame response compared to its response when subjected to the free-field horizontal ground motion only. Although

the imposed shaking is different both in terms of time history and spectral values (**Fig. 6.30a**), the response in terms of column stressing (**Fig. 6.30b**) is practically equivalent although the produced maximum drift ratio is augmented in case of the valley-contaminated input motion (**Fig. 6.30c**). It is therefore pointed out that, were the parasitic vertical acceleration neglected, the valley effect would have been unrealistically considered as minimal.

6.11.3. Response to Very Strong Earthquake Scenario

The detrimental effect of the parasitic vertical acceleration is exaggerated in case of the devastating Tabas (Tabas, Iran, 1981) record (**Fig. 6.31a**) which produces a tremendous 0.83g peak horizontal and 0.62 g peak vertical acceleration (**Fig. 6.31c**). In the absence of vertical acceleration both footings develop significant rotation (**Fig. 6.32b**), hence being able to sustain the imposed shaking with only limited distortion. Yet, the presence of the vertical acceleration pulses results to dramatically enhanced plastification in the left column (**Fig. 6.32a**), despite the increased value of the developed curvature (**Fig. 6.32b**). The effect is less spectacular for the right column. The phenomenon results, as expected, to irrecoverable accumulation of drift which reaches values indicative of total failure (**Fig. 6.32c**).

Finally, for the sake of completeness, **Figure 6.33** compares the response of the frame subjected to simultaneous action of horizontal and parasitic vertical acceleration to that of the frame under horizontal and natural (recorded) vertical component. The plots are self explanatory: the quite high frequency natural vertical component hardly modifies the response of the frame even for the case of the examined devastating long-duration Tabas record.

Figures of Chapter 6

Table 6.1. Structural member dimensions of the idealized typical frame, and synopsis of computed internal forces for static and seismic load combinations.

Structural Member	***Dimensions (cm)***	***Static Combination***			***Seismic Combination***					
		1.35G + 1.5Q			Vertical Loading : **G+0.3Q**			Earthquake Loading : **± E**		
		M^{st} : kNm	Q^{st} : kN	N^{st} : kN	M : kNm	Q : kN	N : kN	M^{E} : kNm	Q^{E} : kN	N^{E} : kN
Ground floor Columns – base	40 x 40	13	10	243	8	6	150	101	41	54
1^{st} floor Columns – base	40 x 40	68	51	153	40	30	96	26	25	19
Ground floor Beam – edges	20 x 50	71	117	0	41	68	0	80	35	0
1^{st} floor Beam – edges	20 x 50	61	117	0	35	68	0	45	19	0

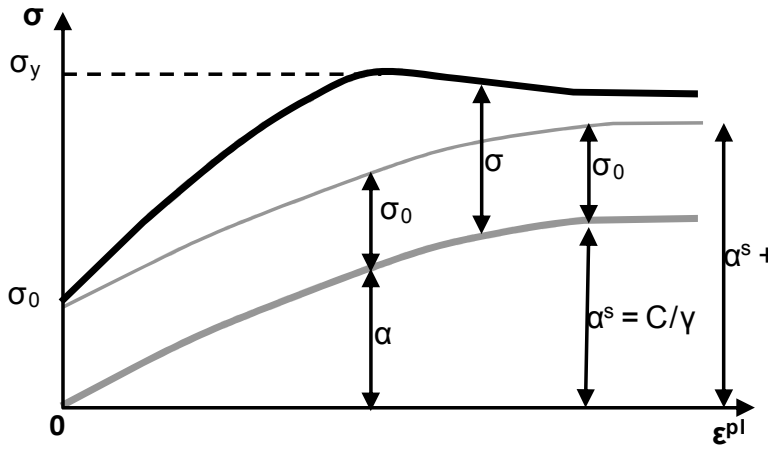

(a)

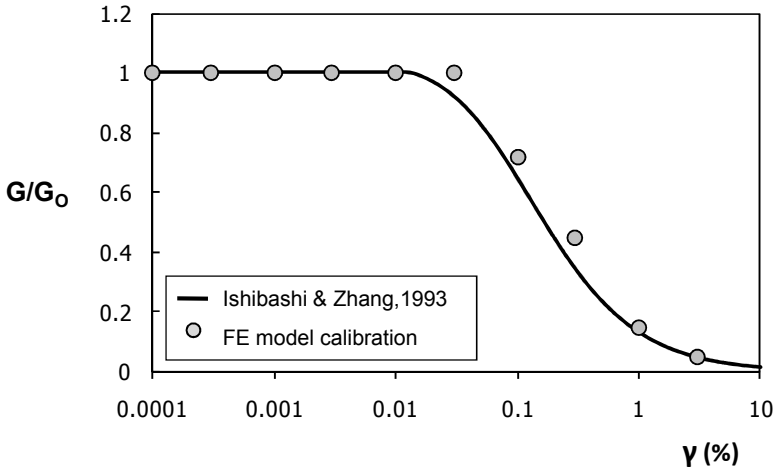

(b)

Figure 6.1. (a) Parameters incorporated into the formulation of the constitutive model and (b) and calibration against published G–γ curves from the literature.

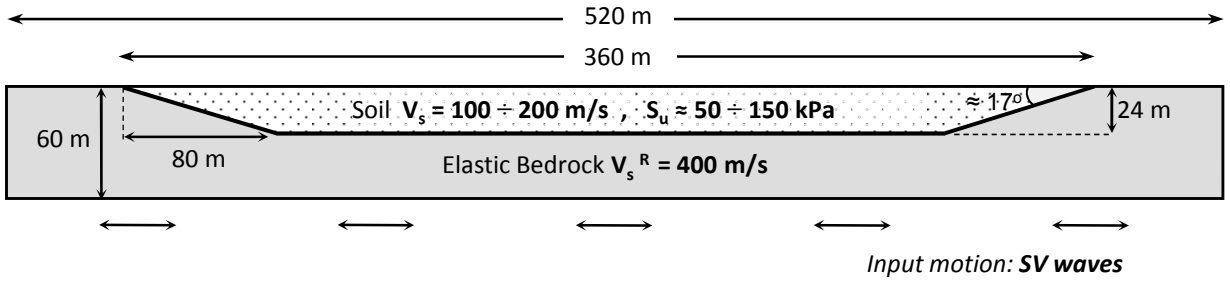

(a)

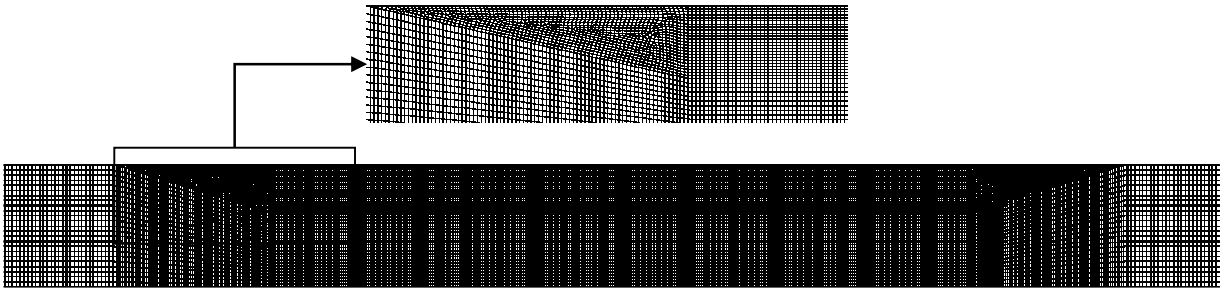

(b)

Figure 6.2. (a) Geometry and Properties of the Valleys utilized for the parametric studies; and (b) finite element discretization, along with zoomed view at the edge of the valley.

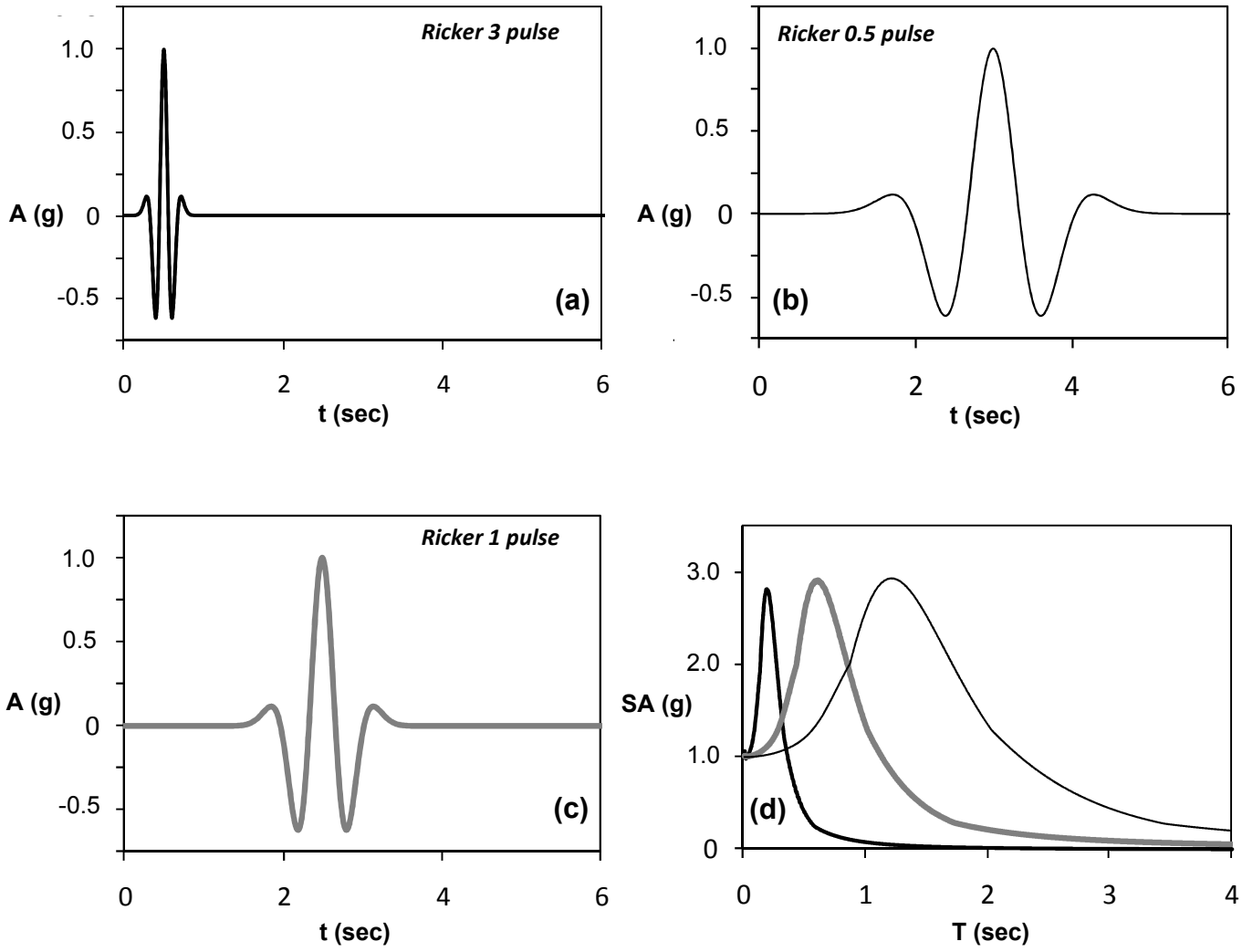

Figure 6.3. The three Ricker wavelets used as seismic excitations: (a) the high-frequency Ricker, f_o = 3 Hz ; (b) the low-frequency Ricker, f_o = 0.5 Hz ; (c) the intermediate Ricker, f_o = 2 Hz ; along with (d) their 5 % damped acceleration elastic response spectra.

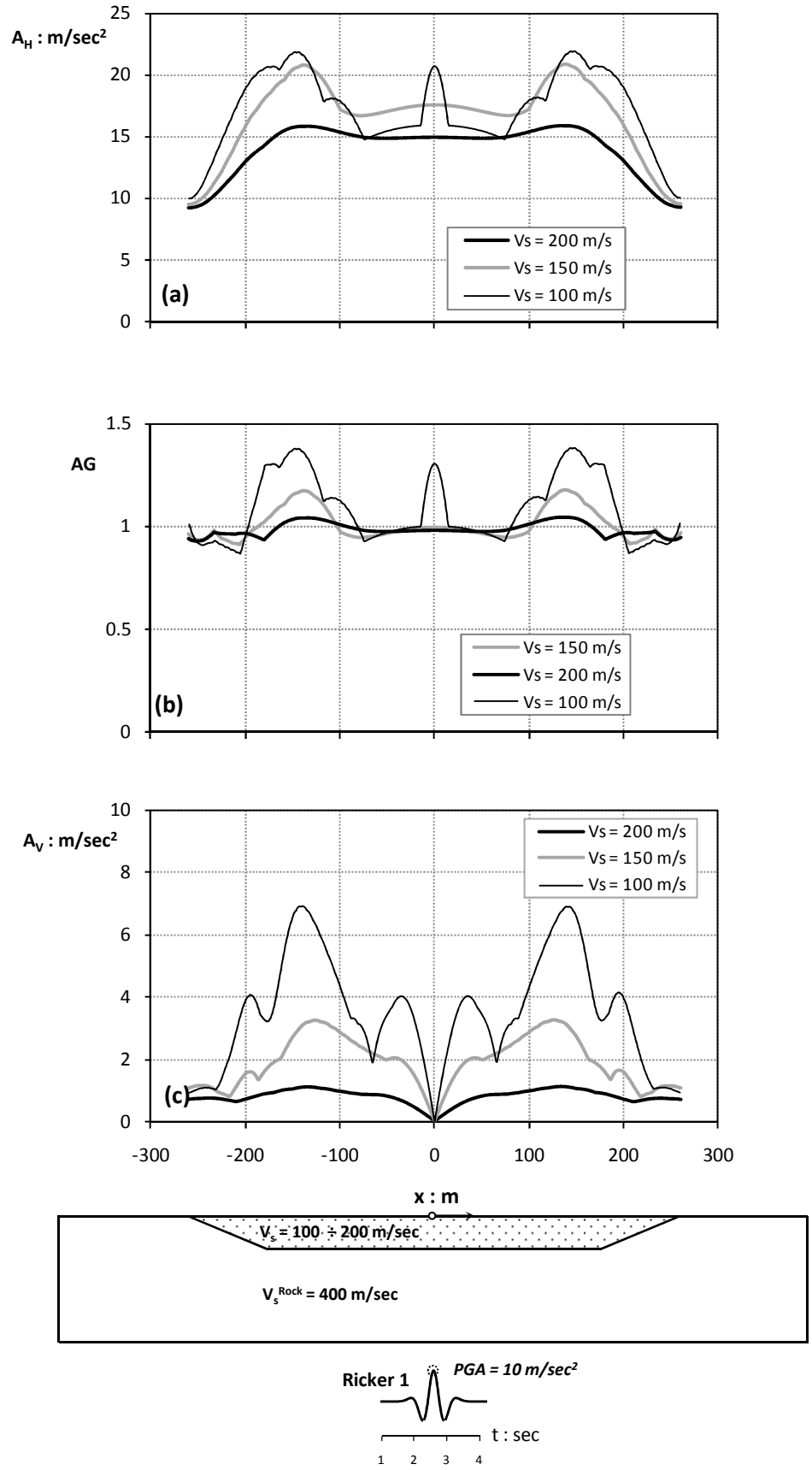

Figure 6.4. Effect of soil stiffness on the viscoelastic response of a Valley subjected to a Ricker1 pulse: Spatial distribution of (a) peak ground acceleration, (b) aggravation factor (ratio of A^{2D}/ A^{1D}) and (c) parasitic vertical acceleration along the valley surface.

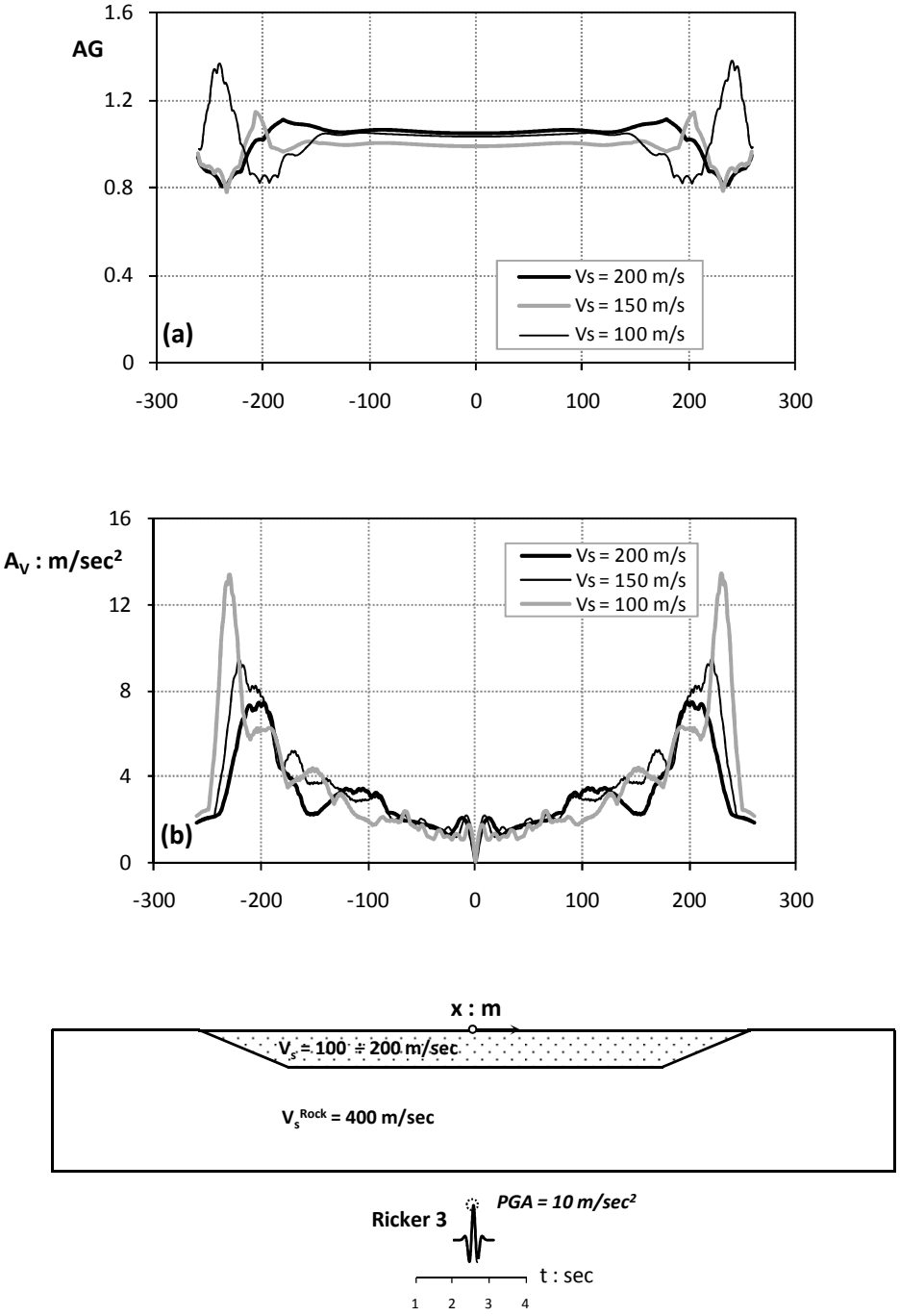

Figure 6.5. Effect of soil stiffness on the viscoelastic response of a Valley subjected to a high frequa*Ricker3* pulse: Spatial distribution of (a) peak ground acceleration, (b) aggravation factor (ratio of A2D/ A1D) and (c) parasitic vertical acceleration along the valley surface.

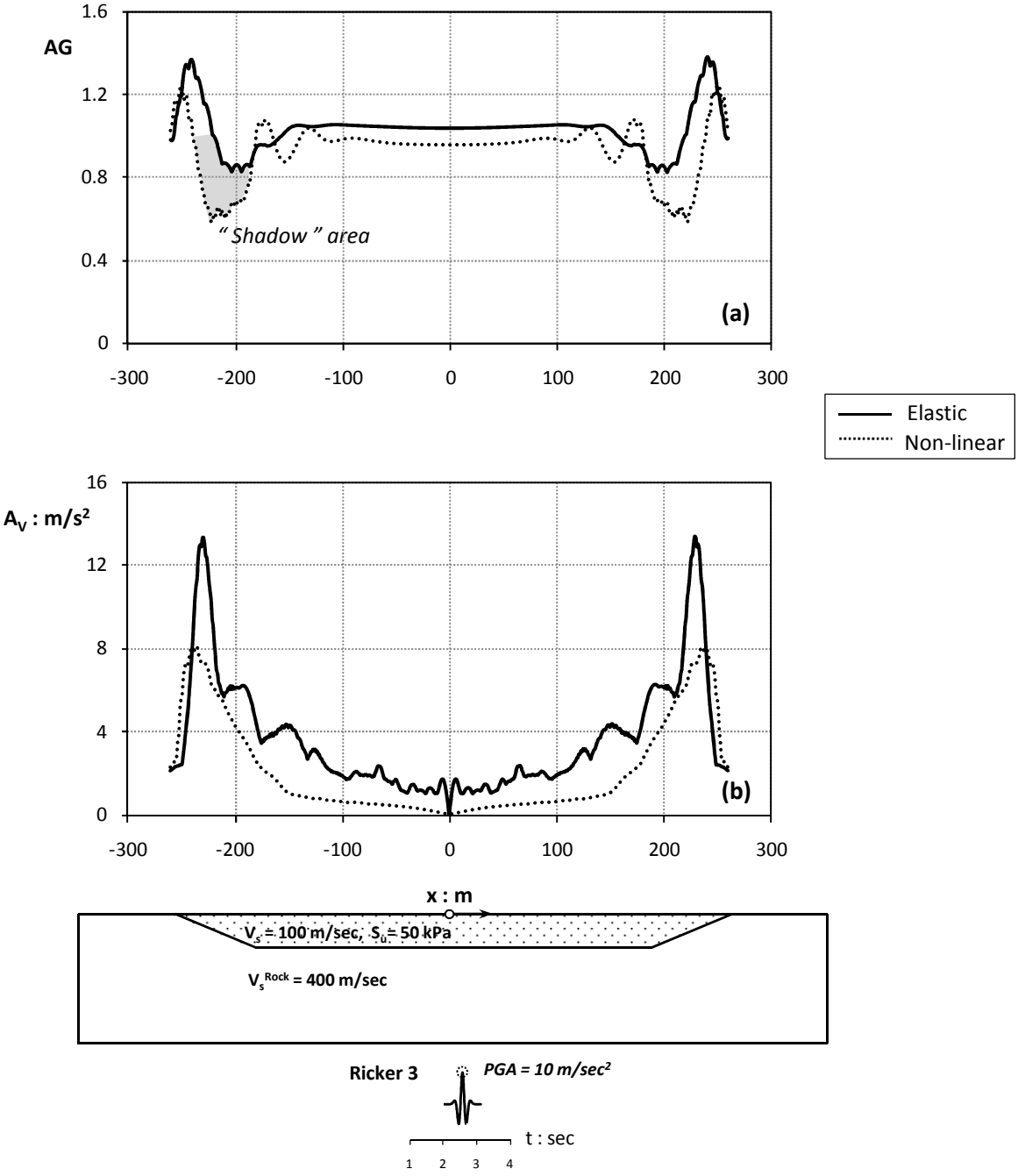

Figure 6.6. Effect of Soil-Nonlinearity on the valley dynamic response : Spatial distribution of (a) Aggravation Factor and (b)maximum values of parasitically generated vertical acceleration along the valley surface. (Case study: Relatively soft valley (Vs = 100 m/s) excited by the high frequency Ricker 3 pulse)

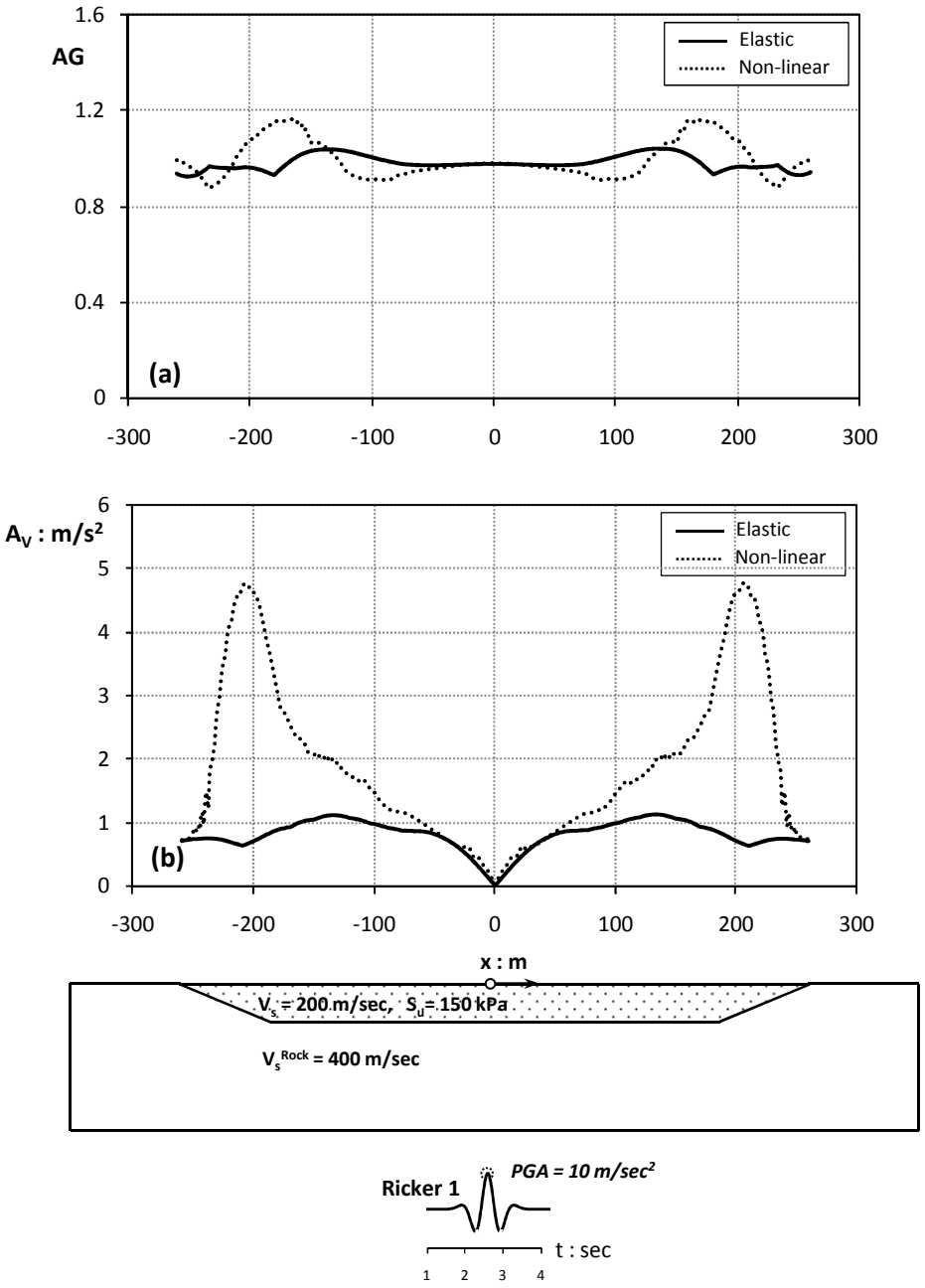

Figure 6.7. Effect of Soil-Nonlinearity on the valley dynamic response : Spatial distribution of (a) Aggravation Factor and (b) maximum values of parasitically generated vertical acceleration along the valley surface. (Case study: stiff valley (Vs =2m/s) excited by the relatively low frequency Ricker 1 pulse)

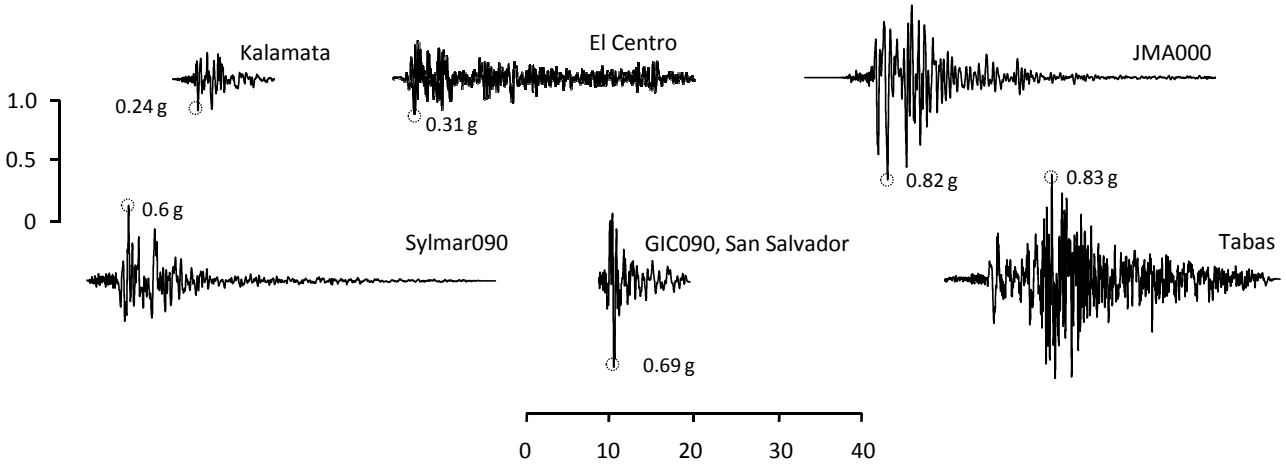

(a)

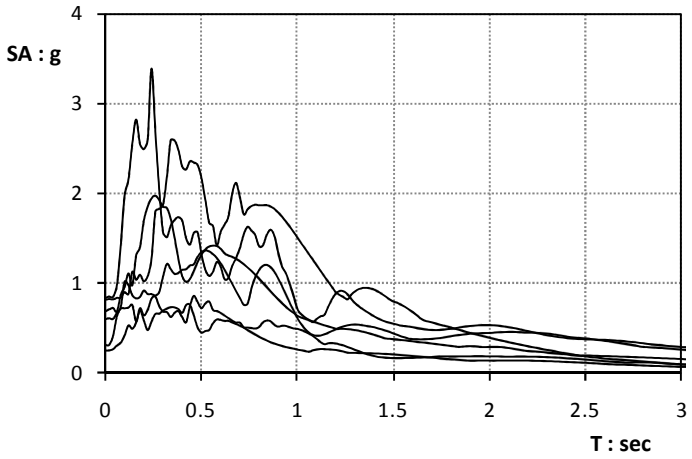

(b)

Figure 6.8. (a) Recorded acceleration time-histories used as excitation frequencies of the valley and (b) their respective elastic response spectra

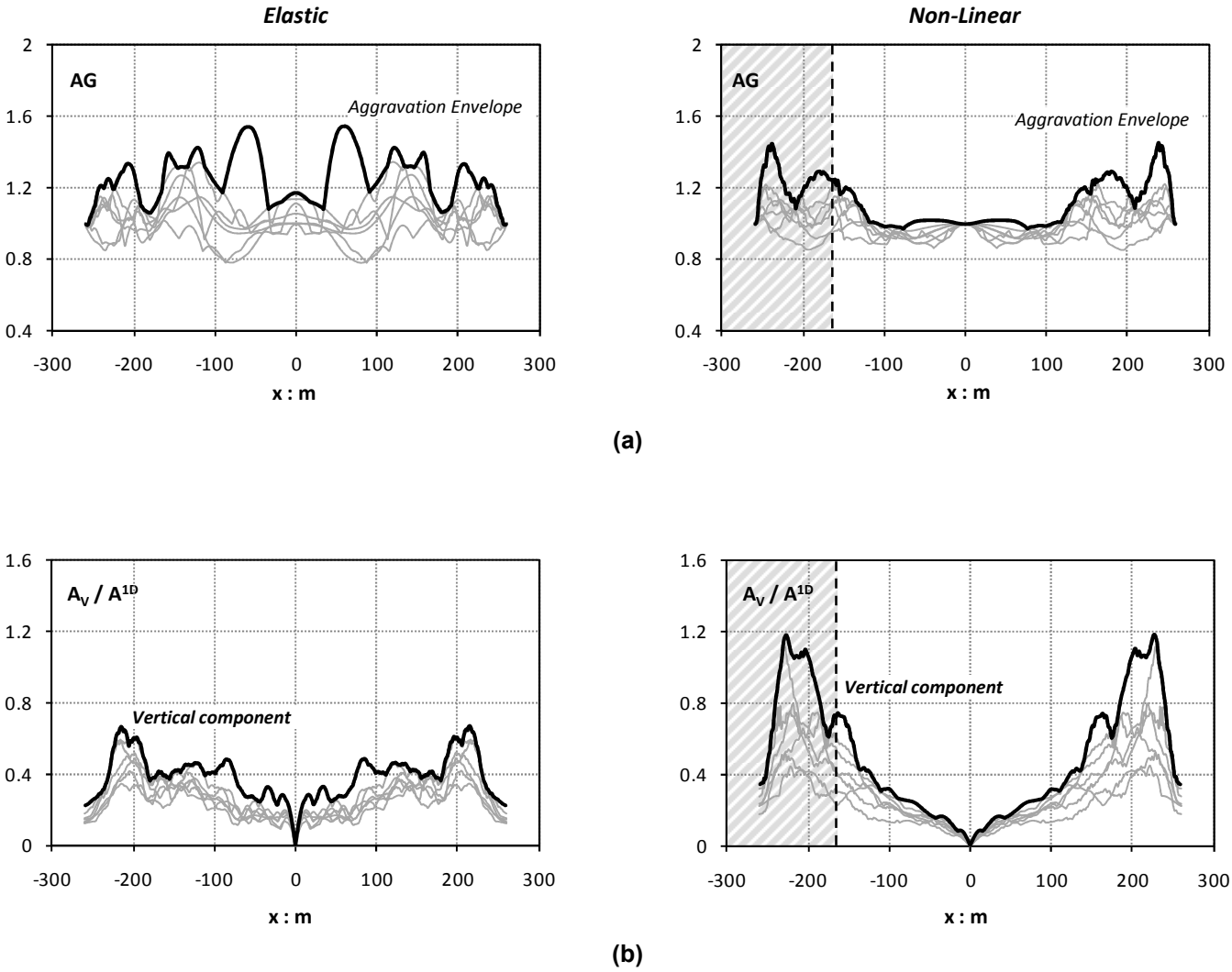

Figure 6.9. Valley subjected to recorded seismic motions: spatial distribution of (a) aggravation factor AG and (b) A_V / A^{1D} ratio considering both elastic (left column) and non-linear (right column) soil response.

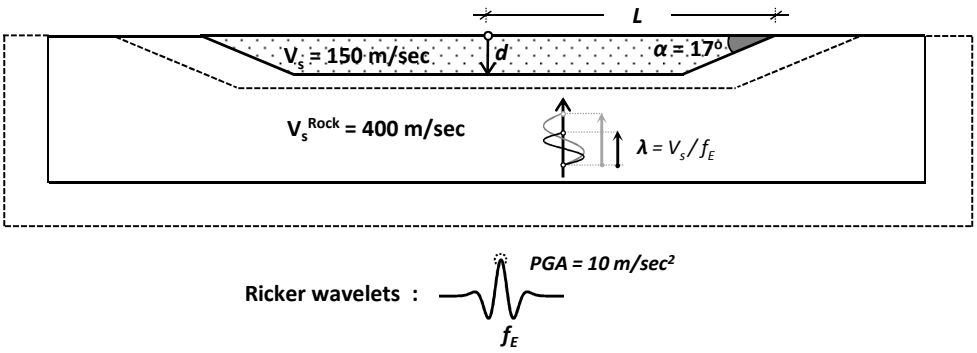

	Dimensions		
	valley 1 [L, d] = [260, 24]	*valley 2* [L, d] = [390, 36]	*valley 3* [L, d] = [520, 48]
x = 6.25	f_E = 1 Hz	f_E = 0.67 Hz	f_E = 0.5 Hz
x = 3.125	f_E = 2 Hz	f_E = 1.33 Hz	f_E = 1 Hz
x = 2.0	f_E = 3 Hz	f_E = 2 Hz	f_E = 1.5 Hz

Figure 6.10. Valley Geometries Investigated during the dimensional analysis and corresponding values of the dimensionless parameter x .

1. x = 6.25

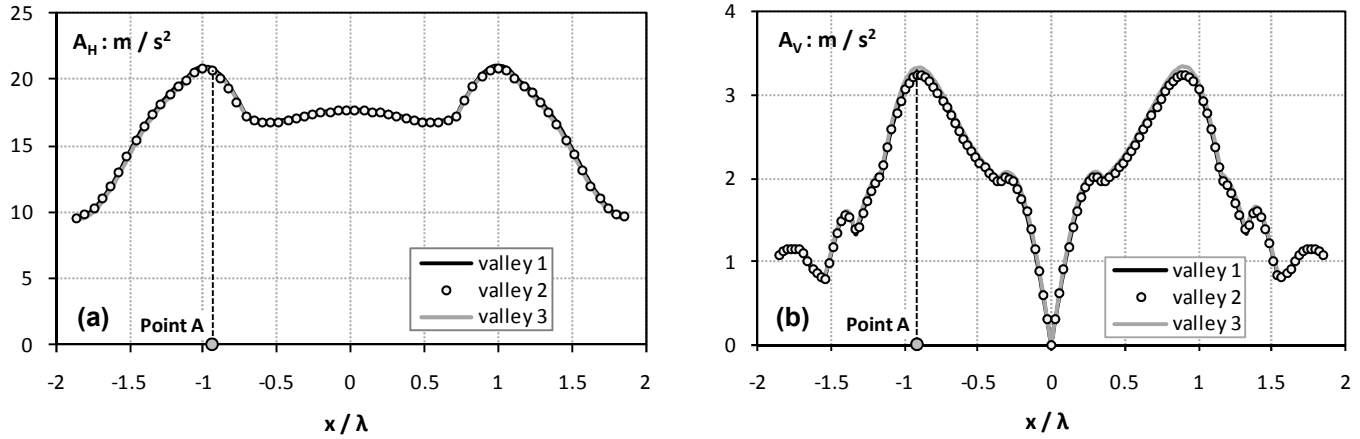

2. x = 3.125

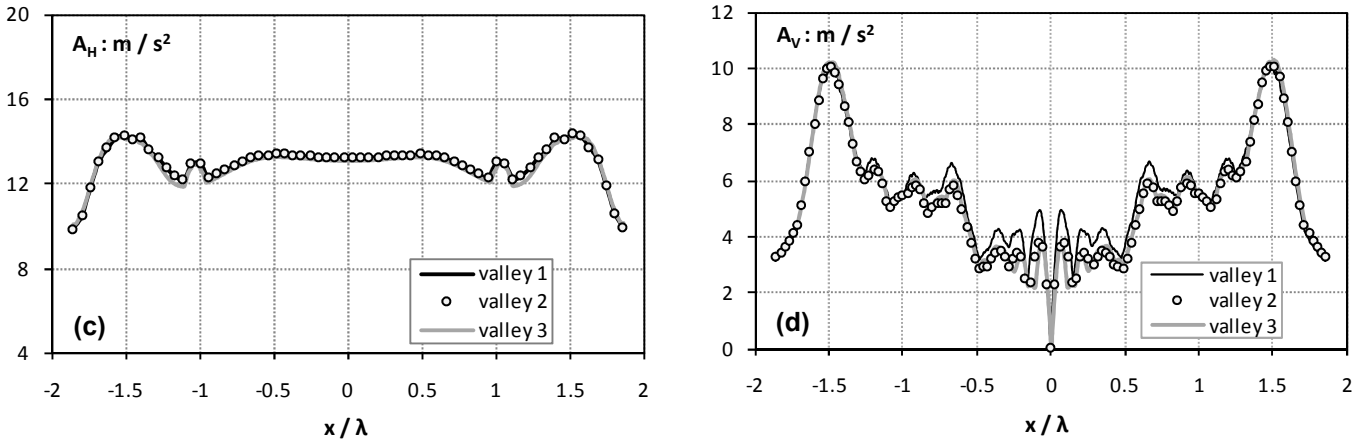

3. x = 2.0

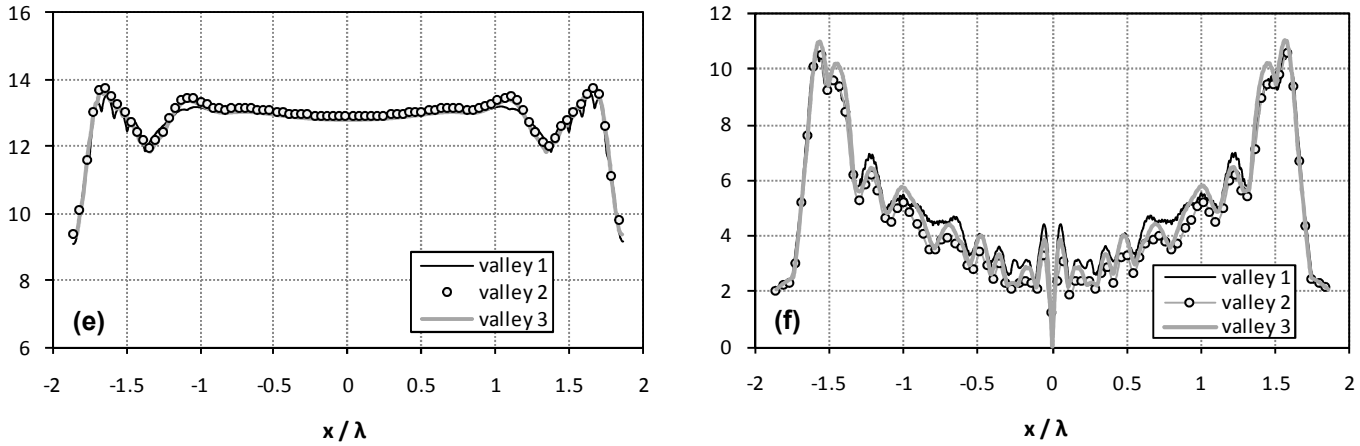

Figure 6.11. Dimensionless analysis results Spatial distribution of peak horizontal and vertical acceleration along the valley surface (viscoelastic soil response when ξ = 2 % is considered)

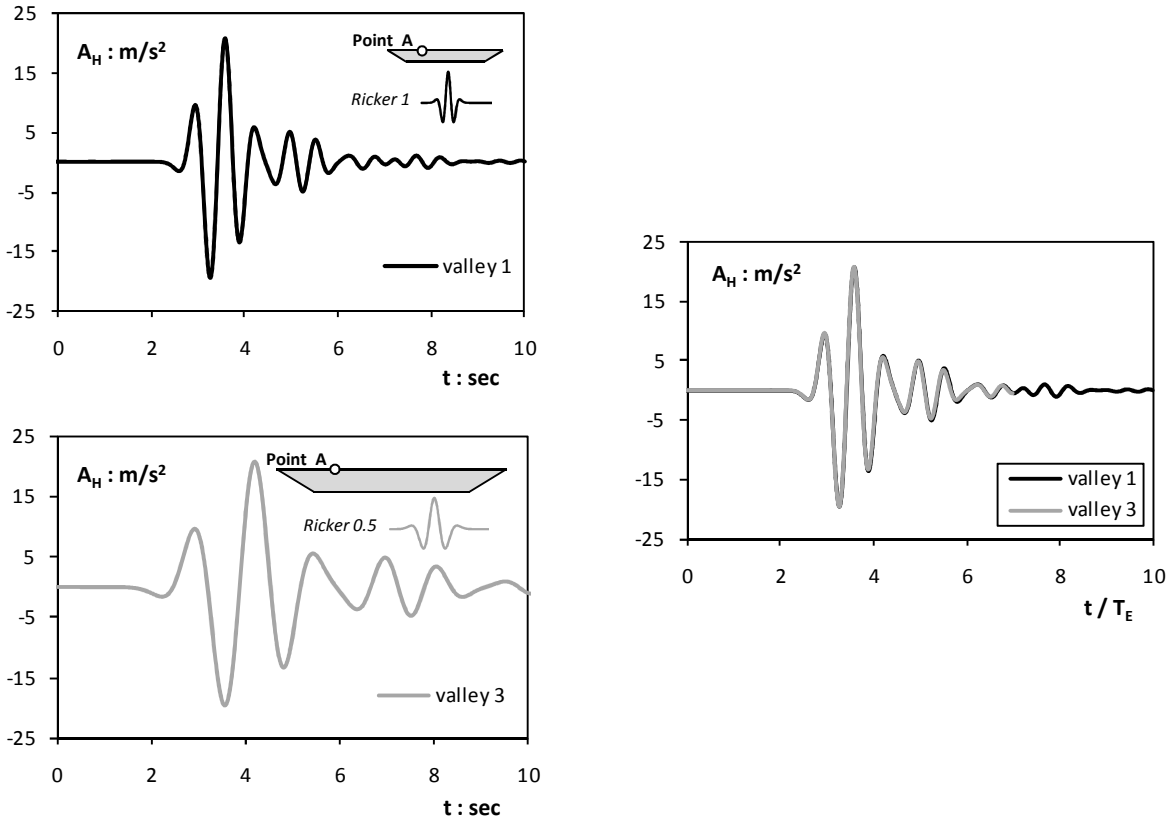

(a)

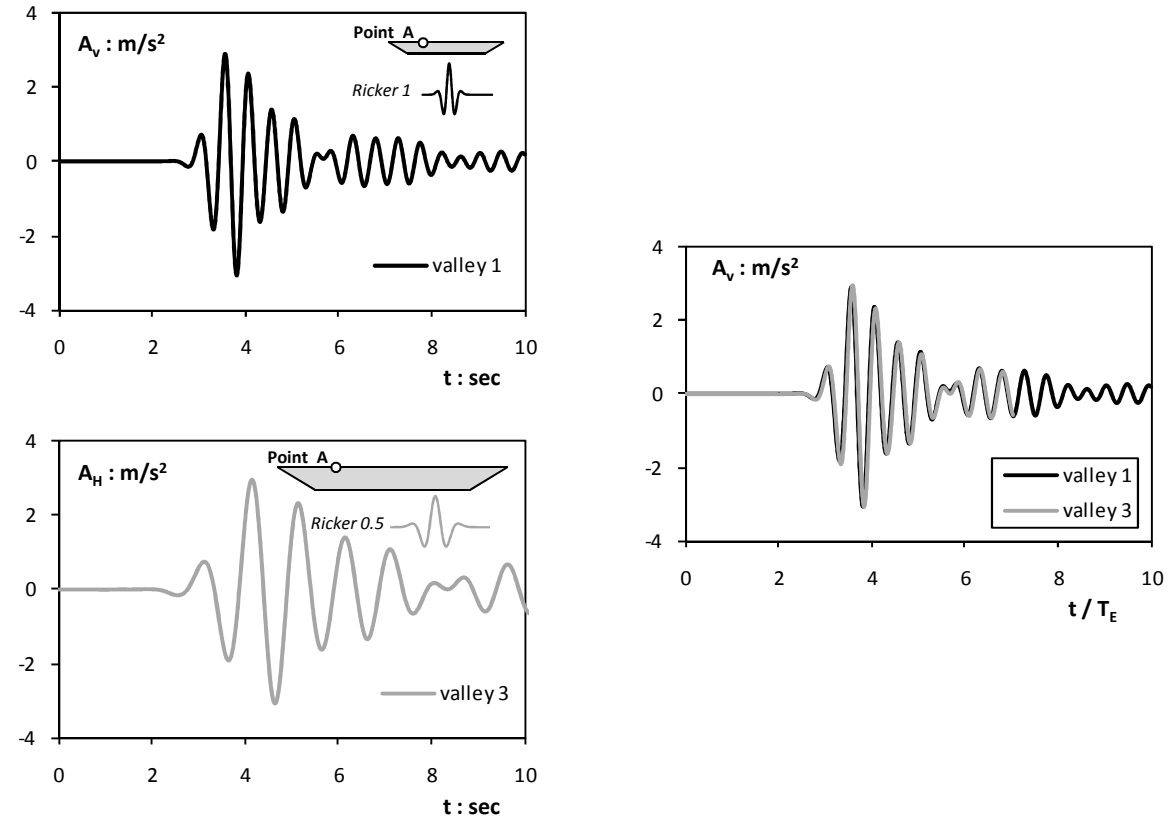

(b)

Figure 6.12. Dimensionless analysis results : Comparison of produced acceleration time histories (horizontal and vertical) at the point A (x/λ = -0.9)of valley surface (viscoelastic soil response with ξ = 2 %)

	Dimensions	
	valley 1 [L, d] = [260, 24]	*valley 3* [L, d] = [520, 48]
x = 6.25	f_E = 0.707 Hz	f_E = 0.5 Hz
x = 2.0	f_E = 2.12 Hz	f_E = 1.5 Hz

1. x = 6.25

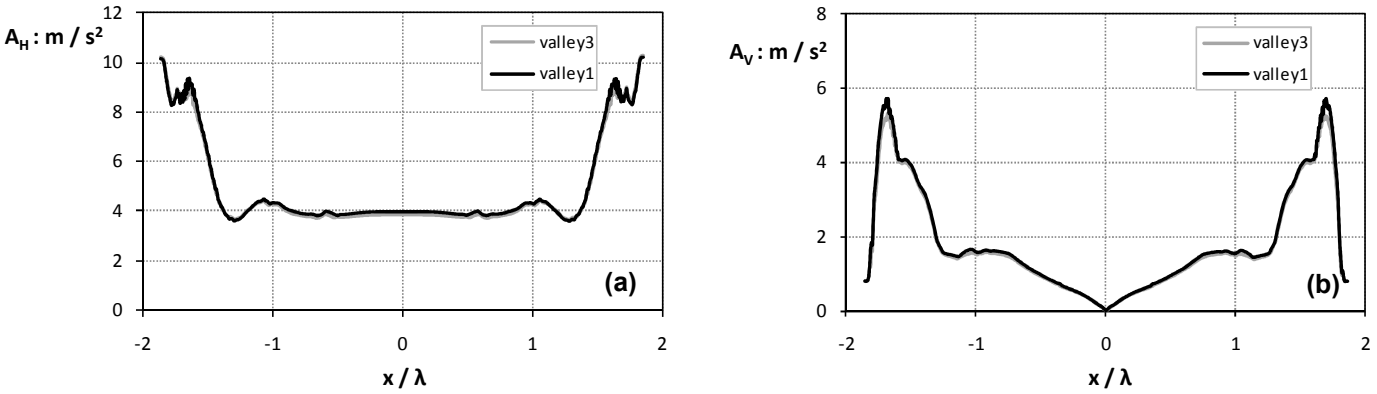

2. x = 2.0

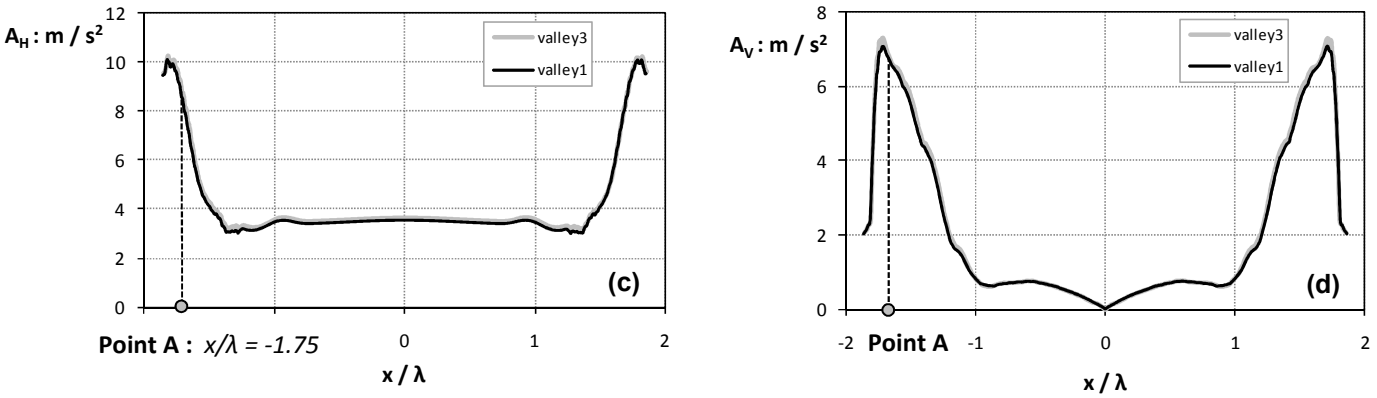

Figure 6.13. Dimensional Analysis Results considering Non-Linear Soil Behavior in terms of distribution of peak horizontal and vertical acceleration values for the two extreme valley geometries examined

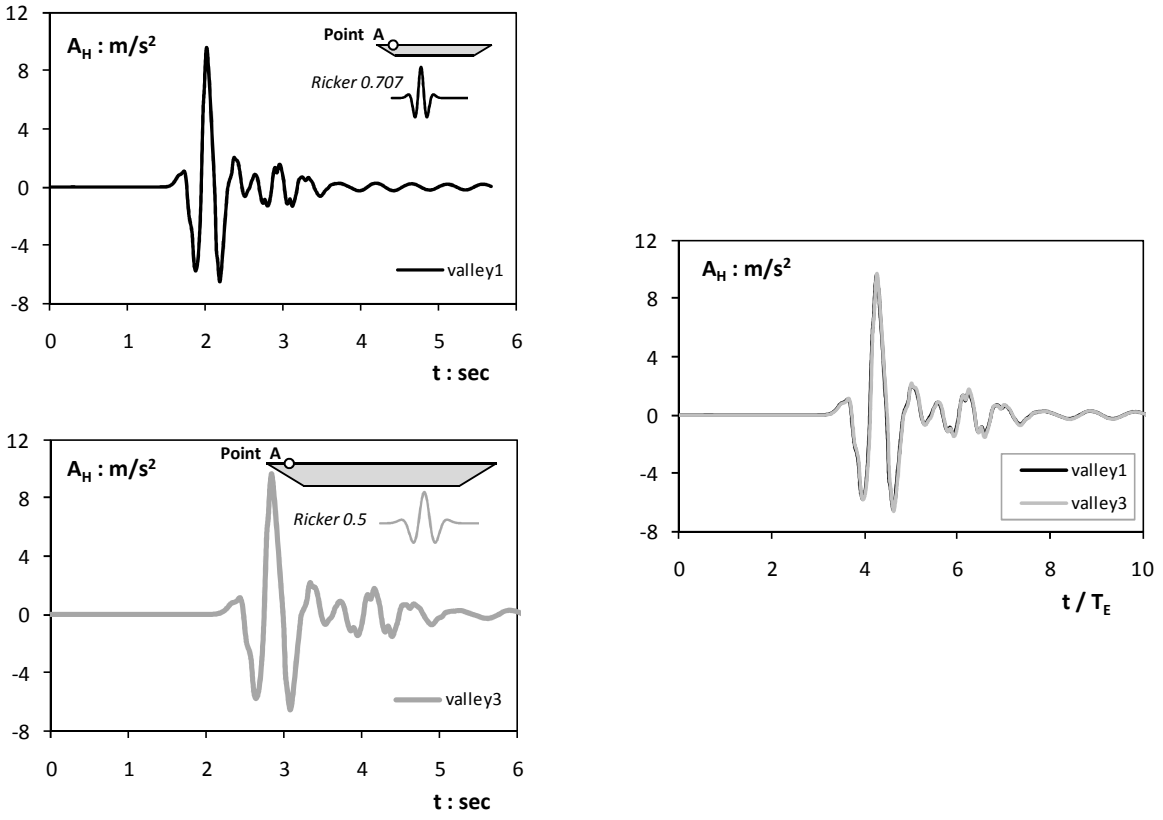

(a)

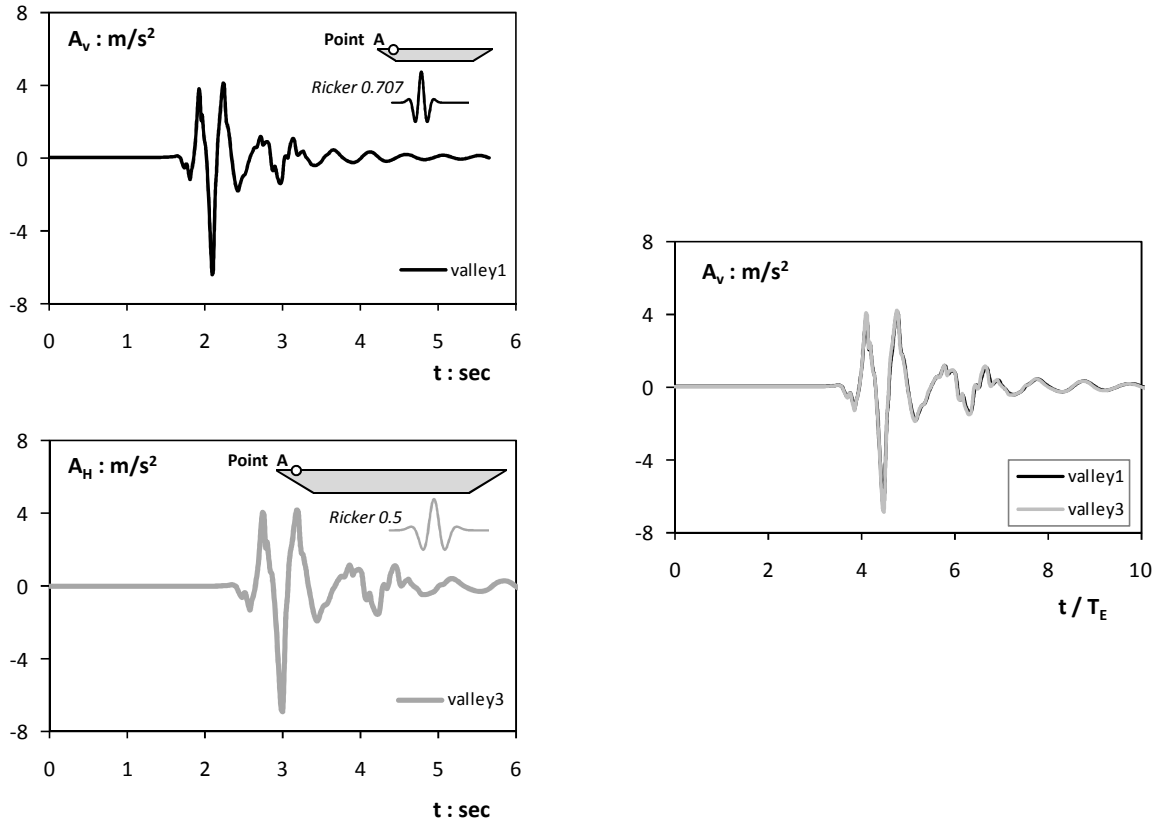

(b)

Figure 6.14 Dimensional Analysis Results Considering Non-Linear Soil Behavior in terms of time histories of horizontal and vertical acceleration for the two extreme valley geometries examined at the point A (x/λ = -1.75) of the valley surface.

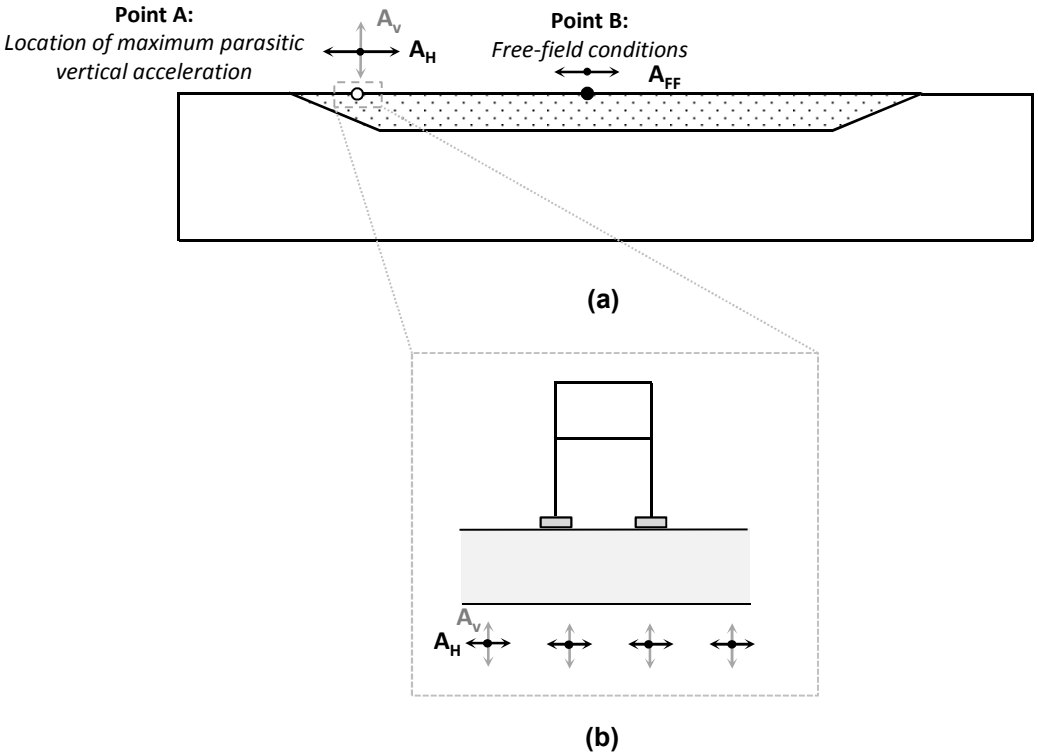

Figure 6.15. (a) First stage: The free field valley response when subjected to horizontal shaking at the bedrock is calculated initially and (b) second stage: the produced horizontal and parasitic vertical acceleration time histories of the first stage are applied as input excitation of the de-coupled model that includes the frame.

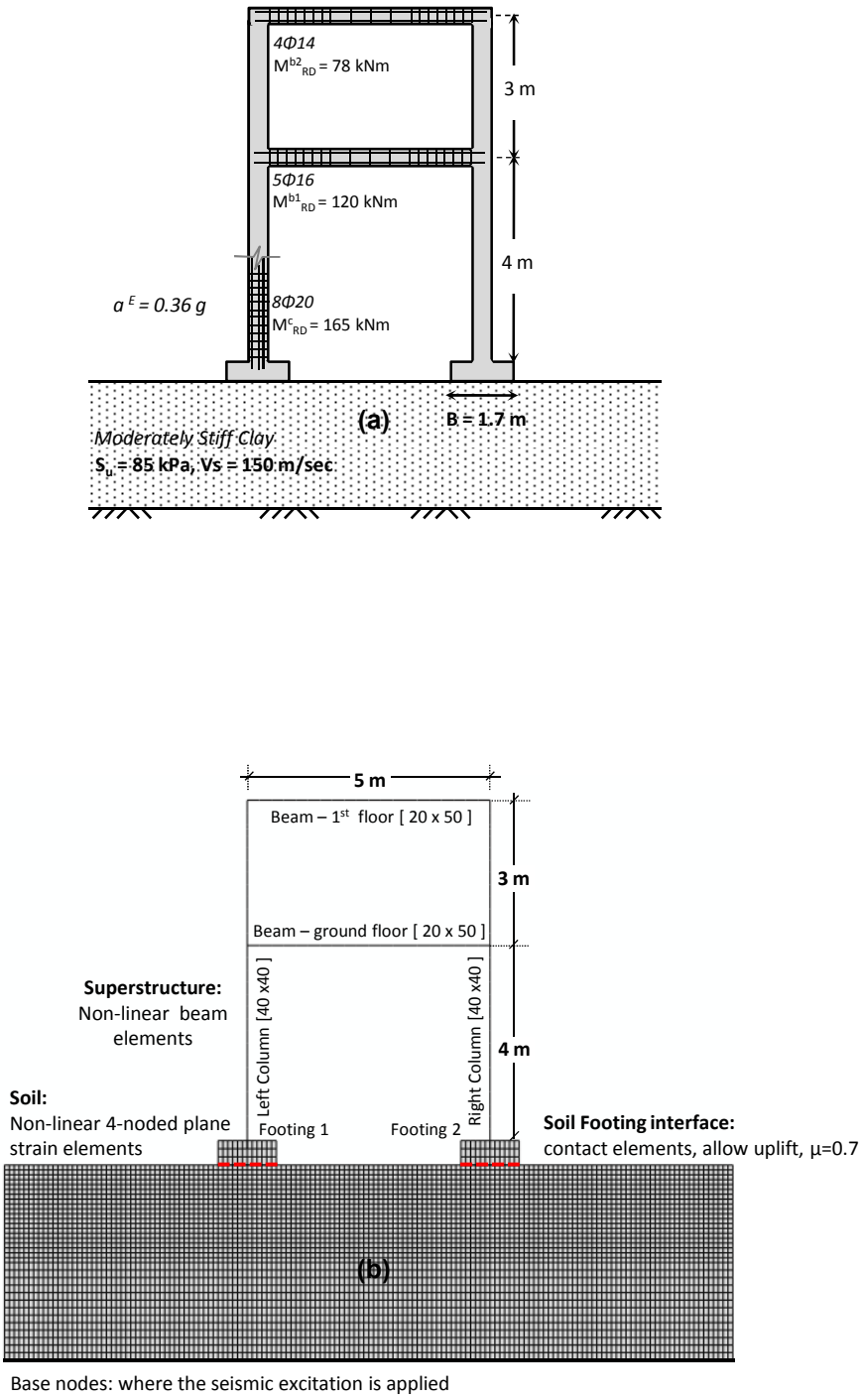

Figure 6.16 (a) Geometry and member properties of the idealized typical frame structure analyzed and (b) finite element model assuming plane-strain conditions: the soil-structure system is modeled so as to consider both material (soil *and* superstructure) and geometric (uplifting and P-δ effects) nonlinearities.

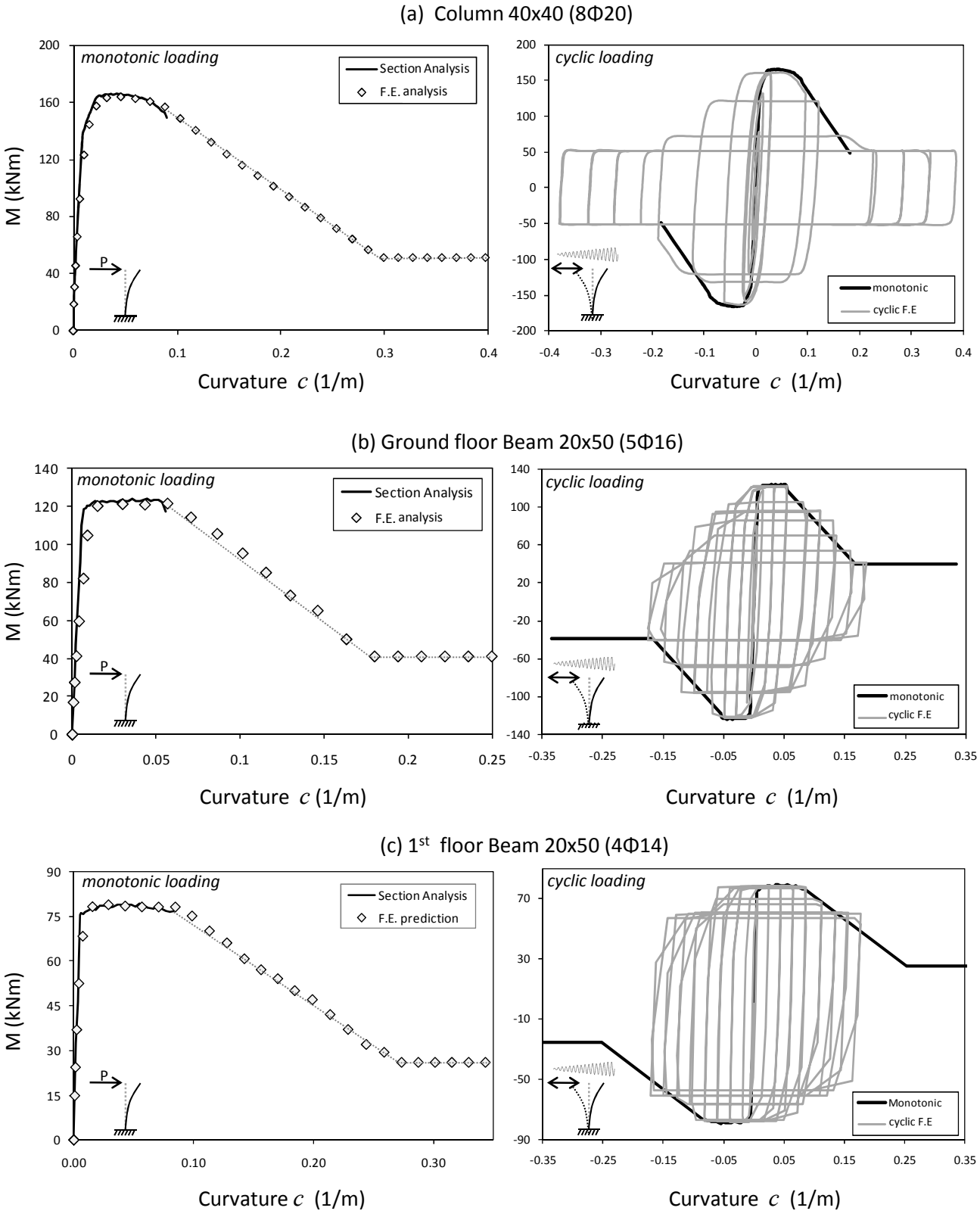

Figure 6.17. Calibration of the superstructure F.E. model against moment–curvature response calculated through reinforced–concrete section analysis under monotonic loading (left column), and FE model response under cyclic loading (right column) : (a) columns (40x40, 8Φ20), (b) ground floor beam (20x50, 5Φ16), and (c) 1st floor beam (20x50, 4Φ14).

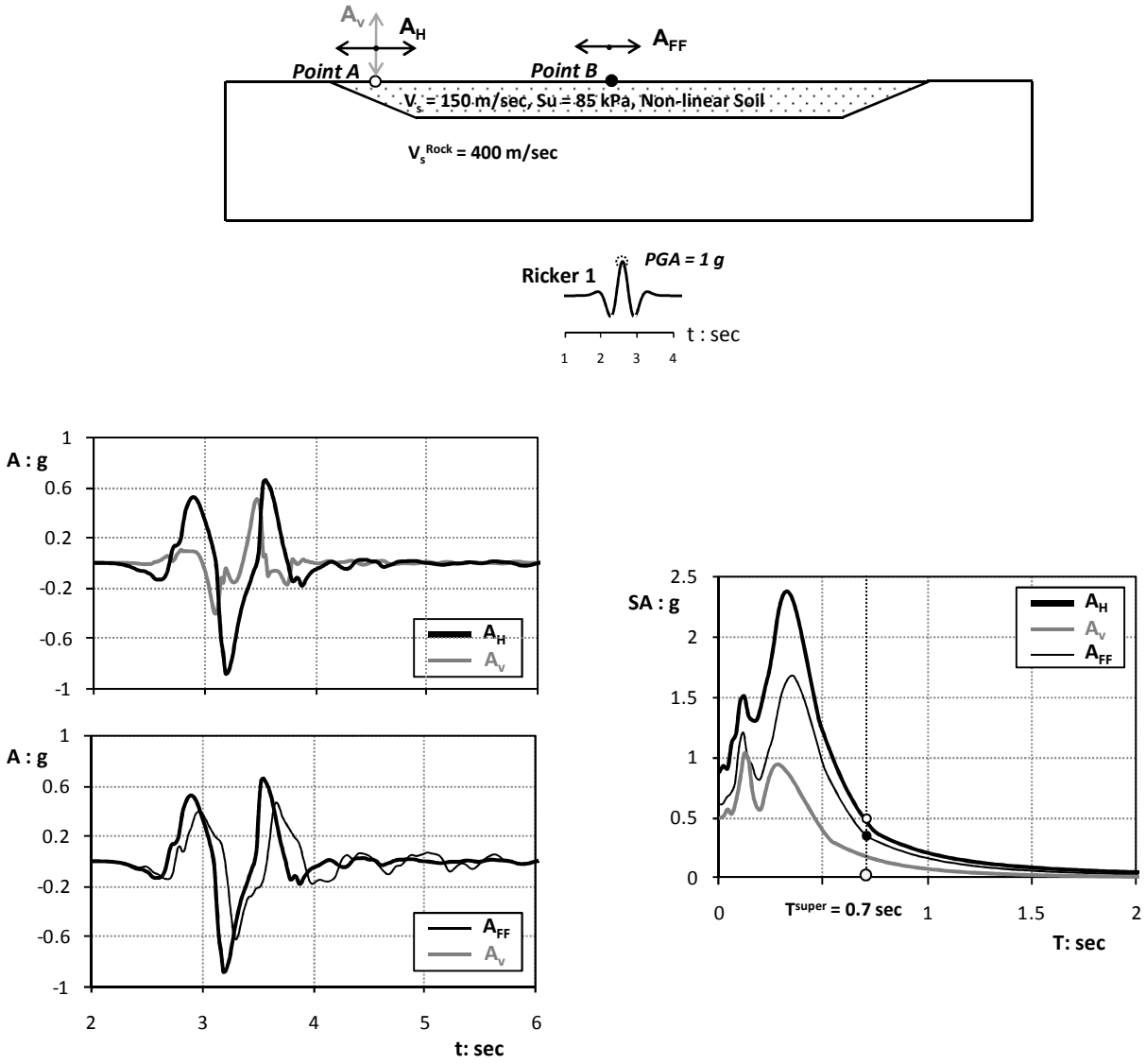

Figure 6.18. (a) Geometry and properties of the Valley utilized for the Valley-Frame Interaction Analyses **(b)** Horizontal and vertical acceleration time histories and respective response spectra on the valley surface points A(edge) and B (quasi free-field)

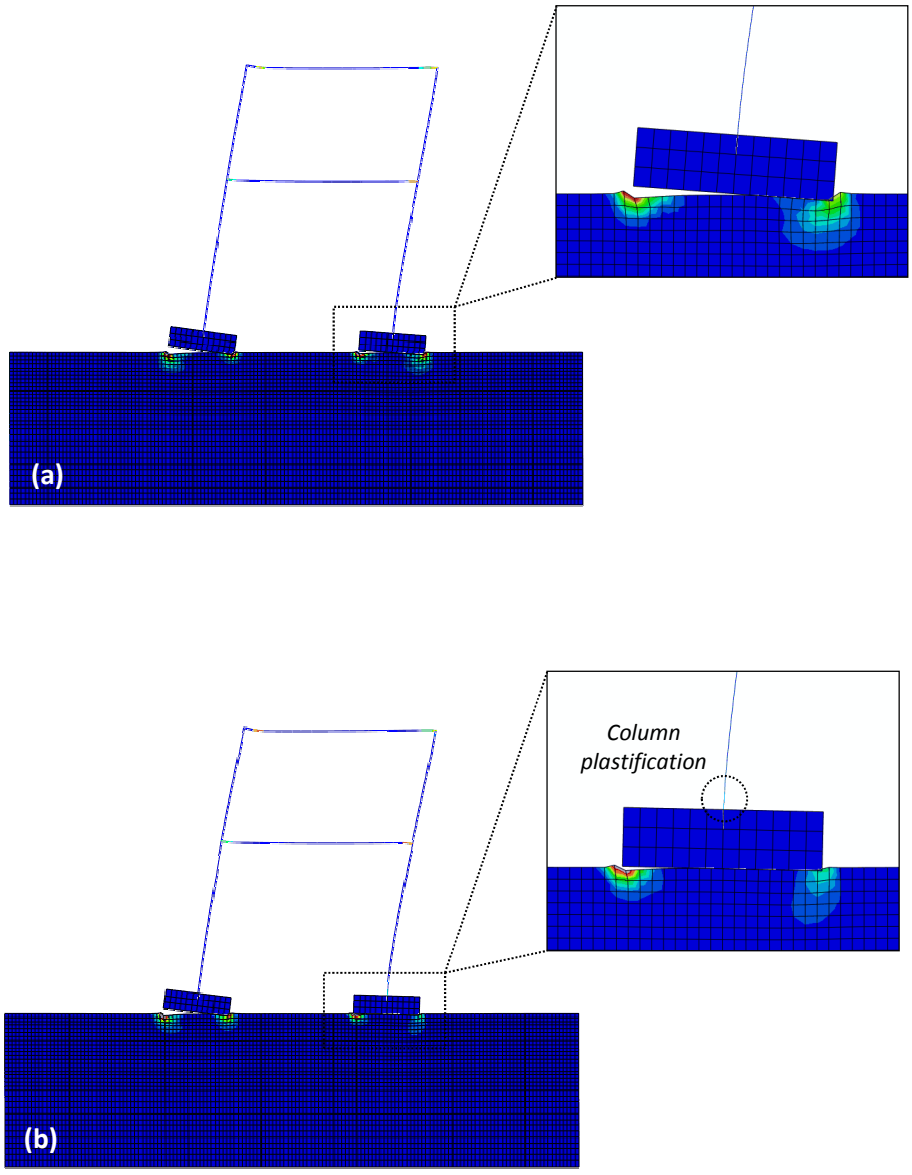

Figure 6.19. Frame response when excited by (a) solely horizontal acceleration and (b) combined horizontal and vertical acceleration (parasitically generated at the valley surface) : Vertical acceleration is associated with increased axial load in the frame column.

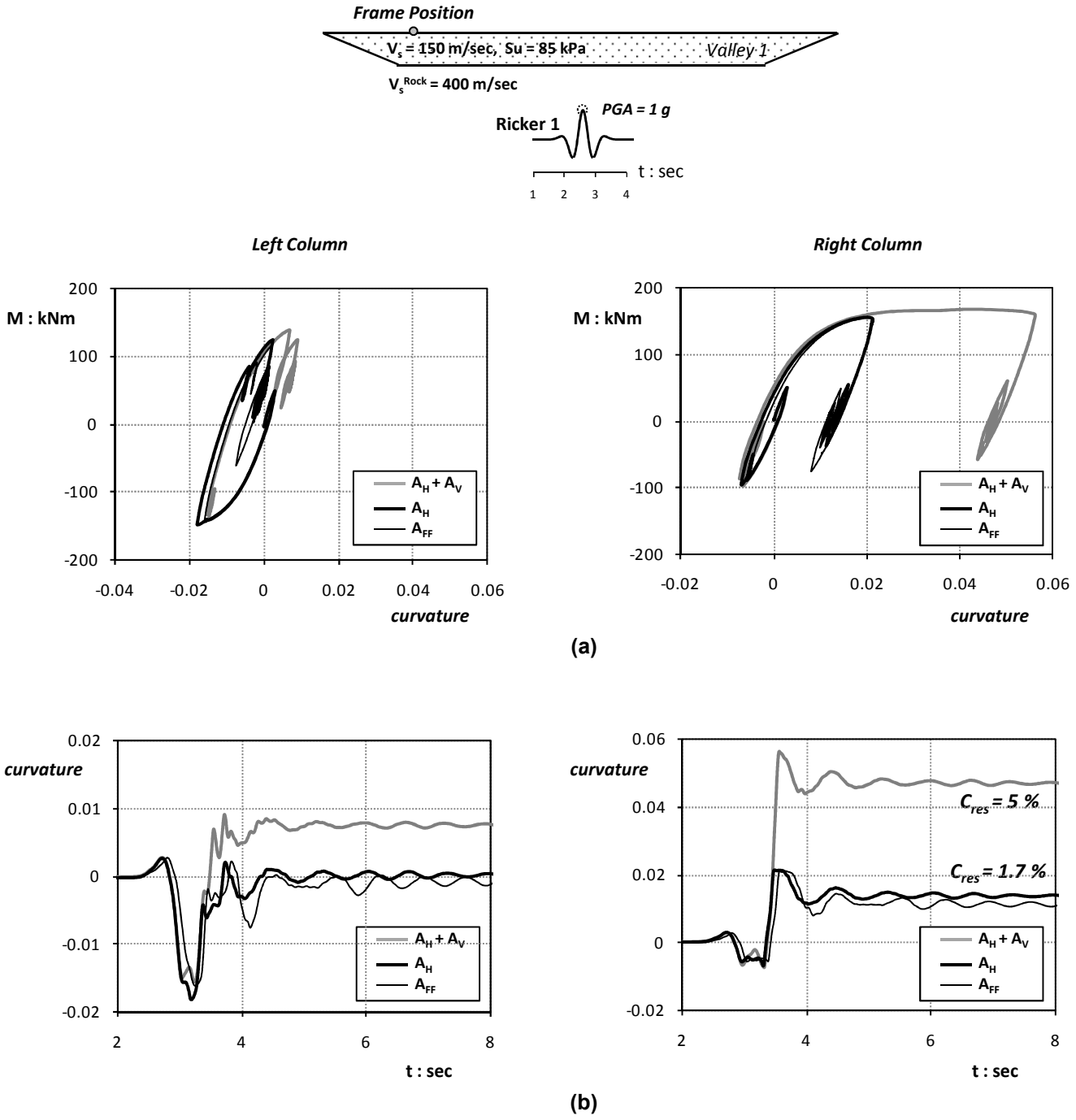

Figure 6.20. Frame response when excited by combined horizontal and vertical acceleration (grey line) and when subjected to horizontal acceleration only (bold black line). For comparison reasons the frame response when excited by the free-field accelation (black line) is plotted together: (a) Moment-curvature loops at the base of both columns , (b) curvature time-history (case study: frame founded on a stiff valley formation and excited by a Ricker 1 pulse).

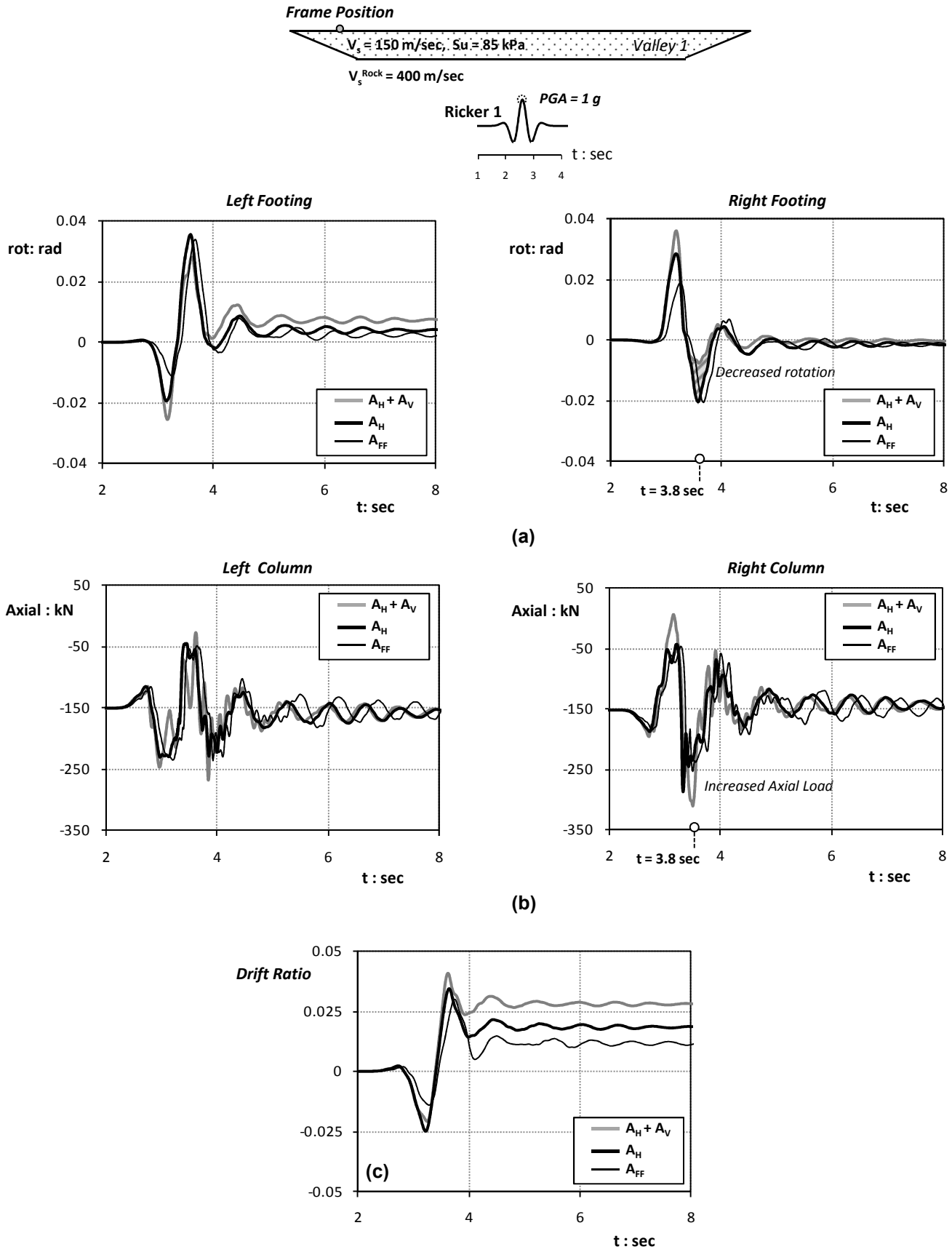

Figure 6.21 Frame response when excited by combined horizontal and vertical acceleration (grey line) and when subjected to horizontal acceleration only (bold black line). For comparison reasons the frame response when excited by the free-field accelation (black line) is plotted together: (a) Rotation time-histories at both footings, (b) time-histories of axial load at the base of the frame columns and (c) ground floor drift ratio time history (case study: frame founded on a stiff valley formation and excited by a Ricker 1 pulse).

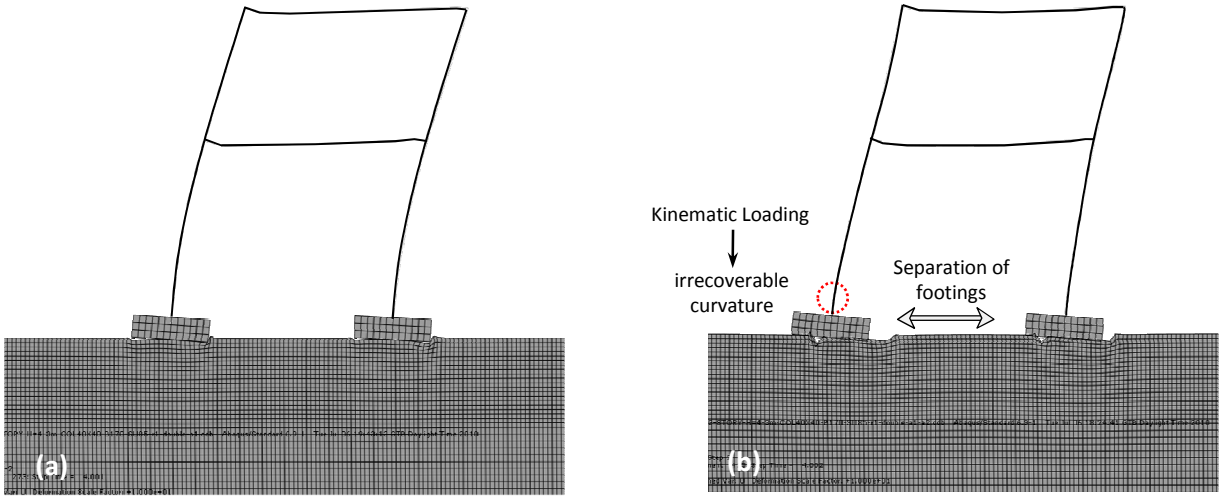

Figure 6.22. Frame deformation when subjected to (a) the valley-contaminated horizontal only component of ground motion and (b) the valley-contaminated horizontal and parasitic vertical component of ground motion with the latter causing a decrease of the column axial load. Case study: Valley 3 (assuming S_u=85 kPa) is excited by Ricker1 at 1g.

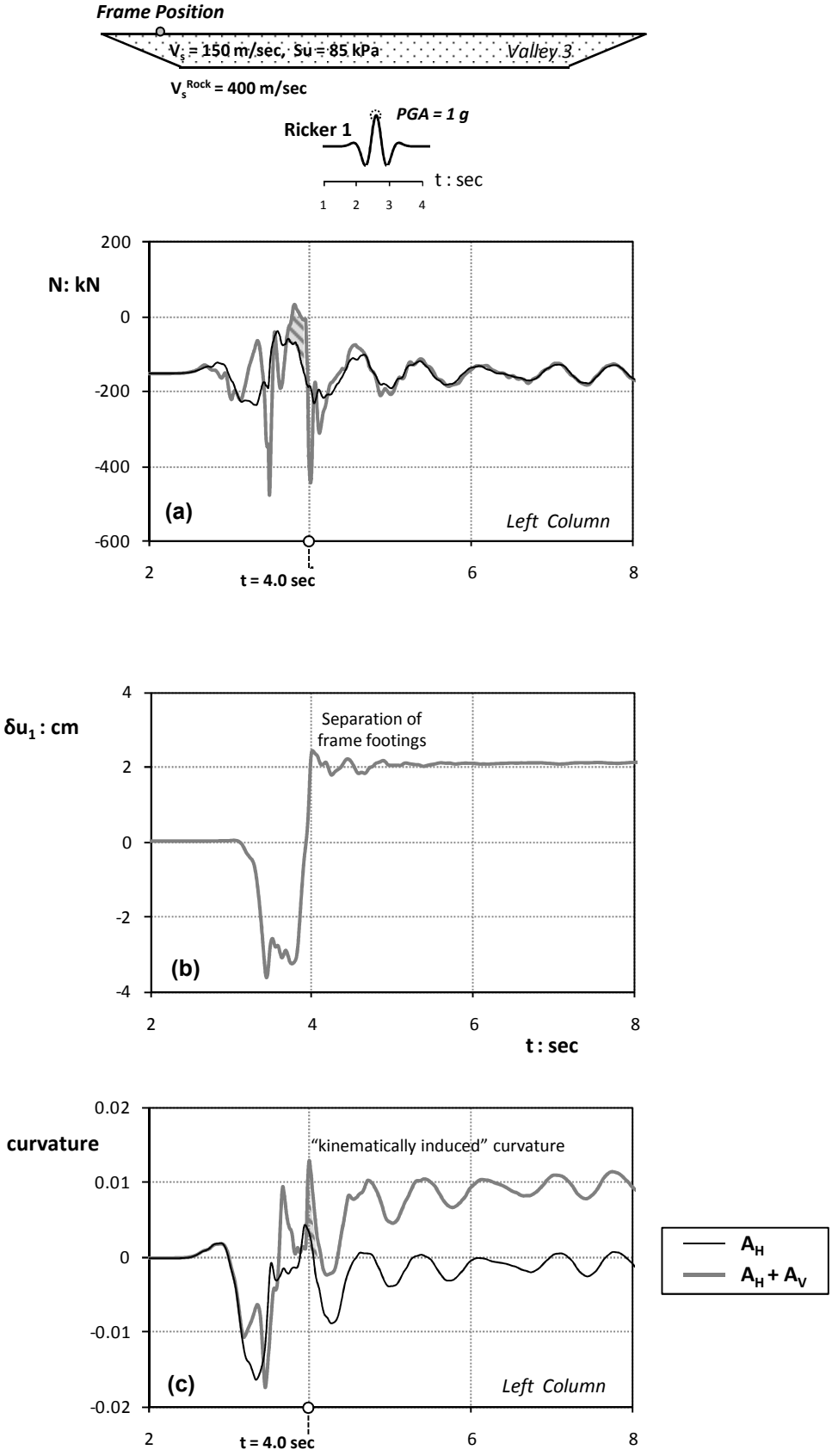

Figure 6.23. Frame response when excited by combined horizontal and vertical acceleration (grey line) and when subjected to horizontal acceleration only (black line): (a) time-history of axial load at the base of the left column, (b) evolution of differential horizontal discplacement of the footings and (c) curvature time history on the left colum (case study: frame founded on a relatively stiff valley formation (S_u=85 kPa) that is excited by a Ricker1 scaled at 1g).

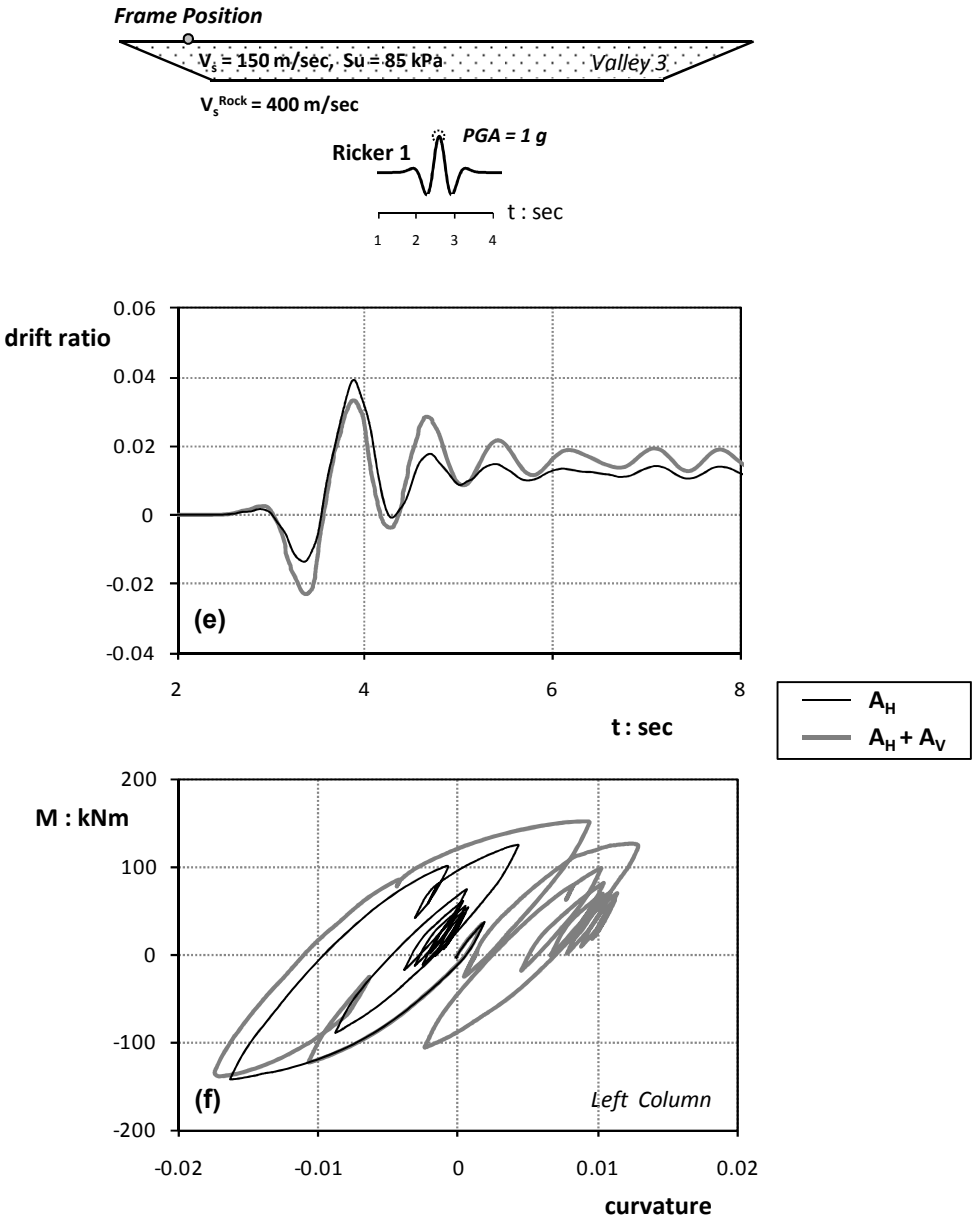

Figure 6.24. Frame response when excited by combined horizontal and vertical acceleration (grey line) and when subjected to horizontal acceleration only (black line): (a) ground floor drift ratio time history and (b) moment-curvature loops at the base of the left column (case study: frame founded on a relatively stiff valley formation (S_u=85 kPa) excited by a Ricker1 scaled at 1g).

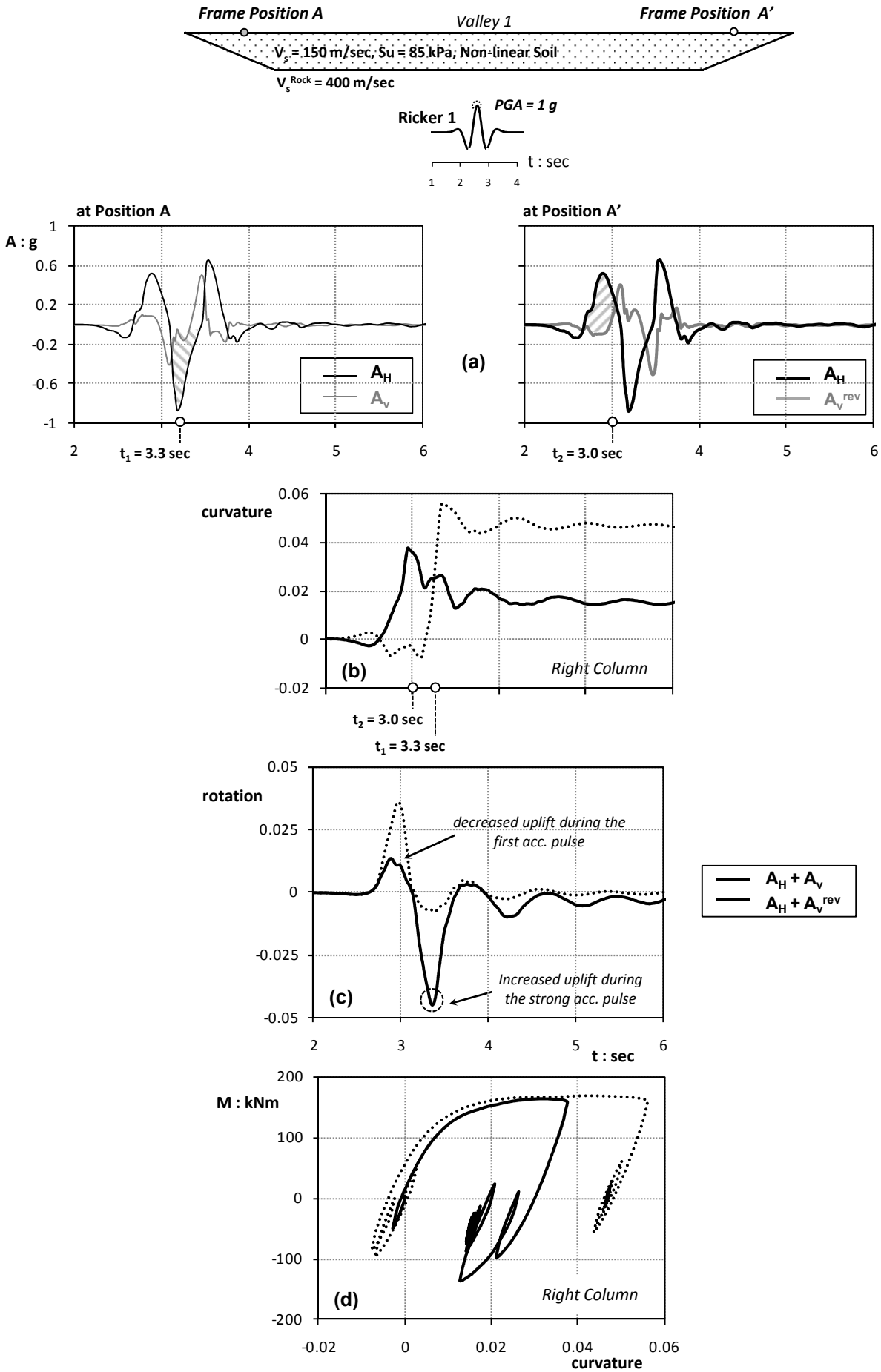

Figure 6.25. Effect of Frame Positioning along the valley: (a) acceleration time histories (horizontal and parasitic vertical) at Position A and A' respectively, (b) curvature time history at the base of the right column, (c) footing rotation time history and (c) moment-curvature-loops for two frames founded on opposite locations along the valley surface (solid line for the frame located at position A' and dotted line for that at position A)

1. Moderate earthquake Scenario –Kalamata earthquake, South Greece

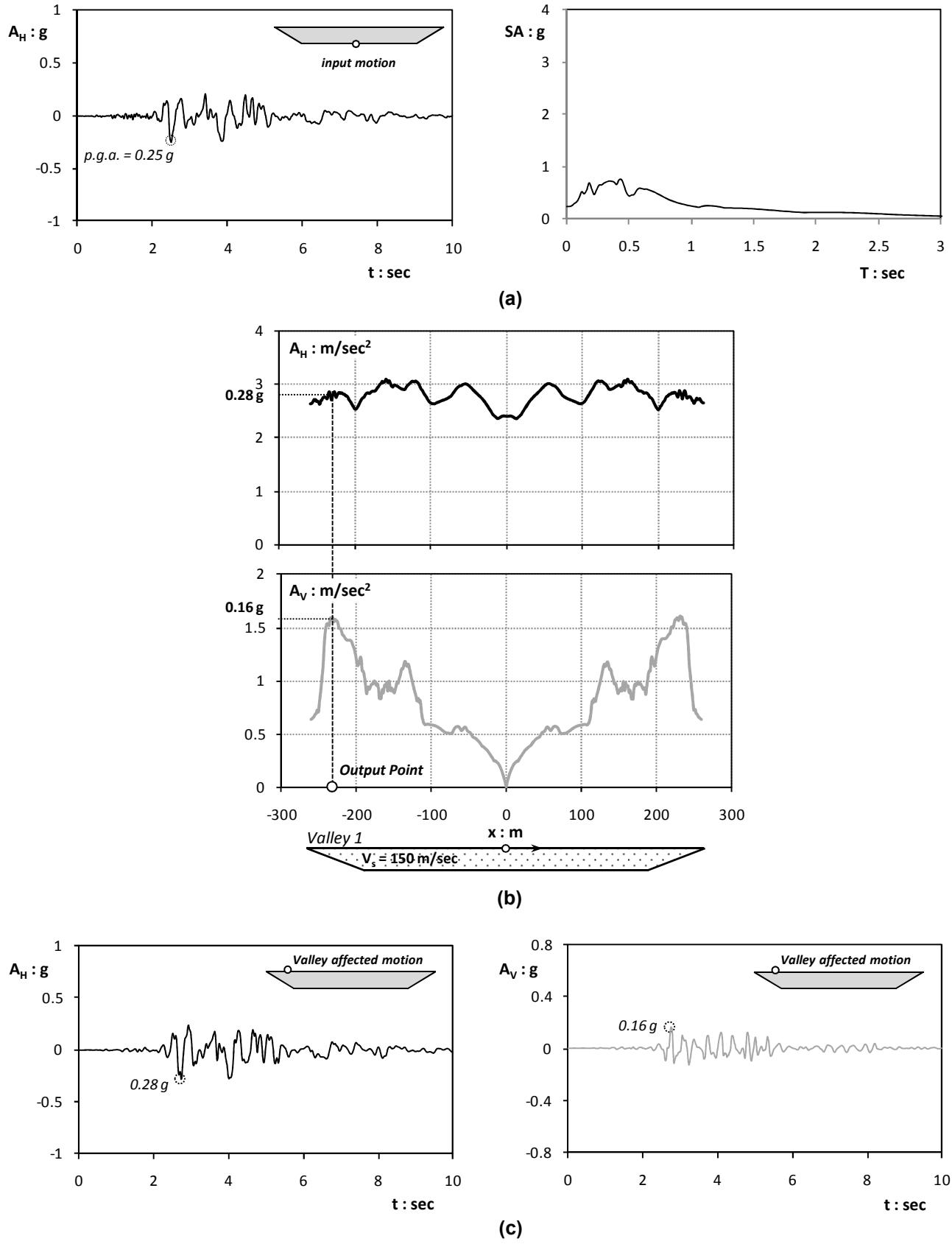

Figure 6.26. Valley Type-1 subjected to a moderate earthquake scenario (Kalamata earthquake, Greece, 1986) : (a) input motion and elastic response spectrum, (b) spatial distribution of horizontal and vertical parasitic acceleration and (c) acceleration time histories at the location where the strongest vertical motion is observed. The outcome of this free-field analysis will serve as input in the subsequent analysis of the decoupled model that involves the frame structure.

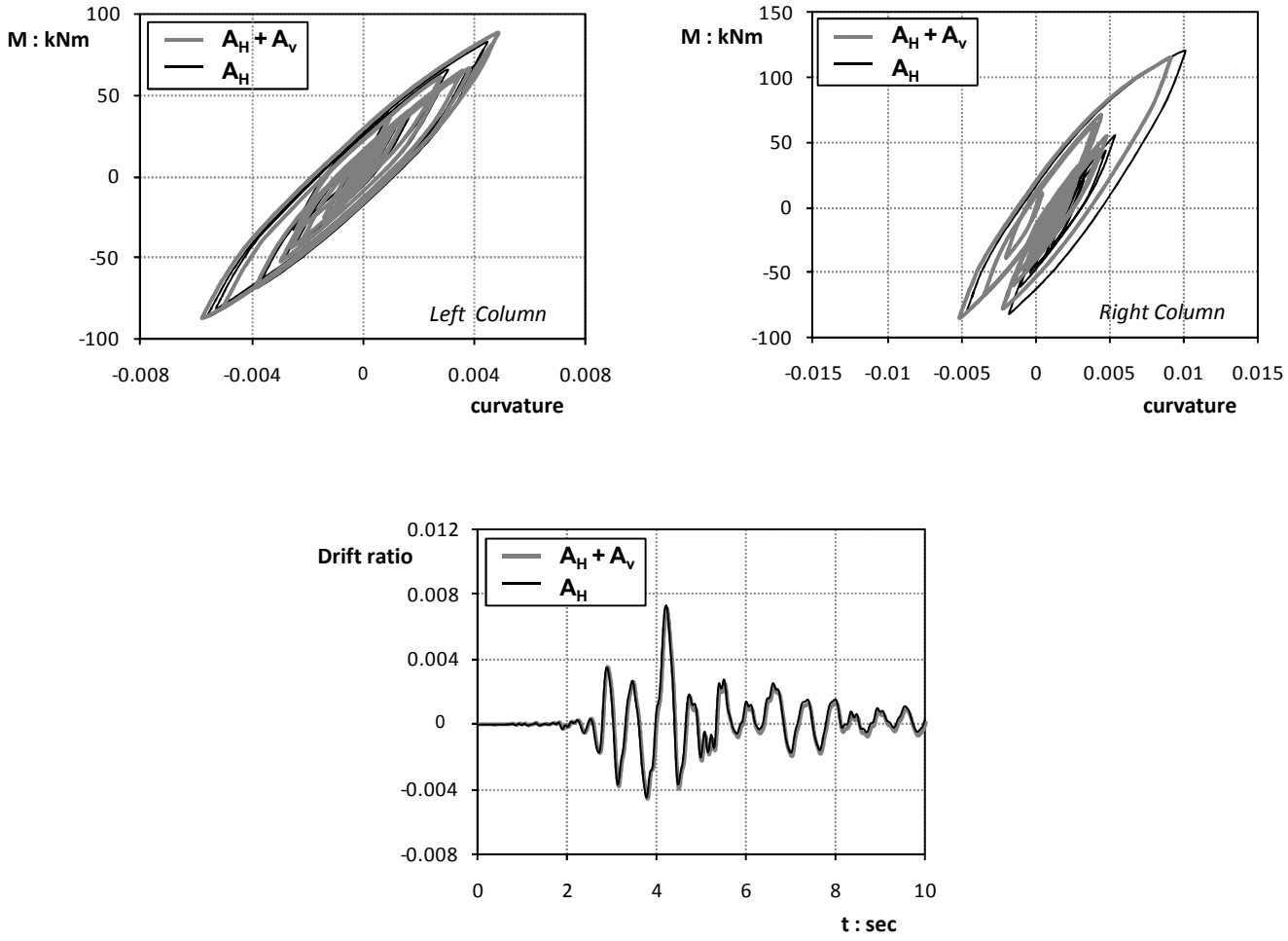

Figure 6.27. Frame subjected to the modified (by the valley presence) Kalamata record. Black lines denotes the case when the frame is excited only by horizontal component and the grey line the case when both horizontal and parasitic vertical are considered: (a) Moment-curvature loops at the base of both frame columns and (b) time history of the ground floor drift ratio.

2. Strong earthquake Scenario – San Salvador earthquake (GIC-090)

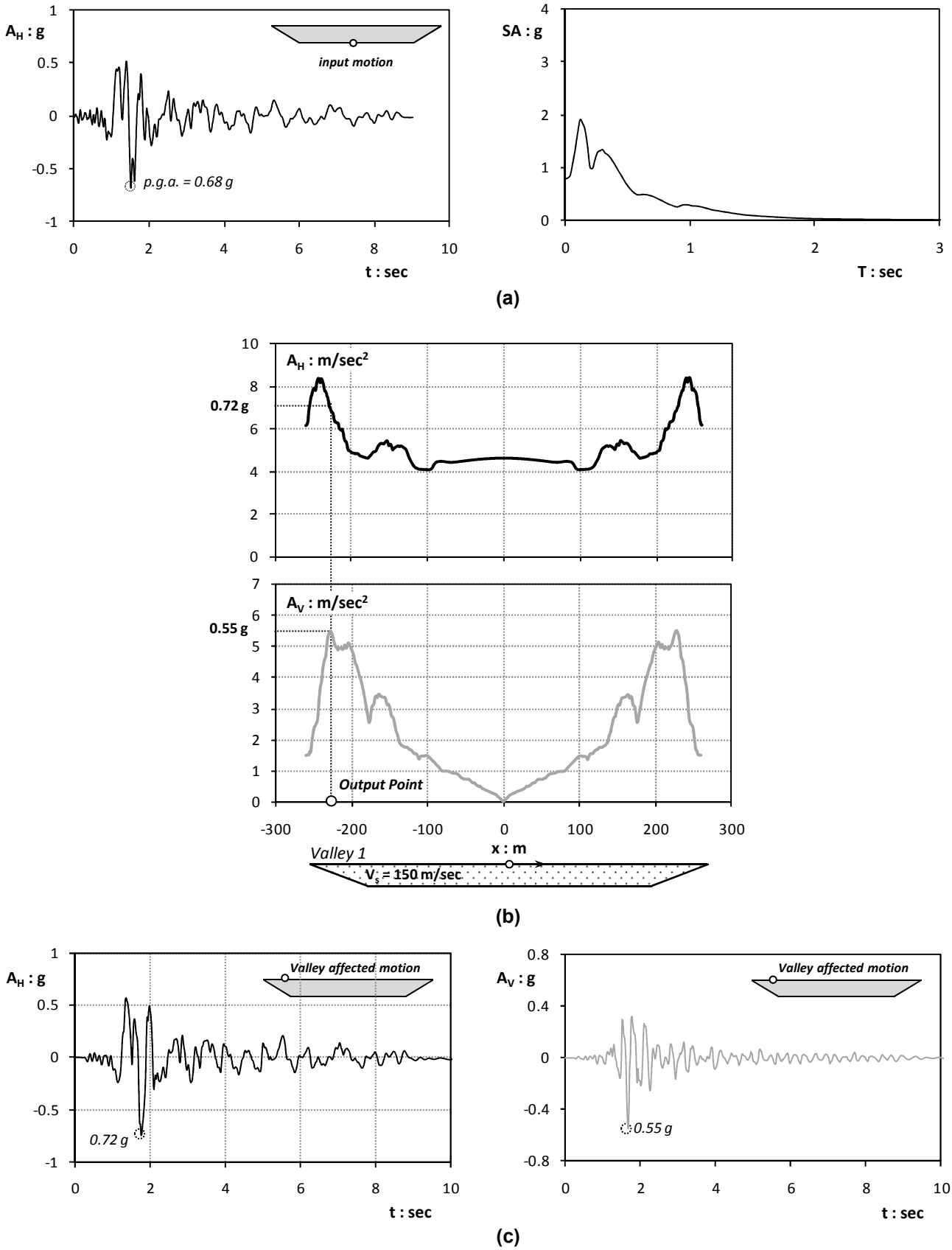

Figure 6.28. Valley Type-1 subjected to a strong earthquake scenario (GIC-090 record, San Salvador earthquake, 1986) : (a) input motion and elastic response spectrum, (b) spatial distribution of horizontal and vertical parasitic acceleration and (c) acceleration time histories at the location where the strongest vertical motion is observed. The outcome of this free-field analysis will serve as input in the subsequent analysis of the decoupled model that involves the frame structure.

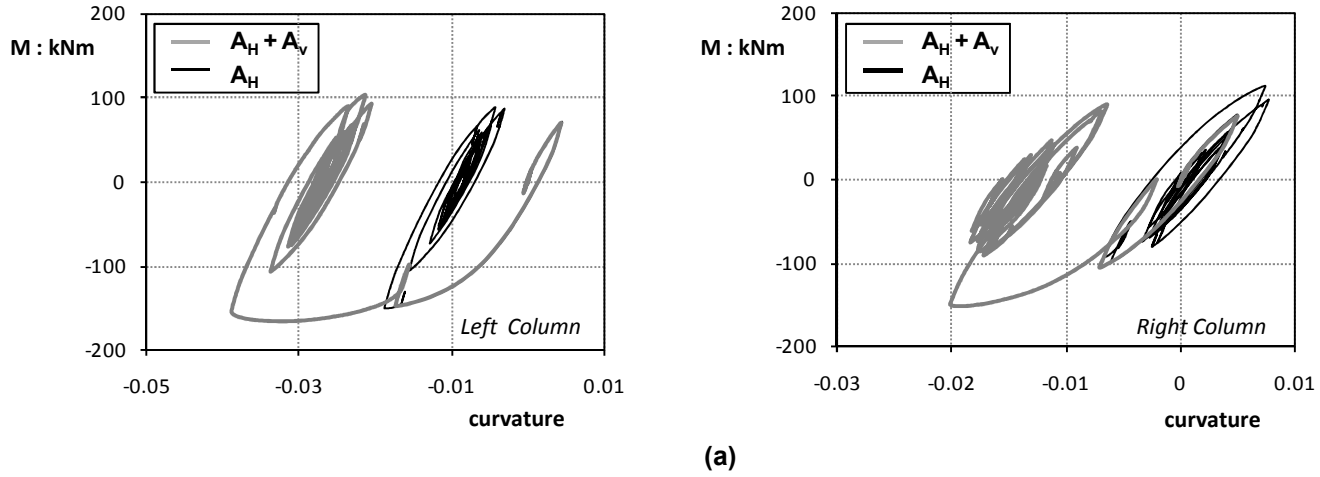

(a)

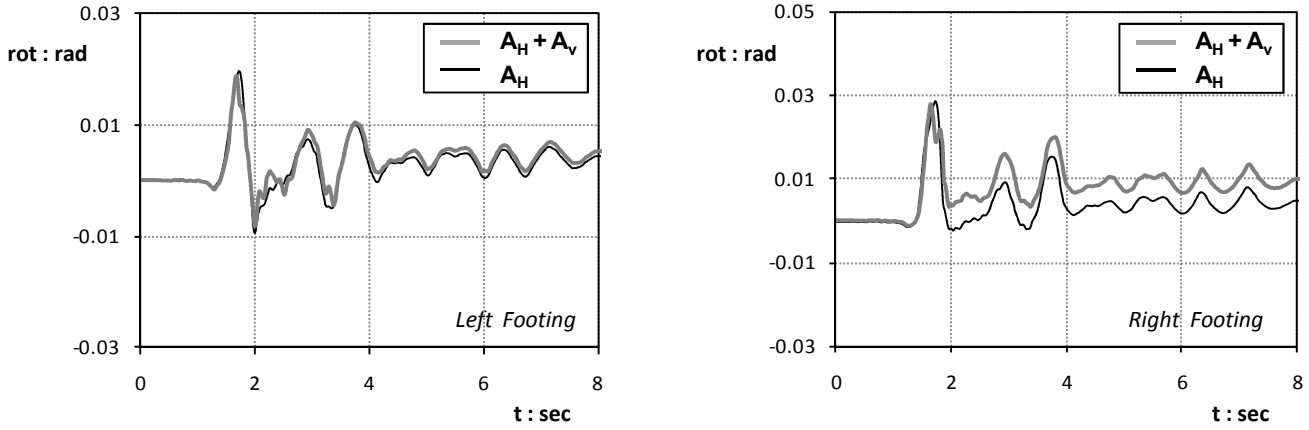

(b)

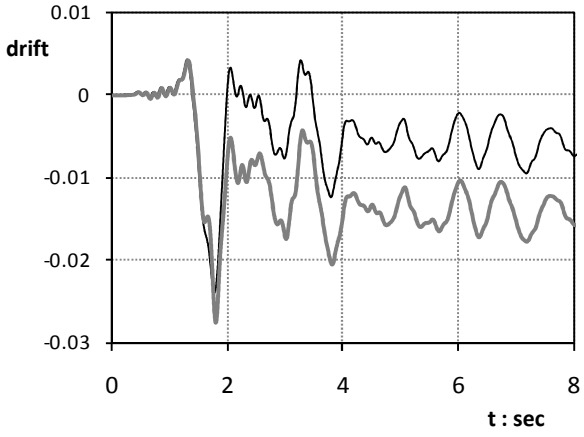

(c)

Figure 6.29. Frame subjected to the modified (due to valley) GIC-090 record (San Salvador, 1986). Black lines denote the case when the frame is excited only by horizontal component and the grey line the case when both horizontal and parasitic vertical components are considered: (a) Moment-curvature loops at the bases of each column, (b) time histories of footing rotations and (c) evolution of ground floor drift ratio.

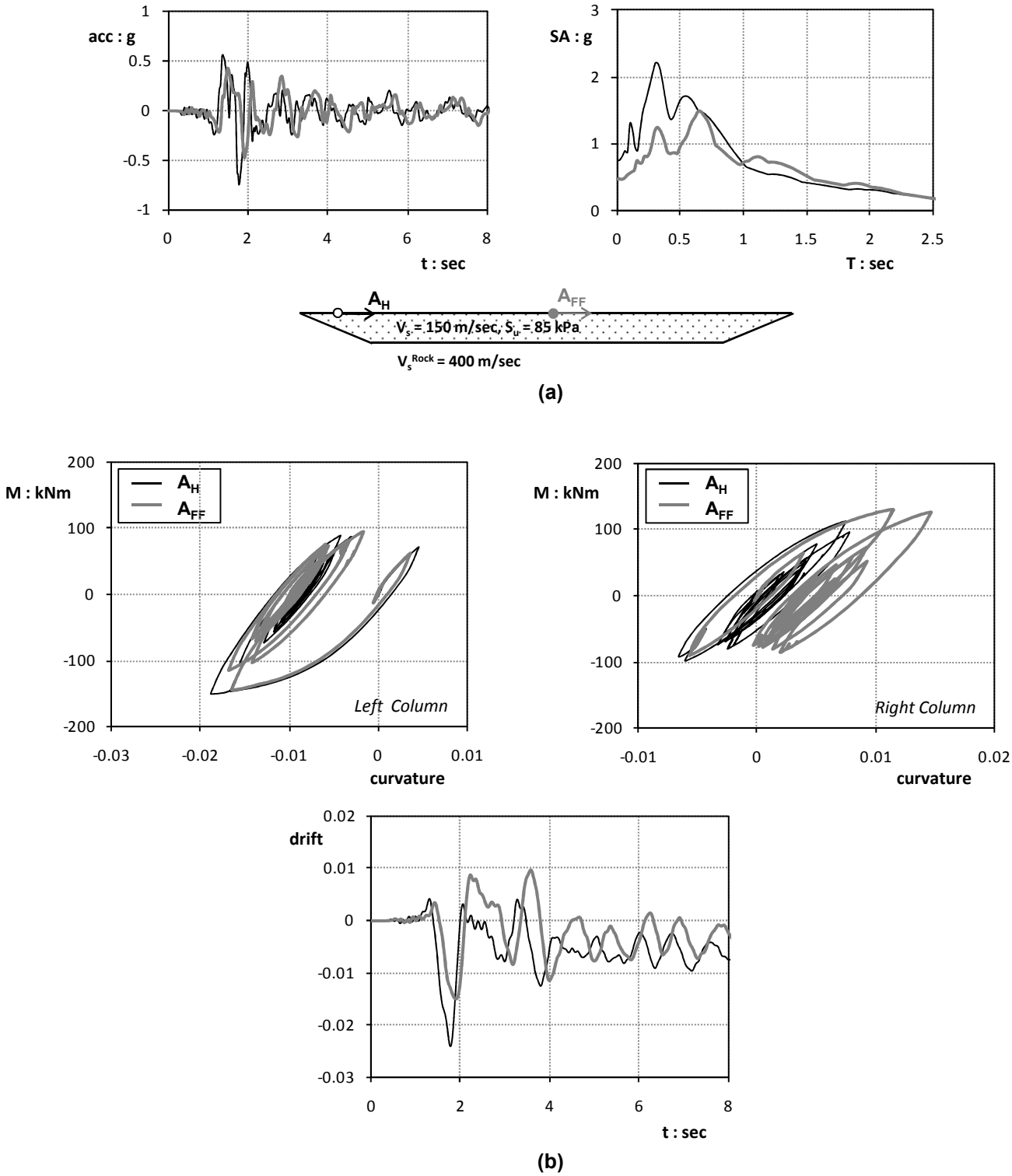

Figure 6.30. "Valley effects" when the parasitic vertical component is ignored: (a) frame excited by the valley-contaminated horizontal acceleration time history (black line) and frame subjected to the free-field horizontal motion (grey line), (b) Moment-curvature loops at the base of each column and (c) evolution of ground floor drift ratio.

3. Very Strong earthquake Scenario – Tabas earthquake (*Tabas-LN* record)

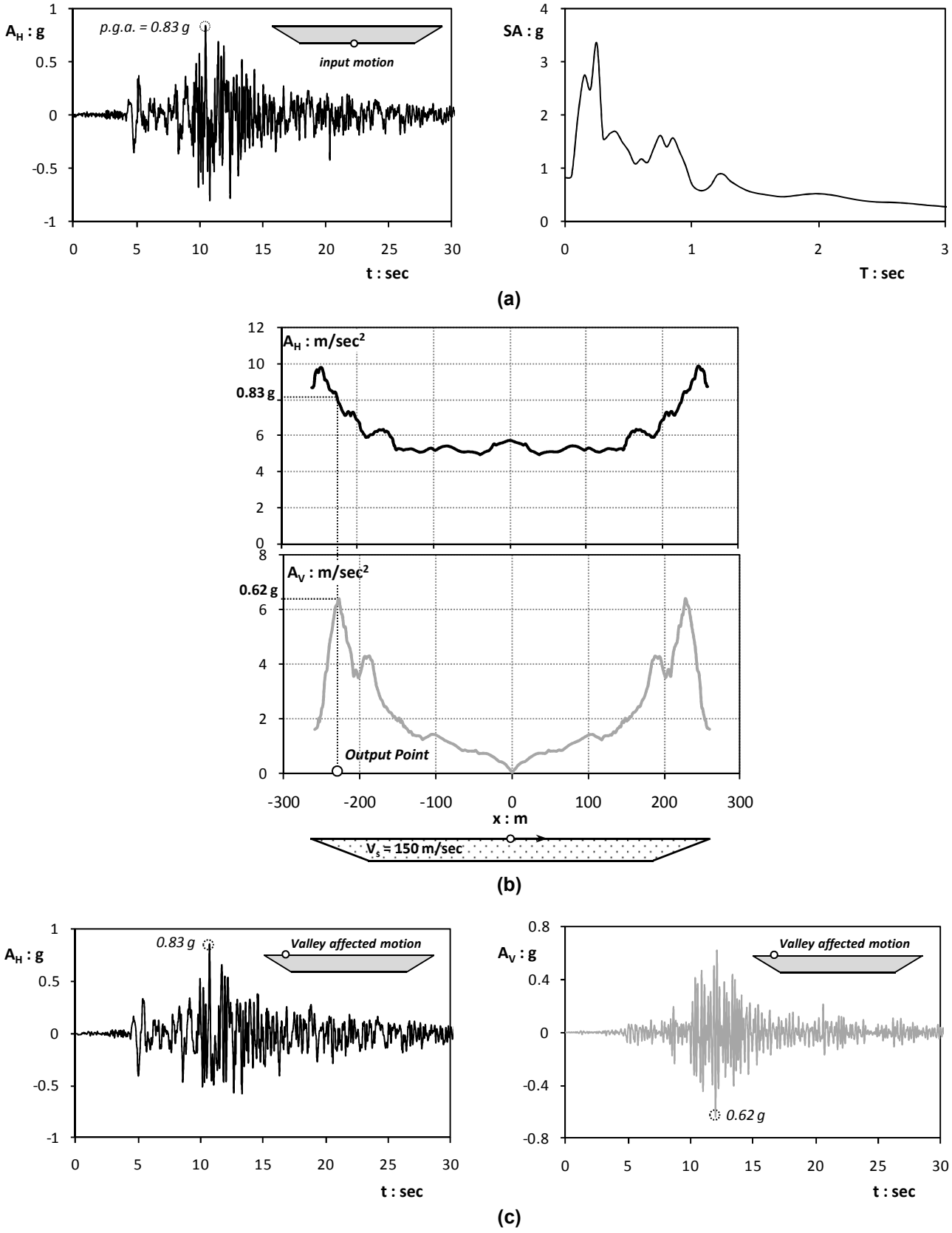

Figure 6.31. Valley Type-1 subjected to a very strong earthquake scenario (Tabas record from Tabas earthquake, Iran 1978) : (a) input motion and elastic response spectrum, (b) spatial distribution of horizontal and vertical parasitic acceleration and (c) acceleration time histories at the location where the strongest vertical motion is observed. The outcome of this free-field analysis will serve as an input in the subsequent analysis of the decoupled model that involves the frame structure.

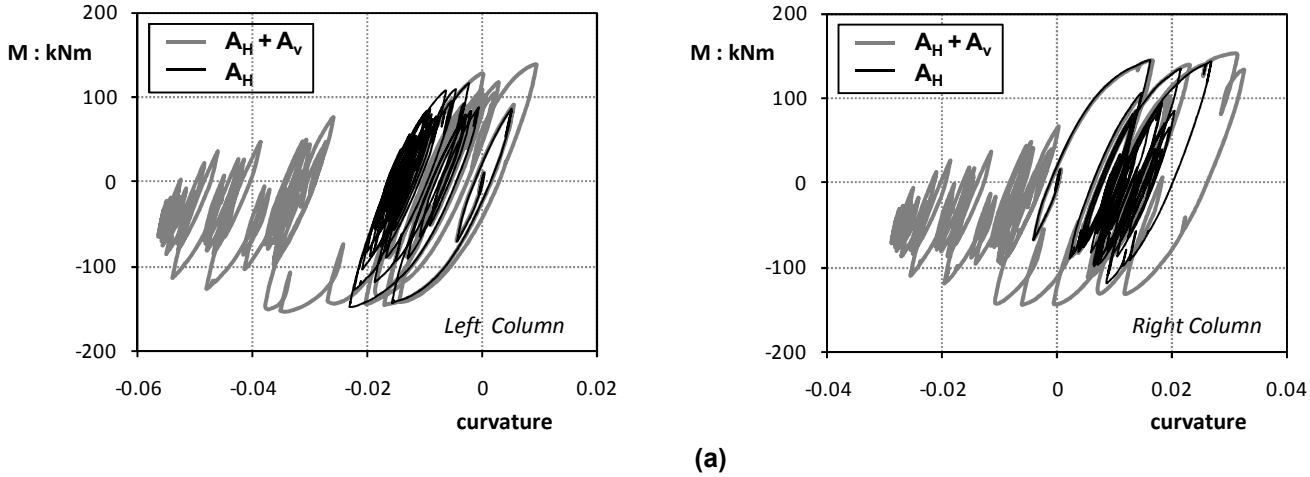

(a)

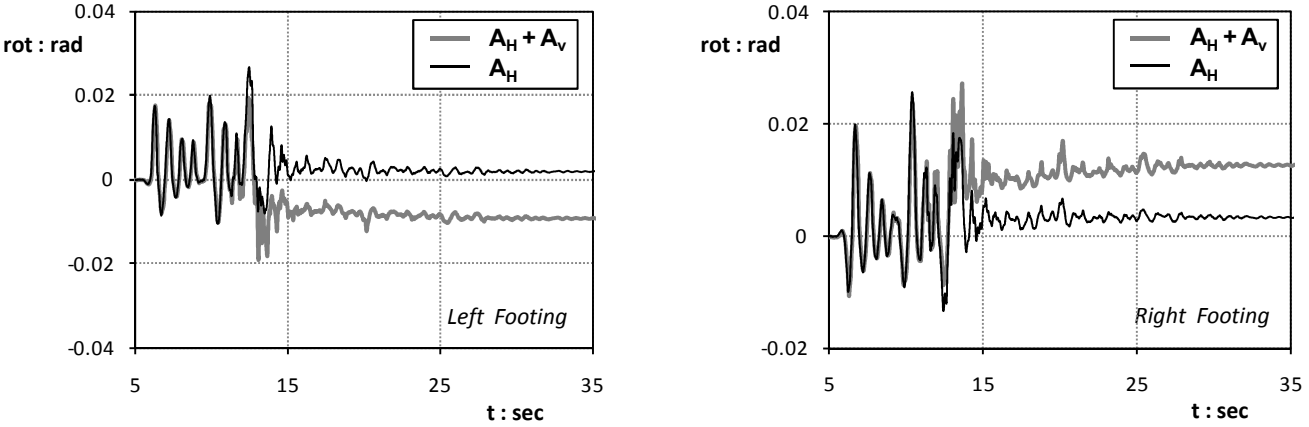

(b)

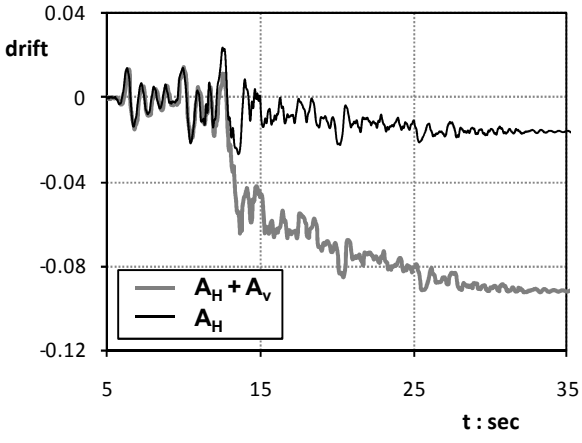

(c)

Figure 6.32. Comparison of the frame response when subjected to either only the horizontal or simultaneous horizontal and parasitic vertical component of the recorded in the Tabas (Iran 1981) ground motion . (a) Moment Curvature plot of each column (b) Footing Rotation Time Histories (c) Ground Floor Drift ratio Time Histories

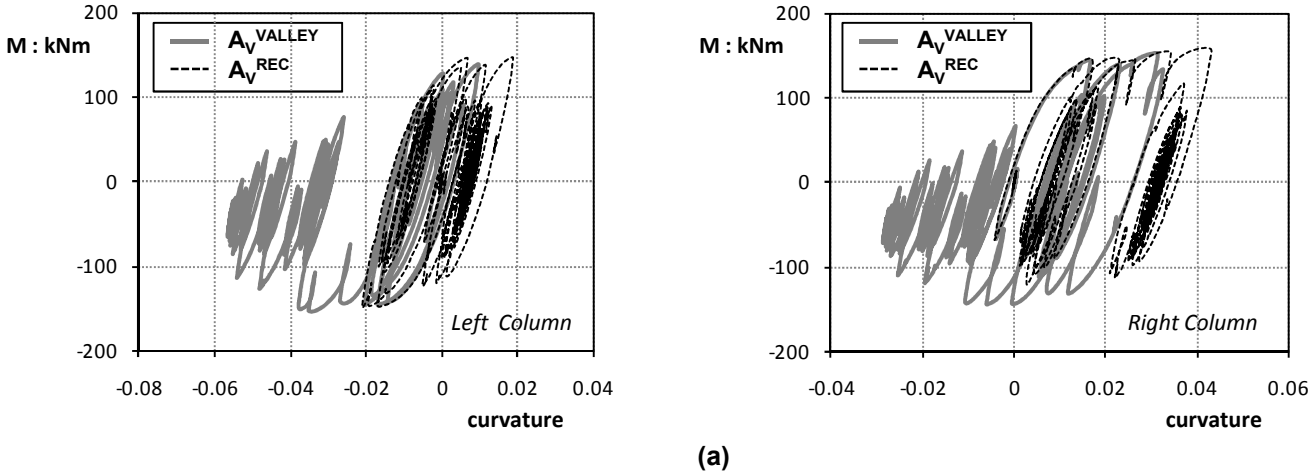

(a)

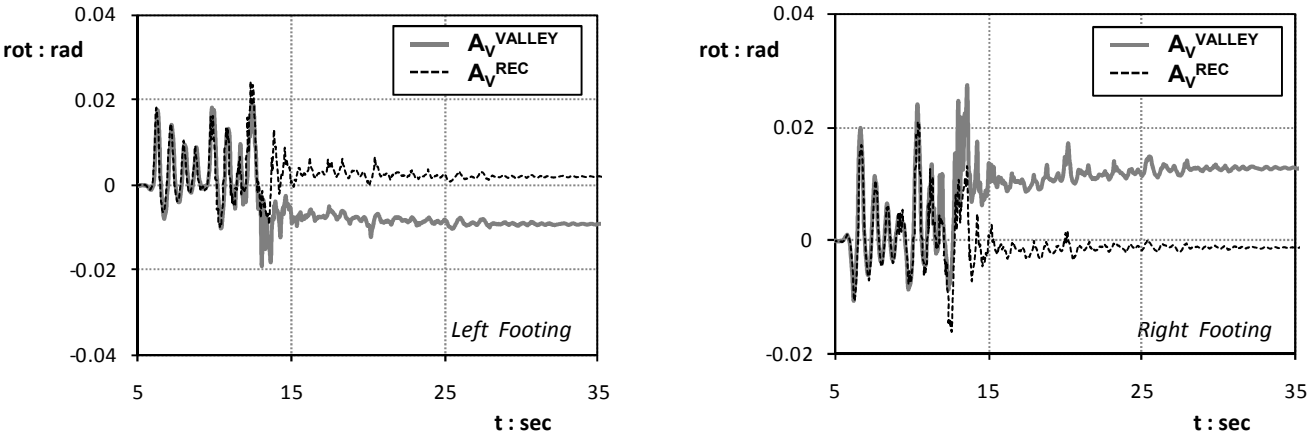

(b)

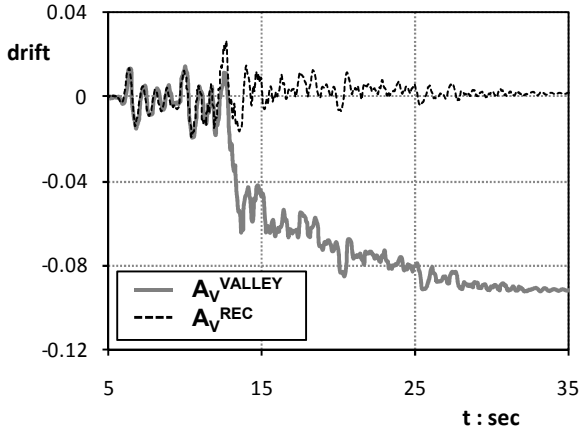

(c)

Figure 6.33. Comparison of the frame response when subjected to the horizontal and either parasitic vertical (grey line) or natural vertical component (dotted black line) of the recorded in the Tabas (Iran 1981) ground motion . (a) Moment Curvature plot of each column (b) Footing Rotation Time Histories (c) Ground Floor Drift ratio Time Histories

References

Chapter 1

Aki, K. and Larner, K. L. (1970), "Surface motion of layered medium having an irregular interface due to incident plane *SH* waves", *Journal of Geophysical Research,* Vol. 70, pp. 933-954

Allotey, N., & Naggar, MHE., (2003), "Analytical moment–rotation curves for rigid foundations based on a winkler model", *Soil Dynamics and Earthquake Engineering* 2003; 23: 367–381.

Allotey, N., & Naggar, MHE., (2007), "An investigation into the winkler modeling of the cyclic response of rigid footings", *Soil Dynamics and Earthquake Engineering* 2007; 28: 44–57.

Allotey, N., & Naggar, MHE., (2008) "A numerical study into lateral cyclic nonlinear soil–pile response", *Canadian Geotechnical Journal*, Vol. 45(9), pp. 1268–1281

Anastasopoulos I., Gazetas G., Loli M., Apostolou M, Gerolymos N. (2009), "Soil Failure can be used for Earthquake Protection of Structures", *Bulletin of Earthquake Engineering*, Vol. 8, No. 1.

Anderson D.L., (2003), "Effect of foundation rocking on the seismic response of shear walls", *Can J Civil Engng;* 30(2): 360–365.

Apostolou M. & Gazetas G. (2004), "Seismic Response of Simple Structures with foundation Uplift", *Proceedings of the 11th International Conference on Soil Dynamics and Earthquake Engineering (11th ICSD) and the 3rd International Conference on Earthquake Geotechnical Engineering, (3rd ICEGE)*, Berkeley, 1, 182−189.

Aslam, M., Scalise, D. T., & Godden, W. G., (1980), ''Earthquake rocking response of rigid bodies.'' *J. Struct. Div.*, ASCE, 106(2), 377–392.

Bard P.Y., & M. Bouchon, (1980), "The seismic response of sediment-filled valleys. Part 2. The case of incident P and SV waves", *Bulletin of the Seismological Society of America*, Vol. 70, No. 5, pp. 1921-1941

Bard, P.-Y. & M. Bouchon, (1980), "The seismic response of sediment-filled valleys. Part 1. The case of incident *SH* waves", *Bulletin of the Seismological Society of America,* Vol. 70, pp. 1263-1286.

Benz, H. M., & Smith R. B, (1988), "Elastic-wave propagation and site amplification in the salt lake, Utah, from simulated normal faulting earthquakes", *Bulletin of the Seismological Society of America*, Vol. 78, No. 6, pp. 1851-1874.

Bertero, V.V, & Zagajeshi, S.W., (1979), "Optimal inelastic design of seismic resistance reinforced concrete framed structures", in "Nonlinear Design of Concrete Structures". *Proc International Symposium*, University of Waterloo, Canada, pp219-272.

Bielak, J., & Christiano, P., (1984), "On the effective seismic input for nonlinear soil-structure interaction systems", *Earthquake Eng. Struct. Dyn.,*12, 107–119.

Bielak, J., MacCamy, R.C., McGhee, D.S., & Barry, A., (1991), "Unified Symmetric BEM-FEM for Site Effects on Ground Motion—SH Waves", *Journal of Engineering Mechanics*, Vol. 117(10), pp. 2265-2285.

Bielak J., Xu J., & O. Ghattas, (1999),"Earthquake ground motion and structural response in alluvial valleys", *Journal of Geotechnical and Geoenvironmental Engineering*, Vol. 125, No. 5, pp. 413-423.

Bielak, J., Loukakis, K., Hisada, Y., & Yoshimura, C., (2003), "Domain Reduction Method for Three-Dimensional Earthquake Modeling in Localized Regions, Part I: Theory", *Bulletin of the Seismological Society of America*, Vol. 93, No. 2, pp. 817–824

Biot M. A., (2006), "Influence of foundation on motion of blocks", *Soil Dynamics and Earthquake Engineering*, 26, pp. 486-490.

Boore, D. (1970), "Love waves in non-uniform wave guides: finite difference calculation", *Journal of Geophysical Research,* Vol. 75, pp. 1512-1527

Bouchon, M., M. Campillo, & S. Gaffett (1989), "A boundary integral equation-discrete wavenumber representation method to study wave propagation in multilayered media having irregular interfaces", *Geophysics,* Vol. 54, pp. 1134-1140.

Boulanger, R. W., Curras, C. J., Kutter, B. L., Wilson, D. W., & Abghari, A. (1999). "Seismic soil-pile-structure interaction experiments and analyses", *Journal of Geotechnical and Geoenvironmental Engineering*, ASCE, 125(9), 750-759.

Bransby M. F. & Randolph M. F (1999), "The effects of skirted foundation shape on behaviour under combined V-M-H loading", *Journal for Offshore and Polar Engineering*, Vol. 9, No. 3, pp.214-218

Butterfield, R., (1981), "Another look at gravity platform foundations", *Soil mechanics and foundation engineering in offshore technology,* Udinei Italy: CISM.

Butterfield, R. & Gottardi, G. (1995). "Simplifying Transformations for the Analysis of Shallow Foundations on Sand", *Proc. 5th Int. Offshore and Polar Eng Conf.*, The Hague, pp. 534-538.

Calvi, G.M., & Kingsley, G.R., (1995), "Displacement based seismic design of multi-degree-of-freedom bridge structures", *Earthquake Engineering and Structural Dynamics*; 24:1247–1266

Chatzigogos, C.T., Pecker, A., & Salençon J., (2009), "Macroelement modeling of shallow foundations", *Soil Dynamics and Earthquake Engineering,* Vol. 29 (5), pp. 765-781

Chatzigogos, C.T., Figini, R., & Pecker, A. and J. Salençon, (2010), "A macroelement formulation for shallow foundations on cohesive and frictional soils", *International Journal for Numerical and Analytical Methods in Geomechanics.*

Chávez-García, F. J., Stephenson, W. R., & M.Rodríguez, (1999), "Lateral Propagation Effects Observed at Parkway, New Zealand. A Case History to Compare 1D versus 2D Site Effects", *Bulletin of the Seismological Society of America*, 89, 3, pp. 718-732

Chen, X. L., & Lai, Y. M., (2003), "Seismic response of bridge piers on elastic-plastic Winkler foundation allowed to uplift", *Journal of Sound and Vibrations*, 266(5), pp. 957 – 965.

Chopra, A.K. & Yim, S.C. (1984), "Earthquake Responses of structures with partial uplift on Winkler foundation", *Journal of Sound and Vibration*, 266(5): 957–965.

Christopoulos, C., Filiatrault, A & B., Folz, (2002a), "Seismic response of self-centering hysteresis SD and F systems", *Earthquake Engineering and Structural Dynamics*, Vol 31, pp. 1131-1150.

Christopoulos, C., Filiatrault, A, Uang C. M., & B., Folz, (2002b), "Post-tensioned Energy Dissipating Connections for Moment Resisting Steel Frames", ASCE Journal of *Structural Engineering*, Vol 128 (9), pp. 1111-1120.

Ciliz, S., Özkan, M. Y., & K. Ö Çetin, (2007), "Effect of basin edge slope on the dynamic response of soil deposits", *4th International Conference on Earthquake Engineering and Geotechnical Engineering* (in CD-ROM).

Cohen, G., Joly, P. & Tordjman, N., (1993), "Construction and analysis of higher-order finite elements with mass lumping for the wave equation", *2nd Int. Conf. on Mathematical and Numerical Aspects of Wave Propagation*, ed. Kleinman, pp. 152-160, SIAM,Philadelphia.

Comartin C.D., Niewiaroski R.W., Freeman S., Turner F.M. (2000), "Seismic evaluation and retrofit of concrete buildings: a practical overview of the ATC-40 document"*, Earthquake Spectra*, 16(1), pp. 241–62.

Cornou, C., P.-Y. Bard, & M. Dietrich, (2003a), "Contribution of dense array analysis to the identification and quantification of basin-edge-induced waves. I. Methodology", *Bulletin of the Seismological Society of America, Vol.* 93(6).

Cornou, C., Bard, P.-Y., & Dietrich M., (2003b), "Contribution of Dense Array Analysis to the Identification and Quantification of Basin-Edge-Induced Waves, Part II: Application to Grenoble Basin (French Alps)", *Bulletin of the Seismological Society of America*, Vol. 93(6), pp. 2624–2648

Cremer C., Pecker A., Davenne L. (2001), "Cyclic macro-element for soil-structure interaction: material and geometrical non-linearities", *International Journal for Numerical and Analytical Methods in Geomechanics*, Vol. 25, pp. 1257–1284.

Cremer C., Pecker A., Davenne L. (2002), "Modelling of nonlinear dynamic behaviour of a shallow strip foundation with macro-element", *Journal of Earthquake Engineering*, Vol. 6, pp. 175-212.

Crémer, C., (2001), "*Modélisation du comportement non lineaire des foundations superficielles sous seisme*", PhD Thesis, LMT-Cachan, France.

Crémer, C., Pecker, A., & Davenne, L., (2001), "Cyclic macro-element for soil–structure interaction: material and geometrical nonlinearities", *International Journal for Numerical and Analytical methods in Geomechanics*; 25(12): 1257–1284.

Cremonini, M. G., Christiano, P., & Bielak J., (1988), "Implementation of effective seismic input for soil-structure interaction systems", *Earthquake Eng. Struct. Dyn.* 16, 615–625.

Dafalias, Y.F., & Hermann, L.R., (1982), "Bounding surface formulation of soil plasticity", *Soil Mechanics – transient and cyclic loading*, Pande GN, Zienkiewicz OC Eds, Wiley: 173 – 218.

Dean, E.T.R., James, R.G., Schofield, A.N., Tan, F.S.C, Tsukamoto, Y., (1992), "The bearing capacity of conical footings on sand in relation to the behaviour of spudcan footings of jack-ups", *Proc. Wroth Memorial Symp. on Predictive Soil Mechanics,* Oxford, pp 230-253.

Dravinski M., & T. K. Mossessian (1987), "Scattering of plane harmonic P, SV and Rayleigh waves by dipping layers of arbitrary shape", *Bulletin of the Seismological Society of America,* Vol. 77, pp. 212-235

Dravinski, M. (1982), "Scattering of *SH* waves by subsurface topography", *Journal of Engineering Mechanics Division Proc. ASCE,* Vol. 108, pp. 1-17

Elsabee, F., Morray, J.P., Roesset, .JM., (1977), "Dynamic behavior of embedded foundations", *Research Report R77-33*, MIT.

Faccioli E., Paolucci R., & Vivero G. (2001), "Investigation of seismic soil–footing interaction by large scale cyclic tests and analytical models", *Proceedings, 4th International Conference on Recent Advances in Geotechnical Earthquake Engineering and Soil Dynamics*, S. Prakash (Ed.), Paper no. SPL-5, San Diego, CA.

Faccioli, E., Maggio, F., Paolucci, R. & Quarteroni, A., (1997), "2D and 3D elastic wave propagation by a pseudo-spectral domain decomposition method", *Journal of Seismology*, 1, 237-251.

Fäh, D, (1992), "*A hybrid technique for the estimation of strong ground motion in sedimentary basins*", Ph.D. thesis Nr. 9796, Swiss Federal Institute of Technology, Zurich.

Fäh, D., Suhadolc P., & Panza G.F., (1993). "Variability of seismic ground motion in complex media: the case of a sedimentary basin in the Friuli (Italy) area", *J. Appl. Geophys.* 30, 131– 48.

Fäh, D., Suhadolc, P., Mueller, St., and Panza G.F., (1994), "A hybrid method for the stimation of ground motion in sedimentary basins: Quantitative modeling for Mexico City, *Bulletin of Seismological Society of America,* 84, 383–399.

Fajfar, P., Gaspersic, P. and Drobnic, D. (1997), "A simplified nonlinear method for seismic damage analysis of structures" in Fajfar P. and Krawinkler, H (Eds) (1997), "Seismic Design Methodologies for the Next Generation of Codes". *Proceedings of International Conference at Bled, Slovenia.* A.A. Balkema, Rotterdam/Brookfield,1997, pp183-194.

Fajfar, P. (1998), "Capacity Spectrum Method based on Inelastic Demand Spectra". *IKPIR Report EE-3/98*, University of Ljubljana, Slovenia

Fardis, M.N. and Panagiotakos, T.B. "*Displacement-based design of RC Buildings : Proposed approach and applications*" in Fajfar P and Krawinkler, pp. 195-206.

Fenves, G.L. (1998), "Effects of footing rotation on earthquake behavior of pile supported bridge piers", *Technical Report for Earth Mechanics, Inc.*

Field E. H., (1996), "Spectral Amplification in a Sediment-Filled Valley Exhibiting Clear Basin-Edge-Induced Waves", *Bulletin of the Seismological Society of America*, Vol. 86, No. 4, pp. 991-1005.

Filiatrault, A., Anderson, D.L., & DeVall, R.H. (1992), "Effect of weak foundation on the seismic response of core wall type buildings", *Can J Civil Engng*; 19(3): 530–9.

Fishman K. L. & S., Ahmad (1995), "Seismic response for alluvial valleys subjected to SH, P and SV waves", *Soil Dynamics and Earthquake Engineering*, Vol. 14, pp. 249-258

Freeman, S.A. (1998), "Development and Use of Capacity Spectrum Method", *Proc. 6th US National Conference on Earthquake Engineering*, Seattle

Gaffet, S. & M. Bouchon (1991), "Source location and valley shape effects on the *P-SV* near displacement field using a boundary integral equation-discrete wavenumber representation method", *Geophy. J. Int.,* Vol. 106, pp. 341-356.

Gajan S., Kutter B.L., Phalen J.D., Hutchinson T.C., Martin G.R. (2005), "Centrifuge modeling of load-deformation behavior of rocking shallow foundations", *Soil Dynamics and Earthquake Engineering,* 25, pp. 773–783.

Gajan, S. & Kutter, B. L. (2008), "Capacity, settlement, and energy dissipation of shallow footings subjected to rocking", *Journal of Geotechnical and Geoenvironmental Engineering, ASCE*, 134 (8), pp 1129-1141.

Gajan, S., & B. L., Kutter, (2009), "Effects of Moment-to-Shear Ratio on Combined Cyclic Load-Displacement Behavior of Shallow Foundations from Centrifuge Experiments", *Journal of Geotechnical and Geoenvironmental Engineering*, ASCE, Vol. 135, No. 8

Gazetas, G. & Roesset, J.M., (1976), "Forced vibrations of strip footing in layered soils", *Method Struct Anal ASCE,* Vol. 1,pp. 115–31.

Gazetas, G., (1980), "Static and dynamic displacements of foundations on heterogeneous multilayered soils", *Geotechnique*, Vol.2, pp.159–77.

Gazetas, G. (1983), "Analysis of machine foundation vibrations: state of the art", *Int. J. Soil Dyn Earthq Eng*; 2:2–42.

Gazetas, G. & Stokoe, K.H. (1991), "Free vibration of embedded foundations: theory versus experiment", *J Geotech Eng ASCE*; 117(9): 1382–401.

Gazetas, G., (1991), "Formulas and charts for impedances of surface and embedded foundations". , *J Geotech Eng ASCE* ; 117(9):1363–81.

Gazetas, G. & Mylonakis, G., (1998), "Seismic soil–structure interaction: new evidence and emerging issues, emerging issues paper", *Geotech Spec Publ ASCE*, (75): 1119–74.

Gazetas G., Apostolou M., and Anastasopoulos I. (2003), "Seismic Uplifting of Foundations on Soft Soil, with Examples from Adapazari (Izmit 1999, Earthquake)", *BGA International Conference on Foundation Innovations, Observations, Design & Practice*, Univ. of Dundee, Scotland, September 25, pp. 37–50.

Gazetas, G., Anastasopoulos, I., & M., Apostolou (2007), "Shallow and Deep Foundations under Fault Rupture or Strong Seismic Shaking", *Earthquake Geotechnical Engineering*, Pitilakis K., Editor, Springer: Berlin, pp. 185–210.

Georgiadis, M. & Butterfield, R. (1988)., "Displacements of footings on sand under eccentric and inclined loads", *Can. Geotech. J.* 25, 199-212.

Gerolymos, N., Apostolou, M., & Gazetas, G., (2007), "Neural network analysis of overturning response under near-fault type excitation", *Earthquake Engineering and Engineering Vibrations*, Vo 4, No.2, pp. 213-228.

Gottardi, G. & Butterfield, R., (1993), "On the bearing capacity of surface footings on sand under general planar loads", *Soils and Foundations,* 33, No. 3,68-79.

Gourvenec, S. & Randolph, M. F. (2003). "Effect of strength nonhomogeneity on the shape and failure envelopes for combined loading of strip and circular foundations on clay" *Geotechnique,* 53, No. 6, 575–586.

Gouvernec S., (2007), "Shape effects on the capacity of rectangular footings under general loading", *Geotechique*, 57, No. 8, 637-646.

Grange, S., Kotronis, P., & Mazars, J., (2008), "A macro-element for the circular foundation to simulate 3D soil-structure interaction", *International Journal for Numerical and Analytical Methods in Geomechanics*, 32.

Gulkan P, Sozen M., "Inelastic response of reinforced concrete structures to earthquake motions", *ACI Journal*,1974; 71(6):604–610.

Gupta, S.,Lin, T.W., Penzien, J., Yen, C.S., (1980), "Hybrid modellingof soil-structure interaction", *EERC report. 80-9*. UC Berkeley.

Guzina, B.B. & Pak, RYS, (1997), "Multi-layer representation of continuous insitu profiles in soil dynamics", *Geotechnical special publication*, vol. 64. New York: ASCE; pp. 1–10.

Haase, J. S., E. Hauksson, F. Vernon, A. Edelman (1996), "Modeling of ground motion from a 1994 Northridge aftershock using a tomographic velocity model of the Los Angeles basin", *Bull. Seism. Soc. Am.,* Vol. 86, pp. 156-167.

Harada, T., Kubo, K., Katayama, T., (1981), "Dynamic soil–structure interaction by continuum formulation method", *Report No. 190, Institute of Industrial Science*, University of Tokyo.

Harden, C.W., Hutchinson, T., Martin, G.R., & Kutter, B.L., (2005), "Numerical modeling of the nonlinear cyclic response of shallow foundations", *Technical Report 2005/04, Pacific Earthquake Engineering Research Center (PEER).*

Harmsen S., & S. Harding, (1981), "Surface Motion over a sedimentary valley for incident plane P and SV waves", *Bulletin of the Seismological Society of America*, Vol. 71, No. 3, pp. 655-67

Hartzell, S., Carver, D., Williams, R. A., Harmsen, S. & A. Zerva, (2003), "Site Response, Shallow Shear-Wave Velocity, and Wave Propagation at the San Jose, California, Dense Seismic Array", *Bulletin of the Seismological Society of America*, Vol. 93(1), pp. 443–464.

Hatamoto, H., Chung, Y.S. and Shinozuka, M. (1990) "Seismic Capacity Enhancement of RC Frames by Means of Damage Control Design", *Proc., 4 USNCEE* (Palm Springs, CA), 2, pp. 279-288.

Hauksson, E., and J. S. Haase, (1997), "Three-dimensional V_p and V_s velocity models of the Los Angeles basin and central Transverse Ranges", California, *J. Geophys.* Res. Vo. 102, pp. 5423-5453.

Helmberger, D. V., & J. E. Vidale, (1988), "Modeling strong motions produced by earthquakes with two-dimensional numerical codes", *Bull. Seism. Soc. Am. Vol.* 78, pp. 109-121.

Herrera, I., (1964), "A Perturbation method for elastic wave propagation: l- non parallel boundaries", *Journal of Geophysical Research,* Vol.69, pp.3845-3851

Hewes J T, & Priestley M J N., (2001), "Experimental Testing of Unbonded Post-tensioned Precast Concrete Segmental Bridge Columns". *Proceedings of the 6th Caltrans Seismic Research Workshop Program*, Sacramento, California.

Hill J., BENZ H., Murphy M., & G. Schuster,(1990), "Propagation and Resonance of the SH waves in the Salt Lake Valley, Utah", *Bulletin of the Seismological Society of America,* Vol. 80, No. 1, pp. 23-42.

Hogan, S. J. (1989), ''On the dynamics of rigid-block motion under harmonic forcing'' *Proc., Royal Soc.*, London, A425, 441–476.

Hogan, S. J. (1990), "The many steady state responses of a rigid block under harmonic forcing.'', *Earthquake Engrg. and Struct. Dyn.*, 19(7), 1057–1071.

Holden T, Restrepo J, Mander J B. (2003), "Seismic Performance of Precast Reinforced and Prestressed Concrete Walls". *Journal of Structural Engineering*, 129(3): 277-424.

Houlsby G. T. , Amorosi A. , & Rojas E., (2005), "Elastic moduli of soils dependent on pressure: a hyperelastic formulation", *Geotechnique*, Vo 55(5), pp. 383 –392.

Houlsby, G.T., Martin, C.M, (1992), "Modelling of the behaviour of foundations of jack-up units on clay", *Proc. Wroth Memorial Symp. on Predictive Soil Mechanics,* Oxford, pp 339-358.

Housner, G. W., (1963), "The Behaviour of Inverted Pendulum Structures during Earthquake"*, Bullettin of Seismological Society of America*, 53(2): 403-417.

Housner, G. W., (1963), "The Behaviour of Inverted Pendulum Structures during Earthquake"*, Bullettin of Seismological Society of America*, 53(2): 403-417.

Huckelbridge, A. A., Jr. & Clough, R. W. "Seismic response of uplifting building frame", *Proc. ASCE* 1978, ST.8, pp. 1211-1229

Ikeda S, Hirose S, Yamaguchi T, Nonaka S., (2002), "Seismic Performance of Concrete Piers Prestressed in the Critical Sections". *Proceedings of the 1st FIB Congress. Osaka*, 207-214, (computer file).

Jacobsen LS. "Steady forced vibrations as in:uenced by damping", *ASME Transactions* 1930; 52:169 –181.

Jennings, P.C., & Bielak, J., (1973), "Dynamics of building-soil interaction", *Bulletin of the Seismological Society of America*, 63(1): 9-48

Kamiyama, M., & Matsukawa, T., (2002), "A new method for estimating nonlinear response of ground," *Proceedings of the 12th European Conference on Earthquake*, pp. 1-10

Kamiyama, M., & K, Fukuchi, (2007), "Nonlinear response analyses of irregular grounds by use of pseudo spectral method", 4th International Conference on Earthquake Engineering and Geotechnical Engineering (in CD-ROM).

Kappos, A.J. (1997) "Partial inelastic analysis procedure for optimum capacity design of RC buildings" in Fajfar, P and Krawinkler, H (Eds) (1997), "Seismic Design Methodologies for the Next Generation of Codes", *Proceedings of International Conference at Bled, Slovenia.* A.A. Balkema, Rotterdam/Brookfield, 1997, pp. 229- 240.

Kausel, E., & Roesset, J.M., (1975), "Dynamic stiffness of circular foundations", *J Eng Mech Div ASCE*; 101:771–85.

Kausel, E., Roesset, J.M., Christian, J.T., (1976), "Nonlinear behavior in soil–structure interaction", *J. Geotech Eng Div ASCE*, 102(GT12): 1159–78.

Kawase, H., (1988), "Time domain response of semi-circular canyon for incident *SV, P and* Rayleigh waves calculated by the discrete wave number Boundary Element Method", *Bulletin of the Seismological Society of America,* Vol. 78 (4), pp. 1415-1437

Kawashima K. "Seismic Design of Concrete Bridges", (2002), Proceedings of the 1st FIB Congress. Osaka, 347-366, (computer file).

Kawashima K., Nagai T., Sakellaraki D. (2007), "Rocking Seismic Isolation of Bridges Supported by Spread Foundations", Proc. Of 2nd Japan-Greece Workshop on Seismic Design, Observation, and Retrofit of Foundations, April 3-4, Tokyo, Japan, pp. 254–265.

Kelly, K. R., R. W. Ward, S. Treitel, and R. M. Alford, (1976), "Synthetic seismograms: a finite difference approach", *Geophysics, Vol.* 41, pp. 2-27.

Kham M., Semblat J.P., Bouden-Romdhane N., Dangla P. (2002), "Numerical Modelling of site amplification vs experimental data from Tunisia", *12th European Conference on Earthquake Engineering*, Ref. 123, 12p.

Kim, S., & Stewart, JP., (2003), "Kinematic soil–structure interaction from strong motion recordings", *J Geotech Geoenv Eng ASCE,* 129(4): 323–35.

King, J. L., & Tucker B. E., (1984), "Observed variations of earthquake motion across a sediment-filled valley", *Bulletin of the Seismological Society of America*, Vol. 74, No. 1, pp. 137-151.

Knappett, J.A., Haigh, S.K., & S.P.G., Madabhushi, (2006), "Mechanisms of failure for shallow foundations under earthquake loading", *Soil Dynamics and Earthquake Engineering,* Vol. 26, pp. 91–102

Komatitsch, D., (1997), *"Méthodes spectrales et éléments spectraux pour l'équation de l'élastodynamique 2D et 3D en milieu hétérogène"*, PhD thesis, Institut de Physique du Globe de Paris, Paris.

Komatitsch, D., Vilotte, J.P., Vai, R., Castillo-Covarrubias, J.M. & Sänchez-Sesma, F.J., (1999), "The spectral element method for elastic wave equations: application to 2D and 3D seismic problems", *Int. J. Num. Meth. Eng.,* 45, 1139-1164.

Komatitsch, D., Barnes, C. & Tromp, J., (2000), "Wave propagation near a uid-solid interface : a spectral element approach", *Geophysics*, Vol. 65, pp.623-663.

Kowalsky, N, Priestley MJN, & G.A., MacRae (1995), "Displacement-based design of RC bridge columns in seismic regions", *Earthquake Engineering and Structural Dynamics*; 24(12):1623–1643.

Kramer S., (1996), "*Geotechnical earthquake engineering*", Englewood Cliffs, NJ: Prentice-Hall

Kurama Y C, Sause R, Pessiki S, Lu L-W.,(2002), "Seismic Response Evaluation of Unbonded Posttensioned Precast Walls", *ACI Structural Journal,* 99(5): 641-651.

Kutter B.L, Martin G., Hutchinson T.C., Harden C., Gajan S., Phalen J.D. (2003), "*Status report on study of modeling of nonlinear cyclic load–deformation behavior of shallow foundations"*, University of California, Davis, PEER Workshop; March.

Kutter B.L. (1995), Recent advances in centrifuge modeling of seismic shaking, Proceedings, *3rd International Conference on Recent Advances in Geotechnical Earthquake Engineering and Soil Dynamics*, St. Louis, Vol. II, pp. 927–941.

Le Pape, Y., & Sieffert, J.P., (2001), "Application of thermodynamics to the global modelling of shallow foundations on frictional material". *International Journal for Numerical and Analytical Methods in Geomechanics*, Vol. 25, pp. 1377-1408.

Lee, V. W. (1984), "Three-dimensional diffraction of plane *P, SV and SH* waves by a hemispherical alluvial valley", *Soil Dynamics and Earthquake Engineering,* Vol. 3, pp. 133-144

Lee, W., & Cao, H., (1989), "Diffraction of plane *SV* waves by circular canyons of various depths", *ASCE Engineering Mechanics Division,* Vol. 115(9), pp. 2035-2056

Loukakis, K. E., (1988), "*Transient response of shallow layered valleys for inclined incident SV waves calculated by the finite element method*, M.Sc. Thesis, Carnegie Mellon University, Pittsburgh.

Luco JE, & Westman RA., (1971), "Dynamic response of circular footings", *J Eng Mech Div ASCE,* 97(EM5): 1381.

Luco, J.E. (1974), "Impedance functions of a rigid foundation on a layered medium", *Nucl Eng Des*; 31:204–17.

M. D. Trifunac, (1971), "Surface motion of a semi-cylindrical alluvial valley for incident plane SH waves", *Bulletin of the Seismological Society of America*, Vol. 61, pp. 1755-1770.

M.F. Bransby, (2002), "The undrained inclined load capacity of shallow foundations after consolidation under vertical loads", *NUMOG VIII*, Rome, pp. 431-437.

Makris, N., & Roussos, Y., (1998), ''Rocking response and overturning of equipment under horizontal pulse-type motions.'' *Rep. No. PEER- 98/05*, Pacific Earthquake Engrg. Res. Ctr., University of California, Berkeley, California.

Makris N., & Roussos Y.S (2000), 'Rocking response of rigid blocks under near-source ground motions", *Géotechnique*, 50(3), pp. 243–262.

Makris *N.* & D. Konstantinidis, (2003), "The rocking spectrum and the limitations of practical design methodologies", *Earthquake Engineering and Structural Dynamics,* Vol32, pp. 265–289.

Malagnini, L., Tricarico, P., Rovelli, A., Herrmann, R. B., Opice, S., Biella, G., & R. de Franco, (1996), "Explosion, Earthquake, and Ambient Noise Recordings in a Pliocene Sediment-Filled Valley: Inferences on Seismic Response Properties by Reference- and Non-Reference-Site Techniques", *Bulletin of the Seismological Society of America*, Vol. 86, No. 3, pp. 670-682.

Mander J B, & Chen C T. "Seismic Resistance of Bridge Piers Based on Damage Avoidance Design". *Technical Report NCEER-97-0014* (National Centre for Earthquake Engineering Research). State University of New York, Buffalo, December 10 1997.

Martin, G., R., & Lam, I. P. (2000). "Earthquake Resistant Design of Foundations : Retrofit of Existing Foundations", *Proc. GeoEng 2000 Conference*, Melbourne

Maugeri, M., Musumeci, G., Novita, D., & Taylor, C.A., (2000), "Shaking table test of failure of a shallow foundation subjected to an eccentric load", *Soil Dynamics and Earthquake Engineering*, Vol. 20, pp. 435-444

Mita, A., & Luco, J.E, (1987), "Dynamic response of embedded foundations: a hybrid approach", *Computer Methods in Applied Mechanics and Engineering,* Vo. 63 (3), pp. 233-256.

Murff, J.D., (1994), "Limit analysis of multi-footing foundation systems", *Proc of the 8th Int. Conf. on Computer Methods and Advances in Geomechanics,* Morgantown, 1, pp. 223-244

Mylonakis, G., Nikolaou, S., Gazetas, G., (2006), "Footings under seismic loading: Analysis and design issues with emphasis on bridge foundations", *Soil Dynamics and Earthquake Engineering*, 26: 824-853.

Nakaki, D.K., & Hart, G.C. (1987), "Uplifiting response of structures subjected to earthquake motions", *Report No. 2.1-3, U.S.–Japan Coordinated Program for Masonry Building Research*.

Natale, M., and Nunziata C., (2004), "Spectral Amplification Effects at Sellano, Central Italy, for the 1997–98 Umbria Seismic Sequence", *Natural Hazards*, Vol. 33, pp. 365–378.

Negro P., Paolucci R., Pedretti S., and Faccioli E., (2000), "Large scale Soil-Structure Interaction experiments on sand under cyclic loading", *12th World Conference on Earthquake Engineering*, New Zealand, (in CD-ROM)

NEHRP Commentary on the Guidelines for the Seismic Rehabilitation of Buildings, FEMA publication 274; October 1997.

Newmark, N. M. (1965), "Effects of earthquakes on dams and embankments", *Geotechnique,* Vol. 15(2), pp. 139 - 160

Niwa, Y. & Hirose, S., (1985), "Scattering problems of plane waves in wedge shaped elastic domains", *Theoretical and Applied Mechanics,* Vol. 33, pp. 393-406, University of Tokyo Press

Nova, R., & Montrasio, L., (1991), "Settlement of shallow foundations on sand", *Geotechnique*, 41(2) : 243-256.

Novak, M. (1985), "Experiments with shallow and deep foundations", in: Gazetas G, Selig ET, editors, *Vibration problems in geotechnical engineering*. New York: ASCE; p. 1–26.

OES, 1995 : California Office of Emergency Services "Vision 2000:Performance Based Seismic Engineering of Buildings", Prepared by Structural Engineers Association of California, Sacramento, CA 1995.

Ohtsuki, A., & K., Harumi, (1983), "Effect of topography and subsurface inhomogeneities on seismic SV waves", *Earthquake Engineering and Structural Dynamics*, Vol. 11, pp. 441-462.

Olsen K. B., Pechmann J. C, & Schuster, G. T., (1995), "Simulation of 3D Elastic Wave Propagation in the Salt Lake Basin", *Bulletin of the Seismological Society of America,* Vol. 85, No. 6, pp. 1688-1710.

Olsen, K. B., R. J. Archuleta, & J. R. Matarese, (1995), "Three-dimensional simulation of a magnitude 7.75 earthquake on the San Andreas fault", *Science,* 270, pp. 1628-1632.

Olsen, K. B., & R. J. Archuleta, (1996), "3-Dimensional simulation of earthquakes on the Los Angeles fault system", *Bull. Seism. Soc. Am. Vol.* 86, pp. 575-596.

Olsen K. B., Nigbor, R. and T. Konno (2000), "3D Viscoelastic Wave Propagation in the Upper Borrego Valley, California, Constrained by Borehole and Surface Data", *Bulletin of the Seismological Society of America*, Vol. 90 (1), pp. 134–150.

Olsen, K. B., Akinci, A., Rovelli, A., Marra, F., & L. Malagnini (2006), "3D Ground-Motion Estimation in Rome, Italy", *Bulletin of the Seismological Society of America*, Vol. 96(1),,pp. 133–146

Palermo A, Pampanin S, Calvi G M. (2004), "The Use of "Controlled Rocking" in Frame-Bridges: Comparisons with Traditional Solutions". Proceedings of 11th Nation Conference on Earthquake Engineering, (in Italian), 25th-29th January, Genova, abstract: pp. 229, CD-ROM file.

Palermo A. (2004), "The *Use of Controlled Rocking in the Seismic Design of Bridges*", Ph.D Dissertation. Technical University of Milan

Palmeri A., & Makris, N., (2008), "Response analysis of rigid structures rocking on viscoelastic foundation", *Earthquake Engineering and Structural Dynamics*, Vol 37(7), pp. 1039- 1063.

Paolucci R., SuáRrez M. M., & Sánchez-Sesma F.J., (1992), "Fast computation of SH seismic Response for a class of alluvial valleys", *Bulletin of the Seismological Society of America*, Vol. 82, No. 5, pp. 2075-2086

Paolucci, R, & Pecker, A., (1997) "Seismic bearing capacity of shallow strip foundation on dry soils", *Soils and Foundations*; Vol. 37(3), pp. 95-105.

Paolucci R. (1997), "Simplified evaluation of earthquake induced permanent displacements of shallow foundations", *Journal of Earthquake Engineering*, Vol. 1, pp. 563–579.

Paolucci, R., Faccioli, E. & Maggio, F., (1999), "3D response analysis of an instrumented hill at Matsuzaki, Japan, by a spectral method", *J. Seism.,* 3, 191-209.

Paolucci R., Shirato M., Yilmaz M.T. (2008), "Seismic behaviour of shallow foundations: Shaking table experiments vs numerical modelling", *Earthquake Engineering and Structural Dynamics*, 37(4), pp. 577–595.

Park R. & Paulay T, (1975), "*Reinforced Concrete Structures"*, John Wiley & Sons. New York

Patera, A.T. (1984), "A spectral element method for fluid dynamics: Laminar flow in a channel expansion", *Journal of Computational Physics,* Volume 54(3), pp. 468-488.

Paulay, T. & Priestley, MJN (1992) "*Seismic Design of Reinforced Concrete and Masonry Buildings*", John Wiley and Sons, New York, 744 p.

Pecker A. (1998), "Capacity Design Principles For Shallow Foundations in Seismic Areas", *Proc. 11th European Conference on Earthquake Engineering*, A.A. Balkema Publishing.

Pecker A. & Pender M.J., (2000), "Earthquake Resistant Design of Foundations: New Construction", Invited paper, *GeoEng2000*, Vol 1, pp. 313-332.

Pecker A. (2002), "Earthquake Resistant Design of Shallow Foundations", *Recent Advances in Earthquake Geotechnical Engineering and Microzonation*, Attila Ansal (Ed.), Springer : Netherlands.

Pecker A. (2003), "Aseismic foundation design process, lessons learned from two major projects: the Vasco de Gama and the Rion Antirion bridges", *ACI International Conference on Seismic Bridge Design and Retrofit*, La Jolla.

Pecker, A., (2006) "Enhanced seismic design of shallow foundations: example of the Rion Antirion bridge", *4th Athenian Lecture on Geotechnical Engineering*, Athens, Greece.

Pedretti, S, (1998), "*Non-linear seismic soil-foundation interaction: analysis and modeling methods*", PhD Thesis, Politechnico di Milano.

Pender, M., (2007), "Seismic design and performance of surface foundations", *4th International Conference on Earthquake Geotechnical Engineering*, Thessaloniki, Greece.

Pevost, J.H., (1978), "Anisotropic stress-strain behavior of clays, *Journal of Geotechnical Engineering*, 116(8): 1255-1263.

Pitarka, A., & K. Irikura, (1996), "Basin structure effects on long-period strong motions in the San Fernando Valley and the Los Angeles basin from the 1994 Northridge earthquake and an aftershock", *Bull. Seism. Soc. Am.* Vol. *86,* pp.126-137.

Priestley MJN, Evison RJ, Carr AJ., (1978), "Seismic response of structures free to rock on their foundations", *Bulletin of the New Zealand National Society for Earthquake Engineering*; 11(3), pp. 141–150.

Priestley M J N, Sritharan S, Conley J R, Pampanin S., (1999), "Preliminary Results and Conclusions from the PRESSS Five-story Precast Concrete Test-building", *PCI Journal*, 44(6): 42-67.

Priestley M J N. (1996), "The PRESSS Program – Current Status and Proposed Plans for Phase III", *PCI Journal*, 41(2): 22-40.

Priestley MJN, Kowalsky MJ, (2000), "Direct displacement-based seismic design of concrete buildings", *Bulletin of the New Zealand National Society for Earthquake Engineering*; 33(4):421– 444.

Priolo, E., Carcione, J.M. & Seriani, G., (1994), "Numerical simulation of interface waves by high-order spectral modeling techniques", *J. acoust. Soc. Am.,* 95, 681-693.

Psycharis, I., (1983), "Dynamics of Flexible Systems with Partial Lift-Off", *Earthquake Engineering and Structural Dynamics*, 2: 201-521.

Psycharis, I.N., & Jennings, P.C., (1983) "Rocking of slender rigid bodies allowed to uplift", *Earthquake Engineering and Structural Dynamics*, Vol 37(7), pp. 1039-1063

Puglia R., Lanzo, G., Pagliaroli, A., Sica, S., & Silvestri F., (2007), "Ground Motion amplification in San Giuliano di Puglia (Southern Italy) during the 2002 Molise earthquake", *4th International Conference on Earthquake Engineering and Geotechnical Engineering* (in CD-ROM).

Raychowdhury, P. and Hutchinson, T.C. (2009), "Performance evaluation of a nonlinear Winkler-based shallow foundation model using centrifuge test results", *Earthquake Engineering and Structural Dynamics*, Vol. 38, pp. 679-698.

Richard R, Elms DG, Budhu M., (1993), "Seismic bearing capacity and settlements of foundations", *Journal of Geotechnical Engineering*, Vol. 119(4), pp. 662-674.

Richart, F.E., Hall, J.R., Woods, R.D. (1970), "*Vibrations of soils and foundations*", Englewood Cliffs, NJ: Prentice-Hall.

Sánchez-Sesma, F. J. and Esquivel, J. A., (1979), "Ground motion of alluvial valleys under the incident plane *SH* waves", *Bulletin of the Seismological Society of America,* Vol. 69, pp. 1107 - 1120

Sánchez-Sesma, F. J., Bravo, M. A. & Herrera, I., (1985), "Surface motion of topographical irregularities for incident *P, SV and* Rayleigh waves", *Bulletin of the Seismological Society of America,* Vol. 75, pp. 297-303

Sanchez-Sesma F. J.,Ramos-Martinez J., & M. Campillo,(1993), "An Indirect boundary element method applied to simulate the seismic response of alluvial valleys for incident P, S, and Rayleigh waves", *Earthquake Engineering and Structural Dynamics,* Vol. 22, pp. 279-295

Scrivner, C. W, & D. V., Helmberger, (1999), "Finite-Difference Modeling of Two Aftershocks of the 1994 Northridge, California, Earthquake", *Bulletin of the Seismological Society of America*, 89, 6, pp. 1505-1518.

Semblat J.F, Duval A.M., Dangla P. (2000), "Numerical analysis of seismic wave amplification in Nice (France) and comparision with experiments", *Soil Dynamics and Earthquake Engineering*, 19 (5), 347-362.

Seriani, G., Priolo, E., Carcione, J.M. & Padovani, E., (1992), "High-order spectral element method for elastic wave modeling", *in Expanded abstracts of the SEG*, pp. 1285-1288, *62nd Int. Mtng of the SEG*, New-Orleans.

Seriani, G., (1998), "3-D large-scale wave propagation modeling by spectral element method on Cray T3E multiprocessor", *Comp.Meth. appl. Mech. Eng.,* 164, 235-247.

Shirato M, Kouno T, Asai R, Nakani S, Fukui J, Paolucci R., (2007) “Large-scale experiments on nonlinear behavior of shallow foundations subjected to large earthquakes’. *Soils and Foundations.*

Shirato, M., Nakatani, S., Fukui, J., Paolucci, R. (2008a), “Large-scale experiments on nonlinear behavior of shallow foundations subjected to strong earthquakes”, *Soils and Foundations*, 48(5): 673-692.

Shirato, M., Paolucci, R, Kuono, R., Nakatani, S., Fukui, J. (2008b), “Numerical Simulation of model tests of pier shallow foundation systems subjected to earthquake loads using an elasto-uplift-plastic macro element”, *Soils and Foundations*, 48(5) : 693-711.

Spanos, P. D. & Koh, A. S. (1984), ‘‘Rocking of rigid blocks due to harmonic shaking.’’ *J. Engrg. Mech.*, ASCE, 110(11), 1627–1642.

Stanton J F, Stone W C, Cheok G S. “A Hybrid Reinforced Precast Frame for Seismic Regions”, *PCI Journal 1997*, 42(2): 20-32.

Stewart JP, Seed RB, Fenves GL., (1999), “Seismic soil–structure interaction in buildings. II: empirical findings”, *J Geotech Eng ASCE*, 125(1): 38–48.

Stokoe, K.H & Richart, F.E. (1974), “Dynamic response of embedded machine foundations”, *J Geotech Eng Div ASCE*; 100(GT-4):427–47.

Stone, W.C. &Taylor, A.W. (1994) “ISDP:Integrated approach to seismic design of reinforced concrete structures”, *Jour. Str. Eng. ASCE*. 120, 12, pp. 3548-3566.

Taiebat, H. A. & Carter, J. P., (2000), “Numerical studies of the bearing capacity of shallow foundations on cohesive soil subjected to combined loading”, *Geotechnique*, 50, No. 4, 409–418.

Takeda, T., M. A. Sozen and N. N. Nielsen: Reinforced Concrete Response to Simulated Earthquakes, ASCE, Journal of the Structural Division, Vol. 96, No. ST12, 1970, pp. 2557 - 2573.

Tan, F.S., (1990). "*Centrifuge and theoretical modelling of conical footings on sand*" Ph.D. thesis, University of Cambridge.

Tani, K., & Craig, W.H., (1995). "Bearing capacity of circular foundations on soft clay of strength increasing with depth", *Soils and Foundations.* Vol 35, No. 4, pp 21-35.

Tassoulas JL., (1984), "An investigation of the effect of rigid sidewalls on the response of embedded circular foundations to obliquely-incident SV and P waves. Dynamic Soil–Structure Interaction", *Rotterdam: A.A. Balkemal*; pP. 55–63.

Ticof, J. (1977), "*Surface footings on sand under general planar loads*", PhD thesis, University of Southampton

Todorovska, M. I. and V. W. Lee, (1991), "Surface motion of shallow circular alluvial valleys for incident plane *SH* waves-analytical solution", *Soil Dynamics and Earthquake Engineering,* Vol. 10

Trifunac, M. D., (1971) "Surface motion of a semi-cylindrical alluvial valley for incident plane *SH* waves", *Bulletin of the Seismological Society of America,* Vol.61, pp. 1755-1770

Trifunac, M. D. (1973), "A note on scattering of plane *SH* waves by a semielliptical canyon", *Int. J. Earthquake Eng. and Struct. Dynamics,* Vol 1, pp.267-281

Tsai, N. C. , (1969), “Influence of local geology on earthquake ground motion”, *Earthquake Engineering Research Laboratory,,* California Institute of Technology, Pasadena.

Tso, W. K., & Wong, C. M. (1989a). ‘‘Steady state rocking response of rigid blocks Part 1: Analysis.’’ *Earthquake Engrg. and Struct. Dyn.*, 18(1), 89–106.

Tso, W. K., & Wong, C. M. (1989b). ‘‘Steady state rocking response of rigid blocks Part 2: Experiment.’’ *Earthquake Engrg. and Struct. Dyn.*, 18(1), 107–120.

Veletsos, A.S., & Nair, V.V., (1975), “Seismic interaction of structures on hysteretic foundations”, *J. Struct. Eng ASCE,* 1975; 101(1) : 109–29.

Vidale, J. E., & D. V. Helmberger, (1988), “Elastic finite-difference modeling of the 1971 San Fernando, California, earthquake”, *Bull Seism. Soc. Am.* Vol. 78, pp. 122-141.

Vrettos, C., (1999),” Vertical and rocking impedances for rigid rectangular foundations on soils with bounded non-homogeneity”, *Earthq Eng Struct Dyn*; 28: 1525–40.

Wolf, J. P. & G. R. Darbre, (1984), “Dynamic-stiffness matrix of soil by boundary-element method: conceptual aspects”, *Earthquake Engineering and Structural Dynamics,* Vo. 12, pp. 385-400

Wolf , J. P., & P. Obernhuber, (1985), “Non-linear Soil-Structure Interaction Analysis using Green’s function of soil in time-domain”, *Earthquake Eng. and Structural Dynamics,* Vo 13. pp.212-223.

Wolf J. P. (1985), “*Dynamic Soil-Structure Interaction*”*,* Prentice-Hall, Englewood Cliffs, New Jersey.

Wolf, J.P. (1994), "*Simple physical models for foundation vibrations*", Englewood Cliffs, NJ: Prentice-Hall.

Wong, H. L. and Trifunac, M. D. (1974), "Scattering of plane *SH* waves by a semi-elliptical canyon", *International Journal of Earthquake Engineering and Structural Dynamics,* Vol. 3, pp. 157-169

Wong, H. L. &Trifunac, M. D., (1974), "Surface motion of a semielliptical alluvial valley for incident plane *SH* waves, *Bulletin of the Seismological Society of America,* 1974, 64, 1389-1408

Wong, H. S. & Jennings, P. C., (1975), "Effect of canyon topography on strong ground motion", *Bulletin of the Seismological Society of America,* Vol 65, pp. 1239-1257

Wong, H. L. (1982), "Effect of surface topography on the diffraction of P, *SV* and Rayleigh waves", *Bulletin of the Seismological Society of America,* Vol. 72, pp. 1167-1183

Wong, H.L., & Luco, J.E., (1985), "Tables of impedance functions for square foundations on layered media", *Soil Dyn Earthq Eng*; Vol. 4, pp.64–81.

Yim, C.S., Chopra, A. K., & Penzien, J., (1980). ''Rocking response of rigid blocks to earthquakes.'' *Earthquake Engineering and Structural Dynamics*, 8(6), 565–587.

Yim, S.C. and Chopra, A.K., (1985), "Simplified earthquake analysis of structures with foundation uplift", *Journal of Structural Engineering* (ASCE), 111(4): 906–930.

Zahradník, J., & Moczo, P., (1996), "Hybrid seismic modeling based on discrete-wavenumber and finite-difference methods", *Pure Appl. Geophys.,148,* 21–38.

Zatar W, Mutsuyoshi H. "Reduced Residual Displacements of Partially Prestressed Concrete Bridge Piers". Proceedings of 12WCEE, 12th World Conference on Earthquake

Zdravkovic L. & Kontoe S., (2008), "Some Issues in Modeling Boundary Conditions in Dynamic Geotechnical Analysis", *12th International Conference of the International Association for Computer Methods and Advances in Geomechanics (IACMAG),* India, (2008)

Zeng, X., & R. S., Steedman (2008), "Bearing capacity failure of shallow foundations in earthquakes", *Geotechnique*, Vol 48(2), pp. 235-256

Zhang, B., & A. S., Papageorgiou, (1996), "Simulation of the Response of the Marina District Basin, San Francisco, California, to the 1989 Loma Prieta Earthquake", *Bulletin of the Seismological Society of America*, Vol. 86(5), pp. 1382-1400.

Zhang, J., & Makris, N., (2001), "Rocking Response of free standing blocks under cycloidal pulses", *Journal of Engineering Mechanics*, p. 472-483.

Chapter 2

ABAQUS, Inc. (2008), ABAQUS user's manual, Providence, R.I.

Ahmadi, M.M., Byrne, P.M., Campanella, R.G. (2005), "Cone trip resistance in sand: modeling, verification, and applications", *Canadian Geotechnical Journal,* Vol.42, pp. 977-993.

Allotey N., El Naggar M. H. (2003), "Analytical moment–rotation curves for rigid foundations based on a Winkler model", *Soil Dynamics and Earthquake Engineering,* Vol. 23, pp. 367–381.

Allotey N.K., El Naggar M.H. (2008), "An investigation into the Winkler modeling of the cyclic response of rigid footings", *Soil Dynamics and Earthquake Engineering*, 28(1), pp. 44–57.

Anastasopoulos I., Gazetas G., Loli M., Apostolou M, Gerolymos N. (2009), "Soil Failure can be used for Earthquake Protection of Structures", *Bulletin of Earthquake Engineering*, Vol. 8, No. 1.

Armstrong P.J., Frederick C.O. (1966), "*A mathematical representation of the multiaxial bauschinger effect"*, CEGB Report No. RD/B/N 731.

Bartlett P. (1979), "*Foundation rocking on a clay soil"*, ME Thesis, University of Auckland, New Zealdand.

Bellotti R., Jamiolkowski M., Lo Presti, D., & O'Neil, D.(1996), "Anisotropy of small strain stiffness in Ticino Sand", *Géotechique,* 46(1), pp. 115-131.

Butterfield R., Gottardi G. (1994), "A complete three-dimensional failure envelope for shallow footings on sand", *Geotechnique*, 44(1), pp. 181–184.

Chatzigogos C.T., Pecker A., Salencon J. (2009), "Macroelement modeling of shallow foundations", *Soil Dynamics and Earthquake Engineering*, Vol. 29, No. 6, pp. 765–781.

Comartin C.D., Niewiaroski R.W., Freeman S., Turner F.M. (2000), "Seismic evaluation and retrofit of concrete buildings: a practical overview of the ATC-40 document"*, Earthquake Spectra*, 16(1), pp. 241–62.

Cremer C., Pecker A., Davenne L. (2001), "Cyclic macro-element for soil-structure interaction: material and geometrical non-linearities". *International Journal for Numerical and Analytical Methods in Geomechanics*, Vol. 25, pp. 1257–1284.

Cremer C., Pecker A., Davenne L. (2002), "Modelling of nonlinear dynamic behaviour of a shallow strip foundation with macro-element", *Journal of Earthquake Engineering*, Vol. 6, pp. 175-212.

Dafalias Y.F., (1986), "An anisotropic critical state soil plasticity model", *Mechanics Research Communications,* 13(6), pp. 341-347.

Dafalias Y.F., & Manzari M.T. (2004), "Simple plasticity sand model accounting for fabric change effects". *ASCE Journal of Engineering Mechanics*, 130(6), pp. 622–34.

Einav I., Puzrin A.M, Houlsby G.T. (2003), "Continuous Hyperplastic Models for Overconsolidated Clays", *Mathematical and Computer Modelling, special issue on Mathematical Models in Geomechanics*, *Proceedings of symposium at Scilla di Reggio Calabria*, 19-22 September, Vol. 37, No. 5/6, pp 515-523

Faccioli E., Paolucci R., and Vanini M. (1999), "*TRISEE: 3D Site Effects and Soil-Foundation Interaction in Earthquake and Vibration Risk Evaluation"*, European Commission Publications.

Faccioli E., Paolucci R., Vivero G. (2001), "Investigation of seismic soil–footing interaction by large scale cyclic tests and analytical models", *Proceedings, 4th International Conference on Recent Advances in Geotechnical Earthquake Engineering and Soil Dynamics*, S. Prakash (Ed.), Paper no. SPL-5, San Diego, CA.

FEMA 356 (2000), *Prestandard and Commentary for the Seismic Rehabilitation of Buildings*.

Gajan S., Phalen J.D., Kutter B.L. (2003a), "*Soil–foundation–structure interaction : shallow foundations"*. *Centrifuge Data Report for test series SSG02*, University of California, Davis, Report No. UCD/CGMDR-03/01.

Gajan S., Phalen J.D., Kutter B.L. (2003b), "*Soil–foundation–structure interaction : shallow foundations". Centrifuge Data Report for test series SSG03*, University of California, Davis, Report No.UCD/CGMDR-03/02.

Gajan S., Kutter B.L., Phalen J.D., Hutchinson T.C., Martin G.R. (2005), "Centrifuge modeling of load-deformation behavior of rocking shallow foundations", *Soil Dynamics and Earthquake Engineering,* 25, pp. 773–783.

Gajan, S. & Kutter, B. L. (2008), "Capacity, settlement, and energy dissipation of shallow footings subjected to rocking", *Journal of Geotechnical and Geoenvironmental Engineering, ASCE*, 134 (8), pp 1129-1141.

Gajo, A., & Muir Wood, D. A.,(1999), "Kinematic hardening constitutive model for sands: a multiaxial formulation", *International Journal of Numerical and Analytical Methods in Geomechanics*, Vol 23, pp. 925–65.

Gazetas G., Apostolou M., & Anastasopoulos I. (2003), "Seismic Uplifting of Foundations on Soft Soil, with Examples from Adapazari (Izmit 1999, Earthquake)", *BGA International Conference on Foundation Innovations,*

Observations, Design & Practice, Univ. of Dundee, Scotland, September 25, pp. 37–50.

Gazetas G., Anastasopoulos I., Apostolou M. (2007), "Shallow and Deep Foundations under Fault Rupture or Strong Seismic Shaking", *Earthquake Geotechnical Engineering*, Pitilakis K., Editor, Springer : Berlin, pp. 185–210.

Georgiadis M., Butterfield R. (1988), "Displacements of footings on sand under eccentric and inclined loads", *Canadian Geotechnical Journal*, 2(1), pp. 2–42.

Gerolymos N., Gazetas G., Tazoh T. (2005), "Seismic Response of Yielding Pile in Non-Linear Soil", *Proc. 1st Greece –Japan Workshop, Seismic Design, Observation, and Retrofit of Foundations*, pp. 25-36, Athens 11-12 October.

Hardin B.O., & Richart F.E. Jr. (1963), "Elastic wave velocities in granular soils", *Journal of Soil Mechanics and Foundations Division*, ASCE, Vol. 89 (SM1), pp. 33–65.

Harden C.W., Hutchinson T.C., Martin G.R., Kutter B.L. (2005), "*Numerical modeling of the nonlinear cyclic response of shallow foundations"*, Report No. PEER-2005/04, Pacific Earthquake Engineering Research Center, University of California, Berkeley.

Harden C.W, Hutchinson T.C. (2009), "Beam-on-nonlinear-winkler foundation modeling of shallow, rocking-dominated footings", *Earthquake Spectra*, 25(2), pp. 277-300.

Houlsby G.T. (1986), "A General Failure Criterion for Frictional and Cohesive Materials", *Soils and Foundations*, Vol. 26, No. 2, pp 97-101.

Houlsby G.T, Puzrin A.M. (1999), "The bearing capacity of a strip footing on clay under combined loading", *Proceedings of the Royal Society of London,* Series A, Vol. 455, pp. 893−916.

Houlsby G.T. & Puzrin A.M. (2006), "*Principles of Hyperplasticity"*, Springer : Berlin.

Ishibashi,I. & Zhang, X. (1993), "Unified dynamic shear moduli and damping ratios of sand and clay", *Soils and Foundations*, Vol. 33(1), pp. 12-191.

Jefferies M.G. (1993), "Nor-sand: A simple critical state model for sand", *Géotechnique*, Vol. 43, pp. 91–103.

Jeremic B., Runesson K., & Sture S. (1999), "A model for elastic-plastic pressure sensitive materials subjected to large deformations", *International Journal of Solids and Structures 36*, 31/32, pp 4901-4918.

Kawashima K., Nagai T., Sakellaraki D. (2007), "Rocking Seismic Isolation of Bridges Supported by Spread Foundations", Proc. of 2nd Japan-Greece Workshop on Seismic Design, Observation, and Retrofit of Foundations, April 3-4, Tokyo, Japan, pp. 254–265.

Kutter B.L. (1995), "Recent advances in centrifuge modeling of seismic shaking", Proceedings, *3rd International Conference on Recent Advances in Geotechnical Earthquake Engineering and Soil Dynamics*, St. Louis, Vol. II, pp. 927–941.

Kutter B.L, Martin G., Hutchinson T.C., Harden C., Gajan S., Phalen J.D. (2003), "*Status report on study of modeling of nonlinear cyclic load–deformation behavior of shallow foundations"*. University of California, Davis, PEER Workshop; March.

Lemaitre J., & Chaboche J.-L. (1990), "*Mechanics of Solid Materials*", Cambridge University Press.

Le Pape Y., Sieffert J.P. (2001), "Application of thermodynamics to the global modelling of shallow foundations on frictional material", *International Journal for Numerical and Analytical Methods in Geomechanics*, Vol. 25, pp. 1377-1408.

Martin, G., R., and Lam, I. P. (2000). "Earthquake Resistant Design of Foundations : Retrofit of Existing Foundations", *Proc. GeoEng 2000 Conference*, Melbourne

Makris N., Roussos Y.S (2000), "Rocking response of rigid blocks under near-source ground motions", *Géotechnique*, 50(3), pp. 243–262.

Mayne, P.W. & Rix, G.J. (1993), "G_{max} – q_c Relationships for Clays", *Geotechnical Testing Journal,* Vol. 16, N_o.1, pp. 54-60

Negro P., Paolucci R., Pedretti S., Faccioli E. (2000), "Large scale soil–structure interaction experiments on sand under cyclic load". *Proceedings of 12th world conference on earthquake engineering*, Paper no. 1191, Auckland, New Zealand.

Paolucci R. (1997), "Simplified evaluation of earthquake induced permanent displacements of shallow foundations", *Journal of Earthquake Engineering*, Vol. 1, pp. 563–579.

Paolucci R., Shirato M., Yilmaz M.T. (2008), "Seismic behaviour of shallow foundations: Shaking table experiments vs numerical modelling", *Earthquake Engineering and Structural Dynamics*, 37(4), pp. 577–595.

Pecker A. (1998), "Capacity Design Principles for Shallow Foundations in Seismic Areas", *Proc. 11th European Conference on Earthquake Engineering*, A.A. Balkema Publishing.

Pecker A. (2002), "Earthquake Resistant Design of Shallow Foundations", *Recent Advances in Earthquake Geotechnical Engineering and Microzonation*, Attila Ansal (Ed.), Springer : Netherlands.

Pecker A. (2003), "Aseismic foundation design process, lessons learned from two major projects: the Vasco de Gama and the Rion Antirion bridges", *ACI International Conference on Seismic Bridge Design and Retrofit*, La Jolla.

Pecker A. (2005), "Design and construction of the foundations of the Rion-Antirrion Bridge", Proceedings*, 1st Greece Japan Workshop on Seismic Design, Observation, and Retrofit of Foundations*, G. Gazetas & T. Tazoh (eds.), Athens, pp. 119-130.

Pecker A. & Pender M.J., (2000), "Earthquake Resistant Design of Foundations: New Construction", Invited paper, *GeoEng2000*, Vol 1, pp. 313-332.

Pender M.J. (2007), "Seismic design and performance of surface foundations", *Earthquake Geotechnical Engineering*, Pitilakis K., Editor, Springer : Berlin, pp. 217–243.

Pestana J.M. (1994), "*A unified constitutive model for clays and sands"*, Sc.D. Thesis, Department of Civil & Environmental Engineering, Massachusetts Institute of Technology, Cambridge, MA.

Pestana J.M., and Whittle A.J. (1995), "Compression model for cohessionless soils", *Géotechnique*, Vol. 45, No. 4, pp. 611-631.

Pestana J.M., and Whittle A.J. (1999), "Formulation of a unified constitutive model for clays and sands", *Int. Journal for Numerical and Analytical Methods in Geomechanics*, 23, pp. 1215-1243.

Phalen J.D. (2003), "*Physical Modeling of the Soil–foundation interaction of spread footings subjected to lateral cyclic loading"*, MS Thesis. University of California at Davis, School of Engineering.

Prandtl, L. (1921), "Uber die Eindringungsfestigkeit (Harte) plastischer Baustoffe und die Festigkeit von Schneiden", *Zeitschrift fur angewandte Mathematik und Mechanik*, Vol. **1**(1), pp. 15–20.

Prévost, J.H., (1980) "Mechanics of Continuous Porous Media", *International Journal of Engineering Science*, 18 (5), pp. 787-800.

Puzrin, A.M. & Houlsby, G.T. (2001a), "Strain-based plasticity models for soils and the BRICK model as an example of the hyperplasticity approach", *Géotechnique*, Vol. 51, No. 2, pp 169-172

Puzrin, A.M. & Houlsby, G.T. (2001b). "Fundamentals of Kinematic Hardening Hyperplasticity", *International Journal of Solids and Structures*, Vol. 38, No. 21, pp 3771-3794

Puzrin, A.M. and Houlsby, G.T. (2001c). "On the Non-Intersection Dilemma in Multi-Surface Plasticity", *Géotechnique*, Vol. 51, No. 4, pp 369-372

Robertson, P.K. & R.G. Campanella (1983a), "Interpretation of Cone Penetration Tests -Part I (Sand)", *Canadian Geotechnical Journal*, Vol. 20, N_o. 4, pp. 718-733.

Robertson, P.K. and R.G. Campanella (1983b), "Interpretation of Cone Penetration Tests -Part II (Clay)", *Canadian Geotechnical Journal*, Vol. 20, N_o. 4,pp. 734-745.

Rosebrook K.R, Kutter B.L.(2001a), "*Soil–foundation–structure interaction : shallow foundations", Centrifuge Data Report for test series KRR01*, University of California, Davis, Report No. UCD/CGMDR-01/09.

Rosebrook K.R, Kutter B.L. (2001b), "*Soil–foundation–structure interaction : shallow foundations", Centrifuge Data Report for test series KRR03*, University of California, Davis, Report No. UCD/CGMDR-01/11.

Rosebrook K.R, Kutter BL. (2001c), "*Soil–foundation–structure interaction : shallow foundations", Centrifuge Data Report for test series KRR02*, University of California, Davis, Report No. UCD/CGMDR-01/10.

Seed, H.B., R. T. Wong, I. M. Idriss, & K. Tokimatsu (1986), "Moduli and damping factors for dynamic analyses of cohesionless soils", *J. Soil Mech. Foundations Division*, ASCE, SM11(112), pp. 1016-1032.

Taylor P.W., Bartlett P.E., and Wiessing P.R. (1981), "Foundation rocking under earthquake loading", *Proceedings of 10th international conference on soil mechanics and foundation engineering*, AA Balkema, Stockholm, Sweden, Rotterdam, Netherlands, Vol. 3, pp. 313–322.

Vucetic M., Dobry R. (1991), "Effect of soil plasticity on cyclic response", *Journal of Geotechnical Engineering*, ASCE, Vol. 117, No. 1, pp. 89–107.

Ziegler H. (1959), "A Modification of Prager's Hardening Rule", *Quart. Appl. Math*., Vol. 17, pp. 55-65.

Chapter 3

ABAQUS, Inc. (2009), ABAQUS user's manual, Providence, R.I.

Allotey, N., El Naggar, M. H. (2003), "Analytical moment–rotation curves for rigid foundations based on a Winkler model", *Soil Dynamics and Earthquake Engineering,* 23, pp. 367–381.

Anastasopoulos I., Gazetas G., Loli M., Apostolou M, Gerolymos N. (2010a), "Soil Failure can be used for Earthquake Protection of Structures", *Bulletin of Earthquake Engineering*, Vol. 8, p.p. 309-326.

Anastasopoulos I. Gelagoti F., Kourkoulis R., Gazetas G. (2010b) "Simplified Constitutive Model for Simulation of Cyclic Response of Shallow Foundations : Validation against Laboratory Tests" *Journal of Geotechnical and Geoenvironmetal Engineering*, ASCE *(accepted for publication, currently under revision).*

Bransby M.F. (2001), "Failure envelopes and plastic potentials for eccentrically loaded surface footings on undrained soil", *International Journal for Numerical and Analytical Methods in Geomechanics*, 25, pp. 329-346.

Chatzigogos C.T., Pecker A., Salencon J. (2009), "Macroelement modeling of shallow foundations", *Soil Dynamics and Earthquake Engineering*, Vol. 29, No. 6, pp. 765–781.

Faccioli E, Paolucci R, Vivero G. (2001), "Investigation of seismic soil– footing interaction by large scale cyclic tests and analytical models", *Proc. 4th*

international conference on recent advances in geotechnical earthquake engrng and soil dynamics, Paper no. SPL-5, San Diego, California.

Fukushima, Y., Irikura, K., Uetake, T., and Matsumoto H. (2000), "Characteristics of observed peak amplitude for strong ground motion from the 1995 Hyogoken Nanbu (Kobe) earthquake", *Bulletin of the Seismological Society of America*, Vol. 90, pp. 545–565.

Gajan, S. & Kutter, B. L. (2008), "Capacity, settlement, and energy dissipation of shallow footings subjected to rocking", *Journal of Geotechnical and Geoenvironmental Engineering, ASCE*, Vol. 134 (8), pp 1129-1141

Gajan, S., Kutter, B.L., Phalen, J. D.,Hutchinson, T. C., Martin, G.R.(2005), "Centrifuge modeling of load-deformation behavior of rocking shallow foundations", *Soil Dynamics and Earthquake Engineering,* 25, pp. 773–783

Gazetas, G., Apostolou, M., & Anastasopoulos, I. (2003), "Seismic Uplifting of Foundations on Soft Soil, with Examples from Adapazari (Izmit 1999, Earthquake)", *BGA Int. Conf. on Found. Innov., Observations, Design & Practice*, Univ. of Dundee, Scotland, September 25, pp. 37–50.

Gourvenec S. (2007), "Shape effects on the capacity of rectangular footings under general loading", *Géotechnique*, 57(8), pp. 637–646.

Houlsby G.T., & Puzrin A.M. (1999), "The bearing capacity of a strip footing on clay under combined loading", *Proceedings of the Royal Society of London*, A 455, pp. 893–916.

Kawashima K., Nagai T., Sakellaraki D. (2007), "Rocking Seismic Isolation of Bridges Supported by Spread Foundations", *Proc. Of 2nd Japan-Greece Workshop on*

Seismic Design, Observation, and Retrofit of Foundations, April 3-4, Tokyo, Japan, pp. 254–265.

Kutter B.L, Martin G., Hutchinson T.C., Harden C., Gajan S., Phalen J.D. (2003), Status report on study of modeling of nonlinear cyclic load–deformation behavior of shallow foundations. University of California, Davis, PEER Workshop; March.

Paolucci, R., Shirato, M., and Yilmaz, M. T. (2007), Seismic behavior of shallow foundations: Shaking table experiments vs numerical modeling, *Earthquake Eng. Struct. Dyn.*, 37(4), pp. 577–595.

Pecker, A., & Pender, M.J., (2000), "Earthquake Resistant Design of Foundations: New Construction", Invited paper, *GeoEng2000*, Vol 1, pp. 313-332.

Priestley, M.J.N. (2000), "Performance based seismic design", *Proc. 12th World Conference on Earthquake Engineering* (12WCEE), Auckland, New Zealand, Paper No. 2831.

Priestley, M.J.N., Calvi G.M., Kowalsky M.J. (2007) "Displacement-Based Seismic Design of Structures" IUSS Press, ISBN 88-6198-000-6

Priestley, M.J.N., Seible, F. and Calvi, G.M. (1996), "*Seismic Design and Retrofit of Bridges"*, John Wiley and Sons, New York.

Taiebat H.A., and Carter J.P. (2002), "Bearing capacity of strip and circular foundations on undrained clay subjected to eccentric loads", *Géotechnique*, 52(1), pp. 61–64.

Trifunac M.D. (1972), "Tectonic stress and the source mechanism of the Imperial Valley, California, earthquake of 1940"*, Bulletin of the Seismological Society of America*, 62(5), pp. 1283-1302.

Ukritchon B., Whittle A.J., and Sloan S.W. (1998), “Undrained limit analyses for combined loading of strip footings on clay”, *Journal of Geotechnical and Geoenvironmental Engineering*, ASCE, 124, pp. 265–276.

Vintzilaiou E., Tassios T.P., Chronopoulos M. (2007) “Experimental validation of seismic code provisions for RC columns’, *Engineering Structures,* 29, p.p., 1153-1164

Chapter 4

ABAQUS, Inc. (2009), ABAQUS user's manual, Providence, R.I.

Allotey, N., El Naggar, M. H. (2003), "Analytical moment–rotation curves for rigid foundations based on a Winkler model", *Soil Dynamics and Earthquake Engineering,* 23, pp. 367–381.

Anastasopoulos I., Gazetas G., Loli M., Apostolou M, Gerolymos N. (2010a), Soil Failure can be used for Earthquake Protection of Structures, *Bulletin of Earthquake Engineering*, 8, pp. 309–326.

Anastasopoulos I., Gelagoti F., Kourkoulis R., Gazetas G. (2010b), "Simplified Constitutive Model for Simulation of Cyclic Response of Shallow Foundations: Validation against Laboratory Tests", *Journal of Geotechnical and Geoenvironmetal Engineering*, ASCE (*accepted for publication).*

Apostolou M., Gazetas G., Garini E. (2007), "Seismic response of slender rigid structures with foundation uplifting", *Soil Dynamics and Earthquake Engineering*, 27 (7), pp. 642–654.

Chatzigogos C.T., Pecker A., Salencon J. (2009), "Macroelement modeling of shallow foundations", *Soil Dynamics and Earthquake Engineering*, Vol. 29, No. 6, pp. 765–781.

Faccioli E, Paolucci R, Vivero G. (2001), "Investigation of seismic soil– footing interaction by large scale cyclic tests and analytical models". *Proc. 4th*

International Conference on Recent Advances in Geotechnical Earthquake Engineering and Soil Dynamics, Paper no. SPL-5, San Diego, California.

FEMA 356 (2000), *Prestandard and Commentary for the Seismic Rehabilitation of Buildings*.

Gajan S., Kutter B.L. (2008), "Capacity, settlement, and energy dissipation of shallow footings subjected to rocking", *Journal of Geotechnical and Geoenvironmental Engineering,* ASCE, 134 (8), pp 1129-1141.

Gajan S., Kutter B.L., Phalen J.D., Hutchinson T.C., Martin G.R. (2005), "Centrifuge modeling of load-deformation behavior of rocking shallow foundations", *Soil Dynamics and Earthquake Engineering,* 25, pp. 773–783

Gajan S., Kutter B.L., Phalen J.D., Hutchinson T.C., Martin G.R. (2005), "Centrifuge modeling of load-deformation behavior of rocking shallow foundations", *Soil Dynamics and Earthquake Engineering,* 25, pp. 773–783.

Gazetas, G., Apostolou, M., & Anastasopoulos, I. (2003), "Seismic Uplifting of Foundations on Soft Soil, with Examples from Adapazari (Izmit 1999, Earthquake)", *BGA Int. Conf. on Found. Innov., Observations, Design & Practice*, Univ. of Dundee, Scotland, September 25, pp. 37–50.

Gerolymos N., Gazetas G., Tazoh T. (2005a), "Seismic Response of Yielding Pile in Non-Linear Soil", *Proc. 1st Greece–Japan Workshop, Seismic Design, Observation, and Retrofit of Foundations*, Athens 11-12 October, pp. 25-36.

Gerolymos N., Apostolou M., Gazetas G. (2005b), "Neural network analysis of overturning response under near-fault type excitation", *Earthquake Engineering and Engineering Vibration*, 4 (2), pp. 213-228.

Harden, C., Hutchinson, T. (2006), "Investigation into the Effects of Foundation Uplift on Simplified Seismic Design Procedures", *Earthquake Spectra*, 22 (3), pp. 663–692.

Housner G.W. (1963), "The behavior of inverted pendulum structures during earthquakes"m *Bulletin of the Seismological Society of America*, 53 (2), pp. 404–417.

Ishiyama Y. (1980), *"Review and discussion on overturning of bodies by earthquake motions"*, Building Research Institute, Research paper 85, Ministry of Construction, Japan.

Kawashima K., Nagai T., Sakellaraki D. (2007), "Rocking Seismic Isolation of Bridges Supported by Spread Foundations", *Proc. of 2nd Japan-Greece Workshop on Seismic Design, Observation, and Retrofit of Foundations*, April 3-4, Tokyo, Japan, pp. 254–265.

Koh A.S., Spanos P., Roesset J.M. (1986), "Harmonic rocking of rigid block on flexible foundation", *Journal of Engineering Mechanics*, ASCE, 112 (11), pp. 1165–1180.

Kutter B.L, Martin G., Hutchinson T.C., Harden C., Gajan S., Phalen J.D. (2003), "*Status report on study of modeling of nonlinear cyclic load–deformation behavior of shallow foundations"*, University of California, Davis, PEER Workshop ; March.

Makris N., Konstantinidis D. (2003), "The rocking spectrum and the limitations of practical design methodologies", *Earthquake Engineering & Structural Dynamics*, 32 (2), pp. 265–289.

Makris, N., Roussos, Y. (2000), "Rocking response of rigid blocks under near source ground motions", *Géotechnique*, 50 (3), pp. 243–262.

Martin, G., R., & Lam, I. P. (2000). "Earthquake Resistant Design of Foundations : Retrofit of Existing Foundations", *Proc. GeoEng 2000 Conference*, Melbourne.

Mergos, P.E., & Kawashima, K. (2005), "Rocking isolation of a typical bridge pier on spread foundation", *Journal of Earthquake Engineering*, 9(2), 395–414.

Paolucci R., Shirato M., Yilmaz M.T. (2008), "Seismic behaviour of shallow foundations: Shaking table experiments vs numerical modelling", *Earthquake Engineering and Structural Dynamics*, Vol. 37, pp. 577–595.

Pecker, A. (1998), "Capacity Design Principles for Shallow Foundations in Seismic Areas", *Proc. 11th European Conference on Earthquake Engineering*, A.A. Balkema Publishing.

Pecker, A., & Pender, M.J., (2000), "Earthquake Resistant Design of Foundations : New Construction", Invited paper, *GeoEng2000*, Vol 1, pp. 313-332.

Pecker, A. (2003), "Aseismic foundation design process, lessons learned from two major projects: the Vasco de Gama and the Rion Antirion bridges", *ACI International Conference on Seismic Bridge Design and Retrofit*, University of California at San Diego, La Jolla, USA.

Priestley M.J.N., Evison R.J., Carr A.J. (1978), "Seismic response of structures free to rock on their foundations", *Bulletin of the New Zealand National Society for Earthquake Engineering*, 11(3), pp. 141–150.

Priestley M.J.N. (2000), "Performance based seismic design", *Proc. 12th World Conference on Earthquake Engineering* (12WCEE), Auckland, New Zealand, Paper No. 2831.

Priestley M.J.N., Calvi G.M., Kowalsky M.J. (2007), "*Displacement-Based Seismic Design of Structures"*, IUSS Press, ISBN 88-6198-000-6.

Priestley M.J.N., Seible F., & Calvi G.M. (1996), "*Seismic Design and Retrofit of Bridges"*, John Wiley and Sons, New York.

Psycharis I., Jennings P. (1983), "Rocking of slender rigid bodies allowed to uplift", *Earthquake Engineering and Structural Dynamics*, 11, pp. 57–76.

Vintzilaiou E., Tassios T.P., Chronopoulos M. (2007) "Experimental validation of seismic code provisions for RC columns", *Engineering Structures*, 29, pp. 1153-1164.

Zhang J., Makris N. (2001), "Rocking response of free-standing blocks under cycloidal pulses", *Journal of Engineering Mechanics*, ASCE, 127 (5), pp. 473–483.

Chapter 5

ABAQUS, Inc. (2008), *ABAQUS user's manual*, Providence, R.I.

Aki K. (1988), "Local site effects on strong ground motion", in J. L. Von Thun (ed.), *Earthquake Engineering and Soil Dynamics II-Recent advances in ground motion evaluation*, Geotechnical Special Publication No. 20, ASCE: New York, pp. 103-155.

Anastasopoulos I., Gazetas G., Loli M., Apostolou M, Gerolymos N. (2010), "Soil Failure can be used for Earthquake Protection of Structures", *Bulletin of Earthquake Engineering*, Vol. 8, No. 2,pp. 309-326.

Bao H., Bielak J., Ghattas O., Kallivokas L.F., O' Hallaron D.R., Shewchuk J., & Xu J. (1996), "Earthquake ground motion modeling on parallel computers, *Proceedings of ACM/IEEE Supercomputing Conference"*, Pittsburgh, USA.

Bard P.Y. & Bouchon M.A. (1980), The seismic response of sediment filled valleys. Parts 1. The Case of incident SH waves, *Bulletin of the Seismological Society of America*, Vol.70, No. 5, pp. 1263-1286.

Bard P.Y. & Bouchon M.A. (1980), "The seismic response of sediment filled valleys. Parts 2. The Case of incident P and SV waves", *Bulletin of the Seismological Society of America*, Vol.70, No. 5, pp. 1921-1941.

Benetatos C., Kiratzi A., Roumelioti Z., Stavrakakis G., Drakatos G., Latoussakis I. (2005), "The 14 August 2003 Lefkada Island (Greece) earthquake: Focal

mechanisms of the mainshock and of the aftershock sequence", *Journal of Seismology*, Vol. 9, No. 2, pp. 171–190.

Bielak J., Xu J. & Ghattas O. (1999), "Earthquake Ground motion and Structural Response in alluvial Valleys". *Journal of Geotechnical and Geoenviromental Engineering,* Vol. 125, No. 5, pp. 413-423.

Bielak J., Hisada Y., Bao H., Xu J & Ghattas O. (2000). "One - vs two - or three-dimensional effects in sedimentary valleys". *Proceedings of the 12th World Conference on Earthquake Engineering*, New Zealand.

Chavez-Garcia F. J., Rodriguez M., & Stephenson W. R. (1998). "1D vs 2D site effects. The case of Parkway basin, New Zealand", *11th European Conference on Eartquake Engineering, Balkema, Rotterdam.*

Chavez-Garcia F., Raptakis D., Makra K., & Pitilakis K. (2000). "Site effects at EURO-SEISTEST – II: Results from 2-D numerical modelling and comparison with observations", *Soil Dynamics & Earthquake Engineering*, Vol. 19, No. 1, pp. 23-39.

Elnashai A.S. (2000), "Analysis of the damage potential of the Kocaeli (Turkey) earthquake of 17 August 1999", *Engineering Structures*, Vol. 22, pp. 746–754.

Fardis, N., Georgarakos, P., Gazetas, G., & Anastasopoulos, I. (2003), "Sliding Isolation of Structures: Effect of Horizontal and Vertical Acceleration", *Proceedings of the FIB International Symposium on "Concrete Structures in Seismic Regions"*, Athens, Greece (in CD-Rom).

Field E. H. (1996), 'Spectral Amplification in a Sediment-Filled Valley exhibiting clear basin-induced waves". *Bulletin of the Seismological Society of America*, Vol. 86, pp. 991-1005.

Fishman K. L. & Ahmad S. (1995). "Seismic response for alluvial valleys subjected to SH, P and SV waves". *Soil Dynamics and Earthquake Engineering*, Vol. 14, pp. 249-258.

Gazetas G., Fan K., Tazoh T., & Shimizu K. (1993). "Seismic response of the pile foundation of Ohba Ohashi bridge". *Proceedings of the 3rd International Conference on Case Histories in Geotechnical Engineering*, pp. 1803-1809.

Gazetas G., Kallou P.V., & Psarropoulos P.N. (2002), "Topography and Soil Effects in the M_S 5.9 Parnitha (Athens) Earthquake: The Case of Adámes", *Natural Hazards,* Vol. 27, pp. 133–169.

Gazetas G., Anastasopoulos I., & Dakoulas P. (2005), "Failure of harbor quaywall in the Lefkada 2003 earthquake", *Proceedings of Geotechnical Earthquake Engineering Satellite Conference – Performance Based Design in Earthquake Geotechnical Engineering : Concepts and Research*, Osaka, pp. 62-69.

Garini E., Gazetas G., & Anastasopoulos I. (2010), "Accumulated Asymmetric Slip Caused by Motions Containing Severe 'Directivity' and 'Fling' Pulses", *Géotechnique*,Vol. 30, No10.

Gerolymos, N., Gazetas, G., & Tazoh, T., (2005), "Seismic Response of Yielding Pile in Non-Linear Soil", *Proc. 1st Greece –Japan Workshop, Seismic Design, Observation, and Retrofit of Foundations*, pp. 25-36, Athens 11-12 October.

Harmsen, S. C., & S. T. Harding (1981). "Surface motion over a sendimentary valley for incident plane P and SV waves", *Bulletin of the Seismological Society of America*, Vol. 72, pp. 655-670.

Hudson M., Idriss I.M., & Beikae M. (1994), *QUAD4M—A computer program to evaluate the seismic response of soil structures using finite element procedures and incorporating a compliant base*, Center for Geotechnical Modeling, Dept. of Civil and Environmental Engineering, Univ. of Calif., Davis.

Ishibashi I. & Zhang X. (1993), "Unified dynamic shear moduli and damping ratios of sand and clay", *Soils and Foundations*, Vol. 33, No. 1, pp. 182-191.

Makra K., Raptakis D., Pitilakis K., Chavez-Garcia F. J., & Pitilakis K. (2001), "Site Effects and Design Provisions", *Pure and Applied Geophysics*, Vol. 158, pp. 2349–2367.

Makra K., Chavez-Garcia F. J., Raptakis D., & Pitilakis K. (2005), "Parametric analysis of the seismic response of a 2D sedimentary valley : implications for code implementations of complex site effects", *Soil Dynamics and Earthquake Engineering*, Vol. 25, pp. 303–315.

Ohtsuki, A. & Harumi, K. (1983). "Effect of topography and subsurface inhomogeneities on seismic SV waves". *Journal of Earthquake Engineering & Structural Dynamics,* Vol. 11, pp. 441-462.

Ohtsuki A., Yamahara H., & Tazoh T. (1984), "Effect of lateral inhomogeneity on seismic waves, II. Observations and analyses", *Earthquake Engineering and Structural Dynamics*, Vol. 12, pp. 795-816.

Papadopoulos G.A., Drakatos G., Papanastasiou D., Kalogeras I., & Stavrakakis G. (2000), "Preliminary results about the catastrophic earthquake of 7-9-99 in Athens, Greece", *Seismological Research Letters*, Vol. 71, pp. 318–329.

Papageorgiou A.S. & Kim J. (1991), "Study of the propagation and amplification of seismic waves in Caracas Valley with reference to the 29 July 1967 earthquake: SH waves", *Bulletin of the Seismological Society of America*, Vol. 81(6), pp. 2214-2233.

Pitilakis K. (2004), "Site Effects. *Recent Advances in Geotechnical Engineering and Microzonation"*, A. Ansal (ed.), Kluver Academic Publ., Ch. 5, pp. 139-197.

Psarropoulos P.N., Tazoh T., Gazetas G., & Apostolou M. (2007), "Linear and Nonlinear Valley Amplification Effects on Seismic Ground Motion", *Soils and Foundations*, Vol. 47, No. 5, pp. 857-871.

Raptakis D., Chavez-Garcia F.J., Makra K., & Pitilakis K. (2000). "Site effects at Euroseistest—I. Determination of the valley structure and confrontation of observations with 1D analysis", *Soil Dynamics and Earthquake Engineering*, Vol. 19, pp. 1-22.

Raptakis D., Makra K., Anastasiadis A., Pitilakis K. (2004a) "Complex site effects in Thessaloniki (Greece) – I: Soil structure and confrontation of observations with 1D analysis", *Bulletin of Earthquake Engineering*, Vol. 2, No. 3, pp. 271-290.

Raptakis D., Makra K., Anastasiadis A., Pitilakis K. (2004b), "Complex site effects in Thessaloniki (Greece) – II: 2D SH modeling and engineering insights", *Bulletin of Earthquake Engineering*, Vol.2, No. 3, pp. 301-327.

Ricker N. (1960). "The form and laws of propagation of seismic wavelets". *Geophysics,* Vol.18, pp. 40.

Sanchez-Sesma, F. J., Chavez-Garcia F., & Bravo M.A. (1988), "Seismic response of a class of alluvial valley for incident SH waves", *Bulletin of the Seismological Society of America,* Vol.78, No.1, pp. 83-95.

Sánchez-Sesma F.J., Pérez-Rocha L.E., & Chávez-Pérez S. (1989), "Diffraction of elastic waves by three-dimensional surface irregularities. Part II", *Bulletin of the Seismological Society of America*, Vol. 79, No. 1, pp. 101-112.

Sánchez-Sesma F.J. & Luzón F. (1995), "Seismic response of three-dimensional alluvial valleys for incident P, S, and Rayleigh waves", *Bulletin of the Seismological Society of America*, Vol. 85, No. 1, pp. 269-284.

Tazoh T., Dewa K., Shimizu K., & Shimada M. (1984), "Observations of earthquake response behavior of foundation piles for road bridge", *Proceedings of the 8th World Conference on Earthquake Engineering*, Vol. 3, pp. 577-584.

Tazoh T., Shimizu K. & Wakahara (1988), "Seismic observations and analysis of grouped piles", *Shimizu Technical Research Bulletin,* Vol. 7, pp. 17-32.

Todorovska M.I. & Lee V.W. (1991), "Surface motion of shallow circular alluvial valleys for incident plane SH waves-analytical solution", *Soil Dynamics and Earthquake Engineering*, Vol. 10, No. 4, pp. 192-200.

Trifunac M.D. (1971), "Surface motion of a semi-cylindrical alluvial valley for incident plane SH waves"*, Bulletin of the Seismological Society of America,* Vol.61, pp.1755-1770.

Vucetic M. & Dobry R. (1991), 'Effect of soil plasticity on cyclic response", *Journal of Geotechnical Engineering*, ASCE, Vol. 117(1), pp. 89-107.

Wong H.L. & Trifunac M.D. (1974), "Surface motion of a semi-elliptical alluvial valley for incident plane SH waves", *Bulletin of the Seismological Society of America*, Vol. 64, No. 5, pp. 1389-1408.

Zhang B. & Papageorgiou A. (1996), "Simulation of the Response of the Marina District Basin, San Francisco, California, to the 1989 Loma Prieta Earthquake", *Bulletin of the Seismological Society of America,* Vol. 86, No. 5, pp. 1382-1400.

Chapter 6

Ελληνικός Αντισεισμικός Κανονισμός ΕΑΚ (2000), ΥΠΕΧΩΔΕ, Αθήνα, Ελλάδα

Ελληνικός Κανονισμός Ωπλισμένου Σκυροδέματος (2000), ΥΠΕΧΩΔΕ, Αθήνα, Ελλάδα

ABAQUS, Inc. (2008), ABAQUS user's manual, Providence, R.I.

Anastasopoulos I., Gelagoti F., Kourkoulis R., Gazetas G. (2010) "Simplified Constitutive Model for Simulation of Cyclic Response of Shallow Foundations: Validation against Laboratory Tests" *Journal of Geotechnical and Geoenvironmetal Engineering*, ASCE *(accepted for publication).*

Bard P.Y. & Bouchon M.A. (1980), 'The seismic response of sediment filled valleys. Parts 1. The Case of incident SH waves", *Bulletin of the Seismological Society of America*, Vol.70, No. 5, pp. 1263-1286.

Chávez-García, F. J., Stephenson, W. R., & M.Rodríguez, (1999), "Lateral Propagation Effects Observed at Parkway, New Zealand. A Case History to Compare 1D versus 2D Site Effects", *Bulletin of the Seismological Society of America*, 89, 3, pp. 718-732

Ciliz, S., Özkan, M. Y., & K. Ö Çetin, (2007), "Effect of basin edge slope on the dynamic response of soil deposits", *4th International Conference on Earthquake Engineering and Geotechnical Engineering* (in CD-ROM).

Cornou, C., Bard, P.-Y., and Dietrich M., (2003), "Contribution of Dense Array Analysis to the Identification and Quantification of Basin-Edge-Induced Waves, Part II: Application to Grenoble Basin (French Alps)", *Bulletin of the Seismological Society of America*, Vol. 93(6), pp. 2624–2648

Fan K., "*Seismic Behavior of Pile Groups*", (1992), PhD Thesis, SUNY at Buffalo.

Gelagoti F., Kourkoulis R., Anastasopoulos I. Gazetas G. (2010), "Seismic Wave Propagation in a Very Soft Alluvial Valley : Sensitivity to Ground Motion Details and Soil Nonlinearity, Generation of Parasitic Vertical Component" *Bulletin of the SSA*, (in print)

Gelagoti F., Kourkoulis R., Anastasopoulos I. Gazetas G. (2010), "Rocking Isolation of Frame Structures Founded on Separate Footings" *Earthquake Engineering and Structural Dynamics* (submitted for possible publication)

Gerolymos, N., Gazetas, G., & Tazoh, T., (2005), "Seismic Response of Yielding Pile in Non-Linear Soil", *Proc. 1st Greece –Japan Workshop, Seismic Design, Observation, and Retrofit of Foundations*, pp. 25-36, Athens 11-12 October.

Harmsen, S. C., & S. T. Harding (1981). "Surface motion over a sendimentary valley for incident plane P and SV waves", *Bulletin of the Seismological Society of America*, Vol. 72, pp. 655-670.

Ishibashi I. & Zhang X. (1993), "Unified dynamic shear moduli and damping ratios of sand and clay", *Soils and Foundations*, Vol. 33, No. 1, pp. 182-191.

Kamiyama, M., & K, Fukuchi, (2007), "Nonlinear response analyses of irregular grounds by use of pseudo spectral method", *4th International Conference on Earthquake Engineering and Geotechnical Engineering* (in CD-ROM).

Kamiyama M. & Matsukawa T., (2002), "A new method for estimating nonlinear response of ground," *Proceedings of the 12th European Conference on Earthquake*, pp. 1-10

King, J. L., & Tucker B. E., (1984), "Observed variations of earthquake motion across a sediment-filled valley", *Bulletin of the Seismological Society of America*, Vol. 74, No. 1, pp. 137-151

Kutter B.L, Martin G., Hutchinson T.C., Harden C., Gajan S., Phalen J.D. (2003), "*Status report on study of modeling of nonlinear cyclic load–deformation behavior of shallow foundations"*. University of California, Davis, PEER Workshop; March.

Olsen, K. B., R. J. Archuleta, & J. R. Matarese, (1995), "Three-dimensional simulation of a magnitude 7.75 earthquake on the San Andreas fault", *Science* 270, pp. 1628-1632.

Olsen K. B., Nigbor, R. and T. Konno (2000), "3D Viscoelastic Wave Propagation in the Upper Borrego Valley, California, Constrained by Borehole and Surface Data", Bulletin of the Seismological Society of America, Vol. 90 (1), pp. 134–150.

Papageorgiou A.S. & Kim J. (1991), "Study of the propagation and amplification of seismic waves in Caracas Valley with reference to the 29 July 1967 earthquake: SH waves", *Bulletin of the Seismological Society of America*, Vol. 81(6), pp. 2214-2233.

Pecker A. & Pender M.J., (2000), "Earthquake Resistant Design of Foundations: New Construction", Invited paper, *GeoEng2000*, Vol 1, pp. 313-332.

Psarropoulos P.N., Tazoh T., Gazetas G., & Apostolou M. (2007), "Linear and Nonlinear Valley Amplification Effects on Seismic Ground Motion", *Soils and Foundations*, Vol. 47, No. 5, pp. 857-871.

Puglia R., Lanzo, G., Pagliaroli, A., Sica, S., & Silvestri F., (2007), "Ground Motion amplification in San Giuliano di Puglia (Southern Italy) during the 2002 Molise earthquake", 4th International Conference on Earthquake Engineering and Geotechnical Engineering (in CD-ROM).

Scrivner, C. W, & D. V., Helmberger, (1999), "Finite-Difference Modeling of Two Aftershocks of the 1994 Northridge, California, Earthquake", *Bulletin of the Seismological Society of America*, 89, 6, pp. 1505-1518.

Tazoh T., Shimizu K. & Wakahara (1988), "Seismic observations and analysis of grouped piles", *Shimizu Technical Research Bulletin,* Vol. 7, pp. 17-32.

Vintzilaiou E., Tassios T.P., Chronopoulos M. (2007) "Experimental validation of seismic code provisions for RC columns", *Engineering Structures* 29, p.p., 1153-1164

Zhang, B., and A. S.,Papageorgiou, (1996), "Simulation of the Response of the Marina District Basin, San Francisco, California, to the 1989 Loma Prieta Earthquake", *Bulletin of the Seismological Society of America*, Vol. 86(5), pp. 1382-1400.